

Moving boundary problems in multi-physics coupling processes

Edited by

Leilei Chen, Pei Li and Elena Atroshchenko

Published in

Frontiers in Physics



FRONTIERS EBOOK COPYRIGHT STATEMENT

The copyright in the text of individual articles in this ebook is the property of their respective authors or their respective institutions or funders. The copyright in graphics and images within each article may be subject to copyright of other parties. In both cases this is subject to a license granted to Frontiers.

The compilation of articles constituting this ebook is the property of Frontiers.

Each article within this ebook, and the ebook itself, are published under the most recent version of the Creative Commons CC-BY licence. The version current at the date of publication of this ebook is CC-BY 4.0. If the CC-BY licence is updated, the licence granted by Frontiers is automatically updated to the new version.

When exercising any right under the CC-BY licence, Frontiers must be attributed as the original publisher of the article or ebook, as applicable.

Authors have the responsibility of ensuring that any graphics or other materials which are the property of others may be included in the CC-BY licence, but this should be checked before relying on the CC-BY licence to reproduce those materials. Any copyright notices relating to those materials must be complied with.

Copyright and source acknowledgement notices may not be removed and must be displayed in any copy, derivative work or partial copy which includes the elements in question.

All copyright, and all rights therein, are protected by national and international copyright laws. The above represents a summary only. For further information please read Frontiers' Conditions for Website Use and Copyright Statement, and the applicable CC-BY licence.

ISSN 1664-8714
ISBN 978-2-8325-3000-9
DOI 10.3389/978-2-8325-3000-9

About Frontiers

Frontiers is more than just an open access publisher of scholarly articles: it is a pioneering approach to the world of academia, radically improving the way scholarly research is managed. The grand vision of Frontiers is a world where all people have an equal opportunity to seek, share and generate knowledge. Frontiers provides immediate and permanent online open access to all its publications, but this alone is not enough to realize our grand goals.

Frontiers journal series

The Frontiers journal series is a multi-tier and interdisciplinary set of open-access, online journals, promising a paradigm shift from the current review, selection and dissemination processes in academic publishing. All Frontiers journals are driven by researchers for researchers; therefore, they constitute a service to the scholarly community. At the same time, the *Frontiers journal series* operates on a revolutionary invention, the tiered publishing system, initially addressing specific communities of scholars, and gradually climbing up to broader public understanding, thus serving the interests of the lay society, too.

Dedication to quality

Each Frontiers article is a landmark of the highest quality, thanks to genuinely collaborative interactions between authors and review editors, who include some of the world's best academicians. Research must be certified by peers before entering a stream of knowledge that may eventually reach the public - and shape society; therefore, Frontiers only applies the most rigorous and unbiased reviews. Frontiers revolutionizes research publishing by freely delivering the most outstanding research, evaluated with no bias from both the academic and social point of view. By applying the most advanced information technologies, Frontiers is catapulting scholarly publishing into a new generation.

What are Frontiers Research Topics?

Frontiers Research Topics are very popular trademarks of the *Frontiers journals series*: they are collections of at least ten articles, all centered on a particular subject. With their unique mix of varied contributions from Original Research to Review Articles, Frontiers Research Topics unify the most influential researchers, the latest key findings and historical advances in a hot research area.

Find out more on how to host your own Frontiers Research Topic or contribute to one as an author by contacting the Frontiers editorial office: frontiersin.org/about/contact

Moving boundary problems in multi-physics coupling processes

Topic editors

Leilei Chen — Huanghuai University, China

Pei Li — Xi'an Jiaotong University, China

Elena Atroshchenko — University of New South Wales, Australia

Citation

Chen, L., Li, P., Atroshchenko, E., eds. (2023). *Moving boundary problems in multi-physics coupling processes*. Lausanne: Frontiers Media SA.

doi: 10.3389/978-2-8325-3000-9

Table of contents

05	Editorial: Moving boundary problems in multi-physics coupling processes Pei Li, Leilei Chen and Elena Atroshchenko
07	Mechanical and cracking behavior of porous rock models containing random circular defects under uniaxial compression Wenqiang Ma, Can Cui and Xiaoxiao Li
23	Sensitivity analysis of structural-acoustic fully-coupled system using isogeometric boundary element method Xiuyun Chen, Yanming Xu, Juan Zhao, Ruhui Cheng and Wenqiang Ma
35	Sensitivity analysis of flexoelectric materials surrogate model based on the isogeometric finite element method Haozhi Li, Juan Zhao, Xiaokun Guo, Yu Cheng, Yanmin Xu and Xiaohui Yuan
45	Design of constrained-layer damping on plates to sound radiation based on isogeometric analysis and non-negative intensity Xinyan Zhang and Yanming Xu
61	Comparative study of surface integral methods in aeroacoustic prediction Chen Xu, Shihao Wang, Dangguo Yang, Rongping Zhang, Shujie Jiang and Yijun Mao
70	Effect of offset distances for rod-airfoil interaction noise Shujie Jiang, Lanqing Li, Xiaokun Guo, Weiming Zhao, Rongping Zhang and Chao Wang
79	Research and application of Rayleigh wave extraction method based on microtremors signal analysis Qingling Du, Yanhui Pan and Youyang Xin
94	Refining large knowledge bases using co-occurring information in associated KBs Yan Wu and Zili Zhang
109	Experimental study of the parameter effects on the flow and noise characteristics for a contra-rotating axial fan Yanjie Zhao, Chen Xu, Zhiwei Zheng, Xiaowen Hu and Yijun Mao
122	Physics informed neural networks for phase field fracture modeling enhanced by length-scale decoupling degradation functions Haojie Lian, Peiyun Zhao, Mengxi Zhang, Peng Wang and Yongsong Li
136	Optimized cabinet parameters for drying lithium-ion batteries based on coupled fluid–thermal field analysis Xuan Peng, Zhaohui Wang, Gang Shen and Yong Yang

- 148 **Numerical simulation study on pore clogging of pervious concrete pavement based on different aggregate gradation**
Qidan Xiao, Yapei Xia, Guanguan Zhang, Xiaoli Lin and Jun Zhao
- 163 **Accelerating fracture simulation with phase field methods based on Drucker-Prager criterion**
Bin Liu, Zhenghe Liu and Lusheng Yang
- 176 **Isogeometric multi-patch topology optimization based on pix2pix**
Qingyuan Hu, Xin Meng and Yangxiu You
- 185 **The method of moments for electromagnetic scattering analysis accelerated by the polynomial chaos expansion in infinite domains**
Xiaohui Yuan, Yujing Ma, Yajun Huang, Ruijin Huo and Zhongwang Wang



OPEN ACCESS

EDITED AND REVIEWED BY
José S. Andrade Jr.,
Federal University of Ceara, Brazil

*CORRESPONDENCE
Pei Li,
✉ mepeili@xjtu.edu.cn

RECEIVED 09 May 2023
ACCEPTED 26 June 2023
PUBLISHED 30 June 2023

CITATION
Li P, Chen L and Atroshchenko E (2023),
Editorial: Moving boundary problems in
multi-physics coupling processes.
Front. Phys. 11:1219806.
doi: 10.3389/fphy.2023.1219806

COPYRIGHT
© 2023 Li, Chen and Atroshchenko. This
is an open-access article distributed
under the terms of the [Creative
Commons Attribution License \(CC BY\)](#).
The use, distribution or reproduction in
other forums is permitted, provided the
original author(s) and the copyright
owner(s) are credited and that the original
publication in this journal is cited, in
accordance with accepted academic
practice. No use, distribution or
reproduction is permitted which does not
comply with these terms.

Editorial: Moving boundary problems in multi-physics coupling processes

Pei Li^{1*}, Leilei Chen^{2,3} and Elena Atroshchenko⁴

¹International Machinery Center, School of Mechanical Engineering, Xi'an Jiaotong University, Xi'an, China, ²College of Intelligent Construction, Wuchang University of Technology, Wuhan, China, ³School of Architectural Engineering, Huanghuai University, Zhumadian, China, ⁴School of Civil and Environmental Engineering, University of New South Wales, Sydney, NSW, Australia

KEYWORDS

editorial, moving boundary problem, multi-physics and coupled problems, fracture, topology optimisation

Editorial on the Research Topic

Moving boundary problems in multi-physics coupling processes

In many problems such as propagation of crack, fluid-structure interaction, flow in deformable porous materials, material forming process and so on, the boundary of material/structure or the interface between different materials/structures varies depending on the *in-situ* responses of associating components and environmental factors. Such problems are also named as moving boundary problems, and the time-dependent boundary poses significant challenges to the numerical modelling of such problems as well as the study of inherent mechanisms dominating the evolution of moving boundaries. Severe nonlinearity caused by the moving boundary requires development of advanced numerical algorithms, while interaction of multi-physics behaviors in moving boundary problems such as mechanical, thermal, electrical and even chemical response, necessitates research of multi-physical modelling methodologies.

This Research Topic “*Moving Boundary Problems in Multi-physics Coupling Processes*” collects 16 papers contributing to the experimental, numerical and theoretical research on moving boundary problems of multi-physics processes. While focusing on “*Moving Boundary Problems in Multi-physics Coupling Processes*,” the selected papers show a good diversity in terms of their research objects, methods and findings. Some contributors have obtained valuable achievements on modelling of cracks. For instance, [Ma et al.](#) used discrete element method to establish a numerical model of porous concrete with random circular defects inside, to study the influence of the porosity or size homogeneity of the defects on the mechanical behavior, crack evolution, and acoustic emission (AE) responses. Their findings can aim the understanding of micro-scale mechanism of crack propagation in porous concrete. To accelerate the numerical simulations of fracture, [Liu et al.](#) employed degradation function that decouples the phase-field and physical length scales, to reduce the mesh density in large structures. By incorporating the Drucker-Prager failure surface into the phase field model to characterize the tension-compression asymmetry of fractures in rocks, they can capture the crack propagation path in rock materials with a good accuracy and efficiency. Instead of using conventional numerical methods, [Lian et al.](#) proposed a novel framework for efficient simulation of crack propagation in brittle materials, whereby the partial differential

equations of the phase field models are solved with physics informed neural networks (PINN) by minimizing the variational energy, enabling accurate and efficient modelling of fracture behavior of brittle materials.

Another important aspect of this Research Topic is directed to the multi-physics problems. [Xiao et al.](#) conducted experimental tests and fluid-structure coupling simulations of pavement-clogging of pervious concretes, and found that the pervious pavement with smaller coarse aggregate is easier to be clogged, and the discontinuous graded coarse aggregate has a good shielding effect on the clogging material. [Yuan et al.](#) focused on electromagnetic problems, and proposed an efficient method of moments (MoM) based on polynomial chaos expansion (PCE) to efficiently calculate the electromagnetic scattering problems. [Li et al.](#) established a Polynomial Chaos Expansion (PCE) surrogate model for flexoelectric materials, and developed a sensitivity analysis method for the surrogate model. Apart from these contributions, some other authors paid efforts on the acoustic-structural coupling problems. For instance, [Jiang et al.](#) studied the interaction between the wake of rods and airfoils by solving the Reynolds average N-S equation and non-linear acoustic equations. [Zhao et al.](#) experimentally investigated the influences of the fan parameters including axial distance, blade number, blade pattern and blade thickness on the performance and noise characteristics under variable rotational speed regulation. [Chen et al.](#) conducted numerical simulation and sensitivity analysis of structural-acoustic fully-coupled systems via combination of FEM and BEM. [Xu et al.](#) employed various surface integral methods to numerically calculate the sound generated from a flow passing through a circular cylinder, and analyzed the pros and cons of each aeroacoustic prediction method.

Optimization and design of moving boundary problems also attracted much attention of researchers. [Zhang et al.](#) introduced an approach to optimizing the patterns of vibrating structures contributing to radiated sound power, and found that the corner radiation properties of the plate can be suppressed by the optimization, minimizing the integration of non-negative intensity. [Peng et al.](#) studied the effect of the geometrical parameters of periodically opening and closing drying cabinets on their drying efficiency, and obtained an optimized configuration. [Hu et al.](#) proposed a new approach for topology optimization of complex structures by combining the pix2pix, an image-to-image translation framework, and the isogeometric multi-

patch analysis. By using a simple centroid design method, [Xiao et al.](#) developed an optimization procedure that can design the mixture of pervious concrete, and obtained some specimens exhibiting obvious improvement of strength. The research work of [Du et al.](#) and [Wu et al.](#) further broaden the scope of this Research Topic, in terms of studying the Rayleigh wave extraction method based on microtremors signal analysis, and refining large knowledge bases using co-occurring information in associated KBs.

The success of this Research Topic owes to all the contributors including the reviewers, authors, editorial office and many colleagues. Reviewers are sincerely acknowledged for their careful and rigorous reviews on the submitted manuscripts, which are the most important step in selecting appropriate work for publication. Many thanks are also given to the authors of submitted manuscripts, which are the key component of this Research Topic. The editors handling this Research Topic also significantly appreciate the help from the editorial office of Frontiers in Physics, and are grateful to friends and others who have offered their help in dissemination of this Research Topic.

Author contributions

PL: Drafting and Revision LC: Revision EA: Revision. All authors contributed to the article and approved the submitted version.

Conflict of interest

The authors declare that the research was conducted in the absence of any commercial or financial relationships that could be construed as a potential conflict of interest.

Publisher's note

All claims expressed in this article are solely those of the authors and do not necessarily represent those of their affiliated organizations, or those of the publisher, the editors and the reviewers. Any product that may be evaluated in this article, or claim that may be made by its manufacturer, is not guaranteed or endorsed by the publisher.



OPEN ACCESS

EDITED BY

Leilei Chen,
Huanghuai University, China

REVIEWED BY

Haojie Lian,
Taiyuan University of Technology, China
Xiao Wang,
Southeast University, China

*CORRESPONDENCE

Wenqiang Ma,
mwq@xyynu.edu.cn

SPECIALTY SECTION

This article was submitted to Statistical and Computational Physics, a section of the journal Frontiers in Physics

RECEIVED 11 October 2022

ACCEPTED 02 November 2022

PUBLISHED 17 November 2022

CITATION

Ma W, Cui C and Li X (2022), Mechanical and cracking behavior of porous rock models containing random circular defects under uniaxial compression. *Front. Phys.* 10:1066555. doi: 10.3389/fphy.2022.1066555

COPYRIGHT

© 2022 Ma, Cui and Li. This is an open-access article distributed under the terms of the [Creative Commons Attribution License \(CC BY\)](#). The use, distribution or reproduction in other forums is permitted, provided the original author(s) and the copyright owner(s) are credited and that the original publication in this journal is cited, in accordance with accepted academic practice. No use, distribution or reproduction is permitted which does not comply with these terms.

Mechanical and cracking behavior of porous rock models containing random circular defects under uniaxial compression

Wenqiang Ma^{1*}, Can Cui¹ and Xiaoxiao Li²

¹College of Architecture and Civil Engineering, Xinyang Normal University, Xinyang, China, ²School of Geographical Sciences, Xinyang Normal University, Xinyang, China

Circular defects are widely distributed in porous rock materials, and the defects greatly affect the mechanical behavior and crack evolution of rock masses. In this paper, numerical models containing random circular defects are constructed based on discrete element method. Then, the uniaxial compressions are numerically performed to reveal the influence of the porosity or size homogeneity of the defects on the mechanical behavior, crack evolution, and acoustic emission (AE) events of the models. The results suggest that a univariant increase in porosity leads to a nonlinear decrease in the peak strength and a linear decrease in the elastic modulus. The number of cracks and AE events decrease with increasing porosity. As the size homogeneity coefficient increases, the peak strengths show a slight linear rise, while the elastic modulus values show a minimal linear downward trend, and the number of cracks and AE events show wave-like increases. The cracks first appear at the location with dense defects, and the cracks initiate from the top and bottom of the circular holes. The crack propagation and intersection modes between two adjacent defects are affected by their positions. These findings provide a reference for the fracture mechanism of rock with random circular defects.

KEYWORDS

porous rock, random circular defects, mechanical behavior, crack evolution, AE event

1 Introduction

Rock is a type of heterogeneous material that contains various kinds of flaws and defects (i.e., cracks, fissures, joints, bedding planes, pores, and holes). All these flaws and defects dramatically influence the mechanical responses, deformation behavior, and failure process of the rock material. Numerous experimental and numerical studies have been performed to investigate the influencing law of the flaw size, shape, distribution, and various flaw combinations on the failure behaviors and cracking development of rock or rock-like materials. Linear flaws, such as cracks [1–3], fissures [4, 5], joints [6–8], and

bedding planes [9], have been extensively studied by many researchers [10–13]. Nevertheless, the research literature on the influence of pore-like flaws (i.e., circular holes, openings, and pores) on rock failure behavior is relatively limited. Among these studies, rock or rock-like specimens containing a single circular hole or opening were the most common research objects in the laboratory and numerical studies [14–22], as depicted in Figure 1. The variations of the circular hole's position and size both affect the strength, acoustic emission (AE) characteristics, and fracture propagation of these specimens. Additionally, some rock or rock-like specimens containing double and three circular or rectangular openings have also been viewed as research targets, as depicted in Figure 2, and have been constantly analyzed and discussed by some researchers [15, 16, 23]. Moreover, some combination forms of flaws (i.e., one circular opening and one linear crack [24–26], one circular opening and some regularly arranged linear cracks [27, 28]) are also prefabricated into rock or rock-like specimens to examine their influences on the rock failure process (see Figure 3).

However, most circular pores or openings in rock are randomly distributed, and their sizes are not uniform. Recently, increasing attention has been given by scholars to the influence of randomly distributed pores on rock strength, microcracking behavior and failure patterns [29–36], as shown in Figure 4. The related research results indicate that the distribution, size, position, and number of random pores all have influence on the mechanical and failure behavior of rock or rock-like materials. As the random pores have different sizes, how to define the size homogeneity and evaluate the influence of the homogeneity index on rock mechanical behavior, microcracking process, and failure pattern have been key issues worthy of research and discussion.

Therefore, in this paper, the Weibull distribution function was introduced to define the size homogeneity index of random circular defects in porous rock material. As it is extremely difficult to obtain experimental rock or rock-like specimens containing random circular defects with various sizes in laboratory, numerical simulation praised by many researchers,

Authors and publication year	Research objects containing a single circular hole or opening											
Huang et al. 2018												
Li et al. 2017												
Li et al. 2019												
Lotidis et al. 2019												
Wong and Peng, 2019												
Zhao et al., 2019												
Zhu et al., 2019												

FIGURE 1
Rock or rock-like specimens containing a single circular hole or opening.

Authors and publication year	Research objects containing double or three circular defects						
Janeiro and Einstein, 2010							
Zhao et al., 2014							
Zhou et al., 2017							

FIGURE 2

Rock or rock-like specimens containing double and three circular or rectangular openings.

has been an effective method to implement corresponding studies on rock failure. In this paper, the particle flow code in two dimensions (PFC2D) was used to build numerical models containing random circular defects with various sizes and porosities based on self-compiled FISH programs. Then, a suite of simulations was performed to investigate the influence of defect size homogeneity and porosities on the mechanical behaviors and crack initiation (CI), propagation, and intersection characteristics of porous rock models.

2 Construction of numerical models containing random circular defects

PFC2D is capable of representing grain-scale microstructural features directly by considering the grains in an actual rock as an assembly of discrete particles [37, 38]. This code can capture and reflect crack initiation, propagation, and intersection in rock specimens better than earlier models constructed in the continuous medium software, and it can be computed rapidly and efficiently [2, 39]. Therefore, it is used in this paper to conduct correlational numerical research.

Relevant literature has shown that the Weibull distribution can better reflect the heterogeneity of the mechanical properties of rocks and rock-like materials [40, 41]. The heterogeneity of mechanical properties can be regarded as the influencing effect of flaws with different sizes. Therefore, in this paper, it is assumed

that the sizes of the circular defects in the model obey the Weibull distribution, and then the related programs could be compiled through FISH language in PFC software to construct models containing random circular defects with heterogeneous sizes.

2.1 Weibull distribution and its application

From the perspective of statistics and probability theory, the Weibull distribution is a continuous probability distribution, and its probability density function is shown in Eq. 1.

$$f(u) = \frac{m}{u_0} \left(\frac{u}{u_0} \right)^{m-1} \exp \left[- \left(\frac{u}{u_0} \right)^m \right] \quad (1)$$

where u is the value of the parameter (radius of the circular defect) satisfying the distribution, u_0 is the average value of characteristic parameters, and m is the shape parameter of the Weibull distribution, i.e., the homogeneity coefficient.

Equation 1 reflects the distribution law of the sizes of random circular defects varying with the homogeneity coefficient m . When m is small, the size distribution of random circular defects is discrete, and the heterogeneity degree is high; when m is large, the size distribution of random circular defects is relatively concentrated, indicating that the circular defects are more uniform in size. The Weibull distribution probability density curve of circular defect sizes under various homogeneity coefficients is shown in Figure 5.

Authors and publication year	Research objects containing combination of one circular and some linear defects
Yin et al., 2018	
Yin et al., 2018	
Liu et al., 2016	
Wang and Tian, 2018	
Yang et al., 2019	
Li et al., 2020	

FIGURE 3

Rock or rock-like specimens containing combination of one circular and some linear defects.

After integrating the probability density function of the Weibull distribution, the random variable obeying a uniform distribution can be transformed into a variable that obeys the Weibull distribution through the transformation relationship between the uniform distribution and the Weibull distribution. After transformation, if the random variable R obeys the uniform distribution of $[0-1]$, then Y will obey the Weibull distribution (see Eq. 2). According to Eq. 2, a self-compiled program was obtained using the built-in FISH language of PFC software. This program can effectively realize the generation of random circular defects with various sizes in the model.

$$Y = u_0 (-\ln R)^{\frac{1}{m}} \quad (2)$$

2.2 Model construction process

The construction process of the whole model requires several steps. In addition to the FISH program in Section 2.1, several

other self-compiled programs are also necessary to build the model. The detailed modeling steps are as follows. First, the model dimension is determined, and the four surrounding walls are built. Second, a FISH program is compiled to generate a group of random circular particles. The center positions of these particles obey a uniform distribution, and the radii of these particles follow the Weibull distribution. The area ratio of random particles to the whole model can be controlled by the FISH program to obtain different model porosities. Third, the coordinates, radii, and ID numbers of these random particles were exported to a text document from the model. Fourth, the random particles generated in step 2 were deleted, and much smaller particles were filled into the whole model area. Fifth, the basic information of the random particles stored in step 3 was imported into the model and used to build circular walls. Sixth, the small particles in these circular walls were deleted, and these circular walls were subsequently deleted. Then, the models containing random circular defects were created successfully. A simple modeling process is depicted in Figure 6.

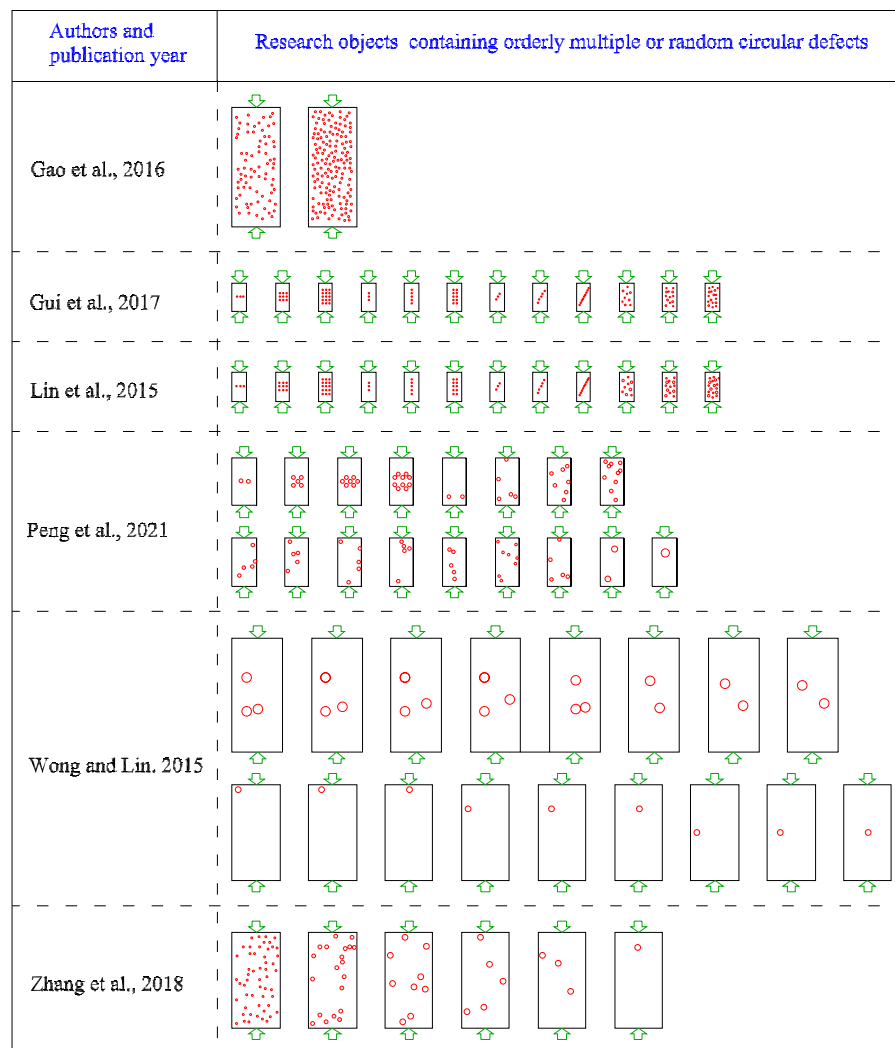


FIGURE 4
Rock or rock-like specimens containing orderly multiple defects or random defects.

As shown in Figure 6, the numerical model is 50 mm in width and 100 mm in height. The particles are bonded together through many contacts. The particle radii exhibit a uniform distribution between the minimum and maximum radii (see Table 1). The flat joint model (FJM) is chosen as the contact bond model of intact rock to simulate the mechanical behavior between micrograins because it is capable of overcoming the defects, i.e., the lower ratio of compression to tension strength, smaller internal frictional angle and the linear strength envelope, of the parallel bonded model (PBM).

2.3 Mesoparameter calibration

The calibrated mesoparameters of the numerical models are summarized in Table 1. This set of mesoparameters has been verified to be capable of reproducing the strength and

deformation behavior, as well as the associated crack propagation of rock specimens under various loading conditions [42]. Uniaxial compression simulations of the numerical models containing random circular defects were conducted based on this set of mesoparameters. The influence of the porosity and size homogeneity of random circular defects on rock mechanical characteristics and the associated crack evolution were then analyzed and discussed.

2.4 Numerical simulation scheme

To study the influence of the porosity and the size homogeneity of random circular defects on the mechanical characteristics and microcracking behavior of the rock models, two types of models were constructed based on the

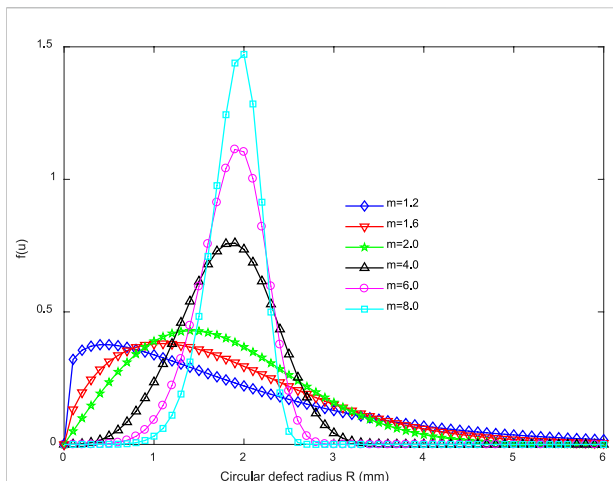


FIGURE 5
Weibull distribution probability density of random circular defects with various size homogeneity coefficients.

method of Section 2.1, as depicted in Figure 7 and Figure 8. The average radius (u_0 in Eq. 2) for these models is 2 mm. The two different types of the models both have six groups, and each group has three models. To save space, only one model in each group is listed here. The size homogeneity coefficient of the random circular defects in the first type of model remains an unchanged value of 1.9, but the porosity of the models between groups varies from 5% to 30% in increments of 5% (see Figure 7). The models in the second type have a constant porosity value of 10%, but the size homogeneity coefficients of the defects in the models between groups are designed as a changing list of 1.2, 1.6, 2.0, 4.0, 6.0, and 8.0 (see Figure 8).

3 Simulation results

In this section, the influence of the porosity and the size homogeneity of random circular defects on the simulation results,

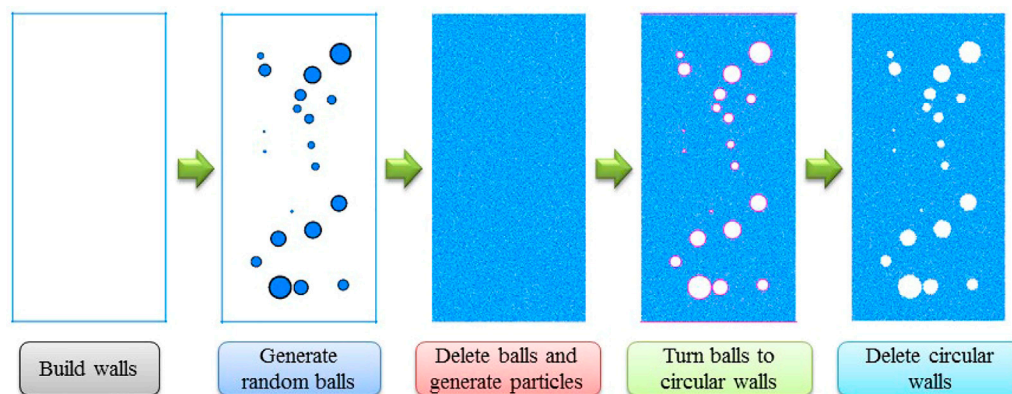


FIGURE 6
Construction process of the models containing random circular defects.

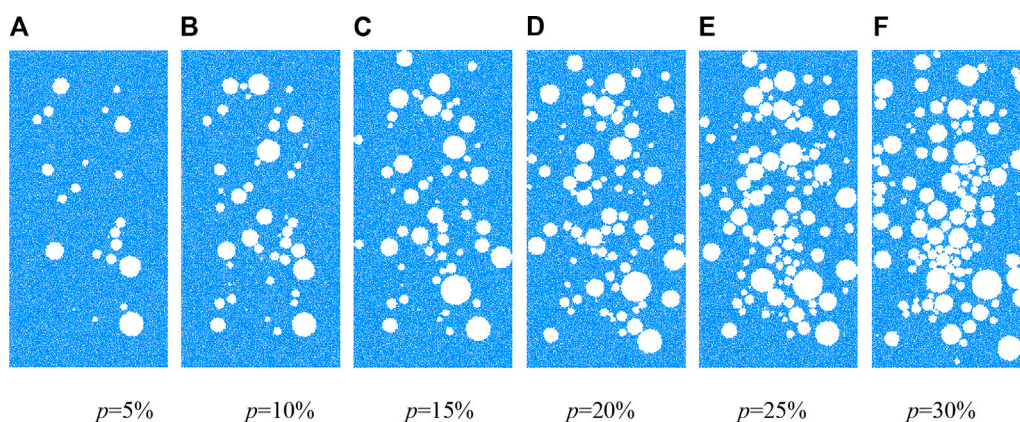


FIGURE 7
Numerical models containing random circular defects under different porosities (Group 3#, $m = 1.9$). (A) $p = 5\%$ (B) $p = 10\%$ (C) $p = 15\%$ (D) $p = 20\%$ (E) $p = 25\%$ (F) $p = 30\%$.

TABLE 1 Summary of the calibrated mesoparameters of the flat-joint model.

Mesoparameters	Values
Particle minimum/maximum radius, r_{\min}/r_{\max} (mm)	0.2/0.3
Particle density, ρ (kg/m ³)	2200
Installation gap ratio, g_{ratio}	0.30
Contact elements, N	4
Effective modulus of both particle and bond, E_c (GPa)	5
Ratio of normal to shear stiffness of both particle and bond, k_{n1}/k_{s1}	1.63
Flat-joint cohesion, c_1 (MPa)	7.2
Flat-joint tensile strength, σ_{c1} (MPa)	6.0
Flat-joint friction angle, φ_1 (°)	35
Flat-joint friction coefficient, μ_1	0.577

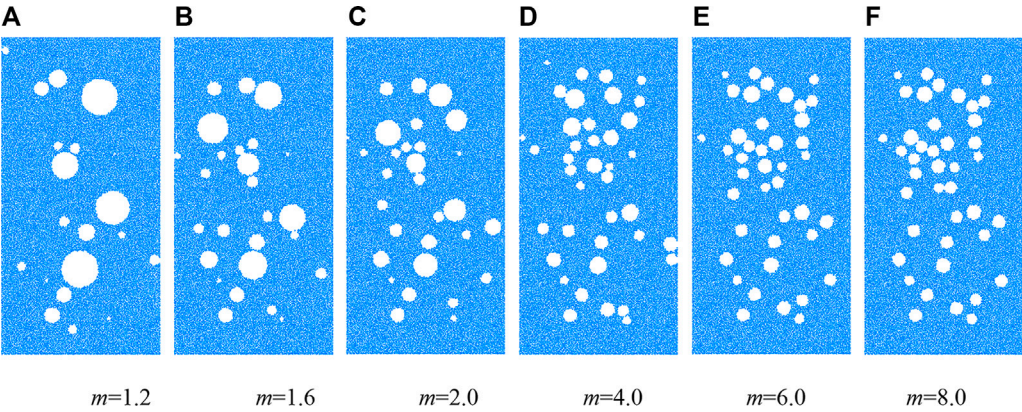


FIGURE 8 Numerical models containing random circular defects with various size homogeneity coefficients (Group 2#, $p = 10\%$). (A) $m = 1.2$ (B) $m = 1.6$ (C) $m = 2.0$ (D) $m = 4.0$ (E) $m = 6.0$ (F) $m = 8.0$.

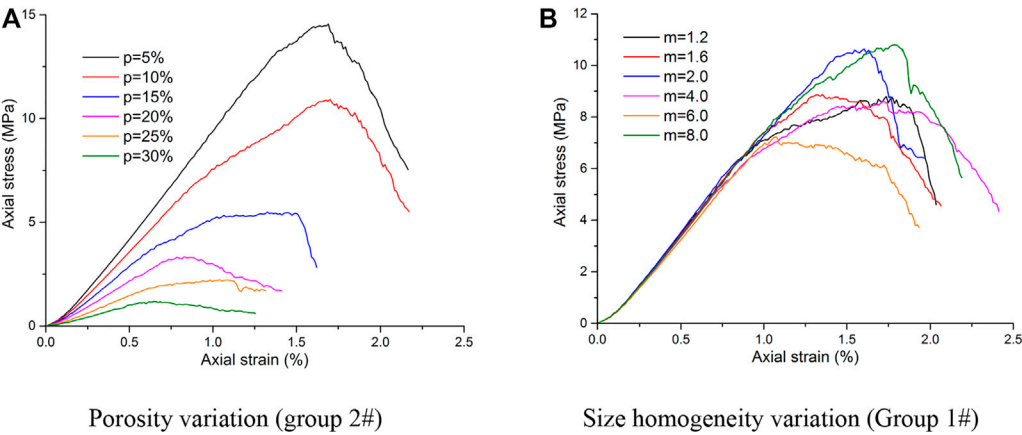
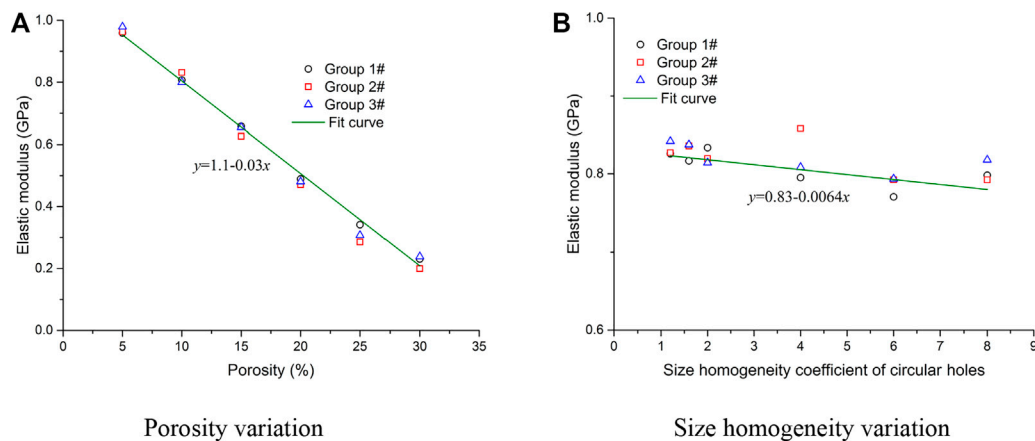
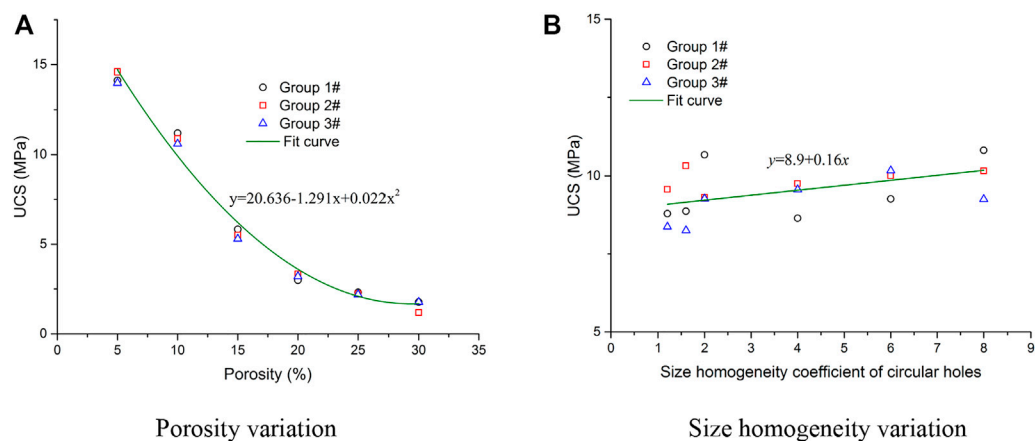


FIGURE 9 Stress-strain curves of the models containing random circular defects. (A) Porosity variation (group 2#) (B) Size homogeneity variation (Group 1#).

**FIGURE 10**

Fitting results of the elastic modulus values of the models containing random circular defects. (A) Porosity variation (B) Size homogeneity variation.

**FIGURE 11**

Fitting results of the peak strengths of the models containing random circular defects. (A) Porosity variation (B) Size homogeneity variation.

including deformation and strength behavior, crack evolution, and AE event characteristics, are examined and discussed.

3.1 Deformation and strength behaviors

The stress-strain curves of the numerical models containing random circular defects are shown in Figure 9. As the porosity of the random circular defects increases, the post-peak parts of the stress-strain curves change from a steep drop to a gentle one, implying that the models have undergone a deformation transformation from brittle to ductile. The slope of the linear part of the stress-strain curve also decreases with increasing porosity, indicating that the elastic

modulus values of these models show a linear decline (see Figure 10A). As shown in Figure 11A, the peak strengths of the models containing circular defects show a nonlinear decline with increasing porosity. These simulation results are in good accordance with the findings simulated in previous studies [30, 33, 34, 36].

However, it is another changing characteristic for the models containing circular defects with various size homogeneity coefficients. As the size homogeneity coefficient increases (see Figure 9B), the elastic parts of the stress-strain curves coincide with each other, and the fitting results of the elastic modulus show a minimal linear downward trend (see Figure 10B). While the stress-strain curves show obvious fluctuations after entering the yield stage, the fitting results of the peak strengths show a

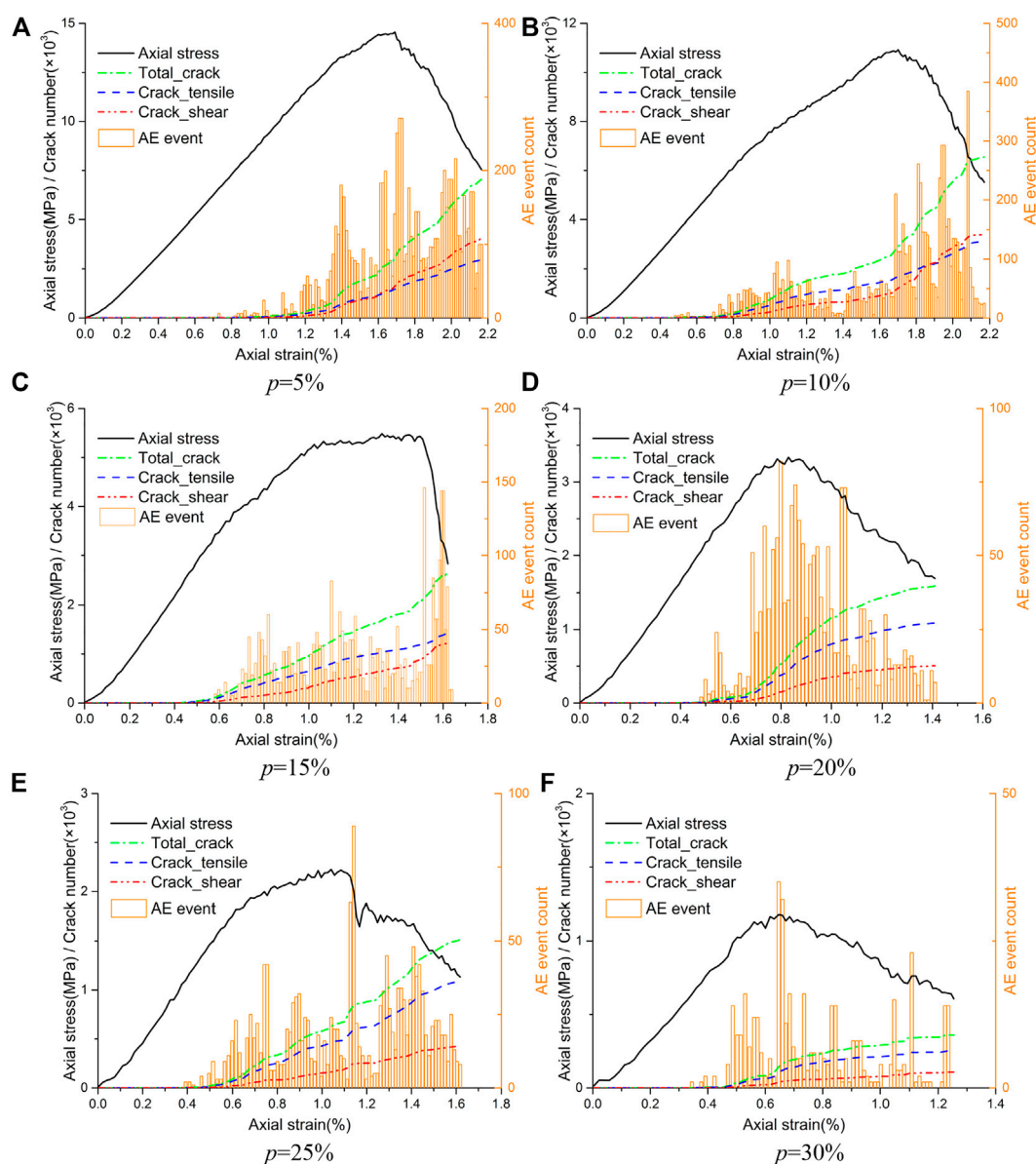


FIGURE 12

Crack development and AE event count of the models with increasing defect porosity. (A) $p = 5\%$ (B) $p = 10\%$. (C) $p = 15\%$ (D) $p = 20\%$. (E) $p = 25\%$ (F) $p = 30\%$.

slight linear rise with increasing size homogeneity coefficient of the circular defects (see Figure 11B).

3.2 Crack evolution and AE event characteristics

The failure of rock materials is a progressive process of damage accumulation. This process is often accompanied by crack initiation, propagation, and intersection. The generation of a group of cracks that are close in time and space can send out a

series of acoustic signals that can be considered an acoustic emission (AE) event. The failure process of rock is always accompanied by many AE events of different intensity levels. The type, location, and quantity of cracks can be tracked and recorded with time in PFC by compiling FISH programs. In this paper, cracks occurring within a certain strain increment range are regarded as an AE event, and the total crack number at this strain interval is regarded as the AE event intensity level. To obtain the crack evolution law and AE event count during the entire compressive process, several self-compiled FISH programs were embedded into the PFC2D software to record the

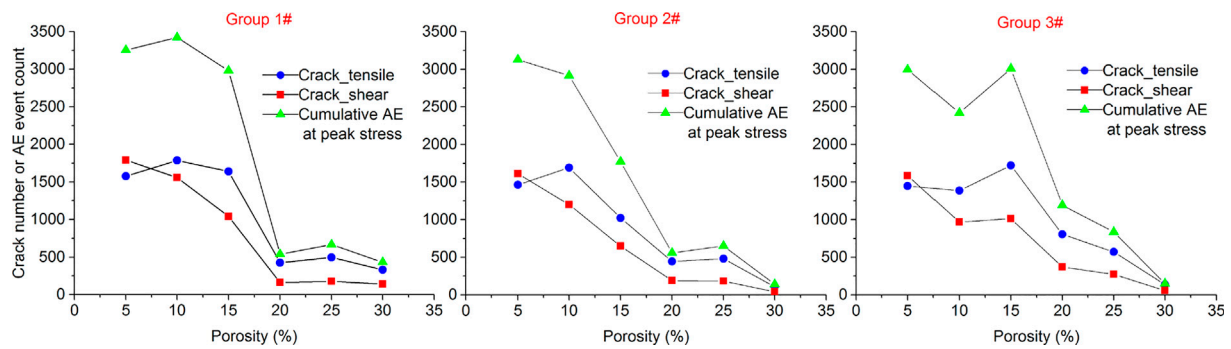


FIGURE 13

Crack number and AE event count of the models at peak stress with increasing defect porosity.

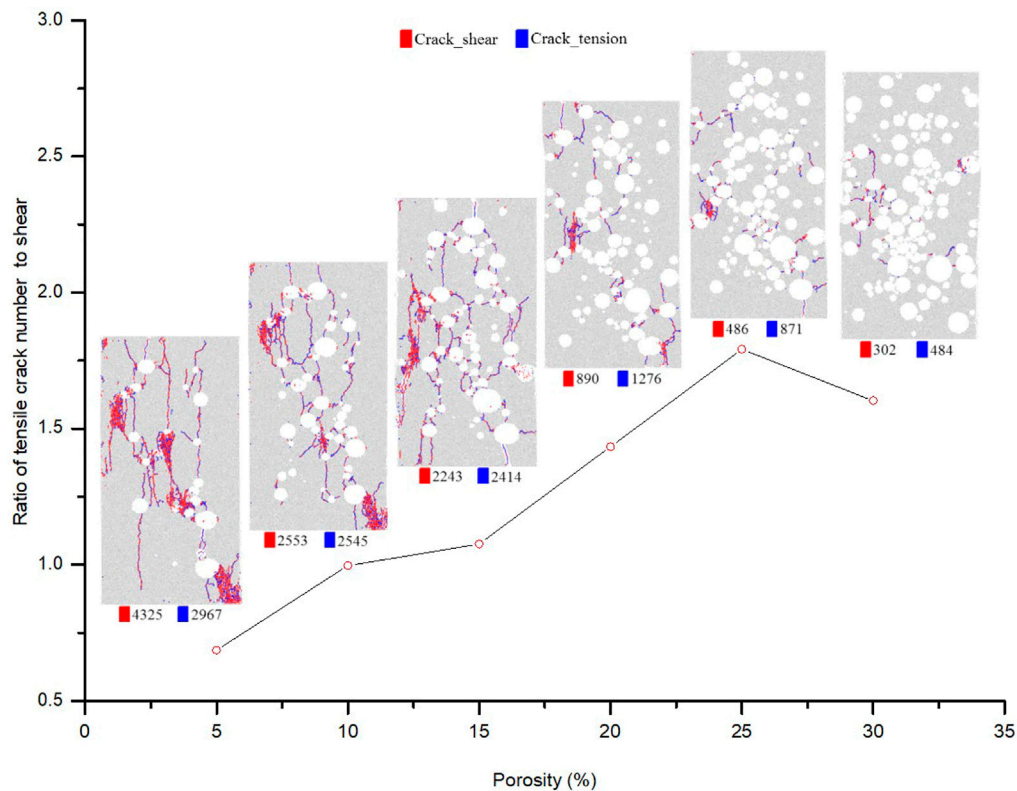


FIGURE 14

Crack distribution of the failure models with increasing defect porosity.

cumulative counts of the shear cracks, tension cracks, and AE events in the model.

- 1) Models containing random circular defects with increasing porosity

The variation curves of the crack amount and the AE intensity histograms of the numerical models containing random circular defects with increasing porosity are shown in Figure 12. The crack amount and the AE intensity both decrease with increasing porosity, but the cumulative AE events before the

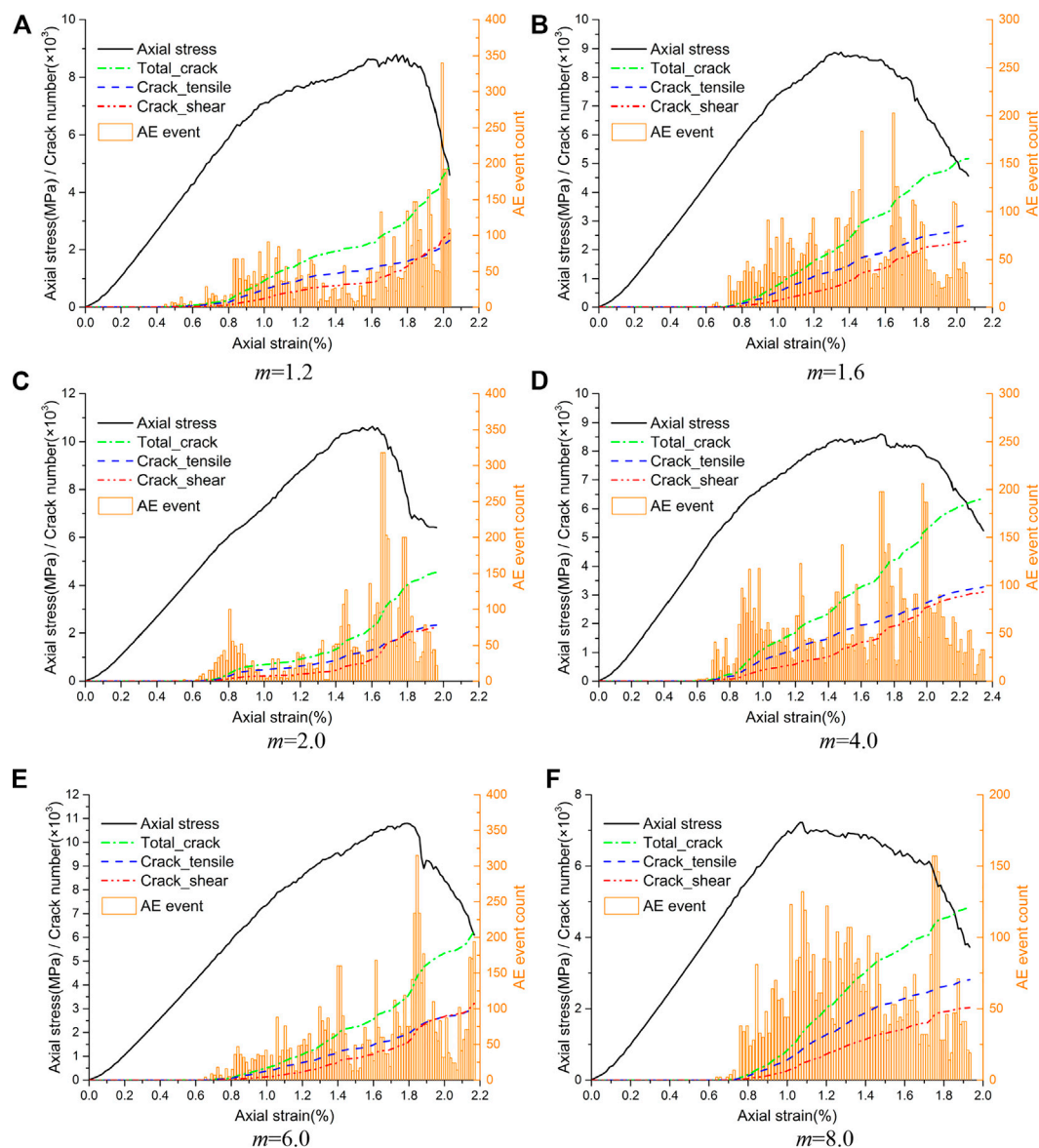


FIGURE 15

Crack development and AE event count of the models with increasing size homogeneity coefficient of the defects. (A) $m = 1.2$ (B) $m = 1.6$. (C) $m = 2.0$ (D) $m = 4.0$. (E) $m = 6.0$ (F) $m = 8.0$.

peak stress increase. When the porosity is less than 15%, there is little difference in the number of tensile and shear cracks, and they change in stages. There are more tensile cracks than shear cracks before the peak stress point, and then the number of shear cracks gradually exceeds that of tensile cracks. When the porosity is greater than 20%, the number of tensile cracks is always much greater than that of shear cracks.

In addition, the number of tensile cracks, shear cracks and AE event intensities of the models with increasing porosity at peak stress are all extracted and illustrated in Figure 13. The three groups of data all indicate that the tensile crack, shear crack, and

AE event intensities at peak stress decrease with increasing porosity.

Figure 14 illustrates the crack distribution of the models having different porosities of random circular defects at 60% of the peak stress after failure. The red and blue lines in Figure 14 represent the shear and tensile cracks that occurred in the model under uniaxial compression, respectively. The Arabic numerals that follow the color legends are the numbers of the corresponding cracks. The number of total cracks, shear cracks, and tensile cracks in the failed specimens all decrease with increasing defect porosity. Furthermore, Figure 14 also

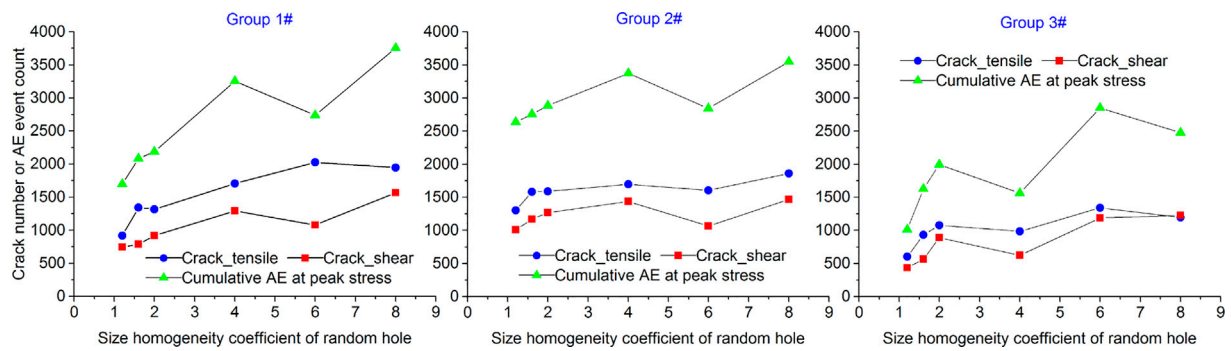


FIGURE 16

Crack number and AE event count at peak stress with increasing size homogeneity coefficient of the defects.

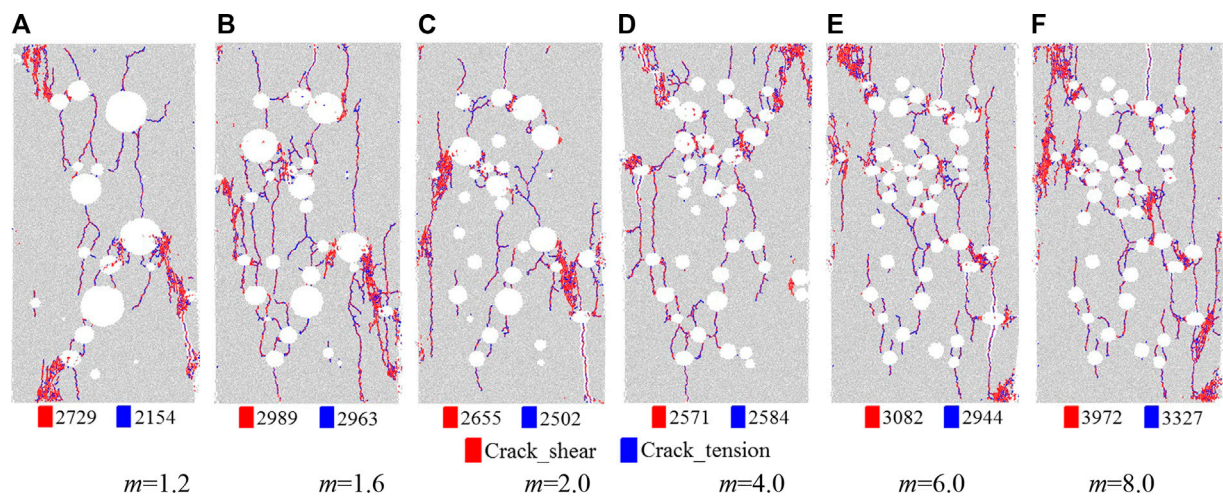


FIGURE 17

Crack distribution of the models with increasing size homogeneity coefficient of the defects ($p = 10\%$). (A) $m = 1.2$ (B) $m = 1.6$ (C) $m = 2.0$ (D) $m = 4.0$ (E) $m = 6.0$ (F) $m = 8.0$.

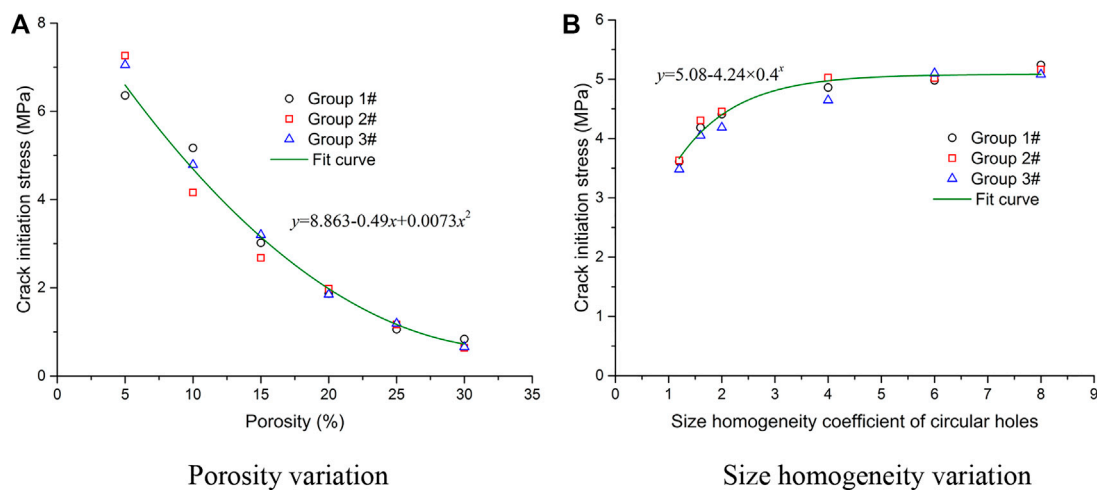
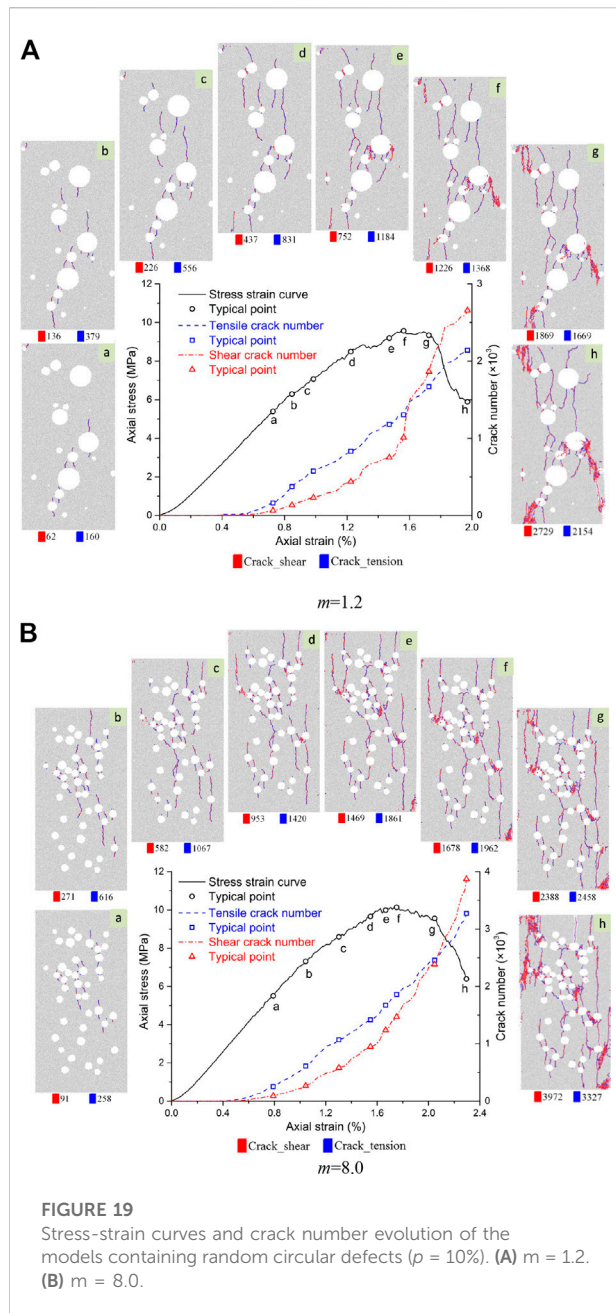


FIGURE 18

Fitting results of the CI stress values of the models containing random circular defects. (A) Porosity variation (B) Size homogeneity variation.



indicates that the proportion of tensile cracks in the total cracks increases with increasing defect porosity.

2) Models containing random circular defects with various size homogeneity coefficients

The variation curves of the crack amount and the AE intensity histograms of the numerical models containing random circular defects with increasing size homogeneity coefficient are shown in Figure 15. The crack amount and the AE event intensity increase with increasing size homogeneity of the defects. The AE events after peak stress also increase

with increasing size homogeneity of the defects. Tensile cracks are the dominant crack type, especially in the stage before the peak stress.

In addition, the number of tensile cracks, shear cracks, and AE event intensity levels of the models with various size homogeneity coefficients of the defects at peak stress are all extracted and illustrated in Figure 16. Three groups of data indicate that the tensile crack, shear crack and AE event intensity at peak stress all show wave-like increases with increasing size homogeneity of the defects.

Figure 17 illustrates the crack distribution of the models containing random circular defects with various size homogeneity coefficients at 60% of the peak stress after failure. The number of total cracks, shear cracks, and tensile cracks in the failed models all show wave-like increases with increasing size homogeneity coefficient of the defects. Furthermore, the proportion of tensile cracks in the total cracks also shows a wave-like increase with increasing size homogeneity of the defects.

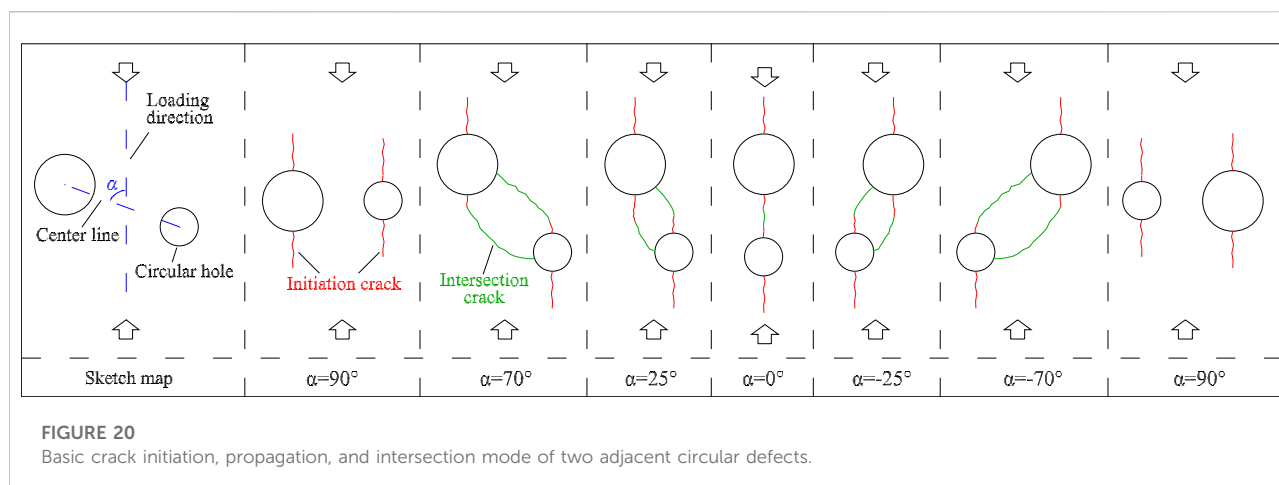
3.3 Crack initiation, intersection and development characteristics

1) Crack initiation stress of the models containing random circular defects

Natural rock materials usually contain a large number of micropores, microcracks, and other defects. The stiffness degradation and failure of rock are often caused by the initiation and propagation of these defects. To determine the initiation mechanism of rock, we must first clarify the stress level at which the rock begins to crack. In this paper, according to the relevant research literature [43], the CI stress is defined as the axial compressive stress when the number of cracks is 1% of the total cracks at the peak stress. The CI stress values of models containing random circular defects with different porosities and size homogeneity are extracted and made into a scatter diagram, and the fitting results are shown in Figure 18. The CI stress decreases in a quadratic curve with increasing defect porosity, but the decreasing rate gradually slows down. The influence of the size homogeneity coefficients on the CI stress of the models changes exponentially, and the influence is more significant when the homogeneity coefficient is less than 4.

2) Crack initiation, propagation and intersection mechanism

To study the crack initiation, propagation and intersection mechanism of the models containing random circular defects, two models having the same porosity and different size homogeneity coefficients of the defects are selected to analyze the crack propagation characteristics during compression. As shown in Figure 19, tensile cracks are the main crack type during



the stage from crack initiation to the peak stress point, and then the number of shear cracks increases rapidly and finally exceeds the number of tensile cracks. After the model reaches the peak strength, its internal structure is destroyed, and the cracks rapidly propagate, intersect, and combine with each other to form macro fracture surfaces. Then, the deformation of rock mainly shows sliding along the macro fracture surfaces, resulting in the rapid growth of shear cracks.

To observe the progressive propagation process of cracks more intuitively, eight typical points ((a-f) in Figure 19) are selected from crack initiation to final failure of the model, and the crack propagation and distribution corresponding to each point is also displayed simultaneously. The cracks first appear at the location of dense defects, and the crack initiation positions usually start from the top and bottom of the circular defects. The direction of crack initiation and propagation is consistent with the loading direction, and tensile cracks (blue lines) are the main crack type.

When the crack just begins to initiate and propagate, depicted as the red lines in Figure 20, the circular and its cracks is like a bead threaded by a string. Subsequently, the propagation and intersection direction of cracks are affected by the adjacent defects. Two adjacent defects can be regarded as a basic unit to illustrate the crack propagation and intersection after crack initiation. As the circular defects are randomly distributed, the angle (α , see Figure 20) between the loading direction and the centerline of two adjacent defects changes. As depicted in Figures 19, 20, there are three basic modes of crack propagation between two circular defects. The crack propagates along the loading direction after initiation and connects the two defects when α approaches 0° . When α approaches 90° , the cracks of the two adjacent defects only propagate along the initiation direction, and no intersection cracks appear. When $|\alpha|$ is between 0° and 90° , the top crack of the bottom defect changes the original initiation direction, approaches the near side of the top defect, and finally penetrates it. Similarly, the bottom crack of the top

defect approaches the near side of the bottom defect and penetrates it after initiation. These three cracking modes constitute the major crack distribution pattern of the whole model. In addition, some cracks that are not induced by the defects are also found at the corners and edges of the model, and most of these cracks appear after the peak stress.

4 Conclusion

The following conclusions can be drawn from numerical simulations of the uniaxial compression of the models containing random circular defects.

- 1) The porosity of the circular defects significantly affects the strength and deformation properties of the models containing random circular defects. As the porosity increases, the model undergo a deformation transformation from brittle to ductile, and the peak strengths and elastic modulus values show a nonlinear and a linear decline, respectively. However, the size homogeneity of the circular defects has a slight impact on the mechanical behaviors of the models containing random circular defects. As the size homogeneity coefficient increases, the peak strengths show a slight linear rise, while the elastic modulus values show a minimal linear downward trend.
- 2) Tensile cracks are the dominant crack type, especially in the stage before the peak stress. The porosity of the circular defects significantly affects the crack number, crack type and AE event intensity of the models containing random circular defects. The number of tensile cracks, shear cracks and AE events all decrease with increasing porosity. There is little difference in the number of tensile and shear cracks when the porosity is less than 15%. However, the number of tensile cracks is always much greater than that of shear cracks when the porosity exceeds 20%. The size homogeneity of the

circular defects has a certain degree of influence on the crack number, crack type and AE event intensity of the models containing random circular defects. The number of tensile cracks, shear cracks, and AE events all show wave-like increases with increasing size homogeneity of the circular defects. The proportion of tensile cracks in the total cracks of the failure models also shows a wave-like increase with increasing size homogeneity of the circular defects.

- 3) The porosity and size homogeneity of the random circular defects significantly affect the CI stresses of the models. The CI stress decreases in a quadratic curve with increasing defect porosity, but the decreasing rate gradually slows down. The influence of the size homogeneity coefficients on the CI stresses of the models changes exponentially, and the influence is more significant when the size homogeneity coefficient is less than 4.
- 4) Tensile cracks are the main crack type during the stage from crack initiation to the peak stress point, and after that, the number of shear cracks increases rapidly and finally exceeds that of tensile cracks. The cracks first appear at the location with dense defects, and the crack initiation positions start from the top and bottom of the circular holes. The direction of crack initiation and propagation is consistent with the loading direction. The propagation and intersection direction of the cracks are significantly affected by adjacent defects. There are three basic modes of crack propagation between the circular defects. When the centerline of two adjacent defects is parallel to the loading direction, the crack propagates along the loading direction after initiation and connects the two holes. When the centerline of two adjacent defects is perpendicular to the loading direction, the cracks only propagate along the initiation direction, and no intersection cracks appear. When the included angle between the centerline and the loading direction is an acute angle, one defect will attract the closer initiation crack of another defect to change its initiation direction, propagate to itself and finally intersect with each other. In addition, a small number of cracks that are not induced by the defects are also found at the corners and edges of the model, and these cracks mostly appear after the peak stress.

References

1. Cheng Y, Jiao YY, Tan F. Numerical and experimental study on the cracking behavior of marble with en-echelon flaws. *Rock Mech Rock Eng* (2019) 52:4319–38. doi:10.1007/s00603-019-01849-x
2. Huang CC, Yang WD, Duan K, Fang LD, Wang L, Bo CJ. Mechanical behaviors of the brittle rock-like specimens with multi-non-persistent joints under uniaxial compression. *Constr Build Mater* (2019) 220:426–43. doi:10.1016/j.conbuildmat.2019.05.159
3. Zhao C, Niu JL, Zhang QZ, Zhao CF, Zhou YM. Failure characteristics of rock-like materials with single flaws under uniaxial compression. *Bull Eng Geol Environ* (2019) 78(1):593–603. doi:10.1007/s10064-018-1379-2
4. Yang SQ, Huang YH. An experimental study on deformation and failure mechanical behavior of granite containing a single fissure under different

Data availability statement

The original contributions presented in the study are included in the article/supplementary material, further inquiries can be directed to the corresponding author.

Author contributions

All authors listed have made a substantial, direct, and intellectual contribution to the work and approved it for publication.

Funding

This research is financially supported by the Science and Technology Project of Henan Province (Grant No. 202102310569), the Nanhu Young Scholars Program of Xinyang Normal University, the Natural Science Foundation of Henan Province (Grant No. 212300410231), the Graduate Student Innovation Fund Project of Xinyang Normal University and the Itasca Consulting Group through its Itasca Education Partnership (IEP) program. The authors gratefully acknowledge the financial or instructional support provided by them.

Conflict of interest

The authors declare that the research was conducted in the absence of any commercial or financial relationships that could be construed as a potential conflict of interest.

Publisher's note

All claims expressed in this article are solely those of the authors and do not necessarily represent those of their affiliated organizations, or those of the publisher, the editors and the reviewers. Any product that may be evaluated in this article, or claim that may be made by its manufacturer, is not guaranteed or endorsed by the publisher.

confining pressures. *Environ Earth Sci* (2017) 76:364. doi:10.1007/s12665-017-6696-4

5. Huang YH, Yang SQ, Tian WL. Crack coalescence behavior of sandstone specimen containing two pre-existing flaws under different confining pressures. *Theor Appl Fracture Mech* (2019) 99:118–30. doi:10.1016/j.tafmec.2018.11.013

6. Bahrani N, Kaiser PK. Numerical investigation of the influence of specimen size on the unconfined strength of defected rocks. *Comput Geotech* (2016) 77:56–67. doi:10.1016/j.compgeo.2016.04.004

7. Farahmand K, Vazaios I, Diederichs MS, Vlachopoulos N. Investigating the scale-dependency of the geometrical and mechanical properties of a moderately

- jointed rock using a synthetic rock mass (SRM) approach. *Comput Geotech* (2018) 95:162–79. doi:10.1016/j.compgeo.2017.10.002
8. Chen S, Qiao CS. Composite damage constitutive model of jointed rock mass considering crack propagation length and joint friction effect. *Arab J Geosci* (2018) 11:283. doi:10.1007/s12517-018-3643-y
9. Chong ZH, Li XH, Hou P. Experimental and numerical study of the effects of layer orientation on the mechanical behavior of shale. *Arab J Sci Eng* (2019) 44: 4725–43. doi:10.1007/s13369-018-3533-3
10. Moomivand H. Effects of orientation, frequency, and number of sets of discontinuities on rock strength under triaxial stresses. *Arab J Geosci* (2014) 7(12): 5345–52. doi:10.1007/s12517-013-1069-0
11. Gao FQ, Kang HP. Effects of pre-existing discontinuities on the residual strength of rock mass - insight from a discrete element method simulation. *J Struct Geol* (2016) 85:40–50. doi:10.1016/j.jsg.2016.02.010
12. Ma WQ, Wang TX. Numerical study of the influence of joint angle on the failure behavior of randomly and nonpersistently jointed rock mass. *Arab J Sci Eng* (2020) 45(5):4023–36. doi:10.1007/s13369-020-04361-5
13. Chen LL, Wang ZW, Peng X, Yang JF, Wu PF, Lian HJ. Modeling pressurized fracture propagation with the isogeometric BEM. *Geomech Geophys Geo-energ Georesour* (2021) 7:51. doi:10.1007/s40948-021-00248-3
14. Wong RHC, Lin P, Tang CA. Experimental and numerical study on splitting failure of brittle solids containing single pore under uniaxial compression. *Mech Mater* (2006) 38:142–59. doi:10.1016/j.mechmat.2005.05.017
15. Janeiro R, Einstein H. Experimental study of the cracking behavior of specimens containing inclusions (under uniaxial compression). *Int J Fract* (2010) 164:83–102. doi:10.1007/s10704-010-9457-x
16. Zhao XD, Zhang HX, Zhu WC. Fracture evolution around pre-existing cylindrical cavities in brittle rocks under uniaxial compression. *Trans Nonferrous Met Soc China* (2014) 24:806–15. doi:10.1016/S1003-6326(14)63129-0
17. Liu JP, Li YH, Xu SD, Xu S, Jin CY, Liu ZS. Moment tensor analysis of acoustic emission for cracking mechanisms in rock with a pre-cut circular hole under uniaxial compression. *Eng Fract Mech* (2015) 135:206–18. doi:10.1016/j.engfracmech.2015.01.006
18. Li DY, Zhu QQ, Zhou ZL, Li XB, Ranjith PG. Fracture analysis of marble specimens with a hole under uniaxial compression by digital image correlation. *Eng Fract Mech* (2017) 183:109–24. doi:10.1016/j.engfracmech.2017.05.035
19. Huang YH, Yang SQ, Hall MR, Tian WL, Yin PF. Experimental study on uniaxial mechanical properties and crack propagation in sandstone containing a single oval cavity. *Arch Civil Mech Eng* (2018) 18(4):1359–73. doi:10.1016/j.acme.2018.04.005
20. Li P, Ren FH, Cai MF, Guo QF, Wang HF, Liu K. Investigating the mechanical and acoustic emission characteristics of brittle failure around a circular opening under uniaxial loading. *Int J Miner Metall Mater* (2019) 26:1217–30. doi:10.1007/s12613-019-1887-5
21. Lotidis MA, Nomikos PP, Sofianos AI. Numerical study of the fracturing process in marble and plaster hollow plate specimens subjected to uniaxial compression. *Rock Mech Rock Eng* (2019) 52(11):4361–86. doi:10.1007/s00603-019-01884-8
22. Wong LNY, Peng J. Numerical investigation of micro-cracking behavior of brittle rock containing a pore-like flaw under uniaxial compression. *Int J Damage Mech* (2020) 29:1543–68. doi:10.1177/1056789520914700
23. Zhou Z, Tan LH, Cao WZ, Zhou ZY, Cai X. Fracture evolution and failure behaviour of marble specimens containing rectangular cavities under uniaxial loading. *Eng Fract Mech* (2017) 187:183–201. doi:10.1016/j.engfracmech.2017.08.029
24. Liu T, Lin BQ, Yang W, Zou QL, Kong J, Yan FZ. Cracking process and stress field evolution in specimen containing combined flaw under uniaxial compression. *Rock Mech Rock Eng* (2016) 49(8):3095–113. doi:10.1007/s00603-016-0982-4
25. Wang X, Tian LG. Mechanical and crack evolution characteristics of coal-rock under different fracture-hole conditions: A numerical study based on particle flow code. *Environ Earth Sci* (2018) 77:297. doi:10.1007/s12665-018-7486-3
26. Yin Q, Jing HW, Su HJ. Investigation on mechanical behavior and crack coalescence of sandstone specimens containing fissure-hole combined flaws under uniaxial compression. *Geosci J* (2018) 22:825–42. doi:10.1007/s12303-017-0081-x
27. Wang XS, Jiang YJ, Li B. Experimental and numerical study on crack propagation and deformation around underground opening in jointed rock masses. *Geosci J* (2017) 21:291–304. doi:10.1007/s12303-016-0051-8
28. Yang SQ, Yin PF, Zhang YC, Chen M, Zhou XP, Jing HW, et al. Failure behavior and crack evolution mechanism of a non-persistent jointed rock mass containing a circular hole. *Int J Rock Mech Min Sci* (1997) (2019) 114:101–21. doi:10.1016/j.ijrmms.2018.12.017
29. Tan X, Konietzky H. Numerical study of variation in Biot's coefficient with respect to microstructure of rocks. *Tectonophysics* (2014) 610:159–71. doi:10.1016/j.tecto.2013.11.014
30. Lin P, Wong RHC, Tang CA. Experimental study of coalescence mechanisms and failure under uniaxial compression of granite containing multiple holes. *Int J Rock Mech Min Sci* (1997) (2015) 77(4-6):313–27. doi:10.1016/j.ijrmms.2015.04.017
31. Wong RHC, Lin P. Numerical study of stress distribution and crack coalescence mechanisms of a solid containing multiple holes. *Int J Rock Mech Min Sci* (1997) (2015) 79:41–54. doi:10.1016/j.ijrmms.2015.08.003
32. Bai QS, Tu SH, Zhang C. Dem investigation of the fracture mechanism of rock disc containing hole(s) and its influence on tensile strength. *Theor Appl Fracture Mech* (2016) 86:197–216. doi:10.1016/j.tafmec.2016.07.005
33. Gao FQ, Stead D, Elmo D. Numerical simulation of microstructure of brittle rock using a grain-breakable distinct element grain-based model. *Comput Geotech* (2016) 78:203–17. doi:10.1016/j.compgeo.2016.05.019
34. Gui YL, Zhao ZY, Zhang C, Ma SQ. Numerical investigation of the opening effect on the mechanical behaviours in rocks under uniaxial loading using hybrid continuum-discrete element method. *Comput Geotech* (2017) 90:55–72. doi:10.1016/j.compgeo.2017.05.021
35. Zhang C, Tu SH, Bai QS. Evaluation of pore size and distribution impacts on uniaxial compressive strength of lithophysal rock. *Arab J Sci Eng* (2018) 43(3): 1235–46. doi:10.1007/s13369-017-2810-x
36. Peng J, Wong LNY, Zhang YH. Influence of pore-like flaws on strength and microcracking behavior of crystalline rock. *Int J Numer Anal Methods Geomech* (2021) 45:521–39. doi:10.1002/nag.3171
37. Jia LC, Chen M, Zhang W, Xu T, Zhou Y, Hou B, et al. Experimental study and numerical modeling of brittle fracture of carbonate rock under uniaxial compression. *Mech Res Commun* (2013) 50:58–62. doi:10.1016/j.mechrescom.2013.04.002
38. Zhang Q, Zhu HH, Zhang LY, Ding XB. Study of scale effect on intact rock strength using particle flow modeling. *Int J Rock Mech Min Sci* (1997) (2011) 48(8): 1320–8. doi:10.1016/j.ijrmms.2011.09.016
39. Saadat M, Tah A. A numerical approach to investigate the effects of rock texture on the damage and crack propagation of a pre-cracked granite. *Comput Geotech* (2019) 111:89–111. doi:10.1016/j.compgeo.2019.03.009
40. Tang CA, Liu H, Lee PKK, Tsui Y, Tham LG. Numerical studies of the influence of microstructure on rock failure in uniaxial compression — Part I: Effect of heterogeneity. *Int J Rock Mech Min Sci* (1997) (2000) 37(4):555–69. doi:10.1016/S1365-1609(99)00121-5
41. Tang CA, Tham LG, Wang SH, Liu H, Li WH. A numerical study of the influence of heterogeneity on the strength characterization of rock under uniaxial tension. *Mech Mater* (2007) 39(4):326–39. doi:10.1016/j.mechmat.2006.05.006
42. Ma WQ, Wang JT, Li XX, Wang TX. Crack evolution and acoustic emission characteristics of rock specimens containing random joints under uniaxial compression. *Acta Geophys* (2021) 69:2427–41. doi:10.1007/s11600-021-00686-3
43. Potyondy DO, Cundall PA. Modeling notch-formation mechanisms in the URL Mine-by Test Tunnel using bonded assemblies of circular particles. *Int J Rock Mech Min Sci* (1997) (1998) 35:510–1. doi:10.1016/S0148-9062(98)00083-7



OPEN ACCESS

EDITED BY

Pei Li,
Xi'an Jiaotong University, China

REVIEWED BY

Yunfei Gao,
Hohai University, China
Chuang Lu,
University of Science and Technology of
China, China

*CORRESPONDENCE

Yanming Xu,
xuyanming@ustc.edu

SPECIALTY SECTION

This article was submitted to Statistical
and Computational Physics,
a section of the journal
Frontiers in Physics

RECEIVED 28 October 2022

ACCEPTED 15 November 2022

PUBLISHED 30 November 2022

CITATION

Chen X, Xu Y, Zhao J, Cheng R and Ma W
(2022), Sensitivity analysis of structural-
acoustic fully-coupled system using
isogeometric boundary
element method.
Front. Phys. 10:1082824.
doi: 10.3389/fphy.2022.1082824

COPYRIGHT

© 2022 Chen, Xu, Zhao, Cheng and Ma.
This is an open-access article
distributed under the terms of the
[Creative Commons Attribution License](#)
(CC BY). The use, distribution or
reproduction in other forums is
permitted, provided the original
author(s) and the copyright owner(s) are
credited and that the original
publication in this journal is cited, in
accordance with accepted academic
practice. No use, distribution or
reproduction is permitted which does
not comply with these terms.

Sensitivity analysis of structural-acoustic fully-coupled system using isogeometric boundary element method

Xiuyun Chen^{1,2}, Yanming Xu^{1,2*}, Juan Zhao^{2,3}, Ruhui Cheng^{2,3}
and Wenqiang Ma³

¹School of Architecture and Civil Engineering, Huanghuai University, Zhumadian, China, ²Henan International Joint Laboratory of Structural Mechanics and Computational Simulation, Huanghuai University, Zhumadian, China, ³College of Architecture and Civil Engineering, Xinyang Normal University, Xinyang, China

In many engineering challenges, the whole interaction between the structural domain and the acoustic domain must be taken into account, particularly for the acoustic analysis of thin structures submerged in water. The fast multipole boundary element approach is used in this work to simulate the external acoustic domain and the finite element method is used to describe the structural components. To improve coupling analysis accuracy, discontinuous higher-order boundary components are created for the acoustic domain. The isogeometric boundary element method (IGABEM) discretizes unknown physical fields by using CAD spline functions as basis functions. IGABEM is inherently compatible with CAD and can perform numerical analysis on CAD models without having to go through the time-consuming meshing process required by traditional FEM/BEM and volume parameterization in isogeometric finite element methods. IGABEM's power in tackling infinite domain issues and combining CAD and numerical analysis is fully used when it is applied to structural form optimization of three-dimensional external acoustic problems. The structural-acoustic design and optimization procedures benefit from the use of structural-acoustic design sensitivity analysis because it may provide information on how design factors affect radiated acoustic performance. This paper provides adjoint operator-based equations for sound power sensitivity on structural surfaces and direct differentiation-based equations for sound power sensitivity on arbitrary closed surfaces surrounding the radiator. Numerical illustrations are provided to show the precision and viability of the suggested approach.

KEYWORDS

iga, FEM/BEM, structural-acoustic coupling, sound power, sensitivity analysis

1 Introduction

A typical issue in underwater acoustics is the analysis of the acoustic radiation or scattering from elastic structures in fluid. Only for basic geometric structures with simple boundary conditions are analytical solutions to structural-acoustic interaction issues accessible [1]. There are still no analytical answers to real-world issues with complex geometries. Therefore, effective numerical techniques must be created.

Due to its high adaptability and suitability for complex real-world model challenges, the finite element method (FEM) is frequently employed to simulate the structural components in these issues [2]. To avoid meshing the commonly infinite or semi-infinite acoustic domain, the sound field is modeled using the boundary element method (BEM) [3]. Researchers have focused a lot of their attention on the FEM/BEM coupling techniques [4]; [5]; [6]; [7]; [8]; [9,10]; [11]; [12], where FEM is used to discretize the structure's components and BEM is utilized to represent the acoustic area. BEM frequently employs continuous linear or quadratic components. Discontinuous elements have been researched as an alternative to them, exhibiting a high level of precision [13]; [14]. When a hypersingular integral is discretized, discontinuous boundary elements are typically used because C^1 -continuity of the surface at the collocation point is necessary in such situation. Applications can be found in fracture analysis [15] and the Navier-Stokes equation solution [16]. When collocation points are situated at the zeros of orthogonal functions for the standard interval, superconvergence for error dependency on the size of discontinuous border elements has been examined by [17]; [14] presents the error dependency of the frequency, element size, and node placement on discontinuous elements. This study discovered that discontinuous border elements outperform continuous components in terms of performance. In-depth research has also been done on how well discontinuous boundary elements perform in acoustic analyses of rigid structures. [18] Discussed how discontinuous boundary elements combined with FEM perform when the interaction between the structure and the sound field is taken into consideration.

Conventional BEM has the well-known drawback of generating a dense and asymmetrical coefficient matrix, which necessitates $O(N^3)$ arithmetic operations to directly solve the system of equations, such as by applying the Gauss elimination technique. The integral problem has been solved more quickly using the fast multipole method (FMM) [19]; [20]; [21]; [22]. Iterative solvers have proven to be effective in solving complex practical issues [23]; [24]. Therefore, large-scale acoustic-structure interaction issues may be successfully solved using the coupling technique based on FEM and fast multipole BEM (FMBEM) [7]; [8]. The diagonal form of the FMM and the original FMM are both utilized to solve the Helmholtz problem. Outside the ranges of their favored frequencies, both

kinds fail in some way. However, the aforementioned issues can be resolved by the wideband FMM created by fusing the original FMM and the diagonal form FMM [25]; [26]. The main use of FMM is for discretization-based numerical analysis using constant boundary elements. Due to the difficulty of the computation process, there are not many articles that employ the FMM for numerical analysis based on discontinuous high-order boundary element discretization [18]. In this research, FMM is employed to speed up the solution of the integral equation using discontinuous boundary elements. Finally, the large-scale acoustic-structure interaction issues are solved using the coupling algorithm FEM/discontinuous wideband FMBEM.

Both conventional FEM and BEM with Lagrange polynomial basis functions rely on polygonal meshes, which leads to time-consuming preprocessing steps, geometric inaccuracies, and poor field variable continuity [27]. The [28] notion of isogeometric analysis (IGA) allows for the resolution of these problems. The core of IGA is to discretize the unknown physical fields while solving partial differential equations by using the same basis functions as those in computer-aided design (CAD) to describe the domain geometry. Geometric accuracy, adjustable order elevation and k-refinement, high order continuous fields, etc. are some benefits of IGA. Although IGA was first created in the context of finite element methods (IGAFEM), there are some situations when it is preferable to combine IGA with boundary element methods (IGABEM) [10, 29]; [30]; [31]; [32, 33]. Several benefits come with IGABEM:

- it can use CAD data right away without the need for volume parameterization from geometric surfaces [34, 35], since both of them are boundary-represented [36]; [37]; [38];
- it inherits the benefits of traditional BEM for addressing problems in infinite domains [39]; [40–42];
- IGABEM is perfect for free boundary problems like crack growth since no volume parameterization is required [43, 44].

As for the singularity problems, singularities and shifting borders are well handled by IGA [43, 44]. Specialized integration methods have been developed to tackle the weakly singular and hypersingular integrals that arise in IGABEM [41].

Acoustic design sensitivity analysis is crucial to the acoustic design and optimization processes because it may provide information about the impact of geometric modifications on the acoustic performance of structures [45]. An overview of recent advancements in structural-acoustic optimization for passive noise suppression was provided by [6]. Gradient-based optimization takes a long time to do a sound power sensitivity analysis for problems involving acoustic-structure interaction. The global finite difference method (FDM) is frequently used in structural-acoustic optimization because it is simple to employ, according to [46], [47], and [48]. However, FDM performs

poorly, especially when several design elements are taken into account at once. The distinction between semi-analytic and analytical sensitivity studies has been made in addition to global finite differences. These classifications have been debated in many studies [49]; [6,50]. Global finite differences are significantly less accurate than analytical and semi-analytical sensitivity studies. Additionally, the former are less expensive computationally than the latter. In [51], coupled structural acoustic issues were addressed using an analytical sensitivity analysis, which has recently emerged as the direct differentiation approach. Using the adjoint operator technique, which has been used to solve structural acoustic problems, allows for still further acceleration in calculation time, particularly for issues with several design variables [52]; [53].

With regard to several design variables, this work constructs equations for sound power sensitivity. To eliminate geometric errors, the fundamental formulations of IGABEM discretization are introduced for acoustic analysis. Directly differentiating the coupled boundary element equation with respect to design variables yields the derivative formulation of the vectors of nodal displacement and sound pressure on the interaction surface with respect to design variables. The coupled boundary element equation is created by fusing the structural equation into the acoustic equation. Utilizing adjoint operators and direct differentiation, respectively, we derive the derivative formulation of the radiated sound power on the structural surface and the derivative formulation of the radiated sound power on any arbitrary closed surface around the radiator. The appropriate formula needed to compute the derivative of the radiated sound power for various design variables are discussed in detail. The FEM/FMBEM coupling system is used to determine the sound power sensitivity. It is shown with numerical examples how accurate and reliable the current method is.

2 Structural-acoustic analysis

2.1 Subdivision surfaces

Since its introduction in the 1970s, subdivision surfaces have been extensively utilized in computer animation and graphics [54]. Additionally, they are accessible in the majority of industrial CAD solid modeling programs (e.g., CATIA, Creo). Subdivision surfaces are often seen in computer graphics literature as a method for repeatedly smoothing and refining a control mesh in order to generate smooth limit surfaces. They may also be seen from the perspective of finite and boundary element analysis as the generalization of splines to arbitrarily connected meshes.

The concept of subdivision schemes is to create a smooth surface out of a rough polygon mesh. Subdivision refinement systems, which may be categorized as interpolating or approximation

schemes, create a smooth surface by a limited process of repetitive refinement beginning with an initial control mesh. All control meshes produced during subdivision refinement describe the exact same spline surface since the subdivision surfaces inherit the refinability attribute from the splines.

In this research, the structural-acoustic coupling analysis is conducted using a Loop subdivision technique [42].

2.2 Acoustic-structure interaction using finite element method/boundary element method

The BEM and FEM are used to simulate the fluid and structural subdomains, respectively. The discretized boundary integral formulation of the fluid solution to the Helmholtz problem is given by [55], as shown in Equation 1:

$$\mathbf{H}\mathbf{p} = \mathbf{G}\mathbf{q} + \mathbf{p}_i, \quad (1)$$

where

\mathbf{H} and \mathbf{G} are the frequency-dependent BEM influencing matrices,

\mathbf{p} is the vector containing the nodal values for pressure,

\mathbf{q} is the vector of normal derivatives of \mathbf{p} ,

\mathbf{p}_i is the incident wave's nodal pressure.

The continuous linear and quadratic element technique is often used, and alternatives to discontinuous elements with good accuracy have already been examined [14]. Discontinuous boundary elements outperform continuous boundary elements [14]. Interpolation nodes are positioned within discontinuous boundary elements, and the expressions of the interpolation functions depend on the position of the node within the element. Thus, by varying the placements of the interpolation nodes, a numerical solution with varied calculation accuracies may be achieved. Both discontinuous and continuous components are employed in the numerical computation in this study.

The steady-state response of the structure may be derived from the frequency-response analysis when a harmonic load with a transitory function $e^{-i\omega t}$ is applied to it. When the acoustic-structure interaction is addressed, Equation 2 derives the linear system of equations to compute the nodal displacements \mathbf{u} [51].

$$(\mathbf{K} - \omega^2\mathbf{M} + i\omega\mathbf{C})\mathbf{u} = \mathbf{f}_s + \mathbf{C}_{sf}\mathbf{p}, \quad (2)$$

$$\mathbf{C}_{sf} = \int_{\Gamma} \mathbf{N}_s^T \mathbf{n} \mathbf{N}_f d\Gamma, \quad (3)$$

where

\mathbf{K} is the structure's stiffness matrix,

\mathbf{M} is the structure's mass matrix,

\mathbf{C} is the structure's damping matrix,

ω is the angular frequency,

\mathbf{f}_s is the vector of the nodal structural forces,

$\mathbf{C}_{sf}\mathbf{p}$ is the acoustic load.

Γ is the coupling boundary surface,

N_s is the global interpolation function for the structural domain,

N_f is the global interpolation function for the fluid domain,

\mathbf{n} is the normal vector of the surface.

The continuity condition across the interaction surface (Fritze et al.2005) is introduced in Equation 4, as follows:

$$\mathbf{q} = i\omega\rho_f\mathbf{v}_f, \quad (4)$$

$$\mathbf{v}_f = -i\omega\mathbf{S}^{-1}\mathbf{C}_{fs}\mathbf{u}, \quad (5)$$

$$\mathbf{S} = \int_{\Gamma} \mathbf{N}_f^T \mathbf{N}_f d\Gamma, \quad (6)$$

$$\mathbf{C}_{fs} = \mathbf{C}_{sf}^T, \quad (7)$$

where

ρ_f is the density of the fluid,

\mathbf{v}_f is the normal velocity vector of the fluid.

Combining Equations 1, 2 and 4, Equation 8 gives the coupled system of equations of an elastic structure submerged in a heavy fluid derived.

$$\begin{bmatrix} \mathbf{K} - \omega^2\mathbf{M} + i\omega\mathbf{C} & -\mathbf{C}_{sf} \\ -\omega^2\rho_f\mathbf{G}\mathbf{S}^{-1}\mathbf{C}_{fs} & \mathbf{H} \end{bmatrix} \begin{Bmatrix} \mathbf{u} \\ \mathbf{p} \end{Bmatrix} = \begin{Bmatrix} \mathbf{f}_s \\ \mathbf{p}_i \end{Bmatrix}. \quad (8)$$

On Equation 8, the application of an iterative solution (e.g., generalized minimum residual approach (GMRES)) results in unsatisfactory convergence. Substituting the finite element formulation into the boundary element equation to obtain a simplified system equation is an appropriate strategy [51]; [44, 56, 57], as shown in Equation 9:

$$\mathbf{H}\mathbf{p} - \mathbf{G}\mathbf{W}\mathbf{C}_{sf}\mathbf{p} = \mathbf{p}_i + \mathbf{G}\mathbf{W}\mathbf{f}_s, \quad (9)$$

$$\mathbf{W} = \omega^2\rho_f\mathbf{S}^{-1}\mathbf{C}_{fs}\mathbf{A}^{-1}, \quad (10)$$

$$\mathbf{A} = \mathbf{K} - \omega^2\mathbf{M} + i\omega\mathbf{C}. \quad (11)$$

It takes much time to solve \mathbf{A}^{-1} directly in Equation 9. In fact, A sparse direct solver could be used to readily solve this symmetric, frequency-dependent system of equations $\mathbf{A}\mathbf{x} = \mathbf{f}_s$, thus obtaining the term $\mathbf{A}^{-1}\mathbf{f}_s$ in Equation 9 quickly. The iterative solver GMRES [24] is introduced in this work to speed up the computing of solutions to the equations for the coupled boundary element system. There is no need to solve $\mathbf{A}^{-1}\mathbf{C}_{sf}$ directly on the left-hand side of Equation 9. Considering the current iterative solution \mathbf{p}_k for vector \mathbf{p} in Equation 9, when a sparse direct solver is employed to solve the symmetric and frequency-dependent system of the linear equation $\mathbf{A}\mathbf{x} = \mathbf{C}_{sf}\mathbf{p}_k$, the solution of $\mathbf{A}^{-1}\mathbf{C}_{sf}\mathbf{p}_k$ could be achieved effectively. Based on this, we could derive the solution of vector \mathbf{u} by solving Eq. 9 and inserting the solution of vector \mathbf{p} into Equation 2.

When dealing with a problem with N unknowns, the coefficient matrices \mathbf{H} and \mathbf{G} are dense and non-symmetrical, resulting in $O(N^2)$ arithmetic operations. FMM is used to speed up the solution of the standard boundary element system of equations and reduces the amount of memory required. The core idea behind FMM is to approximate the fundamental solution for BEM using spherical Hankel functions, Legendre polynomials, and plane waves. The

coefficient matrices are divided into two portions. The first is the near-field component, which is assessed by integration in the region of the source point. The other is the far-field component, which cannot be calculated directly. Using FMM on a cluster hierarchy decreases the complexity of BEM from $O(N^2)$ to $O(N\log N)$. FMM comes in two varieties. The original FMM (low-frequency technique) is based on the fundamental solution's series expansion formula, whereas the diagonal form FMM (high-frequency method) is based on the fundamental solution's plane wave expansion formula. For high-frequency problems, the original FMM is inefficient, while the diagonal form FMM has instability issues when solving low-frequency Helmholtz equations. To circumvent these challenges, the wideband FMM generated by merging the original FMM and the diagonal form FMM can be employed [25]; [26].

2.3 Radiated sound power expression

The radiated sound power W on an arbitrary closed surface around the radiator may be represented as Equation 12 for radiation into open domains:

$$W_A(\omega) = \frac{1}{2} \int_A \Re \{ p(\mathbf{y}, \omega) v_f^*(\mathbf{y}, \omega) \} dA(\mathbf{y}), \quad (12)$$

where

A is a randomly chosen closed surface that encircles the radiator,

p is the sound pressure,

v_f^* is the conjugate complex of the particle velocity v_f ,

\Re is the real part of the quantity.

The real component of complex sound power is radiated into the acoustic far field, whereas the imaginary component only contributes to the evanescent near field.

Using BEM to discretize Equation 12 yields a matrix equation for sound power, which is provided by Equation 13:

$$W_A(\omega) = \frac{1}{2} \Re \{ \mathbf{p}_A^T \mathbf{S}_A \mathbf{v}_A^* \}, \quad (13)$$

$$\mathbf{S}_A = \int_A \mathbf{N}_f^T \mathbf{N}_f dA(\mathbf{y}), \quad (14)$$

where

\mathbf{p}_A is the nodal sound pressure vector on surface A ,

\mathbf{v}_A is the particle velocity vector on surface A .

We may readily replace surface A for sound power assessment with the structural surface Γ when the sound power on the structural surface has to be evaluated. As a result, Equation 13 is changed to Equation 15:

$$W(\omega) = \frac{1}{2} \Re \{ \mathbf{p}^T \mathbf{S}_\Gamma \mathbf{v}_\Gamma^* \}. \quad (15)$$

By resolving Equations 2, 5, 9, respectively, we may obtain the vectors \mathbf{p} , \mathbf{u} , and \mathbf{v}_f in turn. Finally, Equation 15 may be solved to determine the radiated sound power W on the structure surface.

When surface A is not the structural surface, Equation 13 could also be used to determine the sound power W on surface A . The pressure and particle velocity at field point \mathbf{y} on surface A in Equation 13 are $p_A(\mathbf{y})$ and $v_A(\mathbf{y})$, respectively. The vectors \mathbf{p}_A and \mathbf{v}_A may be obtained by solving $p_A(\mathbf{y})$ and $v_A(\mathbf{y})$ at each node on surface A .

Equation 16 may be used to represent the boundary integral equation created on the interaction surface Γ to estimate the sound pressure $p_A(\mathbf{y})$ at a field point \mathbf{y} , as follows:

$$p_A(\mathbf{y}) = \int_{\Gamma} G(\mathbf{x}, \mathbf{y}) q(\mathbf{x}) d\Gamma(\mathbf{x}) - \int_{\Gamma} F(\mathbf{x}, \mathbf{y}) p(\mathbf{x}) d\Gamma(\mathbf{x}), \quad (16)$$

$$G(\mathbf{x}, \mathbf{y}) = \frac{e^{ikr}}{4\pi r}, \quad (17)$$

where

\mathbf{x} is the source point,

\mathbf{y} is the field point,

$q(\mathbf{x})$ is the normal derivative of $p(\mathbf{x})$,

$F(\mathbf{x}, \mathbf{y})$ is the normal derivative of $G(\mathbf{x}, \mathbf{y})$.

Using the continuity condition shown in Equation 18:

$$q_A(\mathbf{y}) = -i\omega\rho v_A(\mathbf{y}), \quad (18)$$

Equation 19 is created by differentiating Equation 16 with regard to $n(\mathbf{y})$:

$$\begin{aligned} v_A(\mathbf{y}) &= \frac{i}{\omega\rho} \frac{\partial p_A(\mathbf{y})}{\partial n(\mathbf{y})} \\ &= \frac{i}{\omega\rho} \int_{\Gamma} \frac{\partial G(\mathbf{x}, \mathbf{y})}{\partial n(\mathbf{y})} q(\mathbf{x}) d\Gamma(\mathbf{x}) - \frac{i}{\omega\rho} \int_{\Gamma} \frac{\partial F(\mathbf{x}, \mathbf{y})}{\partial n(\mathbf{y})} p(\mathbf{x}) d\Gamma(\mathbf{x}). \end{aligned} \quad (19)$$

Discretizing Eqs 16, 19, we get Eqs 20, 21:

$$p_A(\mathbf{y}) = \mathbf{g}^T(\mathbf{y}) \mathbf{q} - \mathbf{h}^T(\mathbf{y}) \mathbf{p}, \quad (20)$$

$$v_A(\mathbf{y}) = \frac{i}{\omega\rho} \mathbf{g}_1^T(\mathbf{y}) \mathbf{q} - \frac{i}{\omega\rho} \mathbf{h}_1^T(\mathbf{y}) \mathbf{p}. \quad (21)$$

By solving Eqs 20, 21, the nodal sound pressure $p_A(\mathbf{y})$ and the particle velocity $v_A(\mathbf{y})$ are available at each node on surface A . Vectors \mathbf{p}_A and \mathbf{v}_A on surface A are thus solved. Finally, Equation 13 allows for the solution of the radiated sound power $W_A(\omega)$ on surface A .

3 Sound power sensitivity analysis

3.1 Sound power sensitivity on structural surface

Equation 8 could be expressed as Equation 22:

$$\begin{bmatrix} \mathbf{K} - \omega^2 \mathbf{M} + i\omega \mathbf{C} & -\mathbf{C}_{sf} \\ -\omega^2 \rho_f \mathbf{G} \mathbf{S}^{-1} \mathbf{C}_{fs} & \mathbf{H} \end{bmatrix} \begin{Bmatrix} \mathbf{u} \\ \mathbf{p} \end{Bmatrix} = \mathbf{B} \begin{Bmatrix} \mathbf{u} \\ \mathbf{p} \end{Bmatrix} = \begin{Bmatrix} \mathbf{f}_s \\ \mathbf{p}_1 \end{Bmatrix}, \quad (22)$$

in which we have Equation 23:

$$\mathbf{B} = \begin{bmatrix} \mathbf{K} - \omega^2 \mathbf{M} + i\omega \mathbf{C} & -\mathbf{C}_{sf} \\ -\omega^2 \rho_f \mathbf{G} \mathbf{S}^{-1} \mathbf{C}_{fs} & \mathbf{H} \end{bmatrix} = \begin{bmatrix} \mathbf{A} & -\mathbf{C}_{sf} \\ -\omega^2 \rho_f \mathbf{G} \mathbf{S}^{-1} \mathbf{C}_{fs} & \mathbf{H} \end{bmatrix}. \quad (23)$$

By differentiating Equation 22 with regard to the design variable θ , we get Equation 24:

$$\frac{\partial \mathbf{B}}{\partial \theta} \begin{Bmatrix} \mathbf{u} \\ \mathbf{p} \end{Bmatrix} + \mathbf{B} \begin{Bmatrix} \frac{\partial \mathbf{u}}{\partial \theta} \\ \frac{\partial \mathbf{p}}{\partial \theta} \end{Bmatrix} = \begin{Bmatrix} \frac{\partial \mathbf{f}_s}{\partial \theta} \\ \frac{\partial \mathbf{p}_1}{\partial \theta} \end{Bmatrix}. \quad (24)$$

Equations 25, 26 are thus conducted:

$$\frac{\partial \mathbf{B}}{\partial \theta} = \begin{bmatrix} \frac{\partial \mathbf{A}}{\partial \theta} & -\frac{\partial \mathbf{C}_{sf}}{\partial \theta} \\ -\frac{\partial (\omega^2 \rho_f \mathbf{G} \mathbf{S}^{-1} \mathbf{C}_{fs})}{\partial \theta} & \frac{\partial \mathbf{H}}{\partial \theta} \end{bmatrix}, \quad (25)$$

$$\mathbf{r} = \begin{Bmatrix} \mathbf{r}_1 \\ \mathbf{r}_2 \end{Bmatrix} = \mathbf{B} \begin{Bmatrix} \frac{\partial \mathbf{u}}{\partial \theta} \\ \frac{\partial \mathbf{p}}{\partial \theta} \end{Bmatrix} = \begin{Bmatrix} \frac{\partial \mathbf{f}_s}{\partial \theta} \\ \frac{\partial \mathbf{p}_1}{\partial \theta} \end{Bmatrix} - \frac{\partial \mathbf{B}}{\partial \theta} \begin{Bmatrix} \mathbf{u} \\ \mathbf{p} \end{Bmatrix}. \quad (26)$$

In the following, several expressions of Eqs 25, 26 are found for different kinds of design variables:

1. When the fluid density ρ_f is chosen to be the design variable θ , Eqs 25, 26 are expressed as Eqs 27, 28:

$$\frac{\partial \mathbf{B}}{\partial \theta} = \begin{bmatrix} \mathbf{0} & \mathbf{0} \\ -\omega^2 \mathbf{G} \mathbf{S}^{-1} \mathbf{C}_{fs} & \mathbf{0} \end{bmatrix}, \quad (27)$$

$$\mathbf{r} = \begin{Bmatrix} \mathbf{r}_1 \\ \mathbf{r}_2 \end{Bmatrix} = \begin{Bmatrix} \mathbf{0} \\ \omega^2 \mathbf{G} \mathbf{S}^{-1} \mathbf{C}_{fs} \mathbf{u} \end{Bmatrix}. \quad (28)$$

2. When the material property of the structural part (e.g., Young's modulus E , the structural density ρ_s) is chosen to be the design variable θ , Eqs 25, 26 are expressed as Eqs 29, 30:

$$\frac{\partial \mathbf{B}}{\partial \theta} = \begin{bmatrix} \frac{\partial \mathbf{A}}{\partial \theta} & \mathbf{0} \\ \mathbf{0} & \mathbf{0} \end{bmatrix}, \quad (29)$$

$$\mathbf{r} = \begin{Bmatrix} \mathbf{r}_1 \\ \mathbf{r}_2 \end{Bmatrix} = \begin{Bmatrix} -\frac{\partial \mathbf{A}}{\partial \theta} \mathbf{u} \\ \mathbf{0} \end{Bmatrix}. \quad (30)$$

3. When some parameters determining the coordinates of structural nodes are taken as design variables, Eqs 25, 26 are expressed as Eqs 31, 32:

$$\frac{\partial \mathbf{B}}{\partial \theta} = \begin{bmatrix} \frac{\partial \mathbf{A}}{\partial \theta} & -\frac{\partial \mathbf{C}_{sf}}{\partial \theta} \\ -\omega^2 \rho_f \frac{\partial (\mathbf{G} \mathbf{S}^{-1} \mathbf{C}_{fs})}{\partial \theta} & \frac{\partial \mathbf{H}}{\partial \theta} \end{bmatrix}, \quad (31)$$

$$\mathbf{r} = \begin{Bmatrix} \mathbf{r}_1 \\ \mathbf{r}_2 \end{Bmatrix} = \begin{Bmatrix} \frac{\partial \mathbf{f}_s}{\partial \theta} \\ \frac{\partial \mathbf{p}_i}{\partial \theta} \end{Bmatrix} - \frac{\partial \mathbf{B}}{\partial \theta} \begin{Bmatrix} \mathbf{u} \\ \mathbf{p} \end{Bmatrix} = \begin{Bmatrix} \frac{\partial \mathbf{f}_s}{\partial \theta} - \frac{\partial \mathbf{A}}{\partial \theta} \mathbf{u} + \frac{\partial \mathbf{C}_{sf}}{\partial \theta} \mathbf{p} \\ \frac{\partial \mathbf{p}_i}{\partial \theta} + \omega^2 \rho_f \frac{\partial (\mathbf{G}\mathbf{S}^{-1}\mathbf{C}_{fs})}{\partial \theta} \mathbf{u} - \frac{\partial \mathbf{H}}{\partial \theta} \mathbf{p} \end{Bmatrix}. \quad (32)$$

When dealing with complicated structures, the direct differentiation approach makes it challenging to determine the derivative of \mathbf{A} , \mathbf{C}_{sf} , \mathbf{C}_{fs} , \mathbf{S}^{-1} , \mathbf{H} , and \mathbf{G} . To overcome this challenge, however, one might use the semi-analytical derivative approach, which uses the finite difference method to compute different coefficient matrices.

Considering the sound power sensitivity on the structure surface Γ , Eq. 33 may be used by differentiating Eq. 15 with regard to design variable θ :

$$\frac{\partial W}{\partial \theta} = \frac{1}{2} \Re \left\{ \left(\frac{\partial \mathbf{p}}{\partial \theta} \right)^T \mathbf{w}_1 + i\omega \mathbf{p}^T \frac{\partial \mathbf{C}_{fs}}{\partial \theta} \mathbf{u}^* + \mathbf{w}_2^T \left(\frac{\partial \mathbf{u}}{\partial \theta} \right)^* \right\}, \quad (33)$$

where

$$\mathbf{w}_1 = i\omega \mathbf{C}_{fs} \mathbf{u}^*,$$

$$\mathbf{w}_2^T = i\omega \mathbf{p}^T \mathbf{C}_{fs}.$$

Introducing the conjugate complex transposed $()^H$, we get Eq. 34:

$$\Re \left\{ \mathbf{w}_2^T \left(\frac{\partial \mathbf{u}}{\partial \theta} \right)^* \right\} = \Re \left\{ \mathbf{w}_2^H \frac{\partial \mathbf{u}}{\partial \theta} \right\}. \quad (34)$$

Applying this to Eq. 33, E. 35 is produced to represent the sound power sensitivity:

$$\frac{\partial W}{\partial \theta} = \frac{1}{2} \Re \left\{ \mathbf{w}_1^T \frac{\partial \mathbf{p}}{\partial \theta} + i\omega \mathbf{p}^T \frac{\partial \mathbf{C}_{fs}}{\partial \theta} \mathbf{u}^* + \mathbf{w}_2^H \frac{\partial \mathbf{u}}{\partial \theta} \right\}. \quad (35)$$

The sum of the first and the third terms in the right side of Eq. 35 can be rewritten as Eq. 36: We may get Eq. 36 by adding the first and third terms of Eq. 35's right side:

$$\mathbf{w}_1^T \frac{\partial \mathbf{p}}{\partial \theta} + \mathbf{w}_2^H \frac{\partial \mathbf{u}}{\partial \theta} = \mathbf{d}^T \begin{bmatrix} \frac{\partial \mathbf{u}}{\partial \theta} \\ \frac{\partial \mathbf{p}}{\partial \theta} \end{bmatrix} = \mathbf{d}^T \mathbf{B}^{-1} \mathbf{r}, \quad (36)$$

where

$$\mathbf{d} = \begin{bmatrix} \mathbf{w}_2^* \\ \mathbf{w}_1 \end{bmatrix}. \quad (37)$$

We may represent the sound power sensitivity on the structure surface as Eq. 38 by substituting Eq. 36 into Eq. 35:

$$\frac{\partial W}{\partial \theta} = \frac{1}{2} \Re \left\{ \mathbf{d}^T \mathbf{B}^{-1} \mathbf{r} + i\omega \mathbf{p}^T \frac{\partial \mathbf{C}_{fs}}{\partial \theta} \mathbf{u}^* \right\}. \quad (38)$$

Two terms make up the structural surface's sound power sensitivity. Eq. 38's first term on the right side can be resolved in one of two ways. One is to first solve $\mathbf{B}\bar{\mathbf{z}} = \mathbf{r}$, a linear system of equations, and then to solve $\mathbf{d}^T \bar{\mathbf{z}}$. The other is to solve $\mathbf{zB} = \mathbf{d}^T$, a linear system of equations, and then \mathbf{zr} . Eq. 26 shows that, in contrast to \mathbf{d} , \mathbf{r} depends on the derivatives of specific terms with respect to the design variable θ . Consequently, m right hand sides \mathbf{r} will be produced by m design variables θ_j with $j = 1, 2, \dots, m$. The linear system of equations $\mathbf{B}\bar{\mathbf{z}} = \mathbf{r}$ must be solved m times using the first method, which takes too much time. The linear system of equations $\mathbf{zB} = \mathbf{d}^T$ only has to be solved once for various design variables when using the second method, though.

When an iterative solver, such as GMRES, is used to solve the adjoint equation $\mathbf{zB} = \mathbf{d}^T$, the convergence is low. Eq. 39 may be used to rewrite the adjoint equation:

$$\mathbf{zB} = [\mathbf{z}_s \quad \mathbf{z}_f] \mathbf{B} = \mathbf{d}^T, \quad (39)$$

where s is the degree of freedom of the structure, f is the degree of freedom of the fluid. Equation 40 illustrates a practical way by splitting the adjoint equation into two reduced coupled sensitivity equations:

$$\mathbf{z}_s \mathbf{A} - \omega^2 \rho_f \mathbf{z}_f \mathbf{G} \mathbf{S}^{-1} \mathbf{C}_{fs} = \mathbf{w}_2^H, \quad (40)$$

$$\mathbf{z}_f \mathbf{H} - \mathbf{z}_s \mathbf{C}_{sf} = \mathbf{w}_1^T. \quad (41)$$

Equation 42 is obtained by transforming Equation 40 into Equation 41 and removing the vector \mathbf{z}_s :

$$\mathbf{z}_f \mathbf{H} - \mathbf{z}_f \mathbf{G} \mathbf{W} \mathbf{C}_{sf} = \mathbf{w}_1^T + \mathbf{w}_2^H \mathbf{A}^{-1} \mathbf{C}_{sf}. \quad (42)$$

The reduced coupled sensitivity equation mentioned above, which is the same as solving Eq. 9, may be used to determine the unidentified fluid vector \mathbf{z}_f . The unknown structural vector \mathbf{z}_s can then be found using Eq. 40. The second term in Eq. 38 vanishes when the design variable is the fluid density ρ , structural density ρ_s , Poisson's ratio ν , Young's modulus E , or structural thickness h because $\frac{\partial \mathbf{C}_{fs}}{\partial \theta} = 0$. However, the term $\frac{\partial \mathbf{C}_{fs}}{\partial \theta}$ does not disappear when the structural form parameter is used as the design variable, such as the radius of the spherical shell r . Although difficult, it is feasible to accurately characterize the sensitivity of \mathbf{C}_{fs} analytically. However, using finite differences provides a straightforward and practical solution to this issue.

3.2 Radiator-peripheral sound power sensitivity on a random closed surface

Equation 43 is created by differentiating Eq. 13 with regard to the design variable θ :

$$\frac{\partial W_A(\omega)}{\partial \theta} = \frac{1}{2} \Re \left\{ \left(\frac{\partial \mathbf{p}_A}{\partial \theta} \right)^T \mathbf{S}_A \mathbf{v}_A^* + \mathbf{p}_A^T \frac{\partial \mathbf{S}_A}{\partial \theta} \mathbf{v}_A^* + \mathbf{p}_A^T \mathbf{S}_A \left(\frac{\partial \mathbf{v}_A}{\partial \theta} \right)^* \right\}. \quad (43)$$

All of the items in vectors $\frac{\partial \mathbf{p}_A}{\partial \theta}$ and $\frac{\partial \mathbf{v}_A}{\partial \theta}$ can be solved using the equations of $\frac{\partial p_A(\mathbf{y})}{\partial \theta}$ and $\frac{\partial v_A(\mathbf{y})}{\partial \theta}$. Eqs 44, 45 may be obtained by differentiating Eqs 16, 19:

$$\begin{aligned} \frac{\partial p_A(\mathbf{y})}{\partial \theta} = & \int_{\Gamma} \frac{\partial G(\mathbf{x}, \mathbf{y})}{\partial \theta} q(\mathbf{x}) d\Gamma(\mathbf{x}) + \int_{\Gamma} G(\mathbf{x}, \mathbf{y}) \frac{\partial q(\mathbf{x})}{\partial \theta} d\Gamma(\mathbf{x}) \\ & + \int_{\Gamma} G(\mathbf{x}, \mathbf{y}) q(\mathbf{x}) \frac{\partial d\Gamma(\mathbf{x})}{\partial \theta} - \int_{\Gamma} \frac{\partial F(\mathbf{x}, \mathbf{y})}{\partial \theta} p(\mathbf{x}) d\Gamma(\mathbf{x}) \\ & - \int_{\Gamma} F(\mathbf{x}, \mathbf{y}) \frac{\partial p(\mathbf{x})}{\partial \theta} d\Gamma(\mathbf{x}) - \int_{\Gamma} F(\mathbf{x}, \mathbf{y}) p(\mathbf{x}) \frac{\partial d\Gamma(\mathbf{x})}{\partial \theta}, \end{aligned} \quad (44)$$

and

$$\begin{aligned} \frac{\partial v_A(\mathbf{y})}{\partial \theta} = & \frac{i}{\omega \rho} \int_{\Gamma} \frac{\partial^2 G(\mathbf{x}, \mathbf{y})}{\partial n(\mathbf{y}) \partial \theta} q(\mathbf{x}) d\Gamma(\mathbf{x}) + \frac{i}{\omega \rho} \int_{\Gamma} \frac{\partial G(\mathbf{x}, \mathbf{y})}{\partial n(\mathbf{y})} \frac{\partial q(\mathbf{x})}{\partial \theta} d\Gamma(\mathbf{x}) \\ & + \frac{i}{\omega \rho} \int_{\Gamma} \frac{\partial G(\mathbf{x}, \mathbf{y})}{\partial n(\mathbf{y})} q(\mathbf{x}) \frac{\partial d\Gamma(\mathbf{x})}{\partial \theta} - \frac{i}{\omega \rho} \int_{\Gamma} \frac{\partial^2 F(\mathbf{x}, \mathbf{y})}{\partial n(\mathbf{y}) \partial \theta} p(\mathbf{x}) d\Gamma(\mathbf{x}) \\ & - \frac{i}{\omega \rho} \int_{\Gamma} \frac{\partial F(\mathbf{x}, \mathbf{y})}{\partial n(\mathbf{y})} \frac{\partial p(\mathbf{x})}{\partial \theta} d\Gamma(\mathbf{x}) - \frac{i}{\omega \rho} \int_{\Gamma} \frac{\partial F(\mathbf{x}, \mathbf{y})}{\partial n(\mathbf{y})} p(\mathbf{x}) \frac{\partial d\Gamma(\mathbf{x})}{\partial \theta} \\ & + \frac{i}{\omega} \frac{\partial \rho^{-1}}{\partial \theta} \int_{\Gamma} \frac{\partial G(\mathbf{x}, \mathbf{y})}{\partial n(\mathbf{y})} q(\mathbf{x}) d\Gamma(\mathbf{x}) - \frac{i}{\omega} \frac{\partial \rho^{-1}}{\partial \theta} \int_{\Gamma} \frac{\partial F(\mathbf{x}, \mathbf{y})}{\partial n(\mathbf{y})} p(\mathbf{x}) d\Gamma(\mathbf{x}), \end{aligned} \quad (45)$$

where

$$\frac{\partial G(\mathbf{x}, \mathbf{y})}{\partial \theta} = -\frac{e^{ikr}}{4\pi r^2} (1 - ikr) \frac{\partial r}{\partial x_i} \left(\frac{\partial x_i}{\partial \theta} - \frac{\partial y_i}{\partial \theta} \right), \quad (46)$$

$$\begin{aligned} \frac{\partial F(\mathbf{x}, \mathbf{y})}{\partial \theta} = & \frac{e^{ikr}}{4\pi r^3} \left[(3 - 3ikr - k^2 r^2) \frac{\partial r}{\partial n(\mathbf{x})} \frac{\partial r}{\partial x_i} - (1 - ikr) n_i(\mathbf{x}) \right] \\ & \times \left(\frac{\partial x_i}{\partial \theta} - \frac{\partial y_i}{\partial \theta} \right) - \frac{e^{ikr}}{4\pi r^2} (1 - ikr) \frac{\partial r}{\partial x_i} \frac{\partial n_i(\mathbf{x})}{\partial \theta}, \end{aligned} \quad (47)$$

$$\begin{aligned} \frac{\partial^2 G(\mathbf{x}, \mathbf{y})}{\partial n(\mathbf{y}) \partial \theta} = & \frac{e^{ikr}}{4\pi r^3} \left[(3 - 3ikr - k^2 r^2) \frac{\partial r}{\partial n(\mathbf{y})} \frac{\partial r}{\partial y_i} - (1 - ikr) n_i(\mathbf{y}) \right] \\ & \times \left(\frac{\partial y_i}{\partial \theta} - \frac{\partial x_i}{\partial \theta} \right) - \frac{e^{ikr}}{4\pi r^2} (1 - ikr) \frac{\partial r}{\partial y_i} \frac{\partial n_i(\mathbf{y})}{\partial \theta}, \end{aligned} \quad (48)$$

$$\begin{aligned} \frac{\partial^2 F(\mathbf{x}, \mathbf{y})}{\partial n(\mathbf{y}) \partial \theta} = & -\frac{e^{ikr}}{4\pi r^4} \left[(15 - 15ikr - 6k^2 r^2 + ik^3 r^3) \frac{\partial r}{\partial n(\mathbf{x})} \frac{\partial r}{\partial n(\mathbf{y})} \frac{\partial r}{\partial y_k} \right. \\ & \left. - (3 - 3ikr - k^2 r^2) \left(n_k(\mathbf{y}) \frac{\partial r}{\partial n(\mathbf{x})} - n_k(\mathbf{x}) \frac{\partial r}{\partial n(\mathbf{y})} - n_j(\mathbf{x}) n_j(\mathbf{y}) \frac{\partial r}{\partial y_k} \right) \right] \\ & \times \left(\frac{\partial y_k}{\partial \theta} - \frac{\partial x_k}{\partial \theta} \right) + \frac{e^{ikr}}{4\pi r^3} \left[(3 - 3ikr - k^2 r^2) \right. \\ & \times \left(\frac{\partial r}{\partial n(\mathbf{y})} \frac{\partial r}{\partial x_i} \frac{\partial n_i(\mathbf{x})}{\partial \theta} + \frac{\partial r}{\partial n(\mathbf{x})} \frac{\partial r}{\partial y_j} \frac{\partial n_j(\mathbf{y})}{\partial \theta} \right) \\ & \left. + (1 - ikr) \left(\frac{\partial n_j(\mathbf{x})}{\partial \theta} n_j(\mathbf{y}) + n_j(\mathbf{x}) \frac{\partial n_j(\mathbf{y})}{\partial \theta} \right) \right], \end{aligned} \quad (49)$$

and

$$\frac{\partial d\Gamma}{\partial \theta} = \left[\frac{\partial^2 x_i}{\partial \theta \partial x_i} - \frac{\partial^2 x_i}{\partial \theta \partial x_j} n_i(\mathbf{x}) n_j(\mathbf{x}) \right] d\Gamma, \quad (50)$$

where $\frac{\partial x_i}{\partial \theta}$ will be determined once the design variable has been used to fully parameterize the examined domain's boundary.

Equations 51 and 52 may be obtained by discretizing Eqs 44, 45:

$$\frac{\partial p_A(\mathbf{y})}{\partial \theta} = \mathbf{g}_2^T(\mathbf{y}, \theta) \mathbf{q} + \mathbf{g}^T(\mathbf{y}) \frac{\partial \mathbf{q}}{\partial \theta} - \mathbf{h}_2^T(\mathbf{y}, \theta) \mathbf{p} - \mathbf{h}^T(\mathbf{y}) \frac{\partial \mathbf{p}}{\partial \theta}, \quad (51)$$

$$\begin{aligned} \frac{\partial v_A(\mathbf{y})}{\partial \theta} = & \frac{i}{\omega \rho} \mathbf{g}_3^T(\mathbf{y}, \theta) \mathbf{q} + \frac{i}{\omega \rho} \mathbf{g}_1^T(\mathbf{y}) \frac{\partial \mathbf{q}}{\partial \theta} - \frac{i}{\omega \rho} \mathbf{h}_3^T(\mathbf{y}, \theta) \mathbf{p} \\ & - \frac{i}{\omega \rho} \mathbf{h}_1^T(\mathbf{y}) \frac{\partial \mathbf{p}}{\partial \theta} + \frac{i}{\omega} \frac{\partial \rho^{-1}}{\partial \theta} [\mathbf{g}_1^T(\mathbf{y}) \mathbf{q} - \mathbf{h}_1^T(\mathbf{y}) \mathbf{p}], \end{aligned} \quad (52)$$

where \mathbf{g}_2 , \mathbf{g}_3 , \mathbf{h}_2 , and \mathbf{h}_3 are coefficient vectors.

Equation 51's \mathbf{g}_2 and \mathbf{h}_2 as well as Equation 52's \mathbf{g}_3 and \mathbf{h}_3 disappear when the fluid density ρ is chosen as the design variable. Eqs 51, 52 may be rewritten as Eqs 53, 54 as a result:

$$\frac{\partial p_A(\mathbf{y})}{\partial \rho} = \mathbf{g}^T(\mathbf{y}) \frac{\partial \mathbf{q}}{\partial \rho} - \mathbf{h}^T(\mathbf{y}) \frac{\partial \mathbf{p}}{\partial \rho}, \quad (53)$$

$$\frac{\partial v_A(\mathbf{y})}{\partial \rho} = \frac{i}{\omega \rho} \mathbf{g}_1^T(\mathbf{y}) \frac{\partial \mathbf{q}}{\partial \rho} - \frac{i}{\omega \rho} \mathbf{h}_1^T(\mathbf{y}) \frac{\partial \mathbf{p}}{\partial \rho} - \frac{i}{\rho^2 \omega} [\mathbf{g}_1^T(\mathbf{y}) \mathbf{q} - \mathbf{h}_1^T(\mathbf{y}) \mathbf{p}]. \quad (54)$$

The variables \mathbf{g}_2 and \mathbf{h}_2 in Equation 51 and \mathbf{g}_3 and \mathbf{h}_3 in Equation 52 disappear when the structural parameter is chosen as the design variable, such as the thickness of the spherical shell, as given in the following numerical example. Eqs 51, 52 are thus equivalent to Eqs 55, 56:

$$\frac{\partial p_A(\mathbf{y})}{\partial \theta} = \mathbf{g}^T(\mathbf{y}) \frac{\partial \mathbf{q}}{\partial \theta} - \mathbf{h}^T(\mathbf{y}) \frac{\partial \mathbf{p}}{\partial \theta}, \quad (55)$$

$$\frac{\partial v_A(\mathbf{y})}{\partial \theta} = \frac{i}{\omega \rho} \mathbf{g}_1^T(\mathbf{y}) \frac{\partial \mathbf{q}}{\partial \theta} - \frac{i}{\omega \rho} \mathbf{h}_1^T(\mathbf{y}) \frac{\partial \mathbf{p}}{\partial \theta}. \quad (56)$$

\mathbf{g}_2 , \mathbf{g}_3 , \mathbf{h}_2 , and \mathbf{h}_3 do not disappear when the structural form parameter, such as the radius of the spherical shell, is specified as the design variable. Eqs 51, 52 may be written as Eqs 57, 58 as a result:

$$\frac{\partial p_A(\mathbf{y})}{\partial \theta} = \mathbf{g}_2^T(\mathbf{y}, \theta) \mathbf{q} + \mathbf{g}^T(\mathbf{y}) \frac{\partial \mathbf{q}}{\partial \theta} - \mathbf{h}_2^T(\mathbf{y}, \theta) \mathbf{p} - \mathbf{h}^T(\mathbf{y}) \frac{\partial \mathbf{p}}{\partial \theta}, \quad (57)$$

$$\begin{aligned} \frac{\partial v_A(\mathbf{y})}{\partial \theta} = & \frac{i}{\omega \rho} \mathbf{g}_3^T(\mathbf{y}, \theta) \mathbf{q} + \frac{i}{\omega \rho} \mathbf{g}_1^T(\mathbf{y}) \frac{\partial \mathbf{q}}{\partial \theta} - \frac{i}{\omega \rho} \mathbf{h}_3^T(\mathbf{y}, \theta) \mathbf{p} \\ & - \frac{i}{\omega \rho} \mathbf{h}_1^T(\mathbf{y}) \frac{\partial \mathbf{p}}{\partial \theta}. \end{aligned} \quad (58)$$

The derivatives of $p_A(\mathbf{y})$ and $v_A(\mathbf{y})$ are both shown to be determined by \mathbf{p} , \mathbf{q} , and their derivatives by Eqs 51, 52. Equations 2, 5, 9, in that order, may be used to produce the vectors \mathbf{p} , \mathbf{u} , and \mathbf{v}_f . Using the continuity condition throughout the interaction surface, the vector \mathbf{q} may then be found. We still need to find the solution to the unknown vectors $\frac{\partial \mathbf{p}}{\partial \theta}$ and $\frac{\partial \mathbf{q}}{\partial \theta}$, though.

Equation 26 cannot be directly solved because the system matrix is too enormous for problems of this kind. Equations 59 and 60 can be used to separate the system Equation 26:

$$\mathbf{A} \frac{\partial \mathbf{u}}{\partial \theta} - \mathbf{C}_{sf} \frac{\partial \mathbf{p}}{\partial \theta} = \mathbf{r}_1, \quad (59)$$

$$\mathbf{H} \frac{\partial \mathbf{p}}{\partial \theta} - \omega^2 \rho \mathbf{G} \mathbf{S}^{-1} \mathbf{C}_{fs} \frac{\partial \mathbf{u}}{\partial \theta} = \mathbf{r}_2. \quad (60)$$

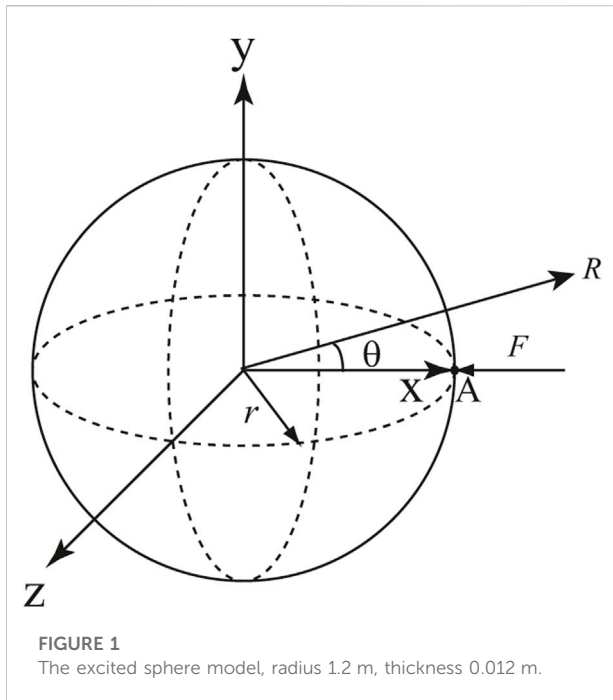


FIGURE 1
The excited sphere model, radius 1.2 m, thickness 0.012 m.

Equation 61 may be obtained by substituting Equation 59 into Equation 60:

$$\mathbf{H} \frac{\partial \mathbf{p}}{\partial \theta} - \mathbf{GWC}_{st} \frac{\partial \mathbf{p}}{\partial \theta} = \mathbf{GWr}_1 + \mathbf{r}_2. \quad (61)$$

Equation 61 and Equation 9 are quite similar, hence the same approach to solving both is used. Equation 59 may be used to solve the unknown vector $\frac{\partial \mathbf{u}}{\partial \theta}$ once the foregoing equation has been solved to get the sensitivity of the nodal sound pressure on the structural surface, denoted by the symbol $\frac{\partial \mathbf{p}}{\partial \theta}$. Equation 62 is obtained by differentiating Equation 5 with respect to the design variable and applying the continuity condition over the interaction surface:

$$\frac{\partial \mathbf{q}}{\partial \theta} = i\omega \frac{\partial \rho}{\partial \theta} \mathbf{v}_f + \omega^2 \rho \left[\frac{\partial (\mathbf{S}^{-1} \mathbf{C}_{fs})}{\partial \theta} \mathbf{u} + \mathbf{S}^{-1} \mathbf{C}_{fs} \frac{\partial \mathbf{u}}{\partial \theta} \right]. \quad (62)$$

We may find $\frac{\partial \mathbf{q}}{\partial \theta}$ by using Equation 62. Equations 51 and 52 may be used to get the derivatives of $p_A(\mathbf{y})$ and $v_A(\mathbf{y})$ at each node on surface A. Equation 63 can be used to describe the derivative of S_A on the right side of Equation 43:

$$\frac{\partial S_A}{\partial \theta} = \int_A \mathbf{N}_f^T \mathbf{N}_r \frac{\partial dA(\mathbf{y})}{\partial \theta}. \quad (63)$$

Once the computing surface does not change when the design variable changes, $\frac{\partial S_A}{\partial \theta} = 0$ causes the second term on the right side of Eq. 43 to disappear. Equation 43 may be used to get the derivative of the radiated sound power on surface A after obtaining the solutions of $\frac{\partial \mathbf{p}_A}{\partial \theta}$ and $\frac{\partial \mathbf{v}_A}{\partial \theta}$.

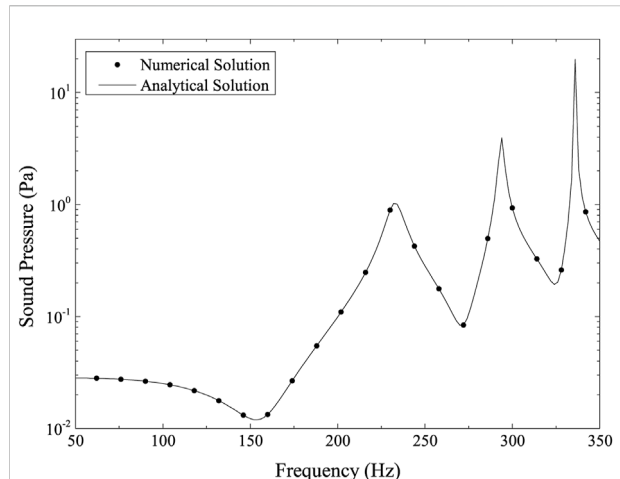


FIGURE 2
Sound pressure at point (2.4, 0, 0).

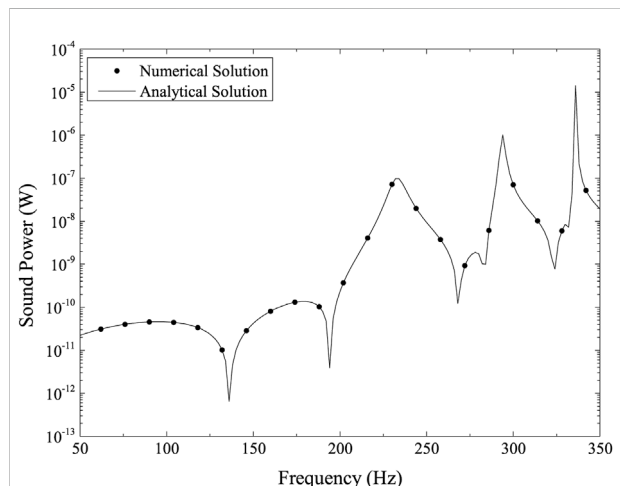


FIGURE 3
Sound power on the structural shell surface.

4 Numerical examples

In this section, some numerical tests are run to look at the reliability and viability of the established approach. In each example, the acoustic analysis employs discontinuous linear boundary element, while the finite element analysis uses shell element. A custom Fortran 95/2003 code written in-house is used for all the computations.

4.1 An elastic sphere excited by a unit force

The sound field of an underwater thin spherical shell centered at position (0, 0, 0) is investigated in this illustration

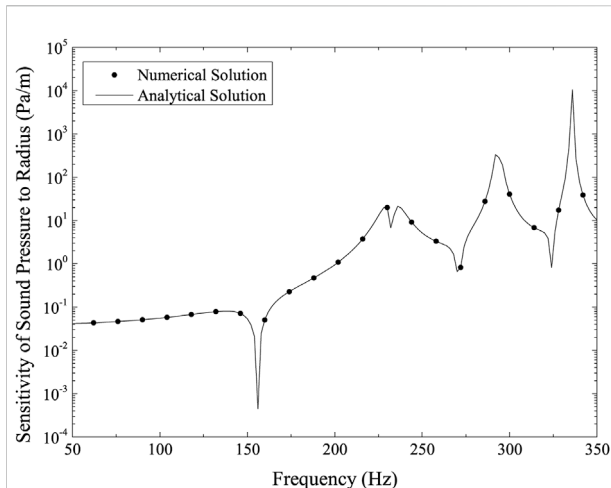


FIGURE 4
Sensitivity of sound pressure at point (2.4, 0, 0) to shell radius.

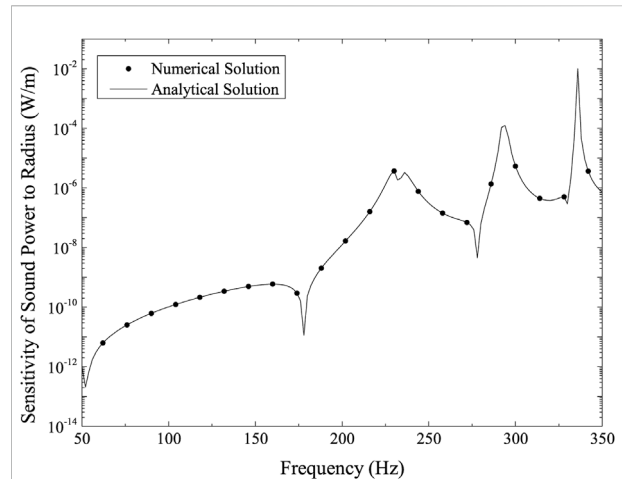


FIGURE 6
Structural surface's sensitivity of sound power to shell radius.

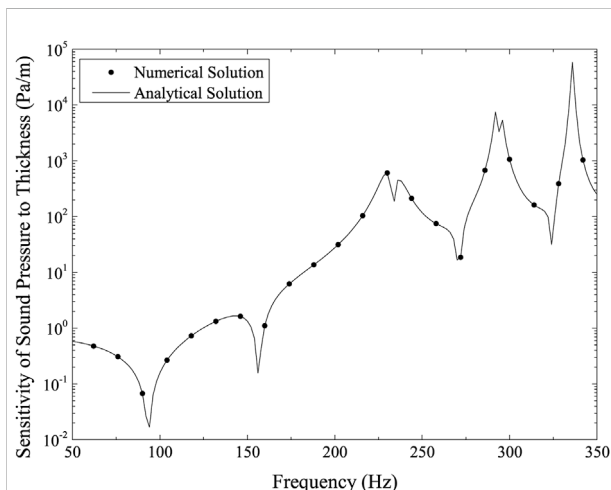


FIGURE 5
Sensitivity of sound pressure at point (2.4, 0, 0) to shell thickness.

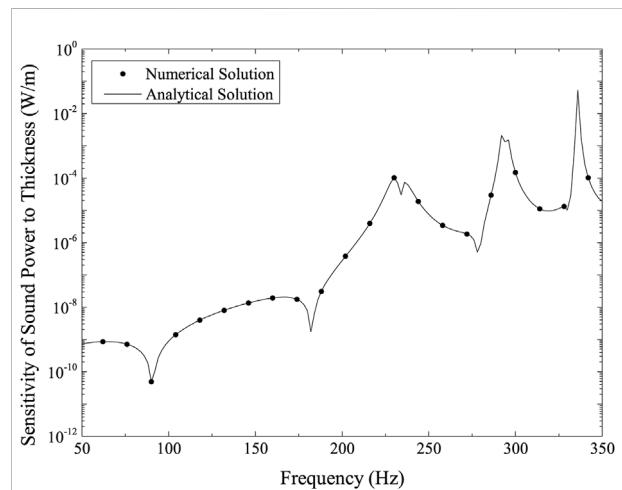
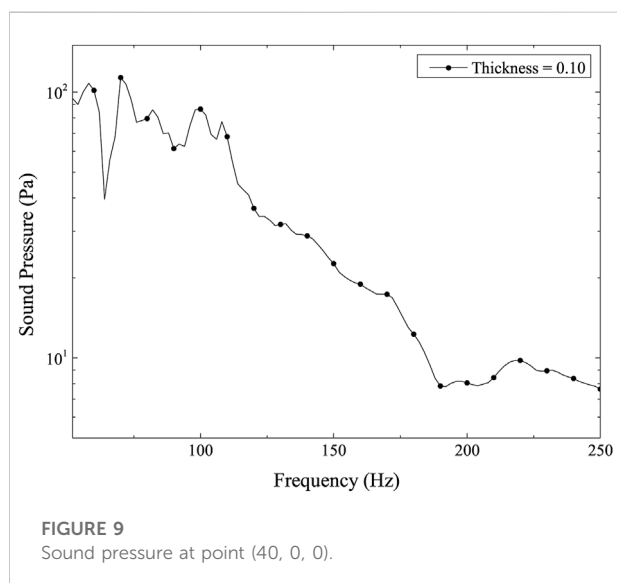
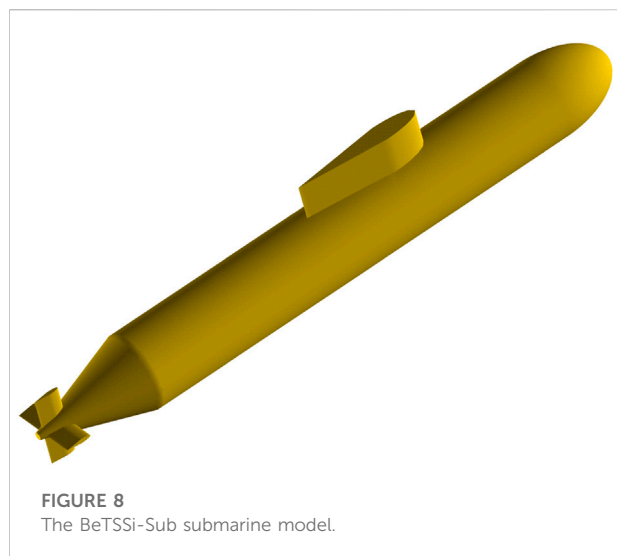


FIGURE 7
Structural surface's sensitivity of sound power to shell thickness.

while accounting for a concentrated force F applied at point A (r , 0, 0), where r stands for the radius of the spherical shell, as seen in Figure 1. The material and geometrical features employed in this example are as follows:

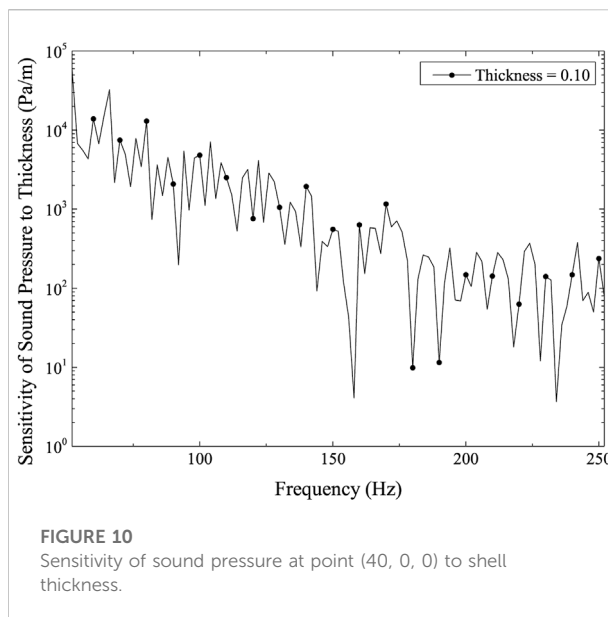
- radius of the shell is 1.2 m,
- thickness of the shell is 0.012 m,
- elasticity modulus of the shell is 2.10×10^{11} Pa,
- Poisson's ratio of the shell is 0.3,
- structural density is 7.86×10^3 kg/m³,
- fluid density is 1.00×10^3 kg/m³,
- sound velocity in water is 1.482×10^3 m/s.

The numerical and analytical solutions, expressed in terms of frequencies, for the sound pressure at point (2.4, 0, 0), are shown in Figure 2. The numerical and analytical solutions, expressed in terms of frequencies, for the sound power on the structural shell surface, are shown in Figure 3. The linear systems are solved using the GMRES implementation without preconditioning, and the wideband FMM algorithm is used to speed up the solving process. 6,144 elements make up the discretized thin-shell model. These figures both demonstrate the good agreement between the numerical and analytical solutions,



demonstrating that the wideband FMM method preserves the excellent accuracy of traditional BEM.

Figures 4, 5 depicts the structure surface's sensitivity of sound pressure to the sphere's radius and its shell thickness, respectively. Figures 6, 7 illustrates the structural surface's sensitivity of sound power to the sphere's radius and its shell thickness, respectively. These four figures show a remarkably similar pattern. These figures show that the numerical and analytical results accord rather well. The figures illustrate how the sound pressure or sound power sensitivity is very modest in the low-frequency range but substantially increases at resonance peaks.



4.2 A BeTSSi-Sub submarine model under incident wave

The scattering sound field of the underwater submarine model under the influence of plane waves is the subject of this section. The incident wave amplitude is 1.0 Pa, and the plane wave propagates positively along the x-axis. The generic model BeTSSi-Sub presented at the World Digital Simulation Conference in 2002 is adopted by the model. The model has a 0.10 m thickness. The positive x-axis direction is from the bow to the stern, and the origin of the coordinate is located at the intersection of the circle that connects the bow and the hull. For the specific geometric characteristics of the BeTSSi-Sub model, please refer to Figure 3, 4 in [58]. Figure 8 displays the submarine model, with a total of 27,034 elements.

The point for the computation is (40, 0, 0). Figure 9 shows the calculation result of sound pressure at point (40, 0, 0), and Figure 10 is the sensitivity of sound pressure at point (40, 0, 0) to shell thickness. Figures 9, 10 show that when the calculation frequency rises, both the sound pressure and its sensitivity to thickness gradually decline. Given that the sound pressure is significantly higher and more sensitive to changes in structural thickness in the lower frequency band, these two figures show that the lower frequency band is a crucial region for the BeTSSi-Sub model with the current material and geometrical specifications.

5 Conclusion

The simulation of acoustic-structure interaction and sensitivity analysis is done using a coupling method based on FEM and BEM. Modelling the problem's structural components is done using the FEM. The BEM is used to discretize the border of the acoustic domain,

which is the boundary of the considered structure under consideration, in order to eliminate the necessity to mesh the acoustic domain. Boundary element analysis uses the FMM to speed up the matrix-vector products. Through the use of IGABEM, structural-acoustic interaction and its sensitivity analysis may be carried out straight from CAD models without the need for meshing, while also eradicating geometric flaws. Equations for the radiated sound power sensitivity are developed for fully linked structural-acoustic systems. The sensitivity of the sound power emitted on the structure surface is calculated using an adjoint operator technique. The sensitivity of the emitted sound power on any closed surface around the radiator is determined using the direct differentiation method. The formulas used to compute the derivative of the radiated sound power for various design factors are provided. Numerical illustrations are provided to show the precision and viability of the suggested approach. The suggested approach may be applied to large-scale practical situations to quantitatively forecast the impact of various design factors on the sound field. Future study will involve extending the created method to real-world engineering issues and using the structural-acoustic design sensitivity analysis to optimization challenges.

Data availability statement

The original contributions presented in the study are included in the article/Supplementary Material, further inquiries can be directed to the corresponding author.

References

1. Junger MC, Feit D. *Sound, structures, and their interaction*, 225. Cambridge, MA: MIT press (1986).
2. Xu Y, Li H, Chen L, Zhao J, Zhang X. Monte Carlo based isogeometric stochastic finite element method for uncertainty quantization in vibration analysis of piezoelectric materials. *Mathematics* (2022) 10:1840. doi:10.3390/math10111840
3. Chen L, Lian H, Xu Y, Li S, Liu Z, Atroshchenko E, et al. Generalized isogeometric boundary element method for uncertainty analysis of time-harmonic wave propagation in infinite domains. *Appl Math Model* (2022) 114: 360–78. doi:10.1016/j.apm.2022.09.030
4. Everstine GC, Henderson FM. Coupled finite element/boundary element approach for fluid-structure interaction. *The J Acoust Soc America* (1990) 87: 1938–47. doi:10.1121/1.399320
5. Chen Z, Hofstetter G, Mang H. A Galerkin-type BE-FE formulation for elasto-acoustic coupling. *Comput Methods Appl Mech Eng* (1998) 152:147–55. Containing papers presented at the Symposium on Advances in Computational Mechanics. doi:10.1016/S0045-7825(97)00187-4
6. Marburg S. Developments in structural-acoustic optimization for passive noise control. *Arch Comput Methods Eng* (2002) 9:291–370. doi:10.1007/BF03041465
7. Schneider S. FE/FMBE coupling to model fluid-structure interaction. *Int J Numer Methods Eng* (2008) 76:2137–56. doi:10.1002/nme.2399
8. Brunner D, Junge M, Gaul L. A comparison of FE-BE coupling schemes for large-scale problems with fluid-structure interaction. *Int J Numer Methods Eng* (2009) 77:664–88. doi:10.1002/nme.2412
9. Merz S, Kinns R, Kessissoglou N. Structural and acoustic responses of a submarine hull due to propeller forces. *J Sound Vibration* (2009) 325:266–86. doi:10.1016/j.jsv.2009.03.011
10. Merz S, Kessissoglou N, Kinns R, Marburg S. Passive and active control of the radiated sound power from a submarine excited by propeller forces. *J Ship Res* (2013) 57:59–71. doi:10.5957/jsr.2013.57.1.59
11. Peters H, Kessissoglou N, Marburg S. Modal decomposition of exterior acoustic-structure interaction. *J Acoust Soc America* (2013) 133:2668–77. doi:10.1121/1.4796114
12. van Opstal T, van Brummelen E, van Zwielen G. A finite-element/boundary-element method for three-dimensional, large-displacement fluid-structure-interaction. *Comput Methods Appl Mech Eng* (2015) 284:637–63. Isogeometric Analysis Special Issue. doi:10.1016/j.cma.2014.09.037
13. Tadeu A, António J. Use of constant, linear and quadratic boundary elements in 3D wave diffraction analysis. *Eng Anal Boundary Elem* (2000) 24:131–44. doi:10.1016/S0955-7997(99)00064-8
14. Marburg S, Schneider S. Influence of element types on numeric error for acoustic boundary elements. *J Comp Acous* (2003) 11:363–86. doi:10.1142/S0218396X03001985
15. Trevelyan J. Use of discontinuous boundary elements for fracture mechanics analysis. *Eng Anal Boundary Elem* (1992) 10:353–8. doi:10.1016/0955-7997(92)90150-6
16. Florez W, Power H. Comparison between continuous and discontinuous boundary elements in the multidomain dual reciprocity method for the solution of the two-dimensional Navier-Stokes equations. *Eng Anal Boundary Elem* (2001) 25: 57–69. doi:10.1016/S0955-7997(00)00051-5
17. Atkinson KE. The numerical solution of integral equations of the second kind. In: *Cambridge monographs on applied and computational mathematics*. Cambridge: University of Cambridge (1996).
18. Chen L, Chen H, Zheng C, Marburg S. Structural-acoustic sensitivity analysis of radiated sound power using a finite element/discontinuous fast multipole boundary element scheme. *Int J Numer Methods Fluids* (2016) 82:858–78. doi:10.1002/flid.4244
19. Greengard L, Rokhlin V. A fast algorithm for particle simulations. *J Comput Phys* (1987) 73:325–48. doi:10.1016/0021-9991(87)90140-9

Author contributions

Conceptualization, XC; Data curation, XC; Formal analysis, RC; Investigation, JZ; Methodology, XC and YX; Project administration, YX; Software, XC and WM; Supervision, YX; Validation, WM; Visualization, RC; Writing—original draft, XC and JZ. All authors have read and agreed to the published version of the manuscript.

Conflict of interest

The authors declare that the research was conducted in the absence of any commercial or financial relationships that could be construed as a potential conflict of interest.

Publisher's note

All claims expressed in this article are solely those of the authors and do not necessarily represent those of their affiliated organizations, or those of the publisher, the editors and the reviewers. Any product that may be evaluated in this article, or claim that may be made by its manufacturer, is not guaranteed or endorsed by the publisher.

20. Coifman R, Rokhlin V, Wandzura S. The fast multipole method for the wave equation: a pedestrian prescription. *IEEE Antennas Propag Mag* (1993) 35:7–12. doi:10.1109/74.250128
21. Schneider S. Application of fast methods for acoustic scattering and radiation problems. *J Comp Acous* (2003) 11:387–401. doi:10.1142/S0218396X03002012
22. Shen L, Liu YJ. An adaptive fast multipole boundary element method for three-dimensional acoustic wave problems based on the Burton-Miller formulation. *Comput Mech* (2007) 40:461–72. doi:10.1007/s00466-006-0121-2
23. Saad Y (2003). *Iterative methods for sparse linear systems* (SIAM). US: Society for Industrial and Applied Mathematics
24. Marburg S, Schneider S. Performance of iterative solvers for acoustic problems. Part I. Solvers and effect of diagonal preconditioning. *Eng Anal Bound Elem* (2003) 27:727–50. doi:10.1016/S0955-7997(03)00025-0
25. Gumerov NA, Duraiswami R. A broadband fast multipole accelerated boundary element method for the three dimensional Helmholtz equation. *J Acoust Soc America* (2009) 125:191–205. doi:10.1121/1.3021297
26. Wolf WR, Lele SK. Wideband fast multipole boundary element method: Application to acoustic scattering from aerodynamic bodies. *Int J Numer Methods Fluids* (2011) 67:2108–29. doi:10.1002/flid.2486
27. Dühring MB, Jensen JS, Sigmund O. Acoustic design by topology optimization. *J Sound Vibration* (2008) 317:557–75. doi:10.1016/j.jsv.2008.03.042
28. Hughes T, Cottrell J, Bazilevs Y. Isogeometric analysis: CAD, finite elements, NURBS, exact geometry and mesh refinement. *Comput Methods Appl Mech Eng* (2005) 194:4135–95. doi:10.1016/j.cma.2004.10.008
29. Simpson R, Bordas S, Trevelyan J, Rabczuk T. A two-dimensional isogeometric boundary element method for elastostatic analysis. *Comput Methods Appl Mech Eng* (2012) 209:212:87–100. doi:10.1016/j.cma.2011.08.008
30. Simpson R, Bordas S, Lian H, Trevelyan J. An isogeometric boundary element method for elastostatic analysis: 2D implementation aspects. *Comput Struct* (2013) 118:2–12. Issue: UK Association for Computational Mechanics in Engineering. doi:10.1016/j.compstruc.2012.12.021
31. Scott M, Simpson R, Evans J, Lipton S, Bordas S, Hughes T, et al. Isogeometric boundary element analysis using unstructured T-splines. *Comput Methods Appl Mech Eng* (2013) 254:197–221. doi:10.1016/j.cma.2012.11.001
32. Chen L, Lian H, Natarajan S, Zhao W, Chen X, Bordas S. Multi-frequency acoustic topology optimization of sound-absorption materials with isogeometric boundary element methods accelerated by frequency-decoupling and model order reduction techniques. *Comput Methods Appl Mech Eng* (2022) 395:114997. doi:10.1016/j.cma.2022.114997
33. Chen L, Wang Z, Peng X, Yang J, Wu P, Lian H. Modeling pressurized fracture propagation with the isogeometric bem. *Geomech Geophys Geo Eng Ge Resour* (2021) 7:51. doi:10.1007/s40948-021-00248-3
34. Xu G, Mourrain B, Duvigneau R, Galligo A. Parameterization of computational domain in isogeometric analysis: Methods and comparison. *Comput Methods Appl Mech Eng* (2011) 200:2021–31. doi:10.1016/j.cma.2011.03.005
35. Xu G, Li M, Mourrain B, Rabczuk T, Xu J, Bordas SP. Constructing IGA-suitable planar parameterization from complex CAD boundary by domain partition and global/local optimization. *Comput Methods Appl Mech Eng* (2018) 328:175–200. doi:10.1016/j.cma.2017.08.052
36. Kostas K, Ginnis A, Politis C, Kaklis P. Ship-hull shape optimization with a T-spline based BEM-isogeometric solver. *Comput Methods Appl Mech Engisogeometric Anal Spec Issue* (2015) 284:611–22. doi:10.1016/j.cma.2014.10.030
37. Lian H, Kerfriden P, Bordas S. Shape optimization directly from CAD: An isogeometric boundary element approach using T-splines. *Comput Methods Appl Mech Eng* (2017) 317:1–41. doi:10.1016/j.cma.2016.11.012
38. Li S, Trevelyan J, Wu Z, Lian H, Wang D, Zhang W. An adaptive SVD-Krylov reduced order model for surrogate based structural shape optimization through isogeometric boundary element method. *Comput Methods Appl Mech Eng* (2019) 349:312–38. doi:10.1016/j.cma.2019.02.023
39. Simpson R, Scott M, Taus M, Thomas D, Lian H. Acoustic isogeometric boundary element analysis. *Comput Methods Appl Mech Eng* (2014) 269:265–90. doi:10.1016/j.cma.2013.10.026
40. Chen L, Liu C, Zhao W, Liu L. An isogeometric approach of two dimensional acoustic design sensitivity analysis and topology optimization analysis for absorbing material distribution. *Comput Methods Appl Mech Eng* (2018) 336:507–32. doi:10.1016/j.cma.2018.03.025
41. Chen L, Lian H, Liu Z, Chen H, Atroshchenko E, Bordas S. Structural shape optimization of three dimensional acoustic problems with isogeometric boundary element methods. *Comput Methods Appl Mech Eng* (2019) 355:926–51. doi:10.1016/j.cma.2019.06.012
42. Chen L, Lu C, Lian H, Liu Z, Zhao W, Li S, et al. Acoustic topology optimization of sound absorbing materials directly from subdivision surfaces with isogeometric boundary element methods. *Comput Methods Appl Mech Eng* (2020) 362:112806. doi:10.1016/j.cma.2019.112806
43. Peng X, Atroshchenko E, Kerfriden P, Bordas S. Isogeometric boundary element methods for three dimensional static fracture and fatigue crack growth. *Comput Methods Appl Mech Eng* (2017) 316:151–85. Special Issue on Isogeometric Analysis: Progress and Challenges. doi:10.1016/j.cma.2016.05.038
44. Peng X, Atroshchenko E, Kerfriden P, Bordas S. Linear elastic fracture simulation directly from CAD: 2D NURBS-based implementation and role of tip enrichment. *Int J Fract* (2017) 204:55–78. doi:10.1007/s10704-016-0153-3
45. Zhang J, Zhang W, Zhu J, Xia L. Integrated layout design of multi-component systems using XFEM and analytical sensitivity analysis. *Comput Methods Appl Mech Eng* (2012) 245:246:75–89. doi:10.1016/j.cma.2012.06.022
46. Lamancusa J. Numerical optimization techniques for structural-acoustic design of rectangular panels. *Comput Structures* (1993) 48:661–75. doi:10.1016/0045-7949(93)90260-K
47. Hambric SA. Sensitivity calculations for broad-band Acoustic radiated noise design optimization problems. *J Vib Acoust* (1996) 118:529–32. doi:10.1115/1.2888219
48. Marburg S, Hardtke H-J. Shape optimization of a vehicle hat-shelf: improving acoustic properties for different load cases by maximizing first eigenfrequency. *Comput Structures* (2001) 79:1943–57. doi:10.1016/S0045-7949(01)00107-9
49. Haftka RT, Adelman HM. Recent developments in structural sensitivity analysis. *Struct Optimization* (1989) 1:137–51. doi:10.1007/BF01637334
50. Marburg S. Efficient optimization of a noise transfer function by modification of a shell structure geometry - Part I: Theory. *Struct Multidiscip Optim* (2002) 24: 51–9. doi:10.1007/s00158-002-0213-3
51. Fritze D, Marburg S, Hardtke H-J. FEM-BEM-coupling and structural-acoustic sensitivity analysis for shell geometries. *Comput Struct* (2005) 83: 143–54. doi:10.1016/j.compstruc.2004.05.019
52. Choi K, Shim I, Wang S. Design sensitivity analysis of structure-induced noise and vibration. *J Vib Acoust* (1997) 119:173–9. doi:10.1115/1.2889699
53. Wang S. Design sensitivity analysis of noise, vibration, and harshness of vehicle body structure. *Mech Structures Machines* (1999) 27:317–35. doi:10.1080/08905459908915701
54. Cirak F, Ortiz M, Schröder P. Subdivision surfaces: a new paradigm for thin-shell finite-element analysis. *Int J Numer Methods Eng* (2000) 47:2039–72. doi:10.1002/(SICI)1097-0207(20000430)47:12<2039::AID-NME872>3.0.CO;2-1
55. Ciskowski RD, Brebbia CA. *Boundary element methods in acoustics*. Germany: Springer (1991).
56. Chen L, Cheng R, Li S, Lian H, Zheng C, Bordas S. A sample-efficient deep learning method for multivariate uncertainty qualification of acoustic-vibration interaction problems. *Comput Methods Appl Mech Eng* (2022) 393:114784. doi:10.1016/j.cma.2022.114784
57. Chen L, Lian H, Liu Z, Gong Y, Zheng C, Bordas S. Bi-material topology optimization for fully coupled structural-acoustic systems with isogeometric fem-bem. *Eng Anal Boundary Elem* (2022) 135:182–95. doi:10.1016/j.enganabound.2021.11.005
58. Nell CW, Gilroy LE. An improved basis model for the betssi submarine. *DRDC Atlantic TR* (2003) 199:2003.



OPEN ACCESS

EDITED BY

Pei Li,
Xi'an Jiaotong University, China

REVIEWED BY

Yunfei Gao,
Hohai University, China
Chuang Lu,
University of Science and Technology of
China, China

*CORRESPONDENCE

Xiaohui Yuan,
✉ yxh@xynu.edu.cn

SPECIALTY SECTION

This article was submitted to Statistical
and Computational Physics,
a section of the journal
Frontiers in Physics

RECEIVED 29 November 2022

ACCEPTED 12 December 2022

PUBLISHED 22 December 2022

CITATION

Li H, Zhao J, Guo X, Cheng Y, Xu Y and
Yuan X (2022), Sensitivity analysis of
flexoelectric materials surrogate model
based on the isogeometric finite
element method.
Front. Phys. 10:1111159.
doi: 10.3389/fphy.2022.1111159

COPYRIGHT

© 2022 Li, Zhao, Guo, Cheng, Xu and
Yuan. This is an open-access article
distributed under the terms of the
[Creative Commons Attribution License](#)
(CC BY). The use, distribution or
reproduction in other forums is
permitted, provided the original
author(s) and the copyright owner(s) are
credited and that the original
publication in this journal is cited, in
accordance with accepted academic
practice. No use, distribution or
reproduction is permitted which does
not comply with these terms.

Sensitivity analysis of flexoelectric materials surrogate model based on the isogeometric finite element method

Haozhi Li^{1,2,3}, Juan Zhao^{1,2,3}, Xiaokun Guo^{1,2,3}, Yu Cheng^{1,2,3},
Yanmin Xu^{3,4} and Xiaohui Yuan^{1,2,3*}

¹College of Architecture and Civil Engineering, Xinyang Normal University, Xinyang, China, ²Henan Unsaturated Soil and Special Soil Engineering Technology Research Center, Xinyang Normal University, Xinyang, China, ³Henan International Joint Laboratory of Structural Mechanics and Computational Simulation, Huanghuai University, Zhumadian, China, ⁴School of Architecture and Civil Engineering, Huanghuai University, Zhumadian, China

In this paper proposes a sensitivity analysis method based on a Polynomial Chaos Expansion (PCE) surrogate model for flexoelectric materials. The non-uniform rational B-splines (NURBS) basis functions to discretize the fourth-order partial differential equation for flexoelectricity and obtains a deterministic solution (electric potential). The mathematical expressions of surrogate model for the flexoelectric materials are established by considering uncertain parameters such as independent Young's modulus, concentrated load and flexoelectric constants. The sensitivity expression is found by derivation the mathematical expression for the surrogate model. Moreover the finite difference method (FDM) are conducted in numerical examples to demonstrate the validity and correctness of the proposed algorithm.

KEYWORDS

isogeometric analysis, polynomial chaos expansion, surrogate model, uncertainty quantification, sensitivity analysis

1 Introduction

Flexoelectricity is a new electromechanical energy conversion mechanism that can be an alternative to piezoelectricity [1]. The flexoelectricity is relatively weak in bulk crystalline materials, resulting in little attention. However, with the advancement of nanotechnology, huge strain gradients can be obtained at small-length scales, leading to a new understanding of the flexoelectricity as a size-dependent phenomenon [2]. As compared to piezoelectricity, flexoelectricity theoretically be present in all dielectrics, including those with centrosymmetric crystal structures, and is therefore a more versatile electromechanical coupling mechanism [3]. The traditional Lagrangian interpolation function of Finite Element Method (FEM) can only provide C^0 continuity requirements. The C^0 continuity of the FEM cannot satisfy the C^1 continuity requirement of the fourth-order partial differential equation for flexoelectricity. This requires other numerical methods to achieve the C^1 continuity requirement. Isogeometric analysis (IGA) is one

of the most popular numerical methods. It satisfies the continuity of C^1 by enhancing the order of NURBS basis function [4]. IGA initially developed to unify computer-aided design (CAD) and computer-aided engineering (CAE), but the remarkable characteristics of IGA basis functions such as NURBS has been applied to many applications including mechanics of fracture [5], electromagnetics [6], acoustics [7–10], and optimizations [11–14].

The input parameters of simulation models are often characterized by high uncertainty, and the model parameters are difficult and inaccurate to estimate [15]. This can largely lead us to make erroneous judgments about the issues of concern. The uncertainty quantification of input parameters is an efficient way to address uncertainty, and it examines the uncertainty in the model from the input parameters. Uncertainty analysis methods including Monte Carlo simulation (MCs) [16–18], the random spectral approach [19, 20] and the perturbation technique [21, 22] are frequently used to take into account the impact of uncertainty on the system response. However, with improving accuracy requirements, modeling of target simulation has become extremely complex, and its implementation is costly and time-consuming. The commonly used MCs approach is costly and challenging to implement for uncertainty quantification when many samples and model observations are required [23]. The surrogate modeling approach uses the relationship between inputs and outputs in a basic mathematical model to establish a new method for replacing complex analytical or computational models. The development of surrogate modeling techniques appropriate for solving practical engineering problems provides the required model observations and can reduce the computational cost of uncertainty quantification.

The Polynomial Chaos Expansion (PCE) becomes a prominent alternative modeling method in the field of uncertainty quantification (UQ) with low training cost when modeling extremely complex systems. The main implementation process of PCE is to use several polynomials to expand the response of random variables. The model response is expressed as a polynomial function of the input by determining the PCE coefficients of the polynomial components. These polynomial functions are orthogonal to the probability density functions of the input variables, which makes the calculation easier. The non-intrusive method does not require information about the control equations and is more suitable than the intrusive method for most problems when solving for the PCE coefficients. The non-intrusive methods include projection methods [24] and regression methods [25, 26] in which regression methods are more popular because of their efficiency in dealing with multivariate problems [27]. The sensitivity analysis (SA) quantitatively measures which the uncertainty of different input parameters contributes to the output uncertainty [28]. The sensitivity index is usually used to indicate the influence of each individual input parameter on the output [29]. Some

complex problems in practical engineering do not have a definite input-output mathematical expression. It makes it difficult for engineers to perform sensitivity analysis on complex problems. The technique of surrogate modeling, such as PCE, can easily quantify the influence of the input parameters on the output by building mathematical expressions for the mechanical properties of complex problems depending on the inputs and outputs.

This paper lays out a procedure for solving the sensitivity problems of flexoelectric materials. This approach consists of two novel points:

- 1 The IGA-FEM and PCE are employed to establish a surrogate model for the flexoelectric materials.
- 2 The sensitivity expressions of the surrogate model are established by considering three kinds of different material parameters, respectively.

The remaining sections of the essay are structured as follows. The foundations of PCE in uncertainty quantification are presented in Section 2. Three introduces the principles of the isogeometric Finite Element Method for the statics of flexoelectric materials. Section 4 validates the IGA-FEM, PCE surrogate models and the sensitivity values of PCE surrogate models of the flexoelectric structure using numerical examples, followed by conclusions in Section 5.

2 Basic formula of polynomial chaos expansion

The basic idea of PCE is to replace the system model with an orthogonal polynomial defined by random variables, and then obtain a surrogate model expression by solving for the PCE coefficients. For the system model with n -dimensional independent random variables, the output function of the truncated PCE model with total expand order p can be expressed as

$$f(\mathbf{r}) = \sum_{\alpha}^{N-1} \theta_{\alpha} \Psi_{\alpha}(\mathbf{r}), \quad (1)$$

where the total number N of polynomial terms of order p is computed by $N = (n+p)!/(n!p!)$. θ_{α} are polynomial coefficients that are unknown. Ψ_{α} are multivariate orthogonal polynomials defined by the tensor product of univariate orthogonal polynomials as

$$\Psi_{\alpha}(\mathbf{r}) = \prod_{i=1}^n \psi_{\alpha_i}(r_i), \quad (2)$$

where $\psi_{\alpha_i}(r_i)$ is a univariate polynomial with respect to the random variable r_i . The inner product of any two functions defined by $\Psi_s(\mathbf{r})$ and $\Psi_t(\mathbf{r})$, and the probability density function $P(\mathbf{r})$ of \mathbf{r} is:

TABLE 1 The probability distributions of different random variables and corresponding orthogonal polynomials [4].

Distribution type of random variable	Orthogonal polynomials	Interval
Gamma	Laguerre	(0, +∞)
Weibull		
Normal	Hermit	(−∞, +∞)
Uniform	Legendre	[a, b]
Beta	Jacobi	[a, b]
Poisson	Charlier	{0, 1, 2, . . . , }
Negative binomial	Meixner-Chaos	{0, 1, 2, . . . , }
Binomial	Krawtchouk	{0, 1, 2, . . . , n}
Hypergeometric	Hahn-Chaos	{0, 1, 2, . . . , n}

$$\langle \Psi_s(\mathbf{r}), \Psi_t(\mathbf{r}) \rangle = \int \Psi_s(\mathbf{r}) \Psi_t(\mathbf{r}) P(\mathbf{r}) d\mathbf{r} = \delta_{st}, \quad (3)$$

where $\langle \cdot \rangle$ is the expectation operator. δ_{st} is the Kronecker symbol, which is equal to one when $s = t$ and otherwise zero.

In general, the probability density functions for different distributions correspond to different orthogonal polynomials, e.g., Legendre polynomials correspond to uniform distributions and Gaussian distributions correspond to Hermite polynomials. Table 1 lists the common univariate orthogonal polynomials and their corresponding probability distributions. There are various approaches to calculating the polynomial chaos expansion coefficient θ_α . The collocation method and the least-squares minimization problem are commonly employed to obtain the PCE coefficients. The orthogonal matrix and the PCE coefficient vector can be obtained according to Eq. 1 as [30].

$$\Psi = \begin{bmatrix} \Psi_0(\mathbf{r}^1) & \dots & \Psi_{N-1}(\mathbf{r}^1) \\ \vdots & & \vdots \\ \Psi_0(\mathbf{r}^Z) & \dots & \Psi_{N-1}(\mathbf{r}^Z) \end{bmatrix} \quad \text{and} \quad \theta = \begin{bmatrix} \theta_0 \\ \vdots \\ \theta_{N-1} \end{bmatrix}, \quad (4)$$

where Z is the number of random variables sample points. The PCE coefficient vector can be expressed as

$$\theta = (\Psi^T \Psi)^{-1} \Psi^T \mathbf{U}, \quad (5)$$

where $\mathbf{U} = \{f(\mathbf{r})\}_{Z=1}^Z$. In this paper, an orthogonal polynomial with random variables satisfying a Gaussian distribution is used as an example. The recurrence relation for the Hermite orthogonal polynomials corresponding to the Gaussian distribution is

$$H_\alpha(r) = \frac{1}{(-1)^\alpha e^{-\frac{r^2}{2}}} \frac{d^\alpha}{dr^\alpha} \left[e^{-\frac{r^2}{2}} \right] = \alpha! \sum_{k=0}^{[\frac{\alpha}{2}]} (-1)^k \frac{1}{k! 2^k (\alpha - 2k)!} r^{\alpha-2k}, \quad (6)$$

where $[\frac{\alpha}{2}]$ is an integer and less than or equal to $\frac{\alpha}{2}$. r denotes the random variable. The three-term recurrence equation for the Hermite orthogonal polynomial is expressed as

$$H_{\alpha+1}(r) = r H_\alpha(r) - \alpha H_{\alpha-1}(r). \quad (7)$$

The first six polynomials of $H_\alpha(r)$ are

$$\begin{aligned} H_0(r) &= 1 & \alpha &= 0, \\ H_1(r) &= r & \alpha &= 1, \\ H_2(r) &= r^2 - 1 & \alpha &= 2, \\ H_3(r) &= r^3 - 3r & \alpha &= 3, \\ H_4(r) &= r^4 - 6r^2 + 3 & \alpha &= 4, \\ H_5(r) &= r^5 - 10r^3 + 15r & \alpha &= 5. \end{aligned} \quad (8)$$

3 IGA discretization of the control equations for flexoelectricity

In this section, we summarize the controlling equations for dielectric solids considering the flexoelectric effect. More information see [31–33] and references included therein. The weak form of the flexoelectric control equation is

$$\int_{\Omega} (C_{ijkl} \delta S_{ij} S_{kl} - e_{kij} E_k \delta S_{ij} - \mu_{ijk} E_i \delta S_{ij,k} - \kappa_{ij} \delta E_i E_j - e_{ikl} \delta E_i S_{kl} - \mu_{ijkl} \delta E_i S_{jkl}) d\Omega - \int_{\Gamma_t} \bar{t}_i \delta u_i d\Gamma_t + \int_{\Gamma_D} \omega \delta \varphi d\Gamma_D = 0, \quad (9)$$

where u_i denotes displacement; φ denotes the electric potential; C_{ijkl} represents the fourth-order elasticity tensor; the mechanical strain is denoted by S_{ij} ; e_{ijk} is the third-order piezoelectric tensor, the electric field is defined as $E_i = -\varphi_{,i}$; the fourth-order total flexoelectric tensor is denoted by μ_{ijkl} ; κ_{ij} is dielectric tensor of second order; \bar{t}_i denotes the mechanical traction; ω is surface charge density. The physical domain is denoted by Ω , with boundaries Γ_t and Γ_D corresponding to mechanical traction and electric displacements, respectively. In order to obtain the

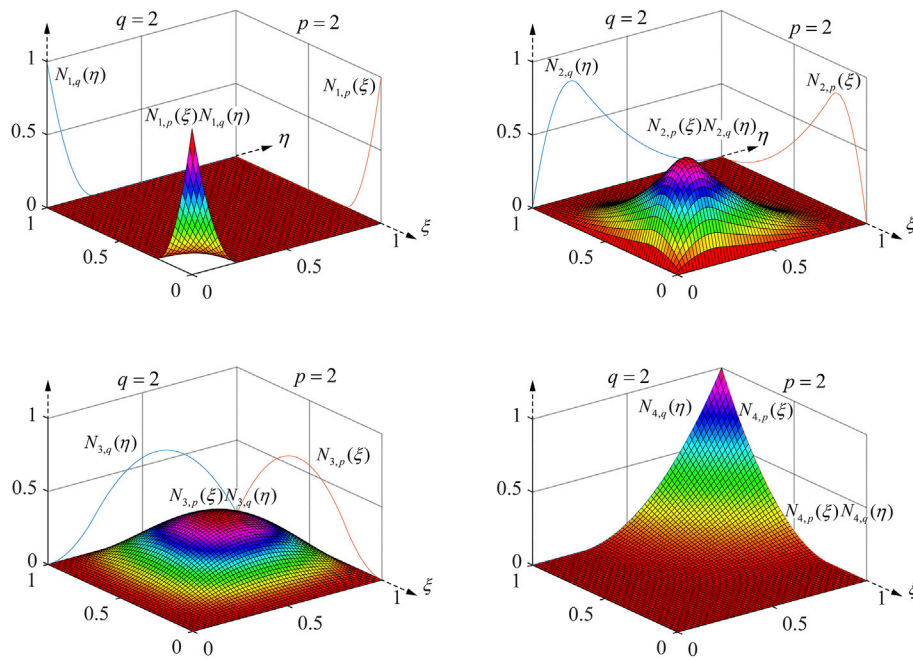


FIGURE 1

The specific B-spline basis functions.

FEM form of the governing Eq. 9, the B-spline basis function $N_{i,p}(\xi)$ obtained by recursively defining the Cox-de-Boor formula is

$$N_{i,0}(\xi) = \begin{cases} 1 & \text{if } \xi_i \leq \xi < \xi_{i+1}, \\ 0 & \text{otherwise} \end{cases}, \quad (10)$$

and for $p = 1, 2, 3$,

$$N_{i,p}(\xi) = \frac{\xi - \xi_i}{\xi_{i+p} - \xi_i} N_{i,p-1}(\xi) + \frac{\xi_{i+p+1} - \xi}{\xi_{i+p+1} - \xi_{i+1}} N_{i+1,p-1}(\xi). \quad (11)$$

Figure 1 illustrates the results of visualizing the B-spline basis functions for both directional knot vectors with $\Xi^1 = [0 \ 0 \ 0 \ 0.5 \ 1 \ 1 \ 1]$ and $\Xi^2 = [0 \ 0 \ 0 \ 0.5 \ 1 \ 1 \ 1]$. The $N_{i,p}$ and $N_{i,q}$ are 2nd order basis functions. The richness of B-spline basis function can be intuitively seen in Figure 1. The richness of the basis functions provides the groundwork for solving the fourth-order partial differential equation for flexoelectricity. Using Eqs. 10, 11 to discretize Eq. 9, the linear algebraic system of equations for the flexoelectricity control equation is obtained as

$$\begin{bmatrix} \mathbf{A}_{uu} & \mathbf{A}_{u\varphi} \\ \mathbf{A}_{\varphi u} & \mathbf{A}_{\varphi\varphi} \end{bmatrix} \begin{bmatrix} \mathbf{u} \\ \Phi \end{bmatrix} = \begin{bmatrix} \mathbf{f}_u \\ \mathbf{f}_\varphi \end{bmatrix}, \quad (12)$$

where the matrix corresponding to the displacements is

$$\mathbf{A}_{uu} = \sum_e \int_{\Omega_e} (\mathbf{B}_u)^T \mathbf{C} (\mathbf{B}_u) d\Omega_e, \quad (13)$$

and

$$\mathbf{B}_u = \begin{bmatrix} \frac{\partial N_1}{\partial x} & \frac{\partial N_2}{\partial x} & \dots & \frac{\partial N_{ncp}}{\partial x} & 0 & 0 & 0 & \dots \\ 0 & 0 & \dots & 0 & \frac{\partial N_1}{\partial y} & \frac{\partial N_2}{\partial y} & \dots & \frac{\partial N_{ncp}}{\partial y} \\ \frac{\partial N_1}{\partial y} & \frac{\partial N_2}{\partial y} & \dots & \frac{\partial N_{ncp}}{\partial y} & \frac{\partial N_1}{\partial x} & \frac{\partial N_2}{\partial x} & \dots & \frac{\partial N_{ncp}}{\partial x} \end{bmatrix}, \quad (14)$$

$$\mathbf{C} = \left(\frac{Y}{(1+\nu)(1-2\nu)} \right) \begin{bmatrix} 1-\nu & \nu & 0 \\ \nu & 1-\nu & 0 \\ 0 & 0 & \left(\frac{1}{2} - \nu \right) \end{bmatrix}, \quad (15)$$

where ν is Poisson's ratio and Y is the Young's modulus. The matrix of displacement and electric field coupling are

$$\begin{aligned} \mathbf{A}_{u\varphi} &= \sum_e \int_{\Omega_e} [(\mathbf{B}_u)^T \mathbf{e}^T (\mathbf{B}_\varphi) + (\mathbf{H}_u)^T \boldsymbol{\mu}^T (\mathbf{B}_\varphi)] d\Omega_e, \\ \mathbf{A}_{\varphi u} &= \sum_e \int_{\Omega_e} [(\mathbf{B}_\varphi)^T \mathbf{e} (\mathbf{B}_u) + (\mathbf{B}_\varphi)^T \boldsymbol{\mu} (\mathbf{H}_u)] d\Omega_e. \end{aligned} \quad (16)$$

The electric field and Hessian matrices are

$$\mathbf{B}_\varphi = \begin{bmatrix} \frac{\partial N_1}{\partial x} & \dots & \frac{\partial N_{ncp}}{\partial x} \\ \frac{\partial N_1}{\partial y} & \dots & \frac{\partial N_{ncp}}{\partial y} \end{bmatrix},$$

$$\mathbf{H}_u = \begin{bmatrix} \frac{\partial^2 N_1}{\partial x^2} & \frac{\partial^2 N_2}{\partial x^2} & \dots & \frac{\partial^2 N_{ncp}}{\partial x^2} & 0 & 0 & \dots & 0 \\ 0 & 0 & \dots & 0 & \frac{\partial^2 N_1}{\partial y \partial x} & \frac{\partial^2 N_2}{\partial y \partial x} & \dots & \frac{\partial^2 N_{ncp}}{\partial y \partial x} \\ \frac{\partial^2 N_1}{\partial y \partial x} & \frac{\partial^2 N_2}{\partial y \partial x} & \dots & \frac{\partial^2 N_{ncp}}{\partial y \partial x} & \frac{\partial^2 N_1}{\partial x^2} & \frac{\partial^2 N_2}{\partial x^2} & \dots & \frac{\partial^2 N_{ncp}}{\partial x^2} \\ \frac{\partial^2 N_1}{\partial x \partial y} & \frac{\partial^2 N_2}{\partial x \partial y} & \dots & \frac{\partial^2 N_{ncp}}{\partial x \partial y} & 0 & 0 & \dots & 0 \\ 0 & 0 & \dots & 0 & \frac{\partial^2 N_1}{\partial y^2} & \frac{\partial^2 N_2}{\partial y^2} & \dots & \frac{\partial^2 N_{ncp}}{\partial y^2} \\ \frac{\partial^2 N_1}{\partial y^2} & \frac{\partial^2 N_2}{\partial y^2} & \dots & \frac{\partial^2 N_{ncp}}{\partial y^2} & \frac{\partial^2 N_1}{\partial x \partial y} & \frac{\partial^2 N_2}{\partial x \partial y} & \dots & \frac{\partial^2 N_{ncp}}{\partial x \partial y} \end{bmatrix}, \quad (17)$$

The piezoelectric constants and flexoelectric constants matrices are

$$\mathbf{e} = \begin{bmatrix} 0 & 0 & e_{115} \\ e_{311} & e_{333} & 0 \end{bmatrix},$$

$$\boldsymbol{\mu} = \begin{bmatrix} \mu_{11} & \mu_{12} & 0 & 0 & 0 & \mu_{44} \\ 0 & 0 & \mu_{44} & \mu_{12} & \mu_{11} & 0 \end{bmatrix}. \quad (18)$$

The matrix corresponding to the electric field is

$$\mathbf{A}_{\varphi\varphi} = - \sum_e \int_{\Omega_e} (\mathbf{B}_\varphi)^T \boldsymbol{\kappa} (\mathbf{B}_\varphi) d\Omega_e, \quad (19)$$

where the permittivity constant matrix is

$$\boldsymbol{\kappa} = \begin{bmatrix} \kappa_{11} & 0 \\ 0 & \kappa_{22} \end{bmatrix}. \quad (20)$$

The force and electrical load vectors are

$$\mathbf{f}_u = \sum_e \int_{\Gamma_{te}} \mathbf{N}_u^T \mathbf{t}_r d\Gamma_{te},$$

$$\mathbf{f}_\varphi = - \sum_e \int_{\Gamma_{De}} \mathbf{N}_\varphi^T \omega d\Gamma_{De}, \quad (21)$$

The subscript e in Ω_e , Γ_{te} and Γ_{De} represents the e th finite element in Eqs. 13, 16, 19, 21.

4 Numerical examples

In this section, we verify the accuracy of the IGA-FEM for solving the fourth-order partial differential equation using a benchmark example of a cantilever beam. After that, some random variable sample points are selected to obtain the

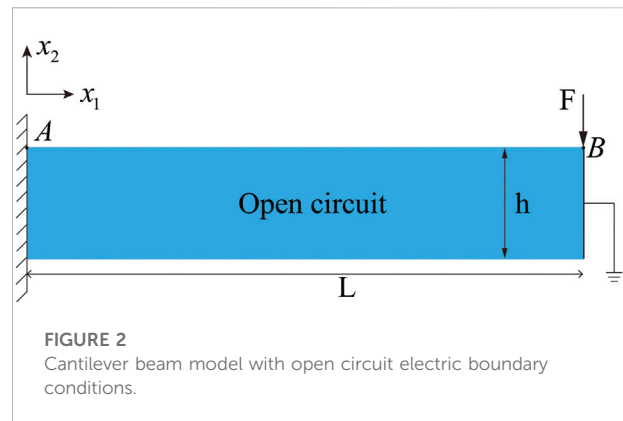


TABLE 2 Material parameters for cantilever beam.

Name	BaTiO ₃
Beam aspect ratio L/h	30
Poisson ratio ν	0.35
Young's modulus Y	120 GPa
Piezoelectric constant e_{311}	-4.3 C/m^2
Flexoelectric constant v_{12}	$1.2 \text{ } \mu\text{C/m}$
Dielectric constants	
κ_{11}	9.9 nC/(Vm)
κ_{33}	11.2 nC/(Vm)
Electric susceptibility χ_{33}	1,408
Concentrated load F	$200 \text{ } \mu\text{N}$

output of IGA-FEM, which is used to build a polynomial chaos expansion surrogate model. Finally, the sensitivity results of the surrogate model for the mechanical properties of flexoelectric materials are verified by several numerical examples. For the cantilever beam model, we postulate that the model satisfies plane strain linear elastic isotropy.

4.1 Model verification

The cantilever beam model with open-circuit electrical boundary conditions and the top free edge subjected to a concentrated load of $200 \text{ } \mu\text{N}$ is depicted in Figure 2. The most commonly used BaTiO₃ material was selected for the cantilever beam model, as summarized in Table 2. The mesh and control point information is demonstrated in Figure 3. The boundary condition of the cantilever beam potential is specified on the right side as 0 V. The FEM uses the traditional Lagrangian basis function, which requires a lot of meshing to achieve higher accuracy, but the processing efficiency is lower. However,

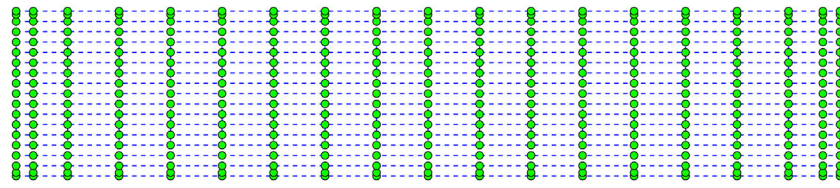


FIGURE 3

FEM discretization showing the control points as green dots.

TABLE 3 The normalized electromechanical coupling coefficient $\bar{\kappa}$ of non-piezoelectric materials with changing normalized thickness h' .

Non-piezoelectric materials			
Normalized thickness h'	IGA-FEM	Analytical solution	Relative error (%)
1	3.4642	3.4641	0.003
2	1.7323	1.7321	0.012
3	1.1549	1.1547	0.017
4	0.8662	0.866	0.023
5	0.6929	0.6928	0.014
6	0.5774	0.5774	0.000

IGA-FEM uses NURBS basis functions to reduce the preprocessing time by enhancing the order, which improves the computational efficiency. This is the main motivation for using IGA-FEM in this work.

The general definition of the electromechanical coupling coefficient \mathcal{K}_{eff} is

$$\mathcal{K}_{eff} = \sqrt{\frac{\mathcal{W}_{elec}}{\mathcal{W}_{mech}}} = \sqrt{\frac{\int_{\Omega} E_i^T \kappa_{ij} E d\Omega}{\int_{\Omega} S_{ij}^T C_{ijkl} S_{ij} d\Omega}}, \quad (22)$$

For the one-dimensional cantilever beam problem, there are only stresses T_{11} and electric fields E_2 [31]. The electromechanical coupling coefficient of the cantilever beam problem is [34].

$$\mathcal{K}_{eff} = \frac{\chi_{33}}{1 + \chi_{33}} \sqrt{\frac{\kappa_{33}}{Y} \left(e_{311}^2 + 12 \left(\frac{\mu_{12}}{h} \right)^2 \right)}, \quad (23)$$

For comparison purposes, we introduce a normalized expression for the electromechanical coupling coefficient as

$$\bar{\kappa} = \frac{\mathcal{K}_{eff}}{\mathcal{K}_{piezo}}, \quad (24)$$

and

$$\mathcal{K}_{piezo} = \frac{\chi_{33}}{1 + \chi_{33}} \sqrt{\frac{\kappa_{33}}{Y} e_{311}^2}. \quad (25)$$

The one-dimensional model can be obtained by setting the Poisson's ratio, the piezoelectric constant e_{333} , flexoelectric constant μ_{11} in the two-dimensional model to zero. The non-piezoelectric material is obtained by setting $e_{311} = 0$. The normalized electromechanical coupling coefficients obtained by IGA-FEM and analytical solutions are presented in Tables 3, 4. From the Tables 3, 4, it can be seen that the normalized electromechanical coupling coefficients obtained by IGA-FEM are very close to the analytical solution, and the relative errors are within a small range. The increase in standardized thickness will decrease the mechanical properties (electric potential) of the flexoelectric material.

4.2 PCE surrogate model verification

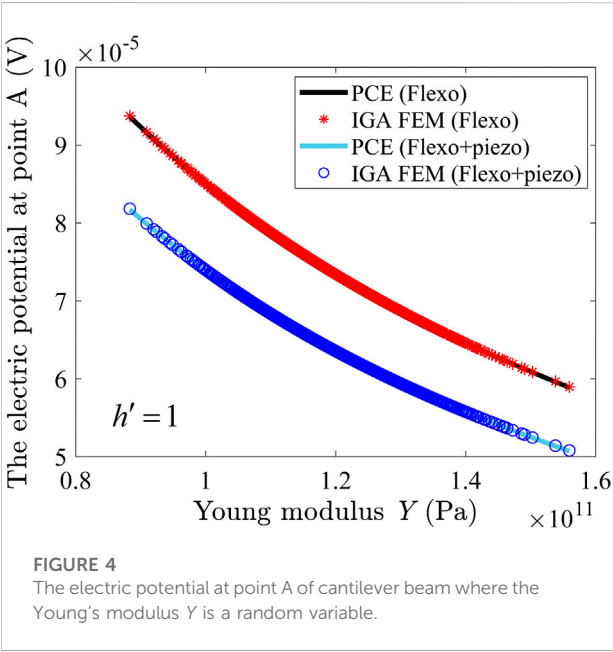
In this section, the output of the IGA-FEM of the cantilever beam model is used to build the PCE surrogate model. The Young's modulus, concentrated load and two flexoelectric constants as the random input variables are adopted, respectively. Table 5 lists the mean values, coefficients of variation, and ranges of sample points for the different random input variables. In this paper, we have used 500 sample points as input parameters for the random variables of the PCE. The Latin Hypercube Sampling (LHS) random number generation module in Matlab is utilized to obtain sample points of

TABLE 4 The normalized electromechanical coupling coefficient \bar{k} of piezoelectric materials with changing normalized thickness h' .

Piezoelectric materials			
Normalized thickness h'	IGA-FEM	Analytical solution	Relative error (%)
1	3.5565	3.6056	1.36
2	1.9793	2.0000	1.04
3	1.5156	1.5275	0.78
4	1.3152	1.3229	0.58
5	1.2112	1.2166	0.44
6	1.1508	1.1547	0.34

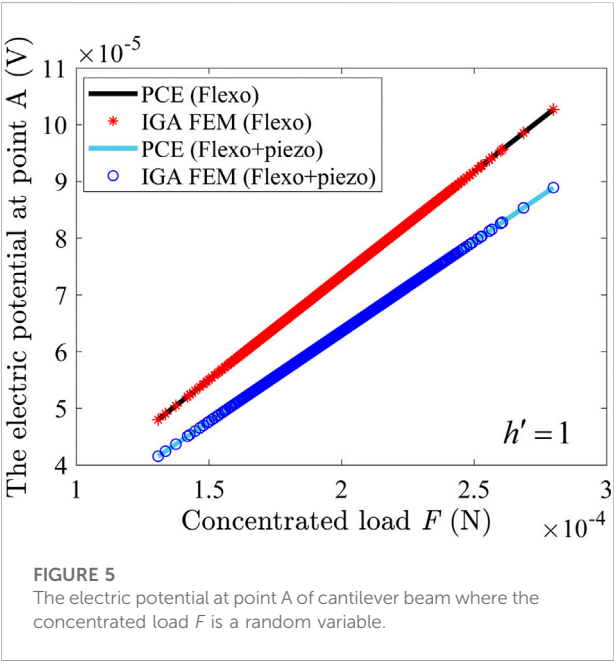
TABLE 5 Definitions and the statistical characteristics of the random input variables.

Variables	Mean values \mathcal{E}	Coefficient of variation γ	The limits of variables: [lower, upper]
Young's modulus Y	120 GPa	0.1	[84,156]
Concentrated load F	200 μ N	0.12	[128,272]
Flexoelectric constant μ_{11} / μ_{12}	1.2 μ C/m	0.14	[0.7,1.7]



random variables. Owing to the potential distribution at the fixed edge is the most obvious, point A is selected as the reference point when establishing the surrogate model.

Figure 4 presents the comparison results of PCE and IGA-FEM for piezoelectric and non-piezoelectric materials with Young's modulus as random variable. As can be seen from Figure 4, the electric potential decreases as the Young's



modulus increases. The PCE calculation results are basically consistent with the IGA-FEM calculation results, which verifies the effectiveness of the algorithm.

Figure 5 depicts the electric potential obtained by PCE and IGA-FEM for piezoelectric and non-piezoelectric materials with concentrated load as random variables. As can be seen from Figure 5, the electric potential of point A increases with increasing

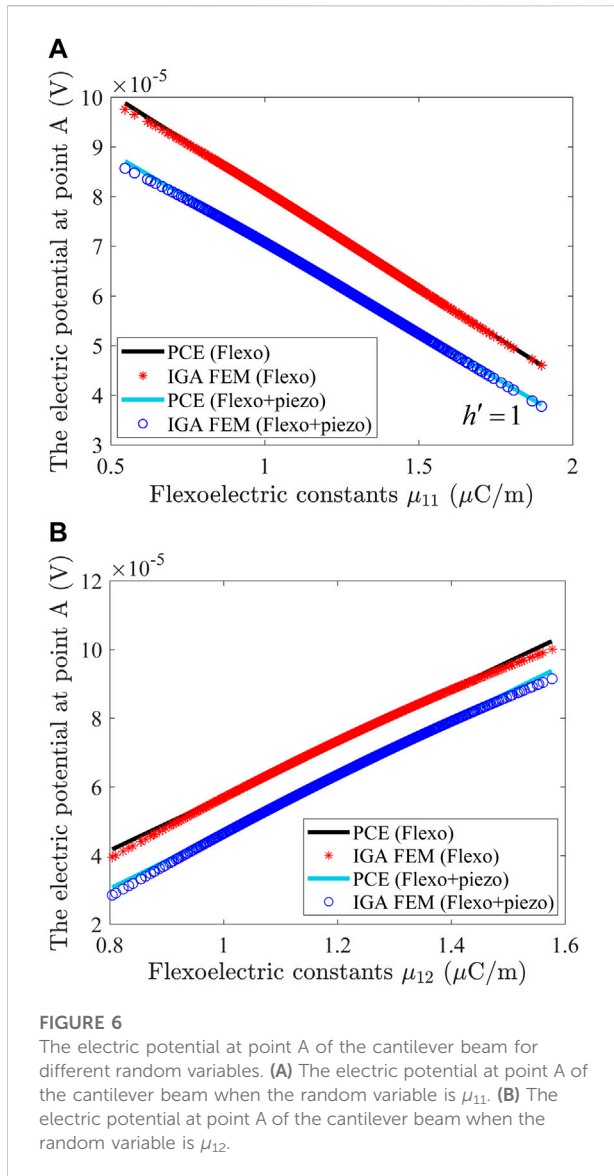


FIGURE 6

The electric potential at point A of the cantilever beam for different random variables. (A) The electric potential at point A of the cantilever beam when the random variable is μ_{11} . (B) The electric potential at point A of the cantilever beam when the random variable is μ_{12} .

concentrated load. The electric potential of a piezoelectric material subjected to the same concentrated force F is less than that of a non-piezoelectric material.

The results of PCE and IGA-FEM for piezoelectric and non-piezoelectric materials are shown in Figure 6, where the random variables are the flexoelectric constants μ_{11} and μ_{12} . It can be seen from Figure 6 that the electric potential presents reverse changes as the two different flexoelectric constants are changed.

4.3 Sensitivity analysis

In this section, we perform a sensitivity analysis of the surrogate model for the mechanical properties of flexoelectric

materials obtained in Section 4.2. The sensitivity expression of the surrogate model for the mechanical properties of flexoelectric materials without considering piezoelectric effect are

$$\begin{aligned}\frac{d\Phi(Y)}{dY} &= -2.42 \times 10^{-15} + 2.48 \times 10^{-26}Y - 7.35 \times 10^{-38}Y^2, \\ \frac{d\Phi(F)}{dF} &= 0.36697, \\ \frac{d\Phi(\mu_{11})}{d\mu_{11}} &= -39.0240, \\ \frac{d\Phi(\mu_{12})}{d\mu_{12}} &= 78.4851.\end{aligned}\quad (26)$$

The sensitivity expression of the surrogate model for the mechanical properties of flexoelectric materials considering piezoelectric effect are

$$\begin{aligned}\frac{d\bar{\Phi}(Y)}{dY} &= -2.24 \times 10^{-15} + 2.34 \times 10^{-26}Y - 6.99 \times 10^{-38}Y^2, \\ \frac{d\bar{\Phi}(F)}{dF} &= 0.31776, \\ \frac{d\bar{\Phi}(\mu_{11})}{d\mu_{11}} &= -36.2533, \\ \frac{d\bar{\Phi}(\mu_{12})}{d\mu_{12}} &= 81.6950.\end{aligned}\quad (27)$$

The sensitivity values obtained from the PCE surrogate model are compared with the global finite difference method (FDM) defined by

$$\frac{d\Phi(r)}{dr} = \frac{\Phi(r + \Delta r) - \Phi(r)}{\Delta r}.\quad (28)$$

To investigate the accuracy of DSM and FDM, one gives the relative error of DSM and FDM for different random variable r . The relative error of the sensitivity results obtained by FDM and PCE is

$$\epsilon_{err} = \frac{|\Phi_{PCE} - \Phi_{FDM}|}{|\Phi_{FDM}|}.\quad (29)$$

Owing to the first sensitivity expressions in Eqs. 27, 28 are a quadratic function of Young's modulus. Therefore, we need to calculate the sensitivity value of the surrogate model through the mean value of Young's modulus. The mean value of Young's modulus is lists in Table 5. The rest of the sensitivity values are directly selected from the derivative results. Tables 6, 7 present a comparison of the sensitivity values of PCE and FDM for non-piezoelectric and piezoelectric materials. From Tables 6, 7, it can be seen that the sensitivity values obtained by PCE and FDM are basically the same, and the relative errors are very small. In terms of the value of sensitivity, the flexoelectric constant μ_{12} has a greater effect on the electric potential of the flexoelectric material and the material is more sensitive to the flexoelectric constant μ_{12} .

TABLE 6 Comparison of PCE and FDM of sensitivity results for non-piezoelectric materials.

Non-piezoelectric			
Random variables	FDM	PCE	Relative error
Young's modulus Y	-5.04×10^{-16}	-5.01×10^{-16}	0.49%
Concentrated load F	0.36697	0.36697	-
Flexoelectric constant μ_{11}	-38.6675	-39.0240	0.9%
Flexoelectric constant μ_{12}	79.0227	78.4851	0.7%

TABLE 7 Comparison of PCE and FDM of sensitivity results for non-piezoelectric materials.

Piezoelectric			
Random variables	FDM	PCE	Relative error
Young's modulus Y	-4.48×10^{-16}	-4.46×10^{-16}	0.49%
Concentrated load F	0.31176	0.31176	-
Flexoelectric constant μ_{11}	-35.7991	-36.2533	1.3%
Flexoelectric constant μ_{12}	82.3133	81.6950	0.8%

5 Conclusion

In this paper, a sensitivity analysis method of surrogate model based on isogeometric stochastic Finite Element Method is proposed for flexoelectric materials. The NURBS basis functions with high-order continuity are used to discretize the fourth-order partial differential equation for flexoelectricity. The Polynomial Chaos Expansion (PCE) is utilized to develop a surrogate model for the mechanical properties of flexoelectric materials. The sensitivity values of the surrogate model are obtained by considering three kinds of different parameters, respectively. Numerical examples illustrate the flexoelectric material is more sensitive to the flexoelectric constant μ_{12} . Additionally, the current technology will also be used to three-dimensional piezoelectric and flexoelectric problems.

Data availability statement

The original contributions presented in the study are included in the article/Supplementary Material; further inquiries can be directed to the corresponding author.

Author contributions

Conceptualization, HL; Data curation, HL; Formal analysis, YC and YX; Investigation, XG; Methodology, HL and JZ; Project administration, XY, Software, HL and JZ; Supervision, XY; Validation, YX; Visualization, YC; Writing—original draft, HL and XG. All authors have read and agreed to the published version of the manuscript.

Conflict of interest

The authors declare that the research was conducted in the absence of any commercial or financial relationships that could be construed as a potential conflict of interest.

Publisher's note

All claims expressed in this article are solely those of the authors and do not necessarily represent those of their affiliated organizations, or those of the publisher, the editors and the reviewers. Any product that may be evaluated in this article, or claim that may be made by its manufacturer, is not guaranteed or endorsed by the publisher.

References

- Hamdia KM, Ghasemi H, Zhuang X, Alajlan N, Rabczuk T. Sensitivity and uncertainty analysis for flexoelectric nanostructures. *Comput Methods Appl Mech Eng* (2018) 337:95–109. doi:10.1016/j.cma.2018.03.016
- Ahmadpoor F, Sharma P. Flexoelectricity in two-dimensional crystalline and biological membranes. *Nanoscale* (2015) 7:16555–70. doi:10.1039/C5NR04722F
- Yudin PV, Tagantsev AK. Fundamentals of flexoelectricity in solids. *Nanotechnology* (2013) 24:432001. doi:10.1088/0957-4484/24/43/432001
- Hughes TJ, Cottrell JA, Bazilevs Y. Isogeometric analysis: CAD, finite elements, NURBS, exact geometry and mesh refinement. *Comput Methods Appl Mech Eng* (2005) 194:4135–95. doi:10.1016/j.cma.2004.10.008
- Chen L, Wang Z, Peng X, Yang J, Wu P, Lian H. Modeling pressurized fracture propagation with the isogeometric BEM. *Geomechanics Geophys Geo-Energy Geo-Resources* (2021) 7:51. doi:10.1007/s40948-021-00248-3
- Chen L, Lian H, Xu Y, Li S, Liu Z, Atroshchenko E, et al. Generalized isogeometric boundary element method for uncertainty analysis of time-harmonic wave propagation in infinite domains. *Appl Math Model* (2023) 114:360–78. doi:10.1016/j.apm.2022.09.030
- Chen L, Lu C, Lian H, Liu Z, Zhao W, Li S, et al. Acoustic topology optimization of sound absorbing materials directly from subdivision surfaces with isogeometric boundary element methods. *Comput Methods Appl Mech Eng* (2020) 362:112806. doi:10.1016/j.cma.2019.112806
- Chen L, Lian H, Liu Z, Gong Y, Zheng C-J, Bordas S. Bi-material topology optimization for fully coupled structural-acoustic systems with isogeometric FEM-BEM. *Eng Anal Boundary Elem* (2022) 135:182–95. doi:10.1016/j.enganabound.2021.11.005
- Chen L, Marburg S, Zhao W, Liu C, Chen H. Implementation of isogeometric fast multipole boundary element methods for 2d half-space acoustic scattering problems with absorbing boundary condition. *J Theor Comput Acoust* (2018) 27:1850024. doi:10.1142/S259172851850024X
- Chen L, Lu C, Zhao W, Chen H, Zheng C-J. Subdivision surfaces—boundary element accelerated by fast multipole for the structural acoustic problem. *J Theor Comput Acoust* (2020) 28:2050011. doi:10.1142/S2591728520500115
- Chen L, Liu C, Zhao W, Liu L. An isogeometric approach of two dimensional acoustic design sensitivity analysis and topology optimization analysis for absorbing material distribution. *Comput Methods Appl Mech Eng* (2018) 336:507–32. doi:10.1016/j.cma.2018.03.025
- Chen L, Lian H, Liu Z, Chen H, Atroshchenko E, Bordas S. Structural shape optimization of three dimensional acoustic problems with isogeometric boundary element methods. *Comput Methods Appl Mech Eng* (2019) 355:926–51. doi:10.1016/j.cma.2019.06.012
- Chen L, Zhang Y, Lian H, Atroshchenko E, Ding C, Bordas SP. Seamless integration of computer-aided geometric modeling and acoustic simulation: Isogeometric boundary element methods based on catmull-clark subdivision surfaces. *Adv Eng Softw* (2020) 149:102879. doi:10.1016/j.advengsoft.2020.102879
- Chen L, Lian H, Natarajan S, Zhao W, Chen X, Bordas S. Multi-frequency acoustic topology optimization of sound-absorption materials with isogeometric boundary element methods accelerated by frequency-decoupling and model order reduction techniques. *Comput Methods Appl Mech Eng* (2022) 395:114997. doi:10.1016/j.cma.2022.114997
- Cheng K, Lu Z. Adaptive sparse polynomial chaos expansions for global sensitivity analysis based on support vector regression. *Comput Structures* (2018) 194:86–96. doi:10.1016/j.compstruc.2017.09.002
- Hurtado J, Barbat A. Monte Carlo techniques in computational stochastic mechanics. *Arch Comput Methods Eng* (1998) 5:3–29. doi:10.1007/BF02736747
- Chen L, Cheng R, Li S, Lian H, Zheng C, Bordas SP. A sample-efficient deep learning method for multivariate uncertainty quantification of acoustic-vibration interaction problems. *Comput Methods Appl Mech Eng* (2022) 393:114784. doi:10.1016/j.cma.2022.114784
- Xu Y, Li H, Chen L, Zhao J, Zhang X. Monte Carlo based isogeometric stochastic finite element method for uncertainty quantization in vibration analysis of piezoelectric materials. *Mathematics* (2022) 10:1840. doi:10.3390/math10111840
- Honda R. Stochastic BEM with spectral approach in elastostatic and elastodynamic problems with geometrical uncertainty. *Eng Anal Boundary Elem* (2005) 29:415–27. doi:10.1016/j.enganabound.2005.01.007
- Liu WK, Belytschko T, Mani A. Random field finite elements. *Int J Numer Methods Eng* (1986) 23:1831–45. doi:10.1002/nme.1620231004
- Kamiński M. Stochastic perturbation approach to engineering structure vibrations by the finite difference method. *J Sound Vibration* (2002) 251:651–70. doi:10.1006/jsvi.2001.3850
- Kamiński M. On generalized stochastic perturbation-based finite element method. *Commun Numer Methods Eng* (2006) 22:23–31. doi:10.1002/cnm.795
- Zhang B-Y, Ni Y-Q. A hybrid sequential sampling strategy for sparse polynomial chaos expansion based on compressive sampling and Bayesian experimental design. *Comput Methods Appl Mech Eng* (2021) 386:114130. doi:10.1016/j.cma.2021.114130
- Le Maître O, Knio OM. *Spectral methods for uncertainty quantification: With applications to computational fluid dynamics*. Berlin, Germany: Springer Science & Business Media (2010).
- Blatman G, Sudret B. Sparse polynomial chaos expansions and adaptive stochastic finite elements using a regression approach. *Comptes Rendus Mécanique* (2008) 336:518–23. doi:10.1016/j.crme.2008.02.013
- Palar PS, Tsuchiya T, Parks GT. Multi-fidelity non-intrusive polynomial chaos based on regression. *Comput Methods Appl Mech Eng* (2016) 305:579–606. doi:10.1016/j.cma.2016.03.022
- Zhou Y, Lu Z, Cheng K, Shi Y. An expanded sparse Bayesian learning method for polynomial chaos expansion. *Mech Syst Signal Process* (2019) 128:153–71. doi:10.1016/j.ymssp.2019.03.032
- Saltelli A, Ratto M, Andres T, Campolongo F, Cariboni J, Gatelli D, et al. *Global sensitivity analysis: The primer*. New York, NY, USA: John Wiley & Sons (2008).
- Hamdia KM, Silani M, Zhuang X, He P, Rabczuk T. Stochastic analysis of the fracture toughness of polymeric nanoparticle composites using polynomial chaos expansions. *Int J Fracture* (2017) 206:215–27. doi:10.1007/s10704-017-0210-6
- Hauseux P, Hale JS, Bordas SP. Accelerating Monte Carlo estimation with derivatives of high-level finite element models. *Comput Methods Appl Mech Eng* (2017) 318:917–36. doi:10.1016/j.cma.2017.01.041
- Majdoub MS, Sharma P, Cagin T. Enhanced size-dependent piezoelectricity and elasticity in nanostructures due to the flexoelectric effect. *Phys Rev B* (2008) 77:125424. doi:10.1103/PhysRevB.77.125424
- Ghasemi H, Park HS, Rabczuk T. A level-set based Iga formulation for topology optimization of flexoelectric materials. *Comput Methods Appl Mech Eng* (2017) 313:239–58. doi:10.1016/j.cma.2016.09.029
- Ghasemi H, Park HS, Alajlan N, Rabczuk T. A computational framework for design and optimization of flexoelectric materials. *Int J Comput Methods* (2020) 17:1850097. doi:10.1142/S0219876218500974
- Abdollahi A, Peco C, Millán D, Arroyo M, Arias I. Computational evaluation of the flexoelectric effect in dielectric solids. *J Appl Phys* (2014) 116:093502. doi:10.1063/1.4893974



OPEN ACCESS

EDITED BY

Pei Li,
Xi'an Jiaotong University, China

REVIEWED BY

Haojie Lian,
Taiyuan University of Technology, China
Bo Yu,
Hefei University of Technology, China

*CORRESPONDENCE

Yanming Xu,
✉ xuyanming@ustc.edu

SPECIALTY SECTION

This article was submitted to Statistical and Computational Physics, a section of the journal Frontiers in Physics

RECEIVED 17 October 2022

ACCEPTED 08 November 2022

PUBLISHED 10 January 2023

CITATION

Zhang X and Xu Y (2023), Design of constrained-layer damping on plates to sound radiation based on isogeometric analysis and non-negative intensity. *Front. Phys.* 10:1072230. doi: 10.3389/fphy.2022.1072230

COPYRIGHT

© 2023 Zhang and Xu. This is an open-access article distributed under the terms of the [Creative Commons Attribution License \(CC BY\)](#). The use, distribution or reproduction in other forums is permitted, provided the original author(s) and the copyright owner(s) are credited and that the original publication in this journal is cited, in accordance with accepted academic practice. No use, distribution or reproduction is permitted which does not comply with these terms.

Design of constrained-layer damping on plates to sound radiation based on isogeometric analysis and non-negative intensity

Xinyan Zhang¹ and Yanming Xu^{1,2*}

¹School of Architecture and Civil Engineering, Huanghuai University, Zhumadian, Henan, China, ²Henan International Joint Laboratory of Structural Mechanics and Computational Simulation, Huanghuai University, Zhumadian, Henan, China

Non-negative intensity (NNI) is a quantity which avoids near-field cancellation effects in sound intensity and provides direct visualization of the surface contributions to the radiated sound power. Hence, minimizing the integration of Non-negative intensity on predefined surfaces is implemented to be the design objective of topology optimization for the constrained-layer damping design on plates in this work. Non-negative intensity can be easily computed based on the radiation modes and the particle velocity on the surfaces of interest. Regarding the radiation modes, an eigenvalue analysis for the acoustic impedance matrix is required. After evaluating the objective function, the gradients of the objective function are computed using an adjoint variable method (AVM). These gradients enable the optimization to be solved by the method of moving asymptotes (MMA). Finally, some numerical examples are presented to validate the proposed optimization approach. Numerical results show that the corner radiation properties of the plate can be suppressed by the optimization, minimizing the integration of Non-negative intensity.

KEYWORDS

topology optimization, constrained-layer damping, non-negative intensity, sound radiation, isogeometric analysis

1 Introduction

Noise control has become an important task in an engineering design. As a commonly used component in engineering, reducing the sound radiation from vibrating plates has drawn much attention. An efficient tool for this job is the topology optimization technique. Topology optimization has rapidly developed since it was introduced by [1] and has been applied to a large range of engineering problems. This technique can flexibly generate holes in the structure and achieve the design objectives, such as reducing the weight or increasing the first natural frequency. Du and Olhoff [2] reduced the radiated sound power of the vibrating plate by optimizing the distribution of bi-materials. In addition, Xu et al. [3] also optimized the material distribution of the plate for minimizing the sound radiation. In their work, damping effects are neglected. To achieve a better design, damping patches can be adopted, for example, free-layer damping and constrained-layer damping (CLD). Compared with the free damping layer, CLD provides considerably more damping effects due to the motion constraints of the damping layer. Zheng et al. [4] investigated the topology optimization of passive constrained-layer damping (PCLD) treatment patches on thin plates with respect to sound radiation at low-frequency resonances.

In addition to the optimization procedure, another alternative to reducing the sound power is to locate the most contributing components of the vibrating structure and then adopt some additional patches on these regions, for example, damping layer, stiffener, or adding mass. This approach is more direct and computationally efficient because it usually does not require an iterative optimization process. It, however, sometimes cannot give a very efficient design for radiation control. Numerical techniques to identify the surface contribution to sound power include supersonic intensity and non-negative intensity. Supersonic intensity (SSI) was first proposed by [5] based on near-field acoustic holography (NAH) and Fourier transformation in wavenumber space. Another method is the surface contribution method proposed by [6]. The surface contribution method is a computational procedure to locate the regions of a vibrating object that radiate far-field sound based on acoustic radiation modes. The surface contributions depend on the acoustic radiation modes, the effectiveness of the acoustic radiation, and either the normal structural velocity or the acoustic pressure. The surface contribution is always positive, avoiding cancellation effects and providing a more direct visualization of the surface contribution to sound power than the sound intensity, compared to the supersonic intensity of the region with positive and negative contributions. Later, [7] renamed this quantity non-negative intensity (NNI) for comparison with the sound intensity. Liu et al. [8] compared these two intensities for predicting radiated sound in detail. By using SSI and NNI, the most contributing regions of vibrating structures can be determined. This information can assist in noise control.

The process of meshing can be costly when performing large-scale calculations, which makes the transition from computer-aided design (CAD) to computer-aided engineering (CAE) very cumbersome [9]. In isogeometric analysis (IGA), conventional Lagrangian basis functions are replaced by a B-spline basis function commonly used in CAD, which alleviates the meshing burden [10–19]. As a boundary representation method, IGABEM is naturally compatible with CAD and can thus perform numerical analysis directly on CAD models without having to go through the time-consuming meshing process required by traditional FEM/BEM, and without having to deal with the challenging volume parameterization required by the isogeometric finite element method. As a result, IGABEM is excellent for solving complicated boundary issues (Chen et al. [20]). IGA handles singularities and moving boundaries effectively [21, 22]. In order to solve the weakly singular and hypersingular integrals that emerge in IGABEM, specialized integration methods have been devised [20, 23]. In this work, non-uniform rational B-spline (NURBS) basis functions are used to discretize partial differential equations.

This article focuses on the adoption of NNI for topology optimization of plate structures with the CLD design. Since NNI can be regarded as the contribution to sound power, reducing the contributions defined as NNI over some partial regions of interest could be another design objective, different from the existing optimizations. By optimizing the distributions of NNI, the contributing pattern to sound power varied. That is to say, the radiation pattern of the vibrating structure is optimized.

The remainder of this article is organized as follows: in Section 2, vibro-acoustic analysis, based on the isogeometric finite element method and the Rayleigh integral equation is presented. NNI is established using the acoustic radiation modes. Section 3 presents the complete optimization problem, including the sensitivity analysis, the definition of objective functions, and updating the scheme of

design variables. The validation of the proposed optimization method is demonstrated in Section 4, by means of a baffled plate example. Finally, this work is concluded in Section 5.

2 Vibro-acoustic analysis

The following governing equations for the structure and fluid are derived in the frequency domain. Throughout this contribution, the time-harmonic term $e^{-i\omega t}$ will be applied, where $i = \sqrt{-1}$ is the imaginary unit, $\omega = 2\pi f$ denotes the angular frequency, with f as the excitation frequency in Hz, and t denoting time.

2.1 Isogeometric finite element modeling for plate vibration

2.1.1 B-splines and non-uniform rational B-splines

Generally, the B-spline is constructed by the knot vector $\Xi = [\xi_0, \xi_1, \dots, \xi_m]$, where $m = n + p + 1$. The B-spline basis function $\{N_{i,p}\}_{i=1}^n$ is defined, as given in Eq. 1 [24]:

$$N_{i,0}(\xi) = \begin{cases} 1 & \text{if } \xi_i \leq \xi < \xi_{i+1}, \\ 0 & \text{otherwise,} \end{cases} \quad (1)$$

and for $p \geq 1$, we have Eq. 2:

$$N_{i,p}(\xi) = \frac{\xi - \xi_i}{\xi_{i+p} - \xi_i} N_{i,p-1}(\xi) + \frac{\xi_{i+p+1} - \xi}{\xi_{i+p+1} - \xi_{i+1}} N_{i+1,p-1}(\xi), \quad (2)$$

where ξ represents the parametric coordinate, p denotes the polynomial order, and n is the number of basis functions or control points. Eqs 1 and 2 are usually obtained using the Cox-de-Boor recursive formula.

NURBS [9] is an important CAD geometric modeling technique developed on the B-splines and is accepted as an industry standard. The NURBS surface is defined, as given in Eq. 3:

$$\mathbf{S}(\xi, \eta) = \sum_{i=1}^n \sum_{j=1}^m \frac{R_{i,j}^{p,q}(\xi, \eta) \mathbf{P}_{i,j}}{\sum_{i'=1}^n \sum_{j'=1}^m \frac{N_{i',p}(\xi) M_{j',q}(\eta) W_{i',j'}}{R_{i',j'}^{p,q}(\xi, \eta)}}, \quad (3)$$

where $N_{i,p}(\xi)$ and $M_{j,q}(\eta)$ are the B-spline basis functions, η represents the parametric coordinate, and $W_{i,j}$ is the weight associated with the control point $\mathbf{P}_{i,j}$.

2.1.2 Boundary element method for exterior acoustic problems

In order to calculate the Kirchhoff–Helmholtz integral equation for exterior acoustic issues, the boundary element method (BEM) is utilized to solve the well-known Helmholtz equation. The Kirchhoff–Helmholtz boundary integral equation can be derived from the Helmholtz equation using Green's second theorem, as shown in Eq. 4:

$$\begin{aligned} c(\mathbf{x})p(\mathbf{x}) + \int_{\Gamma} \frac{\partial G(\mathbf{x}, \mathbf{y})}{\partial \mathbf{n}(\mathbf{y})} p(\mathbf{y}) d\Gamma(\mathbf{y}) \\ = \int_{\Gamma} G(\mathbf{x}, \mathbf{y}) q(\mathbf{y}) d\Gamma(\mathbf{y}), \quad \mathbf{x}, \mathbf{y} \in \Gamma, \end{aligned} \quad (4)$$

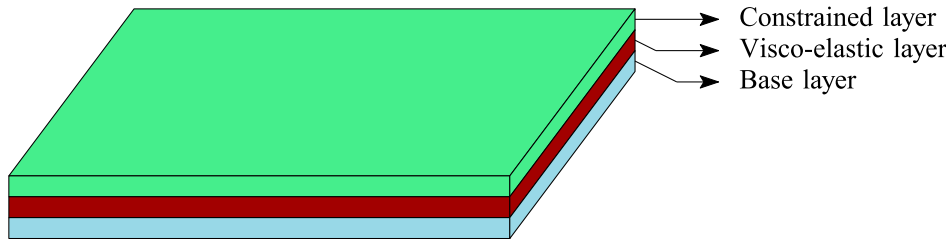


FIGURE 1
Plate structures with constrained-layer damping treatments.

where \mathbf{x} is the field point, \mathbf{y} is the source point situated at the boundary Γ , $\mathbf{n}(\mathbf{y})$ denotes the outward normal vector at point \mathbf{y} , and $\partial(\cdot)/\partial\mathbf{n} = \nabla(\cdot) \cdot \mathbf{n}$ denotes the normal derivative. When the boundary is smooth around point \mathbf{x} , the coefficient $c(\mathbf{x})$ is $1/2$, and when $\mathbf{x} \in \Omega$, it is 1 . The integral equation produced by this formulation can be used to calculate the sound pressure at points of the exterior domain. $G(\mathbf{x}, \mathbf{y})$, as shown in Eq. 5, is Green's function:

$$G(\mathbf{x}, \mathbf{y}) = \frac{e^{ik|\mathbf{x}-\mathbf{y}|}}{4\pi|\mathbf{x}-\mathbf{y}|}. \quad (5)$$

The linear system of the equation that results from discretizing the aforementioned integral equation using the collocation method is given in Eq. 6:

$$\mathbf{H}\mathbf{p} = \mathbf{G}\mathbf{v}, \quad (6)$$

where \mathbf{H} and \mathbf{G} are the BEM influence matrices, which are typically frequency-dependent and asymmetric, and \mathbf{p} and \mathbf{v} are vectors that, respectively, contain unknown sound pressures and given acoustic particle velocities on the boundary. Eq. 7 gives the definition of acoustic intensity:

$$\mathbf{I} = \frac{1}{2} \Re(\mathbf{p}\mathbf{v}^*), \quad (7)$$

where \Re stands for the real portion and $()^*$ for the complex conjugate. Eq. 8 defines the radiated sound power based on acoustic intensity:

$$P = \int_{\Gamma} \mathbf{I} \cdot \mathbf{n} \, d\Gamma(\mathbf{y}), \quad (8)$$

where \mathbf{n} is the outward normal direction on Γ .

2.1.3 Plate vibration analysis

Following [25], the plate structure is assumed to be discretized into three layers, as shown in Figure 1, that is, the constrained-layer damping (CLD) plate. It is composed of a base layer, a visco-elastic layer, and a constrained layer. Shear strains are only considered in the constrained layer. Moreover, we neglect the energy dissipation in the constrained layer and the base layer. In this work, we include the damping effects of the visco-elastic layer by introducing an imaginary component to Young's modulus E as given in Eq. 9:

$$E_d = E(1 - i\gamma), \quad (9)$$

where E_d and γ are the complex Young's modulus and loss factor of damping material, respectively. To model the constrained-layer damping plate, we adopt the finite element model used by [25]. In

this model, the NURBS basis function is used to discretize the partial differential equation, and the elemental matrices are composed of three parts, as shown in Eq. 10:

$$\begin{aligned} \mathbf{K}^e &= \mathbf{K}_b^e + \mathbf{K}_v^e + \mathbf{K}_c^e, \\ \mathbf{M}^e &= \mathbf{M}_b^e + \mathbf{M}_v^e + \mathbf{M}_c^e, \end{aligned} \quad (10)$$

where \mathbf{K}_b^e , \mathbf{K}_v^e , \mathbf{K}_c^e and \mathbf{M}_b^e , \mathbf{M}_v^e , \mathbf{M}_c^e represent the elemental stiffness and mass matrices for the base, visco-elastic, and constrained layers, respectively. By assembling the elemental matrices to the global matrices, we have Eq. 11:

$$(\mathbf{K} - \omega^2 \mathbf{M})\mathbf{u} = \mathbf{f}_s, \quad (11)$$

where \mathbf{u} is the displacement vector and \mathbf{f}_s is the structural load. For convenience, we use \mathbf{K}_d to represent $(\mathbf{K} - \omega^2 \mathbf{M})$ in the following sections.

2.2 Rayleigh integral for sound radiation

Assuming a baffled plate, the sound pressure at any point can be computed via the Rayleigh integral equation, expressed as Eq. 12:

$$p_f(\mathbf{x}) = \frac{i\omega\rho_f}{2\pi} \int_{\Gamma} \frac{e^{ikr}}{r} v_f(\mathbf{y}) \, d\Gamma(\mathbf{y}), \quad (12)$$

where p_f is the sound pressure, $r = |\mathbf{x} - \mathbf{y}|$ is the distance between point \mathbf{x} and \mathbf{y} , k is the wavenumber, and v_f is the particle velocity resulting from the structural vibrations. After discretizing by the collocation method, we obtain Eq. 13:

$$\mathbf{p}_f = \mathbf{G}\mathbf{v}_f, \quad (13)$$

where \mathbf{p}_f denotes the sound pressure on collocation points, and the particle velocity \mathbf{v}_f at the collocation points can be interpolated based on the structural displacement \mathbf{u} by $\mathbf{v}_f = -\dot{\mathbf{u}}_s = i\omega\Theta^{-1}\mathbf{C}_{fs}\mathbf{u}$, where Θ is the boundary mass matrix [6] and \mathbf{C}_{fs} is the coupling matrix. \mathbf{G} is the coefficient matrix, which is dense and asymmetric. Then, the sound power can be computed by the sound pressure and velocity using Eq. 14:

$$P = -\frac{1}{2} \Re(\mathbf{p}_f^T \Theta \mathbf{v}_f^*) = \frac{1}{2} \Re(\mathbf{v}_f^T \mathbf{Z} \mathbf{v}_f^*), \quad (14)$$

where $()^T$ denotes the transposed matrix. Here, the minus sign is introduced because of the direction of the particle velocity. $\mathbf{Z} = -\mathbf{G}^T \Theta$ is the impedance matrix, which is not symmetric due to discretization error when using the collocation method. However, the

symmetrization of Z can be simply achieved by $Z = (Z + Z^T)/2$. The Rayleigh integral equation can be regarded as a special case of the BEM, where $H = H^{-1} = I$. Considering the symmetry, the sound power can be further rewritten as Eq. 15:

$$W = \frac{1}{2} \mathbf{v}_f^T \Re(Z) \mathbf{v}_f = \frac{1}{2} \mathbf{v}_f^T Z_R \mathbf{v}_f, \quad (15)$$

where Z_R is the resistive impedance matrix. Another alternation to obtain Z_R is first computing the sound power as the integration of sound intensity over the surface Γ , as given in Eq. 16:

$$\begin{aligned} W &= \frac{1}{2} \int_{\Gamma} \Re[p^*(\mathbf{x}) v_f(\mathbf{x})] d\Gamma(\mathbf{x}) \\ &= \frac{\omega \rho_f}{4\pi} \int_{\Gamma} \int_{\Gamma} v_f^*(\mathbf{x}) \frac{e^{ikr}}{r} v_f(\mathbf{y}) d\Gamma(\mathbf{x}) d\Gamma(\mathbf{y}). \end{aligned} \quad (16)$$

Then, as given in Eq. 17, the entry of matrix Z_R reads:

$$Z_R^{ij} = \frac{\omega \rho_f}{2\pi} \int_{\Gamma_j} \int_{\Gamma_i} \frac{\sin kr}{r} d\Gamma(\mathbf{x}) d\Gamma(\mathbf{y}). \quad (17)$$

If we use a one-point Gauss–Legendre quadrature scheme, the entry can be approximated as given in Eq. 18:

$$Z_R^{ij} = \frac{\omega \rho_f S_i S_j}{2\pi} \frac{\sin kr_{ij}}{r_{ij}}, \quad (18)$$

where r_{ij} denotes the distance between the collocation points located in elements i and j and S_i and S_j are areas of elements i and j . When $i = j$, $r \rightarrow 0$ and $(\sin kr)/r \rightarrow k$. Apparently, this approach is much more efficient than the collocation method since it does not require integrals. However, this approach cannot yield the sound pressure field because of the singularity in e^{ikr}/r .

2.3 Non-negative intensity

To omit the cancellation effects of sound intensity, we use NNI proposed by [6] and named by [7] to visualize the surface contribution. Following references [6, 26], sound power can be expressed by Eq. 19:

$$P = \int_{\Gamma} I_{\text{NNI}}(\mathbf{x}) d\Gamma(\mathbf{x}) = +\frac{1}{2} \boldsymbol{\beta}^H \boldsymbol{\Theta} \boldsymbol{\beta}, \quad (19)$$

where $I_{\text{NNI}}(\mathbf{x})$ denotes NNI, which is defined by Eq. 20:

$$I_{\text{NNI}}(\mathbf{x}) = +\frac{1}{2} \boldsymbol{\beta}^*(\mathbf{x}) \boldsymbol{\beta}(\mathbf{x}), \quad (20)$$

where $\boldsymbol{\beta}(\mathbf{x})$ is a quantity without physical significance and $()^*$ denotes the conjugate of complex values. Apparently, $I_{\text{NNI}}(\mathbf{x})$ has to be non-negative. After discretizing, the sound power can be reformulated as Eq. 21:

$$P = +\frac{1}{2} \boldsymbol{\beta}^H \boldsymbol{\Theta} \boldsymbol{\beta}, \quad (21)$$

where $()^H$ denotes the transpose conjugate of a complex matrix. As proposed by [6], the complex vector $\boldsymbol{\beta}$ can be calculated by Eq. 22:

$$\boldsymbol{\beta} = \mathbf{B} \boldsymbol{\Theta} \mathbf{v}_f = \boldsymbol{\Phi} \sqrt{\Lambda} \boldsymbol{\Phi}^T \boldsymbol{\Theta} \mathbf{v}_f, \quad (22)$$

where $\boldsymbol{\Phi}$ and Λ are the matrix-storing eigenvector ϕ and diagonal matrix-storing eigenvalue λ by solving the following generalized eigenvalue problem, as shown in Eq. 23:

$$\mathbf{Z}_R \boldsymbol{\phi} = \lambda \boldsymbol{\Theta} \boldsymbol{\phi}. \quad (23)$$

In fact, the computation of the sound power based on $\boldsymbol{\beta}$ is equivalent to mapping the radiation modes, which could apparently reduce the computational efforts the eigensolutions are truncated, since the radiation is dominated by the first fewer radiation modes in the low-frequency range.

3 Optimization problem

3.1 Optimization problem definition

Usually, the objective function of a structural-acoustic system can be categorized into two main types. One is the sound pressure and its variants at one or more points, and the other is the sound power and its variants, which are more suitable for general noise and vibration control in open domains. In this work, we adopt the second type and define the optimization problem as given in Eq. 24:

$$\begin{cases} \min_{\boldsymbol{\mu}} & \Pi = \Pi(\mathbf{u}, \mathbf{p}_f), \\ \text{s.t.} & \sum_{e=1}^{N_e} \mu_e v_e - f_v \sum_{e=1}^{N_e} v_e \leq 0, \\ & 0 \leq \mu_e \leq 1 \quad (e = 1, \dots, N_e), \end{cases} \quad (24)$$

where the objective function Π represents a real-valued function of state variables \mathbf{u} and \mathbf{p}_f . This expression is adopted for convenience because we will investigate more than one objective function. $\boldsymbol{\mu} = [\mu_1, \mu_2, \dots, \mu_{N_e}]^T$ is the design variable vector, and N_e denotes the number of chosen design elements. The symbol v_e denotes the volume of the e th element and f_v denotes the corresponding volume fraction constraint.

3.2 Material interpolation with RAMP formulation

Following the SIMP method, elemental matrices can be interpolated as given in Eq. 25:

$$\begin{aligned} \mathbf{K}^e(\mu_e) &= \mathbf{K}_b^e + \mu_e^p \mathbf{K}_v^e + \mathbf{K}_c^e, \\ \mathbf{M}^e(\mu_e) &= \mathbf{M}_b^e + \mu_e^q \mathbf{M}_v^e + \mathbf{M}_c^e, \end{aligned} \quad (25)$$

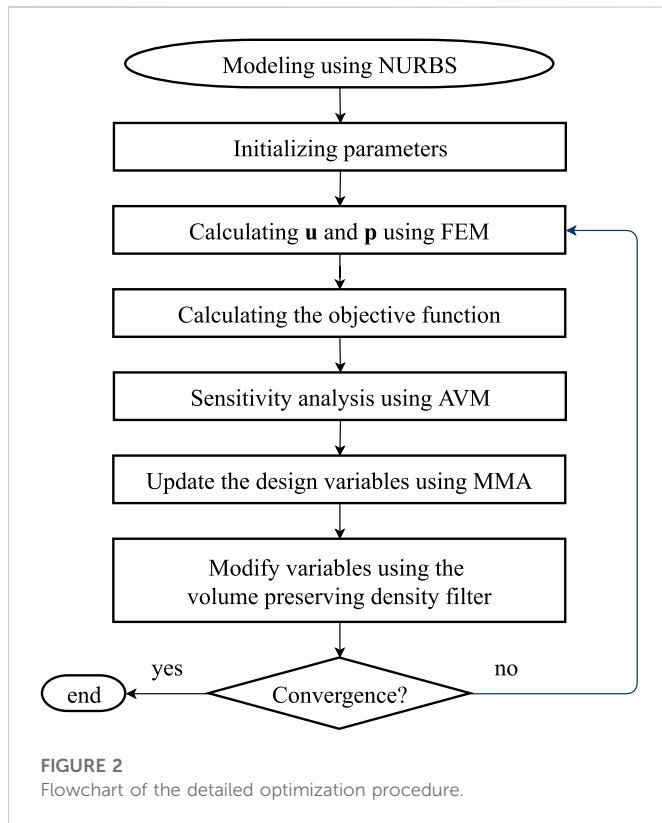
where μ_e is the design variable assigned to the e th element and p and q are the penalization factors and are usually chosen to be 3 and 1, respectively. These factors make the intermediate value approach 0 (no visco-elastic element) or 1 (visco-elastic element). Since the damping layer is attached to the base structure, the problem of localized modes can be avoided, as discussed by [27]. Then, the derivatives of the elemental matrices with respect to the e th design variable can be directly given by Eq. 26:

$$\begin{aligned} \frac{\partial \mathbf{K}^e}{\partial \mu_e} &= p \mu_e^{p-1} \mathbf{K}_v^e, \\ \frac{\partial \mathbf{M}^e}{\partial \mu_e} &= q \mu_e^{q-1} \mathbf{M}_v^e. \end{aligned} \quad (26)$$

Eq. 26 will be used in the sensitivity analysis.

3.3 Design sensitivity analysis

In the present work, we choose the gradient-based algorithm to solve the optimization problem described in Eq. 24. Hence, the derivative of the objective function, that is, the sensitivity



information, is necessary. In the computation of FEM/FMBEM sensitivity, the adjoint variable method (AVM) exhibits excellent accuracy and efficiency [28]. So, AVM is applied for the sensitivity analysis in this work.

First, we can directly write the derivative of the objective function by applying the chain rule as Eq. 27:

$$\frac{\partial \Pi}{\partial \mu_e} = \Re \left(\mathbf{z}_1^T \frac{\partial \mathbf{u}}{\partial \mu_e} + \mathbf{z}_2^T \frac{\partial \mathbf{p}_f}{\partial \mu_e} + z_3 \right), \quad (27)$$

where \mathbf{z}_1^T , \mathbf{z}_2^T , and z_3 are auxiliary variables from [29]. z_3 does not contain the derivatives of state variables, that is, $\partial \mathbf{u} / \partial \mu_e$ and $\partial \mathbf{p}_f / \partial \mu_e$. Since sound pressure can be computed directly from the particle velocity via $\mathbf{p}_f = \mathbf{G} \mathbf{v}_f = i\omega \mathbf{G} \Theta^{-1} \mathbf{C}_{fs} \mathbf{u}$, we get Eq. 28:

$$\frac{\partial \Pi}{\partial \mu_e} = \Re \left[\left(\mathbf{z}_1^T + i\omega \mathbf{z}_2^T \mathbf{G} \Theta^{-1} \mathbf{C}_{fs} \right) \frac{\partial \mathbf{u}}{\partial \mu_e} + z_3 \right]. \quad (28)$$

Then, the direct differentiation of Eq. 11 yields Eq. 29:

$$\frac{\partial \mathbf{K}_d}{\partial \mu_e} \mathbf{u} + \mathbf{K}_d \frac{\partial \mathbf{u}}{\partial \mu_e} = \frac{\partial \mathbf{f}_s}{\partial \mu_e} = 0. \quad (29)$$

Since we only consider design-independent load, the derivative of structural load, that is, $\partial \mathbf{f}_s / \partial \mu_e$ vanishes. Combining Eqs 28 and 29, the derivative of the objective function can be written as Eq. 30:

$$\frac{\partial \Pi}{\partial \mu_e} = \Re \left[z_3 - \left(\mathbf{z}_1^T + i\omega \mathbf{z}_2^T \mathbf{G} \Theta^{-1} \mathbf{C}_{fs} \right) \mathbf{K}_d^{-1} \frac{\partial \mathbf{K}_d}{\partial \mu_e} \mathbf{u} \right]. \quad (30)$$

The derivative of displacement, that is, $\partial \mathbf{u} / \partial \mu_e$, is omitted in Eq. 30. By defining the adjoint equation as given in Eq. 31:

$$\lambda^T \mathbf{K}_d = \left(\mathbf{z}_1^T + i\omega \mathbf{z}_2^T \mathbf{G} \Theta^{-1} \mathbf{C}_{fs} \right), \quad (31)$$

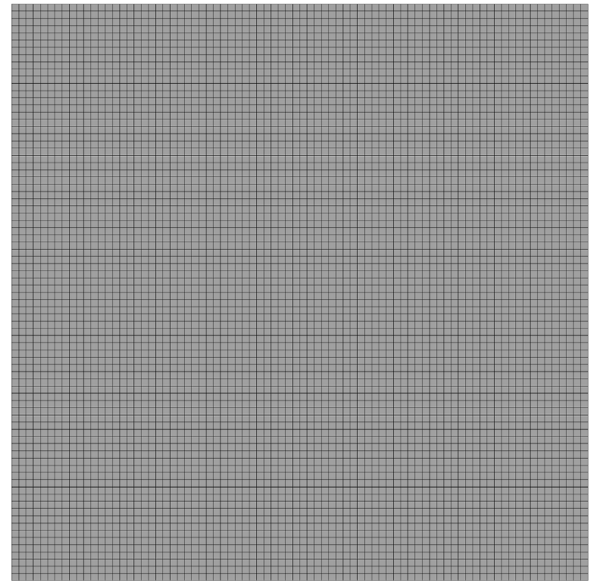


FIGURE 3
Computational grid.

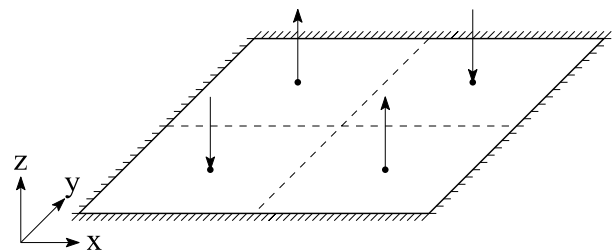


FIGURE 4
Clamped plate example definition.

and the derivative of the objective function can be finally expressed by the adjoint vector λ as given in Eq. 32:

$$\frac{\partial \Pi}{\partial \mu_e} = \Re \left(z_3 - \lambda^T \frac{\partial \mathbf{K}_d}{\partial \mu_e} \mathbf{u} \right). \quad (32)$$

The adjoint method is therefore not free since it requires solving the extra adjoint equation. The adjoint equation, however, only needs to be solved once because it does not contain derivative components. According to the used interpolation scheme for the material properties defined in Section 3.2, the derivative of the matrix \mathbf{K}_d could be simply computed, as given in Eq. 33:

$$\frac{\partial \mathbf{K}_d}{\partial \mu_e} = \frac{\partial \mathbf{K}}{\partial \mu_e} - \omega^2 \frac{\partial \mathbf{M}}{\partial \mu_e}, \quad (33)$$

from which, we have Eq. 34:

$$\frac{\partial \mathbf{D}}{\partial \mu_e} = \begin{bmatrix} \frac{\partial \mathbf{D}^e}{\partial \mu_e} & 0 \\ 0 & 0 \end{bmatrix}, \quad \mathbf{D} = \mathbf{K} \text{ or } \mathbf{M}. \quad (34)$$

TABLE 1 Material properties of the constrained-layer damping plate.

	Density	Modulus	Thickness	Poisson's ratio	Loss factor
	(kg/m ³)	(MPa)	(mm)		
Base layer	2,700	7×10^4	1	0.3	—
Visco-elastic layer	1,200	12	0.3	0.495	0.5
Constrained layer	2,700	7×10^4	0.5	0.3	—

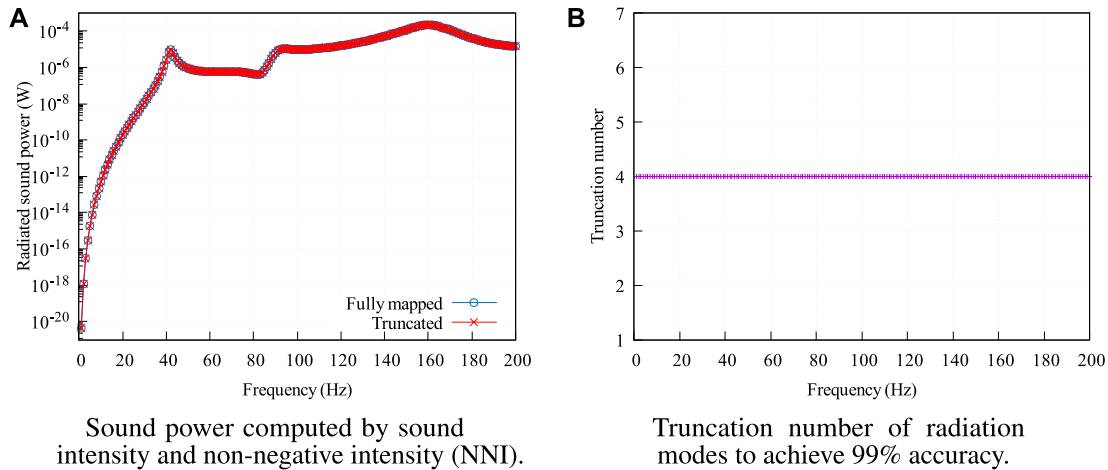


FIGURE 5

Radiated sound power and truncation number versus frequency. (A) Sound power computed by sound intensity and non-negative intensity (NNI). (B) Truncation number of radiation modes to achieve 99% accuracy.

3.4 Objective functions

Since the sound power can be calculated using the sound intensity or NNI, we define two objective functions, as shown in Eq. 35:

$$\begin{aligned} P_{SI} &= -\Re\left(\frac{1}{2}\mathbf{p}^H\mathbf{\Theta}_c\mathbf{v}\right), \\ P_{NNI} &= +\frac{1}{2}\mathbf{\beta}^H\mathbf{\Theta}_c\mathbf{\beta}, \end{aligned} \quad (35)$$

where H denotes the conjugate transpose and $\mathbf{\Theta}_c$ is the corresponding boundary mass matrix for the chosen surface. When $\mathbf{\Theta}_c = \mathbf{\Theta}$, we have $P_{SI} = P_{NNI} = P$. Note that P_{SI} can be negative due to the cancellation effects of sound intensity, whereas P_{NNI} is always non-negative. Following Eq. 27, we obtain Eq. 36 for the objective function P_{SI} :

$$\begin{cases} \mathbf{z}_1^T = i\omega\mathbf{p}_f^H\mathbf{C}_{fs}, \\ \mathbf{z}_2^T = (i\omega\mathbf{C}_{fs}\mathbf{u})^H, \\ \mathbf{z}_3 = 0, \end{cases} \quad (36)$$

and Eq. 37 for the objective function P_{NNI} :

$$\begin{cases} \mathbf{z}_1^T = 2\omega^2\mathbf{u}^H\mathbf{C}_{fs}^T\mathbf{B}^H\mathbf{\Theta}_c\mathbf{B}\mathbf{C}_{fs}, \\ \mathbf{z}_2^T = \mathbf{0}, \\ \mathbf{z}_3 = 0. \end{cases} \quad (37)$$

Based on the derived \mathbf{z}_1^T , \mathbf{z}_2^T , and \mathbf{z}_3 , the derivatives of P_{SI} and P_{NNI} could be easily calculated using Eqs 31 and 32.

3.5 Design variable updating scheme

Based on the sensitivity information, the method of moving asymptotes (MMA), see Svanberg [30], is employed to solve the optimization problem. The iteration procedure is repeated until the relative difference of the objective function values in two adjacent iteration steps is less than a prescribed tolerance τ , as shown in Eq. 38:

$$\text{change} = \frac{|\Pi^{i+1} - \Pi^i|}{\Pi^i} < \tau, \quad (38)$$

where Π^i denotes the objective function at the i th iteration step. The detailed optimization procedure is presented as follows:

1. Modeling using NURBS. The analyzed structural domain is divided into finite elements, and the impedance matrix and its real part are also computed based on the finite element mesh.
2. Setting up the optimization model with an initial distribution given for the design elements.
3. Solving the response problem described in Eq. 11. Then, the objective function is evaluated based on the solutions \mathbf{u} and \mathbf{p} . To achieve an efficient reanalysis, we only assemble matrices \mathbf{Z}_R

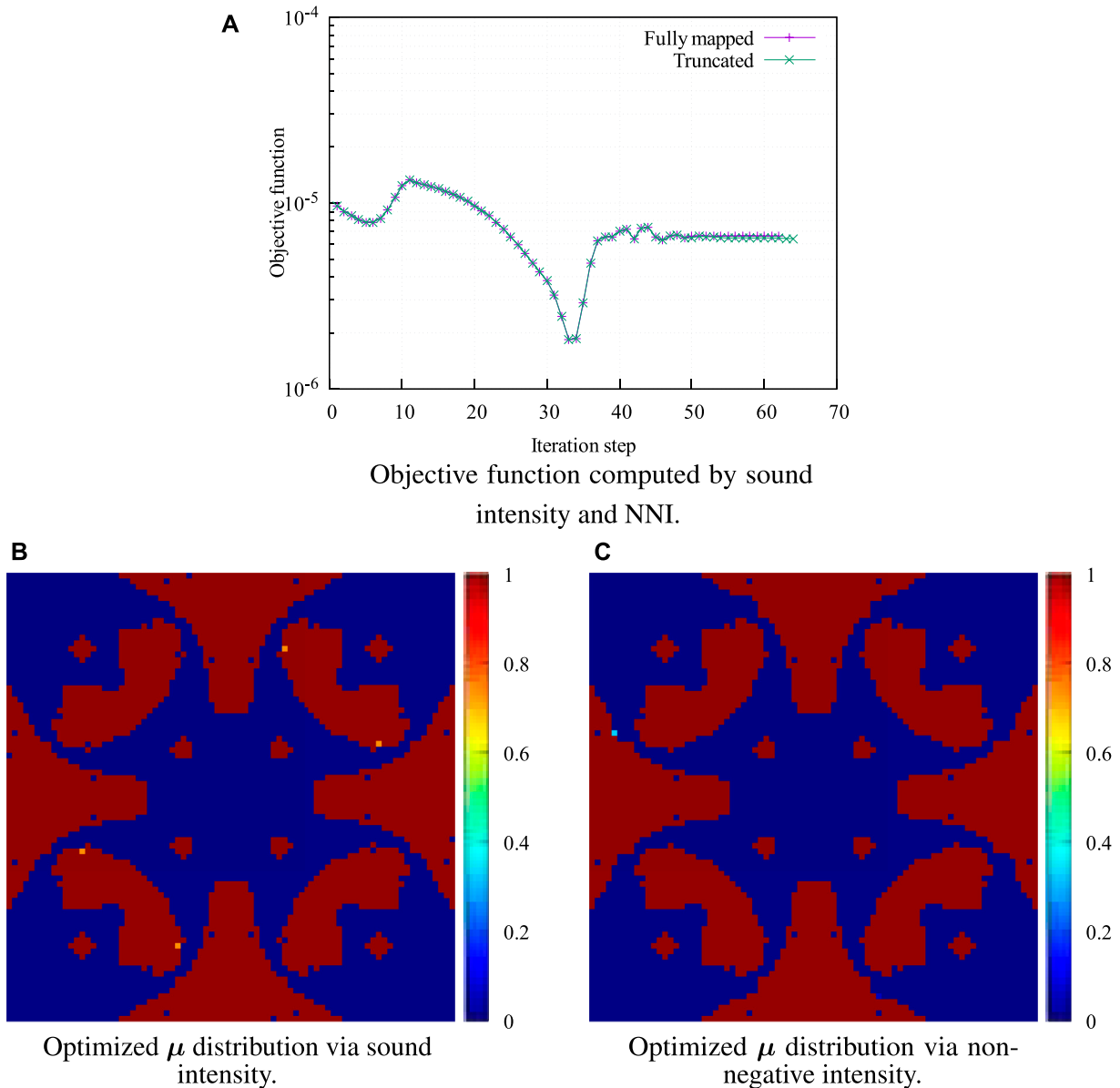


FIGURE 6

Optimization results obtained by sound intensity and NNI. (A) Objective function computed by sound intensity and NNI. (B) Optimized μ distribution via sound intensity. (C) Optimized μ distribution via non-negative intensity.

- (and Z) in the first optimization iteration, and these matrices will be recycled in the following iterations.
4. Solving the generalized eigenvalue problem described in Eq. 23 if required, and computing β based on the solution u . Similarly, we also store the eigenvectors and eigenvalues for a possible recycling step.
 5. Evaluating the chosen objective function (P_{SI} or P_{NNI}). Then, deriving auxiliary variables z_1^T , z_2^T , and z_3 using Eq. 36 or Eq. 37.
 6. Solving the adjoint Eq. 31 for derived z_1^T , z_2^T , and z_3 . With the adjoint variable λ , the sensitivity values are computed using Eq. 32.
 7. When the objective function converges like Eq. 38, optimization is stopped. Otherwise, the design variables are updated using the MMA.

8. Modifying the design variables by the volume-preserving density filter [31], and the procedure is repeated from step 3.

The corresponding flowchart is shown in Figure 2.

4 Numerical examples

To investigate the validity and applicability of the developed optimization approach, some numerical examples are performed in this section. All the computations are implemented in an in-house Fortran 95/2003 code. Sparse direct solver PARDISO is applied to all computations involving the global dynamic stiffness K_d . Eigenvalue

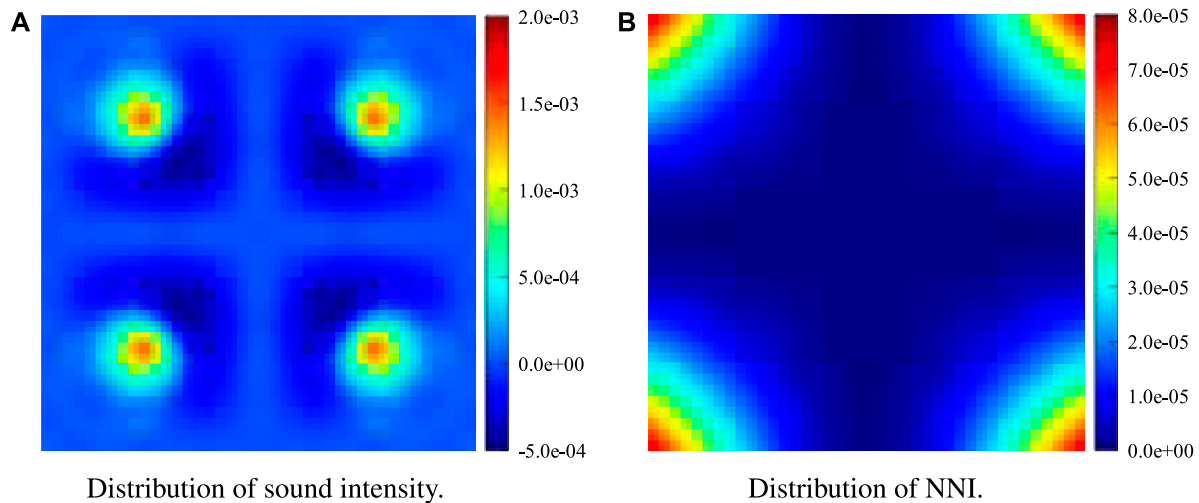


FIGURE 7

Distributions of sound intensity and NNI at 100 Hz. (A) Distribution of sound intensity. (B) Distribution of NNI.

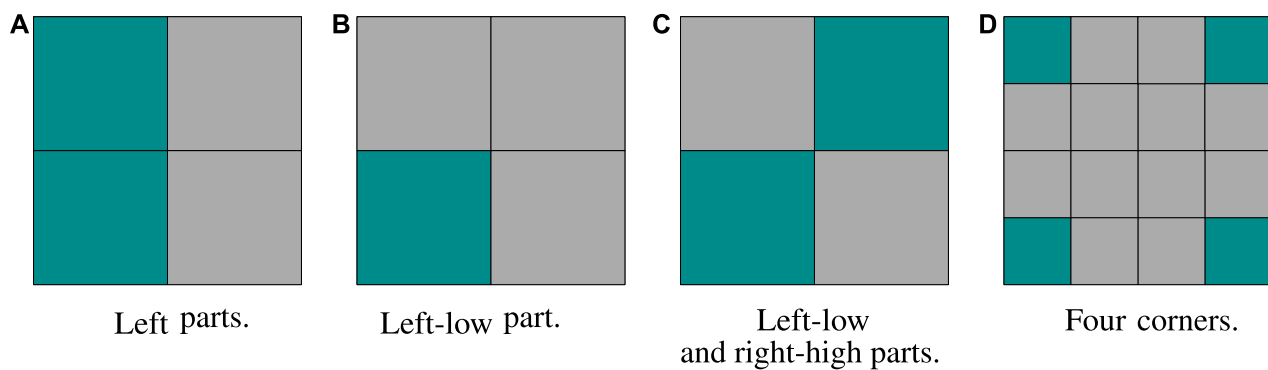


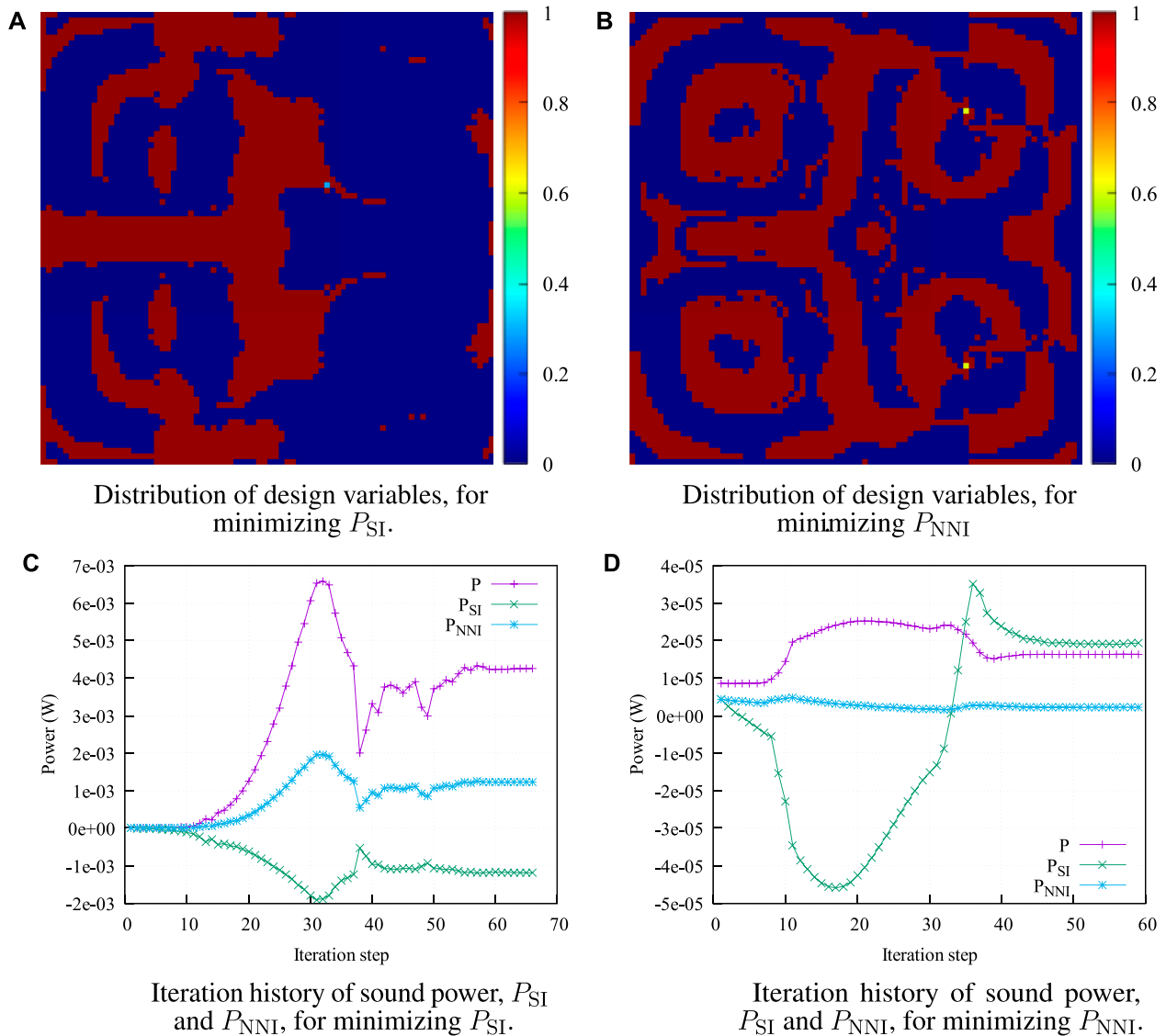
FIGURE 8

Different chosen surface Γ_c , cyan color represents the chosen parts. (A) Left parts. (B) Lower left part. (C) Lower left and upper right parts. (D) Four corners.

problems described in Eq. 23 are solved using the ARPACK routines. The convergence tolerance τ in the optimization is set to 10^{-4} .

A baffled plate of dimensions $1 \text{ m} \times 1 \text{ m}$ will be chosen as the design object in the following example. It is discretized into 80×80 four-node quadrilateral elements, as shown in Figure 3. The finite element model is verified by comparing the natural frequencies and modal loss factors from the present model with those from a closed-form solution [32]. Regarding radiation analysis, the collocation method will be only used when sound intensity is required, otherwise the direct method without integration will be applied instead, in order to save computational costs. We assume the plate to be clamped at its four edges and excited by four harmonic loads $F = F_0 e^{-i\omega t}$ as shown in Figure 4. Air is the acoustic medium, with $c = 343 \text{ m/s}$ and $\rho = 1.21 \text{ kg/m}^3$. The base and constrained layers consist of aluminum with no damping loss, and the core layer is assumed to consist of a visco-elastic material. Detailed material properties are listed in Table 1.

As mentioned previously, the computational efforts will be reduced when truncating eigensolutions in mapping the radiation modes for evaluating NNI and sound power. Figure 5 shows the Radiated sound power and truncation number versus frequency. In Figure 5A, we compare the sound power computed by sound intensity and NNI resulting from mapping truncated radiation modes, and these two results match very well. We also investigate the truncation number to achieve 99% accuracy compared with the sound power computed by sound intensity in Figure 5B. From the result, we notice that a truncation number of 4 is acceptable for the calculation with a frequency range of 200 Hz. In fact, the sound power is dominantly contributed by the fourth radiation mode because the particle velocity corresponds to the fourth modal pattern. This can be confirmed by investigating the coupling factor of particle velocity with the radiation modes [33]. The coupling factor between the particle velocity pattern and the fourth mode is several orders of magnitude larger than the coupling factor with the first three radiation modes. In the

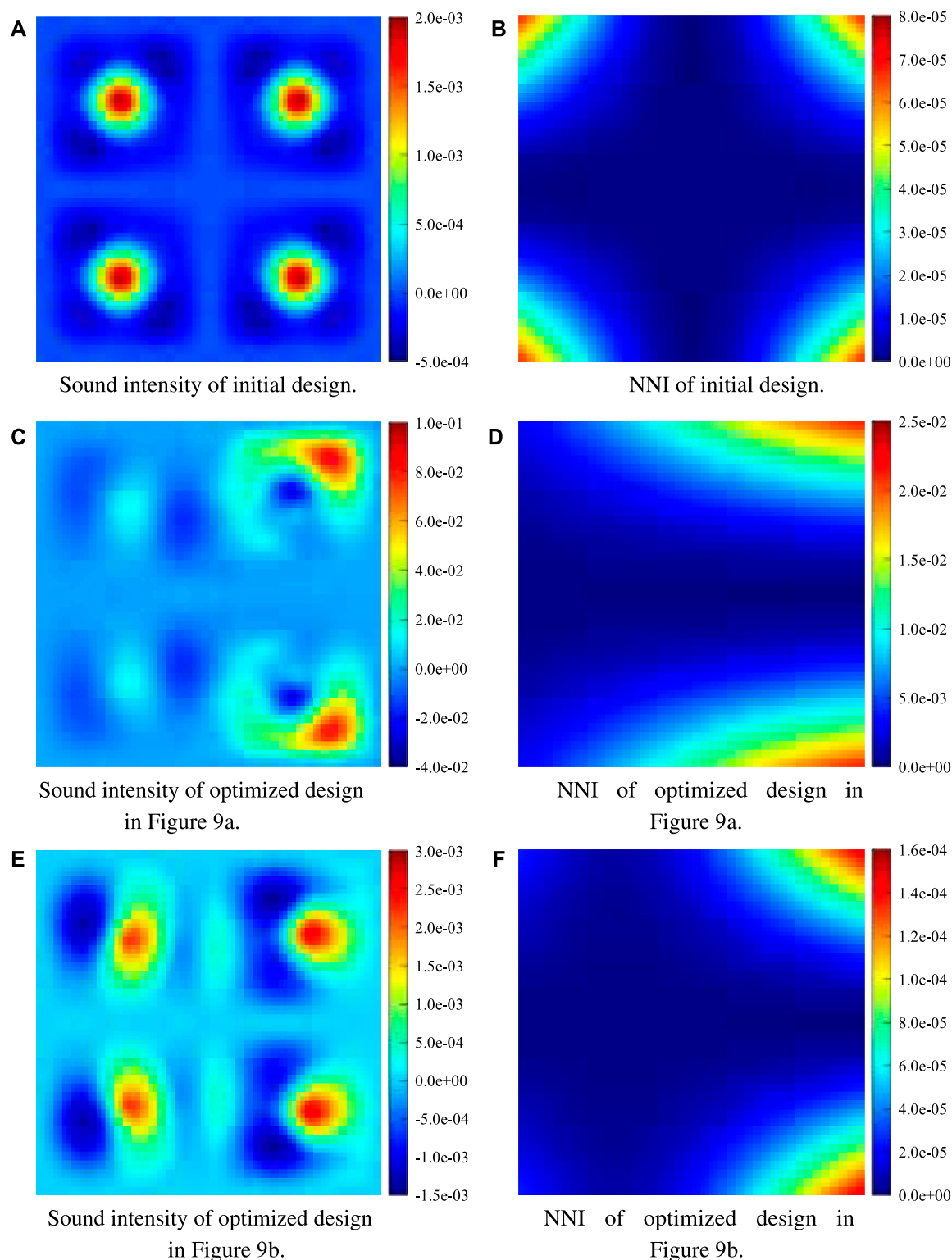
**FIGURE 9**

Optimization results of P_{SI} and P_{NNI} . The left parts are chosen as the investigated surface Γ_c . **(A)** Distribution of design variables, for minimizing P_{SI} . **(B)** Distribution of design variables, for minimizing P_{NNI} . **(C)** Iteration history of sound power, P_{SI} and P_{NNI} , for minimizing P_{SI} . **(D)** Iteration history of sound power, P_{SI} and P_{NNI} , for minimizing P_{SI} .

following calculations, we set a higher truncation number of 30 to guarantee correctness and accuracy, and this still saves considerable costs compared with the computation *via* sound intensity. As a further investigation, we compare the optimization results, which aim at minimizing the radiated computed sound power using truncated acoustic radiation modes. The excitation frequency is assumed to be $f = 100$ Hz. All the initial design variables are given a uniform value of 1 to avoid possible local minimum. The optimization iteration history is illustrated in Figure 6A. Figures 6B, C show the optimized distributions of the design variables μ . Red ($\mu_e = 1$) represents the visco-elastic damping element, and blue ($\mu_e = 0$) indicates that there is no visco-elastic element. Intermediate values ($0 < \mu_e < 1$) are not physical and are difficult to observe in Figures 6B, C. It can be clearly seen that the two optimizations yield almost the same iteration history and optimization solution. Slight

differences between the two optimized designs are possibly caused by numerical error in the eigenvalue analysis and optimization solution. This proves that mapping truncated radiation modes could be an efficient approach to evaluate the sound power without losing accuracy in the response analysis and optimization process at low frequencies. Interestingly, we find that the optimized design yields an even lower sound power (6.6×10^{-12} W) than that (9.7×10^{-12} W) of the initial design with a full visco-elastic damping layer, which is similar to the findings in [29]. This indicates that the investigated optimization is a nonlinear problem and thus stresses the necessity of optimization.

Figure 7 shows the distributions of sound intensity and NNI, which are different. The result of NNI is consistent with the corner radiation introduced by [34] and confirmed by [5] using the supersonic intensity, while the sound intensity is not consistent

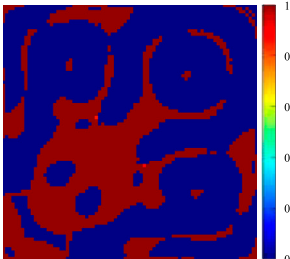
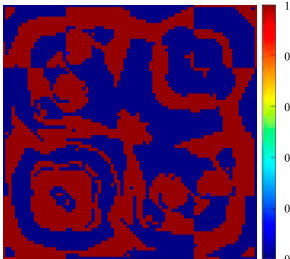
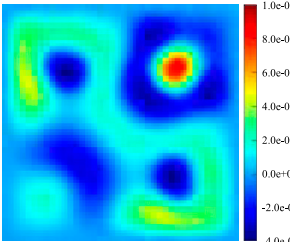
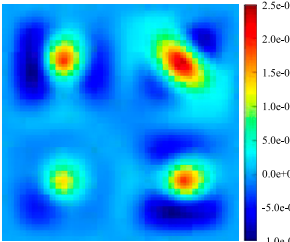
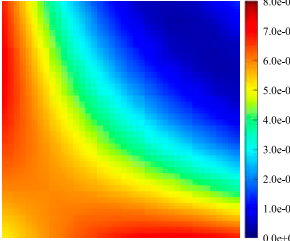
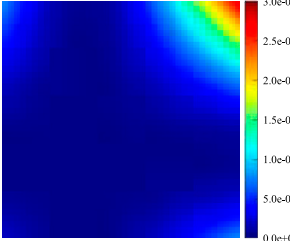
**FIGURE 10**

Distributions of sound intensity and NNI of different designs. (A) Sound intensity of initial design. (B) NNI of initial design. (C) Sound intensity of optimized design in Figure 9A. (D) NNI of optimized design in Figure 9A. (E) Sound intensity of optimized design in Figure 9B. (F) NNI of optimized design in Figure 9B.

since it could be positive or negative. This is similar to the result presented by [6] where the authors used a (1×1) structural modal shape as the particle velocity pattern. It has been clearly shown that NNI (computed *via* mapped radiation modes) could localize

the most contributing areas on structural surfaces, while sound intensity fails due to its cancellation effects. But in the aforementioned optimization, NNI does not outperform sound intensity since they give completely the same objective function

TABLE 2 Optimized results at 100 Hz when the lower left part in Figure 8B is chosen as the investigated surface Γ_c . The left column corresponds to the results with P_{SI} being the objective function, and the right column corresponds to the results with P_{NNI} being the objective function.



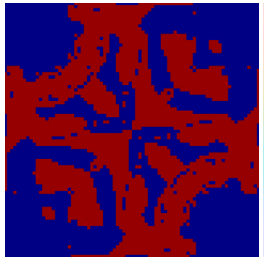
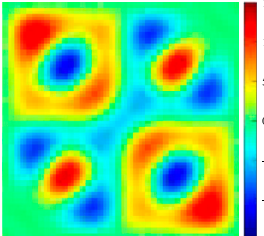
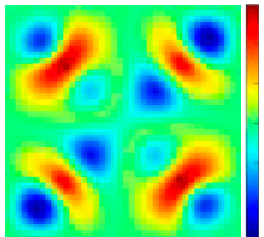
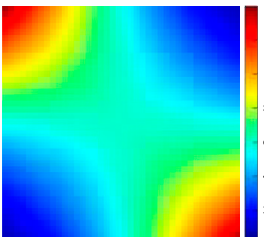
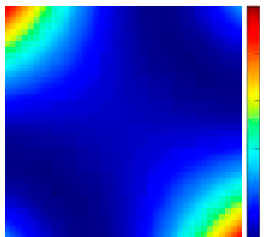
	Objective function	
	Integration of sound intensity (P_{SI})	Integration of NNI (P_{NNI})
Optimized distribution of design variables	 <p>Initial value: $\mu = 0.7$, volume fraction: 0.33</p>	 <p>Initial value: $\mu = 0.7$, volume fraction: 0.47</p>
Sound intensity after optimization	 <p>Maximum: $I_{SI} = 8.7 \times 10^{-2} \text{ W / m}^2$ Minimum: $I_{SI} = -4.0 \times 10^{-2} \text{ W / m}^2$</p>	 <p>Maximum: $I_{SI} = 2.4 \times 10^{-3} \text{ W / m}^2$ Minimum: $I_{SI} = -9.7 \times 10^{-4} \text{ W / m}^2$</p>
NNI after optimization	 <p>Maximum: $I_{NNI} = 7.0 \times 10^{-3} \text{ W / m}^2$ Minimum: $I_{NNI} = 3.1 \times 10^{-4} \text{ W / m}^2$</p>	 <p>Maximum: $I_{NNI} = 2.8 \times 10^{-4} \text{ W / m}^2$ Minimum: $I_{NNI} = 6.8 \times 10^{-10} \text{ W / m}^2$</p>
Power before and after optimization	<p>Initial design: $P = 8.7 \times 10^{-6} \text{ W}$, $P_{SI} = P_{NNI} = P/4$ Optimized design: $P = 3.8 \times 10^{-3} \text{ W}$, $P_{SI} = -5.1 \times 10^{-4} \text{ W}$, $P_{NNI} = 1.4 \times 10^{-3} \text{ W}$</p>	<p>Initial design: $P = 8.7 \times 10^{-6} \text{ W}$, $P_{SI} = P_{NNI} = P/4$ Optimized design: $P = 2.1 \times 10^{-5} \text{ W}$, $P_{SI} = 2.2 \times 10^{-6} \text{ W}$, $P_{NNI} = 4.3 \times 10^{-7} \text{ W}$</p>

when the whole surface is selected, that is, the radiated sound power. NNI, however, makes sense if we only want to decrease the radiation contributed by the partial surface. In this case, integration of the sound acoustic intensity, that is, P_{SI} , on the prescribed region does not directly correspond to the intensity that radiates to the far-field. This is the reason why

we implement the integration of NNI as the objective function instead of P_{SI} .

In Figure 8, we split the plate surface into several pieces and choose different pieces as the investigated area Γ_c where we want to minimize the sound radiation. When choosing the left parts as Γ_c , the optimization results are obtained and illustrated in Figure 9.



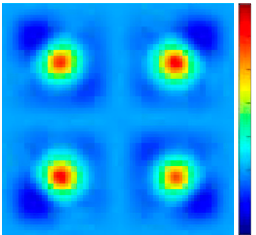
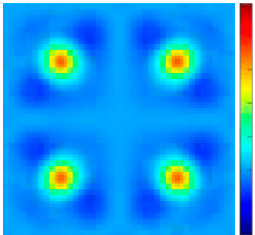
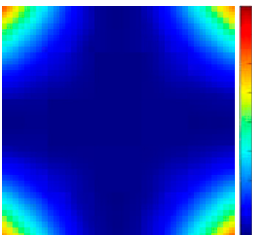
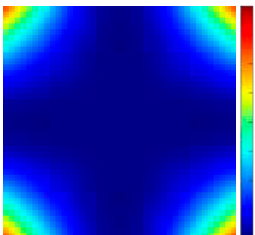
TABLE 3 Optimized results at 100 Hz when the lower left and upper right parts in Figure 8C are chosen as the investigated surface Γ_c . The left column corresponds to the results with P_{SI} being the objective function, and the right column corresponds to the results with P_{NNI} being the objective function.

	Objective function	
	Integration of sound intensity (P_{SI})	Integration of NNI (P_{NNI})
Optimized distribution of design variables	 <p>Initial value: $\mu = 0.7$, volume fraction: 0.21</p>	 <p>Initial value: $\mu = 1.0$, volume fraction: 0.47</p>
Sound intensity after optimization	 <p>Maximum: $I_{SI} = 0.13 \text{ W / m}^2$ Minimum: $I_{SI} = -0.12 \text{ W / m}^2$</p>	 <p>Maximum: $I_{SI} = 1.5 \times 10^{-3} \text{ W / m}^2$ Minimum: $I_{SI} = -1.4 \times 10^{-3} \text{ W / m}^2$</p>
NNI after optimization	 <p>Maximum: $I_{NNI} = 1.4 \times 10^{-2} \text{ W / m}^2$ Minimum: $I_{NNI} = 6.1 \times 10^{-4} \text{ W / m}^2$</p>	 <p>Maximum: $I_{NNI} = 9.4 \times 10^{-5} \text{ W / m}^2$ Minimum: $I_{NNI} = 2.9 \times 10^{-11} \text{ W / m}^2$</p>
Power before and after optimization	<p>Initial design: $P = 8.7 \times 10^{-6} \text{ W}$, $P_{SI} = P_{NNI} = P/2$ Optimized design: $P = 5.9 \times 10^{-3} \text{ W}$, $P_{SI} = -7.8 \times 10^{-4} \text{ W}$, $P_{NNI} = 2.0 \times 10^{-3} \text{ W}$</p>	<p>Initial design: $P = 9.7 \times 10^{-6} \text{ W}$, $P_{SI} = P_{NNI} = P/2$ Optimized design: $P = 1.2 \times 10^{-5} \text{ W}$, $P_{SI} = -5.3 \times 10^{-5} \text{ W}$, $P_{NNI} = 1.6 \times 10^{-6} \text{ W}$</p>

The initial values of the design variables are both set to 0.7. From this figure, it can be clearly seen that these two objective functions yield notably different optimized distributions of design variables, as shown in Figures 9A, B. After the optimization, P_{SI} drops from $4.33 \times 10^{-6} \text{ W}$ to $-1.18 \times 10^{-3} \text{ W}$, while the integration of NNI, that is, P_{NNI} , increases from $4.33 \times 10^{-6} \text{ W}$ to $1.22 \times 10^{-3} \text{ W}$. That is to

say, the real contributions from the left parts are enlarged by the optimization, which indicates that P_{SI} cannot correspond to the energy radiated to the far-field. By contrast, the optimization minimizing P_{NNI} produces a reduction from $4.33 \times 10^{-6} \text{ W}$ to $2.19 \times 10^{-6} \text{ W}$. The coincidence between P_{SI} and P_{NNI} at the beginning is due to the symmetry along the y axis with a

TABLE 4 Optimized results at 100 Hz when the four corners in Figure 8D are chosen as the investigated surface Γ_c . The left column corresponds to the results with P_{SI} being the objective function, and the right column corresponds to the results with P_{NNI} being the objective function.

	Objective function	
	Integration of sound intensity (P_{SI})	Integration of NNI (P_{NNI})
Optimized distribution of design variables	 <p>Initial value: $\mu = 1.0$, volume fraction: 0.47</p>	 <p>Initial value: $\mu = 0.7$, volume fraction: 0.50</p>
Sound intensity after optimization	 <p>Maximum: $I_{SI} = 8.7 \times 10^{-4} \text{ W / m}^2$ Minimum: $I_{SI} = -2.8 \times 10^{-4} \text{ W / m}^2$</p>	 <p>Maximum: $I_{SI} = 7.2 \times 10^{-4} \text{ W / m}^2$ Minimum: $I_{SI} = -1.5 \times 10^{-4} \text{ W / m}^2$</p>
NNI after optimization	 <p>Maximum: $I_{NNI} = 3.2 \times 10^{-5} \text{ W / m}^2$ Minimum: $I_{NNI} = 6.6 \times 10^{-8} \text{ W / m}^2$</p>	 <p>Maximum: $I_{NNI} = 3.2 \times 10^{-5} \text{ W / m}^2$ Minimum: $I_{NNI} = 1.8 \times 10^{-9} \text{ W / m}^2$</p>
Power before and after optimization	<p>Initial design: $P = 9.7 \times 10^{-6} \text{ W}$, $P_{SI} = 4.3 \times 10^{-5} \text{ W}$, $P_{NNI} = 7.3 \times 10^{-6} \text{ W}$ Optimized design: $P = 4.1 \times 10^{-6} \text{ W}$, $P_{SI} = -1.2 \times 10^{-5} \text{ W}$, $P_{NNI} = 3.1 \times 10^{-6} \text{ W}$</p>	<p>Initial design: $P = 8.7 \times 10^{-6} \text{ W}$, $P_{SI} = 1.1 \times 10^{-5} \text{ W}$, $P_{NNI} = 6.5 \times 10^{-6} \text{ W}$ Optimized design: $P = 4.2 \times 10^{-6} \text{ W}$, $P_{SI} = 4.6 \times 10^{-6} \text{ W}$, $P_{NNI} = 3.2 \times 10^{-6} \text{ W}$</p>

uniform distribution of design variables. From Figures 9C, D, we notice that the changing tendency of P_{SI} is opposite to that of P_{NNI} , but P_{NNI} and sound power W show a similar tendency. While the contributions from the left parts are considerably decreased, the sound power almost doubles from $8.66 \times 10^{-6} \text{ W}$ to $1.64 \times 10^{-5} \text{ W}$.

Figure 10 presents the distributions of sound intensity as well as NNI of the initial design (first row) and two optimized designs (second and third rows). To achieve a better optimization result, we conduct the optimization with different initial values of the design variable: $\mu = 0.7$ and $\mu = 1$ and then show the better one here. This

treatment will also be adopted in the following computations. The sound intensity and NNI patterns of the initial design are very similar to those in Figure 7 since they both correspond to a uniform distribution of design variables ($\mu = 0.7$ and $\mu = 1.0$). Hence, homogeneous damping distributions have a very small influence on the patterns of sound intensity and NNI except for detailed values. It is observed the sound intensity and NNI are redistributed by the optimizations in a different manner, which yields inhomogeneous damping distributions. Regarding the sound intensity, there are always adjacent areas exhibiting positive and negative values before and after optimization. From NNI, we notice that two radiating sources located at the left corners become weaker compared with the sources in the right corners after two optimizations. However, compared with the unoptimized source in Figure 10B, the two left sources in Figure 10D correspond to a higher NNI due to improper optimization, with P_{SI} being the objective function. When using P_{NNI} , these two corner sources are successfully suppressed. The optimization makes the contributions from the left corners to the sound power reduce from 50% to approximately 13%. This is attributed to improved cancellation effects of the acoustic source and sink in the left region, and thus less acoustic energy radiates to the far-field. In general, the optimization finally results in an inhomogeneous distribution of structural damping and redistributes the acoustic sink and source accordingly to minimize the objective function. Although the sound intensity performs well when minimizing the sound power is of interest, it shows inferiority in radiation control of the partial or local regions.

In Table 2, we present the optimization results for different investigated surface Θ_c , that is, the lower left part. Integrations of the sound intensity and NNI are also selected as the objective function. The first row shows the optimized distributions of design variables μ , resulting from the two objective functions. The second and third rows show the distributions of sound intensity and NNI, and the last row gives the power values before and after optimization. Since the optimization problem is not symmetric along the x and y axes, the resulting designs are also not symmetric anymore. From Table 2, we can see that P_{SI} decreases from 2.2×10^{-6} W to -5.1×10^{-4} W, showing a large reduction. P_{NNI} , however, increases from 2.2×10^{-6} W to 1.4×10^{-3} W. Since NNI provides a more accurate visualization of the contribution to sound power, optimization based on P_{SI} becomes meaningless because it increases the radiation from the chosen regions. Furthermore, the contributions from the lower left corner are still higher than those from the upper right corner after optimization aiming to decrease P_{SI} . That is to say, P_{SI} fails to give the desirable contributing/radiation pattern. When optimizing the damping distribution based on P_{NNI} , the power radiated from the predefined region reduces to a very low value of 4.3×10^{-7} W. The lower left corner becomes the least contributing compared with all other corners, which is exactly as expected. In addition, two corners adjacent to the lower left corner also become inconspicuous due to the redistributed damping. After optimization, there is only one hot spot located in the upper right corner which is opposite to the chosen region. The four-corner radiator becomes a one-corner radiator. Comparing the sound power, we find that all optimized solutions yield a high sound power because the optimization target is not minimizing the sound power radiated from the entire surface. From the sound

powers, it can be seen that the increase caused by optimization using P_{SI} can be very large, which is unfavorable. Compared with P_{SI} , the increase in sound power introduced by optimization using P_{NNI} is much smaller.

Similar to Tables 2–Tables 4 present optimization results with different investigated surfaces Θ_c . In Table 3, the lower left and upper right parts are selected. It can be clearly seen that two objective functions generate notably different distributions of the design variables with volume fractions of 0.21 and 0.47, respectively. The four-corner radiator becomes a two-opposite-corner radiator after the two optimizations, minimizing F_{SI} and F_{NNI} , respectively. Because Γ_c in Figure 8D is symmetric along both the x and y axes, this finally leads to symmetric distributions of damping, as shown in Table 4. We can notice that the distribution of sound intensity and NNI is very similar to that seen in Figure 7, which results from a homogeneous damping distribution. It can be considered that the waves traveling toward high-damped regions (but with opposite directions in one-fourth of the plate area) cancel each other. Hence, the corner mode remains nearly the same as the homogeneous mode. Interestingly, optimization minimizing F_{SI} produces a lower F_{NNI} than optimization aiming at minimizing F_{NNI} . From this aspect, the optimized solution of F_{NNI} is not optimal, indicating that the applied optimization does not make sense. However, we want to stress that this issue is very common in topology optimization for dynamic and acoustic problems since the optimization problem for these investigated systems are highly non-convex. A local optimum is generally reached by the gradient-based algorithm, and it is very hard to get a global optimum. This is the reason why we conduct optimization with different initial values of the design variables, expecting to obtain a good solution (maybe not optimal). Those optimized solutions, however, are generally good designs, which could provide guidance for design and analysis. Thus, choosing a proper initial value for the design variables is of importance for topology optimization. NNI, which could visualize the contributions of the element/region to sound radiation, has the potential to generate a good initial design. Optimization based on this initial design might converge faster than normal initial values, or converge to a better local minimum. This will be investigated in future work.

From the results discussed previously, it can be clearly seen that the radiation pattern is optimized by using predefined objective functions. Optimized designs usually show higher sound powers than unoptimized designs. However, the increases in sound power caused by optimization using F_{NNI} are not usually very large and can sometimes be acceptable if the sound power is not of high importance. This is attributed to how we select regions with high contributions to sound radiation as the investigated area Γ_c , such as the corners of the plate. This is reasonable because these regions are always of greater interest compared with other less contributing areas. In contrast, optimization possibly produces a sound power several orders of magnitude larger when choosing F_{SI} as the objective function. Such enormous increases are usually unfavorable in engineering. Hence, it is not recommended to optimize the radiation pattern based on the integration of sound intensity.

Finally, we have to admit that the physical meanings of NNI are still unclear, and further research on NNI is required. However, it can be clearly seen that optimization using NNI has the potential to

optimize the radiating pattern and outperforms the sound intensity in designing the radiation pattern.

5 Conclusion

An approach to optimizing the contributing pattern to radiated sound power from vibrating structures has been introduced. Two different predefined objective functions, namely, the integrations of NNI and sound intensity over chosen surfaces, are applied and compared in the optimization. By using these objective functions, an optimized damping layer distribution can be found which reduces the contribution to the sound power from the surfaces of interest. When the entire surface is of interest, these two objective functions are equivalent to the radiated sound power, and two optimizations give almost the same result. However, NNI can be extracted from truncated radiation modes, and usually requires less computational effort than sound intensity. This could improve the computational efficiency of optimization. When only partial surfaces are of interest, two predefined objective functions produce quite different optimized designs. However, optimization using the sound intensity possibly yields an enormous increase in the radiated sound power, which is usually unfavorable in engineering designs. Furthermore, it sometimes fails to generate a desirable radiating pattern. In contrast, optimization using NNI always leads to a desirable radiating pattern with only a slightly increased sound power. Thus, we strongly recommend using NNI to optimize the radiating/contributing pattern. The optimization procedure presented here provides a new way for radiating pattern control.

References

- Bendsøe MP, Kikuchi N. Generating optimal topologies in structural design using a homogenization method. *Comp Methods Appl Mech Eng* (1988) 71:197–224. doi:10.1016/0045-7825(88)90086-2
- Du J, Olhoff N. Minimization of sound radiation from vibrating bi-material structures using topology optimization. *Struct Multidisc Optim* (2007) 33:305–21. doi:10.1007/s00158-006-0088-9
- Xu Z, Huang Q, Zhao Z. Topology optimization of composite material plate with respect to sound radiation. *Eng Anal Boundary Elem* (2011) 35:61–7. doi:10.1016/j.enganabound.2010.05.013
- Zheng W, Yang T, Huang Q, He Z. Topology optimization of PCLD on plates for minimizing sound radiation at low frequency resonance. *Struct Multidisc Optim* (2015) 53:1231–42. doi:10.1007/s00158-015-1371-4
- Williams EG. Supersonic acoustic intensity on planar sources. *The J Acoust Soc America* (1998) 104:2845–50. doi:10.1121/1.423868
- Marburg S, Lösche E, Peters H, Kessissoglou N. Surface contributions to radiated sound power. *J Acoust Soc America* (2013) 133:3700–5. doi:10.1121/1.4802741
- Williams EG. Convolution formulations for non-negative intensity. *J Acoust Soc America* (2013) 134:1055–66. doi:10.1121/1.4812262
- Liu D, Peters H, Marburg S, Kessissoglou N. Supersonic intensity and non-negative intensity for prediction of radiated sound. *J Acoust Soc America* (2016) 139:2797–806. doi:10.1121/1.4948567
- Hughes TJ, Cottrell JA, Bazilevs Y. Isogeometric analysis: CAD, finite elements, NURBS, exact geometry and mesh refinement. *Comp Methods Appl Mech Eng* (2005) 194:4135–95. doi:10.1016/j.cma.2004.10.008
- Gu J, Zhang J, Li G. Isogeometric analysis in BIE for 3-D potential problem. *Eng Anal Boundary Elem* (2012) 36:858–65. doi:10.1016/j.enganabound.2011.09.018
- Zang Q, Liu J, Ye W, Lin G. Isogeometric boundary element method for steady-state heat transfer with concentrated/surface heat sources. *Eng Anal Boundary Elem* (2021) 122:202–13. doi:10.1016/j.enganabound.2020.11.001
- Ibáñez MJ, Barrera D, Maldonado D, Yáñez R, Roldán JB. Non-uniform spline quasi-interpolation to extract the series resistance in resistive switching memristors for compact modeling purposes. *Mathematics* (2021) 9:2159. doi:10.3390/math9172159
- Wang L, Xiong C, Yuan X, Wu H. Discontinuous galerkin isogeometric analysis of convection problem on surface. *Mathematics* (2021) 9:497. doi:10.3390/math9050497
- Yu B, Cao G, Huo W, Zhou H, Atroshchenko E. Isogeometric dual reciprocity boundary element method for solving transient heat conduction problems with heat sources. *J Comput Appl Math* (2021) 385:113197. doi:10.1016/j.cam.2020.113197
- Yu B, Cao G, Meng Z, Gong Y, Dong C. Three-dimensional transient heat conduction problems in FGs via IG-DRBEM. *Comp Methods Appl Mech Eng* (2021) 384:113958. doi:10.1016/j.cma.2021.113958
- Chen L, Lian H, Liu Z, Gong Y, Zheng C, Bordas S. Bi-material topology optimization for fully coupled structural-acoustic systems with isogeometric FEM-BEM. *Eng Anal Boundary Elem* (2022) 135:182–95. doi:10.1016/j.enganabound.2021.11.005
- Chen L, Lian H, Natarajan S, Zhao W, Chen X, Bordas S. Multi-frequency acoustic topology optimization of sound-absorption materials with isogeometric boundary element methods accelerated by frequency-decoupling and model order reduction techniques. *Comp Methods Appl Mech Eng* (2022) 395:114997. doi:10.1016/j.cma.2022.114997
- Peng X, Lian H, Ma Z, Zheng C. Intrinsic extended isogeometric analysis with emphasis on capturing high gradients or singularities. *Eng Anal Boundary Elem* (2022) 134:231–40. doi:10.1016/j.enganabound.2021.09.022
- Chen L, Lian H, Xu Y, Li S, Liu Z, Atroshchenko E, et al. Generalized isogeometric boundary element method for uncertainty analysis of time-harmonic wave propagation in infinite domains. *Appl Math Model* (2023) 114:360–78. doi:10.1016/j.apm.2022.09.030

Data availability statement

The original contributions presented in the study are included in the article/Supplementary Material; further inquiries can be directed to the corresponding author.

Author contributions

Conceptualization, YX; data curation, XZ; formal analysis, XZ; investigation, XZ; methodology, YX; project administration, YX; software, XZ; supervision, YX; validation, XZ; visualization, XZ; and writing—original draft, XZ and YX. All authors have read and agreed to the published version of the manuscript.

Conflict of interest

The authors declare that the research was conducted in the absence of any commercial or financial relationships that could be construed as a potential conflict of interest.

Publisher's note

All claims expressed in this article are solely those of the authors and do not necessarily represent those of their affiliated organizations, or those of the publisher, the editors, and the reviewers. Any product that may be evaluated in this article, or claim that may be made by its manufacturer, are not guaranteed or endorsed by the publisher.

20. Chen L, Lian H, Liu Z, Chen H, Atroshchenko E, Bordas S. Structural shape optimization of three dimensional acoustic problems with isogeometric boundary element methods. *Comp Methods Appl Mech Eng* (2019) 355:926–51. doi:10.1016/j.cma.2019.06.012
21. Peng X, Atroshchenko E, Kerfriden P, Bordas S. Isogeometric boundary element methods for three dimensional static fracture and fatigue crack growth. *Comp Methods Appl Mech Eng* (2017) 316:151–85. doi:10.1016/j.cma.2016.05.038
22. Peng X, Atroshchenko E, Kerfriden P, Bordas S. Linear elastic fracture simulation directly from CAD: 2D NURBS-based implementation and role of tip enrichment. *Int J Fract* (2017) 204:55–78. doi:10.1007/s10704-016-0153-3
23. Keuchel S, Hagelstein NC, Zaleski O, von Estorff O. Evaluation of hypersingular and nearly singular integrals in the Isogeometric Boundary Element Method for acoustics. *Comp Methods Appl Mech Eng* (2017) 325:488–504. doi:10.1016/j.cma.2017.07.025
24. Nguyen VP, Anitescu C, Bordas SP, Rabczuk T. Isogeometric analysis: An overview and computer implementation aspects. *Mathematics Comput Simulation* (2015) 117: 89–116. doi:10.1016/j.matcom.2015.05.008
25. Zheng L, Xie R, Wang Y, Adel E-S. Topology optimization of constrained layer damping on plates using method of moving asymptote (MMA) approach. *Shock and Vibration* (2011) 18:221–44. doi:10.1155/2011/830793
26. Wilkes DR, Peters H, Croaker P, Marburg S, Duncan AJ, Kessissoglou N. Non-negative intensity for coupled fluid-structure interaction problems using the fast multipole method. *J Acoust Soc America* (2017) 141:4278–88. doi:10.1121/1.4983686
27. Olhoff N, Du J. Generalized incremental frequency method for topological design of continuum structures for minimum dynamic compliance subject to forced vibration at a prescribed low or high value of the excitation frequency. *Struct Multidisc Optim* (2016) 54: 1113–41. doi:10.1007/s00158-016-1574-3
28. Chen L, Marburg S, Chen H, Zhang H, Gao H. An adjoint operator approach for sensitivity analysis of radiated sound power in fully coupled structural-acoustic systems. *J Comp Acous* (2017) 25:1750003. doi:10.1142/s0218396x17500035
29. Zhao W, Zheng C, Chen H. Acoustic topology optimization of porous material distribution based on an adjoint variable FMBEM sensitivity analysis. *Eng Anal Boundary Elem* (2019) 99:60–75. doi:10.1016/j.enganabound.2018.11.003
30. Svanberg K. The method of moving asymptotes—A new method for structural optimization. *Int J Numer Meth Engng* (1987) 24:359–73. doi:10.1002/nme.1620240207
31. Xu S, Cai Y, Cheng G. Volume preserving nonlinear density filter based on heaviside functions. *Struct Multidisc Optim* (2010) 41:495–505. doi:10.1007/s00158-009-0452-7
32. Johnson CD, Kienholz DA. Finite element prediction of damping in structures with constrained viscoelastic layers. *AIAA J* (1982) 20:1284–90. doi:10.2514/3.51190
33. Unruh O. Influence of inhomogeneous damping distribution on sound radiation properties of complex vibration modes in rectangular plates. *J Sound Vibration* (2016) 377: 169–84. doi:10.1016/j.jsv.2016.05.009
34. Maidanik G. Response of ribbed panels to reverberant acoustic fields. *J Acoust Soc America* (1962) 34:809–26. doi:10.1121/1.1918200



OPEN ACCESS

EDITED BY

Pei Li,
Xi'an Jiaotong University, China

REVIEWED BY

Yongle Du,
The Pennsylvania State University (PSU),
United States
Jian-Cheng Cai,
Zhejiang Normal University, China

*CORRESPONDENCE

Shujie Jiang,
✉ jiangshujie@cardc.cn

SPECIALTY SECTION

This article was submitted to Statistical and Computational Physics, a section of the journal Frontiers in Physics

RECEIVED 05 January 2023

ACCEPTED 19 January 2023

PUBLISHED 27 January 2023

CITATION

Xu C, Wang S, Yang D, Zhang R, Jiang S and Mao Y (2023), Comparative study of surface integral methods in aeroacoustic prediction. *Front. Phys.* 11:1138027. doi: 10.3389/fphy.2023.1138027

COPYRIGHT

© 2023 Xu, Wang, Yang, Zhang, Jiang and Mao. This is an open-access article distributed under the terms of the [Creative Commons Attribution License \(CC BY\)](#). The use, distribution or reproduction in other forums is permitted, provided the original author(s) and the copyright owner(s) are credited and that the original publication in this journal is cited, in accordance with accepted academic practice. No use, distribution or reproduction is permitted which does not comply with these terms.

Comparative study of surface integral methods in aeroacoustic prediction

Chen Xu¹, Shihao Wang¹, Dangguo Yang², Rongping Zhang², Shujie Jiang^{2*} and Yijun Mao³

¹School of Naval Architecture, Ocean and Energy Power Engineering, Wuhan University of Technology, Wuhan, China, ²Key Laboratory of Aerodynamic Noise Control, China Aerodynamics Research and Development Center, Mianyang, China, ³School of Aerospace Engineering, Huazhong University of Science and Technology, Wuhan, China

Introduction: Surface integral methods based on the acoustic analogy and Kirchhoff formulation are widely employed in computational aeroacoustics. The computational accuracy is usually highly dependent on the selections of the acoustic prediction method and of the integral surfaces.

Methods: This paper analyzes the pros and cons of each aeroacoustic prediction method and studies numerically sound generated from flow past a circular cylinder by employing different surface integral methods. The acoustic analogy based on the impermeable solid surfaces either ignores the quadrupole contribution or needs high computational cost to calculate the quadrupole contribution, and the acoustic analogy based on the permeable integral surfaces usually suffers from the spurious source issue.

Results: Both the pressure-based or density-based Kirchhoff formulations can be used in aeroacoustic prediction, however, the numerical results indicate that the pressure-based Kirchhoff formulation also suffers from the issue of the spurious sound because the pressure fluctuations at the permeable integral surfaces are contaminated by hydrodynamic component.

Discussion: It seems that only the density-based Kirchhoff formulation does not suffer from the issue of the spurious sound, but this formulation requires the acoustic sources should be extracted from compressible flow simulations.

KEYWORDS

aeroacoustics, integral surface, acoustic analogy, spurious sound, kirchhoff method

1 Introduction

Sound generated from turbulence and its interaction with solid boundaries can be predicted with either integral methods or differential methods [1, 2]. Compared with differential methods, integral methods cannot consider the effect of shear mean flow on sound propagation outside the integral surfaces [3]. However, the integral methods usually need less computational cost than the differential methods because the integral methods do not need to discretize the entire domain of acoustic propagation. Therefore, the integral methods are more widely employed in various engineering applications [4].

All integral methods can be classified into the following two types. The first method is based on the acoustic analogy proposed by Lighthill [5] and developed by Ffowcs Williams and Hawkings (FW-H) [6]. In numerical calculations, the integral solutions of FW-H equation, such as time-domain formulations developed by Farassat [7–10], are utilized to predict sound

radiated from sources located on and outside the integral surfaces. Since calculation of sound radiated from the quadrupole sources located outside the integral surfaces usually costs much more time than calculations of monopole and dipole sources on the integral surfaces do, permeable integral surfaces are widely employed in order to reduce or avoid the time consumed at quadrupole calculation.

The second method is based on the Kirchhoff formulation [11, 12], which is derived from the linearized acoustic theory. Therefore, the integral surfaces of the Kirchhoff formulation should enclose all non-linear sources for predicting aerodynamic noise. Detailed reviews of Kirchhoff formulation in computational aeroacoustics can be found in [13].

Both methods have been widely used in computational aeroacoustics, such as jet noise [14–16] and rotor noise [17–19]. Analytical comparison of these two methods have been performed by Brentener and Farassat [20], and they concluded the integral method based on the FW-H equation is superior to that based on the Kirchhoff formulation because the acoustic results based on the FW-H equation is less sensitive than the Kirchhoff formulation to placement of integral surfaces.

However, this conclusion is not supported by all numerical results. For examples, studies of some investigators, such as Wang et al. [21], Sinayoko et al. [22] and Zhong and Zhang [23], have revealed that the FW-H equation with permeable surfaces suffer from the issue of spurious sound owing to vortical disturbances passing through the permeable integral surfaces. Therefore, the acoustic calculation result based on the FW-H equation is still highly dependent on the position of the permeable integral surfaces. In order to reduce the acoustic contamination caused by the spurious sources located at permeable surfaces, various methods, such as, open integral surfaces [24], outflow-disk-averaging technique [25–27], have been developed to suppress the spurious sound radiated from the permeable surfaces over past decades. Detailed reviews can be found in [28].

On the other hand, the input variables of the Kirchhoff formulation do not include the velocity disturbances, thus the Kirchhoff formulation is thought to do not suffer the issue of spurious sound. The static pressure and its gradient are usually used as the input variables of the Kirchhoff formulation in previous numerical studies, such as [20, 29, 30]. However, we must emphasize that the Kirchhoff formulation is derived based on the linearized acoustic theory, thus both the input and output variables should be only acoustic components. In prediction of aerodynamic sound generated from turbulence, the static pressure extracted from the flow simulation results includes not only acoustic but also hydrodynamic (vortical) components [31–33]. Therefore, the pressure-based Kirchhoff formulation is actually also contaminated by the vortical component which is similar to that encountered by the FW-H formulation with permeable integral surfaces. The density fluctuation and its gradient are only relevant to acoustic process in turbulence without external heat sources. Therefore, the density-based Kirchhoff formulation can avoid the issue of spurious sound, to the best knowledge of authors, but no comparative studies on this topic have been performed so far.

This paper aims to perform comparative studies on surface integral methods in aeroacoustic prediction. Aerodynamic sound generated from compressible flow past a circular cylinder is studied numerically using different surface integral methods. The remainder of this paper is structured as follows. Section 2 describes the numerical case. In Section 3, simulation and validation of unsteady flow are performed through comparing the numerical results with previous numerical and experimental data. Acoustic results calculated from different aeroacoustic

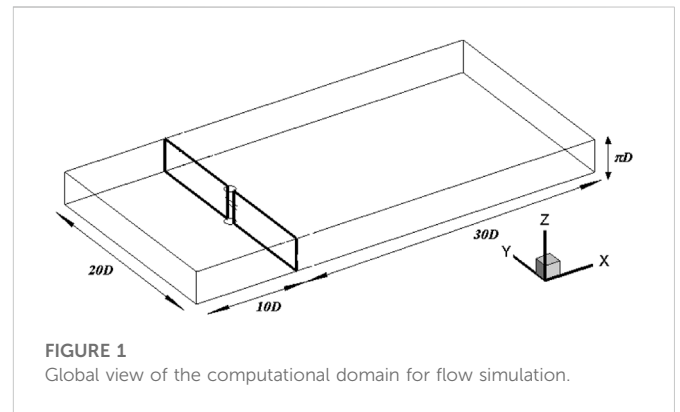


FIGURE 1
Global view of the computational domain for flow simulation.

prediction methods are compared in Section 4. Conclusion are drawn in Section 5.

2 Description of numerical case

Sound generated from compressible flow past a circular cylinder is predicted, where the free stream Mach number and Reynolds number are 0.75 and 2×10^5 , respectively.

Flow physics at this operating condition has been studied numerically and experimentally by some investigators, such as Rodriguez [34], Murthy et al. [35], Xu et al. [36] and Hong et al. [37]. Thus abundant experimental database and numerical results can be used to validate the numerical method used in this paper. The computational domain is $40D \times 20D \times \pi D$ as shown in Figure 1, where D represents the diameter of the circular cylinder. The upstream and downstream boundaries are $10D$ and $30D$ away from the center of the cylinder surface, respectively. A spanwise length of πD is chosen according to recommendation of numerical studies performed by Breuer [38] and Lysenko [39].

3 Simulation and validation of unsteady flow

3.1 Flow simulation setup

Large eddy simulation (LES) technique is employed to solve three-dimensional unsteady compressible Navier-Stokes equations. The well-known Smagorinsky model [40] is used to consider the influence of small scale eddies and to calculate the subgrid scale tensor. All computations are carried out with a Smagorinsky constant of $C_s = 0.1$ [41], which is an empirical value mostly used for practical applications.

Different spatial and temporal discretization schemes are used for the governing equations, in which spatial discretization is achieved by using the bounded central differencing scheme for the convection terms and second-order central difference for the diffusion terms, and an implicit second-order scheme is utilized for the temporal discretization. The SIMPLE algorithm is used for pressure-velocity coupling.

In present study, the initial and boundary conditions are presented as follows. The constant free-stream quantities, i.e., the mass flow and static temperature, are imposed at the

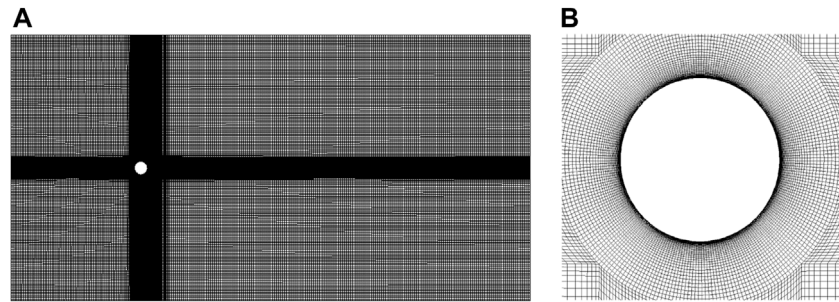


FIGURE 2
Computational mesh for the circular cylinder: (A) entire domain; (B) near-wall region.

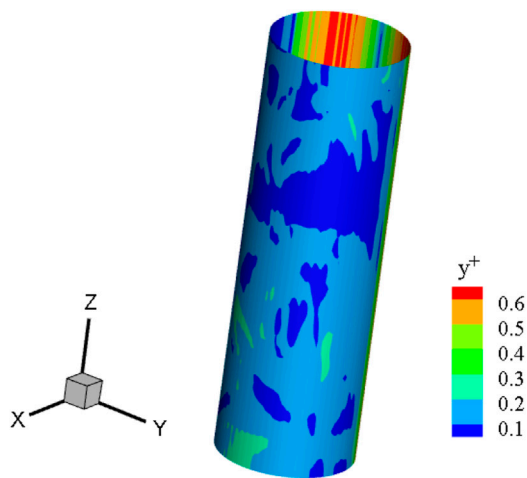


FIGURE 3
 y^+ distribution of the circular cylinder.

inlet boundary without any perturbation. The non-reflecting boundary condition is used at the downstream boundary of the computational domain to avoid acoustic reflection at this surface. No-slip and adiabatic boundary conditions are applied on the solid wall of the cylinder and periodic boundary conditions are used at the rest pairs of surfaces of the computational domain.

The computational domain is discretized with hexahedral meshes and the total number of mesh cells is around 5.8 million, as shown in Figure 2. To avoid any kind of wall functions, the detailed flow inside boundary layer is solved directly using fine grids in the vicinity of the cylinder surface, and the normal distance between the first layer mesh nodes and the cylinder surface is set to be 0.002 mm, with a stretching factor of 1.08.64 and 320 nodes are distributed uniformly along the spanwise and circumferential directions, respectively, which are similar to the grid numbers and distributions utilized in previous simulations [38, 39, 42, 43]. The above grid distribution ensures that the non-dimensional nearest wall distance y^+ is smaller than 1. Figure 3 illustrates the distribution of y^+ , which satisfies the requirement of the LES. Time step $\Delta t = 4.7 \times 10^{-6}$ s is used to ensure temporal resolution of the numerical result, which corresponds to the non-dimensional parameter $U_\infty \Delta t / D = 0.006$.

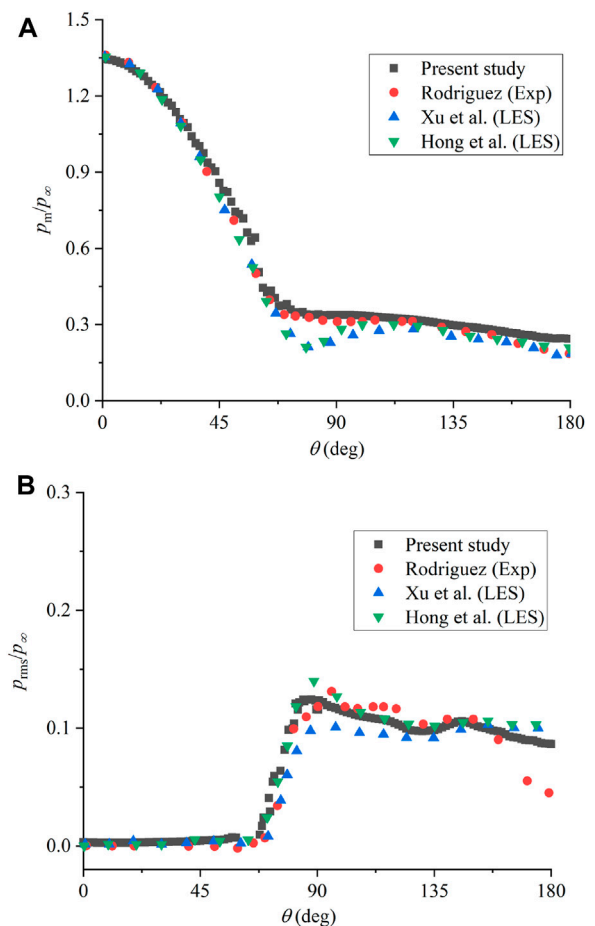


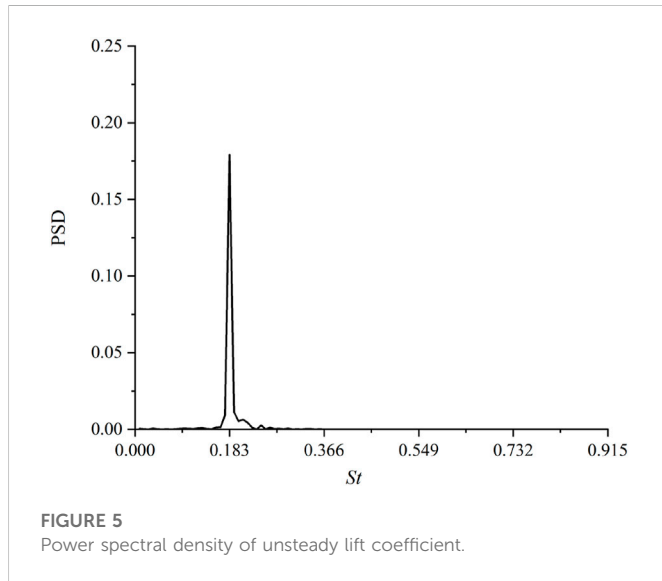
FIGURE 4
Comparison of the calculated results with experimental data: (A) time-averaged wall pressure; (B) RMS of pressure fluctuation.

3.2 Validation of flow simulation results

Based on numerical simulation results, distribution features of the normalized wall pressure, i.e., time-averaged and root-mean-square (RMS) values, are compared with experimental data from Rodriguez [34] as well as the numerical data from Xu et al; [36] and Hong et al; [37]; Figures 4A, B compare time-averaged and root-mean-square

TABLE 1 Comparison of main flow quantities at $Re = 2 \times 10^5$.

	$U_\infty \Delta t / D$	\bar{C}_d	$C_{l_{rms}}$	St
Present results	0.006	1.611	0.264	0.183
[37]	0.02	1.598	0.282	0.187
[36]	0.006	1.572	0.25	0.18
[34]	—	1.618	0.253	0.2
[35]	—	1.50	-	0.18



(RMS) values from different sources, where $\theta = 0$ and $\theta = 180^\circ$ represent the stagnation point and rear point of the cylinder wall, respectively.

In Figure 4A, the time-averaged pressure obtained from present numerical simulation has a good agreement with experimental data of Rodriguez [34], but has a little deviation from the numerical results from Xu et al; [36] and Hong et al [37]; Figure 4B shows that the RMS values from different sources have a disperse feature, but all the numerical results can reach a fair consistency.

To further assess reliability of present numerical results, some quantities together with previous experimental [34, 35] and numerical studies [36, 37] have conducted at the same Reynolds number, including the time-averaged and root-mean square values of lift and drag coefficients based on spanwise length of the cylinder, as well as the Strouhal number, are summarized in Table 1. It can be seen that both the time-average drag coefficient \bar{C}_d and RMS value of the lift coefficient $C_{l_{rms}}$ fall in the range of the existing experimental and numerical results. As is well known, the pressure fluctuation on a cylinder is associated with the alternating vortex shedding. To identify the frequency of the vortex shedding, the power spectral density (PSD) of the instantaneous lift coefficient is shown in Figure 5. The characteristic Strouhal number is defined based on the free stream velocity of U_∞ and the diameter of the cylinder D . As exhibited in Figure 5, an obviously frequency peak value is about 233 Hz

corresponding to the highest peak value $St \approx 0.183$, which is consistent with experimental data in the range from 0.18 to 0.2. Moreover, The time histories of the lift and drag coefficients from the present study are given in Figure 6, and features are consistent with the previous literatures [36, 37].

4 Comparative study of aeroacoustic prediction

4.1 Acoustic formulations

The convective wave equation of the acoustic analogy, developed independently by Najafi-Yazdi et al. [44] and Ghorbaniasl et al. [45] based on the equation of Ffowcs Williams and Hawkings [6], is used to describe sound, generated by turbulence and its interaction with solid boundaries, propagation in a uniform mean flow, which is expressed by

$$\left(\frac{D^2}{Dt^2} - c_0^2 \nabla^2\right)[H(f)\rho'] = \frac{D}{Dt}[Q\delta(f)] - \nabla \cdot [L\delta(f)] + \nabla \cdot \{\nabla \cdot [H(f)\mathbf{T}]\} \quad (1)$$

where three terms at right hand side of Eq. 1 are named as monopole, dipole and quadrupole sources, respectively. These sources are expressed by

$$Q = \rho_0(v_n - U_{\infty n}) + \rho(u_n + U_{\infty n} - v_n) \quad (2)$$

$$\mathbf{L} = ((p - p_0)\mathbf{I} - \boldsymbol{\sigma}) \cdot \mathbf{n} + \rho \mathbf{u}(u_n + U_{\infty n} - v_n) \quad (3)$$

$$\mathbf{T} = [(p - p_0) - c_0^2(\rho - \rho_0)]\mathbf{I} - \boldsymbol{\sigma} + \rho \mathbf{u}\mathbf{u} \quad (4)$$

where $f = 0$ can be either the solid surface or the permeable surface enclosing all solid surfaces, $H(\cdot)$ and $\delta(\cdot)$ respectively represent the Heaviside and Dirac Delta functions, \mathbf{U}_∞ is the velocity of uniform mean flow, \mathbf{u} denotes the fluctuation of the local flow velocity, \mathbf{v} represents the velocity of the surface $f = 0$, \mathbf{n} is the unit vector normal to surface $f = 0$, $\boldsymbol{\sigma}$ is the viscous stress tensor, c_0 and ρ_0 are respectively the speed of sound and density of undisturbed fluid.

By following the derivation method of the time-domain acoustic pressure integral formulations 1 and 1A of Farassat [46], the acoustic pressure integral formulations corresponding to the convective FW-H equations have been derived in [44, 45]. Especially, when the integral surfaces are stationary, the frequency-domain acoustic pressure formulations of the monopole and dipole surface sources can be expressed by:

$$4\pi \tilde{p}'_T(\mathbf{x}, \omega) = - \int_{f=0} \frac{ikc_0 \tilde{Q}(1 - M_{\infty R})}{R^*} e^{ikR} dS - \int_{f=0} \frac{c_0 \tilde{Q} M_{\infty R^*}}{R^{*2}} e^{ikR} dS \quad (5)$$

$$4\pi \tilde{p}'_L(\mathbf{x}, \omega) = - \int_{f=0} \frac{ik \tilde{L}_R}{R^*} e^{ikR} dS + \int_{f=0} \frac{\tilde{L}_{R^*}}{R^{*2}} e^{ikR} dS \quad (6)$$

where subscripts T and L , respectively, represent the monopole and dipole source, and R , which means the acoustic distance between the source and observer in the mean flow, is expressed by

$$R = \gamma^2(R^* - rM_{\infty R}) \quad (7)$$

with $\gamma = \sqrt{1/(1-M_{\infty}^2)}$, $M_{\infty r} = M_{\infty i} \hat{r}_i$, $M_{\infty i} = U_{\infty i}/c_0$, and $L_R = L_j R_j$, $L_{R^*} = L_j R_j^*$, $M_R = M_j R_j$, $M_{R^*} = M_j R_j^*$ and

$$R^* = \frac{\sqrt{r^2 + \gamma^2 (M_{\infty} \cdot \mathbf{r})^2}}{\gamma} = \frac{r \sqrt{1 + \gamma^2 M_{\infty}^2}}{\gamma} \quad (8)$$

where $\mathbf{r} = \mathbf{x} - \mathbf{y}$ is the position vector from the source to the observer, and $r = |\mathbf{r}|$ is the geometrical distance between the source and the observer. Usually, a permeable surface enclosing all solid surfaces can be used to calculate far-field sound in order to reduce the computational time consumed at the volume integral over the quadrupole sources. However, the issue of the spurious sound must be treated carefully in this situation due to vortical disturbances passing through the permeable surface.

Alternative acoustic prediction method is based on the following convective formulation of Kirchhoff formulation [28]:

$$\begin{aligned} 4\pi \tilde{p}'(\mathbf{x}, \omega) = & - \int_{f=0} \left(\frac{\partial \tilde{p}'}{\partial \mathbf{n}} + ik \tilde{p}' R_n \right) \frac{e^{ikR}}{R^*} dS + \int_{f=0} \tilde{p}' R_n^* \frac{e^{ikR}}{R^*} dS \\ & + M_{\infty} \left[\int_{f=0} (-2ik \tilde{p}' + ik M_{\infty R} \tilde{p}' + \mathbf{M}_{\infty} \cdot \nabla \tilde{p}') \frac{e^{ikR}}{R^*} dS \right. \\ & \left. - \int_{f=0} \tilde{p}' M_{\infty R^*} \frac{e^{ikR}}{R^*} dS \right] \quad (9) \end{aligned}$$

with $R_n = \hat{R}_j \hat{n}_j$ and $R_n^* = \hat{R}_j^* \hat{n}_j$. From Eq. 9 we can find that once variables, including the pressure and its spatial derivative in the flow field are known, the acoustic pressure in the far field can be calculated. The pressure fluctuation in the terms at the right hand side of Eq. 9 should be strictly acoustic component, but the pressure fluctuation obtained from the unsteady flow simulation includes both the acoustic and vortical components, thus aeroacoustic prediction results based on Eq. 9 is also prone to be contaminated by the vortical component of the pressure fluctuation. In order to avoid this issue, the following density-based version of the convective Kirchhoff formulation is recommended

$$\begin{aligned} \frac{4\pi \tilde{p}'(\mathbf{x}, \omega)}{c_0^2} = & - \int_{f=0} \left(\frac{\partial \tilde{\rho}'}{\partial \mathbf{n}} + ik \tilde{\rho}' R_n \right) \frac{e^{ikR}}{R^*} dS + \int_{f=0} \tilde{\rho}' R_n^* \frac{e^{ikR}}{R^*} dS \\ & + M_{\infty} \left[\int_{f=0} (-2ik \tilde{\rho}' + ik M_{\infty R} \tilde{\rho}' + \mathbf{M}_{\infty} \cdot \nabla \tilde{\rho}') \frac{e^{ikR}}{R^*} dS \right. \\ & \left. - \int_{f=0} \tilde{\rho}' M_{\infty R^*} \frac{e^{ikR}}{R^*} dS \right] \quad (10) \end{aligned}$$

Eq. 9 is mathematically equivalent to Eq. 10 as the acoustic pressure and density fluctuation has the relationship of $\tilde{p}' = \tilde{\rho}' c_0^2$. Compared Eq. 9 with Eq. 10, density fluctuation in Eq. 10 can be extracted directly from simulation of the unsteady compressible flow but the acoustic pressure component in Eq. 9 could be contaminated by the hydrodynamic component.

4.2 Computational methods

Sound radiated from flow past a circular cylinder is predicted using five numerical methods to compare their pros and cons. Details on these five methods are described below.

In the first method, sound radiated from a stationary solid surface is calculated by means of the convective FW-H equation, where the

integral surface f is the stationary cylinder surface. Thereby, the monopole source disappears and acoustic contribution from only the dipole source is calculated using Eq. 6 when the quadrupole contribution is ignored to save the computational cost.

In the second method, sound is still calculated with the convective FW-H equation but the integral surfaces f corresponds to six permeable surfaces of the computational domain. Aeroacoustic prediction is performed based on formulations (5) and (6), which is capable of reducing the computational time consumed at the volume integral over the quadrupole sources. However, this method is prone to cause the issue of spurious sound owing to vortical velocity disturbances passing through the downstream permeable surface, as discussed by previous investigators, such as [21].

In the present case, the acoustic prediction result is mainly contaminated by the spurious sources located at the downstream permeable surface. Therefore, acoustic computations over the upstream permeable surface and four side permeable surfaces can be calculated based on the formulations (5) and (6). In the third method, the acoustic contribution from the downstream permeable surface is ignored directly, thus this method is usually named open-surface FW-H method.

In the fourth and fifth methods, the acoustic contribution from the closed permeable surfaces is calculated with the pressure-based Kirchhoff formulation (9) and the density-based Kirchhoff formulation (10). As mentioned above, the pressure fluctuation is still contaminated by the hydrodynamic component but the density fluctuation is only related to acoustic process.

All surface integral methods in aeroacoustic prediction are compared and summarized in Table 2.

4.3 Comparison of computational results

Aeroacoustic prediction is performed by means of five methods mentioned above, where the prediction results should be independent of the length of sampling time used in the calculation. Therefore, the effect of the sampling time on the acoustic prediction results should be investigated in advance.

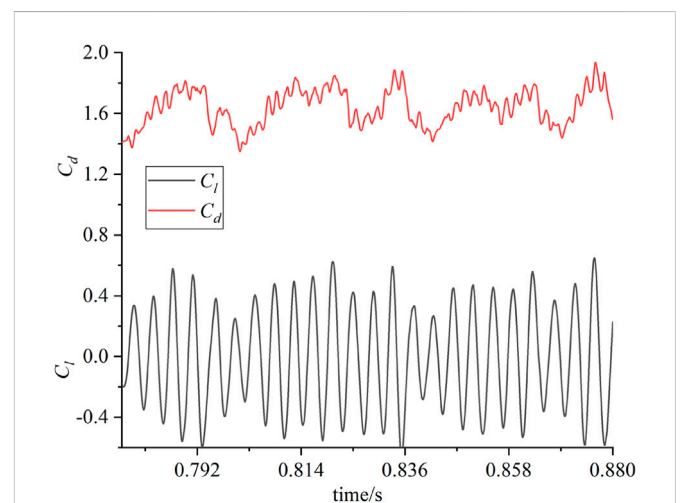
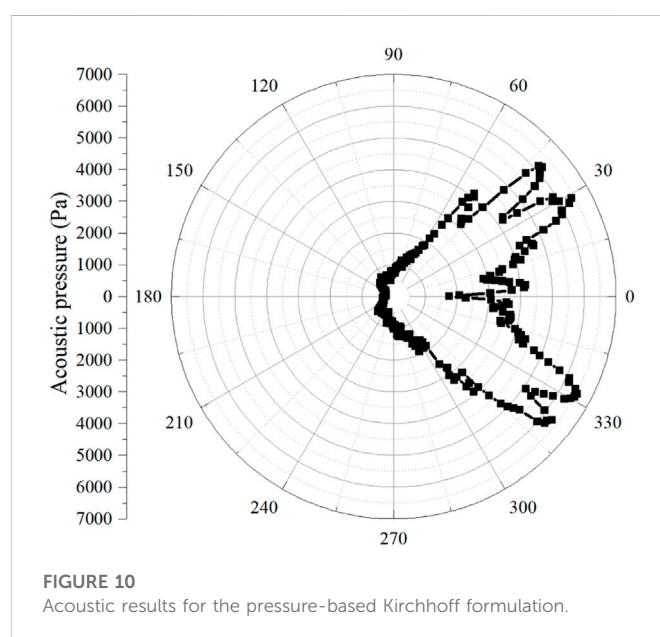
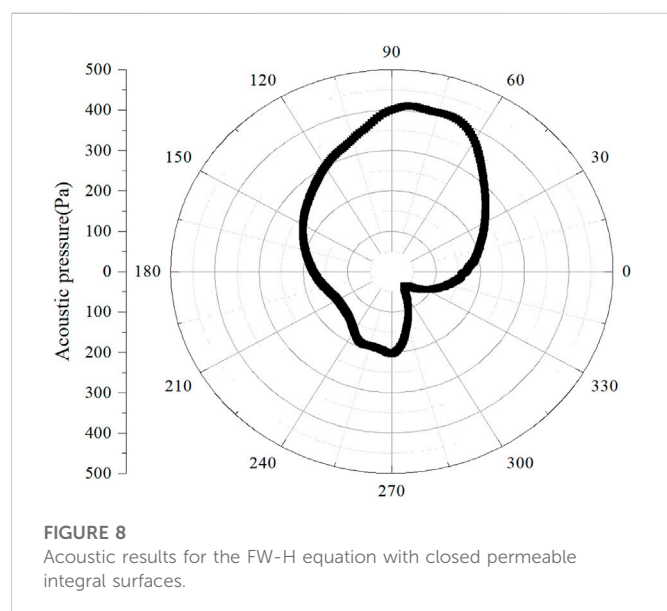
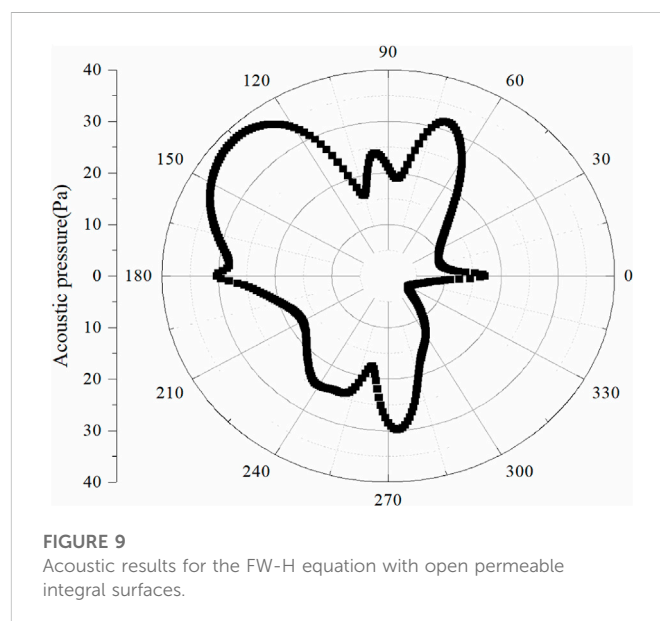
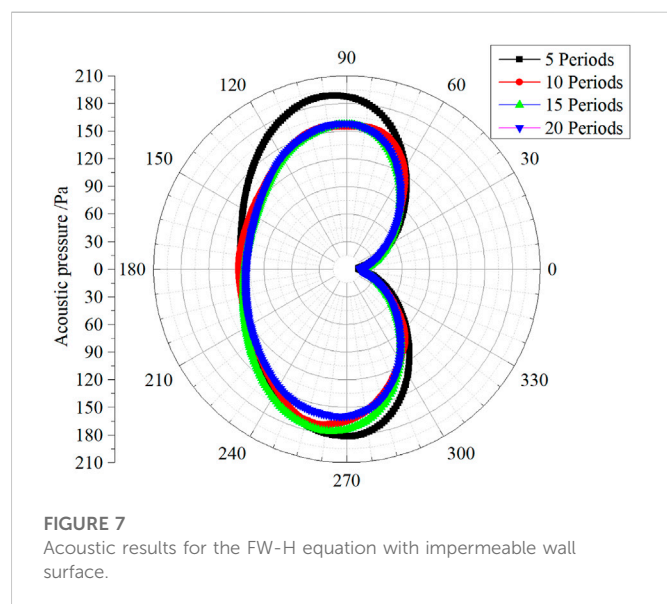


FIGURE 6
Time histories of lift and drag coefficients.

TABLE 2 Comparison of surface integral methods in computational aeroacoustics.

No.	Method	Formulations	Integral surfaces
1	FW-H equation with impermeable surface	(6)	Cylinder wall surface
2	FW-H equation with closed permeable surface	(5, 6)	Closed permeable surfaces
3	FW-H equation with open permeable surface	(5, 6)	Open permeable surfaces
4	Pressure-based Kirchhoff equation	(9)	Closed permeable surfaces
5	Density-based Kirchhoff equation	(10)	Closed permeable surfaces



The flow simulation results shown in Figure 5 indicate that the period of vortex shedding is about 430 time steps, thus unsteady flow simulation results based on 5, 10, 15 and 20 periods are, respectively, used as the input data to predict the acoustic

pressure. 36 acoustic sampling points are uniformly distributed at a circle with a radius of $R = 1$ m in the XY plane and its center is the same as that circular cylinder.

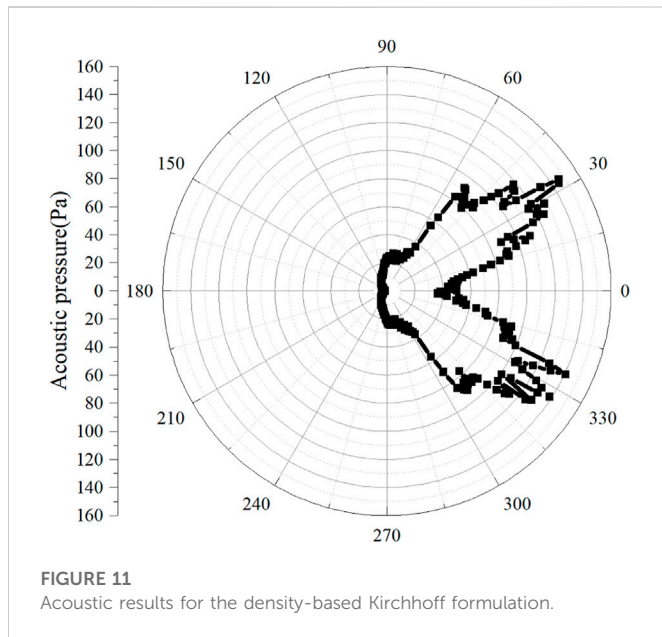


Figure 7 illustrates the directivity pattern of the acoustic pressure calculated from the first acoustic prediction method, i.e., the FW-H equation with the cylinder wall surface. The results indicate that the computational results can reach a converged solution when the sampling times is not smaller than 10 periods of vortex shedding. Therefore, in the following analysis, the aeroacoustic prediction results are performed by extracting sources from 10 periods of vortex shedding.

The FW-H equation with the solid surface does not suffer from the issue of spurious sources but ignores the contribution from the quadrupole sources. The acoustic prediction result is very similar to sound radiated from a compact dipole source immersed in a uniform mean flow, where acoustic pressure at the upstream sampling point is usually higher than that at the downstream sampling point owing to the connective amplification.

Figures 8, 9 illustrate the acoustic results calculated from the FW-H equation with closed and open permeable surfaces, respectively. The results presented in these two figures show a great deviation, implying that the acoustic prediction results are very sensitive to the sources located at the downstream permeable integral surface. It should be noted that the results in both Figures 8, 9 have an obvious difference from that in Figure 7, implying that the FW-H equation with either closed permeable integral surfaces or open permeable integral surfaces cannot output an accurate acoustic prediction result.

Figures 10, 11 display the acoustic pressure prediction results based on the pressure-based Kirchhoff formulation and the density-based Kirchhoff formulation, respectively. The results show that the directivity patterns calculated from two methods are very similar, but the amplitudes of the acoustic pressure have a distinct difference. The reason causing this difference is that the pressure fluctuations at the permeable integral surface are contaminated by the hydrodynamic component, therefore, the acoustic pressure calculated from the pressure-based Kirchhoff formulation is much higher than that from the density-based Kirchhoff formulation.

Moreover, compared Figure 7 with Figure 11, the directivity pattern calculated from these two methods has a distinct difference, which implies that the acoustic contribution from quadrupole sources has a great impact on the acoustic radiation.

5 Conclusion

Sound radiated from flow past a circular cylinder is studied numerically to investigate the effect of different surface integral methods on the prediction results. Conclusions are drawn as follows.

- (1) Acoustic calculation results are highly dependent on selections of the aeroacoustic prediction method and the integral surfaces. The FW-H equation combined with the impermeable wall surface is a suitable choice if the acoustic contribution from the quadrupole sources can be ignored. However, the permeable integral surfaces are recommended in a high-Mach number flow because the acoustic contribution from quadrupole sources has a great impact on acoustic radiation.
- (2) Compared with the FW-H equation with the impermeable wall surfaces, the FW-H equation with the permeable integral surfaces is computationally efficient to predict sound generated from turbulence and its interaction with wall surfaces. However, numerical simulations validate that the acoustic result predicted from the later method has visible computational errors owing to that the monopole and dipole sources are contaminated by vortical velocity at the permeable integral surfaces.
- (3) Acoustic results calculated from the pressure-based Kirchhoff formulation with the permeable integral surfaces also suffers from the issue of spurious sound, but the mechanics of the spurious sound is different from the FW-H equation with the permeable integral surfaces. In the pressure-based Kirchhoff formulation, the spurious sound is caused by the hydrodynamic pressure fluctuations located at the permeable integral surfaces, but the spurious sources in the FW-H equation is caused by the vortical velocity fluctuations located at the permeable integral surfaces.
- (4) Density fluctuation is contributed only from acoustic waves in turbulence without heat transfer. Therefore, the density-based Kirchhoff formulation with the permeable integral surfaces does not suffer from the issue of spurious sound. Difference of acoustic results between the density-based Kirchhoff formulation and the FW-H equation with impermeable wall integral surface can be regarded as the contribution from the quadrupole located in the region between the impermeable wall integral surface and permeable integral surfaces.

However, the density-based Kirchhoff formulation requires that the acoustic sources should be obtained from the compressible flow simulation. Therefore, this method is not suitable for low-Mach-number flows, in which aeroacoustic sources are usually obtained by solving incompressible Navier-Stokes equations.

Data availability statement

The original contributions presented in the study are included in the article/Supplementary Material, further inquiries can be directed to the corresponding author.

Author contributions

CX and SW, Numerical simulation and Analysis; DY and RZ, Formal analysis, YM, Programming; SJ and CX, Writing. All authors have read and agreed to the published version of the manuscript.

Funding

The research is supported by the National Natural Science Foundation of China (No. 52076086) and Laboratory of Aerodynamic Noise Control of China Aerodynamics Research and Development Center (Nos ANCL20220302, SKLA-20200302).

Acknowledgments

The authors gratefully acknowledge high-performance computing facilities IRIDIS4 at the University of Southampton in the completion of this work.

References

- Hardin JC, Hussaini MY. *Computational aeroacoustics*. Hampton, Springer New York: Springer Science and Business Media (1993).
- Tam CKW. *Computational aeroacoustics: A wave number approach*. New York: Cambridge University Press (2012).
- Pan FL, Uzun A, Lyrantzis AS. Surface integral methods in jet aeroacoustics: Refraction corrections. *J Aircraft* (2008) 45:381–7. doi:10.2514/1.23513
- Lyrantzis AS. Surface integral methods in computational aeroacoustics—from the (CFD) near-field to the (acoustic) far-field. *Int J Aeroacoust* (2003) 2:95–128. doi:10.1260/14754720322775498
- Lighthill MJ. On sound generated aerodynamically. I. General theory. *Proc R Soc Lond Ser A, Math Phys Sci* (1952) 211:564–87. doi:10.1098/rspa.1952.0060
- Ffowcs Williams J, Hawkings D. Sound generation by turbulence and surfaces in arbitrary motion. *Philos Trans R Soc Lond A, Math Phys Eng Sci* (1969) 264:321–42. doi:10.1098/rsta.1969.0031
- Farassat F, Succi GP. A review of propeller discrete frequency noise prediction technology with emphasis on two current methods for time domain calculations. *J Sound Vib* (1980) 71:399–419. doi:10.1016/0022-460x(80)90422-8
- Farassat F. Linear acoustic formulas for calculation of rotating blade noise. *AIAA J* (1981) 19:1122–30. doi:10.2514/3.60051
- Farassat F, Brentner KS. Supersonic quadrupole noise theory for high-speed helicopter rotors. *J Sound Vib* (1998) 218:481–500. doi:10.1006/jsvi.1998.1836
- Farassat F, Farris M. Verification and analysis of Formulation 4 of Langley for the study of noise from high speed surfaces. Bellevue: AIAA paper (1999). p. 99–1881.
- Farassat F, Myers MK. Extension of Kirchhoffs formula to radiation from moving surfaces. *J Sound Vib* (1988) 123:451–60. doi:10.1016/s0022-460x(88)80162-7
- Lyrantzis A, Xue Y. Versatile Kirchhoff code for aeroacoustic predictions. *AIAA J* (1997) 35:198–200. doi:10.2514/3.13484
- Lyrantzis AS. Review: The use of Kirchhoffs method in computational aeroacoustics. *J Fluid Eng-t ASME* (1994) 116:665–76. doi:10.1115/1.2911834
- Rahier G, Prieur J, Vuillot F, Lupoglazoff N, Biancherin A. Investigation of integral surface formulations for acoustic post-processing of unsteady aerodynamic jet simulations. *Aerosp Sci Technol* (2004) 8:453–67. doi:10.1016/j.ast.2004.04.005
- Bodony DJ, Lele SK. Current status of jet noise predictions using large-eddy simulation. *AIAA J* (2008) 46:364–80. doi:10.2514/1.24475
- Uzun A, Lyrantzis AS, Blaisdell GA. Coupling of integral acoustics methods with LES for jet noise prediction. *Int J Aeroacoust* (2004) 3:297–346. doi:10.1260/1475472043499290
- Xue Y, Lyrantzis AS. Rotating Kirchhoff method for 3-dimensional transonic blade-vortex interaction hover noise. *AIAA J* (1994) 32:1350–9. doi:10.2514/3.12202
- Lyrantzis AS, Koutsavdis EK. Rotorcraft impulsive noise prediction using a rotating Kirchhoff formulation. *J Aircraft* (1996) 33:1054–61. doi:10.2514/3.47057
- Strawn RC, Biswas R, Lyrantzis AS. Helicopter noise predictions using Kirchhoff methods. *J Comput Acoust* (1996) 4:321–39. doi:10.1142/s0218396x96000106
- Brentner KS, Farassat F. Analytical comparison of the acoustic analogy and Kirchhoff formulation for moving surfaces. *AIAA J* (1998) 36:1379–86. doi:10.2514/3.13979
- Wang M, Lele SK, Moin P. Computation of quadrupole noise using acoustic analogy. *AIAA J* (1996) 34:2247–54. doi:10.2514/3.13387
- Sinayoko S, Wright M, Sandberg R. A generalised Ffowcs-Williams and Hawkings formulation applied to flow simulations with vortical outflow. In: *The 22nd congress on sound and vibration*. Florence, Italy (2015).
- Zhong S, Zhang X. A sound extrapolation method for aeroacoustics far-field prediction in presence of vortical waves. *J Fluid Mech* (2017) 820:424–50. doi:10.1017/jfm.2017.219
- Colonius T, Lele SK. Computational aeroacoustics: Progress on nonlinear problems of sound generation. *Prog Aerosp Sci* (2004) 40:345–416. doi:10.1016/j.paerosci.2004.09.001
- Shur ML, Spalart PR, Strelets MK. Noise prediction for increasingly complex jets. Part I: Methods and tests. *Int J Aeroacoust* (2005) 4:213–45. doi:10.1260/1475472054771376
- Spalart PR, Shur ML, Strelets MK, Travin AK. Initial noise predictions for rudimentary landing gear. *J Sound Vib* (2011) 330:4180–95. doi:10.1016/j.jsv.2011.03.012
- Spalart P, Shur M. Variants of the Ffowcs Williams-Hawkings equation and their coupling with simulations of hot jets. *Int J Aeroacoust* (2009) 8:477–91. doi:10.1260/147547209788549280
- Mao Y, Hu Z. Analysis of spurious sound due to vortical flow through permeable surfaces. *Aerosp Sci Technol* (2020) 96:105544. doi:10.1016/j.ast.2019.105544
- Farassat F. Acoustic radiation from rotating blades - the Kirchhoff method in aeroacoustics. *J Sound Vib* (2001) 239:785–800. doi:10.1006/jsvi.2000.3221
- Wang B, Zhao QJ, Xu GH, Ye L, Wang JY. Numerical analysis on noise of rotor with unconventional blade tips based on CFD/Kirchhoff method. *Chin J Aeronaut* (2013) 26:572–82. doi:10.1016/j.cja.2013.04.045
- Felli M, Grizzi S, Falchi M. A novel approach for the isolation of the sound and pseudo-sound contributions from near-field pressure fluctuation measurements: Analysis of the hydroacoustic and hydrodynamic perturbation in a propeller-rudder system. *Exp Fluids* (2014) 55:1651. doi:10.1007/s00348-013-1651-y
- Mancinelli M, Pagliaroli T, Di Marco A, Camussi R, Castelain T. Wavelet decomposition of hydrodynamic and acoustic pressures in the near field of the jet. *J Fluid Mech* (2017) 813:716–49. doi:10.1017/jfm.2016.869
- Mancinelli M, Pagliaroli T, Camussi R, Castelain T. On the hydrodynamic and acoustic nature of pressure proper orthogonal decomposition modes in the near field of a compressible jet. *J Fluid Mech* (2018) 836:998–1008. doi:10.1017/jfm.2017.839
- Rodriguez O. The circular cylinder in subsonic and transonic flow. *AIAA J* (1984) 22:1713–8. doi:10.2514/3.8842
- Murthy VS, Murthy WC. Detailed measurements on a circular cylinder in cross flow. *AIAA J* (1978) 16:549–50. doi:10.2514/3.60930
- Xu CY, Chen LY, Lu XY. Large-eddy simulation of the compressible flow past a wavy cylinder. *J Fluid Mech* (2010) 665:238–73. doi:10.1017/s0022112010003927
- Hong R, Xia Z, Shi Y, Xiao Z, Chen S. Constrained large-eddy simulation of compressible flow past a circular cylinder. *Commun Comput Phys* (2014) 15:388–421. doi:10.4208/cicp.050513.270513a
- Breuer M. Large eddy simulation of the subcritical flow past a circular cylinder: Numerical and modeling aspects. *Int J Numer Methods Fluids* (1998) 28:1281–302. doi:10.1002/(sici)1097-0363(19981215)28:9<1281::aid-fld759>3.0.co;2-#

Conflict of interest

The authors declare that the research was conducted in the absence of any commercial or financial relationships that could be construed as a potential conflict of interest.

Publisher's note

All claims expressed in this article are solely those of the authors and do not necessarily represent those of their affiliated organizations, or those of the publisher, the editors and the reviewers. Any product that may be evaluated in this article, or claim that may be made by its manufacturer, is not guaranteed or endorsed by the publisher.

39. Lysenko DA, Ertesvåg IS, Rian KE. Large-eddy simulation of the flow over a circular cylinder at Reynolds number 3900 using the OpenFOAM toolbox. *Turbul Combust* (2012) 89:491–518. doi:10.1007/s10494-012-9405-0
40. Smagorinsky J. General circulation experiments with the primitive equations: I. The basic experiment. *Mon Weather Rev* (1963) 91:99–164. doi:10.1175/1520-0493(1963)091<0099:gcwtp>2.3.co;2
41. Rogallo RS, Moin P. Numerical simulation of turbulent flows. *Annu Rev Fluid Mech* (1984) 16:99–137. doi:10.1146/annurev.fl.16.010184.000531
42. Sarkar S. Large-eddy simulation of wake and boundary layer interactions behind a circular cylinder. *J Fluids Eng* (2009) 131. doi:10.1115/1.3176982
43. Breuer M. A challenging test case for large eddy simulation: High Reynolds number circular cylinder flow. *Int J Heat Fluid Flow* (2000) 21:648–54. doi:10.1016/S0142-727X(00)00056-4
44. Najafi-Yazdi A, Bres GA, Mongeau L. An acoustic analogy formulation for moving sources in uniformly moving media. *P Roy Soc A: Math Phys* (2011) 467:144–65. doi:10.1098/rspa.2010.0172
45. Ghorbaniasl G, Lacor C. A moving medium formulation for prediction of propeller noise at incidence. *J Sound Vib* (2012) 331:117–37. doi:10.1016/j.jsv.2011.08.018
46. Farassat F. *Derivation of formulations 1 and 1A of Farassat*. Hampton: NASA TM, 2007-214853 (2007).



OPEN ACCESS

EDITED BY

Leilei Chen,
Huanghuai University, China

REVIEWED BY

Chen Xu,
Wuhan University of Technology, China
Guangda Yang,
Northwestern Polytechnical University,
China
Cheng Ruhui,
Xi'an Jiaotong University, China

*CORRESPONDENCE

Shujie Jiang,
✉ jiangshujie@cardc.cn
Weiming Zhao,
✉ cardc_wmzhao@163.com
Chao Wang,
✉ wangchao3@cardc.cn

SPECIALTY SECTION

This article was submitted to Statistical and Computational Physics, a section of the journal Frontiers in Physics

RECEIVED 03 January 2023

ACCEPTED 27 January 2023

PUBLISHED 16 February 2023

CITATION

Jiang S, Li L, Guo X, Zhao W, Zhang R and Wang C (2023), Effect of offset distances for rod-airfoil interaction noise. *Front. Phys.* 11:1136539. doi: 10.3389/fphy.2023.1136539

COPYRIGHT

© 2023 Jiang, Li, Guo, Zhao, Zhang and Wang. This is an open-access article distributed under the terms of the [Creative Commons Attribution License \(CC BY\)](https://creativecommons.org/licenses/by/4.0/). The use, distribution or reproduction in other forums is permitted, provided the original author(s) and the copyright owner(s) are credited and that the original publication in this journal is cited, in accordance with accepted academic practice. No use, distribution or reproduction is permitted which does not comply with these terms.

Effect of offset distances for rod-airfoil interaction noise

Shujie Jiang^{1*}, Lanqing Li², Xiaokun Guo^{1,3}, Weiming Zhao^{4*}, Rongping Zhang¹ and Chao Wang^{5*}

¹Laboratory of Aerodynamic Noise Control, China Aerodynamics Research and Development Center, Mianyang, Sichuan, China, ²School of Mechanical Engineering, Sichuan University of Science and Engineering, Zigong, Sichuan, China, ³College of Architecture and Civil Engineering, Xinyang Normal University, Xinyang, Henan, China, ⁴Key Laboratory of Icing and Anti/De-icing, China Aerodynamics Research and Development Center, Mianyang, Sichuan, China, ⁵Facility Design and Instrumentation Institute, China Aerodynamics Research and Development Center, Mianyang, China

The noise generated by the interaction between the wake of rods and airfoils is a universal phenomenon in the engineering field. The noise generation mechanism is mainly caused by the violent changes of the pulsating pressure on the airfoil surface, impacted by different vortex scales in the wake of rods. During this process, the energy is radiated outward by sound waves. To capture wakes and the sound generated by the interaction of rod-airfoil with relatively small computing resources is a challenge. In this paper, the sound pressure generated by the rod-airfoil interaction is calculated by solving the Reynolds average N-S equation and non-linear acoustic equations. This numerical method is verified by a rod-airfoil interaction benchmark. This paper focuses on the influence of offset distances between rods and airfoils. The results show that the peak of far-field sound decreases from 89 dB to 80.6 dB as the offset distance from the airfoil to the center of the cylinder increases (the maximum deviation is three times the cylinder diameter). The frequency of peak sound pressure also shifts.

KEYWORDS

aerodynamic noise, RANS/NLAS method, rod-airfoil vortex-structure interaction, wake-airfoil interaction, aeroacoustics

1 Introduction

In recent years, aircraft noise has become one of the major problems due to the rapid increase in air traffic. Aerodynamic noise reduction is also one of the key issues in modern civil aircraft design in the past several decades. However, the noise generation mechanism is very complex for most engineering applications. For example, the strong interactions between the vortex shedding from the upstream flow and the airfoils downstream are one of the most important effects in the noise generation of landing gears [1].

There are mainly four types of numerical aeroacoustic prediction methods [2], including the pure theoretical method [3], the semi-empirical method [4], the direct numerical method, and the hybrid method [5, 6]. At present, the hybrid method is a commonly used numerical simulation method for aeroacoustic calculations. For example, combining computational fluid dynamics (CFD) methods such as URANS, LES [7, 8], and DES [9, 10] with acoustic analogy methods. First, the sound source information is obtained by CFD calculation, and then the source information is brought into the FW-H formula to calculate the far-field noise. Chen et al. [11] used the LES/FW-H combination method to predict the acoustic noise of the rod-airfoil interaction. They found that the first 30% chord length region near the leading edge was the main noise source. Bai et al. [12, 13] compared the aerodynamic noise of the rod-airfoil model by using URANS/FW-H and DES/FW-H



FIGURE 1
Aircraft landing gear.

methods. They pointed out that the DES method was better than the URANS method. Li et al. [14] used the DDES/FW-H method to analyze the effect of distance between rods and airfoils. They found the far-field sound got its maximum when the distance equals the chord length of the airfoil.

Numerical methods have been widely used in acoustic simulation, DES/FW-H and LES/FW-H methods are more widely used by scholars because of their better accuracy, but these two methods have high requirements for computational resources. Many efforts have been made to reduce the computational cost. Chen et al. [15–22] developed the isogeometric boundary element methods to perform acoustic topology optimization for sound absorbing materials. Their method enables acoustic topology optimization to be conducted directly from CAD models without any meshing procedures and meanwhile eliminating geometric errors. In order to save computing resources, Morris et al. [23] first proposed the RANS/non-linear acoustics solver (NLAS) method to predict the noise generation and transmission from an initial statistically steady model of the turbulent flow data, which can be provided by a simple RANS simulation and no requirement from the LES simulation. Batten et al. [24, 25] improved the RANS/NLAS method with more robustness and efficiency. The NLAS method can take sub-grid sound sources into consideration by reconstructing turbulent physical quantities. This can reduce computational resources and keep a relatively high resolution at the same time. In recent years, the RANS/NLAS method has become more and more popular. The application can be found for trains [26, 27], aircrafts [28, 29], and rockets [30].

In practical engineering fields, it is common where the airfoils are not directly behind the upstream rods, such as the landing gear shown in Figure 1. There is a certain offset between the rod and the main branch of a landing gear. Therefore, it is important to consider

the impact of this offset distance on rod-airfoil interaction noise. This paper investigates the effect of different offset distances for sound generation using a combined RANS/NLAS approach.

2 Numerical method

2.1 Non-linear acoustics solver

NLAS provides a more sophisticated subgrid treatment that allows the extraction of acoustic sources from the temporal variation within the modeled subgrid structures. The quasi-steady near-wall RANS solution is obtained a priori so that the grid requirements can be relaxed and reduced in the near-wall region during the NLAS transient calculation, compared to the LES solvers. At the same time, the dissipation effects of a subgrid eddy viscosity model are avoided; Thus, the NLAS solver proves less dissipation than the classic LES or hybrid RANS/LES simulation on course meshes (Figure 2). One of the most important advantages of the NLAS is able to account for both the turbulence-related broadband noise and the discrete tones produced from coherent structures or resonance [24].

The NLAS control equation is derived from the N-S equations by dividing each term in the equation into the mean and the fluctuation terms, $\phi = \bar{\phi} + \phi'$ substituting into the N-S equations, and rearranging the mean and the fluctuation terms to obtain the set of non-linear perturbation Eq. 1 [23, 24]:

$$\frac{\partial Q'}{\partial t} + \frac{\partial F_i'}{\partial x_i} - \frac{\partial (F_i^v)'}{\partial x_i} = -\frac{\partial \bar{Q}}{\partial t} - \frac{\partial \bar{F}_i}{\partial x_i} + \frac{\partial \bar{F}_i^v}{\partial x_i} \quad (1)$$

where.

Q' is the transient fluctuation term;

\bar{Q} is the transient mean term;

F_i' is the linear inviscid fluctuation term;

\bar{F}_i is the inviscid averaging term;

$(F_i^v)'$ is the viscous fluctuation term;

\bar{F}_i^v is the viscous averaging term.

The specific expressions are:

$$\begin{aligned} Q' &= \left[\bar{\rho} u_j' + \rho' \bar{u}_j + \rho' u_j' \right], \bar{Q} = \left[\frac{\bar{\rho}}{\bar{e}} \right] \\ F_i' &= \left[\begin{aligned} &\bar{\rho} u_i' + \rho' \bar{u}_i \\ &\rho' \bar{u}_i u_j' + \bar{\rho} u_i' u_j' + \bar{\rho} u_i' \bar{u}_j + \rho' \delta_{ij} \\ &u_i' (\bar{e} + \bar{p}) + \bar{u}_i (e' + p') \end{aligned} \right] \\ &+ \left[\begin{aligned} &\rho' u_i' \\ &\bar{\rho} u_i' u_j' + \rho' u_i' \bar{u}_j + \rho' \bar{u}_i u_j' + \rho' u_i' u_j' \\ &u_i' (e' + p') \end{aligned} \right] \\ (F_i^v)' &= \left[\begin{aligned} &0 \\ &\tau'_{ij} \\ &-\theta'_i + u'_k \tau'_{ki} + \bar{u}_k \tau'_{ki} \end{aligned} \right] \\ \bar{F}_i &= \left[\begin{aligned} &\bar{\rho} \bar{u}_i \\ &\bar{\rho} \bar{u}_i \bar{u}_j + \bar{p} \delta_{ij} \\ &\bar{u}_i (\bar{e} + \bar{p}) \end{aligned} \right], \bar{F}_i^v = \left[\begin{aligned} &0 \\ &\bar{\tau}_{ij} \\ &-\bar{\theta}_i + \bar{u}_k \bar{\tau}_{ki} \end{aligned} \right] \end{aligned}$$

Neglecting the density fluctuation and taking a time average of the Eq. 2:

$$\overline{LHS} = \overline{RHS} = \frac{\partial R_i}{\partial x_i} \quad (2)$$

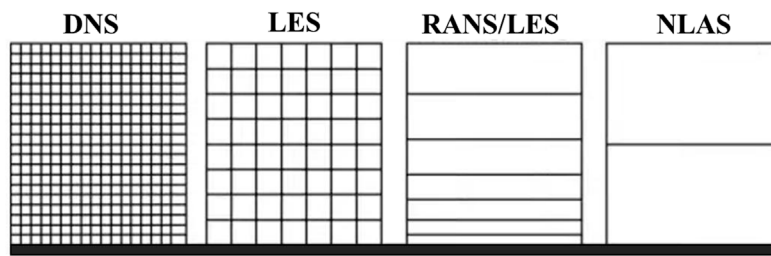


FIGURE 2
Common method near-wall mesh requirement.

R_i is a correlation of the standard Reynolds stress tensor and turbulent heat flux:

$$R_i = \begin{bmatrix} 0 \\ \overline{\rho u'_i u'_j} \\ c_p \overline{\rho T' u'_i} + \overline{\rho u'_i u'_k \overline{u_k}} + \frac{1}{2} \overline{\rho u'_k u'_k u'_i} + \overline{u'_k \tau_{ki}} \end{bmatrix}$$

The key step in NLAS is to obtain these unknown terms in advance from the classical RANS method. The small-scale quantities which cannot be solved are obtained by turbulent reconstruction generated by the subgrid source terms. The turbulent reconstruction method is proposed by Batten [25]. After both the mean levels and subgrid sources are established, the time-dependent calculations can then be carried out to determine the transmitted perturbations around the mean flows by using the above non-linear disturbance equations. The sound pressure in far-field observers can be calculated by the FW-H equations given by Farassat et al. [31, 32]. The flow field information is obtained by NLAS.

2.2 Sound pressure level correction

In order to reduce the amount of mesh during the numerical simulation, the numerical models are usually modified or simplified from the experiment models. For example, the span of the experiment airfoil L is much bigger than the chord c . In order to use the lower mesh number, the span of the numerical simulation can be reduced from L to L_s , which is smaller than the chord c . Then, the aeroacoustic calculation can be speeded up extensively; However, the aeroacoustic sound pressure level (SPL) obtained from the numerical results, and the experimental results cannot be compared directly. In such cases, some corrections have to be introduced to the numerical sound pressure level (SPL). In the paper, we use the correction method first proposed by Kato et al [33, 34].

When

$$\begin{aligned} L_C &\leq L_s \\ SPL &= SPL_s + 10 \log(L/L_s) \end{aligned} \quad (3)$$

when

$$\begin{aligned} L_s &< L_C \leq L \\ SPL &= SPL_s + 20 \log(L_C/L_s) + 10 \log(L/L_C) \end{aligned} \quad (4)$$

when

$$\begin{aligned} L_C &> L \\ SPL &= SPL_s + 20 \log(L/L_s) \end{aligned} \quad (5)$$

3 Numerical validation

3.1 Validation of RANS simulation

The validation benchmark is given by the experiment data of Jacob [35]. In the experiment (Figure 3), the NACA0012 airfoil (with chord length $c = 0.1$ m) is located at one-chord length after the cylinder (with diameter $d = 0.01$ m), both extending by $L = 0.3$ m in the spanwise direction. The acoustic far-field receiver is at 1.85 m from the airfoil center. The incoming flow velocity is 72 m/s and the Reynolds number of the cylinder is 48,000. The experiment was conducted in an anechoic room ($10 \text{ m} \times 8 \text{ m} \times 8 \text{ m}$). The air was supplied by a high-speed subsonic anechoic wind tunnel at Mach numbers ranging up to 0.34.

In order to reduce the computational cost, the span of the numerical model is set as 0.05 m which is smaller than the experiment model ($L = 0.3$ m). The simulation domain was X (-0.2 m, 0.3 m), Y (-0.2 m, 0.2 m), and Z (-0.05 m, 0 m). After the grid convergence check, the multiblock structure meshes with 3 million (mesh cell number) computational grids were used for the RANS/NLAS simulation. The first interior point was located at $y^+ < 1$ from the airfoil surface, yielding a sufficient resolution of the viscous sublayer. In the RANS simulation, the cubic k-ε turbulence model was used. NLAS provided a more sophisticated subgrid treatment that allowed the extraction of acoustic sources from the temporal variation within the modeled subgrid structures. In this paper, the subgrid for NLAS was x (-0.15 m, 0.15 m), y (-0.1 m, 0.1 m), and z (-0.05 m, 0 m) with the resolution ratio 0.002.

Four offset distances ($D = 0d, 0.5d, 1d$, and $3d$) are used to reveal the effect of offset distances. The simulation domain and offset distances can be found in Figure 4.

RANS calculations were carried out to obtain a statistical average of the local Reynolds stress tensor and heat flux. Then they were interpolated into the NLAS noise calculation grid. The turbulence flow is reconstructed based on this statistical average.

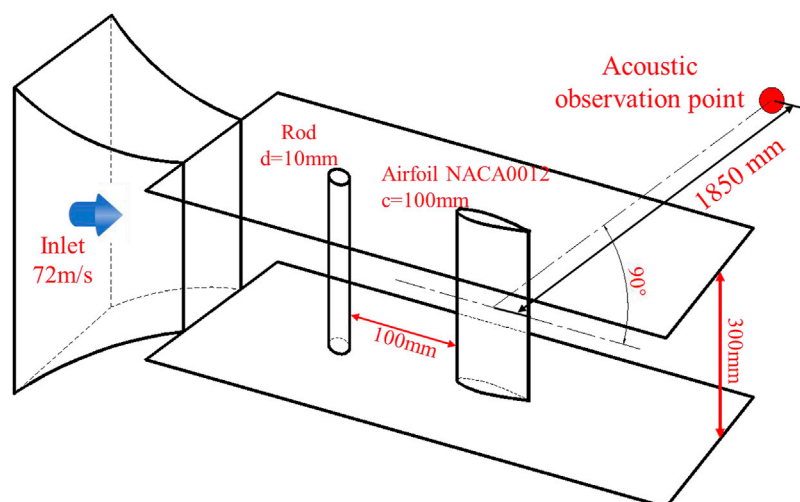


FIGURE 3
Schematic diagram of Jacob test wind tunnel installation.

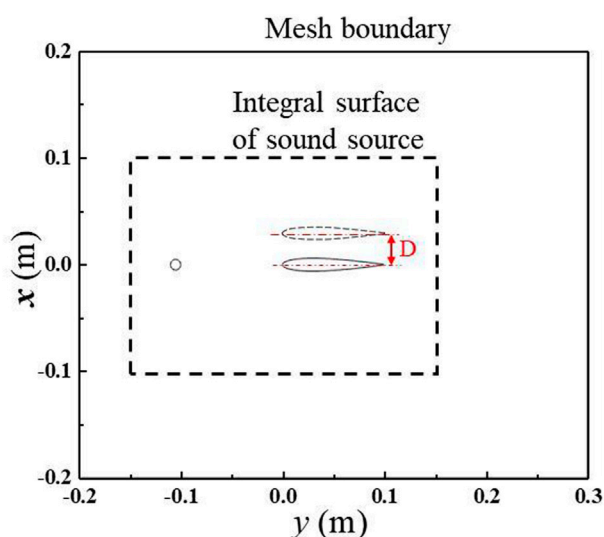


FIGURE 4
Simulation domain and offset distances.

The velocity inlet was applied in the left boundary. The outflow boundary was used in the right boundary. The far-field and periodic boundary are used in the up/down and the spanwise direction. The viscous non-slip adiabatic wall condition was applied for cylinders and airfoils.

The flow velocity (on the line $x/c = 0.25$ and $0 < y/c < 0.6$, as show in Figure 5A.), obtained from the RANS, was compared with the experimental results in Jacob's literature ([35]), as shown in Figure 5B. It can be seen that the velocity variation trend obtained from the RANS calculation in this paper is the same as the URANS method used in the literature ([35]). Both methods differ significantly from the experimental variation trend within

$0.06 < y/c < 0.26$; however, for the region $y/c > 0.26$, the results of the RANS calculations in this paper are closer to the experimental data than the URANS method.

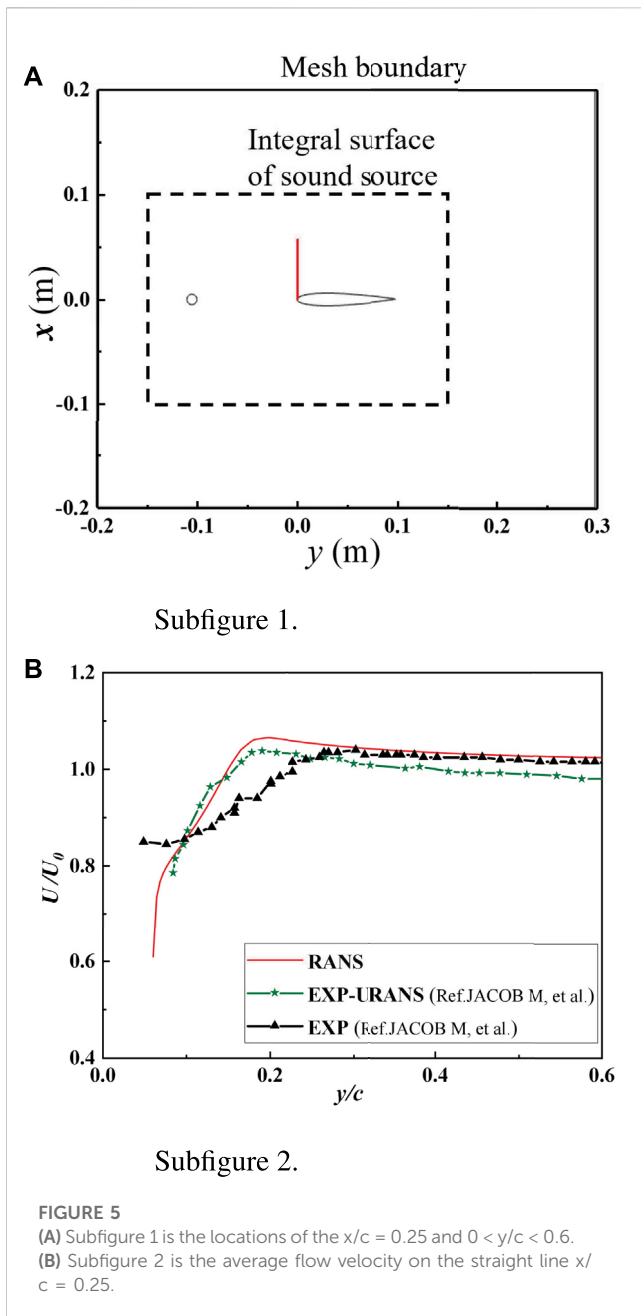
The instantaneous CI for the cylinder is given in Figure 6. The CI presents a sinusoidal oscillation mode which means the convergence.

Figure 7 shows the vorticity contours obtained from the URANS calculations, the large-scale vortices at the trailing edge of the cylinder are continuously shedding and spreading downstream to the leading edge of the wing. The wake of the cylinder interacts with the leading edge of airfoils and generates unsteady pressure fluctuation across the airfoil surface.

3.2 Verification of NLAS calculations

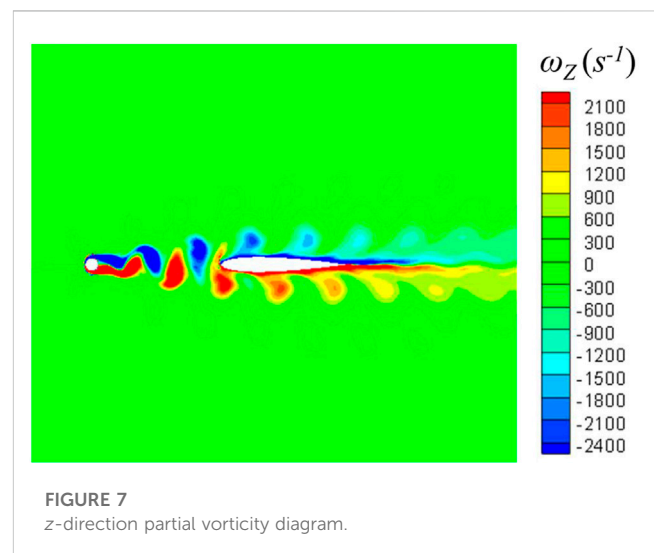
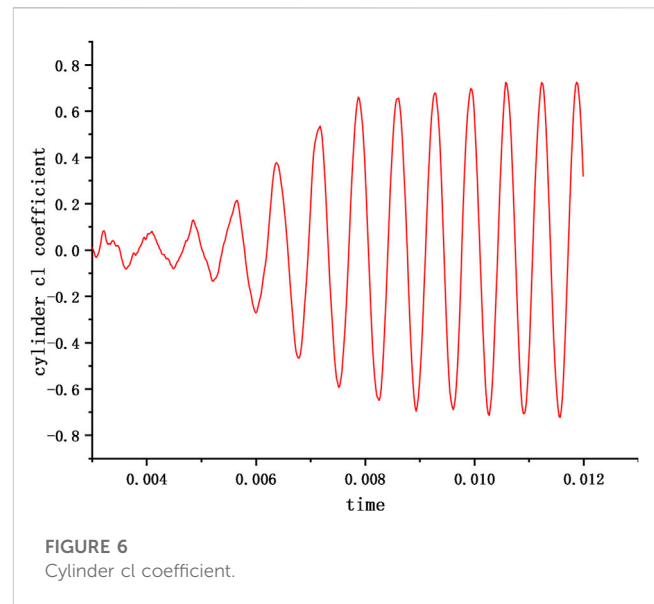
The RANS calculation results were interpolated to the NLAS grid with turbulent reconstruction for acoustic calculations. The numerical time step is $\Delta t = 2 \times 10^{-5}$ s, and the simulation is performed 4,000 steps in total, the simulation is performed using AMD EPYC 7452 with 64 cores for about 20 h. In this paper, the numerical model span is smaller than the experimental model span, and the correction of Eq. 5 is used to correct the acoustic results accordingly.

Figure 8 shows the comparison between the NLAS used in this paper and several calculation methods (LES [35], URANS [13], DES [9]) in the literature. It is found that the sound pressure levels obtained by all four calculation methods are higher than the experimental values in the low-frequency range of 300 Hz–900 Hz. The peak sound pressure obtained by the NLAS method is almost the same as the experimental data and is more accurate than the other methods. Above 1700 Hz, the results obtained by EASM DES and NLAS method are closer to the experimental values. It shows that the NLAS method is able to capture the sound



pressure accurately in most frequencies and with an acceptable computational cost.

Four different sets of computational mesh are used to test the grid independence. As shown in Figure 9, the peak sound pressure level is 91 dB at 1,365 Hz in the experiment [35]. The difference for different computational meshes is quite small. The peak sound pressure level and its frequency are compared in Table 1. The maximum difference of peak sound pressure level is less than 4 dB, and the peak frequency is less than 6 dB, which indicates the calculated results are less correlated with the computational grid. In this paper, the number of meshes is chosen to be 2.41 million to give an error of less than 2 dB for both the peak sound pressure level and its frequency.

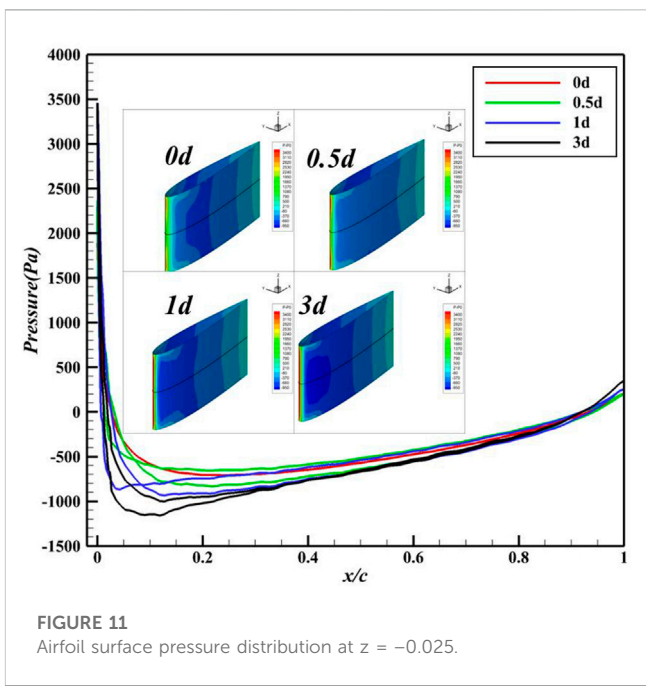
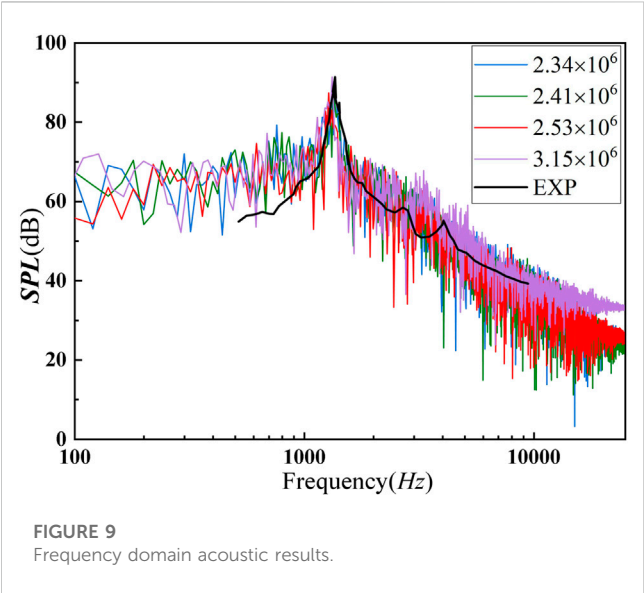
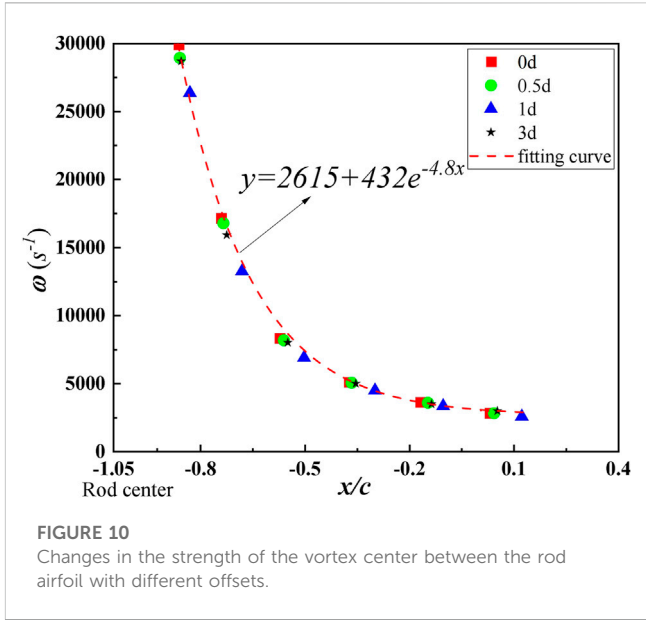
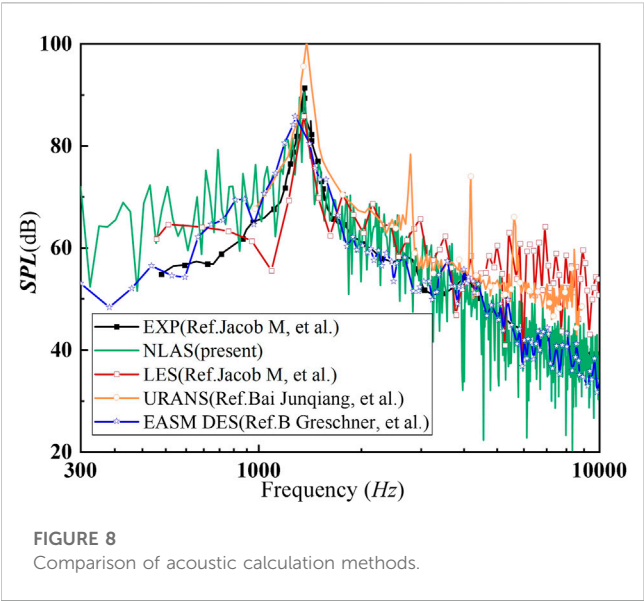


4 The effect of offset distance for rod-airfoil interaction noise

4.1 RANS calculation with different offset distances

In order to analyze the influence of wakes at the trailing edge of the cylinder, different offset distances (0d, 0.5d, 1d, and 3d) are used in this section. The sound pressure is collected in 1.85 m from the center of the wing at zero offset distance. This location is not changed in later research.

Figure 10 shows the variation of vortex intensity at different offset distances calculated by URANS, where the vertical coordinate indicates the vortex intensity ω and the horizontal coordinate indicates distances behind the rod center. The figure shows that the vortex intensities in the wake of the cylinder show



a non-linear decreasing trend, and the offset distance has less effect on them. The vortex in the wake of the cylinder dissipates due to the viscous effect of the fluid. The dissipation rate of the vortex is found to be:

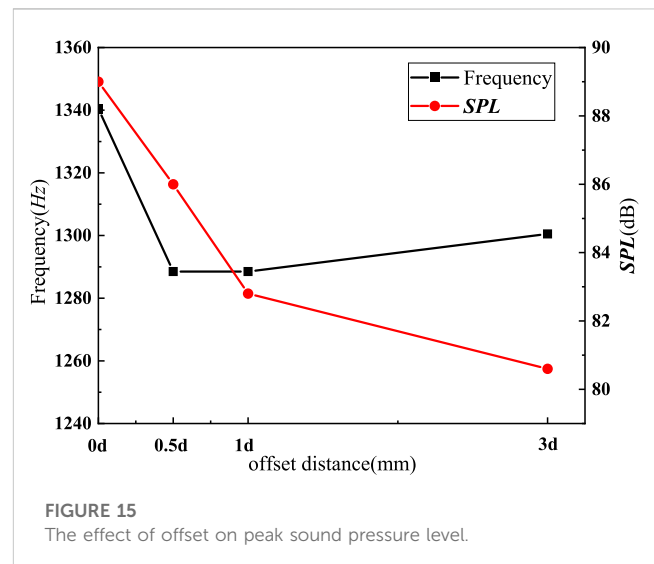
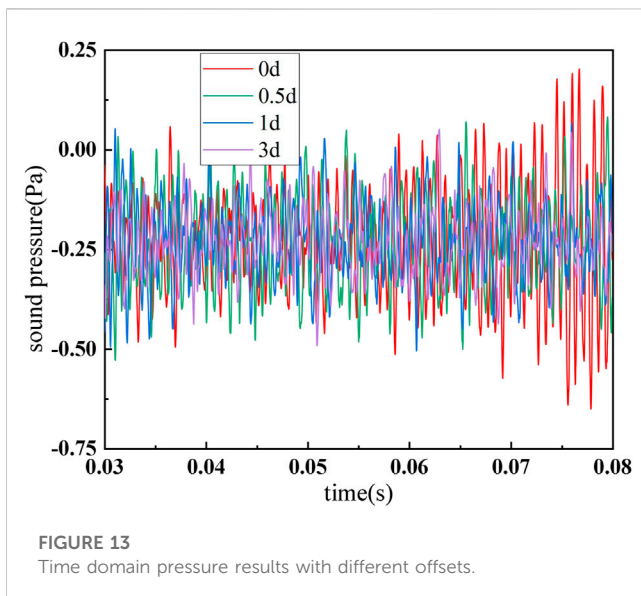
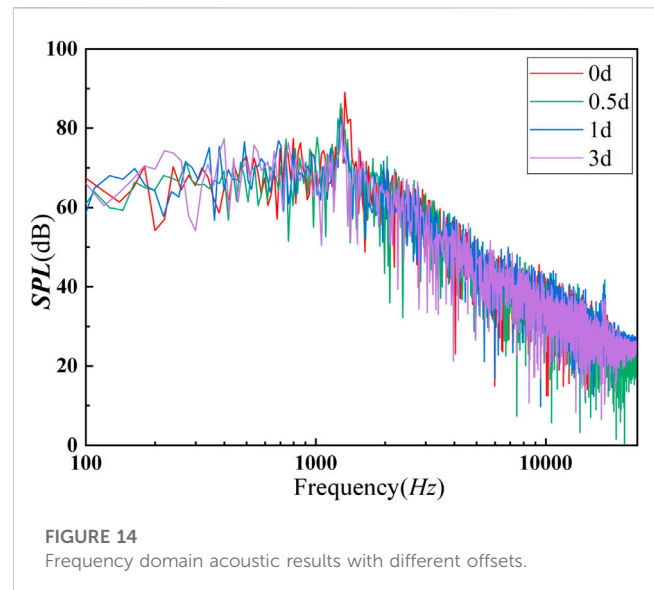
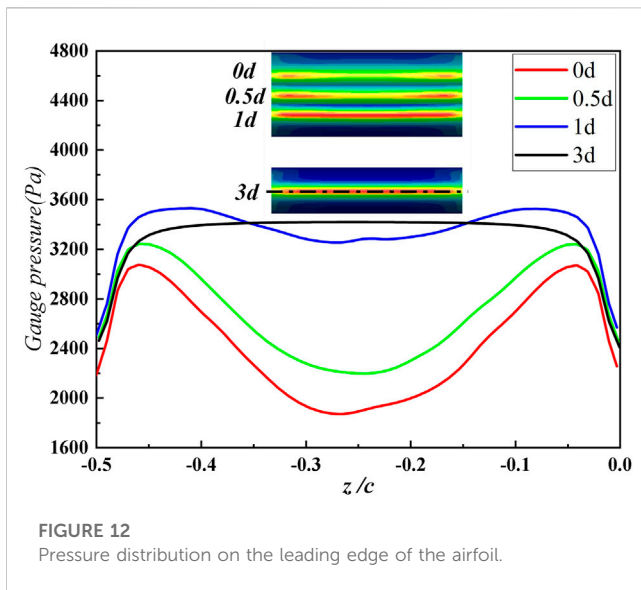
$$y = 2615 + 432e^{-4.8x} \tag{6}$$

where y is the biggest vortex intensity in the wake of the rod and x is the distance behind the rod center.

Figure 11 shows the pressure distribution of the airfoil along the chord in the middle span. It is found that only when the offset

TABLE 1 The effect of the grid on the acoustic results.

Grid ($\times 10^6$)	Frequency difference (Hz)	Frequency error (%)	SPL difference (dB)	SPL error (%)
2.34	4.5	0.3	0.5	1.1
2.41	24.5	1.83	2	2
2.53	84.5	6	3.7	4
3.15	41	3	0.4	0.4



distance $D = 0d$ the pressure on the upper and lower surfaces of the airfoil shows symmetric changes. With the increase of offset distance in the region near the leading edge ($0.014 < x/c < 0.3$), the pressure gradually decreases and with a asymmetric distribution. This may be caused by the fact that with the increase of the offset distance, the higher the flow velocity interacts with the leading edge of the airfoil. When the offset distance increases, the airfoil gradually get out of the vortex street influence area, and the flow field around the body is dominated by the velocity field without cylindrical disturbance.

The pressure distribution at the leading edge of airfoils along the spanwise is presented in Figure 12. The pressure in the center of the leading edge is affected by the vortex shedding dramatically. The pressure difference in the center of the leading edge gets its maximum for about 1,300 Pa by comparing $D = 0d$ and $D = 3d$. This difference decreases with the increase of offset distance D .

4.2 NLAS calculation with different offset distances

The size and mesh resolution for the integral surface of sound sources are the same as the benchmark case. After 4,000 steps of NLAS calculation, Figures 13, 14 show the time domain of sound pressure in the time domain and frequency domain, respectively. The variation of peak sound pressure and its frequency are plotted in Figure 15. It can be seen that the sound pressure level decreases gradually with the increase of offset distance, from 89 dB to 80.6 dB. The peak sound frequency decreased significantly when the offset distance changed from 0d to 0.5d. Its frequency did not change significantly when the offset distance changed from 0.5d to 1d and increased slightly from 0.5d to 3d. With the increase of offset distance, the sound pressure level decreases almost linearly from 0d to 1d; From 1d to 3d, the decrease rate slows down significantly.

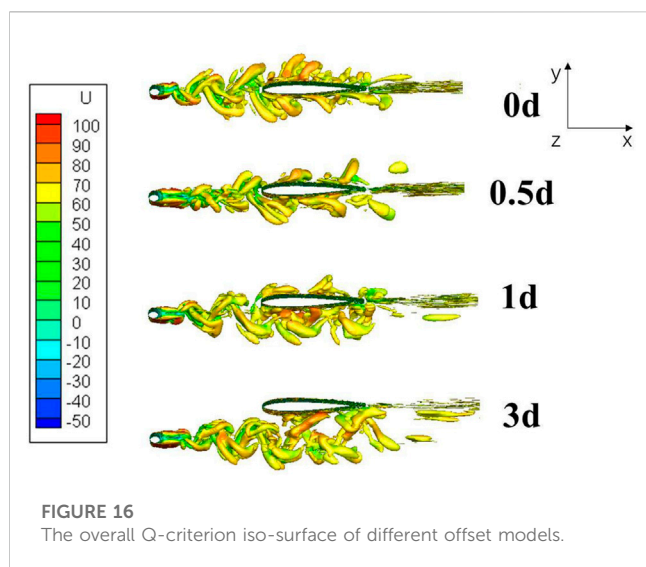


FIGURE 16
The overall Q-criterion iso-surface of different offset models.

The Q-criteria contour surfaces (Figure 16) obtained from NLAS show that there are both large-scale vortices and small-scale vortices generated in the wake of the cylinder. With the increase of the offset distance, the interaction between the wake of the cylinder and the leading edge of the airfoil becomes smaller. So the sound pressure decreases, as predicted in Figure 15.

5 Conclusion

In order to capture the aerodynamic noise with a relatively small computational cost, this paper performs the RANS/NLAS numerical simulation method to study the noise generation by rod-airfoil interaction. This method is verified by experimental results. A very good agreement can be found for four different mesh resolutions. This paper focuses on the effect of offset distance for rod-airfoil interaction noise. It is found the wake behind the cylinder decays with the distance behind the cylinder non-linearly. The offset distance plays no role in this process. The existence of airfoil affects this decay process little. Besides, with the increase of offset distance, the peak sound pressure level decreases, and the corresponding

frequency changes a bit. When the offset distance equals three times the cylinder diameter, the wake of the cylinder has little influence on the leading edge of the following airfoils. The noise can be reduced by about 10 dB by increasing the offset distance to three times of rod diameter. For engineering guidance, the offset distance can affect the noise generated by rod-airfoil interaction dramatically. The noise can be reduced by about 10 dB by increasing the offset distance to three times of rod diameter.

Data availability statement

The original contributions presented in the study are included in the article/supplementary materials, further inquiries can be directed to the corresponding authors.

Author contributions

Conceptualization, SJ; data curation, LL, formal analysis, XG; investigation, LL and XG; methodology, SJ; project administration, WZ; software, LL; supervision, RZ; validation, LL; visualization, LL and SJ; writing, LL, SJ, XG, RZ, and CW. All authors have read and agreed to the published version of the manuscript.

Conflict of interest

The authors declare that the research was conducted in the absence of any commercial or financial relationships that could be construed as a potential conflict of interest.

Publisher's note

All claims expressed in this article are solely those of the authors and do not necessarily represent those of their affiliated organizations, or those of the publisher, the editors and the reviewers. Any product that may be evaluated in this article, or claim that may be made by its manufacturer, is not guaranteed or endorsed by the publisher.

References

1. Song Wenping HZ, Lei Y. Status of investigation on airframe noise computation. *Adv Aeronaut Sci Eng* (2010) 1:125–31. doi:10.3969/j.issn.1674-8190.2010.02.007
2. Dobrzynski W. Almost 40 years of airframe noise research: What did we achieve. *J Aircraft* (2012) 47:353–67. doi:10.2514/1.44457
3. Lockard D. A comparison of fflowcs williams-hawkings solvers for airframe noise applications. In: 8th AIAA/CEAS Aeroacoustics Conference and Exhibit (2002). p. 2580.
4. Boudet J, Casalino D, Jacob M, Ferrand P. Prediction of broadband noise: Airfoil in the wake of a rod. In: 42nd AIAA Aerospace Sciences Meeting and Exhibit (2004). p. 852.
5. Xun H, Xiaoxian C, Zhaokai M, Xin Z. Efficient computation of spinning modal radiation through an engine bypass duct. *AIAA J* (2008) 46:1413–23. doi:10.2514/1.31136
6. de la Puente F, Sanders L, Vuillot F. On lagoon nose landing gear cfd/caa computation over unstructured mesh using a zdes approach. In: 20th AIAA/CEAS aeroacoustics conference (2014). p. 2763.
7. Yang C, Feng H, Peng Y. Noise characteristic analysis and sound sources identification for rod-airfoil interaction using different subgrid-scale models. In: E3S Web of Conferences (EDP Sciences), vol. 233 (2021). p. 04036.
8. Jiang Y, Mao ML, Deng XG, Liu HY. Numerical investigation on body-wake flow interaction over rod-airfoil configuration. *J Fluid Mech* (2015) 779:1–35. doi:10.1017/jfm.2015.419
9. Greschner B, Thiele F, Jacob MC, Casalino D. Prediction of sound generated by a rod-airfoil configuration using EASM DES and the generalised Lighthill/FW-H analogy. *Comput Fluids* (2008) 37:402–13. doi:10.1016/j.compfluid.2007.02.013
10. Zhu W, Luo K, Xiao Z, Fu S. Numerical simulations of the flow dynamics past an oscillating rod-airfoil configuration. In: Progress in Hybrid RANS-LES Modelling: Papers Contributed to the 6th Symposium on Hybrid RANS-LES Methods; 26–28 September 2016. Strasbourg, France: Springer (2018). p. 433–43.
11. Wei-Jie C, Wei-Yang Q, Liang-Feng W, Kun-Bo XU, Fan T. Investigation of rod-airfoil interaction noise using large eddy simulation and FW-H equation. *J Aerospace Power* (2016) 31:2146–55. doi:10.13224/j.cnki.jasp.2016.09.013

12. Peixun Y, Junqiang B, Jiangtao H, Jun Z. Aerodynamic noise of the rod-airfoil computed by using acoustic analogy. *Acta Aerodynamica Sinica* (2013) 31:204–8. doi:10.7638/kqdlxxb-2011.0109
13. Junqiang B, Peixun Y, Guo B. An effective numerical simulation approach to noise induced by flow around rod-airfoil using the hybrid method with solutions of DES and FW-H integration. *J Northwest Polytechnical Univ* (2012) 30:5. doi:10.3969/j.issn.1000-2758.2012.06.009
14. Li Z, Zhang Y, Lu Y. Numerical simulation of the flow and acoustic field of A cylinder wake-airfoil interaction. *Fan Technol* (2020) 3:52–7.
15. Chen L, Cheng R, Li S, Lian H, Zheng C, Bordas SP. A sample-efficient deep learning method for multivariate uncertainty qualification of acoustic-vibration interaction problems. *Comput Methods Appl Mech Eng* (2022) 393:114784. doi:10.1016/j.cma.2022.114784
16. Chen L, Chuang L, Haojie L, ZhaoWei L, Wenchang Z, Shengze L, et al. Acoustic topology optimization of sound absorbing materials directly from subdivision surfaces with isogeometric boundary element methods. *Comput Methods Appl Mech Eng* (2020) 362:112806. doi:10.1016/j.cma.2019.112806
17. Chen L, Haibo C, Changjun Z, Steffen M. Structural-acoustic sensitivity analysis of radiated sound power using a finite element/discontinuous fast multipole boundary element scheme. *Int J Numer Methods Fluids* (2016) 82:858–78. doi:10.1002/ld.4244
18. Chen L, Lian H, Liu Z, Chen H, E A, Bordas S. Structural shape optimization of three dimensional acoustic problems with isogeometric boundary element methods. *Comput Methods Appl Mech Eng* (2019) 355:926–51. doi:10.1016/j.cma.2019.06.012
19. Chen L, Lian H, Liu Z, Gong Y, Zheng C, Bordas S. Bi-material topology optimization for fully coupled structural-acoustic systems with isogeometric FEM-BEM. *Eng Anal Boundary Elem* (2022) 135:182–95. doi:10.1016/j.enganabound.2021.11.005
20. Chen L, Lian H, Natarajan S, Zhao W, Chen X, Bordas S. Multi-frequency acoustic topology optimization of sound-absorption materials with isogeometric boundary element methods accelerated by frequency-decoupling and model order reduction techniques. *Comput Methods Appl Mech Eng* (2022) 395:114997. doi:10.1016/j.cma.2022.114997
21. Chen L, Lian H, Xu Y, Li S, Liu Z, Atroshchenko E, et al. Generalized isogeometric boundary element method for uncertainty analysis of time-harmonic wave propagation in infinite domains. *Appl Math Model* (2023) 114:360–78. doi:10.1016/j.apm.2022.09.030
22. Chen L, Liu C, Zhao W, Liu L. An isogeometric approach of two dimensional acoustic design sensitivity analysis and topology optimization analysis for absorbing material distribution. *Comput Methods Appl Mech Eng* (2018) 336:507–32. doi:10.1016/j.cma.2018.03.025
23. Morris PJ, Long LN, Bangalore A, Wang Q. A parallel three-dimensional computational aeroacoustics method using nonlinear disturbance equations. *J Comput Phys* (1997) 133:56–74. doi:10.1006/jcph.1997.5646
24. Batten P, Ribaldone E, Casella M, Chakravarthy S. Towards a generalized non-linear acoustics solver. In: 10th AIAA/CEAS aeroacoustics conference (2004). p. 3001.
25. Batten P, Goldberg U, Chakravarthy S. Reconstructed sub-grid methods for acoustics predictions at all Reynolds numbers. In: 8th AIAA/CEAS aeroacoustics conference and exhibit (2002). p. 2511.
26. Mo H, An Y, Qingquan L. Influence of the length of high-speed train on the far-field aeroacoustics characteristics. *Chin J Theor Appl Mech* (2019) 51:1310–20. doi:10.6052/0459-1879-19-079
27. Sun Z, Song J, An Y. Numerical simulation of aerodynamic noise of CRH3 high-speed train. *J Peking Univ (Natural Sci Edition)* (2012) 48:701–11. Available from: <http://dspace.imech.ac.cn/handle/311007/47944>.
28. Zhang Y, Duan Z, Hou Y. An application of non-linear acoustics solver in the noise prediction of refueling tube. *Aeronaut Sci Technol* (2015) 26:74–8. doi:10.3969/j.issn.1007-5453.2015.09.017
29. Chen B, Wang Y, Tong M. Cavity noise analysis and passive control using NLAS method. *Aeronaut Comput Tech* (2015) 45:54–7. doi:10.3969/j.issn.1671-654X.2015.05.014
30. Ren S, Zhang S, Yan G. A prediction of fluctuation pressure conditions with transonic rocket by RANS/NLAS method. *J Solid Rocket Technol* (2011) 34:418–22. doi:10.1016/B978-0-444-53599-3.10005-8
31. Farassat F. Discontinuities in aerodynamics and aeroacoustics: The concept and applications of generalized derivatives. *J Sound Vibration* (1977) 55:165–93. doi:10.1016/0022-460x(77)90593-4
32. Casper J, Farassat F. A new time domain formulation for broadband noise predictions. *Int J Aeroacoustics* (2002) 1:207–40. doi:10.1260/147547202320962574
33. Agrawal B, Sharma A. Aerodynamic noise prediction for a rod-airfoil configuration using large eddy simulations. In: 20th AIAA/CEAS Aeroacoustics Conference (2014). doi:10.2514/6.2014-3295
34. Kato C, Iida A, Takano Y, Fujita H, Ikegawa M. Numerical prediction of aerodynamic noise radiated from low mach number turbulent wake. In: 31st aerospace sciences meeting (1993). p. 145.
35. Jacob M, Boudet J, Casalino D, Michard M. A rod-airfoil experiment as a benchmark for broadband noise modeling. *Theor Comput Fluid Dyn* (2005) 19:171–96. doi:10.1007/s00162-004-0108-6



OPEN ACCESS

EDITED BY

Pei Li,
Xi'an Jiaotong University, China

REVIEWED BY

Lijuan Sun,
Jilin Jianzhu University, China
Baoliang Wang,
Yellow River Engineering Consulting Co.,
Ltd, China

*CORRESPONDENCE

Qingling Du,
✉ duqingling@huanghuai.edu.cn

SPECIALTY SECTION

This article was submitted to Statistical
and Computational Physics,
a section of the journal
Frontiers in Physics

RECEIVED 03 February 2023

ACCEPTED 14 February 2023

PUBLISHED 22 February 2023

CITATION

Du Q, Pan Y and Xin Y (2023), Research
and application of Rayleigh wave
extraction method based on
microtremors signal analysis.
Front. Phys. 11:1158049.
doi: 10.3389/fphy.2023.1158049

COPYRIGHT

© 2023 Du, Pan and Xin. This is an open-
access article distributed under the terms
of the [Creative Commons Attribution
License \(CC BY\)](#). The use, distribution or
reproduction in other forums is
permitted, provided the original author(s)
and the copyright owner(s) are credited
and that the original publication in this
journal is cited, in accordance with
accepted academic practice. No use,
distribution or reproduction is permitted
which does not comply with these terms.

Research and application of Rayleigh wave extraction method based on microtremors signal analysis

Qingling Du^{1,2*}, Yanhui Pan¹ and Youyang Xin¹

¹School of Architectural Engineering, Huanghuai University, Zhumadian, China, ²Henan International Joint Laboratory of Structural Mechanics and Computational Simulation, Huanghuai University, Zhumadian, China

This study investigates the method and application of single-channel, three-component microtremor signal co-directional Rayleigh surface-wave extraction. The research focuses on filtering linear polarization waves using polarizability wave and phase-difference filtering, which were analyzed based on both simulated data and real microtremor signals. Additionally, the study examines the use of time-frequency analysis to analyze microtremor signals and identify Rayleigh wave propagation direction. The combination of these methods leads to a set of procedures for extracting high-SNR co-directional Rayleigh surface waves from microtremor signals, which was applied to the elliptical polarizability imaging method. Results indicate that the proposed data processing process effectively filters linear polarization waves and accurately determines the propagation direction of the Rayleigh wave, leading to significant improvement in the accuracy of elliptical polarizability exploration results. This provides a reference for obtaining high signal-to-noise ratio data in microtremor Rayleigh wave seismic exploration.

KEYWORDS

microtremors, Rayleigh wave, numerical simulation, elliptical polarizability, filtering method

1 Introduction

There are continuous weak vibrations of various frequencies on the Earth's surface at all times. Microtremors, also known as micromotions, are continuous weak vibrations that occur on the Earth's surface and vary irregularly with space and time in the field of seismic engineering. With advancements in seismic wave monitoring technology, the study of microtremor signals has advanced, and its applications in seismic wave exploration have broadened.

Although complex, microtremor signals provide valuable information about geological structures. Tokimatsu et al. studied the components of the microtremor signal, and the results showed that the microtremor signal was mainly composed of body waves (P and S waves) and surface waves (Rayleigh and Love waves) [1–5]. Toksöz and Lacoss found that high-frequency microtremor signals contain body waves and Rayleigh surface wave components, whereas low-frequency microtremor signals are mainly composed of a fundamental Rayleigh surface wave. The main source of signals with frequencies higher than 1 Hz is human activities of near-field sources [6]. Rayleigh surface waves are dominant in microtremor signals with far-field source characteristics, and the energy of Rayleigh

surface waves accounts for 2/3 of the total excitation energy. The spectrum distribution characteristics of microtremor signals change with changes in the detection location. The main frequency and amplitude of data at different locations have obvious differences that are closely related to the site [7]. The research results not only show the complexity of the composition of the pulsation signal, but also lay the foundation for the application of the microtremor signal to geological structure exploration and promote the vigorous development of the microtremor seismic wave exploration method.

In recent years, the microtremor seismic exploration method has become increasingly popular among engineers, especially for the exploration of Rayleigh surface waves through microtremor analysis. One approach is the velocity dispersion method, which utilizes the kinematic properties of Rayleigh surface waves. For example, Aki proposed the spatial autocorrelation method (SPAC) to extract the velocity dispersion curve from ground pulsation records [8, 9], the frequency-wave number spectrum proposed by Capon in 1969 [10], and Claerbout's seismic interference technique for interpreting the internal structure of the medium by extracting Green's function from the microtremor signal [11]. On the other hand, the elliptical polarization method based on the dynamic characteristics of Rayleigh surface waves, such as Boore and Toksöz, was proposed in 1969 to study the feasibility of using the dynamic characteristics of the elliptical polarization of Rayleigh surface wave particles to study the crustal structure. Research shows that the elliptical polarization of particle motion in layered media changes with the frequency, and can interpret the geological structure in the same way as the velocity dispersion method [12]. Nakamura studied the field effect in 1989 by utilizing the Fourier spectral ratio (HVSr) on three-component data from a single detector [13]. The elliptical polarizability method is widely used worldwide.

However, the application of these exploration methods is mostly based on the stationary characteristics of the microtremor signals. In fact, Toksöz (1964) found that the conditions required for the microtremor signals of different frequency bands to meet the stationary characteristics are different [14], that not all the randomly intercepted seismic records meet the stationary characteristics, and that stationarity can be established only under very harsh conditions [15]. This significantly affected the accuracy of the exploration results. This limitation significantly restricts the applicability of exploration methods relying on stationary microtremor signals. For example, Du et al. theoretically deduced the influence mechanism of the interference wave of the microtremor recording on elliptical polarizability. The results show that linear polarization waves, Rayleigh surface waves in different directions, and other interference waves strongly interfere with the calculation of elliptical polarizability, and the imaging shifts in the direction [16, 17]. This conclusion provides a direction for extracting the elliptical polarizability of Rayleigh surface waves using microtremor signals. Therefore, in addition to extracting stationary microtremor signals, geological structure exploration can also be realized by extracting high signal-to-noise ratio co-directional Rayleigh waves through wave-field separation.

In recent years, many achievements have emerged in the research of wave field separation [18–20], and different methods have been adopted according to different data types and application directions. For example, the P-wave and S-wave separation of multi-

wave seismic data are generally based on the kinematic characteristics (wave velocity, vibration direction) and dynamic characteristics (wave amplitude, frequency, and phase) of seismic waves, mainly the F-K filtering τ -P transform, Radon transform, polarization filtering, full waveform inversion, divergence, and curl methods [21–24]. At present, the separation methods of mixed mining wave fields are mainly based on inversion theory and filtering denoising [25–28]. Wave field separation and suppression methods of multiples mainly include filtering methods based on signal analysis and prediction methods based on wave equation (29)–(33). However, there are few studies on the wave field separation of Rayleigh waves in microtremor signals. In the 1940 s, the concept of time-frequency analysis that refines the overall features to local features was proposed, which can determine the energy distribution at any time and frequency and clearly express the relationship between the frequency spectrum and time, providing a favorable tool for the analysis and research of non-stationary signals. In 1932, Winger proposed the concept of time-frequency joint analysis, and then Ville introduced it into signal processing to form the classic video analysis method, Winger-Ville [34]. In 1968, Rihaczek proposed the concept of a complex energy density function when studying the distribution of the signal energy in the time and frequency domains. On this basis, Ren é RM provided a solution—instantaneous polarization characteristics of signals in Complex Trace Analysis of signal processing [35]. However, for the superimposed signal, filtering directly according to the instantaneous polarization characteristics causes significant errors. Galiana-Marino designed an optimized filtering scheme based on the multi-scale characteristics of the wavelet transform, which can effectively filter linearly polarized waves. The above wave-field separation methods and research conclusions still have many shortcomings when applied to the extraction of Rayleigh surface waves from microtremor signals; however, they provide a theoretical basis for the research content of this paper. In addition, the finite element method, which is widely used in solid mechanics, acoustics, and other aspects [36–41], was used in this study, providing technical support for this study.

In summary, the microtremor signal is common on Earth, Rayleigh surface waves are dominant in the far field, and the spectral characteristics are closely related to the site changes; therefore, they can be used as a signal source for seismic wave exploration. However, its signal composition is complex and cannot meet the requirements of high signal-to-noise ratio of active source signals, and it is difficult to strictly meet the requirements of signal stability, which seriously affects the accuracy of Rayleigh surface wave exploration results. At the same time, the complexity of the signal components makes simple wave field separation unable to meet the requirements of engineering applications. In view of the above problems, this study combines polarization filtering, phase difference filtering, and directional filtering, and uses numerical simulation and time-frequency analysis to study the method of extracting the same direction high signal-to-noise ratio surface wave from the microtremor signal, and applies it to the Rayleigh surface wave ellipse polarizability imaging method. The purpose was to improve the imaging accuracy of microtremor Rayleigh wave exploration and promote the application of microtremor signals in engineering exploration.

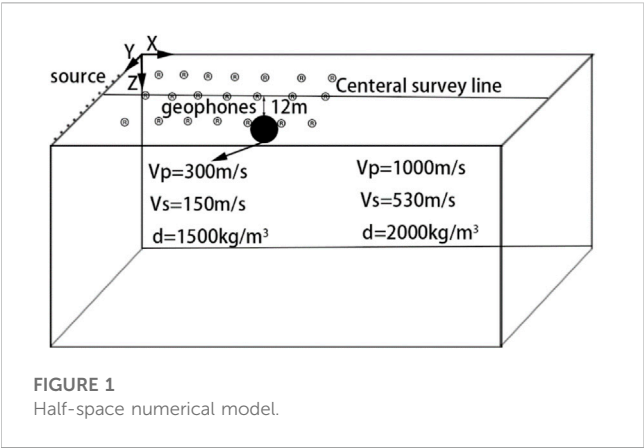


FIGURE 1
Half-space numerical model.

2 Numerical simulation

This study mainly focused on the extraction method of high-quality Rayleigh surface waves in a microtremor signal. The experimental data were obtained from numerical simulations and actual site data. This section introduces the numerical model and parameters of the simulation data used in this study. A homogeneous half-space model is shown in Figure 1. To simulate the microtremor signal more realistically, a spherical cavity was set in the inhomogeneous half-space to simulate the inhomogeneous geological characteristics as required. Considering the far-field characteristics of the microtremor signal, a plane-wave source was used in the numerical simulation. Each plane wave source was composed of a linear array of point sources. According to the Huygens principle, the wavefront of a Rayleigh wave radiated by a linear array of point sources is a plane type, and the plane wave field in the full text is simulated in this manner. The model grid was divided into 2 m, and the 20 Hz dominant frequency of the Rick wavelet was selected as the source. The array spacing between the geophones was 2 m. A central line was set at the center of the model. The spherical cavity was directly below the line.

Different source distributions were set according to the different research contents in this study. Seismic wave data in different directions and from multiple sources can be simulated by adjusting the source location and number of sources. Table 1 shows the elastic parameters of the half-space model; medium one is selected for the local abnormal body, and medium two is selected for the homogeneous semi-infinite space.

Figure 2 shows a snapshot of the wave field of the seismic wave propagation in homogeneous media. At 0.2 s, it can clearly see the P wave, S wave and Rayleigh surface wave; At 0.35 s and 0.4 s, since the longitudinal wave propagates to the boundary of the model, the reflected wave at the boundary of the model can be seen. The finite element software can clearly describe the propagation of seismic

waves in elastic media. The simulated seismic-wave data used in this study were obtained using this software.

3 Linear polarization wave filtering method

Microtremor signals include not only linearly polarized waves such as body waves and longitudinal waves, but also elliptically polarized Rayleigh surface waves propagating in different directions, and signals from multiple sources may be received in the same time period. Therefore, using the Rayleigh surface wave method to extract geological structure information from microtremor signals requires a feasibility analysis of wave selection according to the characteristics of microtremor signals to ensure that Rayleigh surface waves with high signal-to-noise ratios can be extracted from the microtremor signal. The particle trajectory of Rayleigh surface waves is elliptical and has elliptical polarization characteristics. However, the trajectories of particles such as body waves and longitudinal waves are linearly polarized waves. At the same time, the phase difference between the horizontal and vertical components of Rayleigh wave is $\pi/2$; Both the body wave and the longitudinal wave are waves with linear polarization characteristics, and the horizontal component and the vertical component have the same phase. Based on the above wave characteristics, this summary studies the filtering methods of microtremor signals from two aspects: polarization filtering and phase difference filtering. The two methods were applied to the simulation data and site microtremor data, and the advantages and disadvantages of the filtering methods and their applicability to the microtremor signal were compared and analyzed.

3.1 Polarizability filtering method

Polarization filtering is primarily used to separate linearly polarized waves according to the elliptical polarization characteristics of the particle trajectory of Rayleigh surface waves. The polarizability of the particle trajectory of the Rayleigh surface wave, which is an ellipse, can be determined through the ratio of its short to long half axis or by analyzing the spectral ratio of its horizontal and vertical components with Fourier transform. Then, the wave fields of linearly and elliptically polarized waves were separated based on the determined polarizability. However, when a section of the signal contains both a linear polarization wave and an elliptical polarization wave, the spectrum ratio does not truly reflect the polarization characteristics of the Rayleigh surface wave related to the site because the Fourier transform is the average characteristic of the entire seismic record spectrum. The linearly polarized wave in the signal can be effectively filtered out by separating the wave field at different scales and reconstructing the signal through a wavelet transform. The Hilbert transform converts the real signal into an analytic complex signal, which is then divided into different scales

TABLE 1 Elastic parameters of medium.

Media properties	Longitudinal wave velocity VP(m/s)	Shear wave velocity VS.(m/s)	Density ρ (g/cm ³)
Media 1	300 m/s	150 m/s	1,500 g/cm ³
Media 2	1,000 m/s	530 m/s	2000 g/cm ³

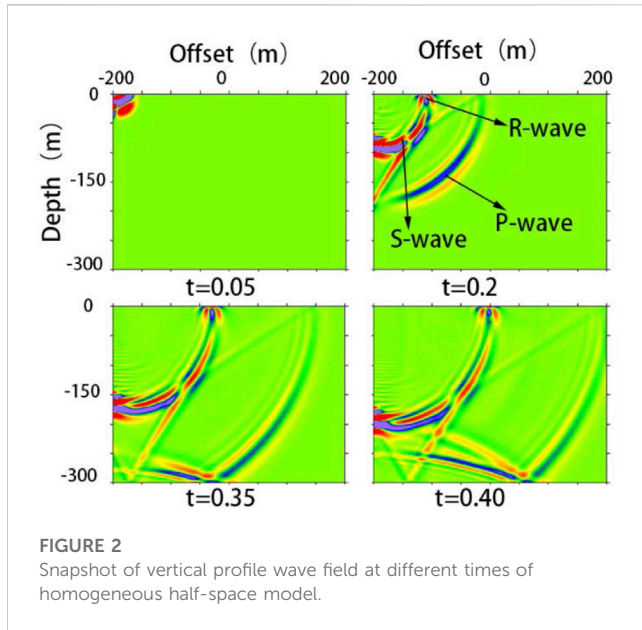


FIGURE 2
Snapshot of vertical profile wave field at different times of homogeneous half-space model.

using wavelet transform. Finally, the Stokes parameters were used to calculate the instantaneous long and short half axes of the signals at different scales. The filter function was set according to the elliptic polarization parameters. The basic principles are as follows:

The Hilbert transform can transform the real signal $x(t)$ in the time domain into an analytic signal and transform a one-dimensional signal into a two-dimensional signal on the complex plane as follows:

$$Z(t) = x(t) + i\hat{x}(t) \quad (1)$$

It can also be written as:

$$Z(t) = A(t)e^{-i\varphi(t)} \quad (2)$$

Where $A(t)$ envelope of the Hilbert transform, and is the instantaneous amplitude of signal $x(t)$,

$$A(t) = \sqrt{x^2(t) + \hat{x}^2(t)} \quad (3)$$

$\varphi(t)$ is called instantaneous response signal, namely, instantaneous phase:

$$\varphi(t) = \arctan\left(\frac{\hat{x}(t)}{x(t)}\right) \quad (4)$$

The instantaneous frequency can be expressed as:

$$f = \frac{1}{2\pi} \frac{\partial \varphi(t)}{\partial t} \quad (5)$$

Three types of instantaneous signal information can be obtained by the Hilbert transform: instantaneous amplitude, instantaneous phase, and instantaneous frequency. Owing to the large overall wave filtering error, it is necessary to perform a wavelet transform on the analytical signal to obtain the instantaneous information of signals with different scales. The instantaneous long and short half-axes of the seismic records can be calculated using the following formula:

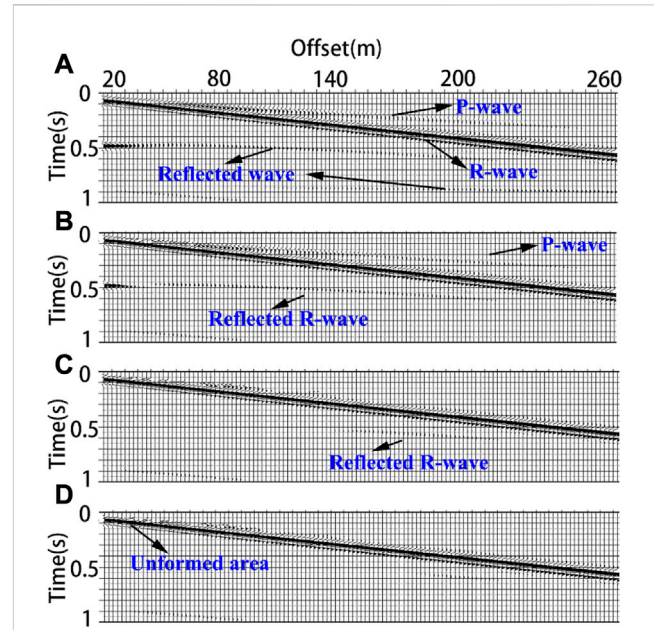


FIGURE 3
Seismic record. (A) Is the original signal simulated by the homogeneous half-space model; (B–D) are seismic records after polarization filtering with parameters of 0.1, 0.3 and 0.4 respectively.

$$a(t) = \sqrt{\frac{S_0(t) + (S_1^2(t) + S_2^2(t))^{1/2}}{2}} \quad (6)$$

$$b(t) = \sqrt{\frac{S_0(t) - (S_1^2(t) + S_2^2(t))^{1/2}}{2}} \quad (7)$$

$a(t)$ and $b(t)$ are the instantaneous long half axis and instantaneous short half axis of the signal, respectively; S_0 , S_1 , S_2 are the three Stokes parameters,

$$S_0(t) = A_z^2(t) + A_h^2(t) \quad (8)$$

$$S_1(t) = A_z^2(t) - A_h^2(t) \quad (9)$$

$$S_2(t) = 2A_z(t)A_h(t)\cos(\theta(t)) \quad (10)$$

$\theta(t)$ is the instantaneous phase difference between the vertical and horizontal components and $A_z(t)$, $A_h(t)$ are the instantaneous amplitudes of the vertical and horizontal components, respectively.

The following paper analyzes the filtering characteristics and effects of polarization filtering through the simulation data of homogeneous half-space and transverse non-homogeneous half-space.

Figure 3A shows 120 channels of original seismic records simulated by the homogeneous medium model with a sampling rate of 0.0005 and a duration of 1 s. It can be seen from the figure that the seismic record contains direct P wave, direct Rayleigh surface waves, Rayleigh surface waves, and S wave reflected from the model side boundary and bottom boundary. The wave field was relatively complex. To compare the effects of polarization filtering, the filtering parameters were set to 0.1, 0.3, and 0.4, and the corresponding seismic records were 3b, c, and d, respectively. When the filtering parameter was set to 0.1, only part of the

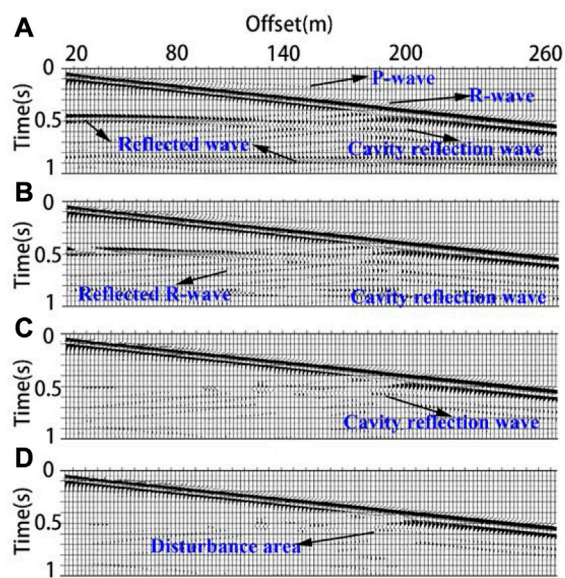


FIGURE 4

Seismic record. (A) is the original signal simulated by the transverse inhomogeneous half-space model; (B–D) are seismic records after polarization filtering with parameters of 0.1, 0.3 and 0.4 respectively.

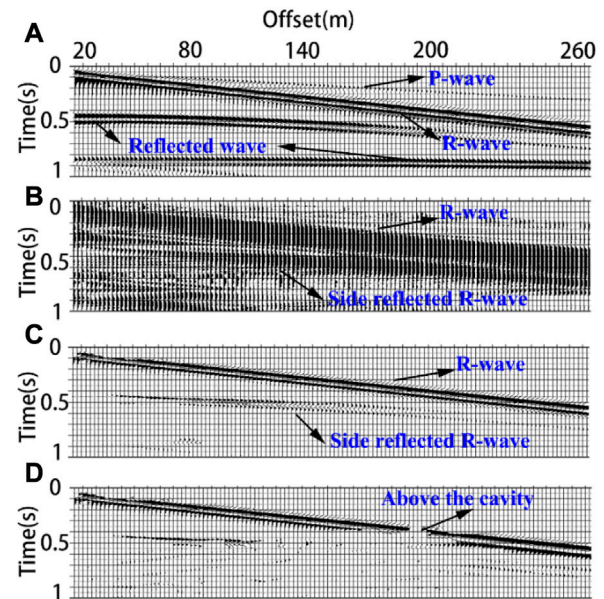


FIGURE 5

Seismic record. (A) is the original seismic record simulated by the homogeneous half-space model; (B) is the corresponding instantaneous phase difference between the horizontal component and the vertical component, (C, D) are the phase difference filtering results of seismic records of homogeneous model and transverse inhomogeneous model respectively.

S-wave reflected from the bottom edge in Figure 3B was filtered, and the rest was basically unchanged; when the parameter was set to 0.3, the reflected wave and the direct P-wave in Figure 3B. Were filtered, but the boundary-reflected Rayleigh wave was also filtered as a linearly polarized wave. When the parameter is set to 0.4, in the near-source section, because the stable Rayleigh wave has not yet formed, excessive filtering will distort the signal, and polarization filtering can filter the linear polarization wave well.

Considering the complexity of the natural geological structure, the seismic records were processed with local inhomogeneity in the model in the same manner, and the results are shown in Figure 4.

Figure 4A shows the original simulated seismic record propagating in the transverse inhomogeneous half-space model. Compared with Figure 3A, seismic record 4a has more reflected waves from the local inhomogeneous media. When the filtering parameter was 0.1, the linear polarization wave could not be filtered (Figure 4B). When the parameter was increased to 0.3, it can be seen in Figure 4C that most of the linear polarization wave and the reflection wave near the local abnormal body were filtered. However, from the comparison of 4a, c, and d, it can be seen that polarization filtering can still eliminate most linear polarization waves for seismic records containing local abnormal bodies. However, because the surface wave generates strong emission when passing through an abnormal body, the signal received by the geophone is no longer a stable surface wave; thus, the Rayleigh surface wave signal near the abnormal body becomes more distorted as the filtering degree increases.

From the above numerical experimental results, it can be found that polarization filtering has a good filtering effect for simple body waves and stable Rayleigh surface wave superposition. However, for

complex signals, it is difficult to filter the linear polarization wave without causing signal distortion, especially for signals that have not formed stable surface waves. At the same time, this method needs to undergo column operations such as wavelet transform and data reconstruction when processing the data. Processing a large amount of microtremor data takes a long time. This method is not suitable for preliminary screening of a large amount of data. After determining the high-quality microtremor signal segment, the polarization filtering method can be used as a fine processing method to filter body wave interference without causing signal distortion.

3.2 Phase difference filtering method

In addition to the polarization characteristics, the phase difference of $\pi/2$ between the horizontal and vertical components of the Rayleigh wave is also a very important feature. Because the amplitude of seismic records is not considered when calculating the phase, the amplitude of seismic records is also not considered in phase difference filtering; as long as it is a Rayleigh surface wave, it can be recognized. Moreover, the two horizontal components in the three-component seismic record have the same phase; therefore, the wave propagation direction cannot be considered when considering the wave. The phase-difference filtering method and its effects are discussed below.

According to the relevant introduction in the previous section, the instantaneous phase, instantaneous amplitude, and instantaneous frequency of each seismic record can be obtained

using the Hilbert transform, and the instantaneous phase difference formula of the horizontal component $x(t)$ and vertical component $z(t)$ can be expressed as (11),

$$\theta(t) = \arctan\left(\frac{x(t)\hat{z}(t) - z(t)\hat{x}(t)}{x(t)\hat{z}(t) + \hat{z}(t)\hat{x}(t)}\right) \quad (11)$$

Where $\hat{x}(t)$, $\hat{z}(t)$ is obtained by Hilbert transformation.

To improve the accuracy of filtering, this study does not directly perform phase difference on seismic records, but does wavelet transform on signals, and then sets the filtering function with phase difference as the filtering condition. The filtering effect was verified using homogeneous and inhomogeneous model data; the results are shown in Figure 5.

Figure 5A shows the original seismic record of the homogeneous model, in which the linear polarization wave includes the P-wave and the body wave reflected from the bottom boundary, and the elliptical polarization wave includes the direct Rayleigh surface wave R and the two groups of Rayleigh surface waves reflected from the side boundary. The original seismic records of the transverse inhomogeneous model are not presented in this figure. To illustrate the characteristics of the phase difference more clearly, Figure 5B. Shows the absolute value of the phase difference between the horizontal and vertical components. It can be seen from the figure that the direct Rayleigh surface wave and Rayleigh surface wave reflected from the sides of the two models can reflect all Rayleigh surface waves in the seismic record. Although the amplitude of the lowest reflected Rayleigh wave in the seismic record is very weak, it is still clear in the figure; however, the linear polarization wave is not shown.

Figure 5C is obtained after phase-difference filtering. Only Rayleigh surface waves can be seen in the figure, and the linearly polarized waves are well filtered. Compared with the effect of polarization filtering (Figure 4C), the Rayleigh surface wave reflected from the side boundary is still retained because the horizontal component must be consistent with the propagation direction of the wave through polarizability conditional filtering. Otherwise, Rayleigh surface waves with different propagation directions are filtered to different degrees while filtering body waves. The phase-difference filter does not have this problem because it does not consider the amplitude strength. For three-component data, the two horizontal components have the same phase; therefore, the wave propagation direction can be ignored for filtering. This method is more suitable for the preliminary filtering of microtremor data. Figure 5D shows the filtering results of the phase-difference method on the seismic records containing local abnormal bodies, which can also effectively filter the linear polarization wave. However, owing to the existence of local abnormal bodies, the Rayleigh surface wave near the abnormal body is seriously disturbed, and after filtering, there is a more serious distortion than in the elliptical polarizability wave method.

3.3 Comparative analysis of case application

The principles of elliptic polarization filtering, phase difference filtering, and the filtering effect of numerical simulation data were studied. Next, the two methods were applied to the microtremor case data, and their filtering effects were compared. The geophone selected for data acquisition in this study was an EPS-3 digital seismometer

produced by the Chongqing Instrument Factory. This instrument is a three-component data collector with a signal acquisition range of 150 Hz. The data were collected in Luxian County, Sichuan Province, China in October 2015. The sampling interval and sampling time interval were 10 m and 0.01 s, respectively. The seismic records are shown in Figure 6. Figure 6A shows the 600 s three-component seismic records of the sampling market. It can be seen from the amplified seismic records (Figures 6B, C) that some of the samples tend to be stable and some contain strong earthquake signals in the 10 s sampling time.

To illustrate the filtering effect of polarization filtering and phase difference filtering methods on the microtremor case data, three groups of special microtremor data were selected for the experiment. Figure 7A Shows the vertical component of the original data for the three groups of data, and the signal length was 10 s. Figures 7B, C correspond to the three groups of vertical component data after polarization filtering and phase-difference filtering, respectively.

The results show that the group A data almost retains the complete signal after being processed by the two filtering methods, which indicates that the Rayleigh surface wave of the signal in group A is dominant. The missing part of the signal after filtering is caused by a combination of high-frequency body waves in the signal and the filtering parameter settings. It is explained here that both methods automatically recognize Rayleigh surface waves and can separate the wave field. A specific application analysis will be provided in the article on microtremor data processing. The signals in Group B are almost completely removed after being processed by the two filtering methods, which indicates that the signals in Group B are body waves. For this type of signal with a high body wave content, both filtering effects were very good. The Group C seismic records contained several wave groups. After filtering, the results of the two methods retained one group, whereas the rest were filtered. The only wave group in Group C was a Rayleigh surface wave.

In conclusion, both polarization filtering and phase-difference filtering can eliminate the body wave in the signal to a certain extent and complete the separation of body waves and Rayleigh surface waves. Polarization filtering is highly dependent on the amplitude and requires a long operating time. In the case of an unknown direction, Rayleigh surface waves propagating from some directions may be mistaken for body wave filtering, but the wave field separation effect is better than that of phase difference filtering. The phase difference filtering method does not consider the amplitude strength, and because the two horizontal components have the same phase, it can filter without knowing the propagation direction of the wave. However, the low-amplitude Rayleigh wave signal will cause great interference, and the disturbance caused by the local abnormal body is more likely to cause distortion. Therefore, the phase-difference filtering method is more suitable for the preliminary Rayleigh surface-wave filtering of microtremor data, and the polarization filtering method is more suitable for the final fine filtering of body waves. Based on the research objectives of this study, these two methods can be applied to different stages of data processing.

4 Direction recognition of Rayleigh wave

The propagation direction of Rayleigh surface waves plays an important role in extracting geological structural images using non-

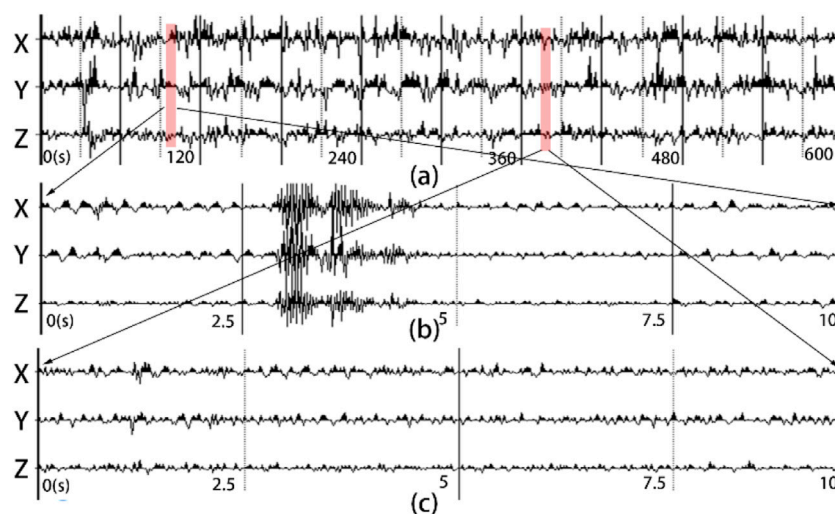


FIGURE 6
A group of three-component seismic records.

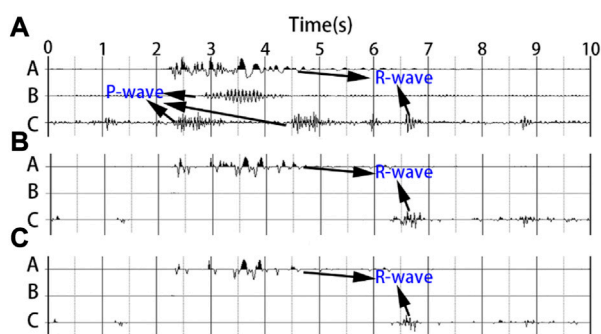


FIGURE 7
Seismic records, A, B and C are vertical component seismic records including Rayleigh surface wave, body wave and Rayleigh surface wave respectively. (A) Is the original record; (B, C) are the results of (A) polarization filtering and phase difference filtering, respectively.

stationary microtremor signals. For example, in the Rayleigh surface-wave elliptic polarizability method, the imaging of abnormal bodies in the profile shifts along the propagation direction. Therefore, this section studies the time-frequency analysis method of microtremor signals and extracts the principal components of Rayleigh surface waves through a time-frequency analysis method. The directional filtering method of Rayleigh surface waves is studied through time-frequency analysis and the anti-clockwise rotation characteristics of surface wave particle motion.

4.1 Application of time-frequency analysis

The microtremor signal is composed of harmonics of various frequencies, amplitudes, and initial phases that propagate in

different directions. The harmonics with the strongest energy had the greatest impact on the characteristics of the entire signal. In this study, the instantaneous frequency and instantaneous phase at the moment of strongest energy are called the dominant frequency and dominant phase, respectively. The specific processing flow for extracting the principal component information of the signal through time-frequency analysis is as follows: First, the signal is analyzed in the time-frequency domain to determine the time t_0 and frequency point f_0 with the strongest energy, and then bandpass filtering is performed on the signal centered on f_0 . The principal component of the microtremor signal can be used to identify both the wave type and wave propagation direction. Different signals are used to study the practicability of the time-frequency analysis and principal component extraction method. First, the simulated body-wave seismic records were analyzed, and the results are shown in Figure 8.

Figure 8A shows the body wave propagating in a homogeneous medium, and its time-frequency distribution is shown in Figure 8B. The energy distribution in a homogeneous medium is relatively smooth and concentrated, with 14.16 Hz as the dominant frequency, and the maximum energy point located at (0.3655 s, 14.16 Hz), as the signal is not affected by other waves. It can also be clearly seen from the superposition diagram of the horizontal and vertical components of the filtered seismic records that the phases of the two components were almost the same (Figure 8C). The instantaneous phase difference at 0.3655 s was 0.0614° or 3.52°. The phase difference is very small and can be regarded as in-phase. This is consistent with the fact that the horizontal and vertical components of the linearly polarized wave are in phase.

Figure 9A shows the simulated Rayleigh surface wave seismic record of the homogeneous medium, and Figure 9B shows the time-frequency energy distribution diagram of the Z component. The maximum energy points is (0.425 s, 20.99 Hz). There was an obvious phase difference in the filtered seismic record stack diagram (Figure 9C). The instantaneous phase difference between the horizontal and vertical components at 0.425 s was 1.5709° or

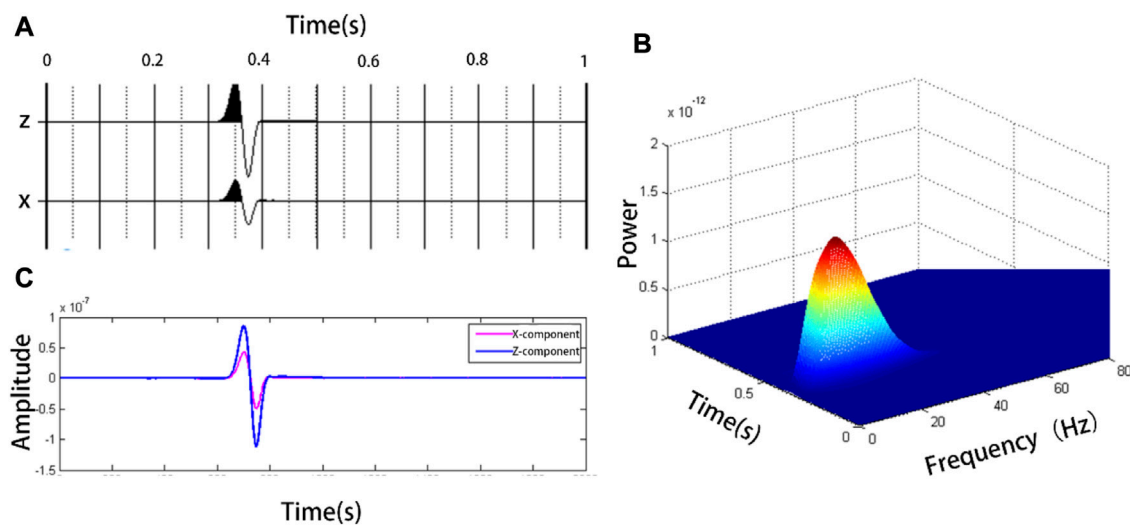


FIGURE 8

(A) shows the horizontal and vertical component seismic records of the simulated body wave, (B) is the time-frequency distribution diagram of the vertical component in (A), (C) is the comparison of seismic records after bandpass filtering.

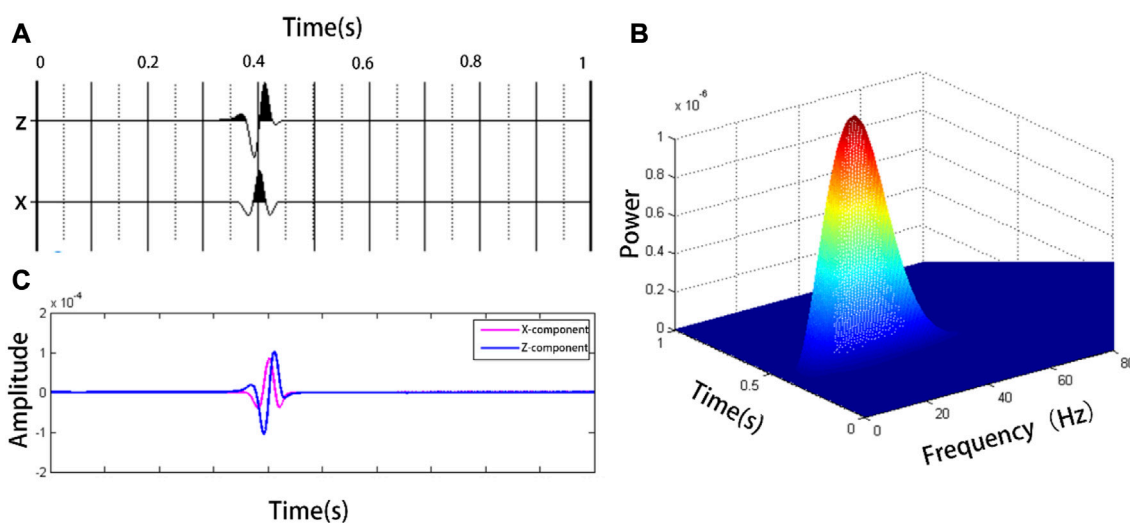


FIGURE 9

(A) Is the horizontal and vertical component seismic records of simulated Rayleigh wave, and (B) is the time-frequency distribution diagram of the vertical component in (A); (C) is the comparison of seismic records after bandpass filtering.

90.01°. This is consistent with the expected phase difference of 90° between the horizontal and vertical components of the Rayleigh surface wave. In the numerical simulation signal, without interference from other waves, many methods can easily distinguish its signal characteristics; however, the components of the microtremor signal are more complex, and the extraction of the principal components is more complex. At this time, the time-frequency analysis method has more prominent advantages. The practicability of this method was verified using two groups of microtremor signals dominated by Rayleigh surface waves and body waves.

Figure 10A shows a group of three-component original microtremor seismic records dominated by body waves with a duration of 10s. From the time-frequency energy distribution diagram (Figure 10B) of the vertical component seismic record Z, it can be seen that the energy of the microtremor signal in this section is approximately 20 Hz, and there is a series of wave groups with strong energy in approximately 5 s. The maximum point of its energy is (4.96 s, 24 Hz). The three-component seismic record was band-pass filtered at 24 Hz and the filtering range was determined according to the energy distribution. The seismic record stacking diagrams of the filtered vertical and horizontal components are

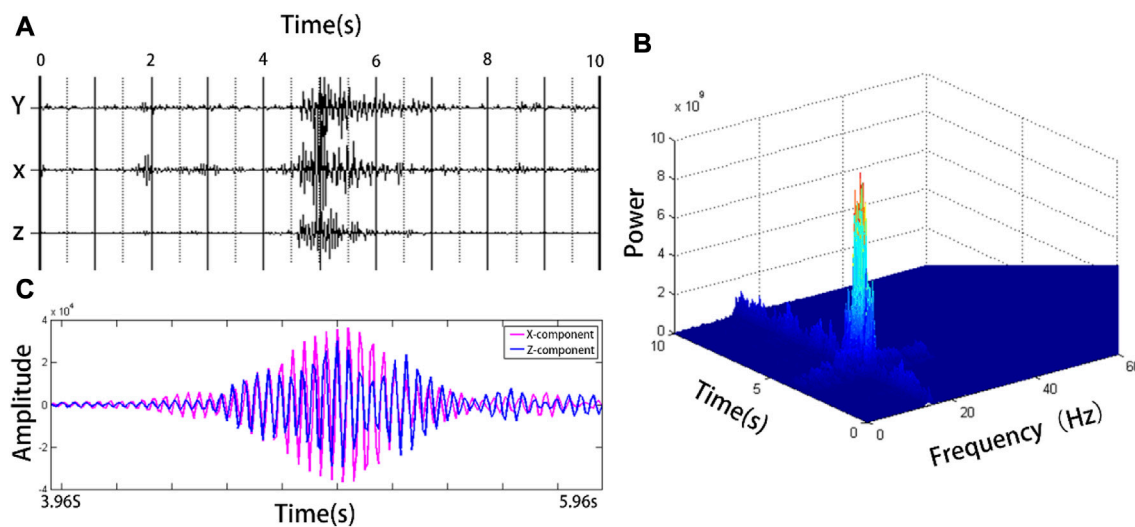


FIGURE 10
(A) shows the horizontal and vertical component seismic records of the body wave dominant microtremor signal, and (B) shows the time-frequency distribution of the vertical component in (A); (C) is the comparison of seismic records after bandpass filtering.

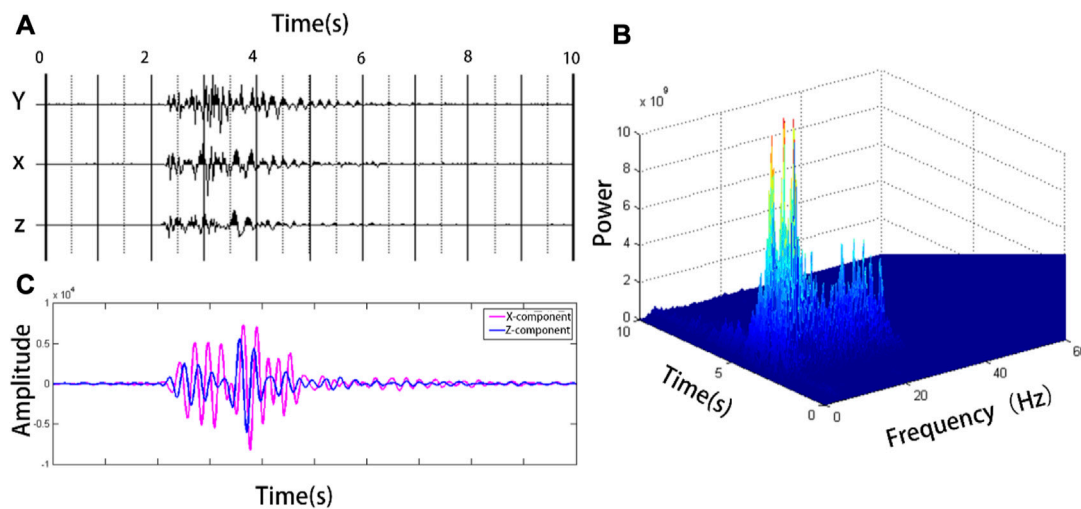


FIGURE 11
(A) shows the horizontal and vertical component seismic records of the Rayleigh wave dominant microtremor signal, and (B) shows the time-frequency distribution of the vertical component in (A); (C) is the comparison of seismic records after bandpass filtering.

shown in Figure 10C. Since the dominant frequency of the signal in this section is high, in order to clearly display the signal characteristics, only the records between 3.96 s and 5.96 s are selected in Figure 10C. The figure illustrates that the phases of the vertical and horizontal components are largely in phase. At the same time, the instantaneous phase difference at 4.96 s is 0.2085 (11.9°), which is very small and can be considered to be the same phase wave.

Figure 11A shows a group of three-component original microtremor seismic records dominated by Rayleigh surface waves with duration of 10 s. From the time-frequency energy

distribution of the vertical component seismic record Z, it can be seen that there is a series of wave groups with strong energy between 2 s and 5 s. From the perspective of frequency, the microtremor signals in this section have strong energy from 2 Hz to 30 Hz. The maximum energy point is (2.47 s, 3.71 Hz), and the three-component seismic record was band-pass filtered with a 3.71 Hz as the center. The filtered vertical and horizontal component seismic record stack diagram is shown in Figure 9C., which shows that the vertical and horizontal component phases are obviously out of sync. After calculation, the instantaneous phase difference at 2.47 s was 1.8629 (106.7°). Near $\pi/2$, although $\pi/2$ is not as accurate as the

analog signal, it can still be considered to have the characteristics of a Rayleigh surface wave.

The nonstationary characteristics of the microtremor signal change its frequency distribution over time. The time-frequency domain can clearly reflect the energy distribution of each time and frequency point of the microtremor record, which is more suitable for the analysis of non-stationary microtremor seismic records. In this study, the time-frequency analysis method was used to study the active source seismic records and site microtremor records. The findings indicate that the utilization of time-frequency analysis does not significantly enhance the analysis of active source seismic records, which possess low levels of interference. However, for microtremor signals that consist of complex components, the main components can be effectively isolated through the application of time-frequency analysis. The principal components of the microtremor signal are extracted using a time-frequency analysis method, which effectively improves the accuracy of the characteristic analysis of the microtremor Rayleigh wave. It plays an important role in the identification and direction determination of polarization characteristics.

4.2 Analysis of Rayleigh wave propagation direction

Determining the direction of wave propagation is a crucial aspect of seismic exploration. The identification of the propagation direction through single-channel three-component Rayleigh surface wave data is based on the fact that the Rayleigh surface wave travels in a counterclockwise elliptical motion along the wave's propagation direction. Methods for discrimination will be discussed below.

The Rayleigh surface wave had the strongest energy among all the received waves in the dominant microtremor signals. The vertical component of the Rayleigh surface wave had the strongest energy when the source was vertically loaded in the homogeneous half-space model. Therefore, in this study, we determined the moment with the strongest energy at all sampling points through the Z component, and then took the X, Y and X component values x , y corresponding to the corresponding time, respectively, took the positive direction of X as the starting direction, and used cosine $\cos(a)$ to calculate the included angle between the propagation direction and the X axis.

When $y > 0$,

$$a = \arccos\left(\frac{x}{\sqrt{x^2 + y^2}}\right) \quad (12)$$

When, $y < 0$ according to the properties of inverse trigonometric function,

$$a = 2\pi - \arccos\left(\frac{x}{\sqrt{x^2 + y^2}}\right) \quad (13)$$

Angle a is the included angle between the propagation direction and positive direction of the X-axis. a may differ from the actual propagation direction of Rayleigh surface waves. As long as the Rayleigh surface wave travels along a straight line, we can synthesize two horizontal components into a radial horizontal component $d(t)$,

thus transforming the three-component data into two-component data. When the Z-axis is downward, the Rayleigh surface wave rotates counterclockwise along the propagation direction. The horizontal and vertical components are constructed as complex numbers:

$$T(t) = d(t) + iz(t) \quad (14)$$

The direction of signal propagation can be determined based on the difference between the spoke value of the imaginary part and the difference between the spoke value of the complex number at time t_0 and t_0+h . If this difference is greater than zero, the signal propagates in one direction, and if it is less than zero, it propagates in the opposite direction. The value of h , which represents the time difference, is determined based on the dominant frequency of the wave.

To verify the reliability of the method, numerical simulation, experimental verification, and case data verification were designed. A plane diagram of the homogeneous half-space medium model designed in this study is shown in Figure 12. Figure 12A shows the arrangement of geophones and their sources. The wave field in this experiment was excited by point sources with a total of 11 rows, 21 columns, and 231 geophones arranged. The geophone is 15 m from the source, and a stable Rayleigh surface wave can be formed at the minimum offset. Although there is still a small amount of p-waves, they do not affect the determination of the Rayleigh surface wave propagation direction. Figure 12B shows the direction arrow drawn according to the propagation direction of the Rayleigh surface wave calculated from 231 sets of single-channel, three-component seismic records. Compared with Figures 12A, B, the distribution of the propagation direction is consistent with the case of Rayleigh surface waves spreading from the point source to the outside. This method can determine the propagation direction of Rayleigh waves when there is almost no other wave interference.

For microtremor signal data, a Rayleigh surface wave with a strong signal was selected for the experiment. Field data acquisition was based on 11 groups. Eleven groups of three-component seismic records were collected for each group. In this study, nine channels with three-component seismic records were selected. Each data channel intercepts a segment of the signal with a sampling time of 10 s, including a group of Rayleigh surface waves. These nine groups of data contain Rayleigh surface wave signals from the same seismic source, with the same propagation direction.

Figure 13A shows the vertical component seismic record and Figure 13C shows the time-frequency energy distribution of one of the data. The time-frequency distribution of the microtremor seismic record is relatively scattered, and the direct determination of the propagation direction of the wave is interfered with by other waves. According to the energy distribution, the maximum energy point in the time and frequency domains is (2.46 s, 3.7 Hz), and the bandpass filter is carried out with 3.7 Hz as the center to suppress the interference of other waves as much as possible. Figure 11B shows the results of the band-pass filtering in Figure 11A. Finally, the propagation direction of each data point was determined by the propagation direction determination procedure of the wave, and the results are shown in Figure 11D. Taking the positive direction of the

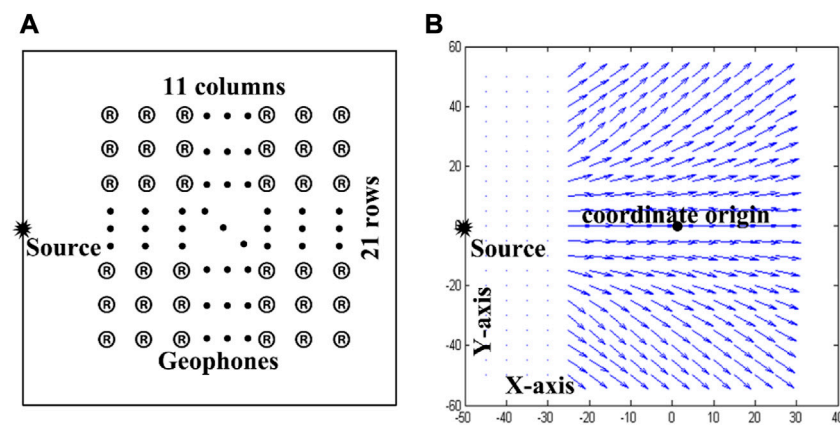


FIGURE 12

(A) shows the geophone and source distribution of the numerical model, and (B) shows the distribution diagram of the Rayleigh wave propagation direction in seismic records.

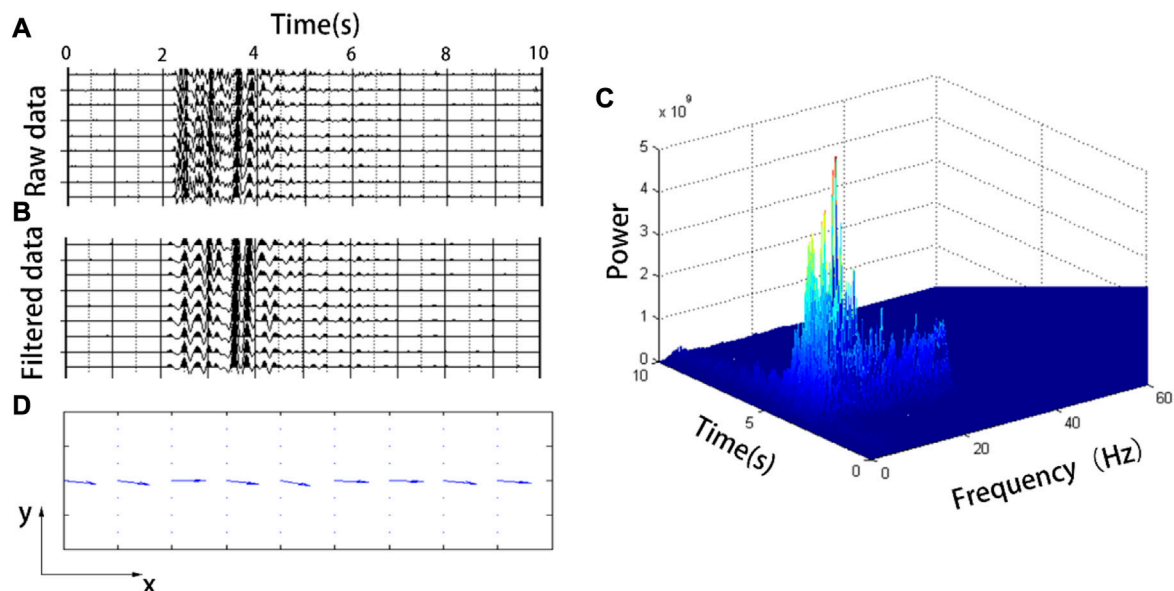


FIGURE 13

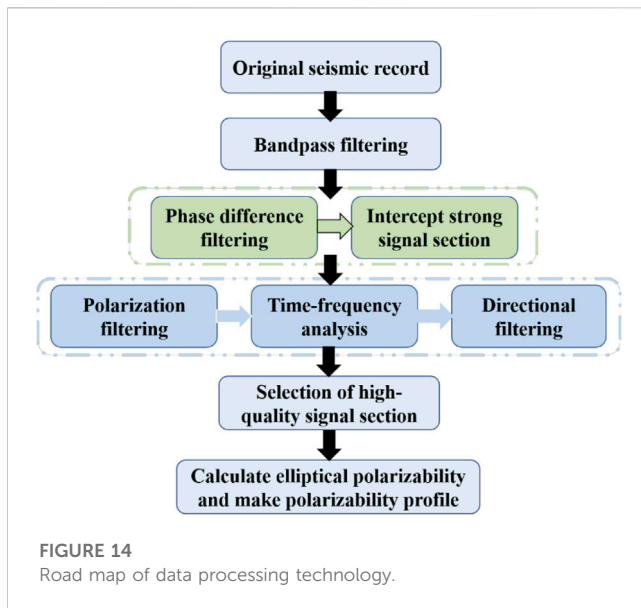
(A) shows a three-component microtremor vertical component seismic record dominated by a Rayleigh surface wave. (B) Seismic record after the main frequency filtering of (A); (C) time-frequency distribution diagram of the vertical component in (A, D) directional distribution of the Rayleigh wave.

x -axis as a reference, the specific angles are 341, 337, 356, 339, 331, 348, 351, 342, and 345. From these results, it can be inferred that the propagation direction of this group of signals is an angle of approximately 20° along the positive direction of the x - and y -axes. Theoretically, the propagation direction of the nine groups of data should be completely consistent. Due to interference from other waves in the signal and inaccuracies in the placement of the three-component detector during data collection, the result deviated somewhat from the theoretical value. In summary, by combining the time-frequency analysis and anti-clockwise rotation characteristics of Rayleigh surface

waves, the propagation direction of microtremor Rayleigh surface waves can be effectively identified.

5 Experimental analysis

The purpose of this study was to extract a high signal-to-noise ratio co-propagating Rayleigh surface wave from the microtremor signal. Based on the research results of the filtering methods analyzed above, a set of high signal-to-noise ratio co-directional Rayleigh surface wave extraction processes for microtremor signals



is summarized, and the application effect of this method in seismic wave imaging is verified by taking the elliptical polarizability geological structure imaging method as an example.

The data processing technology roadmap is shown in Figure 14: Detailed data processing steps are as follows.

- (1) Band-pass filtering: Band-pass filtering is performed on the original seismic records, DC interference is filtered out, and the appropriate frequency band range is selected according to the exploration depth.
- (2) Phase difference filtering: Phase difference filtering was performed on all seismic records to remove the strong linear polarization wave signal in the microtremor signal to facilitate the selection of the surface wave dominant signal section.
- (3) Intercept the signal segment: According to the phase-difference filtering results, the dominant signal segment of the strong surface wave was initially intercepted from the band-pass filtered signal, and several high-quality signal segments were intercepted from each group of three-component seismic records.
- (4) Polarization filtering: Polarization filtering is performed on the preliminarily intercepted surface wave dominant signal to filter the linear polarization interference wave in the signal.
- (5) Time-frequency analysis: time-frequency analysis is performed on the filtered signal segment to determine the main components of the signal.
- (6) Direction filtering: Identify the propagation direction of Rayleigh surface waves for all processed signal segments according to the results of the signal principal components.
- (7) High-quality signal selection: The best signal segment of the Rayleigh surface wave with a high signal-to-noise ratio propagating in the same direction is selected from the signal segments of all seismic channels.
- (8) Seismic wave imaging: Calculate the elliptical polarizability of different frequencies of each signal segment and obtain the polarizability profile.

The elliptical polarizability method was used to study the crustal structure using the dynamic characteristics of the elliptical polarization of Rayleigh surface wave particles. The research shows that the elliptical polarizability of particle motion in layered media changes with frequency and can interpret the geological structure in the same way as the velocity dispersion method. However, when the signal is in a non-stationary state, the superposition of linear polarization waves and Rayleigh surface waves in different directions will have an impact on the imaging results and cannot accurately identify the geological structural features. Using the above method of extracting the microtremor Rayleigh surface wave, a co-propagating Rayleigh surface wave with a high signal-to-noise ratio can be extracted from the microtremor signal, which meets the application conditions of the elliptical polarizability method. Therefore, this study uses the elliptical polarizability method and numerical simulation to verify the viability of extracting co-propagating Rayleigh surface waves with high signal-to-noise ratios.

In this study, two plane wave sources with opposite directions are set on the homogeneous half-space model, and then white noise with a noise level of 20% is added to the three-component records by a numerical method. The excitation source simultaneously generates a longitudinal wave and a model boundary reflection body wave to simulate a simple three-component microtremor signal. Figure 15A shows the 40-channel homogeneous model vertical component seismic records, with a sampling frequency of 0.0005, sampling duration of 2 s, sampling interval of 2 m, and dominant frequency of 20 Hz. Seismic records include longitudinal waves, model boundary reflector waves, Rayleigh surface waves in different propagation directions, and noise. The simulated signals should be used as far as possible to restore the characteristics of the micromotion signals.

Figure 15B shows the elliptical polarizability profile, where the exploration depth is converted from a half-wavelength. The polarizability profile was calculated directly from the 40-channel unprocessed simulated three-component seismic records of micromotion. From the figure, we can clearly see many abnormal areas with high and low elliptical polarizabilities. The data were derived from a uniform half-space model. According to the calculation of the model parameters, the theoretical elliptical polarizability value of each frequency is 0.654 when the Rayleigh surface wave propagates in a homogeneous medium. Due to various interference factors present in the signal, the polarizability profile does not accurately reflect the characteristics of the homogeneous model. This shows that the geological structure information cannot be accurately extracted from the unprocessed non-stationary micromotion signals using the Rayleigh surface wave elliptical polarizability method.

For an experimental comparison, we applied the high signal-to-noise ratio co-directional microtremor Rayleigh surface wave extraction method summarized above to the simulation data. The detailed data processing process and parameters are as follows.

- (1) Band-pass filtering: 20 Hz as the frequency center
- (2) Phase difference filtering: Phase difference filtering was performed on all simulated micromotion seismic records, and then the region of the strong amplitude Rayleigh surface wave in each seismic record was determined.

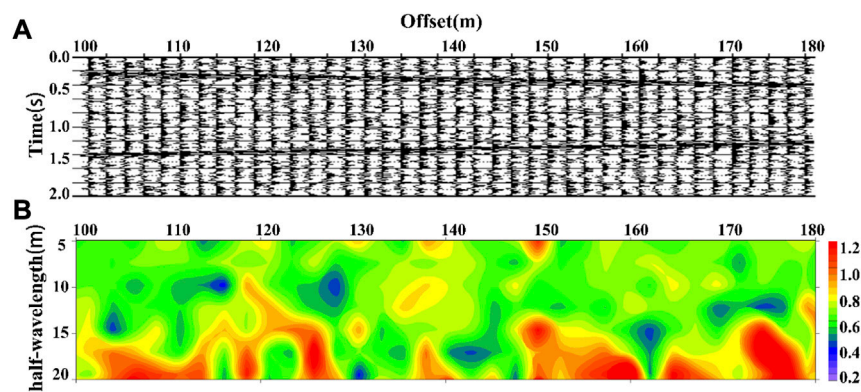


FIGURE 15

(A) Vertical component of the original synthetic seismic record, and (B) vertical slice of the estimated ellipticity at an apparent depth of 0.5λ .

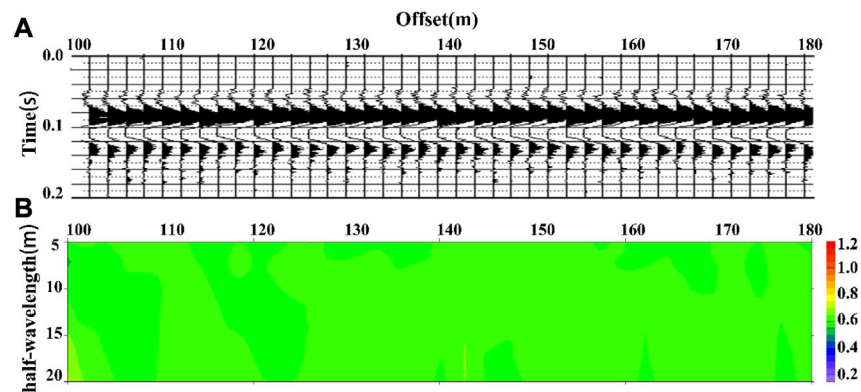


FIGURE 16

(A) is the processed synthetic vertical component seismic record and (B) is the vertical slice of the estimated ellipticity at an apparent depth of 0.5λ .

- (3) Intercept signal segments: and initially intercept all strong surface wave dominant signal segments with a duration of 0.2 s from the band-pass filtered signal;
- (4) Polarization filtering: the filtering parameter of polarization filtering for all intercepted surface wave dominant signals is set to 0.3 to filter the linear polarization interference wave in the signal.
- (5) Time-frequency analysis: time-frequency analysis is performed on the filtered signal segment to determine the main components of the signal.
- (6) Direction filtering: The propagation direction of the Rayleigh surface wave in the signal segment is identified according to the principal component.
- (7) High-quality signal selection: Select the best signal segment of the Rayleigh surface wave with high SNR in the same direction from each signal segment and select 40 groups of Rayleigh surface wave signals with 0.2 s in the same direction.
- (8) Seismic wave imaging: Calculate the elliptical polarizability of different frequencies of each signal segment and obtain the polarizability profile.

The processing results are shown in Figure 16:

The processed seismic record is shown in Figure 16A., which is the vertical component seismic record of the same direction propagation Rayleigh wave with a sampling time of 0.2 s; it can be seen from the seismic records that after a series of processing, the signal only contains a set of Rayleigh surface waves, and the strong linear polarization wave and white noise are filtered, resulting in a relatively clear surface wave waveform. Figure 16B shows the elliptical polarizability profile. It can be clearly seen from the profile that the polarizability is approximately the theoretical value of 0.654, which clearly reflects the uniform characteristics of the model.

The comparative test results in Figures 15B, 16B Show that the combination of elliptical polarizability waves, phase difference filtering, time-frequency analysis, and directional filtering can extract a high signal-to-noise ratio co-directional Rayleigh surface wave from the complex components of the micromotion signal, effectively improving the imaging accuracy of the micro-motion Rayleigh surface wave elliptical polarizability method. In the future, our goal

is to extend the use of this method to real-world data and integrate it with other seismic wave imaging techniques, thereby expanding the utilization of micromotion signals in seismic wave exploration.

6 Conclusion

In this study, the study focuses on extracting a high signal-to-noise ratio Rayleigh surface wave from microtremor signals through numerical simulation data and site data, with the aim of improving the imaging accuracy of the microtremor Rayleigh surface wave exploration method. The conclusions of this study are as follows:

First, polarization filtering and phase-difference filtering methods were studied, and the two filtering methods were applied to the simulation data and site data. Both filtering methods were found to effectively eliminate the linear polarization wave in the signal, but the polarization filtering is highly dependent on the amplitude, the operation time is long, and the filtering effect is better than that of phase difference filtering. The phase-difference filtering method does not consider the amplitude strength and can filter without knowing the propagation direction of the wave, but the low-amplitude Rayleigh wave signal will cause significant interference, and the disturbance caused by the local abnormal body is more likely to cause distortion. The two filtering methods can be applied at different stages of microtremor Rayleigh wave extraction, considering their advantages and disadvantages.

Second, the Rayleigh wave propagation direction was identified. The non-stationary microtremor signals were studied using a time-frequency analysis method, and the principal component information was extracted from the signal segments. The simulation data and field data experimental results show that this method can effectively improve the accuracy of data analysis and accurately extract the principal component information of the data. At the same time, combined with the principal component information of the signal and the anti-clockwise rotation characteristics of Rayleigh surface wave, the method for identifying the propagation direction of Rayleigh surface waves was studied. The results show that the method can effectively identify the propagation direction of Rayleigh surface waves from single-point three-component seismic records, both simulated and site data.

Finally, the data extraction process of high-SNR co-directional Rayleigh surface waves from microtremor signals is summarized and

applied. Based on the filtering method results, a summary of the extraction process for high-SNR co-directional Rayleigh surface waves from microtremor signals is provided. By comparing the imaging results before and after data processing, it was found that using this method to extract Rayleigh surface waves can effectively improve the accuracy of the polarizability profile. Furthermore, the research results can broaden the application scope of the Rayleigh surface wave exploration method and provide a reference for future research on microtremor seismic wave exploration. It has broad application prospects in large-scale crustal research and small-scale engineering geophysical exploration.

Data availability statement

The raw data supporting the conclusion of this article will be made available by the authors, without undue reservation.

Author contributions

Conceptualization, QD; data curation, YP; formal analysis, QD; investigation, QD; methodology, QD; project administration, QD; software, YP; supervision, YX; validation, YP; visualization, QD; and YP writing—original draft, QD and YP. All authors have read and agreed to the published version of the manuscript.

Conflict of interest

The authors declare that the research was conducted in the absence of any commercial or financial relationships that could be construed as a potential conflict of interest.

Publisher's note

All claims expressed in this article are solely those of the authors and do not necessarily represent those of their affiliated organizations, or those of the publisher, the editors and the reviewers. Any product that may be evaluated in this article, or claim that may be made by its manufacturer, is not guaranteed or endorsed by the publisher.

References

- Konno K, Ohmachi T. Ground-motion characteristics estimated from spectral ratio between horizontal and vertical components of microtremor[J]. *Bull Soc Am* (1998) 88(1):228–41.
- Tokimatsu K, Arai H, Asaka Y. Deep shear-wave structure and earthquake ground motion characteristics in Sumiyoshi area, Kobe city, based on microtremor measurements[J]. *J Struct Constr Engng AIJ* (1997) 491:37–45. (in Japanese).
- Nakamura Y. On the H/V spectrum[C]. In: The 14th world conference on earthquake engineering; October, 2008; Beijing, china (2008).
- Arai H, Tokimatsu K. Effects of Rayleigh and Love waves on microtremors H/V spectra[C]. In: Proc. 12th World Conf. on Earthquake Engineering (2000). p. 2232. CD-ROM.
- Thomson WT. Transmission of elastic waves through a stratified solid medium. *J Appl Phys* (1950) 21:89–93. doi:10.1063/1.1699629
- Omori F. On micro-tremors[J]. *Bull Imperial Earthquake Invest Committee* (1908) 2(1):1–6.
- Sakaji K. *Temporal variation of the power spectra of microtremors observed at soil and rock site*[C]. Graduation thesis. Sapporo, Japan: Hokkaido University (1998). (in Japanese).
- Aki K. Space and time spectra of stationary stochastic waves, with special reference to microtremors[J]. *Bull Earthq Res Inst* (1957) 35:415–56.
- Aki K. A note on the use of microseisms in determining the shallow structures of the earth's crust. *Geophysics* (1965) 30(4):665–6. doi:10.1190/1.1439640
- Capon J. High-resolution frequency-wavenumber spectrum analysis. *Proc IEEE* (1969) 57(8):1408–18. doi:10.1109/proc.1969.7278
- Claerbout JF. Synthesis of a layered medium from its acoustic transmission response[J]. *Geophysics* (1968) 33(2):264–9. doi:10.1190/1.1439927

12. Boore DM, Toksöz MN. Rayleigh wave particle motion and crustal structure[J]. *Bull Seismol Soc Am* (1969) 59(1):331–46.
13. Nakamura Y. A method for dynamic characteristics estimation of subsurface using microtremors on the ground surface[J]. *Q.Rept RTRI Jpn* (1989) 30:25–33.
14. Toksöz MN. Microseisms and an attempted application to exploration[J]. *Geophysics* (1964) 29(2):154–77. doi:10.1190/1.1439344
15. Okada H, Suto K. *The microtremor survey method*[M]. Houston, Texas, USA: Society of Exploration Geophysicists (2003). p. 1–53.
16. Du Q, Liu Z, Liu S. Analysis of influencing factors and numerical simulation of horizontal-to-vertical spectral ratio method[J]. *J Earthquake Tsunami* (2019) 14(1):2050004.
17. Du Q, Liu Z, Liu S, Zhang L, Yu W. A study of the lateral heterogeneity with the ellipticity of Rayleigh waves derived from microtremors. *Geophys J Int* (2021) 225(3): 2020–34. doi:10.1093/gji/ggab075
18. Shi Y, Zhang W, Wang Y. Seismic elastic RTM with vector-wavefield decomposition. *J Geophys Eng* (2019) 16(3):509–24. doi:10.1093/jge/gxz023
19. Wang WH, Zhang W, Shi Y, Ke X. Elastic reverse time migration based on wavefield separation[J]. *Chin J. Geophys.* (2017) 60(7):2813–24. (in Chinese).
20. Wei Y, Li YE, Yang J, Zong J, Fang J, Fu H. Multi-task learning based P/S wave separation and reverse time migration for VSP[J]. *SEG Tech Program Expanded Abstr* (2020) 2020:1671–5.
21. Devaney A, Oristaglio M. A plane-wave decomposition for elastic wave fields applied to the separation of *P*-waves and *S*-waves in vector seismic data. *Geophysics* (1986) 51(2):419–23. doi:10.1190/1.1442102
22. Stoffa PL, Buhl P, Diebold JB, Wenzel F. Direct mapping of seismic data to the domain of intercept time and ray parameter—a plane-wave decomposition. *Geophysics* (1981) 46(3):255–67. doi:10.1190/1.1441197
23. Beylkin G. Discrete radon transform[J]. *Acoust IEEE Trans Speech Signal Process* (1987) 35(2):162–02.
24. Shimshoni M, Smith SW. Seismic signal enhancement with three-component detectors. *Geophysics* (1964) 29(5):664–71. doi:10.1190/1.1439402
25. Gan S, Wang S, Chen Y, Chen X, Xiang K. Separation of simultaneous sources using a structural-oriented median filter in the flattened dimension. *Comput Geosciences* (2016) 86:46–54. doi:10.1016/j.cageo.2015.10.001
26. Chen Y. Deblending using a space-varying median filter[J]. *Exploration Geophys* (2015) 46(4):5183.
27. Chen Y, Fomel S. Random noise attenuation using local signal-and-noise orthogonalization. *Geophysics* (2015) 80(6):1–9. doi:10.1190/geo2014-0227.1
28. Zu S, Cao J, Qu S, Chen Y. Iterative deblending for simultaneous source data using the deep neural network. *Geophysics* (2020) 85(2):V131–41. doi:10.1190/geo2019-0319.1
29. Dellinger J, Etgen J. Wave-field separation in two-dimensional anisotropic media. *Geophysics* (1990) 55(7):914–9. doi:10.1190/1.1442906
30. Sun R, McMechan GA, Hsiao HH, Chow J. Separating *P*- and *S*-waves in prestack 3D elastic seismograms using divergence and curl. *Geophysics* (2004) 69(1):286–97. doi:10.1190/1.1649396
31. Hu TY, Hong F, Wang RQ, Li G, Wen S. Multiple attenuation using beamforming onshore and offshore China. *The Leading Edge* (2002) 21(9):906–10. doi:10.1190/1.1508949
32. Hong F, Hu T, Wang R. Target multiple attenuation using 3D beamforming[C]. In: The 73th SEG Annual Meeting, Expanded Abstracts (2003). p. 1969–72.
33. Trad D, Ulrych T, Sacchi M. Accurate interpolation with high-resolution time-variant Radon transforms. *Geophysics* (2002) 67:644–56. doi:10.1190/1.1468626
34. Ville J. Théorie et. Application de la notion de signal analytique[J]. *Câbles et Transmissions 2eA* (1948) 1948:61–74.
35. René RM, Fitter JL, Forsyth PM, Kim KY, Murray DJ, Walters JK, et al. Multicomponent seismic studies using complex trace analysis. *Geophysics* (1986) 51: 1235–51. doi:10.1190/1.1442177
36. Chen L, Lian H, Xu Y, Li S, Liu Z, Atroshchenko E, et al. Generalized isogeometric boundary element method for uncertainty analysis of time-harmonic wave propagation in infinite domains. *Appl Math Model* (2023) 114:360–78. doi:10.1016/j.apm.2022.09.030
37. Chen L, Cheng R, Li S, Lian H, Zheng C, BORDAS SPA. A sample-efficient deep learning method for multivariate uncertainty qualification of acoustic-vibration interaction problems. *Comput Methods Appl Mech Eng* (2022) 393:114784. doi:10.1016/j.cma.2022.114784
38. Chen L, Lian H, Natarajan S, Zhao W, Chen X, BORDAS SPA. Multi-frequency acoustic topology optimization of sound-absorption materials with isogeometric boundary element methods accelerated by frequency-decoupling and model order reduction techniques. *Comput Methods Appl Mech Eng* (2022) 395:114997. doi:10.1016/j.cma.2022.114997
39. Chen L, Lian H, Liu Z, Chen H, Atroshchenko E, BORDAS S. Structural shape optimization of three dimensional acoustic problems with isogeometric boundary element methods. *Comput Methods Appl Mech Eng* (2019) 355:926–51. doi:10.1016/j.cma.2019.06.012
40. Chen L, Lu C, Lian H, Liu Z, Zhao W, Li S, et al. Acoustic topology optimization of sound absorbing materials directly from subdivision surfaces with isogeometric boundary element methods. *Comput Methods Appl Mech Eng* (2020) 362:112806. doi:10.1016/j.cma.2019.112806
41. Chen L, Liu C, Zhao W, Liu L. An isogeometric approach of two dimensional acoustic design sensitivity analysis and topology optimization analysis for absorbing material distribution. *Comput Methods Appl Mech Eng* (2018) 336:507–32. doi:10.1016/j.cma.2018.03.025



OPEN ACCESS

EDITED BY

Leilei Chen,
Huanghuai University, China

REVIEWED BY

Xin Zhang,
Southwest Jiaotong University, China
Fang-Yuan Shi,
Ningxia University, China

*CORRESPONDENCE

Zili Zhang,
✉ zhangzl@swu.edu.cn

SPECIALTY SECTION

This article was submitted to Statistical and Computational Physics, a section of the journal Frontiers in Physics

RECEIVED 09 January 2023

ACCEPTED 23 January 2023

PUBLISHED 23 February 2023

CITATION

Wu Y and Zhang Z (2023), Refining large knowledge bases using co-occurring information in associated KBs. *Front. Phys.* 11:1140733. doi: 10.3389/fphy.2023.1140733

COPYRIGHT

© 2023 Wu and Zhang. This is an open-access article distributed under the terms of the [Creative Commons Attribution License \(CC BY\)](#). The use, distribution or reproduction in other forums is permitted, provided the original author(s) and the copyright owner(s) are credited and that the original publication in this journal is cited, in accordance with accepted academic practice. No use, distribution or reproduction is permitted which does not comply with these terms.

Refining large knowledge bases using co-occurring information in associated KBs

Yan Wu and Zili Zhang*

College of Computer and Information Science, Southwest University, Chongqing, China

To clean and correct abnormal information in domain-oriented knowledge bases (KBs) such as DBpedia automatically is one of the focuses of large KB correction. It is of paramount importance to improve the accuracy of different application systems, such as Q&A systems, which are based on these KBs. In this paper, a triples correction assessment (TCA) framework is proposed to repair erroneous triples in original KBs by finding co-occurring similar triples in other target KBs. TCA uses two new strategies to search for negative candidates to clean KBs. One triple matching algorithm in TCA is proposed to correct erroneous information, and similar metrics are applied to validate the revised triples. The experimental results demonstrate the effectiveness of TCA for knowledge correction with DBpedia and Wikidata datasets.

KEYWORDS

abnormal information, matching algorithm, knowledge correction, Q&A systems, negative candidates

1 Introduction

Domain-oriented knowledge bases (KBs) such as Wikidata [1] and DBpedia [2] are extracted from Wikipedia articles. Since KBs are constructed automatically, some errors are imported from Wikipedia, including inconsistencies, typing errors, and numerical outliers [3–6]. One of the major errors is a range violation of triples in KBs. The problem arises when triples contain some abnormal information. For example, one triple `<dbr:Andreas_Baum, dbo:nationality, dbr:Germans>` is extracted from the sentence “Andreas Baum is a German politician” in DBpedia. The erroneous nationality of Andreas_Baum is “Germans,” and the correct target is “Germany”. Some facts use language values as the target of predicate “nationality,” such as `<dbr:Ami_Haruna, dbo:nationality, dbr:japanese_language>`, `<dbr:Amelia_Rosselli, dbo:nationality, dbr:italian_language>`, and `<dbr:Diederik_Grit, dbo:nationality, dbr:dutch_language>`. Some triples consider the value of their ethnic group or language as the object for nationality, and they violate the range value of the predicate. These incorrect triples are called abnormal information in KBs. Some triples with abnormal information have some implicit features in KBs. Usually, these abnormal triples are removed during data cleaning. Therefore, some interesting details are ignored in the application of KBs. The accuracy of knowledge greatly affects the results of question and answer (Q&A) systems with these KBs. Several published datasets explore the balance of natural language questions and SPARQL queries, ignoring errors in answers [7]. In SQuAD 2.0 [8] from extractive reading comprehension systems, there are some questions about “nationality” with erroneous answers, such as “question”: “Along with German immigrants, immigrants of what nationality supported Tammany Hall?”, “answers”: [“Irish”] and “question”: “What was Diogo Cao’s nationality?”, “answers”: [“text”: “Portuguese”]. The incorrect answers,

Irish and Portuguese, are replaced by the correct items (Ireland and Portugal). These answers have similar triples in KBs constructed from Wikipedia. KBs are used effectively in the backend of question-answering systems, e.g., IBM Watson System [9] containing YAGO [10] KBs. In order to improve the accuracy of answers in Q&A systems, our work is shifted to refine large KBs at the backend of the Q&A systems. The task focuses on cleaning and correcting errors by finding co-occurring similar triples in KBs.

Fact validation and a rule-based model are applied to detect erroneous information by searching candidates in KBs [11–15]. These cleaning algorithms are designed to look for existing errors in training datasets, but they cannot search for more errors in KBs. This study analyzes the characteristics of incorrect information and extracts the featurization of triples to improve the effectiveness of mining incorrect triples in KBs. For correcting these errors [6, 16, 17], some semantic embedding methods were designed to build a correction framework. The accuracy of the model depends on the pre-training model. For these methods, some pre-trained parameters are applied to make the correction decision. Every triple is checked for consistency. The framework is not suitable for tons of errors, i.e., for large KBs. Correction rules are acquired by rule models [18] for solving large KBs. However, positive and negative rules are generated before constructing correction rules. Correction rules are applied to solve a batch of errors. For a single error, it takes a lot of time to obtain the correction rule. Similarly, for errors without redundant information, the corresponding correction rules are not obtained.

In this study, an automatic framework, triples correction assessment (TCA), is developed to clean abnormal triples and revise these facts for refining large KBs. First, statements of erroneous triples are analyzed to acquire some new negative candidates and more negative sampling by small erroneous triples with range violations. After the process of data cleaning in TCA, small samples are used to obtain a large amount of abnormal information to clean up a large knowledge base. In our framework, the abnormal information in data cleaning is transmitted to mine interesting features for data correction. So, one triple matching method is proposed to find some repairs in target KBs by matching co-occurring triples between original and target KBs in the part of data correction. Other parts assist the whole framework to screen better correction results by similarity measures. Here, one new correction similarity is designed to acquire final repair to perform the alteration in incorrect triples. Our TCA framework is designed to correct range violations of the triple by discovering evidence triples from an external knowledge base. There are already a large number of Wikipedia-related knowledge bases, and they are quite mature and have a higher quality of triples. Our framework skips the pre-training part and further explores the relationship between KBs with the original source to correct the knowledge base. Also, our framework bridges sample inconsistencies between data cleaning and data rectification, further refining large knowledge bases.

1.1 Contributions

The novel contributions are as follows:

- An automatic framework, TCA, is developed to clean abnormal information and find consensus from other knowledge bases to correct the range errors of RDF triples.
- Some negative candidate search strategies are collected to filter abnormal information, and cross-type negative sample methods are applied to clean erroneous knowledge. Here, correction similarity metrics are designed to evaluate candidates for gathering final repairs.
- One co-occurring triple matching algorithm is designed to match similar triples to find candidates for correcting abnormal information in two different KBs.

The organization of this paper is as follows: In [Sections 2 and 3](#), related work and preliminary materials are presented. [Section 4](#) introduces the proposed framework containing negative candidate searching strategies and a correction model, respectively. [Section 5](#) shows the experiments and analysis of our model. At last, the conclusion is presented in [Section 6](#).

2 Related work

Some mistaken tails of the triples are recognized by wrong links between different KBs, and each link is embedded into a feature vector in the learning model [19]. In addition, the PaTyBRED [20] method incorporated type and path features into local relation classifiers to search triples with incorrect relation assertions in KB. Integrity rules [21] and constraints of functional dependencies [22–24] are considered to solve constraint violations in KBs. Preferred update formulations are designed to repair ABox concepts in KBs through active integrity constraints [25]. Data quality is improved with statistical features [26] or graph structure [27] by type. Liu et al. [11] proposed consensus measures to crawl and clean subject links in data fact validation. Usually, a fact-checking model is trained to detect erroneous information in KBs. Some rules are generated to perform correctness checking by searching candidate triples [13]. So, candidate triples are leveraged to find more erroneous triples for cleaning KBs. Wang et al. [14] used relational messages for passing aggregate neighborhood information to clean data. It seems inevitable that knowledge acquisition [28] is strongly affected by the noise that exists in KBs. Triples accuracy assessment (TAA) [12] is used to filter erroneous information by matching triples between the target KB and the original KBs.

Piyawat et al. [29] correct the range violation errors in the DBpedia for data cleaning. The Correction of Confusions in Knowledge Graphs [16] model was designed to correct errors with approximate string matching. The correction tower [30] was designed to recognize errors and repair knowledge with embedding methods. The incorrect facts are removed by the embedding models with the Word2vec method in KBs [17]. Embedding algorithms, rule-based models, edit history, and other approaches are leveraged to correct errors in KBs. A new family of models to predict corrections has received increasing attention in the domain of embedding methods, such as TransE [31], RESCAL [32], TransH [33], TransG [34], DistMult [35], HolE [36], or ProjE [37]. Our work focuses on associated KBs to search for similar triples and connections for KB repairs. Bader et al. [38] considered previous repair methods to correct abnormal knowledge with source codes. One error correction system [39] contains the majority of fault values in the tables and leverages the correction values as the sample

repairs. Baran et al. [39] without these prerequisites was designed for data correction in tabular data. The edit history [40] of KBs was considered in the correction models for repairing Wikidata. They ignored contextual errors in the edit history of KBs.

Mahdavi et al. [41] designed an error detection system (Raha) and updated a system (Baran) for error correction by transfer learning. Other studies correct entity type [5, 16, 42] in the task of cleaning KBs. The work of fixing bugs is carried out by checking whether the KB violates the constraints of the schema [6, 43] automatically. Some erroneous structured knowledge in Wikipedia is repaired by using pre-trained language model (LM) probes [44]. Natural language processing methods are combined with knowledge-correction algorithms [45]. Some models were designed to validate the syntax of knowledge and clean KBs, such as ORE [46], RDF:ALERTS [47], VRP [48], and AMIE [49]. Some clean systems were proposed to solve inconsistencies in tabular data [50–53]. Also, some correction systems [30, 41] are designed to refine KBs. Usually, some correction methods focus on solving specific problems [5, 6, 16, 42, 43]. Extending these studies, natural language processing methods are combined with knowledge correction algorithms [44, 45]. To solve the errors existing in structured knowledge, pre-trained models are trained to set parameters and a framework to correct errors or eliminate them [54, 55]. In these correction models, errors are predefined in the training datasets and not in the KBs. Such models ignore the process of exploring errors and fail to achieve good correction results in large KBs.

These methods are used when there is a lack of association between KBs, and these cannot be scaled to multiple large KBs. While the problem of correcting errors has been neglected in the field of knowledge application, the available repair methods mainly result in the undesired knowledge loss caused by the data removal. Triples with the correct subject are considered in this study. A method to correct these errors is posited by a post factum investigation of the KB.

3 Preliminaries

A KB (such as Wikidata) following Semantic Web standards covering RDF (Resource Description Framework), RDF Schema, and the SPARQL Query Language [56] is considered in our experiment. A KB is composed of a TBOX (terminology) and an ABox (assertions). Through the TBox level, the KB defines classes, a class hierarchy (*via* `rdfs:SubClassOf`), properties (relations), and property domains and ranges. The ABox contains a set of facts (assertions) describing concrete entities represented by a Uniform Resource Identifier (URI). Let K_1 and K_2 represent two KBs. K_1 is the original knowledge base for validation, and K_2 is the additional KB that is leveraged to provide matching information or correction features. The entities of two KBs are represented as E_1 and E_2 , respectively. The predicates are R_1 and R_2 , and the type sets of entities are T_1 and T_2 which include the domain and range of relation, respectively.

3.1 Overlapping type of entity

Two entities $e_1 \in E_1$ and $e_2 \in E_2$ are selected: e_i ($i = 1, 2$) is an entity with overlapping type, if e_1 and e_2 denote the same real-world facts. The connection of e_1 and e_2 , can be represented as $e_1 = e_2$, and the

connection of types in two entities, τ_{e_1} and τ_{e_2} , can be represented as $\tau_{e_1} = \tau_{e_2}$. Here, the entities of the KB are represented as E and the predicate as R . The KB can be symbolized as a set of triples (e_s, r, e_o) indicated as S , where e_s and $e_o \in E$ mark head and tail, respectively. $r \in R$ expresses the predicate name (relation/property) between them. For every fact (e_s, r, e_o) , the formulation ϕ of KB-embedding models assigns a score, $\phi(e_s, r, e_o) \in R$, showing whether this triple is correct or not.

Most of the KB-embedding algorithms [31, 33] follow the open-world assumption (OWA), stating that KBs include only positive samples and that non-observed knowledge is either false or just missing. The negative samples (i.e., (\cdot, r, e_o) or (e_s, r, \cdot)) are found by applying the type property of source triple (e_s, r, e_o) . For instance, (\cdot, r, e_o) has wrong domain property of relation and (e_s, r, \cdot) has wrong range property of predicate name.

3.2 Overlapping type pair of entities

Given two triples and type pair, (e_s^1, r^1, e_o^1) and (e_s^2, r^2, e_o^2) are from different KBs. If $e_s^1 = e_s^2$ and $e_o^1 = e_o^2$, (e_s^1, e_o^1) and (e_s^2, e_o^2) are defined as a strict overlapping entity pair for r_1 and r_2 . The pair group of entities for r_1 and r_2 is written as $O(r_1, r_2)$ strictly.

If $\tau_{e_s^1} = \tau_{e_s^2}$ and $\tau_{e_o^1} = \tau_{e_o^2}$, $\tau_{(e_s^1, e_o^1)}$ and $\tau_{(e_s^2, e_o^2)}$ are described as a rough overlapping type pair for r_1 and r_2 . The pair group of type for r_1 and r_2 is written as $O_\tau(r_1, r_2)$.

Example 1. (Monte_Masi, nationality, Australia), (Person, Country) are in K_1 . (Monte Masi, country of citizenship, Egypt), (Person, country) are in K_2 . For the relations “nationality” and “country of citizenship,” they share the overlapping entities “Monte_Masi” and “Egypt” and the overlapping type pair (Person, country). Hence, the overlapping entity pair of predicates “nationality” and “country of citizenship” is (Monte_Masi, Australia), i.e., $O(\text{nationality, country of citizenship}) = (\text{Monte_Masi, Australia})$. At the same time, the overlapping type pair of relations “nationality” and “country of citizenship” is (Person, Country), i.e., $O_\tau(\text{nationality, country of citizenship}) = (\text{Person, Country})$.

Example 1. In Figure 1, (Berlin, locatedat, Germany), (Germany, city), (Germany, country) are in the target base, and (Berlin, locatedin, Germany), (Germany, city), (Germany, country) is in the external base. The overlapping entities (“Berlin”, “Germany”) and the overlapping type pair (city, country) are shared in the predicates “locatedat” and “locatedin.” Therefore, the overlapping entities group of predicates “locatedat” and “locatedin” is (Berlin, Germany), i.e., $O(\text{locatedat, locatedin}) = (\text{Berlin, Germany})$. At the same time, the overlapping type group of predicates “locatedat” and “locatedin” is (city, country), i.e., $O_\tau(\text{locatedat, locatedin}) = (\text{city, country})$.

3.3 Evaluation measures

To fairly validate the performance of algorithms, three classical evaluation measures are used in our experiment, i.e., **Mean_Raw_Rank**, **Precision@K**, and **Recall** [57]. To mathematically explain the measures, the evaluation set is defined as D , consisting of positive/negative feedback set D^+/D^- . For the i_{th} triple, the rank i represents

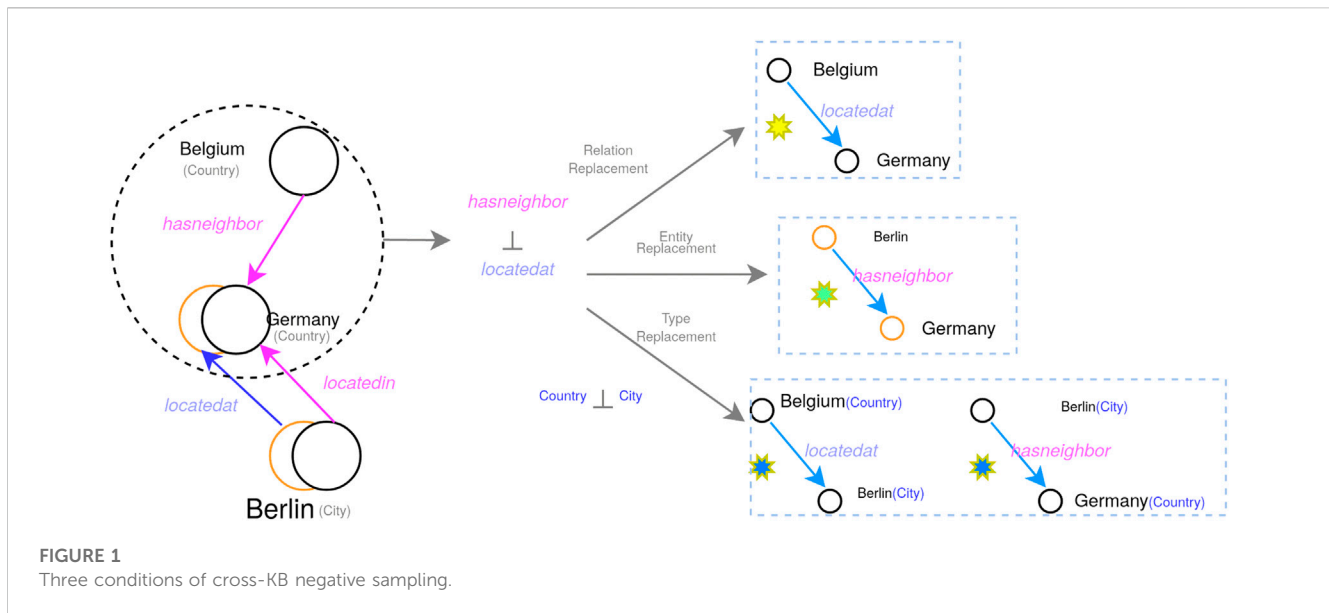


FIGURE 1
Three conditions of cross-KB negative sampling.

its rank in the evaluation set D . Triples with higher scores are filtered out as positive feedback. The rank of incorrect triples has lower values with better performance.

3.3.1 Triple semantic similarity

Word-to-word similarity is leveraged to calculate the consensus confidence of two entities in triples. By the confidence, some co-similar entities have near confidences and they are leveraged in matching methods.

3.3.2 Correction similarity

For calculating the correction similarity for repairs, a harmonic average similarity is proposed to validate the revised triples. The d_L denotes the distance in similarity of words for entities. Also, some special features are considered in similarity measures, e.g., the predicate *wikiPageWikiLink* discovers the same parts of two triples in the original sources, regarded as *semantic_measure*(e_0, e_i). The outer semantic measure calculates the quantity of matching parts in (P_{e_i} , *wikiPageWikiLink*) to acquire the common source, as explained in Func. 1. The part *semantic_measure*(e_0, e_i) considers the best similarity of two entities with soft cardinality [58]. Here, some similarity algorithms are leveraged to validate matching methods, considering their inner features, such as *theLevenshtein_distance*, *Cosine_similarity*, *Sorensen_Dice*, and *Jaro_Winkler*. Last, the harmonic correction similarity is shown in Func. 2.

$$\text{semantic_measure}(e_0, e_i) = \frac{|P_{e_0}|_{soft} \cap |P_{e_i}|_{soft}}{|P_{e_0}|_{soft}}, \quad (1)$$

$$s(e_0, e_i) = 1 - \frac{d_L(e_0, e_i)}{\max(|e_0|, |e_i|)} + \text{semantic_measure}(e_0, e_i). \quad (2)$$

3.3.3 Soft harmonic similarity

A new soft harmonic means function is generated with character-level measure and semantic-relatedness in Func. 1, in order to balance the features of semantics and characters. The consensus is acquired by searching repair similarity of the

optimal correction. Let single word T be a set of n tokens: $T = \{T^1, T^2, \dots, T^n\}$. $d(T^i, T^j)$ is a character-level similarity measure scaled in the interval $[0, 1]$. The soft cardinality of the single word T is calculated as in Function 3.

$$|T|_{soft} = \sum_{i=1}^n \left[\frac{1}{\sum_{j=1}^n d(T^i, T^j)} \right] \quad (3)$$

$$f_{sim} = \frac{2 \times \text{character-level}(e_0, e_i)_{soft} \times \text{semantic-related}(e_0, e_i)}{\text{character-level}(e_0, e_i)_{soft} + \text{semantic-related}(e_0, e_i)}. \quad (4)$$

Cross-similarity measures are leveraged to validate repairs of erroneous triples in KBs. After our model operations, some mistaken assertions are matched with multiple values in the process of repairs. Here, a new cross-similarity measure is proposed to analyze final revised assertions of triples in KBs, aiming to discover common features between original entities and repairs after correction. In Eq. (6), the *Jaro-Winkler* distance [59] is suitable for calculating the similarity between short strings such as names, where d_j is the *Jaro-Winkler* string similarity between e_0 and e_i , m is the number of strings matched, and t is the number of transpositions. Then *sim_external*(.) analyzes the external similarity probability, matching co-occurrence Wikipages in the (*wikiPageWikiLink*) property. *s*(e_0, e_i) is a pair of compared objects. A new cross-function, f_{cross} , in Eq. (7) is the harmonic mean of distance and external similarity, which is designed to cover all correlations of assertions and candidate repairs.

$$\text{sim_external}(e_0, e_i) = (|P_{e_0}| \cap |P_{e_i}|) / |P_{e_0}|, \quad (5)$$

$$d_j = \frac{1}{3} \left(\frac{m}{|e_0|} + \frac{m}{|e_i|} + \frac{m-t}{m} \right), \quad (6)$$

$$f_{cross} = \frac{2 \times d_j \times \text{sim_external}(e_0, e_i)}{d_j + \text{sim_external}(e_0, e_i)}. \quad (7)$$

3.3.4 Relation semantic similarity

The framework uses a method to calculate the semantic similarity between two relations based on word-to-word

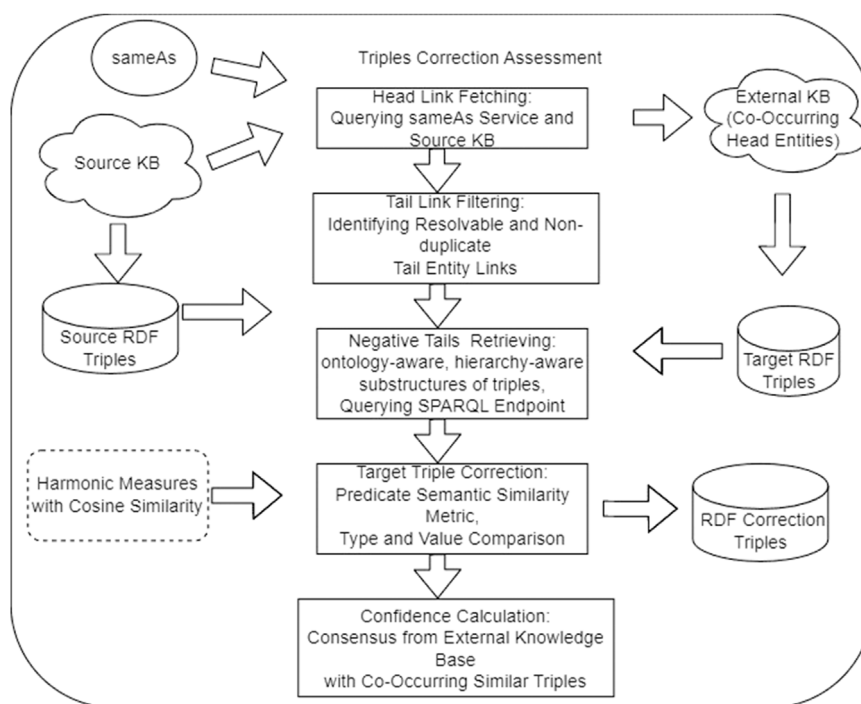


FIGURE 2
TCA framework.

similarity and the abstract-based information content (IC) of words, which is a measure of concept specificity. More specific type concepts (e.g., scientist) have higher values of IC over some type concepts (e.g., person). Generally, types of entities have underlying hierarchy concepts and structures, such as the structure among types with sub-concepts {actor, award_winner, person} in types of Freebase. Given the weights of hierarchy-based concepts [60], entity e and its type set are denoted as T_e . A hierarchy structure among concepts is presented as $C = /t_1/t_2/\dots/t_i/\dots/t_n$, where $t_i \in T_e$, n is the counts of hierarchy levels, t_n is the most specific semantic concept, and t_1 is the most general semantic concept. Usually, the range concept of a relation picks t_1 as the value.

4 The proposed framework

The TCA framework comprises five units (Figure 2). The first two elements recognize equivalent head entity links for a group of source triples, while the middle two parts select negative candidates with erroneous ranges from the source triples and perform the correction. The last item calculates a confidence score for each repair, representing the level of accuracy of the corrected entities.

The Head Link Fetching (HLFFetching) is used to attain similar links of the candidate instance of a source entity. Since there may be duplicate and non-resolvable tails for different head entities, the second part, Tail Link Filtering (TLFFiltering), makes a genuine attempt to find these tail links of tuples co-occurring in two KBs. Then, the Negative Tails Retrieving (NTR) accumulates target values

including the identified candidate property links from external KBs. The third component, target triple correction (TTC), integrates a set of functions to identify repaired triples semantically similar to the source triple. The last component, confidence calculation (CC), calculates the confidence score for corrected triples from external KBs.

4.1 Problem statements

In knowledge bases, there is some noisy and useless information. Before the utilization of the knowledge base, some invalid data are removed and some knowledge is corrected for reuse in the application of KBs. So, knowledge base completion (KBC) is a hot research topic in the field of web science. Most research studies of KBC focus on predicating new information. Here, removing some invalid data and correcting some erroneous facts are our tasks. Aiming at the abnormal information in the knowledge base, this topic filters out invalid data and corrects error information for cleaning and completing KBs. In our approach, the first step is to find more error triples in KBs. Then, some valid erroneous triples are corrected to expand KBs.

Even when the selected entities are correct in KBs, incorrect relations between entities can still cause these triples to go wrong. Here, some other problem statements are explained.

4.1.1 Triple with conflict range type.

For instance, one selected triple $\langle dbr:Hiro_Arikawa, dbo:nationality, dbr:Japanese_people \rangle$ has the correct predicate

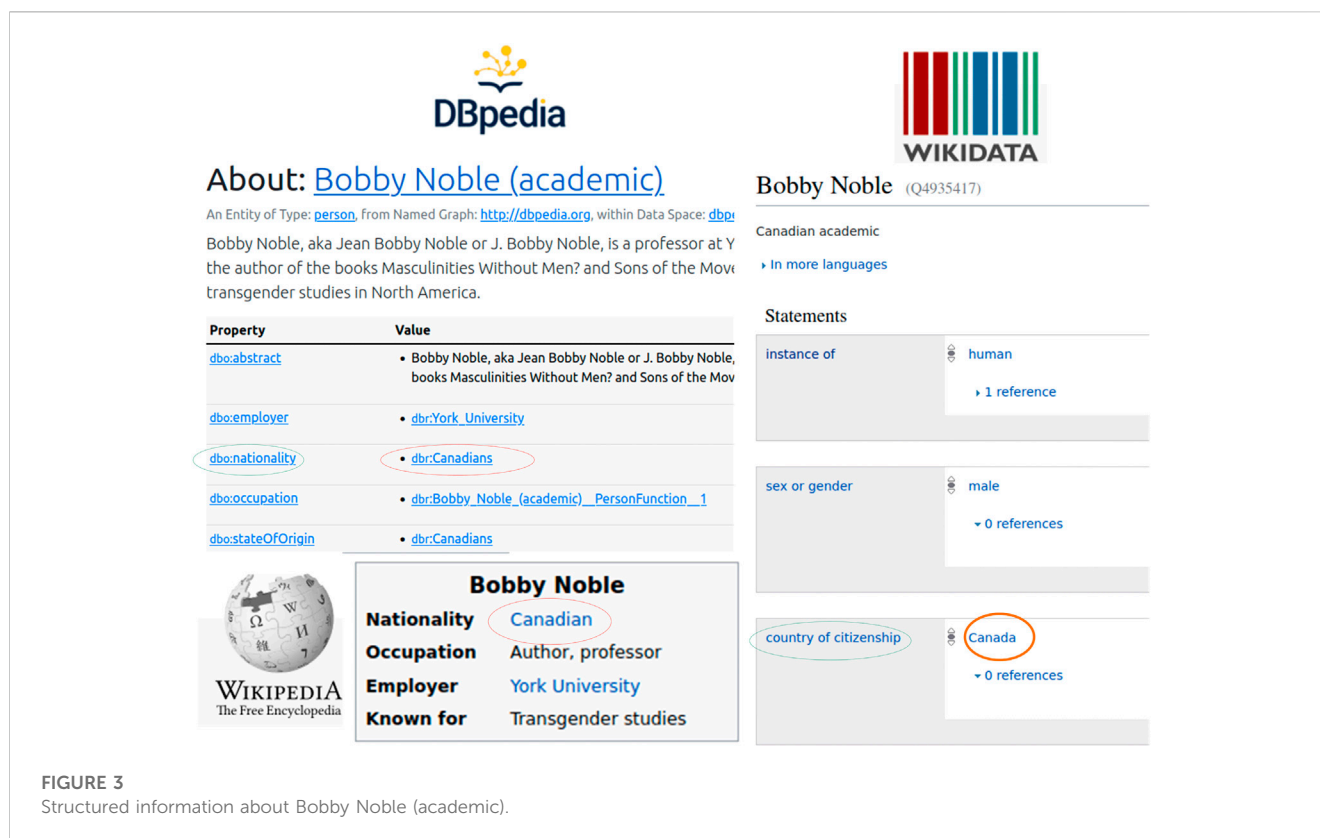


FIGURE 3
Structured information about Bobby Noble (academic).

range property (`dbo:Country`), but the `dbo:Japanese_people` has a conflicting `rdf:type` (`dbo:EthnicGroup`). Here, `dbo:EthnicGroup` and `dbo:Country` has strict conflict ($dbo:EthnicGroup \perp dbo:Country$). The incorrect triple is revised to $\langle dbr:Hiro_Arikawa, dbo:nationality, dbr:Japan \rangle$. In the entity errors, the “nationality” specifies that a particular person comes from a particular country. The errors violate inconsistencies of type. The correct triple based on the type should be $(dbr:Hiro_Arikawa, dbo:nationality, dbr:Japan)$. After analysis of predicate errors, the new correct triple based on the type should be $(dbr:Hiro_Arikawa, ethnic_group, dbr:Japan)$.

4.1.2 Error information in original source

The following two triples (illustrated in Figure 3) are about professor Bobby Noble: (Bobby Noble (academic), nationality, Canadians) in DBpedia as of September, 2022, and (Bobby Noble, nationality, Canadian) in Wikipedia. The triples from the two associated knowledge bases have the same errors since their original source contains incorrect information. Referring to the Wikidata database, the corrected triple (Bobby Noble, country of citizenship, Canada) equals (Bobby Noble (academic), nationality, Canada), since the predicate name *nationality* has the equivalent property of “country of citizenship.”

4.1.3 Type errors

Given a fixed relation “birthplace” in the DBpedia as the sample, the noise type information is detected by the TBox

property. Here, the hierarchical property `rdfs:subClassOf` is considered in the experiment to find the erroneous types. By the manual evaluation, the precision of corrected type is 95% in the relation of *birthplace*. Similarly, the quantity of the incorrect type (`dbo:Organisation`, `dbo:SportsClub`, `dbo:Agent`, etc.) is small. The corrected type contains some more subcategories, i.e., `dbo:City` $<$ `dbo:Settlement` $<$ `dbo:PopulatedPlace` $<$ `dbo:Place`. So, searching the errors of types refers to the range of type and their inner property. In the closed-world assumption (CWA), negative triples with erroneous type are found by the type property, i.e., the range of the predicate. Then, in the open world assumption, the tail of the triple is replaced with another type of property.

For example, the positive triple: $\langle \text{Albert_Einstein}, \text{birthPlace}, \text{Ulm} \rangle$ and type pair $\langle \text{Person}, \text{birthPlace}, \text{Place} \rangle$. Here, we remove the premise of `dbo`: all examples exist in the DBpedia. CWA: $\langle \text{Javed_Omar}, \text{birthPlace}, \text{Bangladesh_national_cricket_team} \rangle$ exists in the KB. OWA: a. $\langle \text{Albert_Einstein}, \text{birthPlace}, \text{University_of_Zurich} \rangle$, $\langle \text{Person}, \text{birthPlace}, \text{Organization} \rangle$. The negative type for the range of birthplaces is replaced. b. $\langle \text{Balquhain_Castle}, \text{birthPlace}, \text{Ulm} \rangle$, $\langle \text{Building}, \text{birthPlace}, \text{Place} \rangle$. Both of these triples are not in the KB, but in general knowledge: Albert_Einstein graduated from the University_of_Zurich. The triple *a* is regarded as unknown knowledge in the DBpedia or similar triples are not extracted from Wikipedia. But the triple *b* is actually false. Finally, the study exclusively uses the tail type replacement in the process of negative triples detection.

TABLE 1 Some examples of conflict feedbacks.

Fact	Feedback
< dbr: Wang_Zeng, dbo: birthPlace, dbr: Song_dynasty >	×
< dbr: Wang_Zeng, dbo: birthPlace, dbr: Qingzhou >	✓
< dbr: Novotel, dbo: locationCountry, dbr: Évry_Essonne >	×
< dbr: Novotel, dbo: locationCountry, dbr: France >	✓
< dbr: Averroes, dbo: birthPlace, dbr: Almohad_Caliphate >	×
< dbr: Averroes, dbo: birthPlace, dbr: Córdoba_Andalusia >	✓
< dbr: Pope_Telesphorus, dbo: birthPlace, dbr: Calabria >	×
< dbr: Pope_Telesphorus, dbo: birthPlace, dbr: Greece >	✓

4.1.4 Conflict feedback

Conflict feedback is assumed to consist of binary *true/false* assessments of facts that have the same subjects contained in the KB. Two different triples have the same subject and predicate but different objects. Not all positive examples can find corresponding counterexamples; conflict feedback cannot be obtained with a small number of examples. Two different paths are proposed to find the conflict feedback. First, range violation errors of triples are considered to search abnormal facts. The default settings are that subjects are always correct and objects have range violations. For example, the triple < dbr: Wang_Zeng, dbo: birthPlace, dbr: Song_dynasty > in DBpedia is incorrect since the predicate *dbo: birthPlace* requires a tail with the *dbo: Place* property (the best type following the characteristic distribution), which *dbr: Song_dynasty* is devoid of since *Song_dynasty* was an era of Chinese history, not a place. The inconsistency damages the effectiveness of any applications in KBs. To correct the instance, the *dbr: Song_dynasty* should be removed and *dbr: Qingzhou*, where *Wang_Zeng* was born, is saved in KBs. In Table 1, some examples are acquired from conflict feedback in DBpedia 2016 version. Such conflict feedback strictly disturbs information for further predictions, causes data distortion, and increases noise. The conflict errors are removed after searching all abnormal facts, and erroneous triples of one-to-many attributes are corrected in our proposed method for knowledge base correction.

4.2 Generated erroneous entities

Negative statements are regarded as incorrect triples. One major problem statement is that an object of triple has a type without a matching range of predicate. This error is also called a range violation of relation [61]. For the erroneous triples, cross-type negative sampling is used to generate erroneous entities. Also, the convenient way of error generation is to refer to TBox property, such as a class hierarchy (*via* *rdfs:subClassOf*) and *owl:equivalentClass*. In the incorrect examples, the subject is not unique. For some conflict feedback, the same subject and the same property have different objects. Conflict feedback is considered to clean KBs, since some conflict feedback contains negative statements obfuscating facts in the real world.

4.2.1 Cross-type negative sampling

The model presents how to produce cross-KB negative samples over two KBs based on cross-KB negative predicates. The cross-KB negative samples can be caused by three strategies: predicate replacement, entity substitution, and type replacement.

4.2.1.1 Cross-KB negative type of predicate

There are two predicates: $r_1 \in R_1$ and $r_2 \in R_2$. r_i , $i = 1, 2$ has an empty overlapping type pair, i.e., $O_r(r_1, r_2) = \emptyset$; then the predicates r_1, r_2 are shown as $\tau_{r_1} \perp \tau_{r_2}$, called as generalized cross-KB negative type of predicate. The cross-KB negative relation [57] is defined by the strict cross-KB negative relation. For a given relation $r_1^1 \in K_1$ and the type $\tau_{r_1^1} \in K_1$, the cross-KB negative type of predicate set $N(\tau_{r_1^1})$ of r_1^1 is expressed as $N(\tau_{r_1^1}) = \{\tau_{r_2} | \tau_{r_2} \perp \tau_{r_1^1}, \tau_{r_2} \in K_2\}$, and the cross-KB negative set $N(\tau_{r_2^1})$ of the predicate $\tau_{r_2} \in K_2$ is described as $N(\tau_{r_2^1}) = \{\tau_{r_1} | \tau_{r_1} \perp \tau_{r_2^1}, \tau_{r_1} \in K_1\}$. All the types of entities in the set of T_i , $i = 1, 2$.

Example 2. Let us assume that $K_1 = \{\text{Germany, Berlin, Albert_Einstein, Belgium}\}$ and $R_1 = \{\text{locatedat, livesin}\}$. Three observed triples are (Berlin, locatedat, Germany), (Berlin, locatedin, Germany), and (Albert_Einstein, livesin, Berlin). The predicate “livesin” in Figure 1 is taken as an instance. The pair of entities on this predicate is (Albert_Einstein, Berlin). This pair of entities does not fulfill any predicate in the additional links. Thus, all predicates in the external links are its cross-KB negative type of predicates, i.e., $N(\text{livesin}) = \{\text{locatedin, hasneighbor}\}$. For the property “hasneighbor” in another knowledge base, its cross-KB negative type of predicate is $N(\text{livesin, locatedat})$.

4.2.1.2 Predicate replacement

Let us assume Q_2 represents the set of triples in the other KB K_2 . For a triple $(e_s^2, r_2, e_o^2) \in Q_2$, if r_2 is replaced by any predicate $r_1 \in N(r_2)$, new triple (e_s^2, r_1, e_o^2) is regarded as a cross-KB negative sample. This new negative candidate is composed of entities $e_s^2, e_o^2 \in K_2$ and $r_1 \in R_1$. S_r' is denoted as the set of cross-KB negative samples acquired by predicate replacement. The intuition of predicate replacement is that if a triple (e_s^2, r_2, e_o^2) is correct, r_1 and r_2 do not have any overlapping entity pair, i.e., no triples can fulfill predicates r_1 and r_2 simultaneously and the new incorrect triple is (e_s^2, r_1, e_o^2) .

Example 3. As shown in Figure 1, since *hasneighbor* \perp *locatedat*, “hasneighbor” is alternated by “locatedat” between the entities “Belgium” and “Germany” to obtain a negative sample (Belgium, locatedat, Germany).

4.2.1.3 Entity substitution

Given a triple $(e_s^2, r_2, e_o^2) \in Q_2$ and $r_1 \in N(r_2)$, (e_s^2, e_o^2) is replaced with any entity pair (e_s^1, e_o^1) of triples satisfying r_1 , the new (e_s^1, r_2, e_o^1) is seen as a cross-KB negative sample.

Example 4. Since (Berlin, Germany) contains the predicate “locatedat” shown in Figure 1, and *hasneighbor* \perp *locatedat*, substituting the negative predicate “locatedat,” the entity pairs have alternates on the predicate “hasneighbor.” So, a new negative candidate is acquired, i.e., (Berlin, hasneighbor, Germany).

The cross-KB negative sampling efficiently acquires validation knowledge from additional KB for the source KB. Although tons of negative samples are produced without semantic similarity, such negative samples are still very instructive for embedding learning.

Since the method needs to learn from easy examples (e.g., negative relations “hasneighbor” and “hasPresident”) to difficult instances (e.g., “hasneighbor” and “locatedat”), negative sample sets containing many simple conditions are beneficial for simple model learning. Difficult negative triples are more informative for complex models.

4.2.1.4 Type replacement

There are $(e_s^2, r_2, e_o^2) \in Q_2$ and its type $(T_{e_s^2}, r_2, T_{e_o^2}) \in T_2$. The positive triple and type pair is the $(e_s^2, r_2, e_o^2) \in Q_2$ and $(T_{r_{domain}}, r_2, T_{r_{range}}) \in T_2$. If the new samples satisfy the condition that $T_{e_i} \in T_2, \neq T_{r_{domain}}$, the set of triples are new negative samples, i.e., $(T_{e_i}, r_2, T_{r_{range}})$. In the same assumption, the type of target entity is replaced by other types. The new negative samples $((T_{r_{domain}}, r_2, T_{e_i}))$ satisfies the condition that $T_{e_i} \in T_2, \neq T_{r_{range}}$.

positivetriples:

$$(e_s, r, e_o) \in K, \quad type \in (T_{r_{domain}}, r, T_{r_{range}}).$$

negativetriples:

$$a. (e_s, r, e_o^*) \notin K, \quad (8)$$

$$type \in (T_{r_{domain}}, r, T^*), \quad T^* \in T, T^* \neq T_{r_{range}}.$$

$$b. (e_s', r, e_o) \notin K,$$

$$type \in (T^*, r, T_{r_{range}}), \quad T^* \in T, T^* \neq T_{r_{domain}}.$$

$r_1 \in N(r_2)$ and $t_1 \in N(r_2)$, (e_s^2, e_o^2) is replaced with any entity group (e_s^1, e_o^1) of triples which includes r_1 ; the new (e_s^1, r_2, e_o^1) is regarded as a cross-KB negative sample.

4.2.2 Search strategy to generate negative candidates

In the CHAI model [13], they regard the candidate triples as true when the original triples are correct. Extending this idea; the negative candidates are also false. Considering the criteria from the CHAI model and the RVE model [29], a new search strategy is defined to explore more negative candidates. In short, $\langle s, p, o \rangle$ is a triple in K and one erroneous triple is taken as negative feedback.

4.2.2.1 Existing subject and object

The criterion collects all candidates whose subject and object appear as such for some triples in K ; p' and p have the same *ObjectPropertyRange*:

$$exist_{KB1}(s, p, o) \Leftrightarrow \exists p' \in \xi | (s, p', o) \in K. \quad (9)$$

4.2.2.2 Existing subject and predicate:

The criterion collects all candidates whose subject and predicate occur as such for some triples in K . There exists no candidate with the correct property type:

$$exist_{KB2}(s, p, o) \Leftrightarrow \exists o' \in \xi | (s, p, o') \in K. \quad (10)$$

4.2.2.3 Existing predicate and object

The criterion collects all candidates whose object entity replaces the subject one or more times in a triple that has another predicate p' or the object entity appears at least once as the object in a triple that has another predicate p' :

$$exist_{KB3}(s, p, o) \Leftrightarrow \exists s' \in \xi | (s', p, o) \in K. \quad (11)$$

For instance, one negative triple (*Bobby Noble (academic), nationality, Canadians*) is chosen as the example. In criterion *a*, one candidate (*Bobby Noble (academic), dbo:stateOfOrigin, Canadians*) can be generated. In criterion *b*, one erroneous triple is (*Bonipert, nationality, French_people*) and the candidate is (*Bonipert, nationality, Italians*). In criterion *c*, there are erroneous objects *Canadians, French_people, Italians, etc.* The number of candidate samples about (*?a, nationality, Canadians*) is over 4,900. The number of candidates about *French_people* is over 1,300 and the quantity about *Italians* is near 1,000. For positive triples, the results of candidates have a lower number of incorrect or noisy candidates, which also exist in the original KB. So, sparsity negative examples can be crawled by some features, and then our previous work produced a GILP model [15] to acquire more negative examples in iterations.

Combining the search strategy of negative candidates with the method of cross-type negative sampling, erroneous entities, and their triples can be generated for cleaning. Also, some interesting negative statements are selected to be corrected as new facts for knowledge base completion.

4.3 Fetching and filtering erroneous tails links

The HLFetching part acquires the tail of a source triple as input by the <http://sameas.org> service and equivalent links of the candidate instances are fetched in external KB. The *sameAs* property supplies service to quickly get equivalent links with arbitrary URIs, and 200 million URIs are served, currently. The *SameAs4J* API is used to fetch equivalent tails links from the *sameAs* service [62].

In a KB, a target predicate $P_r, \langle s, o \rangle$ is used to detect a negative example if $\langle s, P_r', o \rangle \in KB$, with $P_r' \neq P_r$, for every $\langle s, o \rangle$ is semantically connected by at least one predicate. To refine the quality of training triples and delete cases of mixed types, all the subjects must have the same type, and the same is true for the object values. For example, the pseudo-SPARQL query is leveraged to present how to get negative examples in the predicate of child in the DBpedia database. Such as the pseudo-SPARQL query: *select distinct ?head ?tail where { ?head rdf:type dbr: Person. ?tail rdf:type dbr: Person. ?subject ?relation ?tail. {{ ?head dbr: child ?realTail. } UNION { ?realHead dbr: child ?tail.}} FILTER NOT EXISTS{?head dbr: child ? tail. }*

4.4 Target triple correction

For target triple correction, the model takes co-occurring similar entities into consideration. One fixed predicate name is chosen as the sample to illustrate the process of correction. In the CWA, some simple queries can be serviced to find erroneous entities without correct *ObjectPropertyRange*, i.e., $\langle subject, predicate, object \rangle$ and $\langle object, a, wrong_ObjectPropertyRange \rangle$. For example, the correction type of the “nationality” range is *Country*. The DBpedia contains over 1,800 different values of objects with the correct type. Also, there are some false positive items, e.g., *dbr:Canadians, dbr:Germans, dbr:*

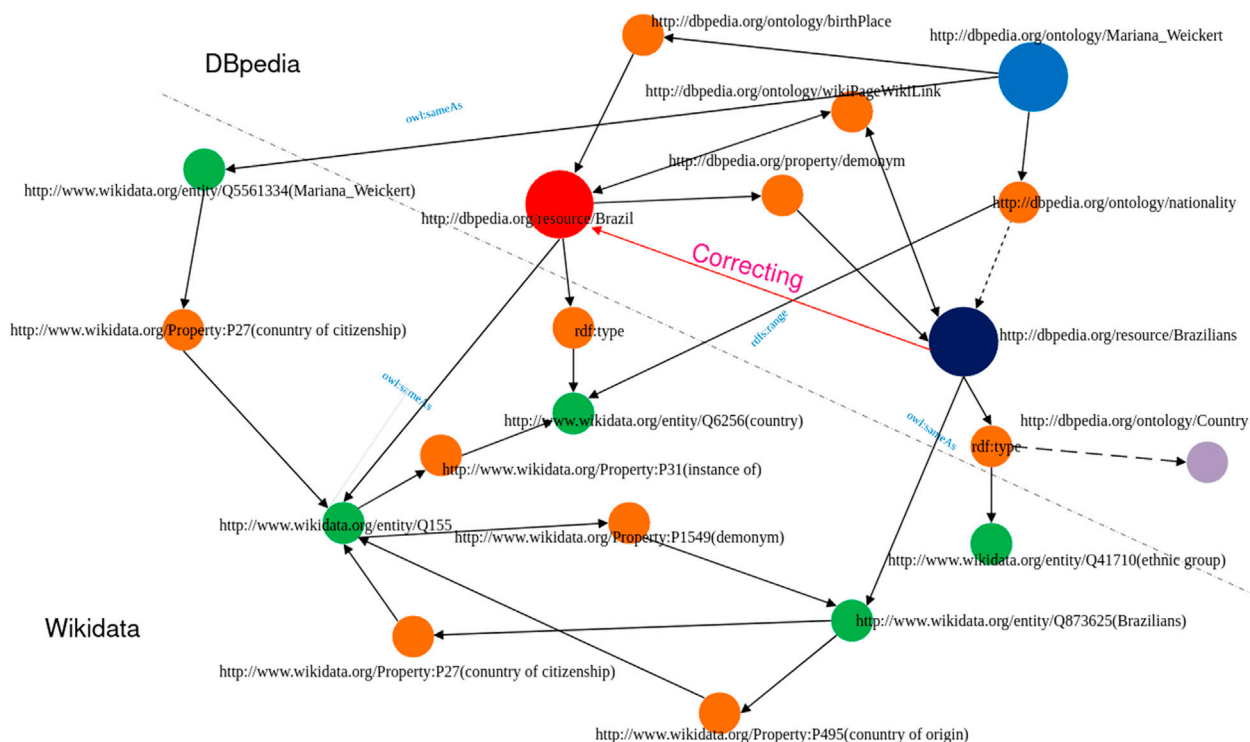


FIGURE 4
Evidence graph as displayed in the TCA (the dark dot denotes erroneous entity and the red one is corrected. Orange dots denote predicate property, and other colors show the entities between DBpedia and Wikidata).

French_language, and *dbr:Pakistanis* Comparatively, the KB holds over 1,000 different incorrect entities of triples. Next, the co-occurring similar entities in the Wikidata are leveraged to validate the repairs in the DBpedia. The algorithms assess the correctness of entity values by cross-checking them with properties of type from a new KB, shown in [Algorithm 1](#). The system automatically checks the conformity of the entity inside the old KB (DBpedia) to all the same entities inside the Wikidata with the property of *sameAs*. In the CWA, the YAGO has the precise information of type by the property of *wordnet*. Referring to Wikidata, we can also leverage the features to verify the repairs of YAGO in the rule correction algorithms.

Algorithm 1 describes the triple matching algorithm to correct negative candidates. First, in the former methods, it is proposed to generate erroneous triples. Then, conflict feedback is removed from sets of erroneous entities. The predicate name is extracted from one erroneous triple. True *ObjectPropertyRange* τ is leveraged to find candidate property p' in associated KB K' . Also, p' can be found by overlapping type pairs of entities. At the same time, corresponding candidate instance s' is acquired by *owl:sameAs* relation from original subject s of $\langle s, p, o \rangle$. Next, new objects are found in K' from $\langle s', p', ? \rangle$ and stored in $set\{obj\}$. Finally, some similarity measures are used to filter consensus and make the final correction. The TCA iterations are terminated either when no triples are in E or when $Corr_n$ remains unchanged among two iterations.

Our problem is simplified to finding the corresponding property in Wikidata based on a co-occurring similar triple in DBpedia. Especially, the equivalent property of the predicate name of triples is selected to find repairs for the wrong entity. One entity *Mariana_Weickert* extracted from DBpedia is regarded as an example of a correcting task. An evidence graph is shown in the TCA, in Figure 4. For erroneous triple $\langle \textit{Mariana_Weickert}, \textit{dbo:nationlity}, \textit{Brazilians} \rangle$, it violates the range constraint of a predicate name. The dashed lines represent wrong relations.

```

Input:  $\text{pand} \rightarrow \langle s, p, o \rangle$  ;
Output:  $\text{Corr}_n$ ;
 $\text{Corr}_i = \text{null}$ ,  $i = 0$ ;
Erroneous_entities_sets:  $\{s, p, o\} \in E$ ;
while  $K \neq \emptyset$  or  $\text{Corr}_i$  changed do
     $p \rightarrow \text{ObjectPropertyRange}(\tau(\text{true}) \text{ or } \tau'(\text{false}))$ ;
     $(p, \tau, \text{owl: equivalentProperty}) \rightarrow \text{candidate\_property: } p'$ ;
     $(s, \text{owl: sameAs}) \rightarrow \text{candidate\_instance: } s'$ ;
     $\langle s', p', ? \rangle \rightarrow \text{property\_value: } o'$ ;
     $(o', \text{owl: sameAs}, ?) \rightarrow \text{repairs: set}\{\text{obj}\}$ ;
     $\text{correction}(\text{obj}) = \text{filterConsensus}(\text{set}\{\text{obj}\})$ ;
     $\langle s, p, o \rangle \rightarrow \langle s', p', o' \rangle \rightarrow \langle s, p, \text{obj} \rangle$  ;
     $\text{Corr}_i := \langle s, \text{obj} \rangle \cup \text{Corr}_i$ ;  $i = ++$ ;
end
return  $\text{Corr}_n$ ;

```

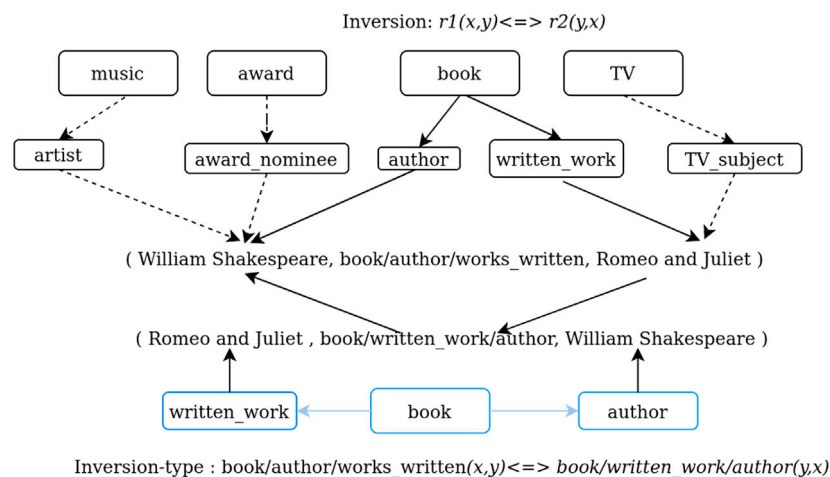



FIGURE 5

Example of logic relations with entity hierarchical types in Freebase.

Algorithm 1 Co-occurring Triple Matching Algorithm.

Two major paths are expressed in the process of repairing the wrong range constraint. First, based on subject *Mariana_Weickert*, a similar entity in Wikidata is filtered by *owl:sameAs* and the equivalent property of nationality is replaced by Wikidata:P27 (country of citizenship). So, the repair entity is *wikidata:Q155*, and the corresponding entity is Brazil in DBpedia. *dbr:Brazilians* has wrong type *dbo:Country*. Second, referring to the wrong object and the correct range type, *Brazilians* and *Brazil* are related by properties *wikidata:P495* (country of origin) and *wikidata:P27*. Finally, $\langle \text{Mariana_Weickert}, \text{dbo:nationlity}, \text{Brazilians} \rangle$ can be corrected to $\langle \text{Mariana_Weickert}, \text{dbo:nationlity}, \text{Brazil} \rangle$. Before application in the answer-question system, some results are validated by our algorithm. Some constructed KBs, such as DBpedia or YAGO, have high precision. For these KBs, our approach can be used to validate the final results in the question-answer system.

4.4.1 Hierarchy information for knowledge correction

The taxonomy and hierarchy of knowledge can be applied to many downstream tasks. Hierarchical information originated from concept ontologies, including semantic similarity [63, 64], facilitating classification models [65], knowledge representation learning models [66], and question-answer systems [67]. Well-organized algorithms or attentions of hierarchies are widely applied in the works of relation extraction, such as concept hierarchy, relation hierarchy with semantic connections, a hierarchical attention scheme, and a coarse-to-fine-grained attention [68, 69].

4.4.2 Hierarchical type

In Freebase and DBpedia, selecting one hierarchical type c with k layers as example, $c(i)$ is the i_{th} sub-type of c . The most precise sub-type is considered the first layer, and the most general sub-type is regarded as the last layer, while each sub-type $c(i)$ has only one parent sub-type $c(i+1)$. Taking a bottom-up path in the hierarchy, the form of hierarchical type is represented as $c = c(1), c(2), \dots, c(k)$. In YAGO, subclass Of is used to connect the

concepts (sub-types). In logic rules, like the inversion, $r_1(x, y) <=> r_2(y, x)$ and the variables x, y can be the entities in general. Here, we expand the logic relations with entity hierarchical types and acquire the fixed domain entities.

As shown in Figure 5, the inversion-type logic are $r_1(\text{author}, \text{written_work}) <=> r_2(\text{written_work}, \text{author})$. So, the relations r_1 and r_2 are *book/author/works_written* and *book/written_work/author*. Especially, the entity of freebase contains the type information in the label of the entity. One negative triple is inversion-type, so negative candidates can be acquired by inversion relations. For instance, nationality has *InversePath* (is nationality of. In DBpedia, an entity page displays statements in which an entity may be not only a subject but also an object. In the latter case, the respective property appears as “is . . . of.” If one negative triple $\langle s, p, o \rangle$ has inverse path, all candidates extracted from the condition satisfies $\langle o, \text{is_p_of}, s' \rangle$ are incorrect.

For example, the object of *irthplace* in entity *Nick_Soolsma* follows the type path: *Andijk(dbo:Village) < Medemblik(dbo:Town) < North_Holland(dbo:Region) < Netherlands(dbo:Country)*. One logic path: country containing one birthplace of a person is the person's nationality. By hierarchical property, *dbr:Nick_Soolsma* acquires one new nationality, *dbr:Netherlands*. Repair results can be obtained by predicting erroneous information by hierarchical type. The correction method was proposed in our previous work [18]. For the explanation of hierarchical correction, related paths, and relationships can be used to acquire corrections for negative triples.

5 Experiments

Our approach is tested by using four datasets from four predicate names. Here, mean reciprocal ranking (MRR), HITS@1, and HITS@10 [6] are selected to measure the confidence

calculation of corrected triples in the knowledge base. All training datasets are leveraged in the experiments from <http://ri-www.nii.ac.jp/FixRVE/Dataset8>. Some baseline algorithms were realized in Python, using Ref. 6. Our framework is constructed in the Ubuntu 20.04.5 system and Java 1.8.0, and experimental analysis is run on a notebook with a 12th Gen Intel Core i9-12900KF × 24 and 62.6 GB memory.

5.1 Negative feedback generation

P is given a constraint predicate. A constraint has several lines when it leverages a specified relation. *#constr* is the total quantity of constraints of the *errors type* in Dbpedia. *#triple* is the number for calculating all these constraints of triples with the predicate P . *#violations* is the quantity of violations for this constraint in Dbpedia in October 2016. *#current_cor* is the quantity of current corrections collected from Dbpedia in 2020.

In type classification of nationality, objects with the *country* property are up to 67%, and entities with *ethnic group* is 31%. Other types are less than 2%, such as language, island, and human settlement. After analysis of negative constraints of *nationality*, there are duplicate triples between problem statements. In Dbpedia, the type of the entity is a parallel relationship in the SPARQL query results, and the hierarchical relationship between the attributes cannot be obtained from the query results. Therefore, there are overlapping parts among all these errors because the object value of the predicate “*nationality*” is not unique. Nearly 20% of the triples determined as can be corrected to complete KBs since the objects can have multiple values for *nationality*, explained in Table 2. For the relation *birthplace*, the conflict feedback is removed because the predicate objects have a single value. Also, there are over 70% conflict types in error types for nationality. Here, some examples extracted from nationality are applied to validate our correction model.

For a single incorrect triple, a search strategy is proposed to generate negative candidates. Following strategy *a* for *nationality*, some new predicate names *isCitizenOf*, *stateOfOrigin* are acquired from KBs. In strategy *b*, the object types of triples are all exception properties. Negative candidates are obtained by determining the type of a multi-valued object. In search *c*, the set of all errors for such a predicate name can be found with a single incorrect entity object.

5.2 Discussion

Some examples of repairs with predicate *nationality* are shown in Table 3. Most subjects have word similarity of repair and tail. The results of some samples about nationality are shown in Figure 6. For predicate *nationality*, there are a large number of different subjects for one incorrect object. Therefore, for triples with the same erroneous object, such subjects from triples are aggregated into a set, which can ignore the quantity of subjects. Incorrect triples are revised from the perspective of the object. For each pair of error object and repair, the correction similarity is calculated by harmonic correction similarity with different distance methods. In TCA framework, the confidence calculation component holds maximum similarity to filter corrections. The precision of repairs is focused on the interval of [0.3, 0.6], since the great majority of incorrect objects have few connections. In our

TABLE 2 Negative constraints of *nationality* in Dbpedia.

Items	Numbers	Rates (%)
<i>#triple</i>	150,332	
<i>#current_cor</i>	92,995	61.86
<i>#constr</i>	57,337	38.14
<i>conflict_type</i>	45,405	30.20
<i>conflict_feedback</i>	32,594	21.68

TABLE 3 Repairs examples.

Subject	Tail	Repair	Correction
Walter_Mignolo	Argentinians	Argentina	Argentina
Moirra_Gatens	Australians	Australia	Australia
Bobby_Noble	Canadian	Canada	Canada
Oisín_Kelly	Dublin	Australia; Belarus	Ireland
Jerry_Weyer	Luxembourgish	Germany; Luxembourg	Luxembourg

validation part, the precision of repairs is over 0.5, and these revised triples are regarded as final corrections.

In Figure 7, string similarity methods are leveraged to replace distance methods in harmony correction similarity. String similarity measures are extracted from two aspects, i.e., character-level measures and token-level measures. Nine repair examples are randomly used to validate the correction rates. Fourteen similarity measures are separated by their values. By the nature of repairs, TCA only focuses on the words, not the sentences. So, the results show the Qgram(2) and NGram(i), NormalizedLevenshtein has the better performance. Compared with word and string features, correction similarity is suitable to acquire repairs with word similarity.

Some similarity measures are used to compare these repairs in TCA, as shown in Figure 8. The mistaken entities have single values as the final correction. For multiple values as repairs, cross-similarity is proposed to discover final corrections. Distance similarity measures are leveraged to validate repairs, such as the longest common subsequence (LCS), Optimal String Alignment (OSA), and normalized Levenshtein distance (NLD). Compared to Dbpedia, the similarity of repairs in Wikidata focuses on word similarity. For a single erroneous triple, Jaro–Winkler similarity is used to validate repairs, and the revised correction has an interval with high precision. In the experiment, 2,000 negative entities were randomly selected to verify the TCA model. The best performance of cross-similarity is shown in Figure 8 and Eq. (7). So, cross-similarity is leveraged to filter final repairs in the EILC model. The final pairs of errors and corrections exhibit unique characteristics that have a high degree of word similarity. Here, multiple repairs indicate that some examples have over 90% similarity probability, i.e., Jaro–Winkler similarity.

The traditional measures, e.g., Mean_Raw_Rank, Precision, and Recall, are used to evaluate the effect of our correction model and to make comparisons with other classic algorithms. The bold value of **M** stands for Mean_Raw_Rank, explained in evaluation measures. And the

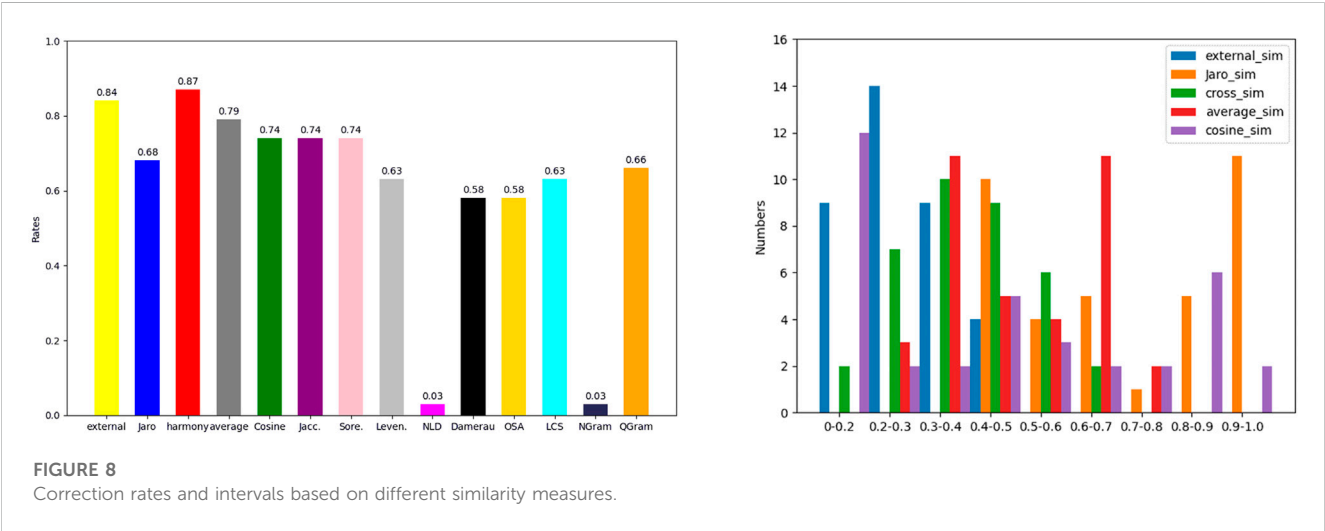
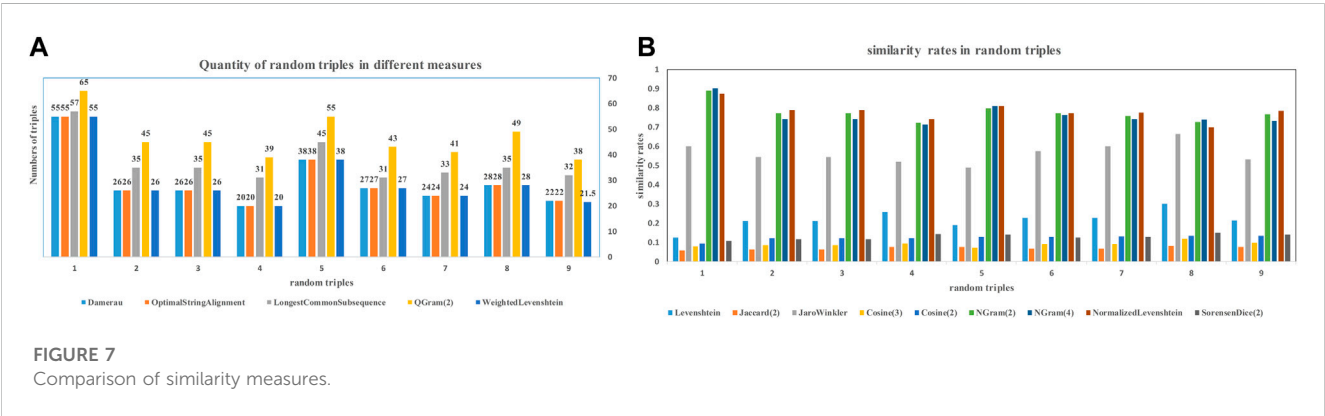
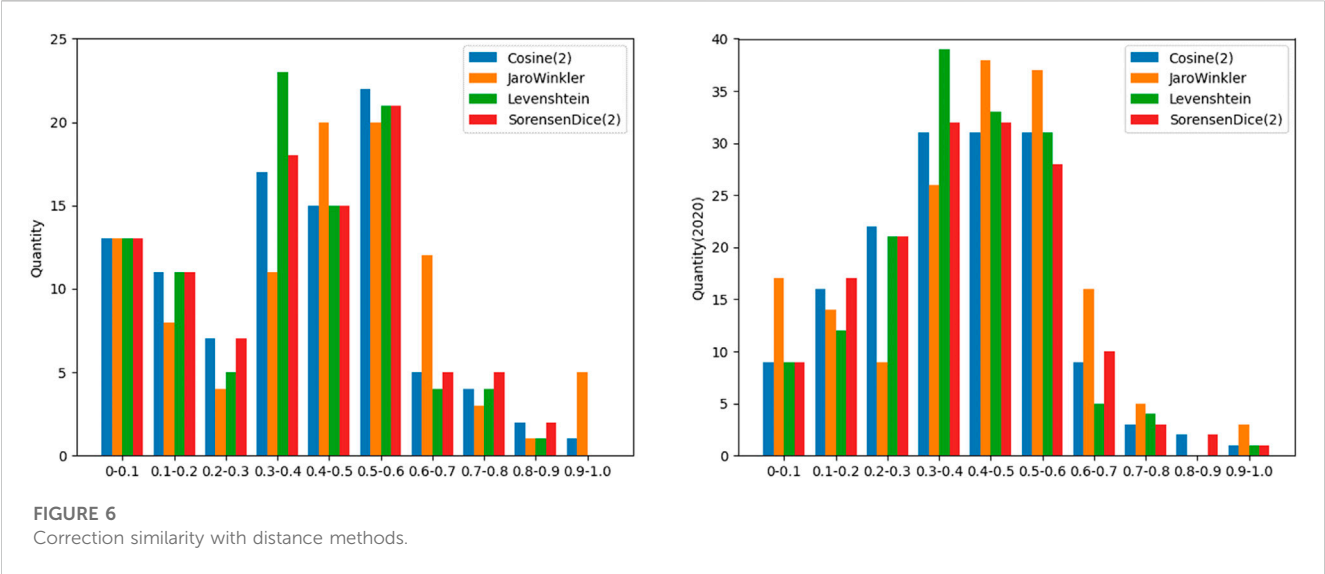


TABLE 4 Comparison of baseline methods.

Method	locationCountry			formerTeam			Employer			birthPlace		
	M	@1	@10	M	@1	@10	M	@1	@10	M	@1	@10
DBpedia lookup	0.02	1	3	0.06	6	6	0.07	6	10	0.04	3	5
WikiDisambiguates	0.04	3	4	0.04	3	4	0.04	3	7	0.11	8	18
TransE	0.19	11	37	0.02	1	1	0.00	0	3	0.24	20	35
AMIE+	0.42	40	43	0.06	6	6	0.00	0	0	0.01	1	1
Graph method	0.89	88	91	0.37	25	61	0.62	53	74	0.44	24	75
Keyword method	0.58	48	77	0.60	49	78	0.36	33	45	0.48	36	72
TCA	0.95	87	98	0.38	32	46	0.76	64	87	0.55	54	61

The bold value of **M** stands for Mean_Raw_Rank, explained in evaluation measures. And the @1 and @10 present the value of **precision @K**.

TABLE 5 Some examples overlapping type pair of entities.

DBpedia (predicate)	Wikidata (property)
dbo: locationCountry	P17(country); P27 (country of citizenship); P495 (country of origin)
dbo:formerTeam	P5138(season of club or team); P463(member of); P664(organizer)
dbo:employer	P108(employer); P127(owned by); P112(founded by); P123 (publisher)
dbo: birthPlace	P27 (country of citizenship); P495 (country of origin)

@1 and @10 present the value of **precision @K**. The comparison results are shown in Table 4 Our approach is compared to six baseline methods. Two are normally leveraged for entity search (DBpedia lookup and dbo: wikiPageDisambiguates) to find entities with the correct range type of predicate name and object. Two baseline methods were originally created for knowledge graph completion (TransE [70] and AMIE+ [49]) for finding the correct object from a given subject and a predicate name. Also, the graph method and keyword method [2] are leveraged to correct triples with range violations.

For positive examples in DBpedia and Wikidata, one example of overlapping type pair is $O_r(\text{dbo: locationCountry, country of citizenship}) = (\text{person, country})$. The negative triple follows the equation: $O_r(r_1, r_2) = (?a, \text{country})$. Here, ?a does not equal country. Following an overlapping type pair of entities, corresponding predicates are acquired from positive examples in target KBs. Predicate comparisons from DBpedia and Wikidata are explained in Table 5. By the comparisons, some properties are used to search the repairs from co-occurring similar subjects. For these type pairs, some predicate names in external KBs are acquired for correcting negative candidates.

Three evaluation measures are used to calculate the correct object provided for each method. It is evident that our model outperforms common algorithms for all training sets. One condition is that the incorrect object of an erroneous triple has a unique corresponding subject (e.g., locationCountry). TCA and graph methods work closely, since the pair of object and subject has more connections and the paths of triples contain more details. In another condition, one incorrect object has multiple subjects and a graph method. There is a lot of redundant and ambiguous information provided by the

graph algorithm with graph structure, which makes it impossible to find the correct object. In this condition (e.g., formerTeam), the keyword method is more effective because it takes advantage of external information from abstracts of triples, including subject and object. In order to be faster and more efficient in the algorithm, TCA explores knowledge correction methods from different perspectives.

TCA is more effective than other basic methods and the keyword method. For these basic methods, they can only correct some single error entity. To make up for such shortcomings and save time complexity, TCA is leveraged to correct range violations by using co-occurring similar entities. By making full utilization of other related knowledge bases for knowledge correction, it is beneficial to think about linked open data. The predefined paths are applied for hierarchy correction. The paths are derived from positive examples. In AMIE+, some paths can be provided by AMIE+. Not all predicates have a logical relationship, and hierarchical learning is very dependent on path information. The final result is close to AMIE+. After analysis of all methods, our proposed TCA model has better performance in base methods. If the source is not Wikipedia, or if the target is not DBpedia or YAGO, the original data sets need to do some changes. While the correction model is applied to other background knowledge bases, the training sets are changed to a triple formulation. All testing facts are transferred to $\langle \text{subject, predicate, object} \rangle$. Also, the corresponding knowledge is matched by the associated knowledge bases with the same conditions. Our correction algorithm is, indeed, applicable to Wikipedia-linked knowledge bases.

6 Conclusion

This paper proposed a TCA framework to detect abnormal information and correct negative statements that exist in Wikipedia automatically by co-occurring similar facts in external KBs. Based on ontology-aware substructures of triples, fixing extracted errors is a significant research topic for KB curation. Additionally, our framework is executed post factum, with no changes in the process of KB construction. Two new strategies are applied to search for negative candidates for cleaning KBs. One triple matching algorithm in TCA is proposed to correct erroneous information. Our compared experimental results show that TCA is effective over some baseline methods and widely applied in large knowledge bases. Our framework is straightforwardly adapted to detect erroneous knowledge on other KBs, such as YAGO and Freebase.

In the future, conflicting feedback facts or predictions can be used to refine the KBs. Also, our framework will focus on the search space of triples with other similar contents, such as the abstracts, the labels, and the derived peculiarities. Moreover, more features of similar facts with logic rules are detected in the hub research of knowledge base completion. In our next work plan, a neural network is added to explore more paths for searching for mistakes in KBs. Next, the number of associated knowledge bases can be expanded and the problem of completing large knowledge bases can be solved by associating and matching more effective information toward the goal of completing large KBs.

References

- Vrandečić D, Krötzsch M. Wikidata: A free collaborative knowledgebase. *Commun ACM* (2014) 57:78–85. doi:10.1145/2629489
- Auer S, Bizer C, Kobilarov G, Lehmann J, Cyganiak R, Ives Z. Dbpedia: A nucleus for a web of open data. *The semantic web*. Springer (2007). p. 722–35.
- Raimbault F, Ménier G, Marteau PF, et al. On the detection of inconsistencies in rdf data sets and their correction at ontological level (2011). p. 1–11. Available at: <https://hal.archives-ouvertes.fr/hal-00635854> (Oct 26, 2011).
- Zaveri A, Kontokostas D, Sherif MA, Böhmann L, Morsey M, Auer S, et al. User-driven quality evaluation of dbpedia. Proceedings of the 9th International Conference on Semantic Systems (2013). p. 97–104.
- Paulheim H, Bizer C. Type inference on noisy rdf data. *International semantic web conference*. (Springer) (2013). p. 510–25.
- Lertvittayakumjorn P, Kertkeidkachorn N, Ichise R. Resolving range violations in dbpedia. Joint international semantic technology conference. Springer (2017). p. 121–37.
- Dubey M, Banerjee D, Abdelkawi A, Lehmann J. Lc-quad 2.0: A large dataset for complex question answering over wikidata and dbpedia. Springer. Proceedings of the 18th International Semantic Web Conference (ISWC) (2019). p. 1–8.
- Rajpurkar P, Jia R, Liang P. "Know what you don't know: Unanswerable questions for squad," in Proceedings of the 56th annual meeting of the association for computational linguistics (short papers), Melbourne, Australia, July 15 - 20, 2018. arXiv preprint arXiv:1806.03822 (2018). p. 784–9.
- Ferrucci D, Brown E, Chu-Carroll J, Fan J, Gondek D, Kalyanpur AA, et al. Building watson: An overview of the deepqa project. *AI Mag* (2010) 31:59–79. doi:10.1609/aimag.v31i3.2303
- Suchanek FM, Kasneci G, Weikum G. Yago: A core of semantic knowledge. Proceedings of the 16th international conference on World Wide Web (2007). p. 697–706.
- Liu S, d'Aquin M, Motta E. Towards linked data fact validation through measuring consensus. Springer, Cham. Portoro, Slovenia: LDQ@ ESWC (2015). p. 21.
- Liu S, d'Aquin M, Motta E. Measuring accuracy of triples in knowledge graphs. *International conference on language, data and knowledge*. Springer (2017). p. 343–57.
- Borrego A, Ayala D, Hernández I, Rivero CR, Ruiz D. Generating rules to filter candidate triples for their correctness checking by knowledge graph completion techniques. Proceedings of the 10th International Conference on Knowledge Capture (2019). p. 115–22.

Data availability statement

The original contributions presented in the study are included in the article/Supplementary Material; further inquiries can be directed to the corresponding author.

Author contributions

YW and ZZ contributed to the design and implementation of the research, to the analysis of the results, and to the writing of the manuscript.

Conflict of interest

The authors declare that the research was conducted in the absence of any commercial or financial relationships that could be construed as a potential conflict of interest.

Publisher's note

All claims expressed in this article are solely those of the authors and do not necessarily represent those of their affiliated organizations, or those of the publisher, the editors, and the reviewers. Any product that may be evaluated in this article, or claim that may be made by its manufacturer, is not guaranteed or endorsed by the publisher.

- Wang H, Ren H, Leskovec J. Entity context and relational paths for knowledge graph completion. arXiv preprint arXiv:2002.06757 (2020).
- Wu Y, Chen J, Haxhidaui P, Venugopal VE, Theobald M. Guided inductive logic programming: Cleaning knowledge bases with iterative user feedback. *EPiC Ser Comput* (2020) 72:92–106.
- Melo A, Paulheim H. An approach to correction of erroneous links in knowledge graphs. *CEUR Workshop Proc (Rwth)* (2017) 2065:54–7.
- Chen J, Chen X, Horrocks I, B Myklebust E, Jimenez-Ruiz E. Correcting knowledge base assertions. Proceedings of The Web Conference (2020). p. 1537–47.
- Wu Y, Zhang Z, Wang G. Correcting large knowledge bases using guided inductive logic learning rules. *Pacific rim international conference on artificial intelligence*. Springer (2021). p. 556–71.
- Paulheim H. Identifying wrong links between datasets by multi-dimensional outlier detection. *WoDOOM* (2014) 27–38.
- Melo A, Paulheim H. Detection of relation assertion errors in knowledge graphs. Proceedings of the Knowledge Capture Conference (2017). p. 1–8.
- Zhang L, Wang W, Zhang Y. Privacy preserving association rule mining: Taxonomy, techniques, and metrics. *IEEE Access* (2019) 7:45032–47. doi:10.1109/access.2019.2908452
- Fan W, Geerts F. *Foundations of data quality management*. Springer, Cham: Morgan and Claypool Publishers (2012). doi:10.1007/978-3-031-01892-3
- Galarraga LA, Teflioudi C, Hose K, Suchanek F. "Amie: Association rule mining under incomplete evidence in ontological knowledge bases," in WWW '13: Proceedings of the 22nd international conference on World Wide Web. Rio de Janeiro, Brazil: WWW (2013). p. 413–22. doi:10.1145/2488388.2488425
- Zeng Q, Patel JM, Page D. QuickFOIL: Scalable inductive logic programming. *PVLDB* (2014) 8:197–208. doi:10.14778/2735508.2735510
- Rantsoudis C, Feuillade G, Herzig A. "Repairing aboxes through active integrity constraints. 30th international workshop on description logics (DL 2017)," in 30th international workshop on description logics (DL workshop 2017), 18 July 2017 - 21 July 2017. Montpellier, France: CEUR-WS: Workshop proceedings (2017). p. 1–13. <https://oatao.univ-toulouse.fr/22739/>.
- Paulheim H, Bizer C. Improving the quality of linked data using statistical distributions. *Int J Semantic Web Inf Syst (Ijswis)* (2014) 10:63–86. doi:10.4018/ijswis.2014040104

27. Liang J, Xiao Y, Zhang Y, Hwang SW, Wang H. "Graph-based wrong isa relation detection in a large-scale lexical taxonomy," In Proceedings of the thirty-first AAAI conference on artificial intelligence. San Francisco California USA (2017). p. 1–6. doi:10.1609/aaai.v31i1.10676
28. Manago M, Kodratoff Y. Noise and knowledge acquisition. *IJCAI* (1987) 348–54.
29. Lertvittayakumjorn P, Kertkeidkachorn N, Ichise R. Correcting range violation errors in dbpedia. *International semantic web conference*. Kobe, Japan. (Springer): Posters, Demos and Industry Tracks (2017). p. 1–4. <https://ceur-ws.org/Vol-1963/>.
30. Abedini F, Keyvanpour MR, Menhaj MB. Correction tower: A general embedding method of the error recognition for the knowledge graph correction. *Int J Pattern Recognition Artif Intelligence* (2020) 34:2059034. doi:10.1142/s021800142059034x
31. Bordes A, Usunier N, Garcia-Duran A, Weston J, Yakhnenko O. Translating embeddings for modeling multi-relational data. *Adv Neural Inf Process Syst* (2013) 26.
32. Nickel M, Trespe V, Kriegl HP. A three-way model for collective learning on multi-relational data. *ICML* (2011) 1–8.
33. Wang Z, Zhang J, Feng J, Chen Z. Knowledge graph embedding by translating on hyperplanes. *Proc AAAI Conf Artif Intelligence* (2014) 28:1112–9. doi:10.1609/aaai.v28i1.8870
34. Xiao H, Huang M, Hao Y, Zhu X. "Transg: A generative mixture model for knowledge graph embedding," in Proceedings of the 54th annual meeting of the association for computational linguistics (Germany) (2015). p. 2316–25. doi:10.48550/arXiv.1509.05488
35. Yang B, Yih WT, He X, Gao J, Deng L. "Embedding entities and relations for learning and inference in knowledge bases. Proceedings of the international conference on learning representations. San Diego, CA, USA: ICLR (2014). p. 1–13. doi:10.48550/arXiv.1412.6575
36. Nickel M, Rosasco L, Poggio T. Holographic embeddings of knowledge graphs. *Proc AAAI Conf Artif Intelligence* (2016) 30:1955–61. doi:10.1609/aaai.v30i1.10314
37. Shi B, Weninger T. Proje: Embedding projection for knowledge graph completion. *Proc AAAI Conf Artif Intelligence* (2017) 31:1236–42. doi:10.1609/aaai.v31i1.10677
38. Bader J, Scott A, Pradel M, Chandra S. Getafix: Learning to fix bugs automatically. *Proc ACM Programming Languages* (2019) 3:1–27. doi:10.1145/3360585
39. Mahdavi M, Baran AZ. Effective error correction via a unified context representation and transfer learning. *Proc VLDB Endowment* (2020) 13:1948–61.
40. Pellissier Tanon T, Suchanek F. *Neural knowledge base repairs*. European Semantic Web Conference (Springer) (2021). p. 287–303.
41. Mahdavi M, Abedjan Z, Castro Fernandez R, Madden S, Ouzzani M, Stonebraker M, et al. Raha: A configuration-free error detection system. Proceedings of the 2019 International Conference on Management of Data (2019). p. 865–82.
42. Zhao Y, Hou J, Yu Z, Zhang Y, Li Q. Confidence-aware embedding for knowledge graph entity typing. *Complexity* (2021) 2021:1–8. doi:10.1155/2021/3473849
43. Chen J, Jiménez-Ruiz E, Horrocks I, Chen X, Myklebust EB. *An assertion and alignment correction framework for large scale knowledge bases*. Semantic Web Prepress, IOS Press (2021). p. 1–25. doi:10.3233/SW-210448
44. Arnaout H, Tran TK, Stepanova D, Gad-Elrab MH, Razniewski S, Weikum G. Utilizing language model probes for knowledge graph repair. *Wiki Workshop* (2022) 2022:1–8.
45. Petroni F, Rocktäschel T, Lewis P, Bakhtin A, Wu Y, Miller AH, et al. "Language models as knowledge bases?," In Proceedings of the 2019 conference on empirical methods in natural language processing and the 9th international joint conference on natural language processing (EMNLP-IJCNLP). Hong Kong, China: Association for Computational Linguistics (2019). p. 2463–73. doi:10.18653/v1/D19-1250
46. Lehmann J, Böhmann L. Ore-a tool for repairing and enriching knowledge bases. *International semantic web conference*. Springer (2010). p. 177–93.
47. Knuth M, Hercher J, Sack H. "Collaboratively patching linked data," In Proceedings of 2nd international workshop on usage analysis and the web of data (USEWOD 2012) p. 1–6. doi:10.48550/arXiv.1204.2715
48. Ma Y, Qi G. *An analysis of data quality in dbpedia and zhishi. me*. China Semantic Web Symposium and Web Science Conference. Springer (2013). p. 106–17.
49. Lajus J, Galárraga L, Suchanek F. *Fast and exact rule mining with amie 3*. European Semantic Web Conference. Springer (2020). p. 36–52.
50. Chu X, Morcos J, Ilyas IF, Ouzzani M, Papotti P, Tang N, et al. Katara: Reliable data cleaning with knowledge bases and crowdsourcing. *Proc VLDB Endowment* (2015) 8:1952–5. doi:10.14778/2824032.2824109
51. Krishnan S, Franklin MJ, Goldberg K, Wang J, Wu E. Activeclean: An interactive data cleaning framework for modern machine learning. Proceedings of the 2016 International Conference on Management of Data (2016). p. 2117–20.
52. Rekatsinas T, Chu X, Ilyas IF, Holoclean RC. Holistic data repairs with probabilistic inference. *Proc. VLDB Endow.* (2017) 10(11):1190–201. arXiv preprint arXiv:1702.00820.
53. Krishnan S, Franklin MJ, Goldberg K, Wu E. *Boostclean: Automated error detection and repair for machine learning*. arXiv preprint arXiv:1711.01299 (2017).
54. De Melo G. *Not quite the same: Identity constraints for the web of linked data*. Twenty-Seventh AAAI Conference on Artificial Intelligence (2013). p. 1092–8.
55. Ngonga Ngomo AC, Sherif MA, Lyko K. Unsupervised link discovery through knowledge base repair. *European semantic web conference*. Springer (2014). p. 380–94.
56. Domingue J, Fensel D, Hendler JA. *Handbook of semantic web technologies*. Springer Science and Business Media (2011).
57. Wang Y, Ma F, Gao J. Efficient knowledge graph validation via cross-graph representation learning. Proceedings of the 29th ACM International Conference on Information and Knowledge Management (2020), 1595–604.
58. Vargas SGJ. *A knowledge-based information extraction prototype for data-rich documents in the information technology domain*. [Dissertation/master's thesis]. Columbia: National University (2008).
59. Wang Y, Qin J, Wang W. Efficient approximate entity matching using jaro-winkler distance. *International conference on web information systems engineering*. Springer (2017). p. 231–9.
60. Cui Z, Kapanipathi P, Talamadupula K, Gao T, Ji Q. "Type-augmented relation prediction in knowledge graphs," in The thirty-fifth AAAI conference on artificial intelligence (AAAI-21). Vancouver, Canada (2020). doi:10.1609/aaai.v35i8.16879
61. Dimou A, Kontokostas D, Freudenberg M, Verborgh R, Lehmann J, Mannens E, et al. *International semantic web conference*. Springer (2015). p. 133–49. Assessing and refining mappings to rdf to improve dataset quality
62. Fiorentino A, Zangari J, Darling MM. DaRLing: A datalog rewriter for owl 2 RL ontological reasoning under SPARQL queries. *Theor Pract Logic Programming* (2020) 20:958–73. doi:10.1017/s1471068420000204
63. Leacock C, Chodorow M. Combining local context and wordnet similarity for word sense identification. *WordNet: Electron lexical database* (1998) 49: 265–83.
64. Zhang K, Yao Y, Xie R, Han X, Liu Z, Lin F, et al. Open hierarchical relation extraction. Proceedings of the 2021 Conference of the North American Chapter of the Association for Computational Linguistics: Human Language Technologies (2021). p. 5682–93.
65. Weinberger KQ, Chapelle O. Large margin taxonomy embedding for document categorization. *Adv Neural Inf Process Syst* (2009) 1737–44.
66. Xie R, Liu Z, Sun M, et al. Representation learning of knowledge graphs with hierarchical types. *IJCAI* (2016) 2965–71.
67. Toba H, Ming ZY, Adriani M, Chua TS. Discovering high quality answers in community question answering archives using a hierarchy of classifiers. *Inf Sci* (2014) 261:101–15. doi:10.1016/j.ins.2013.10.030
68. Han X, Yu P, Liu Z, Sun M, Li P. Hierarchical relation extraction with coarse-to-fine grained attention. Proceedings of the 2018 Conference on Empirical Methods in Natural Language Processing (2018). p. 2236–45.
69. Zhang N, Deng S, Sun Z, Wang G, Chen X, Zhang W, et al. "Long-tail relation extraction via knowledge graph embeddings and graph convolution networks," In Proceedings of the 2019 conference of the north american chapter of the association for computational linguistics: Human language technologies, Volume 1 (Long and Short Papers). Minneapolis, Minnesota: Association for Computational Linguistics (2019). p. 3016–25. doi:10.18653/v1/N19-1306
70. Lin Y, Liu Z, Sun M, Liu Y, Zhu X. *Learning entity and relation embeddings for knowledge graph completion*. Twenty-ninth AAAI conference on artificial intelligence (2015). p. 1–7.



OPEN ACCESS

EDITED BY

Leilei Chen,
Huanghuai University, China

REVIEWED BY

Shanju Yang,
Northwest A&F University, China
Lingling Chen,
Northwestern Polytechnical University,
China

*CORRESPONDENCE

Chen Xu,
✉ chenxu@whut.edu.cn

SPECIALTY SECTION

This article was submitted to Statistical
and Computational Physics,
a section of the journal
Frontiers in Physics

RECEIVED 29 January 2023

ACCEPTED 14 February 2023

PUBLISHED 24 February 2023

CITATION

Zhao Y, Xu C, Zheng Z, Hu X and Mao Y
(2023), Experimental study of the
parameter effects on the flow and noise
characteristics for a contra-rotating
axial fan.
Front. Phys. 11:1153380.
doi: 10.3389/fphy.2023.1153380

COPYRIGHT

© 2023 Zhao, Xu, Zheng, Hu and Mao.
This is an open-access article distributed
under the terms of the [Creative
Commons Attribution License \(CC BY\)](#).
The use, distribution or reproduction in
other forums is permitted, provided the
original author(s) and the copyright
owner(s) are credited and that the original
publication in this journal is cited, in
accordance with accepted academic
practice. No use, distribution or
reproduction is permitted which does not
comply with these terms.

Experimental study of the parameter effects on the flow and noise characteristics for a contra-rotating axial fan

Yanjie Zhao¹, Chen Xu^{2*}, Zhiwei Zheng³, Xiaowen Hu⁴ and
Yijun Mao¹

¹School of Aerospace Engineering, Huazhong University of Science and Technology, Wuhan, China,

²School of Naval Architecture, Ocean and Energy Power Engineering, Wuhan University of Technology,
Wuhan, China, ³Foshan Shunde Midea Washing Appliances Mfg. Co., Ltd., Foshan, China, ⁴Corporate
Research Center, Midea Group, Foshan, China

Introduction: In the present paper, experiments for a contra-rotating axial fan have been conducted to investigate the influences of the fan parameters including axial distance, blade number, blade pattern and blade thickness on the performance and noise characteristics under variable rotational speed regulation.

Methods: The characteristic curves and spectrum characteristics of the contra-rotating axial fan with different structural configurations are compared and analyzed. Moreover, the spectrum density of the velocity obtained from the experiment is compared with the classic turbulence models.

Results: The results show the characteristic curves of the shaft power and the sound pressure level (SPL) are nearly identical, which indicates the axial distance and blade number are not sensible factors for the contra-rotating axial fan under variable rotational speed regulation. The blade profiles of the fan have an impact on the characteristic curves of the SPL and the shaft power curves of the fan decrease evidently with increase of the blade thickness, while the shaft power curves are very close with different blade patterns.

Discussion: In general, the blade profiles are sensible factors for the contra-rotating axial fan under variable rotational speed regulation. Through the SPL spectrum analysis of the contra-rotating axial fan with different blade profile, it can be concluded that the blade profile of the rotors has an obvious impact on the broadband noise characteristics under moderate and high frequency range.

KEYWORDS

contra-rotating axial fan, acoustic noise, fan configuration, experimental study, spectrum analysis

Abbreviations: BPF, blade passing frequency; SPL, sound pressure level.

1 Introduction

Contra-rotating axial fans have been widely applied in the ventilation and air conditioning systems for its merits of the compact size and high pressure rise. Generally, a contra-rotating axial fan is composed of two rotors that rotate in opposite directions with a casing enclosing them. Compared with the traditional fans, the contra-rotating axial fan has the advantage of high efficiency, while with the disadvantage of high noise level. In recent years, many experimental and numerical works have been performed by researchers focusing on contra-rotating fans [1–9].

Compared to fans with a single rotor, the axial spacing of rotors as well as the mounting position for contra-rotating fans has significant impact on the flow and noise characteristics. Roy et al [10] designed a contra-rotating fan unit and tested the flow behavior to improve the performance and to develop an effective design principle. The study found that the contra-rotating unit could enhance the overall stall margins and that at different axial distance between two rotors the performance characteristics varied by 7% at most. In addition, the best performance was observed when the axial distance of two rotors was equal to around 50% of the first rotor chord. Shigemitsu et al [11] developed a high speed contra-rotating axial fan and investigated the performance and the internal flow conditions by experimental and numerical methods. They discussed the influences of the axial distance on the performance and the noise characteristics and illustrated the interaction of the flow field between the rotors. Nouri et al [12] conducted an experimental investigation on the inverse design method of contra-rotating axial fans and the effects of varying the axial distance and rotational speed ratios on the overall performance were analyzed. Mao et al [13] investigated the effects of axial distance on the performance of a contra-rotating axial fan by unsteady numerical simulation. The results suggested that the unsteady effects dominated the flow behavior at smaller axial spacing ranges, while the variation of aerodynamic force for two rotors was different as the axial spacing increased. Sun et al [14] designed a contra-rotating fan for mine ventilation and analyzed the performance and flow characteristics under different speed combinations. The results showed that depending on the flow rate and the resistance of the pipe network, variable speed operation of two rotors expanded the stable working range. In addition, Chen et al [15] conducted experimental and numerical investigations on the performance and detailed flow structure of a contra-rotating fan under different rotational speed ratios. Ravelet et al [16] designed three contra-rotating stages with different rotational speed ratios, mean stagger angles of blades and repartitions of blade loads between two rotors to study the global characteristics and the unsteady features of the flow. Luan et al [17] studied the acoustic and vibration effects of the axial spacing based on the experimental analysis and numerical calculation. Ai et al [18] performed experimental studies on the rotational speed matching of two rotors and analyzed its impact on the stable margin and efficient working range.

As is the case in traditional fans, geometric parameters of the rotor have great impact on the flow and noise in contra-rotating axial fans. Joly et al [19] utilized a multidisciplinary optimization methodology to design a low-weight and high-load contra-rotating fan. Cao et al [20] employed the model of forced vortex and free

vortex, in which the real inflow velocity distribution of downstream rotor was considered, to improve the performance and optimize the flow field. Mohammadi et al [21] optimized the blade thickness of a ducted contra-rotating axial flow fan and studied the flow characteristics inside it by numerical simulation. They compared the flow behavior and obtained the characteristic map under the optimum blade thickness. Additionally, the influences of different rotational speed ratios and axial gaps of the contra-rotating fan were also investigated in the paper. Xu et al [22] studied the tip clearance flow and associated loss mechanism of a contra-rotating axial fan and compared the stage efficiency and pressure loss coefficient with different tip clearance based on unsteady numerical simulation. The results indicated that on the same tip clearance variation, the efficiency of the downstream rotor decreased more dramatically than that of the upstream rotor, though the contra-rotating fan efficiency almost linearly changed with tip clearance variation. Wang et al [23] investigated the effects of tip clearance on the performance and found isentropic efficiency and stable operating range decreased with increasing tip clearance size. Furthermore, the negative effect on the performance of the upstream rotor was greater than that of the downstream rotor. Grasso et al [24] presented a multi-objective efficiency-noise optimization approach of the blades of a contra-rotating fan on the basis of artificial neural networks by means of RANS-based hybrid methods that split the description of the flow field from the quantification of the source of noise and of its propagation. Wang et al [25] applied the perforated trailing-edge for the upstream rotor and perforated leading-edge for the downstream rotor of a contra-rotating fan and obtained an overall noise reduction of 6–7 dB with similar aerodynamic characteristics.

Most of the previous investigations on the contra-rotating axial fan focus on the flow and noise characteristics under design point and off-design points at the fixed rotational speed, while in some circumstances, variable rotational speed regulation of the contra-rotating fan is the only practical approach to satisfy the requirement of air quantity. Despite a great deal of research on contra-rotating axial fans, there have been few experimental studies carried out to investigate the influence of the contra-rotating fan parameters on the performance and noise characteristics of the contra-rotating axial fan under variable rotational speed regulation. In the present paper, an experimental study on the performance and noise characteristics of a contra-rotating axial fan under variable rotational speed regulation has been conducted to analyze the influence of the fan parameters. The remainder of this paper is organized as follows. In [section 2](#), the schematics and dimensions of the contra-rotating axial fan model are introduced and the parametric fan configurations are illustrated in detail. [Section 3](#) describes the test rig setup for the contra-rotating fan performance and noise characteristics, as well as the outlet velocity of the main flow region. [Section 4](#) analyzes the tonal noise characteristics of the contra-rotating fan under different rotational speeds and compares the obtained energy spectrum characteristics from experiments with that from classic models. In [section 5](#), the performance and noise characteristics of the contra-rotating axial fan under variable rotational speed regulation are obtained, and on the basis of which the influences of the fan configurations are compared and analyzed. [Section 6](#) draws conclusions.

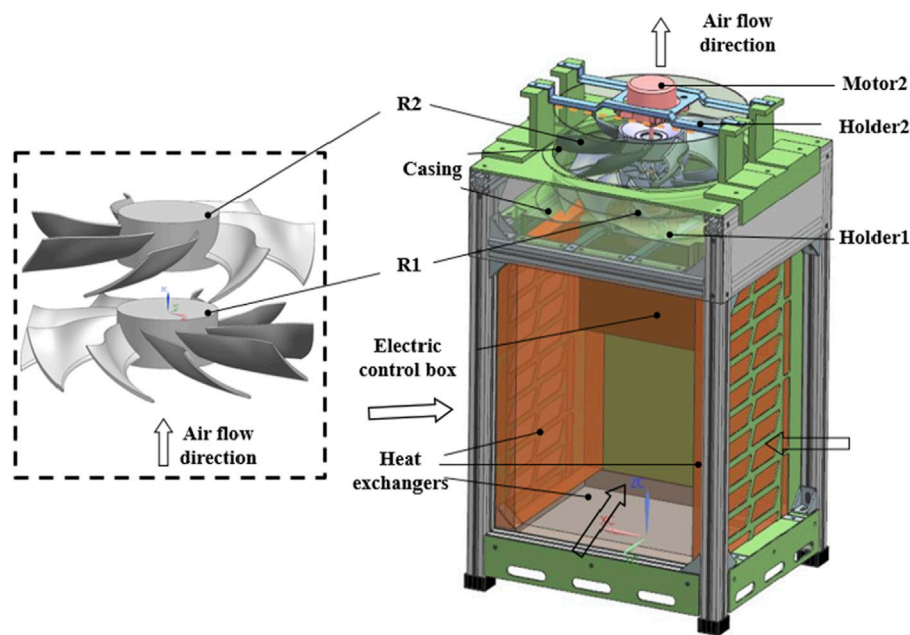


FIGURE 1
Model of the studied contra-rotating axial fan in the apparatus.

2 Tested models

2.1 The studied contra-rotating axial fan

The present investigation is based on a contra-rotating axial fan installed in the air conditioning system due to the high energy efficiency. Figure 1 illustrates the configuration of the contra-rotation axial fan used in this study, which is applied in an outdoor unit of central air conditioner with an overall dimension of $920 \text{ mm}^3 \times 640 \text{ mm}^3 \times 600 \text{ mm}^3$. The air enters the fan after passing by the three heat exchangers located on the side wall brackets and the electric control box is located on the other side. The air exits from the top side where the axial flow fans are located. The two rotors are fixed by the support brackets and electric motors.

The normal volume flow rate for the outdoor unit is around $2,750 \text{ m}^3/\text{h}$, and the two rotors rotate at the same speed and to the opposite directions. The diameter of two rotors are 350 mm with a tip clearance of around 5 mm and a hub to tip ratio of 0.35. The tip axial chord length of R2 is slightly smaller than that of R1.

2.2 Parametric scheme of contra-rotating axial fan

The contra-rotating axial fan consists of two rotors, and the fan structural parameters such as axial spacing and the blade parameters including the blade number and blade profile have an impact on the performance and noise characteristics.

The axial distance between the upstream rotor and downstream rotor significantly affects the performance and the noise characteristics, as well as the flow field, under the fixed rotational speed [1, 13]. In the present paper, the influence of the axial positions of the two rotors on

the performance and noise characteristics of the contra-rotating axial fan under variable rotational speed regulation is also studied. Three schemes with different axial positions of the two rotors are implemented to compare the flow and noise characteristics under variable rotational speed regulation in the experiment. Scheme A represents the original fan with the axial distance of 30 mm. In scheme B, the position of the upstream rotor is fixed and the axial shift of downstream rotor is about 7 mm toward the outlet. In scheme C, the two rotors of the fan are both shifted by 7 mm toward the outlet direction, keeping the axial distance between the two rotors unchanged.

In the present paper, three combinations of blade number for two rotors of the contra-rotating axial fan have been employed to study its influence on the performance and noise characteristics. The scheme 1 is consisted of nine blades for rotor 1 and 7 blades for rotor 2. For scheme 2 and 3, there are both 5 blades for rotor 2, while the blades for rotor 1 respectively are nine and 7.

Apart from the structural parameters of the fan and the rotor, the blade profile such as the blade pattern and thickness, also has a notable impact on the fan performance and noise, as is the case in the rotor-stator blade rows [19, 21]. To study the effect of the blade profile on the flow and noise characteristics of the contra-rotating axial fan, models with three blade pattern and four blade thickness are applied in the present experiment. Figure 2 shows three different distribution models of blade pattern and blade thickness. In the Figure 2, convex, straight and concave represent the three different blade pattern models, and T5, T10, T15, and T20 represent the four blade thickness models.

3 Experimental facilities

To study the aerodynamic and noise characteristics of the contra-rotating axial fan, the experimental measurement setups

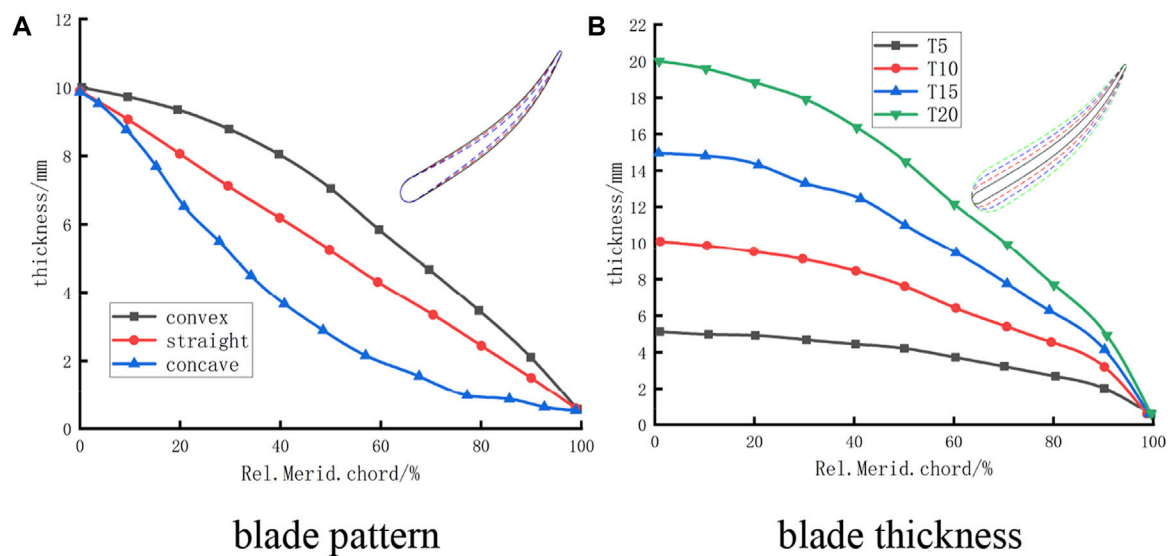


FIGURE 2
Distribution of blade pattern and blade thickness: (A) blade pattern; (B) blade thickness.

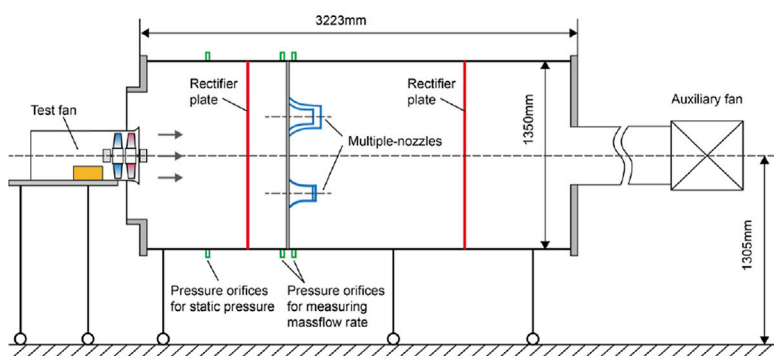
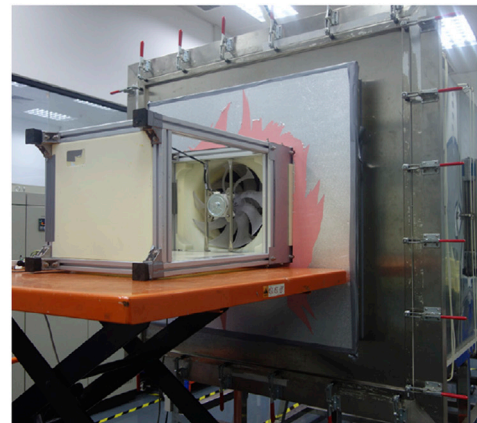


FIGURE 3
Schematic and photograph of the performance test rig.



for the performance and noise characteristics have been performed in Midea Corporate Research Center. Besides, the local velocity of the main flow region downstream the outlet of the contra-rotating fan has also been measured to obtain the energy spectrum characteristics of the main flow field.

Figure 3 shows the schematic and photograph of the performance test rig, which has been built according to the Chinese National Standard GB/T7725-2004 and GB/T1236-2000 for the industrial fan performance testing. The volume flow rate which ranges from 500–5,000 m³/h is calculated according to the pressure difference between the upstream and downstream of the multi-nozzles. The uncertainties of the pressure and airflow rate are 0.15 Pa and 0.004 m³/h, respectively. As shown in Figure 3, the outlet of the contra-

rotating axial fan faces toward the test rig, and the three inlet sides of the model should be unobstructed. Pressure orifice 1 is set to measure the static pressure, while pressure orifices 2 and 3 are set to measure the flow rate. The rotational speed of the motor is regulated by a SIMENS MicroMaster frequency converter and measured by a photoelectric digital tachometer. The shaft power is measured by two AC power meters.

The aeroacoustics test has been carried out in a semi-anechoic chamber in Midea Corporate Research Center. The size of the semi-anechoic chamber is 9.6 m long by 5.2 m wide by 3.9 m high and the inside surfaces are lined with mineral wool wedges of 69 cm deep. Figure 4 illustrates the schematic and photograph of the noise test rig, which has been built based on the Chinese National Standard GB/T17758. Four sampling points of

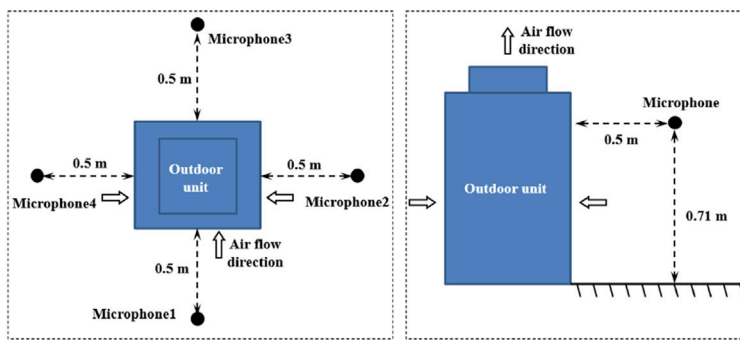


FIGURE 4
Schematic and photograph of the noise test rig.

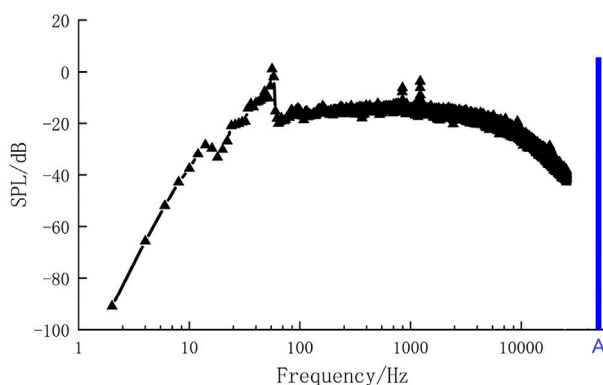


FIGURE 5
SPL spectrum of the background noise.

the noise spectra around the contra-rotating axial fan have been sampled in a semi-anechoic chamber and four microphones are arranged on the four sides of the fan to test the noise characteristics. The height between the measuring points and the ground is 0.71 m, and the distance of the measuring points from the model is 0.5 m.

During the noise test, PCB microphones and preamplifiers, combined with LMS data acquisition system SCADAS Mobile SCM01, are implemented to proceed the measurement and data acquisition of the noise signals. The data acquisition frequency is 10 kHz and the acquisition time is 15 s at each sampling.

To obtain the energy spectrum characteristics of the main flow region downstream the contra-rotating axial fan, the outlet velocity of the main flow field has been measured *via* the hotwire anemometer. The sampling point is located at 50% span of the rotor 2 outlet and 80% of the tip axial chord length downstream the rear rotor trailing edge opposite the side of the electric control box. The acquisition frequency is 32 kHz and the acquisition time is 32 s for the experimental sampling.

4 Noise and flow characteristics of the contra-rotating axial fan

4.1 Background noise

Figure 5 gives a typical SPL spectrum of the background noise in the hemi-anechoic chamber, and the overall A-weighted SPL of the background noise is around 17.6 dB, which is much lower than the studied fan noise level. In consequence, the effect of the background noise on the noise experiments of the contra-rotating axial fan in the hemi-anechoic chamber in Midea Corporate Research Center is rather negligible.

4.2 SPL comparison of four measuring points

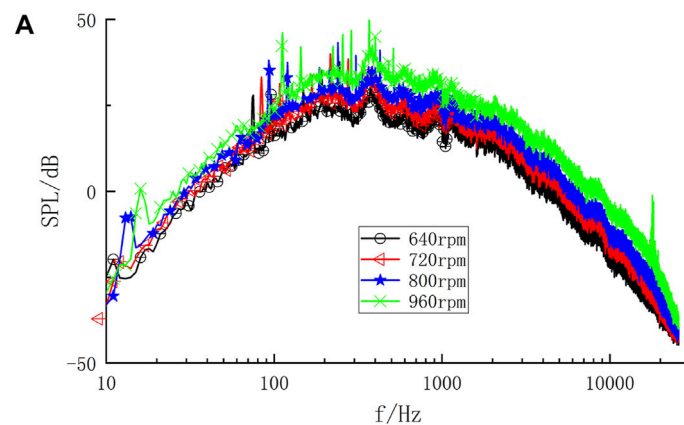
As demonstrated in the previous section, four PCB microphones are arranged on the four sides of the fan unit to test the sound pressure level. Table 1 compares the sound pressure levels at four measuring points, and the results indicate that the overall sound pressure levels of the contra-rotating fan are nearly independent of the circumferential angle, thus the noise feature at only one sampling point is analyzed in the following text. Therefore, in the following investigation, the noise data obtained from Microphone1 is applied.

4.3 Noise characteristics of the contra-rotating axial fan

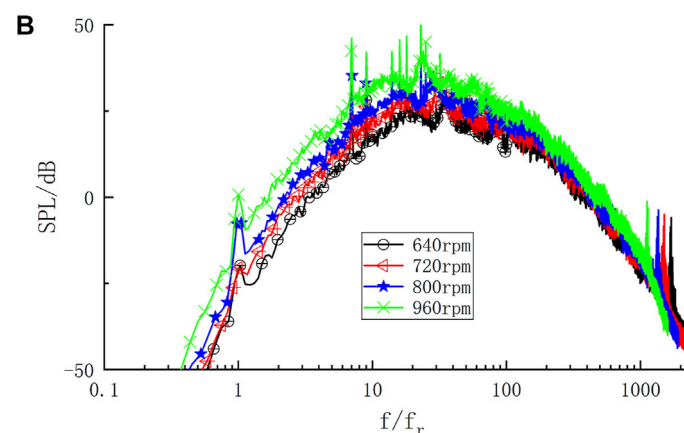
The SPL spectra of the model with nine blades for rotor 1 and 7 blades for rotor 2 under different frequencies at different rotational speeds is shown in Figures 6A, B, the frequency is non-dimensionalized by the rotational frequency. It can be seen in Figure 6A, the broadband noise components of the SPL spectra from 100 Hz to 1,000 Hz show the highest value under different rotational speeds. From Figure 6B, the first peak of the SPL under non-dimensional frequency of 1 at different rotational speeds

TABLE 1 A-weighted SPL of four measuring points at different rotational speeds.

(rpm)	Mircophone1/0° (dB)	Mircophone2/90° (dB)	Mircophone3/180° (dB)	Mircophone4/270° (dB)
640	55.03	54.69	54.91	55.19
720	57.39	57.11	56.92	57.25
800	60.78	60.39	60.21	60.57
960	65.53	65.16	64.99	65.37



SPL spectrum under different frequencies



SPL spectrum under nondimensionalized frequencies by the rotational frequency

FIGURE 6

SPL spectrum of the contra-rotating axial fan at different rotational speeds: (A) original SPL spectrum; (B) nondimensional SPL spectrum.

appears, and the following peaks of the SPL at different rotational speeds all appear under the blade passing frequency of rotor 1 and rotor 2 and their harmonic. It then can be concluded that the primary tonal noise is probably caused by the electric box and by the interaction of two blade rows. It also can be seen that with the increase of the rotational speed of the fan, the tonal noise at the blade passing frequency and its harmonic, as well as the tonal noise at the rotational frequency, becomes higher. Besides, the noise peak value at around 18,000 Hz in Figure 6A is probably generated from the

frequency converter, which remains unchanged at different rotational speeds.

Figure 7 shows the non-linear fitting of the tonal SPL for fundamental frequency of rotor 1 and rotor 2 under different rotational speeds. From Figure 7, it can be obtained that the expressions of the fitted curve for fundamental frequency of rotor 1 and rotor 2 are as follows,

$$SPL_{f_{r1}} = 89.95 \lg n - 225.8 \quad (1)$$

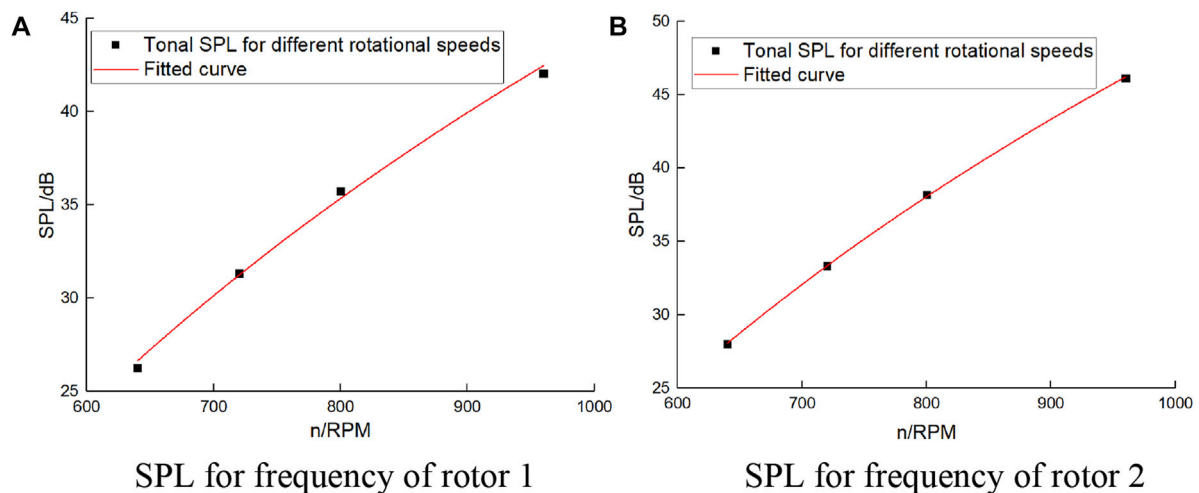


FIGURE 7
Tonal SPL for fundamental frequency of rotor 1 and rotor 2: (A) SPL for rotor 1; (B) SPL for rotor 2.

$$SPL_{f_{r2}} = 103.05 \lg n - 261.09 \quad (2)$$

where n represents the rotational speed of the fan.

The expression of SPL is as following,

$$SPL = 20 \lg \frac{P}{P_{ref}} \quad (3)$$

where P represents the sound pressure and P_{ref} represents reference sound pressure, which is 2×10^{-5} Pa.

It then can be concluded that

$$P_{f_{r1}} \propto U^{4.55} \quad (4)$$

$$P_{f_{r2}} \propto U^{5.15} \quad (5)$$

where U represents the characteristic velocity and is proportionate to the rotational speed n .

With the increase of the rotational speed of the fan, the tonal noise at the blade passing frequency and its harmonic becomes higher, which indicates the interaction of the blade rows grows intense. Based on the analysis above, the SPL of the tonal noise under fundamental frequency of rotor 1 and rotor 2 can be predicted under different rotational speeds.

4.4 Flow characteristics of the contra-rotating axial fan

The accuracy of computing the fan broadband noise, in a very large part, relies on the accuracy of the flow characteristics, thus the adequacy of the turbulence model is one of the principal elements for the accurate simulation of broadband noise. The flow in the simulation of the fan is commonly assumed as isotropic turbulence, for which the Liepmann and von Karman models are the most popular models.

The Liepmann model based on the exponential law assumption of turbulence longitudinal correlation coefficient

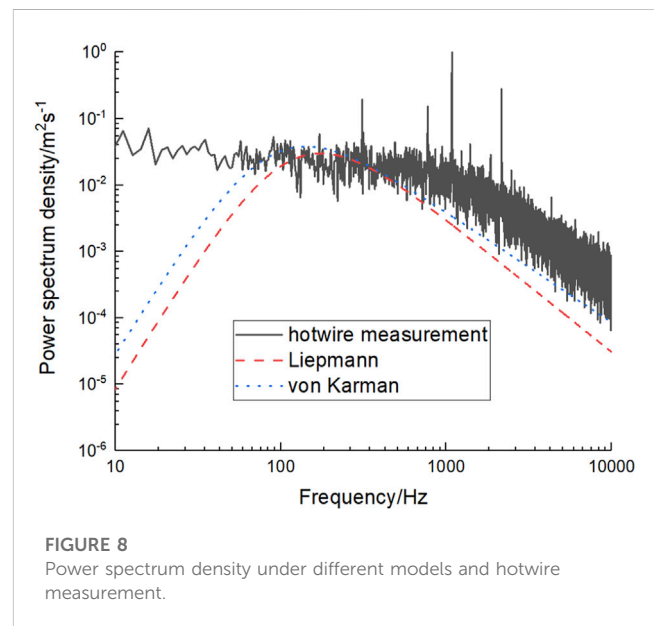


FIGURE 8
Power spectrum density under different models and hotwire measurement.

presents the expression of the three-dimensional energy spectrum as following,

$$E_L(k) = \frac{8u_{rms}^2 \Lambda^5}{\pi} \frac{k^4}{(1 + \Lambda^2 k^2)^3} \quad (6)$$

where $E(k)$ is the three-dimensional energy spectrum, k represents the wave number and Λ represents the turbulence integral scale, and u_{rms} is the root mean square turbulence velocity. For the large eddies with most of the turbulence energy, the Liepmann model shows the law of k^4 well, while for the inertial subrange, it shows the law of k^{-2} which has a discrepancy from the $-5/3$ exponential law presented in experiments.

The von Karman model, which is presented in the following, exhibits similar feature for the range of large eddies, while for the inertial subrange, it shows the $-5/3$ exponential law.

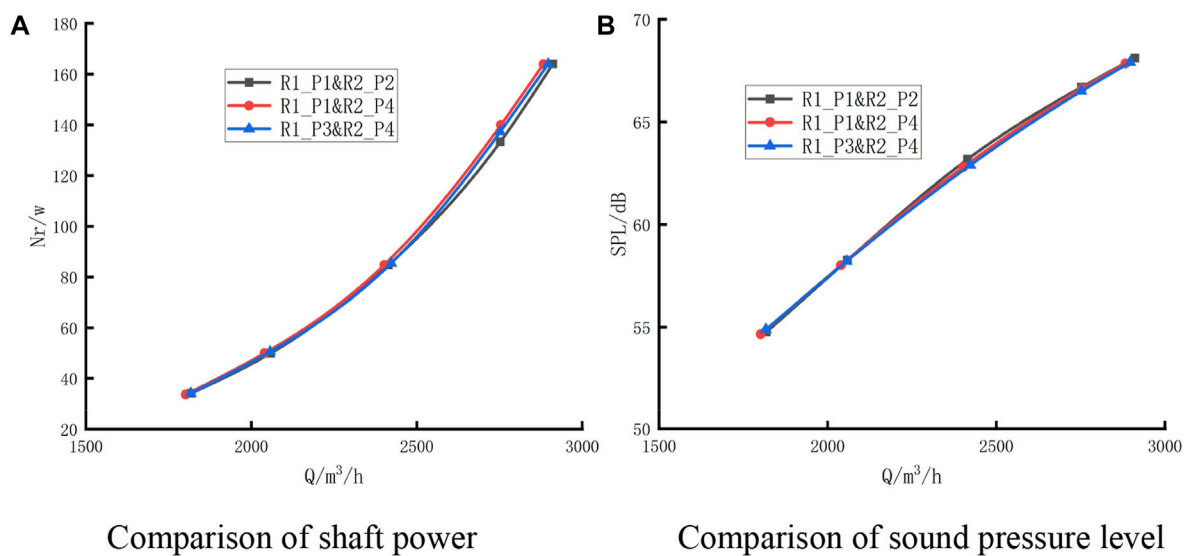


FIGURE 9
Variable rotational speed regulation characteristics of the fan with different axial distances: (A) comparison of shaft power; (B) comparison of SPL.

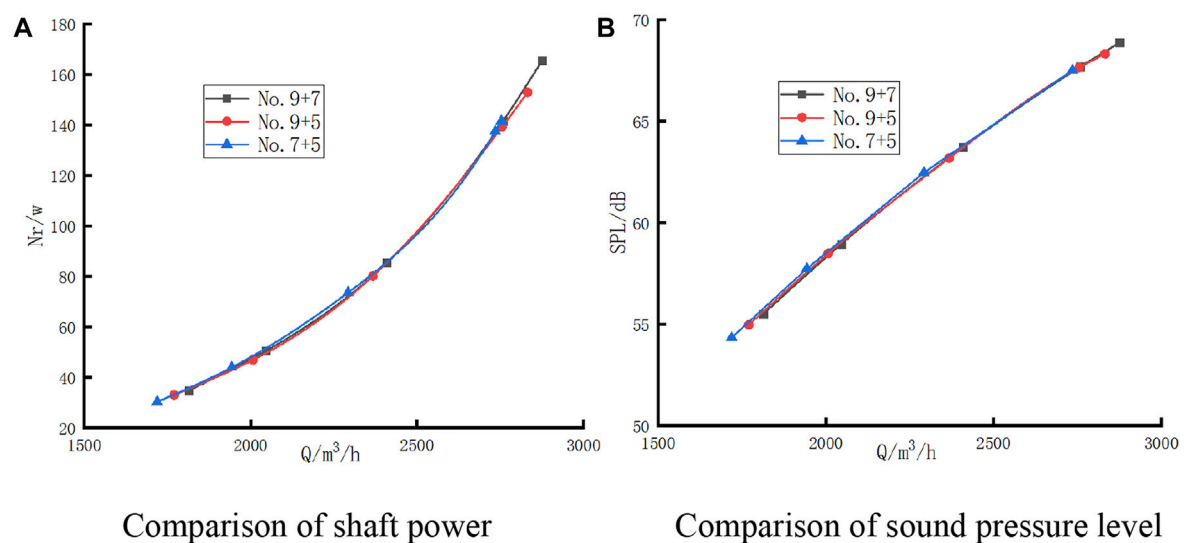


FIGURE 10
Variable rotational speed regulation characteristics of the fan with different blade number combinations: (A) comparison of shaft power; (B) comparison of SPL.

$$E_v(k) = \frac{55\Gamma(5/6)}{9\sqrt{\pi}\Gamma(1/3)} u_{rms}^2 \Lambda^5 \left(\frac{\Gamma(1/3)}{\sqrt{\pi}\Gamma(5/6)} \right)^4 \frac{k^4}{\left(1 + \left(\frac{\Gamma(1/3)}{\sqrt{\pi}\Gamma(5/6)} \right)^2 \Lambda^2 k^2 \right)^{17/6}} \quad (7)$$

where k , u_{rms} and Λ represent the parameters shown in the Liepmann model.

In order to compare the energy spectrum density of the measured velocity with that of the Liepmann and von Karman models. Figure 8 compares the power spectrum density under the Liepmann and von Karman models with that obtained from hotwire measurement. It

then can be seen that for $f < 100$ Hz, $psd_v(f) = 2.26psd_L(f)$, and spectral density of the two models largely varies with f^4 . Meanwhile, the power spectral density of the measured velocity changes slightly for this range of frequency, in which the spectral density obtained from hotwire measurement is apparently higher than that obtained from the two models. This is probably because in the lower frequency range, the scale of vortex is large and the flow is anisotropic turbulence, which leads to significant difference between the experimental results and that obtained from Liepmann and von Karman models. While for $100 \text{ Hz} < f < 1,000 \text{ Hz}$, the difference between $psd_v(f)$ and $psd_L(f)$ is very small. In this frequency range,

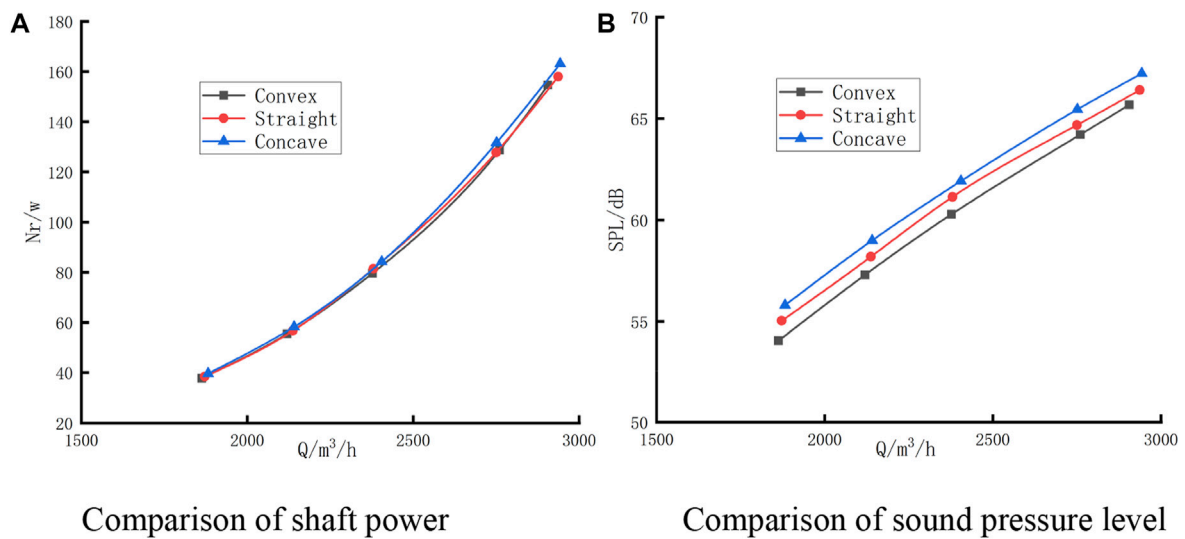


FIGURE 11

Variable rotational speed regulation characteristics of the fan with different blade patterns: (A) comparison of shaft power; (B) comparison of SPL.

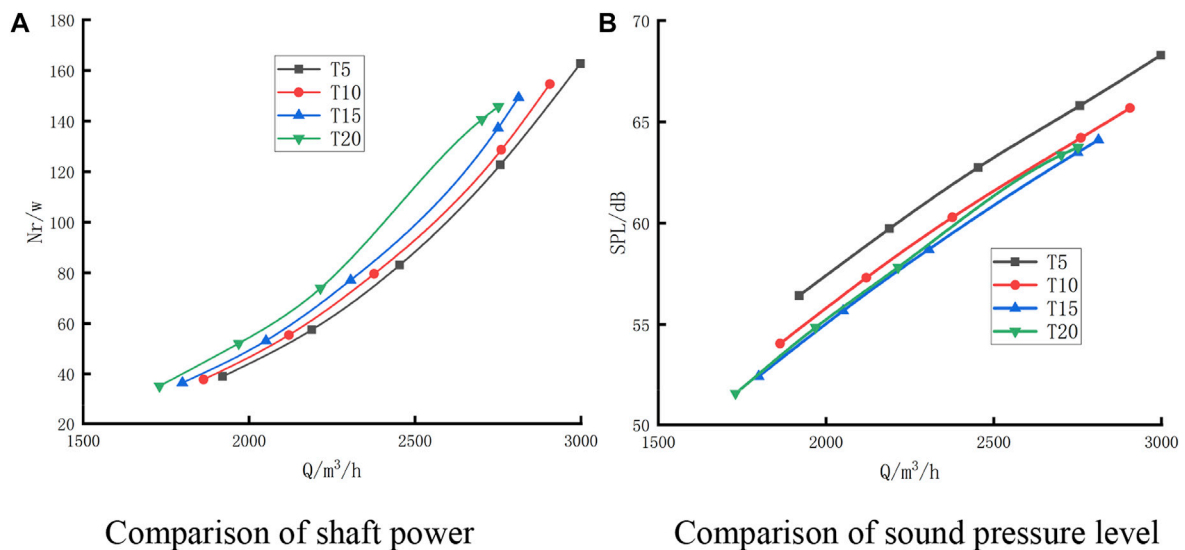


FIGURE 12

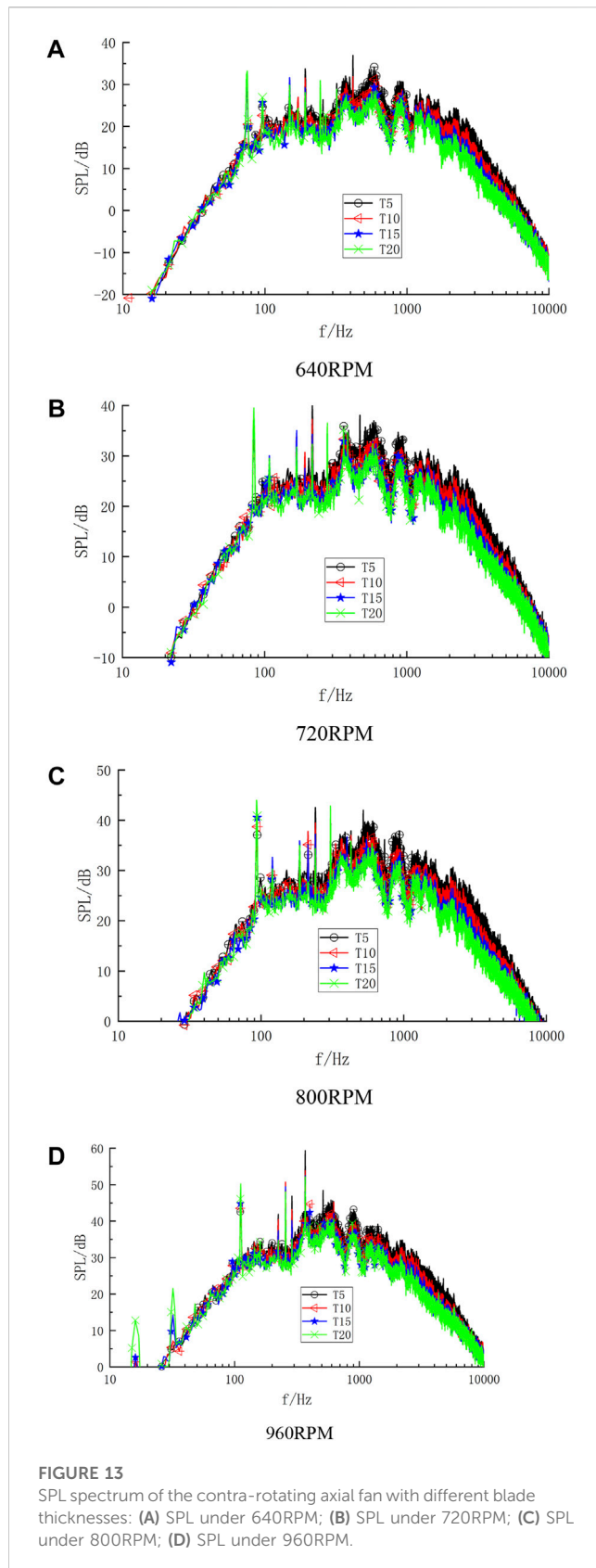
Variable rotational speed regulation characteristics of the fan with different blade thicknesses: (A) comparison of shaft power; (B) comparison of SPL.

the scale of vortex is relatively small and the turbulent flow is approximately local isotropic, thus the experimental results and that obtained from Liepmann and von Karman models agree well. Besides, in this range of frequency, the power spectral density of the measured velocity is pretty close to that obtained from the Liepmann and von Karman models. In addition, the variance of spectral density obtained from the Liepmann and von Karman models gradually increases for $f > 1,000$ Hz owing to the fact that $psd_L(f)$ decays slightly faster than $psd_V(f)$, and the power spectral density of von Karman model is closer to that of the measured velocity in this range of frequency.

5 Influence of the fan parameters on the performance and noise characteristics

5.1 Investigation of variable rotational speed regulation characteristics of the fan

Due to the limitation of certain conditions, variable rotational speed regulation of the contra-rotating fan is probably the only practical approach to satisfy the requirement of air quantity. In the present experiment, the



performance and noise characteristics under variable rotational speed regulation are obtained to investigate the influences of the fan parameters.

Figure 9 shows variable rotational speed regulation characteristics of the fan with different axial distances. It can be seen that under variable rotational speed regulation, there is remarkably little variation of characteristic curves of shaft power and SPL.

Through the variable rotational speed regulation, the three fan models nearly reach the same volume flow rate. It can be seen that not only the shaft power and SPL are fairly close, but the rotational speed is also basically unchanged at the design point for all of the three models.

Figure 10 shows variable rotational speed regulation characteristics of the fan with different blade number. It can be seen that under variable rotational speed regulation, the characteristic curves of the shaft power and SPL are nearly identical.

It can be seen that the shaft power and SPL of the fan show rather small differences under the three blade number combinations, while there is an increase of the rotational speed with decrease of the blade number.

Figure 11A shows that the shaft power curves of the fan with the three different blade patterns are very close, especially for the cases with straight and concave blade patterns, the characteristic curves of the shaft power are basically identical. For the fan with the three blade patterns, the characteristic curves of SPL under variable rotational speed regulation vary obviously, as shown in Figure 11B, and the convex blade gets the lowest noise level of all three patterns.

It can be seen that near the design flow rate, the fan model with the convex blade pattern shows slightly better performance and noise characteristics. Meanwhile, to achieve the required design flow rate, the rotational speed for the fan models with different blade pattern varies slightly.

Figure 12A shows that the shaft power curves of the fan with the different blade thicknesses under variable rotational speed regulation increase evidently with the increase of the blade thickness. Meanwhile, it can be seen in Figure 12B that with increase of the blade thickness, the SPL curves of the fan decrease evidently first, and with the blade thickness of 15 mm, it shows the lowest noise characteristics. While with the increase of the blade thickness from 15 mm to 20 mm, the SPL curves are quite close. This indicates there might be an optimum blade thickness to get the best noise characteristics.

It can be seen that with the increase of the blade thickness, to reach the flow rate near design point, the required rotational speed and shaft power of the fan model both increase, while the SPL decreases first and then increases slightly. Besides, the disparity of the rotational speed for the fan models with the blade thickness is obviously larger than that for the fan models with the blade pattern.

5.2 Spectrum analysis of the fan with different blade profiles

To analyze the influence of the blade thickness on the noise characteristics, Figure 13 shows the SPL spectra of the contra-rotating axial fan with the different blade thicknesses under four different rotational speeds. It can be seen from that below the fundamental frequency of rotor 1 and rotor 2, the SPL varies slightly for the model fan with different blade thicknesses under four different rotational speeds. For the frequencies between 100 Hz

and 5,000 Hz, the broadband noise of the model fan decreases with the increase of the blade thickness, which indicates that the blade thickness has an obvious impact on the band noise of the contra-rotating axial fan in this frequency range. Meanwhile, in this frequency range, the SPL of the broadband noise varies evidently for the model with the blade thickness from 5 mm to 15 mm, compared with that from 15 mm to 20 mm. While for the higher frequency range ($f > 5,000$ Hz), the influence of the blade thickness on the SPL gradually decreases.

Additionally, the tonal SPL for fundamental frequency of rotor 1 and rotor 2 of the fan slightly increases with the increase of the blade thickness, which is evidently different from the influence of the blade thickness on the broadband components. Moreover, at its harmonic of the BPF, the variation of tonal SPL is inconsistent with that at fundamental frequency for the model fan with different blade thickness.

In general, the broadband noise of the model fan with the different blade thicknesses between 100 Hz and 5,000 Hz is obviously lower than that out of this frequency range ($f < 100$ Hz or $f > 5,000$ Hz), and this also applies to the models with the different blade pattern. It then can be concluded that the blade profile of the contra-rotating fan has an obvious impact on the broadband noise characteristics under moderate and high frequencies.

6 Conclusion

In the present experimental study, the performance and noise characteristics of a contra-rotating fan under variable rotational speed regulation are studied, and models with different parameters of the fan are applied in the experiments. Compared with the existing experimental and numerical investigations, the present research attempts to discuss the influences of structural and blade parameters of the contra-rotating fan on variable rotational speed regulation characteristics of performance and noise, thus provides instructions for designing contra-rotating axial fans. Conclusions are drawn as follows.

- 1) It can be concluded that the tonal sound pressure for fundamental frequency of rotor 1 and rotor 2 is proportionate to 4.55th and 5.15th power of the characteristic velocity, respectively, which is proportionate to the rotational speed. For the accurate prediction of flow characteristics which to a great extent determine the accurate prediction of the broadband noise, the Liepmann and von Karman models yield close results for the power spectrum density at moderately high frequencies, where the two models effectively predict the spectrum density of the velocity. It probably because in this frequency range, the scale of vortex is relatively small and the turbulent flow is approximately local isotropic, thus the experimental results and that obtained from Liepmann and von Karman models agree well. While at higher frequencies, the power spectral density of von Karman model, compared with that of Liepmann model, is closer to that of the measured velocity.
- 2) For the contra-rotating axial fans with different axial distances between rotors or blade number combinations, the characteristic curves of the shaft power and SPL are nearly identical, which indicates the axial distance and blade number are not sensible factors for the contra-rotating axial fan under variable rotational

speed regulation. Under variable rotational speed regulation, the blade profiles of the fan, including the blade pattern and thickness, have an impact on the characteristic curves of the SPL. The shaft power curves of the fan with the different blade thicknesses decrease evidently with increase of the blade thickness, while the shaft power curves are very close with different blade patterns. In general, the blade profiles, especially the blade thickness, are sensible factors of the performance and noise characteristics for the contra-rotating axial fan under variable rotational speed regulation.

- 3) The SPL varies slightly for the model fan with different blade profile below the fundamental frequency of rotor 1 and rotor 2, while the blade profile of the rotors has an obvious impact on the broadband noise characteristics under moderate and high frequency range. Moreover, for the higher frequency range ($f > 5000$ Hz), the influence of the blade thickness on the SPL gradually decreases.

Data availability statement

The original contributions presented in the study are included in the article/supplementary material, further inquiries can be directed to the corresponding author.

Author contributions

YZ: writing original draft, data analysis; CX: writing-review and editing; ZZ: software and editing; XH: analysis and reviewing; YM: conceptualization, reviewing and editing.

Funding

The research is supported by the National Natural Science Foundation of China (No. 52076086).

Conflict of interest

Authors ZZ was employed by Foshan Shunde Midea Washing Appliances Mfg. Co., Ltd. and XH was employed by Midea Group.

The remaining authors declare that the research was conducted in the absence of any commercial or financial relationships that could be construed as a potential conflict of interest.

Publisher's note

All claims expressed in this article are solely those of the authors and do not necessarily represent those of their affiliated organizations, or those of the publisher, the editors and the reviewers. Any product that may be evaluated in this article, or claim that may be made by its manufacturer, is not guaranteed or endorsed by the publisher.

References

- Mistry C, Pradeep AM. Effect of variation in axial spacing and rotor speed combinations on the performance of a high aspect ratio contra-rotating axial fan stage. *P Mech Eng A-j Pow* (2013) 227(2):138–46. doi:10.1177/0957650912467453
- Mistry C, Pradeep AM. Influence of circumferential inflow distortion on the performance of a low speed, high aspect ratio contra rotating axial fan. *J Turbomach* (2014) 136(7):0710091–11. doi:10.1115/1.4025953
- Fukutomi J, Shigemitsu T, Yasunobu T. Performance and internal flow of sirocco fan using contra-rotating rotors. *J Therm Sci* (2008) 17(1):35–41. doi:10.1007/s11630-008-0035-8
- Shigemitsu T, Fukutomi J, Okabe Y. Performance and flow condition of small-sized axial fan and adoption of contra-rotating rotors. *J Therm Sci* (2010) 19(1):1–6. doi:10.1007/s11630-010-0001-0
- Heinrich M, Khaleghi H, Friebe C. Effect of circumferential casing treatment on low-speed contra-rotating fans. *J Appl Fluid Mech* (2020) 13(6):1719–26. doi:10.47176/JAFM.13.06.31492
- Dong B, Jiang C, Liu X, Deng Y, Huang L. Theoretical characterization and modal directivity investigation of the interaction noise for a small contra-rotating fan. *Mech Syst Signal Pr* (2020) 135:106362–15. doi:10.1016/j.ymssp.2019.106362
- Dong B, Xie D, He F, Huang L. Noise attenuation and performance study of a small-sized contra-rotating fan with microperforated casing treatments. *Mech Syst Signal Pr* (2021) 147:107086107086–16. doi:10.1016/j.ymssp.2020.107086
- Wang C, Huang LX. Theoretical acoustic prediction of the aerodynamic interaction for contra-rotating fans. *AIAA J* (2018) 56(5):1855–66. doi:10.2514/1.j055845
- Sarraf C, Nouri H, Ravelet F, Bakir F. Experimental study of blade thickness effects on the overall and local performances of a controlled vortex designed axial-flow fan. *Exp Therm Fluid Sci* (2011) 35(4):684–93. doi:10.1016/j.expthermflusci.2011.01.002
- Roy B, Ravibabu K, Rao PS, Basu S, Raju A, Murthy PN. Flow studies in ducted twin-rotor contra-rotating axial flow fans. In: ASME 1992 International Gas Turbine and Aeroengine Congress and Exposition; June 1–4, 1992; Cologne, Germany (1992). V001T01A131-92-GT-390.
- Shigemitsu T, Fukutomi J, Okabe Y, Iuchi K, Shimizu H. Unsteady flow condition of contra-rotating small-sized axial fan. *J Therm Sci* (2011) 20(6):495–502. doi:10.1007/s11630-011-0501-6
- Nouri H, Ravelet F, Bakir F, Sarraf C, Rey R. Design and experimental validation of a ducted counter-rotating axial-flow fans system. *J Fluid Eng-t ASME* (2012) 134(10):104504.1–6. doi:10.1115/1.4007591
- Mao XC, Liu B. A numerical study on the unsteady effect of axial spacing on the performance in a contra-rotating axial compressor. *P Mech Eng C-j Mec* (2017) 231(14):2598–609. doi:10.1177/0954406216638881
- Sun XB, Meng DW, Liu BW, Wang Q. Numerical investigation of differential speed operation of two impellers of contra-rotating axial-flow fan. *Adv Mech Eng* (2017) 9(10):168781401772008168781401772008–16. doi:10.1177/1687814017720083
- Chen YY, Liu B, Xuan Y, Xiang XR. A study of speed ratio affecting the performance of a contra-rotating axial compressor. *P Mech Eng G-j Aer* (2008) 222(G7):985–91. doi:10.1243/09544100jaero364
- Ravelet F, Bakir F, Sarraf C, Wang J. Experimental investigation on the effect of load distribution on the performances of a counter-rotating axial-flow fan. *Exp Therm Fluid Sci* (2018) 96:101–10. doi:10.1016/j.expthermflusci.2018.03.004
- Luan H, Weng L, Liu R, Li D, Wang M. Axial spacing effects on rotor-rotor interaction noise and vibration in a contra-rotating fan. *Int J Aerospace Eng* (2019) 2019:21259761–15. doi:10.1155/2019/2125976
- Ai ZJ, Qin GL, Lin JX, Chen XF. Experimental study on the speed matching of two rotors for a counter-rotating fan. In: ASME Power Conference 2018; June 24–28, 2018; Lake Buena Vista, USA (2018). V002T09A001.
- Joly M, Verstraete T, Paniagua G. Full design of a highly loaded and compact contra-rotating fan using multidisciplinary evolutionary optimization. In: ASME Turbo Expo 2013: Turbine Technical Conference & Exposition; June 3–7, 2013; San Antonio, USA (2013). p. GT2013–94433.
- Cao LL, Watanabe S, Imanishi T, Yoshimura H, Furukawa A. Experimental analysis of flow structure in contra-rotating axial flow pump designed with different rotational speed concept. *J Therm Sci* (2013) 22(4):345–51. doi:10.1007/s11630-013-0634-x
- Mohammadi A, Boroomand M. Design and internal flow analysis of a ducted contra-rotating axial flow fan. In: ASME 2014 International Mechanical Engineering Congress and Exposition; November 14–20, 2014; Montreal, Canada (2014). p. IMECE2014–39883.
- Xu J, Tan C, Chen H, Zhu Y, Zhang D. Influence of tip clearance on performance of a contra-rotating fan. *J Therm Sci* (2009) 18(3):207–14. doi:10.1007/s11630-009-0207-1
- Wang YG, Chen WX, Wu CH, Ren SY. Effects of tip clearance size on the performance and tip leakage vortex in dual-rows counter-rotating compressor. *P Mech Eng G-j Aer* (2015) 229(11):1953–65. doi:10.1177/0954410014562483
- Grasso G, Moreau S, Christophe J, Schram C. Multi-disciplinary optimization of a contra-rotating fan. *Int J Aeroacoust* (2018) 17(6):655–86. doi:10.1177/1475472x18789000
- Wang C, Huang LX. Passive noise reduction for a contra-rotating fan. *J Turbomach* (2015) 137(3):031007.1–10. doi:10.1115/1.4028357

Nomenclature

Q_v volume flow rate

N_r shaft power

n rotational speed

P_{ref} reference sound pressure

f_{r1} fundamental frequency of rotor 1

f_{r2} fundamental frequency of rotor 2

u_{rms} root mean square turbulence velocity

k wave number

Λ turbulence integral scale



OPEN ACCESS

EDITED BY

Pei Li,
Xi'an Jiaotong University, China

REVIEWED BY

Peng Yu,
Guangxi University, China
Li Chen,
University of Luxembourg, Luxembourg

*CORRESPONDENCE

Yongsong Li,
✉ liys@huanghuai.edu.cn

SPECIALTY SECTION

This article was submitted to Statistical and Computational Physics, a section of the journal Frontiers in Physics

RECEIVED 28 January 2023

ACCEPTED 23 February 2023

PUBLISHED 07 March 2023

CITATION

Lian H, Zhao P, Zhang M, Wang P and Li Y (2023), Physics informed neural networks for phase field fracture modeling enhanced by length-scale decoupling degradation functions.
Front. Phys. 11:1152811.
doi: 10.3389/fphy.2023.1152811

COPYRIGHT

© 2023 Lian, Zhao, Zhang, Wang and Li. This is an open-access article distributed under the terms of the [Creative Commons Attribution License \(CC BY\)](#). The use, distribution or reproduction in other forums is permitted, provided the original author(s) and the copyright owner(s) are credited and that the original publication in this journal is cited, in accordance with accepted academic practice. No use, distribution or reproduction is permitted which does not comply with these terms.

Physics informed neural networks for phase field fracture modeling enhanced by length-scale decoupling degradation functions

Haojie Lian¹, Peiyun Zhao², Mengxi Zhang³, Peng Wang⁴ and Yongsong Li^{5*}

¹Key Laboratory of In-situ Property-improving Mining of Ministry of Education, Taiyuan University of Technology, Taiyuan, Shanxi, China, ²College of Mining Engineering, Taiyuan University of Technology, Taiyuan, Shanxi, China, ³State Key Laboratory of Hydraulic Engineering Simulation and Safety, Tianjin University, Tianjin, China, ⁴Beijing Huituo Infinite Technology Co., Ltd., Beijing, China, ⁵School of Architectural and Civil Engineering, Huanghuai University, Zhumadian, China

The paper proposed a novel framework for efficient simulation of crack propagation in brittle materials. In the present work, the phase field represents the sharp crack surface with a diffuse fracture zone and captures the crack path implicitly. The partial differential equations of the phase field models are solved with physics informed neural networks (PINN) by minimizing the variational energy. We introduce to the PINN-based phase field model the degradation function that decouples the phase-field and physical length scales, whereby reducing the mesh density for resolving diffuse fracture zones. The numerical results demonstrate the accuracy and efficiency of the proposed algorithm.

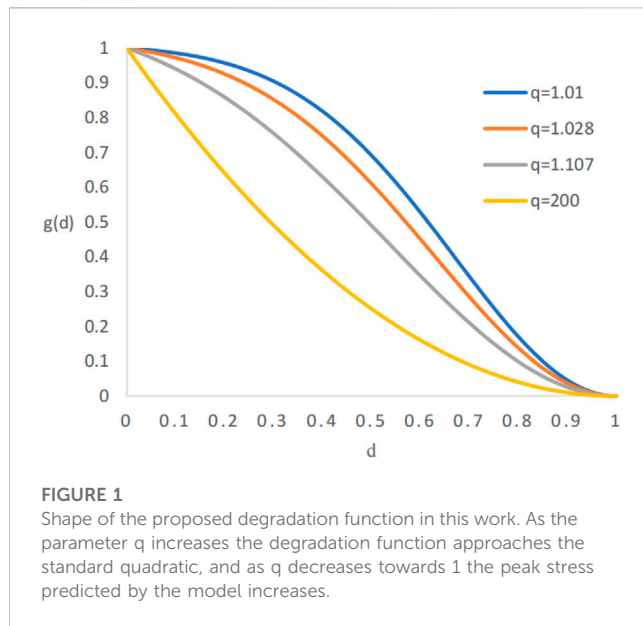
KEYWORDS

phase-field, fracture, large structures, physics informed, deep neural network

1 Introduction

Predicting material and structural failure due to crack nucleation and extension is central to many engineering applications. Several numerical methods are developed to capture complex fracture phenomena, such as the finite element method [1], the boundary element method [2], the cohesion zone method [3,4], the extended finite element methods [5], the peridynamics Ha and Bobaru [6] and the phase field methods. In these methods, the phase field method has demonstrated advantages in description of complex fracture patterns. By introducing additional continuous field variables to track discrete discontinuities with diffuse fracture zones, the phase field method Bourdin et al. [7] unifies crack initiation, propagation, branching, and merging in structures.

In phase field method, the *diffuse fracture region* must be resolved with sufficient degrees of freedom to obtain an accurate solution. The length scale of the *physical process zone* is proportional to the ratio of the fracture energy to the square of the material strength. For most problems modeled by linear elastic fracture mechanics, the length scale of the physical process zone is very small compared to structures, but the commonly used formulas in fracture phase field approach does not distinguish between the *phase field crack length scale* the physical process zone length scale, which leads to prohibitive meshing requirement when extending the models with nanoscale phase field length to large structures. To alleviate the meshing burden, Wu et al. proposed a length-scale insensitive phase-field model [8], but the method



is practically applicable to the scenario that the phase-field length scale and physical process zone length scale are in the same order of magnitude. Lo et al. [9] proposes a degradation function that separates the phase field length scale from physical length-scale, which enables one to simulate crack propagation in large scale structures.

As a branch of artificial intelligence, the deep learning based on Artificial Neural Networks has made tremendous progress with the explosive growth of data in the past decade [10–12] and applied in a wide range of areas. ANN were initially trained for Computer Visualization and Natural Language Processing tasks [13,14]. When it comes to the field of physical simulation, two major problems arise: firstly, it is cumbersome to obtain the data from complex engineering systems; secondly, the result predicted by the training data cannot ensure that the physical principles of the problem are satisfied. Hence, the effectiveness and reliability of ANN in characterizing physical phenomena are questionable. To overcome the difficulties, physics informed neural networks (PINN) [12,15–19] were put forward, which comply with the distribution of the training data as much as possible and meanwhile obey the laws of physics which are commonly formulated by partial differential equations. Compared to purely data-driven neural network learning, PINN allows learning with fewer data samples and obtaining models with greater generalization capability. Goswami et al. [20], Goswami et al. [21] firstly applied PINN to solve the phase field model for simulating the growth and propagation of fractures in brittle materials. Their results offer improved accuracy and efficiency, demonstrating the advantages of PINN in simulating moving boundary problems.

In the present work, we introduce the degradation function proposed by Lo et al. [9] to the PINN-based phase field method [20,21], in order to analyse crack growth in large structures with a data driven and mechanism based hybrid approach. We use three numerical simulation examples to demonstrate that the physical neural network combined with the proposed degradation function is correct and advantageous. The remaining of the paper is organized as

follows. Section 2 introduces fracture phase field method and shows how the phase field length scale and the physical process zone length are decoupled. Section 3 elaborates on how the fracture phase field model is discretized with the PINN. The numerical examples are given and analysed in Section 4, and Section 5 is the conclusion and outlook of future work.

2 Phase field model of cracks

2.1 Conventional phase field crack modeling

The phase-field crack modeling of brittle fractures involves the integration of two fields: the elastic field u and the phase field d , and the crack propagation is determined according to the free energy minimization principle. Based on the energy decomposition proposed by Francfort and Marigo [22], the free energy of the fracture system is given as:

$$E(u, \Gamma) = \int_{\Omega} \psi_e(\varepsilon(u)) dx + G_c \int_{\Gamma} ds \quad (1)$$

where: G_c is the critical energy release rate, ψ_e is the elastic energy density, Γ is the fracture surface, and Ω is the problem domain. The right hand side of the equation is the sum of the elastic strain energy and the fracture surface energy, and the fracture phase field method in mechanics assumes that the crack should follow the direction of minimum free energy and be irreversible.

Since the boundary integral involved in the surface energy is not easy to handle, it is replaced by the crack density equation in the following:

$$\psi_c = \frac{G_c}{2l_0} (d^2 + l_0^2 |\nabla d|^2) \quad (2)$$

where: d is the order parameter; l is the diffuse crack width. Theoretically, the model draws on the elliptic regularization method of the Mumford-Shah generalization Lie et al. [23] in computer image segmentation (hence the model is also known as AT2).

Since the elastic strain energy cannot distinguish between positive and negative for stress and strain, Amor et al. [24] and Miehe et al. [25] proposed a tension-compression split of the elastic strain energy, which is defined as:

$$\psi_e(\varepsilon, d) = g(d) \psi_e^+ + \psi_e^- \quad (3)$$

where the elastic energy is determined by both the strain and the order parameter d . $g(d)$ represents the degradation function, which is used to reduce the strength of material around the cracked region. To model material failure and crack propagation, the material should be fully elastic when it is intact and disappears when it is completely cracked. This is achieved by multiplying the elastic energy by the degradation function in the phase field description of the damaged materials.

In addition, to prevent the release of elastic energy after unloading from causing crack healing, Miehe et al. [26] proposed a very concise and effective solution by introducing a historical strain function:

$$H(x, t) = \max_{\tau \in [0, t]} \psi_e^+ \quad (4)$$

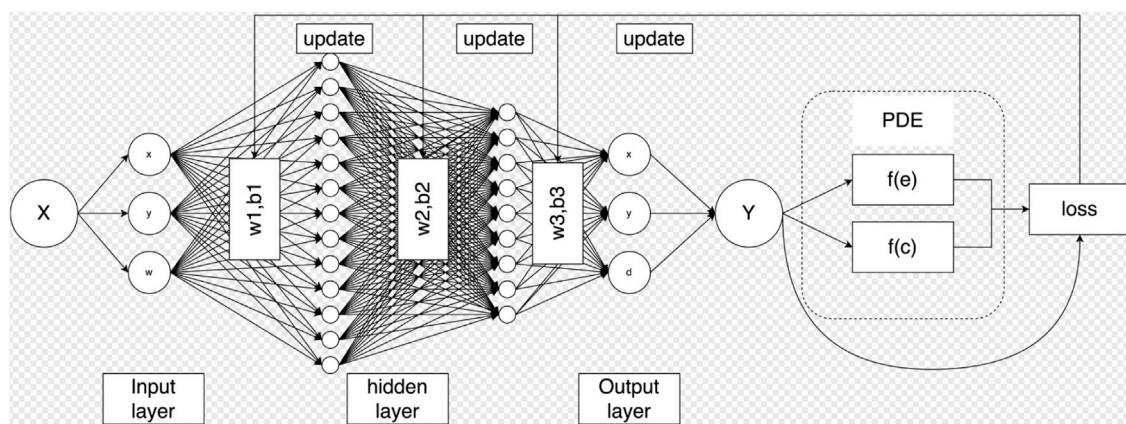


FIGURE 2

Schematic representation of the proposed physics informed neural network. X represents the input of the neural network, Y represents the output of the neural network, $f(e)$ represents the elastic strain energy, and $f(c)$ represents the fracture energy. For training, we have used the ADAM optimizer followed by L-BFGS.

Eq. 4 indicates that the crack driving force is taken as the historical maximum tensile elastic energy. Even after re-unloading, the tensile elastic energy maintains its maximum value and thus prevents crack healing.

Substituting the crack density in Eq. 2 and the elastic energy in Eq. 5 into the free energy of the fracture system in Eq. 1:

$$E(u, d) = g(d)\psi_e^+ + \psi_e^- + \frac{G_c}{2l} (d^2 + l^2 |\nabla d|^2) + g(d)H(x, t) \quad (5)$$

Finally, we seek the solution to minimize the free energy E , which consists of the elastic strain energy ψ_e and the fracture surface energy ψ_c .

2.2 Degradation function

The degradation function needs to satisfy the following conditions:

$$\begin{aligned} g(1) &= 1 \\ g(0) &= 0 \\ g'(0) &= 0 \end{aligned} \quad (6)$$

The most widely used degradation function in the literature is a quadratic function,

$$g(d) = (1 - d)^2. \quad (7)$$

With this degradation function, for the AT2 model (d^2) with uniform uniaxial tension, the peak stress is obtained as:

$$\sigma_c = \sqrt{\frac{27G_c E}{256l_0}} \quad (8)$$

Eq. 8 shows that the phase-field length, l_0 is not an independent parameter but dependent on the material strength, σ_c , fracture energy, G_c , and Young's modulus, E . This length scale, which represents the size of the physical process zone, l_p , can be quite small for real materials. In the past, the typical approach has been to set l_p equal to l_0 . However, this means that numerical solutions must

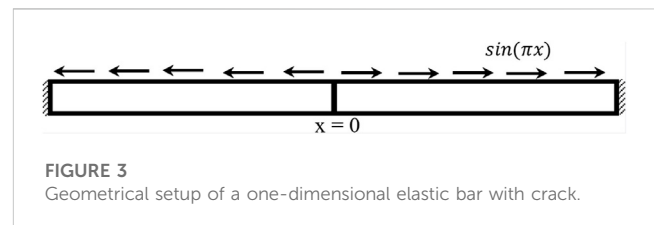


FIGURE 3

Geometrical setup of a one-dimensional elastic bar with crack.

have the ability to resolve the small l_p , which can be a challenge for large engineering structures. This is because the mesh size around cracks must be a fraction of l_0 , at most $l_0/2$, leading to computationally intensive simulations. To overcome the difficulties, Lo et al. [9] proposed a new degradation as:

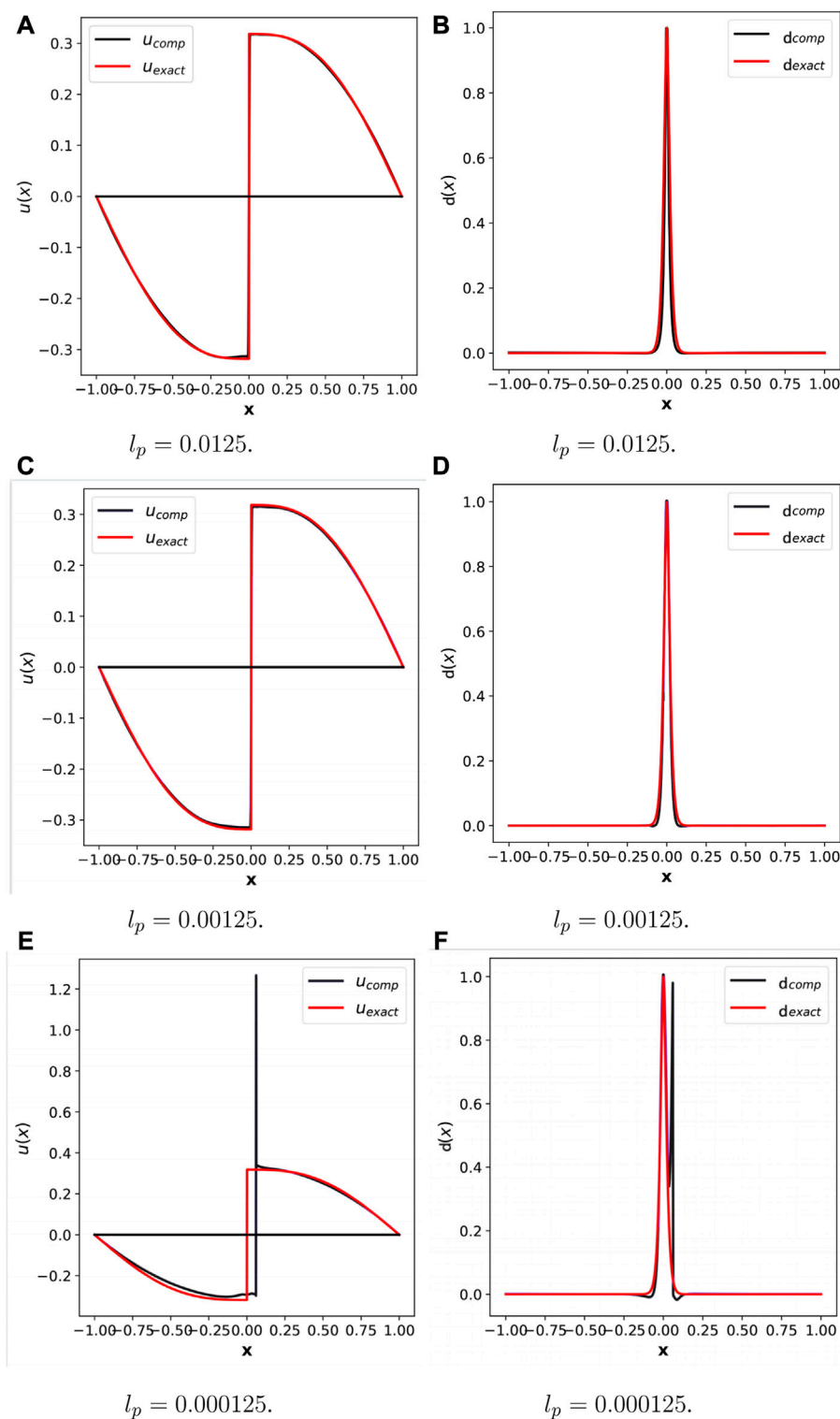
$$g(d) = q * \left[1 - \left(\frac{q-1}{q} \right)^{(1-d)^2} \right] \quad (9)$$

This degradation function meets all the requirements of Eq. 6. Its shape depends on the value of q . When q is 200, the shape of the proposed degradation function in Eq. 23 is close to that of the classical degradation function in Eq. 7. When the value of q is slightly larger than 1, the shape of the degradation function $g(d)$ will dramatically alter following marginal change of the value of q . This can be seen in Figure 1.

The peak stress for a bar under homogeneous uniaxial tension can be determined using the proposed degradation function, as follows:

$$\sigma_c^* = \frac{\sqrt{\frac{27G_c E}{256l_0}}}{\sqrt{(q-1)\ln\left(\frac{q}{q-1}\right)}} \quad (10)$$

It's worth mentioning that we've introduced the notation σ_c^* to represent the peak stress calculated using the alternative degradation function, differentiating it from the conventional peak stress (σ_c). Additionally, the physical length scale l_p in the case of the alternative degradation function is given as:

**FIGURE 4**

1D elastic bar with crack using variation energy based PINN. Left column compares the exact displacement u_{exact} and the computed displacement u_{comp} . The right column compares the exact phase field d_{exact} and the computed phase field d_{comp} . (A) $l_p = 0.0125$, (B) $l_p = 0.0125$, (C) $l_p = 0.00125$, (D) $l_p = 0.00125$, (E) $l_p = 0.000125$, (F) $l_p = 0.000125$.

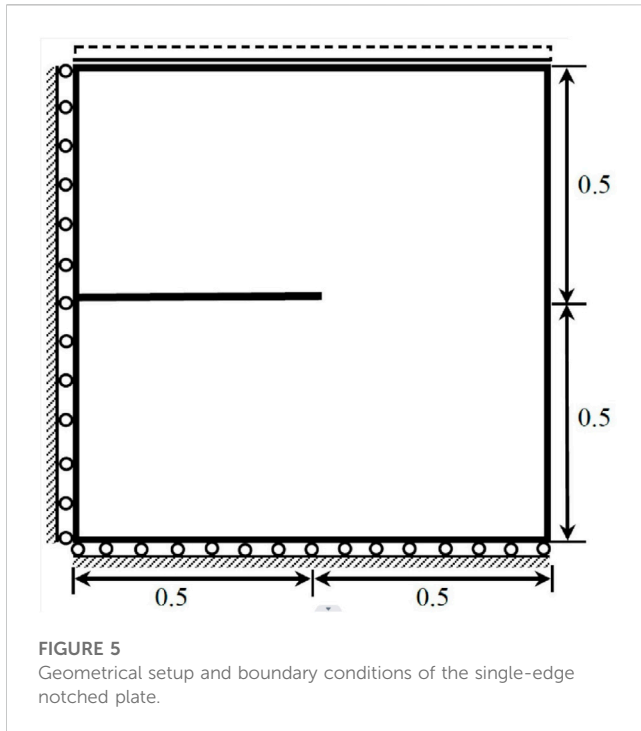


FIGURE 5
Geometrical setup and boundary conditions of the single-edge notched plate.

$$l_p = (q - 1) \ln \left(\frac{q}{q - 1} \right) l_0. \quad (11)$$

This allows us to also express the peak stress with the proposed degradation function as follows:

$$\sigma_c^* = \sqrt{\frac{27G_c E}{256l_p}} \quad (12)$$

q can be used to maintain the same peak stress σ_c^* in numerical simulations with the increase of the phase-field length, which allows for a coarser mesh in the proximity of cracks. Supposing G_c , E , and σ_c^* are given as constants, when q is large, the sizes of the physical process zone, l_p , and the phase-field process zone, l_0 , are comparable. Moreover, the finite element mesh must be refined according to l_0 . If we would like to increase the l_0 by 4 times without changing the peak stress, σ_c^* or the l_p , q needs to be 1.107 according to Eq. 10. If we aim to increase the length scale l_0 by 16 times while still maintaining the same peak stress, we find that $q \approx 1.0148$. If we increase l_0 by 100 times, we find that $q \approx 1.00155$. This demonstrates that the proposed degradation function allows for decoupling l_0 from l_p . Note that these results assume homogeneous post-peak behavior and that localized deformations have been suppressed. Importantly, it's worth noting that the resulting peak stress remains the same for different phase-field length scales. Also note that the material is not damaged, i.e., d begins to increase from 0, until the strains exceed peak strains.

3 PINN-based fracture phase-field modeling

This section details the implementation of the phase field method based on PINN [20, 21]. Firstly, the deep neural network will be described, and secondly, the synthesis between the PINN

phase field method with the degradation function mentioned in the above section is explained.

3.1 Deep neural networks

Deep learning is a branch of machine learning based on deep neural networks. In comparison with shallow neural networks, deep learning has more hidden layers and is more capable of fitting non-linearities. Neural network training consists of two steps, i.e., forward propagation and backward propagation. The forward propagation is used to train the neural network parameters, while the backward propagation is used to update the neural network parameters and find the optimal solution. In this paper, a feed-forward deep neural network is used for the study. The hidden layer of the deep neural network contains its main parameter weights W and biases b , and the parameters are continuously optimized by optimization algorithms (e.g., adaptive moment estimation (ADAM), proposed Newton method (L-BFGS), etc.) to find the optimal solution. Supposing that the network consists of L hidden layers, with layer 0 denoting the input layer and layer $(L + 1)$ denoting the output layer, the expression of the neural network can be written as:

$$z_i^l = \sigma_{l-1} \left(\sum_{j=1}^{m_{l-1}} (W_{i,j}^l (z_j^{l-1}) + b_i^l) \right) \quad (13)$$

The calculation of the output Y in the feed-forward algorithm can be represented as follows: the activation function σ_{l-1} in layer l is used in conjunction with the number of neurons m_{l-1} in layer $l - 1$.

$$\begin{aligned} Y_l &= \sigma_l (W_{l+1} z_l + b_{l+1}), \\ z_l &= \sigma_{l-1} (W_l z_{l-1} + b_l), \\ z_{l-1} &= \sigma_{l-2} (W_{l-1} z_{l-2} + b_{l-1}), \\ &\vdots \\ z_1 &= \sigma_0 (W_1 x + b_1) \end{aligned} \quad (14)$$

where x represents the input to the neural network in Eq. 14. Forward propagation is used to train the neural network parameters, (w , b), which represent all the W_l and b_l parameters that appear in Eq. 14. We evaluate a neural network prediction result by the loss function, and if the loss value reaches low enough, (which is generally not possible to be 0) we end the neural network training. The common loss functions for regression are MAE loss, MSE loss, and smooth L1 loss. Their expressions are given by the following equations.

$$L = \frac{1}{n} \sum_{i=1}^n |Y_i - N(x_i; W, b)| \quad (15)$$

$$L = \frac{1}{n} \sum_{i=1}^n (Y_i - N(x_i; W, b))^2 \quad (16)$$

$$\text{smoothL}_1(x) = \begin{cases} 0.5(Y_i - N(x_i; W, b))^2 & \text{if } |Y_i - N(x_i; W, b)| < 1 \\ |Y_i - N(x_i; W, b)| - 0.5 & \text{otherwise,} \end{cases} \quad (17)$$

Y_i represents the target value and $N(x_i; W, b)$ represents the predicted value of the neural network. Backward propagation is automatically performed based on the value of the loss function. Automated differentiation and weight update implemented in TensorFlow or PyTorch allow algorithm designers to perform their tasks without coding the back propagation from scratch.

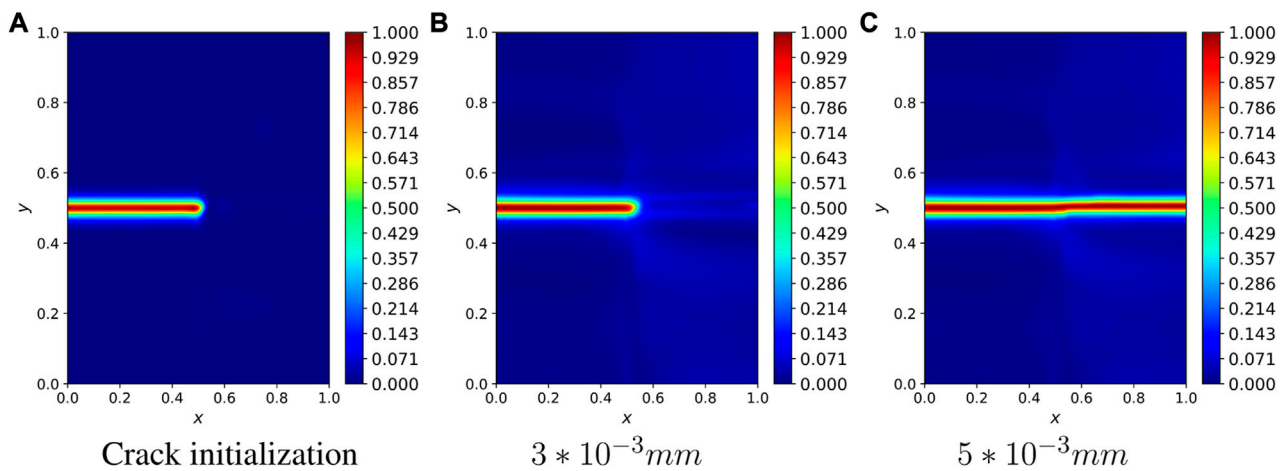


FIGURE 6

Phase field image of the single-edge notched plate at $l_0 = l_p$ (A) Crack initialization, (B) 3×10^{-3} mm, (C) 5×10^{-3} mm.

The reader is referred to LeCun et al. [27] for details of the adopted gradient calculation method and the layer-by-layer chain rule gradient derivation process. In the following section we focus on an algorithmic approach for solving problems using the variational energy-based physics informed neural network.

3.2 Variational energy based PINN

We can define the problem by a one-dimensional time-independent differential equation:

$$F(u, u_x, \dots, u_{x \dots x}, x, f(x)) = 0, \quad (18)$$

together with the Dirichlet boundary condition, which is defined as:

$$u(x_D) = u_D \quad (19)$$

The deep neural network can be utilized to compute the field variable, represented by u , by considering variables such as the Dirichlet boundary point, represented by x_D , and the source term, represented by $f(x)$. Furthermore, the first, second, and higher-order derivatives with respect to the independent variable x can be calculated using u_x , u_{xx} and $u_{x \dots x}$ respectively. The variational energy principle has the distinctive benefit of automatically satisfying homogeneous Neumann boundary conditions. At this point, the expression for the variational energy is:

$$V = \int_{\Omega} y(u, u_x, \dots, u_{x \dots x}, x, f(x)) d\Omega \quad (20)$$

where y is the differentiable functional. Ω is the problem domain for which a solution is required, so the problem for which we require a solution can be expressed as follows:

$$\text{subject to: } \begin{aligned} u^* &= \operatorname{argmin}_u V(u) \\ u(x_D) &= u_D. \end{aligned} \quad (21)$$

The steps for solving the differential equation using a neural network are detailed as follows: First, we construct a neural network, $N(x; W, b)$ with initial parameters. Second, we revise the neural network

according to the boundary conditions. In terms of addressing the boundary conditions in the context of neural network, weak form and the strong form. When dealing with boundary conditions in a weak form, a penalty term reflecting the boundary condition is added to the loss function. But this may cause interference among different loss terms, which slows or even cripples the convergence of the problem. So, we prefer the strong form here and we redesign the output of the neural network so as to comply with the Dirichlet boundary condition. To this end, we set:

$$u \approx \tilde{u}_D + B(x) \cdot N(x; W, b). \quad (22)$$

The function \tilde{u}_D is selected such that it matches the value of u_D at the Dirichlet boundary points. Meanwhile, $B(x)$ is equal to zero at the same boundary. There is no requirement for a boundary component in the calculation of the loss function. Thirdly, the output of the neural network existing in variable energy expression is calculated using an automatic differential technique. Having computed the first and higher-order derivatives of u , we can now calculate the variational energy at each quadrature point. This is done by using u_x from Eq. 22 and its derivatives obtained previously. The total variational energy of the system is then obtained by summing the energies at each point, as defined in Eq. 20. In this step we use the PDE (partial differential equation), i.e., the total variational energy, as the loss function of the neural network. The neural network constructed above is named *physics informed neural network*. The final step is to update the neural network parameters W and b by adjusting them so that the next neural network output value is closer to the target value.

According to the above steps, Goswami et al. [20], Goswami et al. [21] proposed a PINN combined with phase field method to simulate the fracture problem. The displacement control is applied for the loading process. To train the PINN, a fixed displacement step, denoted by Δu , is taken and the strain-history function is updated at each displacement increment. Before training the network, the weights are initialized randomly from a Gaussian distribution with the Xavier initialization technique [11]. In order to calculate the parameters of the neural network at the first

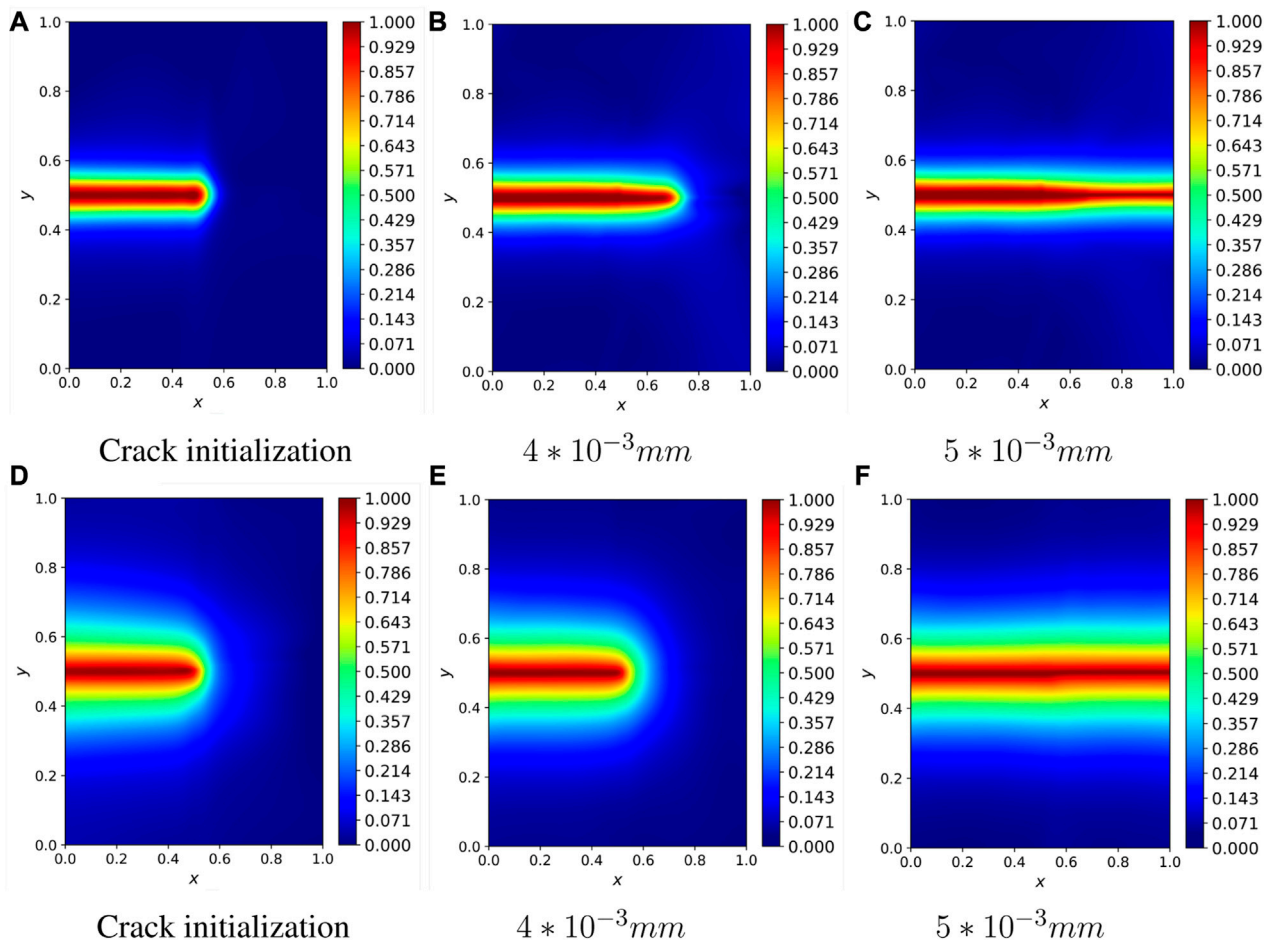


FIGURE 7

Phase field images of single-edge notched plates with the same model size and different l_0 values. The upper half: $l_0 = 4l_p = 0.05$. The low half: $l_0 = 10l_p = 0.125$. (A) Crack initialization, (B) 4×10^{-3} mm, (C) 5×10^{-3} mm, (D) Crack initialization, (E) 4×10^{-3} mm, (F) 5×10^{-3} mm.

displacement step i , the Gaussian quadrature points and their corresponding weights are generated using the above process, and in the subsequent step, the automatic differentiation method is employed to calculate the displacement increment, Δu , and the eigenvalues of the strain, $(\lambda_1, \dots, \lambda_d)$, where d denotes the number of spatial dimensions. These eigenvalues are then utilized to determine ψ_e^+ and ψ_e^- .

Next we modify the degradation function in the initial PINN model as Lo et al. [9]:

$$g(d) = q * \left[1 - \left(\frac{q-1}{q} \right)^{(1-d)^2} \right] \quad (23)$$

The initial crack is defined by the initial strain-history function, $H(x, 0)$. This function is determined based on the closest distance between a point x in the domain and the initial crack, which represents the discrete crack [28]. The local strain-history functional approach allows for the specification of initial cracks in the system [26]. In particular, we set

$$H(x, 0) = \begin{cases} \frac{BG_c}{2l_0} \left(1 - \frac{2d(x, l)}{l_0} \right) & d(x, l) \leq \frac{l_0}{2} \\ 0 & d(x, l) \geq \frac{l_0}{2} \end{cases} \quad (24)$$

where G_c is a material property known as the critical energy release rate, representing the energy needed to produce a fracture surface with a unit area. The parameter l_0 controls how the crack spreads. In Eqs. 24, B is a scalar parameter that controls the magnitude of the scalar history field and is calculated as:

$$B = \frac{1}{1-d} \quad \text{for } d < 1 \quad (25)$$

As is shown in Eq. 22, the output of the neural network is modified to meet the boundary conditions.

As explained in Section 2, the solution to the crack problem is obtained by minimizing the free energy E , which consists of the elastic strain energy ψ_e and the fracture surface energy ψ_c . To use the variational energy based PINN approach to study the growth of fracture, the problem is formulated as:

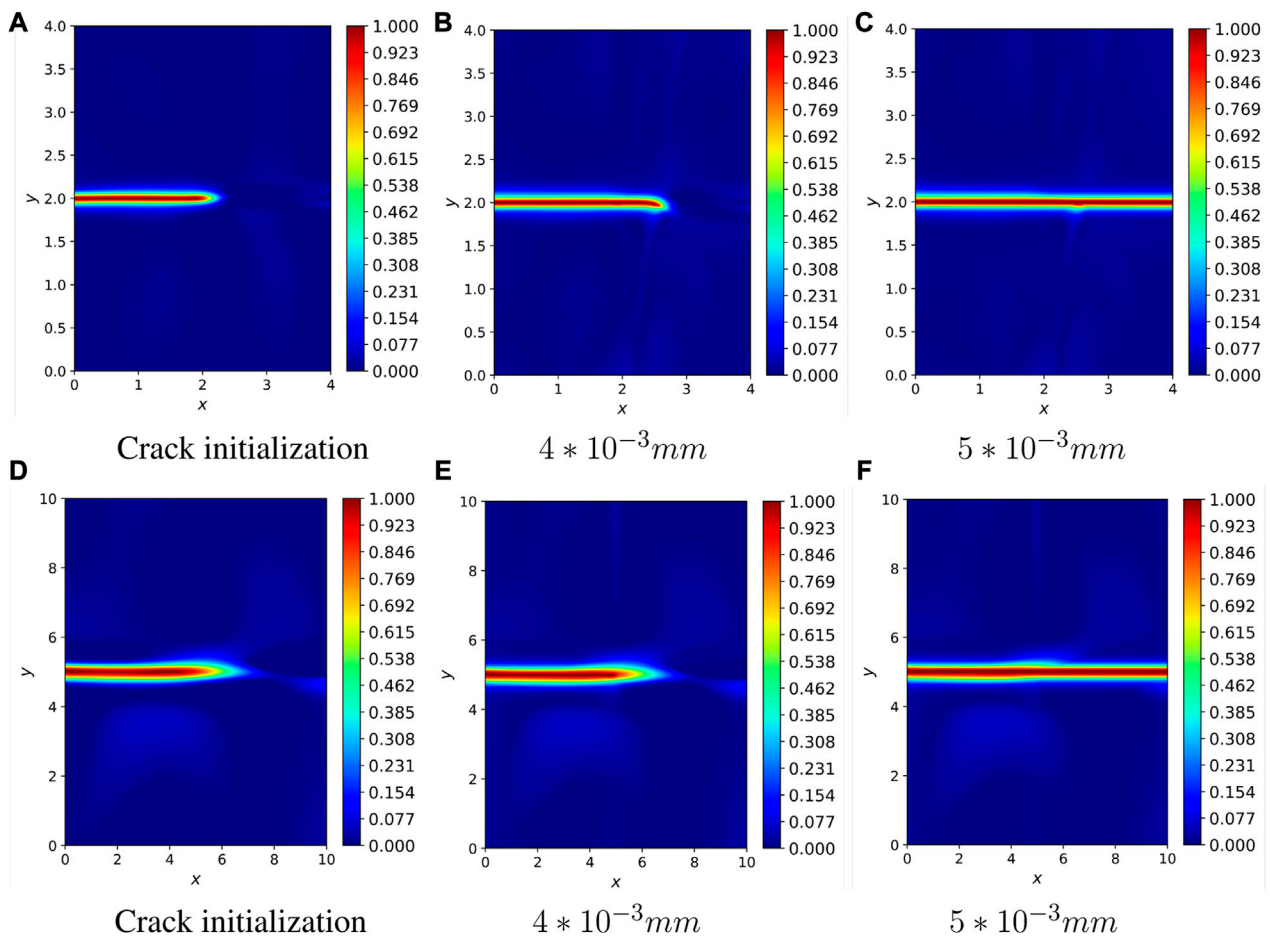


FIGURE 8

Phase field images of single-edge notched plates with 4 and 10 times of model enlargement while maintaining the peak stress unchanged. The upper half: $l_0 = 4l_p$. The low half: $l_0 = 10l_p$. (A) Crack initialization, (B) 4×10^{-3} mm, (C) 5×10^{-3} mm, (D) Crack initialization, (E) 4×10^{-3} mm, (F) 5×10^{-3} mm.

$$\begin{aligned}
 &\text{Minimize: } E = \psi_e + \psi_c \\
 &\text{subject to: } u = \bar{u} \quad \text{on } \partial\Omega_D \\
 &\text{where: } \psi_e = \int_{\Omega} (g(d)\psi^+(\epsilon) + \psi^-(\epsilon)) d\Omega \\
 &\quad \psi_c = \int_{\Omega} \left(\frac{G_c}{2l_0} [d^2 + l_0^2 |\nabla d|^2] + g(d)H(x,t) \right) d\Omega
 \end{aligned} \quad (26)$$

Note that integration is needed to calculate ψ_e and ψ_c in Eq. 26 for obtaining the elastic strain energy and the surface energy over the whole domain. Figure 2 shows a schematic diagram of the proposed PINN framework. For simplicity, only one layer of hidden layers is explicitly shown.

4 Numerical examples

4.1 One dimensional cracked elastic bar

We are analyzing a bar with a crack located at the center ($x = 0$) and it is fixed at both ends ($x = -1$, $x = 1$). This bar is subjected to a sinusoidal load. The geometric setup is shown in Figure 3. For a given material, we take into account the elastic property E , material

strength σ_c , and fracture energy G_c as the primary parameters. This implies that for the commonly used quadratic degradation function in Eq. 7, the length scale l_0 is not a separate variable and is valued as $l_0 = 27G_cE/256\sigma_c^2$. We choose the following parameters for this model: $\sigma_c = 0.15\text{MPa}$, $G_c = 2.7\text{N/m}$, $E = 1\text{MPa}$, and $l_0 = l_p = 12.5\text{ }\mu\text{m}$. The mesh size h in the vicinity of the crack is $h = l_0$. The crack at center is imposed by the following initial strain-history function:

$$H(x, 0) = \begin{cases} 1000 & \text{if } d(x) \leq l_0 \\ 0 & \text{if } d(x) > l_0 \end{cases} \quad (27)$$

where l_0 is the length scale parameter. The displacement field satisfies the Dirichlet boundary conditions, i.e.,

$$u(1) = u(-1) = 0 \quad (28)$$

The analytical solution of the displacement field Schilling et al. [29] is discontinuous and is given by the following equation:

$$u_{ex} = \begin{cases} \frac{1}{\pi^2} \sin(\pi x) - \frac{1+x}{\pi} & \text{if } x < 0 \\ \frac{1}{\pi^2} \sin(\pi x) + \frac{1-x}{\pi} & \text{if } x \geq 0 \end{cases} \quad (29)$$

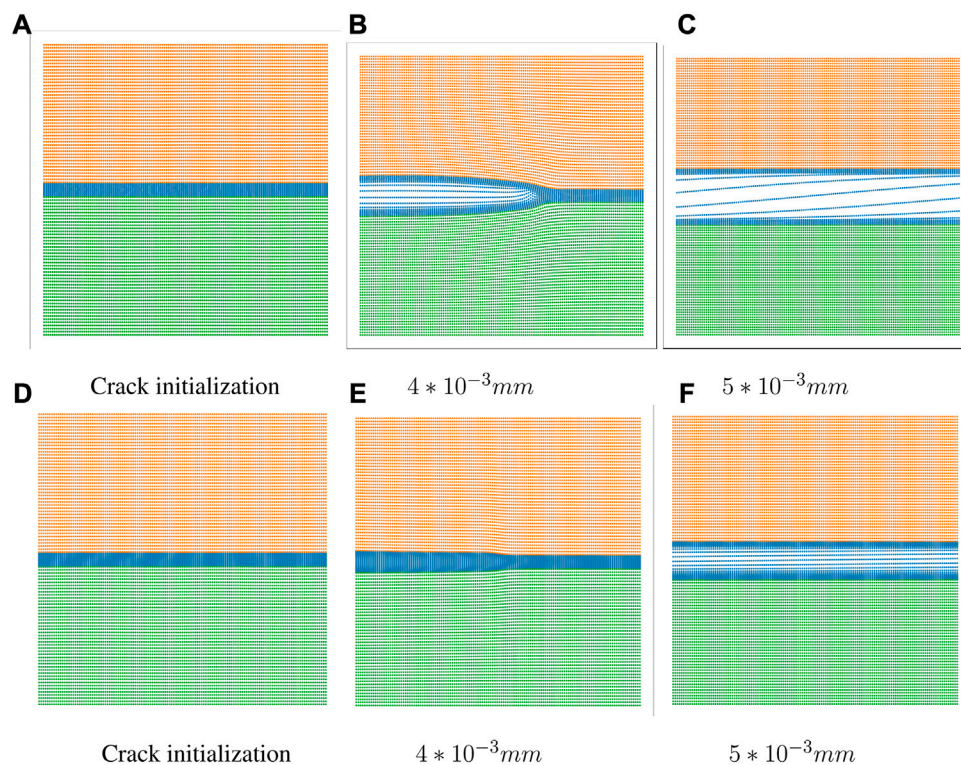


FIGURE 9

Scatter plots of single-sided notched plates with 4 and 10 times of model enlargement while maintaining the peak stress unchanged. The upper half: $l_0 = 4l_p$. The low half: $l_0 = 10l_p$, (A) Crack initialization, (B) 4×10^{-3} mm, (C) 5×10^{-3} mm, (D) Crack initialization, (E) 4×10^{-3} mm, (F) 5×10^{-3} mm.

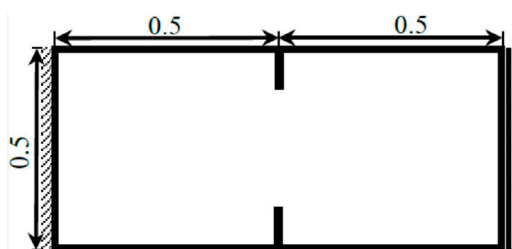


FIGURE 10

Geometrical setup and boundary conditions of the symmetrically double-edge notched plate.

and phase field solutions is,

$$d_{ex} = \exp\left(\frac{-|x - a|}{l_0}\right) \quad (30)$$

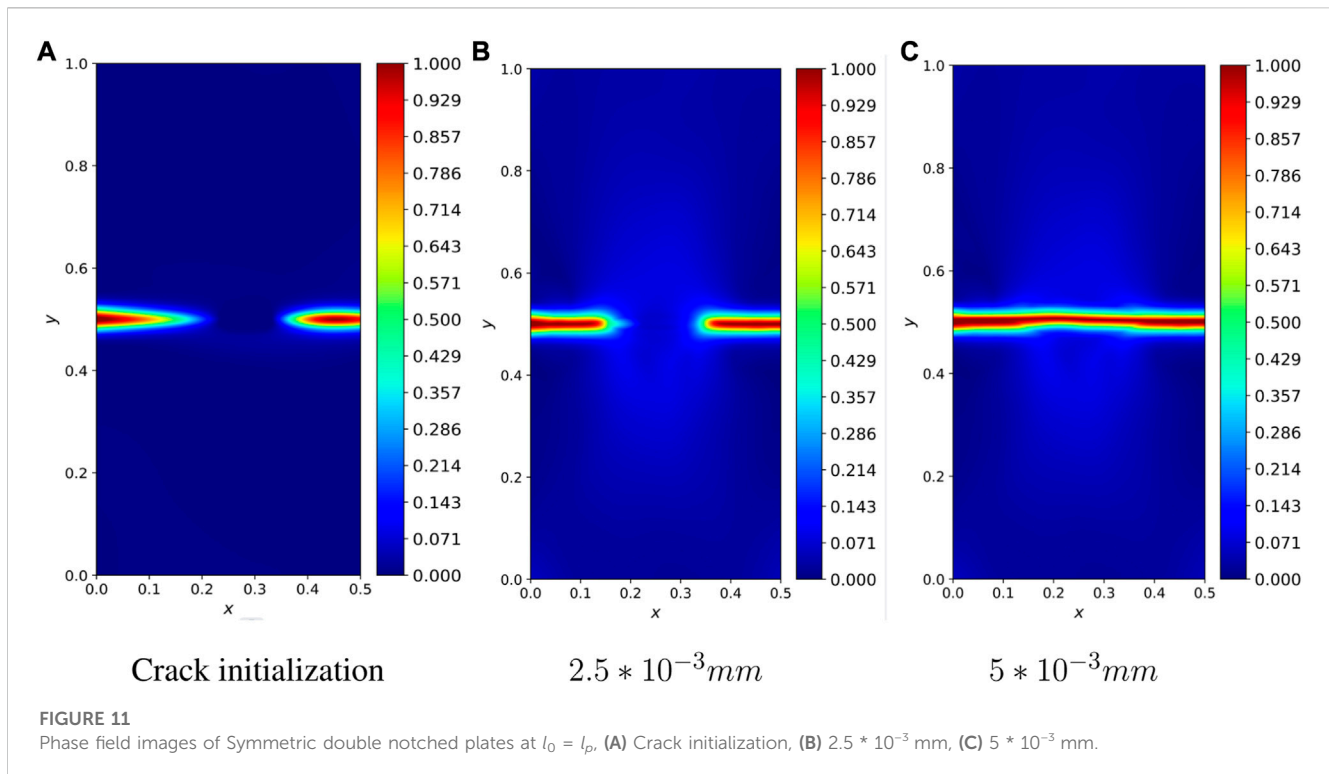
where the crack is located at 'a'. For this problem, the configurations of the neural network are: three hidden layers and a subsequent linear layer, we use adaptive tanh activation function in the hidden layer, while for the last layer, we adopt a linear activation function. The optimization is first performed using the Adam optimizer, and then the L-BFGS optimizer is used, where the learning rate of the L-BFGS optimizer is $\alpha = 0.001$. The one-dimensional elastic bar is

divided into three regions: $l_c: [-1, -2L_0]$, $c: [-2L_0, 2L_0]$, $r_c: [2L_0, 1]$, where l_c and r_c respectively represent the left and right crack regions, and c is the crack region. To ensure that the output of the neural network fully satisfies the boundary conditions of Dirichlet, we set:

$$u = [(x + 1)(x - 1)]u_\theta \quad (31)$$

where u_θ is the displacement field obtained as the output of the neural network. To optimize the proposed Physics-Informed Neural Network (PINN), we minimize the total variational energy of the system, which is defined in Eq. 20. To evaluate the precision of the results derived using this approach, we adopt two metrics: the relative error L_2^{rel} and the root mean square error (RMSE).

Next, we study the effect of the proposed degradation function on the model. First, for the proposed degradation function, it can decouple between the length of the coupling field, l_0 , and the physical length, l_p . By setting different q values, we can make l_0 multiple times larger than l_p . For instance, $l_0 = 100l_p$ when $q = 1.00155$. Figure 4 shows the simulation results in cases of $l_0 = l_p = 0.0125$, $1/10L_0 = l_p = 0.00125$ and $1/100L_0 = l_p = 0.000125$. To ensure an impartial evaluation, both methods were tested using the same neural network architecture and the number of integral points. The results from the proposed method were then compared to those obtained from the AT2-based PINN approach. Figures 4A,B show the displacement field u and phase field d obtained using $l_p = 0.0125$. Visually, the obtained results overlap with the analytical solutions obtained using formulas Eqs. 29, 30. To quantify the accuracy of the



proposed PINN method, relative errors and RMSEs corresponding to u and d are calculated. For u and d , the observed relative errors are 3.32% and 2.77%. In terms of the model size, 800 Gaussian points are involved. Corresponding to $l_p = 0.00125$ for u and d , relative prediction errors of 2.46% and 1.01%. Relative errors of u and d in case of $l_p = 0.000125$ of 20.56% and 48.28%. Note that the difference in Figures 4E,F is actually due to a lack of resolution at the material length scale. Therefore increasing the integration points appropriately and adjusting the number of training iterations may narrow the difference. The results shown in Figures 4E,F are not perfect. However, as the linear elastic fracture mechanics must meet the constraint of the phase-field process on a small scale zones, the constraint of the phase-field process on a small scale zones also applies to the proposed modeling method. Nevertheless, the phase field length scale can be selected independent of the inherent material process zone length scale, provided that the material processing zone length scale is sufficiently refined.

4.2 Single-edge notched plate subjected to tension

In this case, we take into consideration a unit square plate with a horizontal crack running from the midpoint of the left outer edge to the center of the plate. The problem's geometry and boundary conditions are illustrated in Figure 5. The plate material has a tensile strength of $\sigma_c = 2.54$ MPa, a fracture energy of $G_c = 2.7$ N/m, a Young's modulus of $E = 282.69$ MPa, and a phase field length scale of $l_0 = l_p = 12.5$ μ m. The mesh size, h , near the crack is $h = l_0/4$. The constant displacement increment applied during the computation is $\delta v = 10^{-3}$ mm. The crack path for the single-edge

notched plate under tension was obtained using a fully connected neural network with three hidden layers, each of which has 50 neurons. The activation function for the first two layers adopt the tanh function, and for the last layer adopt the linear function. The initial crack was determined using the strain history functional described in Eq. 24. The boundary conditions imposed were Dirichlet boundary conditions.

$$u(0, y) = v(x, 0) = 0, \quad v(x, 1) = \Delta v \quad (32)$$

where u and v are the solutions of the elastic field along the x and y -axes, respectively. To satisfy the Dirichlet boundary conditions, the neural network outputs for the elastic field are modified as:

$$u = [x(1-x)]\hat{u} \quad (33)$$

$$v = [y(y-1)]\hat{v} + y\Delta v \quad (34)$$

where \hat{u} and \hat{v} are obtained from the neural network. Figure 6 illustrates the crack propagation process in case of $l_p = l_0 = 0.0125$ mm. The result is very close to that of Goswami et al. [20].

As in the previous case, we first study the effect of the proposed degradation function on different physical length scale, l_p for the same size model. The ratio between l_0 and l_p is varied by setting different values of q . Figure 7 shows the simulation results for the cases $l_0 = l_p = 0.0125$ mm, $l_0 = 4l_p = 0.05$ mm and $l_0 = 10l_p = 0.125$ mm. In the above simulation, we observe that when the length of the phase field increases, the number of required Gaussian integration points decreases considerably, when $l_0 = l_p = 0.0125$ mm, the number of required integration points is: $20 \times 20 \times 16$ (20 represents the mesh of elements and 16 represents the number of required integration points per element), when $l_0 = 4l_p = 0.05$ mm, the number of required integration points is:

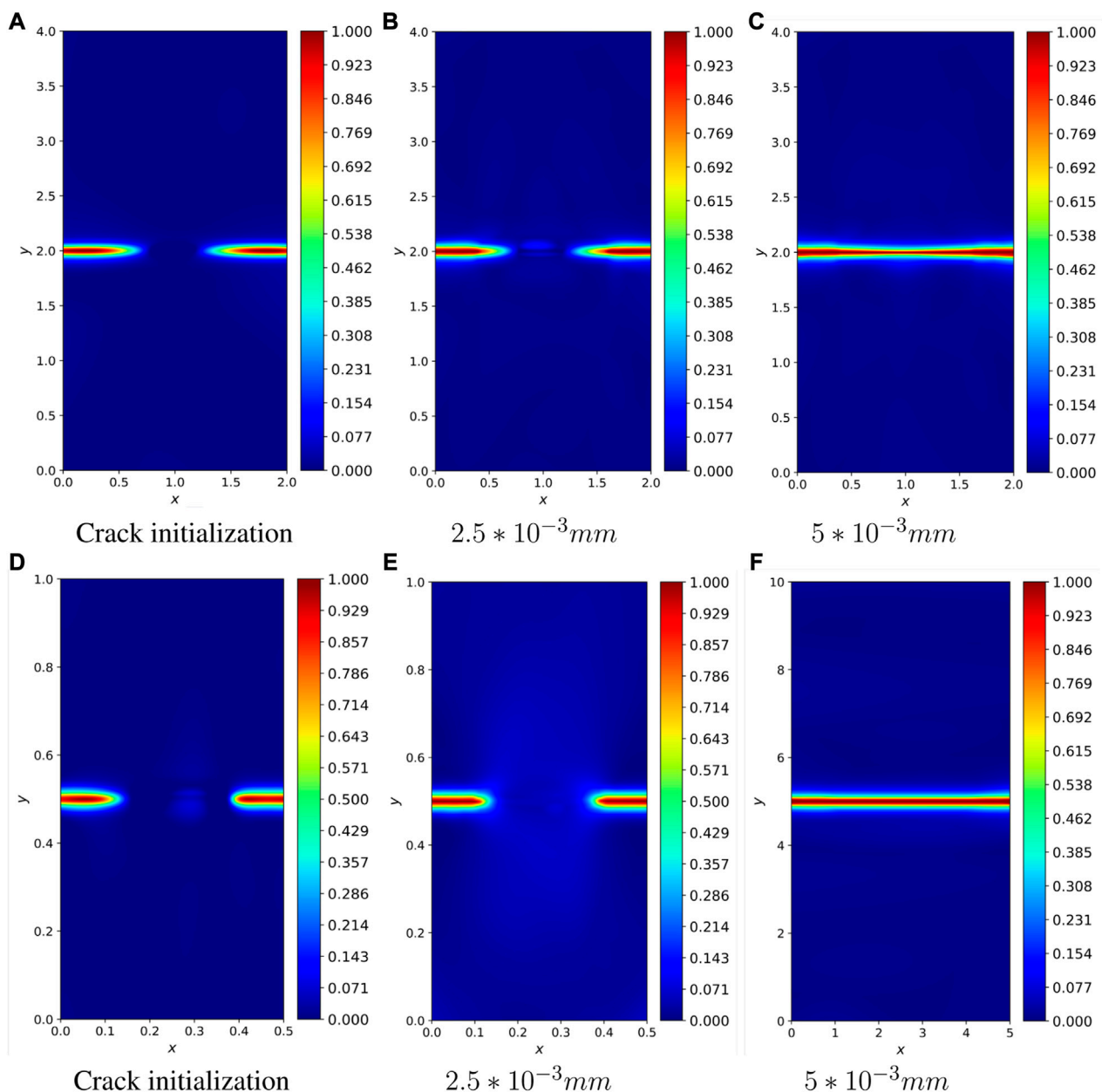


FIGURE 12

Phase field images of Symmetric double notched plates with 4 and 10 times of model enlargement while maintaining the peak stress unchanged.

The upper half: $l_0 = 4l_p$. The low half: $l_0 = 10l_p$, (A) Crack initialization, (B) 2.5×10^{-3} mm, (C) 5×10^{-3} mm, (D) Crack initialization, (E) 2.5×10^{-3} mm, (F) 5×10^{-3} mm.

$15 \times 15 \times 16$, When $l_0 = 10l_p = 0.125$ mm, the number of integration points required is: $12 \times 12 \times 16$, and the same simulation speed is also increased. Therefore, assuming that the model is enlarged and the l_p is unchanged, does it mean that we can simulate the harsh conditions in the large-scale model where the physical length scale, l_p has to be small. We will therefore next investigate increasing the size of the model while keeping the length scale of the physical process zone constant. The previous example in Section 4.1 shows that decoupling the physical length scale from the phase field length is achievable albeit with limitations. The proposed degradation function allows to solve large-scale problem with

much less computational cost. Suppose we multiply the length of the model edge by a factor of 4 and 10. In the meanwhile, the value of q is modified so that $l_0 = 4l_p$ and $l_0 = 10l_p$. The value of σ_c remains constant all the time. The proposed degradation function allows to increase the size of l_0 and decrease the mesh, $\frac{1}{h}$ (which is closely related to the size of l_0 , usually $h = l_0/4$), while keeping the physical length scale l_p constant. Simulation results for $l_0 = 4l_p$ and $l_0 = 10l_p$ are shown in figures Figure 8 and Figure 9. With the classical degradation function, if we want to increase the model by a factor of 10, we would need to add more integration points, whereas with the proposed degradation function, we can keep the number of

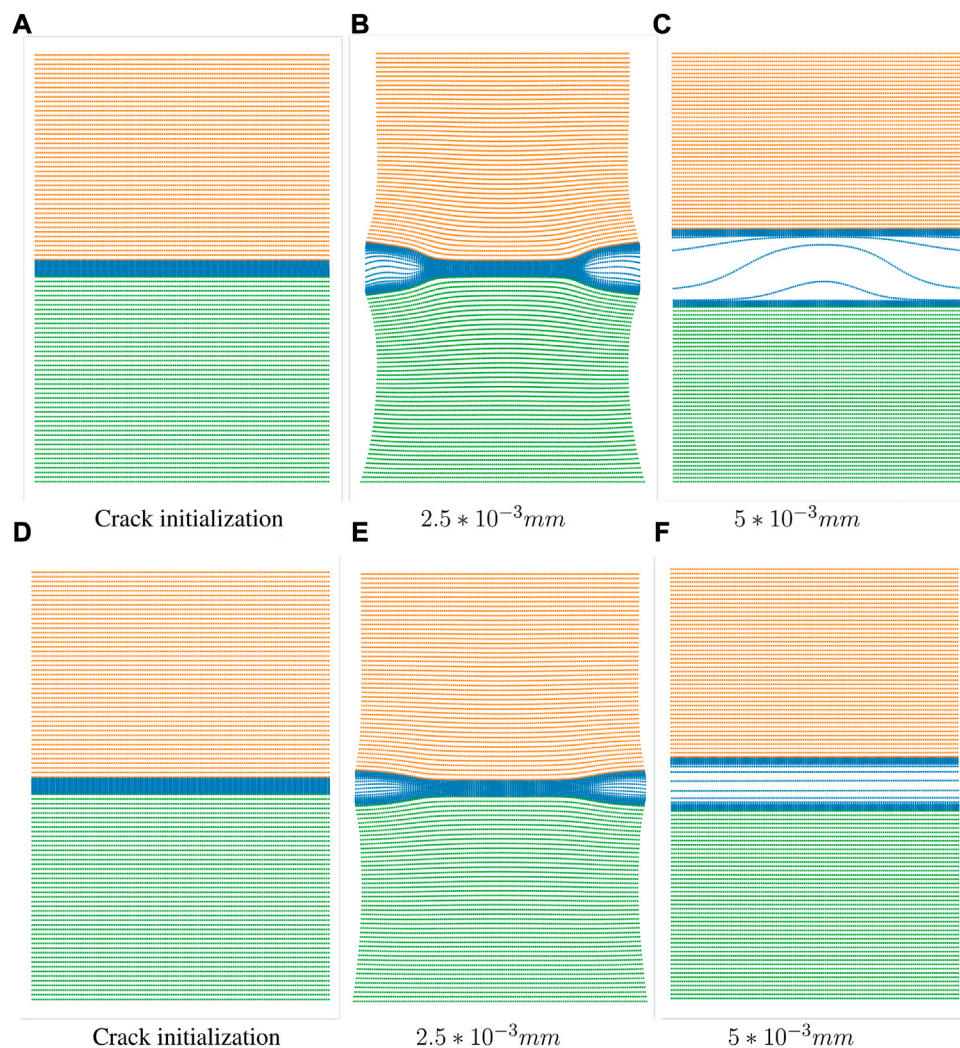


FIGURE 13

Scatter plots of Symmetric double notched plates with 4 and 10 times of model enlargement while maintaining the peak stress unchanged. The upper half: $l_0 = 4l_p$. The low half: $l_0 = 10l_p$. (A) Crack initialization, (B) 2.5×10^{-3} mm, (C) 5×10^{-3} mm, (D) Crack initialization, (E) 2.5×10^{-3} mm, (F) 5×10^{-3} mm.

integration points almost unchanged while increasing the model size by a factor of 10. We observe that the crack path shape is accurately captured by the larger length scale of the phase field. This adjustment to the phase field model formulation, therefore, allows for an increased sample size without the need for a significant increase in the computational volume of the length scale of the material processing zone.

4.3 Symmetrically double-edge notched plate subjected to tension

To verify the proposed method, we add another case, in which a double-edge notched plate subjected to a tensile load (see Figure 10) is considered. The material parameters are $\sigma_c = 2.54$ Mpa, $G_c = 2.7 \times 10$ N/m, $E = 282.69$ Mpa, and $l_0 = l_p = 12.5$ μ m.

To determine the crack path, we employed a fully connected neural network that includes four hidden layers, each of which has

50 neurons. The first three layers use the tanh activation function, while the final layer uses the linear activation. Both of cracks were initiated using the strain history functional, and the Dirichlet boundary conditions are specified:

$$u(x, 0) = v(x, 0) = 0, \quad v(x, 1) = \Delta v \quad (35)$$

The solution for the elastic field along the x and y -axes are represented by u and v , respectively. In order to determine the crack path, a constant displacement increment of $\delta u = 0.5 \times 10^{-4}$ mm has been applied. The output from the neural network for the elastic field is adjusted to conform with the Dirichlet boundary conditions:

$$u = y\hat{u} \quad (36)$$

$$v = [y(y-1)]\hat{v} + y\Delta v \quad (37)$$

where \hat{u} and \hat{v} are obtained from the neural network. The value of q is set to be 200. Figure 11 show the predicted crack propagation as a function of the tensile displacement. The predicted results are

compared with the results in Goswami et al. [20], and our findings are highly consistent with the results reported in the literature.

We multiply the lengths of the model edges by factors of 4 and 10, and modify the value of q so that $l_0 = 4l_p$ and $l_0 = 10l_p$. The value of σ_c is kept constant. The simulation results are shown in Figure 12 and Figure 13. Compared to the classical degradation function, there is no substantial increase in the running time when the model is expanded by a factor of 10 (mainly a small increase in the number of neural network iterations). We can find that with by introducing the length-scale separating degradation function to the PINN-based phase field model, maintaining a given mesh density sufficient to solve a larger scale model.

5 Conclusion and outlook

In this paper, we enhanced PINN-based phase field method (Goswami et al. [20], Goswami et al. [21]) with the degradation functions proposed by Lo et al. [9] in order to simulate fracture propagation in large structures. In conventional phase field method, the length scale of the phase field length scale is set to equate the physical length scale, which is very small compared to the structure size. Because a very refined mesh is needed to represent the diffuse fracture zone, it is impractical to apply PINN-based phase field method to large-scale models. To solve this problem, we introduce to PINN-based phase field simulation the degradation function that decouples the length scales of the phase field and the physical process zone. The merits and limitations of the modified phase field approach are discussed through several numerical examples. The proposed method combines the advantages of data driven and mechanism based computational approaches and improved its efficiency in fracture simulation. Although these examples are only for 2D problems, it is expected that the method could be applied to 3D situations without issue. In the future, we will investigate the uncertainty quantification of fractures with the present method. In addition, we will extend the present method to the hydraulic fracture problems.

References

- Moës N, Dolbow J, Belytschko T. A finite element method for crack growth without remeshing. *Int J Numer Methods Eng* (1999) 46:131–50. doi:10.1002/(sici)1097-0207(19990910)46:1<131::aid-nme726>3.0.co;2-j
- Aliabadi MH. *The boundary element method, volume 2: Applications in solids and structures, vol. 2*. New York, NY, USA: John Wiley & Sons (2002).
- Pereira K, Wahab MA. Fretting fatigue lifetime estimation using a cyclic cohesive zone model. *Tribology Int* (2020) 141:105899. doi:10.1016/j.triboint.2019.105899
- Pereira K, Bhatti N, Wahab MA. Prediction of fretting fatigue crack initiation location and direction using cohesive zone model. *Tribology Int* (2018) 127:245–54. doi:10.1016/j.triboint.2018.05.038
- Zi G, Belytschko T. New crack-tip elements for XFEM and applications to cohesive cracks. *Int J Numer Methods Eng* (2003) 57:2221–40. doi:10.1002/nme.849
- Ha YD, Bobaru F. Studies of dynamic crack propagation and crack branching with peridynamics. *Int J Fracture* (2010) 162:229–44. doi:10.1007/s10704-010-9442-4
- Bourdin B, Francfort GA, Marigo J-J. Numerical experiments in revisited brittle fracture. *J Mech Phys Sol* (2000) 48:797–826. doi:10.1016/s0022-5096(99)00028-9
- Wu J.Y., Nguyen V.P. (2018). A length scale insensitive phase-field damage model for brittle fracture. 392 *Journal of the Mechanics and Physics of Solids*. 119, 20–42.
- Lo Y-S, Hughes TJ, Landis CM. Phase-field fracture modeling for large structures. *J Mech Phys Sol* (2023) 171:105118. doi:10.1016/j.jmps.2022.105118
- Li Z, Liu F, Yang W, Peng S, Zhou J. A survey of convolutional neural networks: Analysis, applications, and prospects. *IEEE Trans Neural networks Learn Syst* (2021) 33: 6999–7019. doi:10.1109/tnnls.2021.3084827
- Glorot X, Bengio Y. Understanding the difficulty of training deep feedforward neural networks. In: *Proceedings of the thirteenth international conference on artificial intelligence and statistics (JMLR Workshop and Conference Proceedings)* (2010). p. 249–56.
- Karumuri S, Tripathy R, Bilonis I, Panchal J. Simulator-free solution of high-dimensional stochastic elliptic partial differential equations using deep neural networks. *J Comput Phys* (2020) 404:109120. doi:10.1016/j.jcp.2019.109120
- Simonyan K, Zisserman A. *Very deep convolutional networks for large-scale image recognition* (2014). *arXiv preprint arXiv:1409.1556*.
- Albawi S, Mohammed TA, Al-Zawi S. Understanding of a convolutional neural network. In: *2017 international conference on engineering and technology (ICET)*. Antalya, Turkey: IEEE (2017). p. 1–6. doi:10.1109/ICETechnol.2017.8308186
- Raissi M, Perdikaris P, Karniadakis GE. Physics-informed neural networks: A deep learning framework for solving forward and inverse problems involving nonlinear partial differential equations. *J Comput Phys* (2019) 378:686–707. doi:10.1016/j.jcp.2018.10.045

Data availability statement

The original contributions presented in the study are included in the article/supplementary material, further inquiries can be directed to the corresponding author.

Author contributions

HL: Software, Methodology, Writing, Administration; PZ: Software, Writing; MZ: Methodology, Revision; PW: Methodology; YL: Methodology, Administration. All authors contributed to the article and approved the submitted version.

Funding

The authors appreciate the financial support from the National Natural Science Foundation of China (NSFC) under Grant Nos. 52274222 and 51904202.

Conflict of interest

Author PW was employed by Beijing Huituo Infinite Technology Co., Ltd.

The remaining authors declare that the research was conducted in the absence of any commercial or financial relationships that could be construed as a potential conflict of interest.

Publisher's note

All claims expressed in this article are solely those of the authors and do not necessarily represent those of their affiliated organizations, or those of the publisher, the editors and the reviewers. Any product that may be evaluated in this article, or claim that may be made by its manufacturer, is not guaranteed or endorsed by the publisher.

16. Raissi M. Deep hidden physics models: Deep learning of nonlinear partial differential equations. *J Machine Learn Res* (2018) 19:932–55.
17. Raissi M, Yazdani A, Karniadakis GE. *Hidden fluid mechanics: A Navier-Stokes informed deep learning framework for assimilating flow visualization data* (2018). *arXiv preprint arXiv:1808.04327*.
18. Zhu Y, Zabaras N, Koutsourelakis P-S, Perdikaris P. Physics-constrained deep learning for high-dimensional surrogate modeling and uncertainty quantification without labeled data. *J Comput Phys* (2019) 394:56–81. doi:10.1016/j.jcp.2019.05.024
19. Geneva N, Zabaras N. Modeling the dynamics of PDE systems with physics-constrained deep auto-regressive networks. *J Comput Phys* (2020) 403:109056. doi:10.1016/j.jcp.2019.109056
20. Goswami S, Anitescu C, Chakraborty S, Rabczuk T. Transfer learning enhanced physics informed neural network for phase-field modeling of fracture. *Theor Appl Fracture Mech* (2020) 106:102447. doi:10.1016/j.tafmec.2019.102447
21. Goswami S, Anitescu C, Rabczuk T. Adaptive phase field analysis with dual hierarchical meshes for brittle fracture. *Eng Fracture Mech* (2019) 218:106608. doi:10.1016/j.engfracmech.2019.106608
22. Francfort GA, Marigo JJ. Revisiting brittle fracture as an energy minimization problem. *J Mech Phys Sol* (1998) 46:1319–42. doi:10.1016/s0022-5096(98)00034-9
23. Lie J, Lysaker M, Tai X-C. A binary level set model and some applications to mumford-shah image segmentation. *IEEE Trans image Process* (2006) 15:1171–81. doi:10.1109/tip.2005.863956
24. Amor H, Marigo JJ, Maurini C. Regularized formulation of the variational brittle fracture with unilateral contact: Numerical experiments. *J Mech Phys Sol* (2009) 57:1209–29. doi:10.1016/j.jmps.2009.04.011
25. Miehe C, Welschinger F, Hofacker M. Thermodynamically consistent phase-field models of fracture: Variational principles and multi-field fe implementations. *Int J Numer Methods Eng* (2010) 83:1273–311. doi:10.1002/nme.2861
26. Miehe C, Hofacker M, Welschinger F. A phase field model for rate-independent crack propagation: Robust algorithmic implementation based on operator splits. *Comput Methods Appl Mech Eng* (2010) 199:2765–78. doi:10.1016/j.cma.2010.04.011
27. LeCun Y, Bengio Y, Hinton G. Deep learning. *Nature* (2015) 521:436–44. doi:10.1038/nature14539
28. Borden MJ, Verhoosel CV, Scott MA, Hughes TJ, Landis CM. A phase-field description of dynamic brittle fracture. *Comput Methods Appl Mech Eng* (2012) 217:77–95. doi:10.1016/j.cma.2012.01.008
29. Schilling D, Borden MJ, Stolarski HK. Isogeometric collocation for phase-field fracture models. *Comput Methods Appl Mech Eng* (2015) 284:583–610. doi:10.1016/j.cma.2014.09.032



OPEN ACCESS

EDITED BY

Leilei Chen,
Huanghuai University, China

REVIEWED BY

Jianfeng Yang,
Xi'an University of Science and
Technology, China
Lixing Zheng,
Shanxi University, China

*CORRESPONDENCE

Xuan Peng,
✉ pengxuan89@sina.com

SPECIALTY SECTION

This article was submitted to Statistical
and Computational Physics,
a section of the journal
Frontiers in Physics

RECEIVED 13 January 2023

ACCEPTED 24 February 2023

PUBLISHED 13 March 2023

CITATION

Peng X, Wang Z, Shen G and Yang Y
(2023), Optimized cabinet parameters for
drying lithium-ion batteries based on
coupled fluid–thermal field analysis.
Front. Phys. 11:1143477.
doi: 10.3389/fphy.2023.1143477

COPYRIGHT

© 2023 Peng, Wang, Shen and Yang. This
is an open-access article distributed
under the terms of the [Creative
Commons Attribution License \(CC BY\)](#).
The use, distribution or reproduction in
other forums is permitted, provided the
original author(s) and the copyright
owner(s) are credited and that the original
publication in this journal is cited, in
accordance with accepted academic
practice. No use, distribution or
reproduction is permitted which does not
comply with these terms.

Optimized cabinet parameters for drying lithium-ion batteries based on coupled fluid–thermal field analysis

Xuan Peng*, Zhaohui Wang, Gang Shen and Yong Yang

Department of mechanical engineering, Suzhou University of Science and Technology, Suzhou, China

Hot-airflow desiccation is a commonly applied technique for drying lithium-ion batteries. However, most drying cabinet designs currently suffer from poor efficiency because they evacuate steam by ejecting the hot air in the cabinet to the open air continuously. This can be addressed by closing and opening the cabinet periodically, where the temperature of the heating zone is increased as quickly as possible through internal air recirculation in the closed position, and the steam is ejected with the hot air only during the open period. Nonetheless, drying cabinet designs of this nature have been rarely subjected to numerical analysis based on computational fluid dynamics and heat transfer, and the design factors enhancing the rate of temperature increase during the closed period remain poorly understood. The present work addresses these issues by outlining a detailed numerical approach for simulating the airflow temperature of a drying cabinet during internal air recirculation in its closed position, and the characteristics of the airflow and the temperature distribution in the dryer are evaluated *via* transient fluid–thermal coupling analysis. The results of the numerical investigation indicate that the heating efficiency is substantially influenced by the inlet airflow velocity, the distance between the trays holding the batteries, and the size of the free space between the front door and the trays. The results demonstrate that the developed model provides a useful means of evaluating and optimizing the heating efficiency of these types of drying cabinets.

KEYWORDS

drying cabinet, computational fluid dynamics, numerical simulation, thermal analysis, structure design

1 Introduction

The drying process is a crucial component in the manufacture of lithium-ion batteries, and hot-airflow desiccation is very commonly applied for this purpose. However, an optimal hot-airflow drying cabinet design is crucial for maximizing drying efficiency and minimizing energy use, which are essential considerations in industrial manufacturing operations. Nonetheless, this issue is seriously complicated by the fact that optimal drying cabinet design varies significantly according to the material to be heated or dried.

The process of optimizing the designs of all types of drying cabinets has been substantially streamlined by applying numerical analysis based on computational fluid dynamics (CFD) and heat transfer because these tools provide a powerful and economic method for evaluating the airflow and temperature distributions in the dryer. Accordingly, a great number of studies have been devoted to constructing CFD models for the thermal

devices used in manufacturing, food, and pharmaceutical engineering fields. For example, Amanlou and Zomorodian [1] studied the impact of geometrical shapes on the drying capabilities of drying cabinets. Park et al. [2] demonstrated that the direction and location of the hot air injection have a significant influence on the thermal field in a gas oven cavity. Wang et al. [3] optimized the design of a room for drying American ginseng based on numerically modeled airflow and heat transfer characteristics, and the results demonstrated that inhomogeneity in the airflow and temperature distributions are mainly influenced by the inlet airflow rate, inlet diameter, and number of partition boards employed in the drying room. Moreover, the results indicated that the drying process is highly affected by the convective heat transfer characteristics of the room, which can be adjusted by varying its structural parameters and the inlet airflow rate.

Analogous results to those discussed previously can be found in a number of studies involving cooling devices [4–7]. In addition to convective heat transfer, the role of radiative heat transfer in the airflow and temperature distributions of ovens and drying devices has also been investigated numerically. For example, Kokolj et al. [8] adopted a Monte Carlo-based radiation model that enabled numerical evaluations of the baking performance of a forced convection oven, and a linear relationship was established between the oven temperature and the level of bread browning. Román-Roldán et al. [9] modeled radiative heat transfer using the discrete ordinate method in a mixed greenhouse food dryer, where solar energy served as the heat source, and the impact of various design features on the airflow and wall temperature distributions were analyzed. However, the time dependence of the wall temperature was not verified. Rek et al. [10] again modeled radiative heat transfer based on the discrete ordinate method to investigate the impacts of various structural features on the airflow and temperature distributions in a new-generation heating oven. The results indicated that the oven temperature had an insignificant effect on the radiative heat transfer in the oven because the temperature was relatively low.

A further complication arises in the modeling of ovens and drying devices because water is vaporized from the material in the heating process and enters the hot airflow, which forms a coupled thermal and moisture diffusion phenomenon that must be included in numerical models. These considerations are further crucial because the moisture content in food is of critical concern in food engineering applications. For example, Lemus-Mondaca et al. [11] coupled thermal and mass transfer phenomena in the drying process of olive waste cake using a temperature-dependent latent heat of vaporization and the effective diffusivity of moisture defined by an Arrhenius-type equation, where modeling was conducted in conjunction with the finite volume method. Nasser et al. [12] considered water evaporation and condensation in the bread baking process using a multi-flow fluid model. Specific to lithium-ion battery desiccation, Zhao et al. [13] calculated an effective diffusion coefficient for water vapor by means of Fick's equation and an Arrhenius-type equation when analyzing the vacuum drying kinetics of a lithium cathode material through empirical models related to the moisture and drying rate. However, the characteristics of drying for the cathode material differ from those of the battery core. The drying process specific to the cores of lithium-ion batteries was investigated by Jiang et al.

[14], where a high-temperature environment was generated within a cylindrical vacuum oven by injecting hot nitrogen gas. Both radiative and conductive heat transfer inside the battery core were analyzed in detail *via* CFD simulations.

However, most reported drying cabinets reported in the literature suffer from poor efficiency because they evacuate the steam by ejecting the hot air in the cabinet to the open air continuously. This issue is addressed by periodically closing and opening the cabinet, where the temperature of the heating zone is increased as quickly as possible through internal air recirculation in the closed position, and the steam is ejected with the hot air only during the open period. However, relatively few studies have evaluated the thermal and airflow characteristics for these types of drying cabinets. Moreover, most of the few existing studies have focused on improving the homogeneity of the airflow and temperature in the steady state, while the factors influencing the rate of temperature increase in the closed position remain poorly understood.

The present work addresses these issues for lithium-ion battery desiccation by outlining a detailed numerical approach for simulating the airflow temperature of a drying cabinet during internal air recirculation in its closed position, and the characteristics of the airflow and temperature distributions in the drying cabinet are evaluated *via* thermal-mass transfer coupling analysis. Moreover, an analysis of the homogeneity in the airflow and temperature distributions is important to ensure that the batteries can be heated uniformly. The ultimate goal of the present work is to obtain a maximum possible rate of temperature increase in the drying cabinet during its closed period because this rate of temperature increase plays a crucial role in improving the drying efficiency of the cabinet. To this end, we explore several structural factors affecting the rate of temperature increase in the drying cabinet in an effort to obtain the optimal parameters.

The remainder of this paper is organized as follows. The physical and CFD models and simulation settings are presented in [Section 2](#), where the geometrical structure of the drying cabinet is first outlined, and the governing equations involved in the fluid-thermal coupling analysis are reviewed. In addition, the process of simplifying the batteries as a porous medium and the simplified treatment of the fan inlets are presented in detail. [Section 3](#) presents the numerical results based on CFD and thermal simulations, where the characteristics of the airflow and temperature distributions in the drying cabinet are first analyzed. Then, the structural factors influencing the rate of temperature increase in the cabinet and the homogeneity in the airflow and temperature distributions are explored, and the optimized combination of parameters is adopted for simulation. Finally, [Section 4](#) summarizes the conclusions of the study and suggests topics for future study.

2 Numerical modeling of the drying cabinet

A physical model of the drying cabinet investigated herein is presented in [Figure 1A](#). As can be seen, the cabinet is mainly composed of fans, thin porous plates, cylindrical batteries stacked

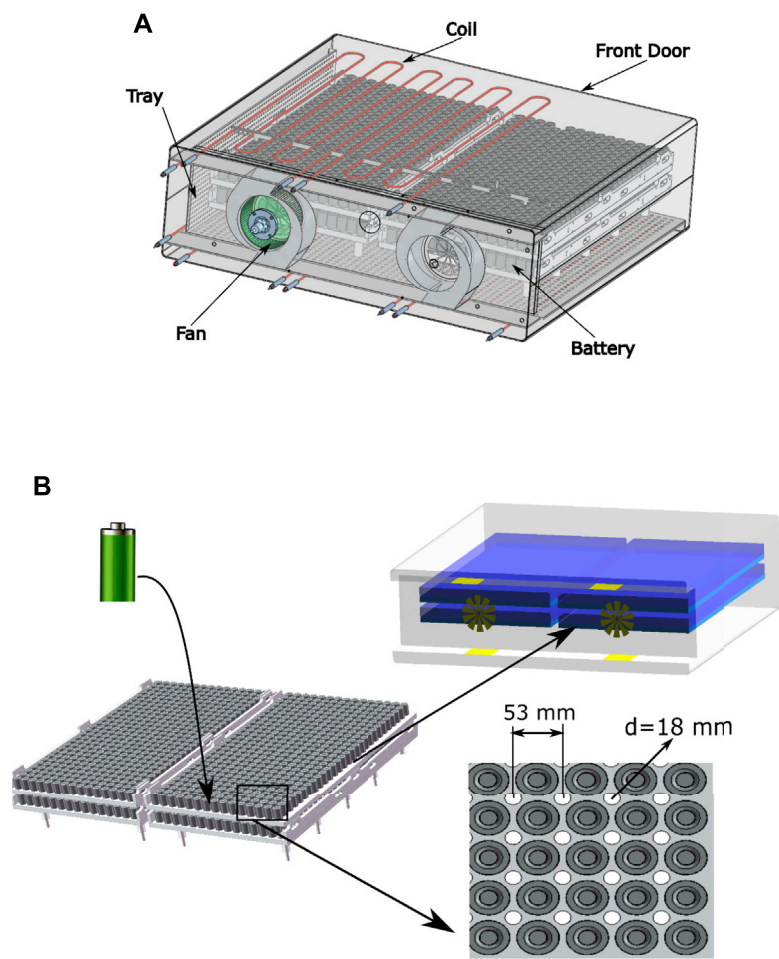
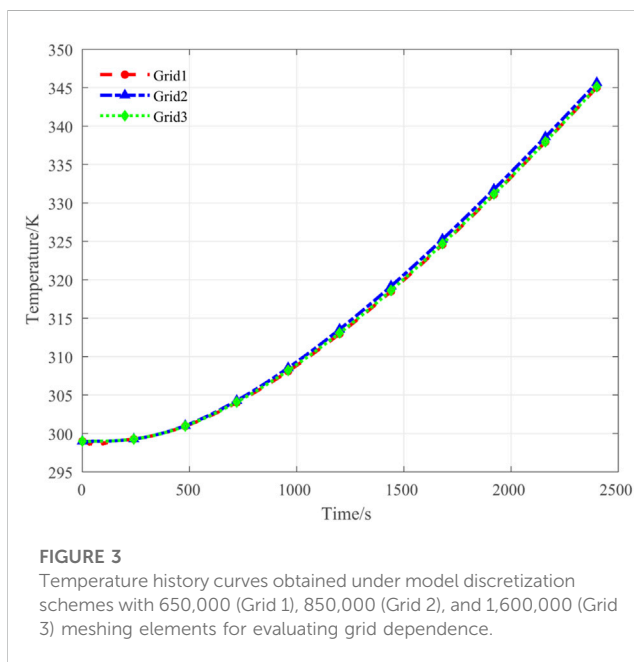
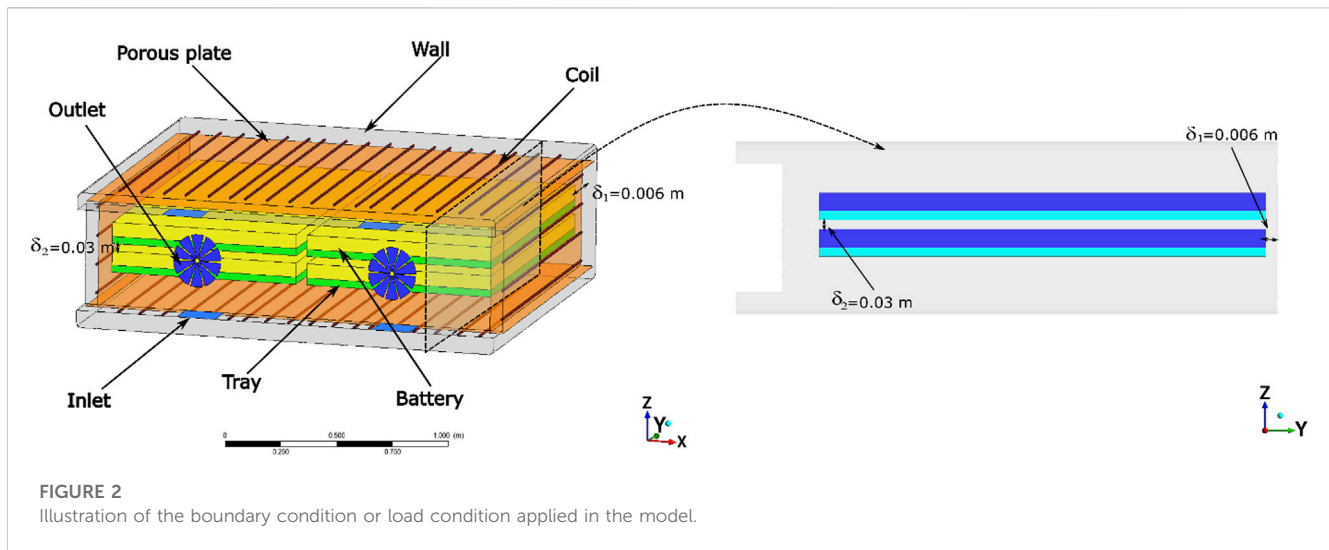


FIGURE 1 Illustrations of the drying cabinet investigated in the present work: **(A)** physical model that is mainly composed of fans, heating coils, porous plates, cylindrical batteries stacked on trays, and a front door for loading and unloading; **(B)** simplified model applied for CFD analysis.

TABLE 1 Parameters obtained experimentally for boundary conditions.

Inlet	$ u = 4.47 \text{ m/s}$	Initial temperature $T_{in} = 300 \text{ K}$
Outlet	Pressure outlet	Initial temperature $T_{out} = 300 \text{ K}$
Porous plate	$C_2 = 1029.3 \text{ m}^{-1}$	Thermal resistance rate $k = 5.928 \times 10^{-6} (\text{m}^2\text{K})/\text{W}$
	$\alpha = 4.765 \times 10^{-10} \text{ m}^2$	
Wall	Non-slip boundary	Adiabatic
Coil	—	Heat source density
		$Q = 1.25 \times 10^7 \text{ W/m}^3$
Battery region	$C_2 = 10.84 \text{ m}^{-1}$	—
	$\frac{1}{\alpha} = 2.21 \times 10^7 \text{ m}^{-2}$	
Trays	$C_2 = 64.22 \text{ m}^{-1}$	—
	$\frac{1}{\alpha} = 1.31 \times 10^8 \text{ m}^{-2}$	

on trays, and a front door for loading and unloading. The regions of the drying chamber surrounding the porous plates represent spaces of free airflow, and the airflow is directly heated by electric coils. The porous plates then permit the warm air access to the batteries for drying when air is drawn from the internal space of the drying cabinet and blown into the airflow space by the fans. The four trays



and battery configurations are illustrated in Figure 1B, which also presents a properly simplified drying cabinet structure for CFD analysis. The trays include holes with diameters $d = 18$ mm evenly spaced about the batteries at 53 mm intervals to improve airflow. The overall size of the cabinet is of 1,300 mm \times 1,500 mm \times 565 mm. The height and diameter of the lithium ion batteries are 89 mm and 46 mm, respectively.

2.1 Governing equations

All simulations were conducted using the commercial CFD software package Ansys Fluent. The governing equations employed for a compressible Newtonian fluid include the continuum equation and the momentum equations in the x ,

y , and z directions, which can be specified, respectively, as follows:

$$\frac{\partial \rho}{\partial t} + \nabla(\rho \mathbf{u}) = 0, \quad (1)$$

$$\frac{\partial(\rho u)}{\partial t} + \nabla(\rho u \mathbf{u}) = -\frac{\partial p}{\partial x} + \nabla(\mu \nabla u) + S_x, \quad (2)$$

$$\frac{\partial(\rho v)}{\partial t} + \nabla(\rho v \mathbf{u}) = -\frac{\partial p}{\partial y} + \nabla(\mu \nabla v) + S_y, \quad (3)$$

$$\frac{\partial(\rho w)}{\partial t} + \nabla(\rho w \mathbf{u}) = -\frac{\partial p}{\partial z} + \nabla(\mu \nabla w) + S_z, \quad (4)$$

where t is the time, p is the pressure, ρ is the density, μ is the dynamic viscosity, u , v , and w are the scalar components of the fluid velocity \mathbf{u} , and the momentum source terms S_x , S_y , and S_z denote the contributions of the body force in the x , y , and z directions, respectively. For free airflow, S_x , S_y , and S_z are zeros.

Ignoring the viscous dissipation effect, the energy equation can be written as

$$\frac{\partial(\rho h)}{\partial t} + \nabla(\rho h \mathbf{u}) = -p \nabla \cdot \mathbf{u} + \nabla(k \nabla T) + S_T, \quad (5)$$

where h is the total enthalpy, k is the thermal conductivity, T is the temperature, and S_T is the heat source term.

2.2 Modeling batteries as a porous medium

Direct modeling of the batteries residing in the trays to be dried is quite challenging because of the complexity of the geometry due to the great number of batteries involved, which imposes a substantial burden when applying the computational mesh to the system. However, this issue can be largely resolved by modeling the batteries loaded on the trays as a porous medium with a porosity that is easily calculated based on their alignment (Figure 1B). In addition, the porous plates separating the airflow channels and the internal space of the drying cabinet can be treated analogously as porous boundaries. Simplifications based

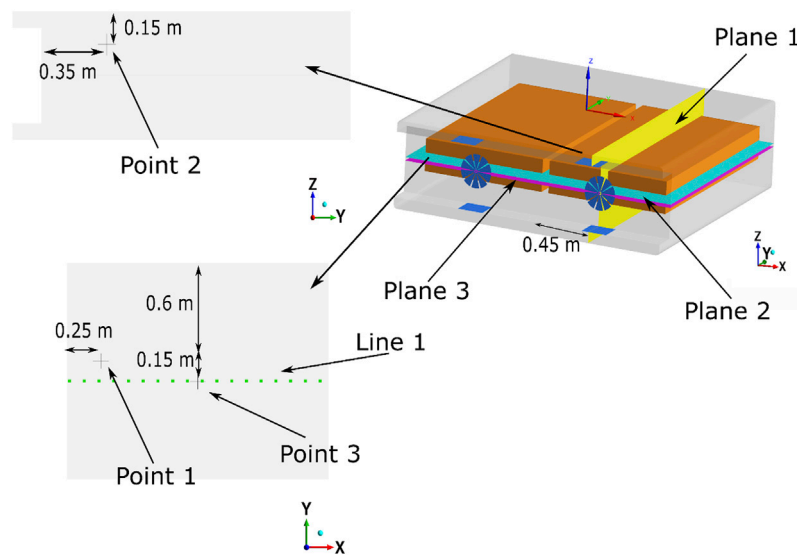


FIGURE 4
Sampling positions applied in the numerical experiments.

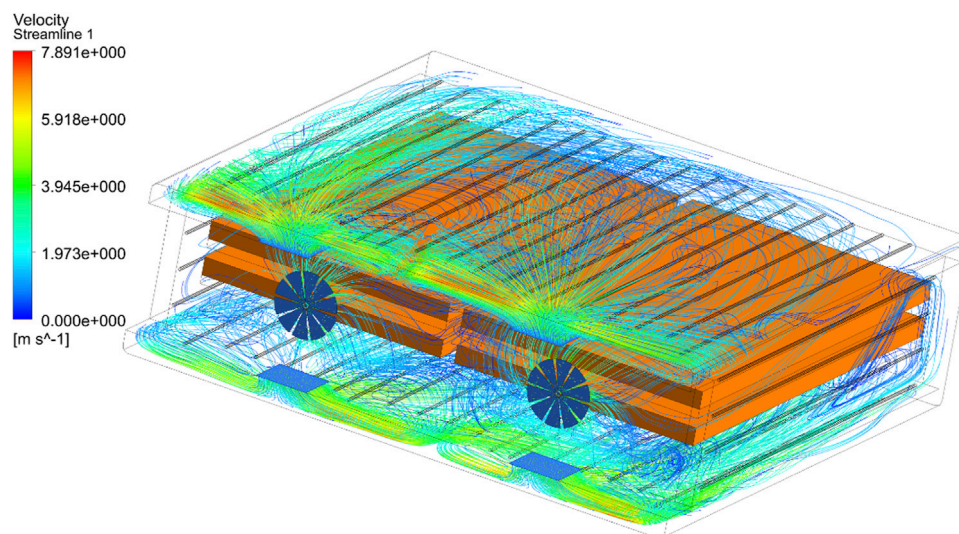


FIGURE 5
Instantaneous airflow velocity streamlines of the model at a simulation time of 2,400 s.

on porous media have been widely used in CFD simulations applied in the food engineering field [15–17].

The resistance to airflow induced by a porous medium is accounted for as an additional source term S in the momentum equations, which is defined according to viscous and inertial components as follows:

$$S_i = \frac{\Delta P}{\Delta n} = -\left(\sum_{j=1}^3 D_{ij} \mu u_j + \sum_{j=1}^3 F_{ij} \rho \frac{1}{2} |u| u_j\right), \quad (6)$$

where u_j is the velocity in the j -th direction and $|u|$ is the magnitude of the velocity inside the porous medium. Δn is the thickness of the porous zone, and D_{ij} and F_{ij} are the elements of coefficient matrices that represent the pressure drop due to viscous and inertial resistances, respectively. For a uniformly porous medium, the off-diagonal entries of D_{ij} and F_{ij} are 0. Therefore, Eq. 6 can be simplified as

$$S_i = -\left(\frac{\mu}{\alpha} u_i + C_2 \rho |u| u_i\right), \quad (7)$$

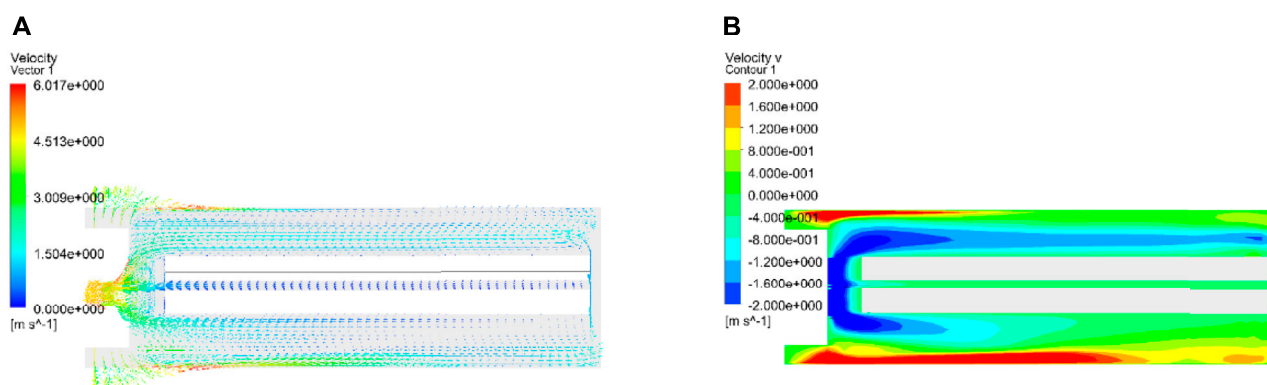


FIGURE 6
Instantaneous velocity vector field (A) and velocity contour plot of the u_y component (B) for Plane 1 at 2,400 s.

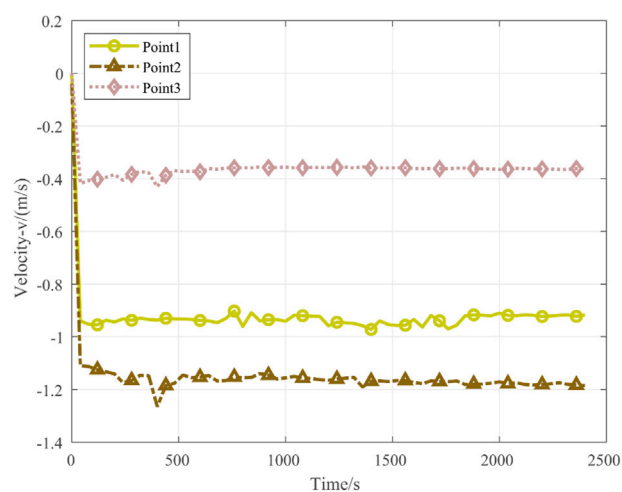


FIGURE 7
History of u_y at sample Points 1, 2, and 3.

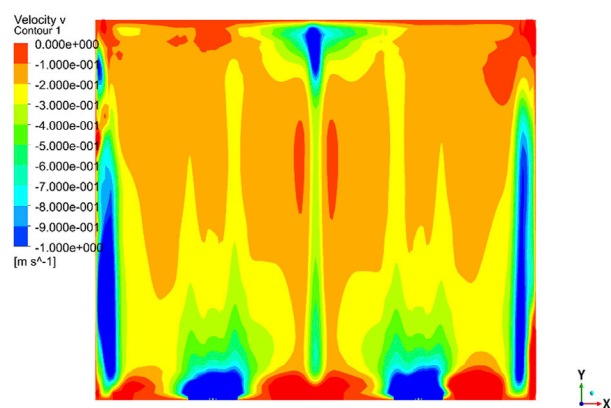


FIGURE 8
Instantaneous contour plot of u_y for Plane 2 at 2,400 s.

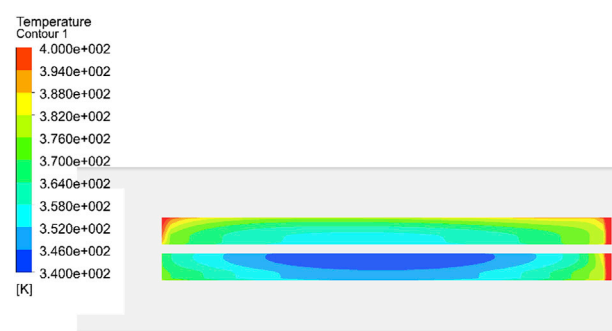


FIGURE 9
Instantaneous temperature distribution of Plane 1 at 2,400 s.

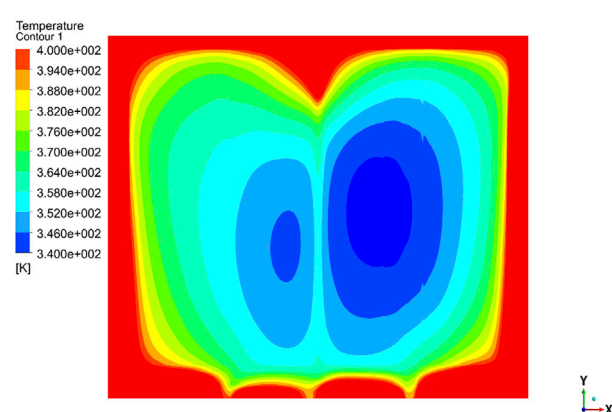


FIGURE 10
Instantaneous temperature distribution of Plane 3 at 2,400 s.

where α is the permeability and C_2 is the inertial resistance coefficient. These two parameters can be determined by least-squares fitting to experimental plots of the pressure drop through

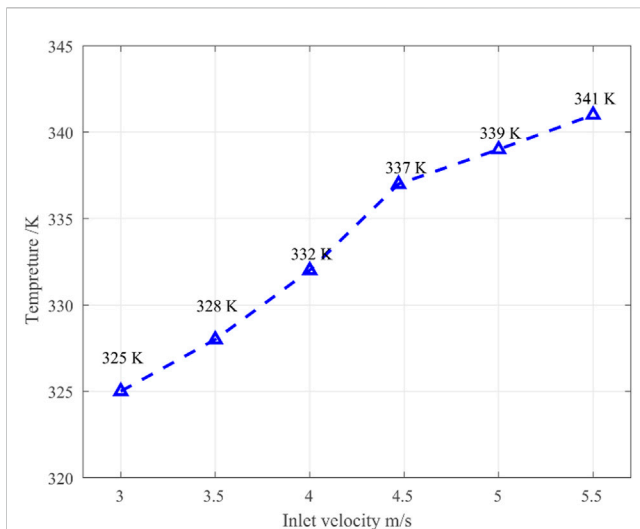


FIGURE 11

Lowest instantaneous temperature observed in the battery region at 2,400 s as a function of the magnitude of the inlet airflow velocity.

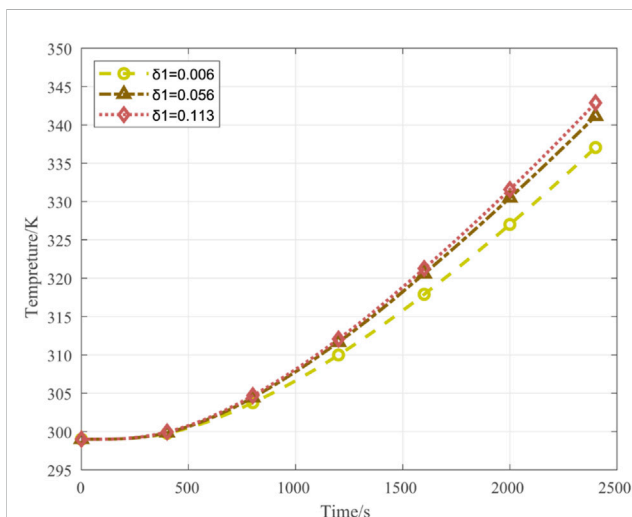


FIGURE 12

Effect of the distance δ_1 between the front door and the battery region on the lowest temperature in the drying cabinet as a function of simulation time.

porous media with respect to the airflow velocity [18]. The resulting parameters obtained for the inlet boundary conditions are listed in Table 1.

2.3 Boundary conditions

The regions associated with boundary conditions or load conditions are defined herein according to the simplified CFD model presented in Figure 2. Hexahedral-dominant meshing elements were used to discretize the computational domain.

The process of determining the boundary conditions was simplified by applying the following assumptions:

- 1) The influence of the wall on the heat transfer of air in the exterior zone is ignored
- 2) The wall thickness is uniform
- 3) No chemical reactions occur on the battery surfaces during the heating process
- 4) Heat variations in the airflow due to fan rotation are ignored

The model is further simplified by removing the fans and applying only two inlets and four outlets. An airflow velocity boundary is set for the inlets based on the actual flow rate of the fan, and the outlets are set as pressure outlet boundaries. Moreover, the temperature of the air at the inlets and outlets remains constant during the computations because the total thermal energy does not change when the air flows through the fan zones. This is realized by modifying the user-defined function (UDF) in Fluent. The boundary and load conditions applied in the simulations are listed in Table 1. Meanwhile, the operating pressure of the drying cabinet was set at 80 kPa.

2.4 Computational parameters and methods

The Semi-Implicit Method for Pressure-Linked Equations (SIMPLE) algorithm was used to solve the continuum and momentum equations. A second-order upwind scheme was applied for differentiation of the convective term. The divergence theorem was applied for the pressure gradient source term and diffusion term with quadratic precision discretization applied for the surfaces of the control volume. The convergence criterion of the error norm for the continuum and momentum equations was set at 3×10^{-3} , and that for the energy equation was set at 1×10^{-5} . All simulations were conducted on a personal computer with an Intel Xeon dual CPU operating at 3.40 GHz and 64 GB of RAM.

3 Numerical results

As discussed, the ultimate goal of the present work is to determine the structural design parameters that provide a maximum possible rate of temperature increase in the battery region of the drying cabinet during its closed period. This can be determined based on the temperature history curve obtained for the battery region during simulations. However, the temperature is not uniform throughout the battery region. The present work addresses this inconsistency by applying temperature history curves based on the position in the battery region with the lowest temperature. However, this position is not being fixed for all configurations. Therefore, we employ a Fluent UDF to locate this position during each simulation.

We first conducted a grid dependence study to determine the optimal grid density. To this end, we compared the temperature history curves obtained with 20 iterations applied for each 1 s time step under discretization schemes with 650,000, 850,000, and 1,600,000 meshing elements, and the results are given in

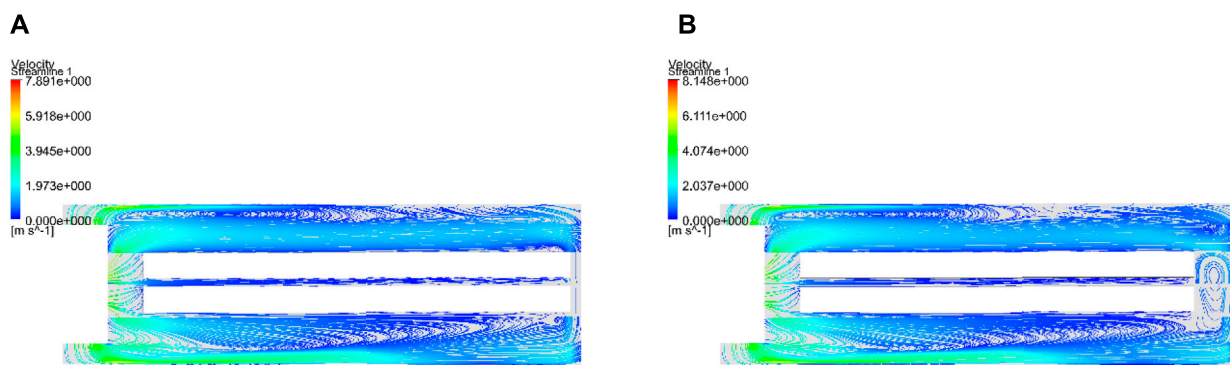


FIGURE 13

Instantaneous airflow velocity streamlines at 2,400 s for different values of δ_1 : (A) $\delta_1 = 0.06$ m and (B) $\delta_1 = 0.113$ m.

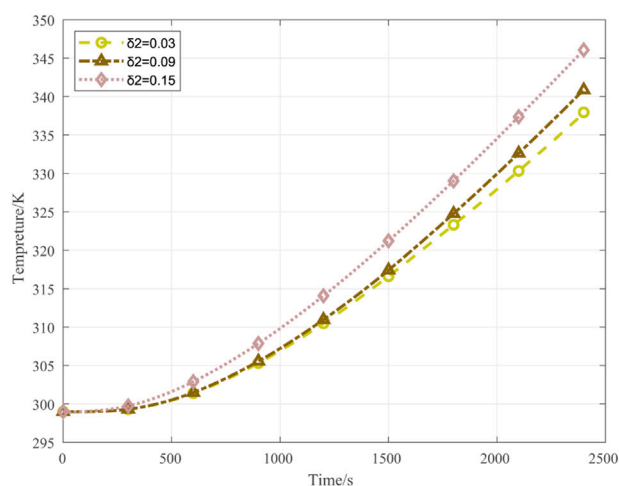


FIGURE 14

Effect of the distance δ_2 between the top of the batteries in the lower tray and the bottom of the upper tray on the lowest temperature in the drying cabinet as a function of simulation time.

Figure 3 with respect to 2,400 time steps in 1 s intervals. As can be seen, the lowest temperature position in the battery region increases exponentially, where the temperature increases slowly at the beginning and then rapidly after 800 s of heating. We further note that the different meshing schemes produce very little difference among the obtained temperature history. Therefore, 850,000 meshing elements were uniformly applied in all subsequent simulations, and 20 iterations were applied for each 1 s time step.

A uniform discussion of results was ensured by restricting analysis to specific planes in the numerical model (Figure 2) and at specific points within those planes. As illustrated in Figure 4, Plane 1 resides in the yz plane at $x = 0.45$ m and includes a cross section of the battery region, two inlets, and an outlet, Plane 2 resides in the xy plane between the lower and upper battery regions at $z = -0.278$ m, and Plane 3 also resides in the xy plane near the lower

battery region at $z = -0.3$ m. In addition, the position of sample Point 2 on Plane 1 is shown in the top left corner of the figure, while the positions of sample Points 1 and 3 and Line 1 on Plane 2 are clearly defined in the bottom left corner of the figure.

3.1 Airflow and temperature fields of the basic configuration

The instantaneous airflow velocity streamlines of the entire model in its basic configuration at a simulation time of 2,400 s is presented in Figure 5. As can be seen, high-velocity regions exist near the top and bottom wind channels close to the inlets, and a maximum velocity of 7.8 m/s is obtained. The velocity decreases substantially near the front door and when passing through the battery region under the resistance generated by the porous medium. Meanwhile, the velocity recovers near the outlets.

This behavior in the airflow is further illustrated by the instantaneous velocity vectors and the velocity contour of components u_y presented for Plane 1 at 2,400 s in Figures 6A, B, respectively. These results clearly demonstrate how the airflow direction and magnitude change in the y direction. Basically, the airflow travels in the positive y direction in the wind channels with the magnitude decreasing as the airflow approaches the front door. Then, the airflow changes to the negative y direction and the air moves back toward the fan with a velocity that increases with decreasing distance from the fan. However, the airflow velocity between the lower and upper battery trays is uniformly low at around 0.1 m/s.

The history curves of u_y at the three samples points are plotted in Figure 7. As can be seen, the velocity at these points tends to be stable after rapidly increasing in the negative direction within the first few seconds. Therefore, we focused on the velocity field observed at a simulation time of 2,400 s. The instantaneous contour plot of u_y observed for Plane 2 at 2,400 s is presented in Figure 8. As can be seen, the velocity generally decreases gradually from the outlets to the front door. However, the velocity around the battery trays is higher than that in the interior area of Plane 2. The mean value of u_y calculated over an array of 8×9 uniformly

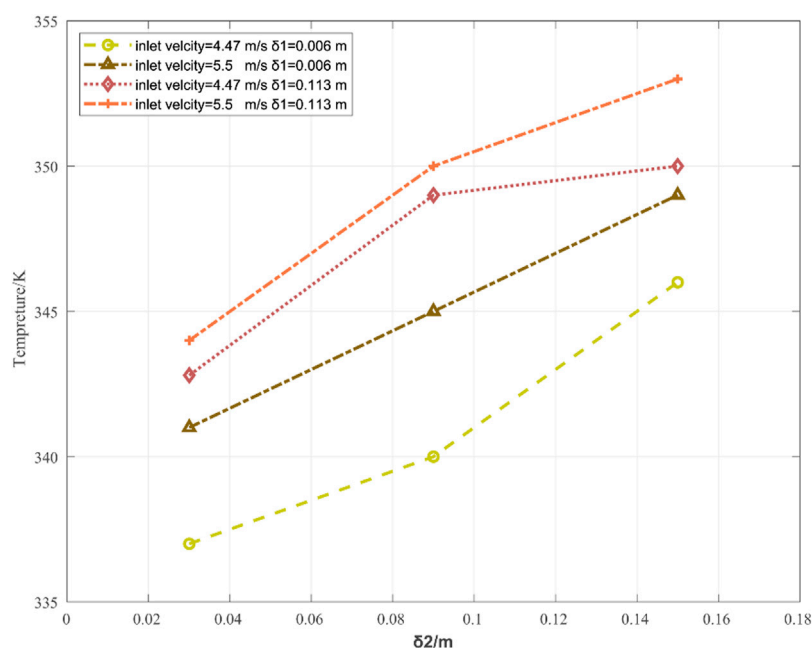


FIGURE 15

Lowest instantaneous temperature observed in the battery region at 2,400 s as a function of δ_2 for different values of the inlet airflow velocity and δ_1 .

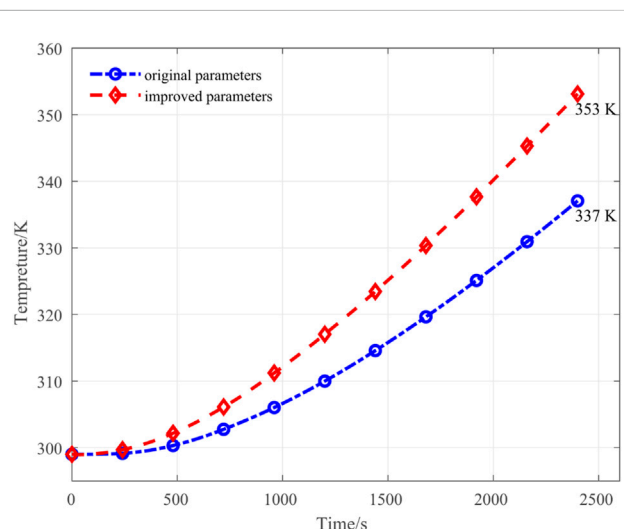


FIGURE 16

Lowest temperature in the drying cabinet for the basic configuration and optimized configuration as a function of simulation time.

distributed points was -0.13 m/s with a standard deviation of 0.08. This non-uniformity in the velocity field may result in uneven heat transfer.

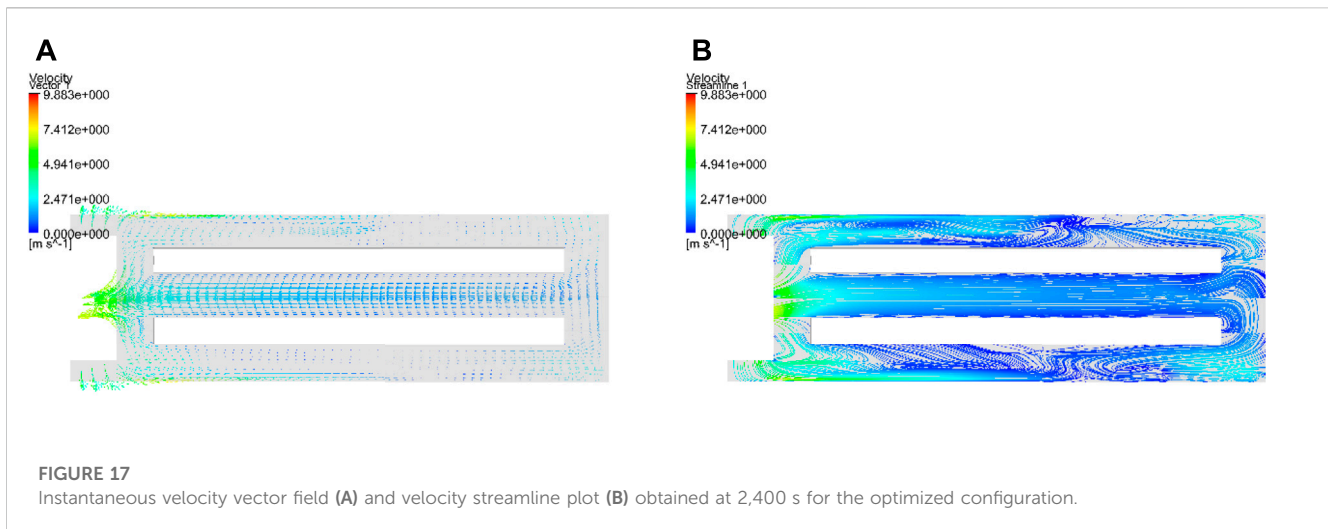
The instantaneous temperature distribution of Plane 1 is presented in Figure 9. As can be observed, the temperature decreases gradually from the exterior to the interior zone, and the region of the upper battery tray is warmer than the region of

the lower battery tray, while the central area of the lower battery tray at the top is the coolest zone. We expect that the temperature in this lowest-temperature zone can be further decreased by optimizing the cabinet structure.

The instantaneous temperature distribution of Plane 3 at 2,400 s is presented in Figure 10. We note that the temperature of this region between the battery trays decreases from the exterior to the interior zone, but the distribution is not symmetric as was observed directly between the battery trays for Plate 2. At this lower point between the battery trays, the temperature distributed over the right-hand side is less compared to that distributed over the left-hand side, and the maximum temperature difference was 70 K on this plane. The asymmetric temperature distribution is observed on the upper part of the battery region. This is because of the asymmetric airflow caused by the skewed inlet, as shown in Figure 1.

3.2 Factors affecting heat efficiency

The aforementioned discussion has demonstrated that the central area at the top of the batteries in the lower battery tray is the coolest zone, while the airflow velocity in the space between the batteries in the upper and lower battery trays is relatively low. This indicates that a relatively low rate of heat convection results in the relatively low rate of temperature increase in the drying cabinet. Moreover, the inlet airflow velocity has been a common subject of investigation [3, 4, 6], while other studies have demonstrated that the efficiency of convective heat transfer in, for example, solar-based drying devices can be improved effectively by selecting a suitable inlet airflow velocity [19, 20]. In addition, the aforementioned results



demonstrated that the airflow velocity is low in the free space between the front door and the battery region. Therefore, the distance between the front door and the battery region can be expected to have a substantial effect on the rate of temperature increase in the drying cabinet. Finally, the aforementioned results demonstrated that the airflow velocity is relatively low between the batteries in the upper and lower battery trays. Therefore, the distance between the upper and lower battery trays also can be expected to have a substantial effect on the rate of temperature increase in the drying cabinet because the lowest temperature is observed near this zone. Accordingly, the structural factors investigated in an effort to maximize the rate of temperature increase in the drying cabinet include the airflow velocity at the inlet, the free space between the front door and the battery region, and the distance between the upper and lower battery trays. Here, each of these parameters is varied in the simulations with the values of the other two parameters held at the standard values applied in the basic configuration. The exception to this is that a value of $\delta_1 = 0.09$ m is generally applied as the standard value.

3.2.1 Inlet airflow velocity

The influence of inlet airflow velocity was evaluated by comparing the lowest temperatures in the battery region observed instantaneously at 2,400 s when simulating the battery drying process with $|u|$ values of 3.5, 4, 4.47, 5, and 5.5 m/s. The lowest temperatures are plotted in Figure 11 as a function of $|u|$. As can be seen, the lowest temperature increases monotonically with increasing $|u|$. Nevertheless, we did not consider $|u|$ values greater than 5.5 m/s, owing to limitations in fan power. We later consider the impact of inlet airflow velocity together with changes in the other parameters.

3.2.2 Width of the free space between the front door and the battery region

The effect of the distance δ_1 between the front door and the battery region on the lowest temperature in the drying cabinet is presented in Figure 12 as a function of simulation time. As can be

seen, the temperature at the lowest-temperature position increases at an increasing rate as the value of δ_1 increases. The rationale for this behavior can be determined according to the instantaneous airflow velocity streamlines obtained at 2,400 s for δ_1 values of 0.06 and 0.113 m, which are presented in Figures 13A, B, respectively. Accordingly, we can surmise that the free space close to the front door helps to gather the airflow and drive the airflow through the gap between the upper and lower battery trays. Hence, the convective heat transfer increases with increasing δ_1 . However, the benefit of increasing δ_1 incurs an obvious penalty because the proportion of the available space that can be loaded with batteries decreases with increasing δ_1 , which detracts from the efficiency of the drying cabinet in a different way. Fortunately, we further note from Figure 12 that the change in the rate of temperature increase is relatively large when δ_1 changes from 0.006 m to 0.056 m, but this change diminishes substantially when δ_1 increases from 0.056 m to 0.113 m. Hence, the improvement gained by further enlarging the free space is limited.

3.2.3 Distance between upper and lower battery trays

The effect of the distance δ_2 on the lowest temperature in the drying cabinet battery regions is presented in Figure 14 as a function of simulation time. Clearly, the rate with which the temperature increases improves greatly with increasing δ_2 . However, the benefit of this dimension is once again limited due to the restriction on the size of the drying cabinet.

3.2.4 Multi-parameter effects

The aforementioned results demonstrate that changes in the value of a single parameter can indeed improve the heat transfer efficiency of the drying cabinet. However, the combined effects of inlet airflow velocity, δ_1 , and δ_2 remain unexamined. This is addressed by plotting the lowest instantaneous temperature observed in the battery region at 2,400 s as a function of δ_2 for different values of inlet airflow velocity and δ_1 in Figure 15. As can be seen, an inlet airflow velocity of 5.5 m/s and $\delta_1 = 0.113$ m yield maximum instantaneous temperatures for all values of δ_2 .

considered. Accordingly, we selected the parameter values of 5.5 m/s for the inlet airflow velocity, $\delta_1 = 0.113$ m, and $\delta_2 = 0.15$ m as the optimal parameters and plotted the lowest temperature in the drying cabinet for the basic configuration and optimized configuration as a function of simulation time in Figure 16. The results demonstrate that the optimal parameters yield a much greater rate of heating than the standard parameters, where the temperature difference is 10 K at 1800 s and 16 K at 2,400 s.

The benefits of the optimal parameters are further evaluated based on the instantaneous velocity vector field and velocity streamline plot obtained at 2,400 s for the optimized configuration, which are, respectively, presented in Figures 17A, B. The comparison between Figure 17B and Figure 6 indicates that the density of streamlines between the upper and lower battery trays increases after optimizing the configuration. This indicates that the airflow in the gap zone is faster than that observed for the basic configuration. Moreover, the absolute value of u_y exceeded 1 m/s, and the mean value of u_y calculated over an array of 8×9 uniformly distributed points was -1.5 m/s, which has a greater magnitude than the value of -0.13 m/s observed for the basic configuration.

4 Conclusion and future work

The present work addressed the poorly understood effect of the parameter values of periodically opening and closing drying cabinets on their drying efficiency by outlining a numerical approach for simulating the airflow temperature in the drying cabinet in its closed position and then evaluating the characteristics of the airflow and temperature distributions in the drying cabinet *via* thermal–mass transfer coupling analysis. The main contribution of this work can be stated as follows:

- 1) The simulation process was simplified by modeling the fan zone as inlet/outlet boundaries, and a UDF was applied to maintain equivalent temperatures at these boundaries during each iteration of the process to obtain a consistent heating process without directly modeling the fans.
- 2) Rather than applying the homogeneity of the temperature distribution in the steady state as a measure of the heating efficiency, this was evaluated in the present work based on the history of the lowest temperature in the battery region over a specified heating period. This criterion represents a direct measurement of the heating rate of the drying cabinet.
- 3) The heat efficiency of the cabinet depends on the uniformity of the temperature in the battery region, which is highly influenced by convective heat transfer. Therefore, we evaluated the temperature history at the position with the lowest temperature in the battery region near the gap between the upper and lower trays. Meanwhile, the velocity of the airflow through the gap was low.
- 4) The numerical results demonstrated that increasing the inlet velocity, the distance between upper and lower battery trays, and the distance between the front door and the battery region collaboratively generates better airflow conditions. Compared

to the basic configuration, the optimized configuration increased the lowest temperature in the battery region by 13 K after heating for 40 min.

Accordingly, the results presented demonstrate that the developed model provides a useful means of evaluating and optimizing the heating efficiency of these types of drying cabinets. Future work will focus on developing a more intelligent approach for obtaining optimal cabinet design parameters with the help of advanced optimization methods, such as particle swarm methods. Machine learning can be also incorporated to improve the efficiency of the numerical model.

Data availability statement

The original contributions presented in the study are included in the article/Supplementary Material; further inquiries can be directed to the corresponding author.

Author contributions

XP, ZW, YY, and GS contributed to the conception and design of the study. ZW organized the database. XP performed the statistical analysis. ZW wrote the first draft of the manuscript, while XP, GS, YY, and ZW wrote specific sections of the manuscript. All authors contributed to the manuscript revision and reading processes and approved the final submitted version.

Acknowledgments

The supply of data related to the geometry of the drying cabinet and operation by Wujiang Jingling[®] drying-oven manufacturers is gratefully acknowledged.

Conflict of interest

The authors declare that the research was conducted in the absence of any commercial or financial relationships that could be construed as a potential conflict of interest.

Publisher's note

All claims expressed in this article are solely those of the authors and do not necessarily represent those of their affiliated organizations, or those of the publisher, the editors, and the reviewers. Any product that may be evaluated in this article, or claim that may be made by its manufacturer, is not guaranteed or endorsed by the publisher.

References

- Amanlou Y, Zomorodian A. Applying CFD for designing a new fruit cabinet dryer. *J Food Eng* (2010) 101:8–15. doi:10.1016/j.jfoodeng.2010.06.001
- Park SH, Kim YH, Kim YS, Park YG, Ha MY. Numerical study on the effect of different hole locations in the fan case on the thermal performance inside a gas oven range. *Appl Therm Eng* (2018) 137:123–33. doi:10.1016/j.applthermaleng.2018.03.087
- Wang P, Liu G, Ao S, Sun D, Yu B, Wu X. Numerical investigation of airflow and heat transfer characteristics and optimal design of the American ginseng drying room. *Appl Therm Eng* (2021) 183:115885. doi:10.1016/j.applthermaleng.2020.115885
- Wang G-B, Zhang X-R. Enhanced airflow by additional axial fans for produce cooling in a cold room: A numerical study on the trade-off between cooling performance and irreversibility. *Int J Refrigeration* (2021) 130:452–65. doi:10.1016/j.ijrefrig.2021.06.030
- Saw LH, Ye Y, Tay AAO, Chong WT, Kuan SH, Yew MC. Computational fluid dynamic and thermal analysis of Lithium-ion battery pack with air cooling. *Appl Energy* (2016) 177:783–92. doi:10.1016/j.apenergy.2016.05.122
- Chauhan A, Trembley J, Wrobel LC, Jouhara H. Experimental and CFD validation of the thermal performance of a cryogenic batch freezer with the effect of loading. *Energy* (2019) 171:77–94. doi:10.1016/j.energy.2018.12.149
- Zhao C-J, Han J-W, Yang X-T, Qian J-P, Fan B-L. A review of computational fluid dynamics for forced-air cooling process. *Appl Energy* (2016) 168:314–31. doi:10.1016/j.apenergy.2016.01.101
- Kokolj U, Škerget L, Ravnik J. A numerical model of the shortbread baking process in a forced convection oven. *Appl Therm Eng* (2017) 111:1304–11. doi:10.1016/j.applthermaleng.2016.10.031
- Román-Roldán NI, Ituna Yudson JF, López-Ortiz A, Rodríguez-Ramírez J, Sandoval-Torres S. A new air recirculation system for homogeneous solar drying: Computational fluid dynamics approach. *Renew Energy* (2021) 179:1727–41. doi:10.1016/j.renene.2021.07.134
- Rek Z, Rudolf M, Zun I. Application of CFD simulation in the development of a new generation heating oven. *Strojniški vestnik - J Mech Eng* (2012) 58:134–44. doi:10.5545/sv-jme.2011.163
- Lemus-Mondaca R, Zambra C, Rosales C. Computational modelling and energy consumption of turbulent 3D drying process of olive-waste cake. *J Food Eng* (2019) 263:102–13. doi:10.1016/j.jfoodeng.2019.05.036
- Al-Nasser M, Fayssal I, Moukalled F. Numerical simulation of bread baking in a convection oven. *Appl Therm Eng* (2021) 184:116252. doi:10.1016/j.applthermaleng.2020.116252
- Zhao F, Han F, Zhang S, Tian H, Yang Y, Sun K. Vacuum drying kinetics and energy consumption analysis of LiFePO₄ battery powder. *Energy* (2018) 162:669–81. doi:10.1016/j.energy.2018.08.023
- Jiang Z, Zhao F, Guan Y, Qiu Z. Research on vacuum drying process and internal heat conduction of Li-ion battery core. *Theor Appl Mech Lett* (2019) 9:120–9. doi:10.1016/j.taml.2019.02.008
- Rong L, Aarnink AJA. Development of ammonia mass transfer coefficient models for the atmosphere above two types of the slatted floors in a pig house using computational fluid dynamics. *Biosyst Eng* (2019) 183:13–25. doi:10.1016/j.biosystemseng.2019.04.011
- Xin Y, Rong L, Wang C, Li B, Liu D. CFD study on the impacts of geometric models of lying pigs on resistance coefficients for porous media modelling of the animal occupied zone. *Biosyst Eng* (2022) 222:93–105. doi:10.1016/j.biosystemseng.2022.07.015
- Doumbia EM, Janke D, Yi Q, Amon T, Krieger M, Hempel S. CFD modelling of an animal occupied zone using an anisotropic porous medium model with velocity depended resistance parameters. *Comput Elect Agric* (2021) 181:105950. doi:10.1016/j.compag.2020.105950
- Zhou D, Du Y, Wang P, Qian H, Zhou Y. Experimental study on the influence of gas flux on flow resistance in porous media. *J Logistical Eng Univ* (2011) 27:50–3+81. doi:10.3969/j.issn.1672-7843.2011.04.0117843.2011.04.011
- Getahun E, Delele MA, Gabbiye N, Fanta SW, Demissie P, Vanierschot M. Importance of integrated CFD and product quality modeling of solar dryers for fruits and vegetables: A review. *Solar Energy* (2021) 220:88–110. doi:10.1016/j.solener.2021.03.049
- Demissie P, Hayelom M, Kassaye A, Hailesilassie A, Gebrehiwot M, Vanierschot M. Design, development and CFD modeling of indirect solar food dryer. *Energy Proced* (2019) 158:1128–34. doi:10.1016/j.egypro.2019.01.278



OPEN ACCESS

EDITED BY

Leilei Chen,
Huanghuai University, China

REVIEWED BY

Kunming Li,
China Three Gorges University, China
Cheng Ruhui,
Xi'an Jiaotong University, China

*CORRESPONDENCE

Qidan Xiao,
✉ xiaoqidan253@163.com

SPECIALTY SECTION

This article was submitted to Statistical
and Computational Physics,
a section of the journal
Frontiers in Physics

RECEIVED 10 February 2023

ACCEPTED 24 February 2023

PUBLISHED 20 March 2023

CITATION

Xiao Q, Xia Y, Zhang G, Lin X and Zhao J
(2023), Numerical simulation study on
pore clogging of pervious concrete
pavement based on different
aggregate gradation.
Front. Phys. 11:1162899.
doi: 10.3389/fphy.2023.1162899

COPYRIGHT

© 2023 Xiao, Xia, Zhang, Lin and Zhao.
This is an open-access article distributed
under the terms of the [Creative
Commons Attribution License \(CC BY\)](#).
The use, distribution or reproduction in
other forums is permitted, provided the
original author(s) and the copyright
owner(s) are credited and that the original
publication in this journal is cited, in
accordance with accepted academic
practice. No use, distribution or
reproduction is permitted which does not
comply with these terms.

Numerical simulation study on pore clogging of pervious concrete pavement based on different aggregate gradation

Qidan Xiao^{1,2*}, Yapei Xia^{1,2}, Guanguan Zhang^{1,2}, Xiaoli Lin^{1,2} and Jun Zhao³

¹College of Architecture and Civil Engineering, Xinyang Normal University, Xinyang, China, ²Henan New Environmentally-Friendly Civil Engineering Materials Engineering Research Center, Xinyang Normal University, Xinyang, China, ³School of Water Conservancy and Civil Engineering, Zhengzhou University, Zhengzhou, China

Pervious concrete (PC) pavements can effectively reduce surface runoff, but it will be clogged with time and its service life will be affected. In this study, based on three groups of PC specimens with different aggregate gradations optimized by previous experiments, the pavement-clogging simulation test is carried out using the two-way coupling of the particle flow code with computational fluid dynamics (PFC-CFD). The results show that when the gradation of aggregates in the pervious pavement is different, the volume fraction of clogging material in the pavement and the time when the volume fraction of the clogging material reaches the maximum are also different. It is related to the zigzag degree and size of the pore in the pervious pavement. The smaller the particle size of coarse aggregate in the pervious pavement, the easier it is to be clogged, and the discontinuous graded coarse aggregate has a good shielding effect on the clogging material. Different clogging material gradations have different effects on the clogging of pervious pavements. According to the aforementioned research results, researchers can select different mix ratios of anti-clogging PC according to different areas of use. The law obtained from the experiment can provide a reference for further study of the double-layer pervious pavement structure design.

KEYWORDS

pervious concrete, PFC-CFD simulation, different aggregate gradation, clogging material, pore clogging

1 Introduction

Pervious concrete (PC) generally contains no or minimal fine aggregate; due to the low cement content, coarse aggregates can form a large number of interconnected pores [1], so rainwater can freely infiltrate into the PC pavement and reduce the problem of urban waterlogging [2]. With time, different types of clogging material will be transported to the interior of a PC pavement under the action of rainwater or natural settlement [3], which will eventually reduce the permeability of PC and seriously reduce the service life of the pervious pavement [4].

B. Debnath et al. [5] showed that the clogging of PC mainly depends on the coarse aggregate's size, and the smaller the particle size of coarse aggregate, the higher the clogging rate. V. V. Hung et al. [6] found that porosity and permeability decrease with the increase in

fine aggregate proportion. G. Brunetti et al. [7] used different sizes of sand as clogging materials and found that fine sand could significantly reduce the permeability of pervious concrete. J. Zhang et al. [8] believed that the active time of fine sand in pores is longer than that of coarse sand, and when the clogging particles are only coarse sand, the peak is shorter than that in the case of fine sand. G. F. B. Sandoval et al. [9] studied the results showing that the plugging particles with smaller particle sizes (clay and sediment C) significantly harm the decrease of permeability. J. P. Coughlin et al. [10] found clay can clog pervious roads about ten times as much as sand. J. W. Lee et al. [11] showed that in the case of small-size aggregate (1.0 mm–2.8 mm), the clogging depth is 15 mm, and in the case of large-size aggregate (>6.0 mm), the clogging depth can reach more than 35 mm. M. Kayhanian et al. [12] found that most of the clogging substance of a PC pavement occurs near the pavement's surface, and the clogging substance is mainly in the 25-mm depth of the pavement with low porosity. X. Nan et al. [13] showed that clogged particles of 0.6–2.2 mm are clogged in the pervious pavement of 2 cm, and particles smaller than 0.3 mm can enter the pervious pavement and form a deep blockage. Q. Yang et al. [14] found that rainfall intensity and duration will affect infiltration performance and clogging. M. Brugin et al. [15] showed that the rainfall mode and the pavement slope significantly influence the clogging of the pervious pavement. X. Cui et al. [16] believed that clogging is easy when the value of the particle size ratio is between 0.6 and 0.8. J. Zhang et al. [17] believed that clogging material of the full gradation is more likely to block the specimens with higher porosity.

G. F. B. Sandoval et al. [18] believed that the permeability coefficient of a pervious pavement decreases significantly in the first 5 years; so, it is necessary to maintain the pervious pavement once a year in the first 5 years. J. Huang et al. [19] found that cleaning with pressurized water is only effective for the top 30 mm of the pervious specimen. A. Singh et al. [20] showed that pressurized water is also effective in removing up to 3.18 mm sediments but is less efficient at deeper depths. A research study by N. Hu et al. [21] showed that the combination of pressure cleaning and vacuum suction best removes clogging material in a pervious pavement. G. F. B. Sandoval et al. [22] believed that according to the type of clogging material, it is necessary to maintain pervious pavements regularly to prevent the decrease of the permeability coefficient. A. Kia et al. [23] developed a new type of pervious pavement with a low curvature pore structure, which has anti-clogging performance, high permeability, and strength but a high preparation and installation cost. A research study by I. Barišić et al. [24] showed that when the aggregate of PC is a mixture of small and large particle sizes, the permeability coefficient decreases slowly and has a favorable effect on mechanical properties. K. S. Elango et al. [25] showed that the PC prepared with binder has good permeability and can meet the requirements of pervious concrete. A. Garcia et al. [26] believed that in order to prepare the mix proportion of PC with a low clogging rate, it is necessary to analyze the clogging material in this area and prepare the PC mixture which is less than or larger than the pore diameter. H. Zhou et al. [27] found that the equivalent diameter of the pore is determined by CT scanning and image processing. The open and closed pores' geometric properties are calculated using the algorithm code [28]. A. Parvan et al. [29] obtained the real pore

structure to explore the development process of hydraulic characteristics.

G. Ma et al. [30] developed a numerical simulation to study the hydraulic characteristics of pervious pavements and to visualize the clogging process. J. Xu et al. [31] studied the distribution of clogging material and the development of clogging depth in the PC pavement under the action of natural deposition and seepage through the discrete element method (DEM) and computational fluid dynamics (CFD). J. Hu et al. [32] showed that based on the CFD-DEM model, the clogging development process of pervious pavements under the action of rainfall is simulated by considering the factors of climate, pavement porosity, flow velocity, blocking material quality, and pavement structure. S. Remond et al. [33] showed that the motion and clogging of small spherical particles in the random accumulation of large balls are simulated by the DEM. In a study by X. Nan et al. [34], the CT scanning technique and Avizo software were used to reconstruct the inner hole structure, and the DEM model in CFD simulates the multiphase flow of surface particles in pervious concrete. J. Zhang et al. [35], based on the numerical simulation method, studied the anti-clogging performance of different pervious pavement structures. In a study by J. Zhang et al. [36], the mechanism and development law of pore clogging in the pervious pavement were studied using the CFD-DEM model. A research study by W. Zhao et al. [37] showed that the numerical simulation method could minimize the dependence on the real experimental work [38] and solve the problems that cannot be carried out in the laboratory [39, 40].

The aforementioned numerical simulation method simplifies the aggregate of PC to spherical particles, which is always different from the real aggregate shape. There are few experimental studies on the clogging of PC pavement with high compressive strength and good permeability in the literature. In this study, based on three groups of PC specimens with different aggregate gradations optimized by previous experiments, the pavement clogging simulation test is carried out using the CFD module in discrete element software PFC3D. The coarse aggregate in the PC specimen is composed of the real aggregate's clump, making the virtual specimen more authentic and scientific. In this study, the internal clogging of three pavement structures is studied through experiments and numerical simulation. Using the method of two-way coupling of the particle flow code with computational fluid dynamics (PFC-CFD), the clogging simulation experiments of different pervious pavements are carried out, and three clogging states of pervious pavements are obtained. The effects of coarse aggregate gradation and clogging material gradation on the anti-clogging ability of pervious pavements are analyzed. According to the research results, researchers can select different mix ratios of anti-clogging PC according to different areas of use. The law obtained from the experiment can provide a reference for the further study of the design of double-layer pervious pavement structures.

2 Experimental program

2.1 Materials

The cement used in this experiment is ordinary Portland cement with a strength grade of 42.5. The main parameters are shown in Table 1.

TABLE 1 Physical properties of P.O42.5 ordinary Portland cement.

Density (kg/m ³)	Specific surface area (m ² /kg)	Setting time		Flexural strength (MPa)		Compressive strength (MPa)	
		Initial setting (min)	Final setting (h)	3d	28d	3d	28d
3,110	389	130	6.6	5.6	9.2	33.7	56.4

TABLE 2 Physical properties of natural coarse aggregate.

Name	Aggregate size (mm)	Bulk density (kg/m ³)	Apparent density (kg/m ³)	Crushing value (%)	Water absorption (%)
Size A	5–10	1,441	2,680	13.9	1.15
Size B	10–15	1,453	2,680	11.5	0.79
Size C	15–20	1,502	2,680	9.8	0.42



FIGURE 1 Natural coarse aggregate with different particle sizes: (A) 5–10 mm; (B) 10–15 mm; (C) 15–20 mm.

Three kinds of aggregates are selected, which are 5–10 mm, 10–15 mm, and 15–20 mm. The performance indexes of the aggregates are shown in Table 2. The shape and appearance of the aggregates are shown in Figure 1.

2.2 Sediments

In the actual seepage process of pervious pavements, the clogging substance of different particle sizes in rainwater will reduce the performance of pervious pavements; so, the clogging simulation should be as close as possible to the clogging process in real life. The clogging material of the PC pavement was collected, as shown in Figure 2.

In this study, in order to better understand the range of particle size and clogging depth of clogging material, colored sand with different particle sizes is used as clogging material, as shown in Figure 3. The composition content of clogging material in each particle size range is shown in Table 3.

The colored sand is divided into fine sand, coarse sand, and full-grade sand using the screening method, and the particle size ranges are 0.15–0.6 mm, 0.6–4.75 mm, and 0.15–4.75 mm, respectively.

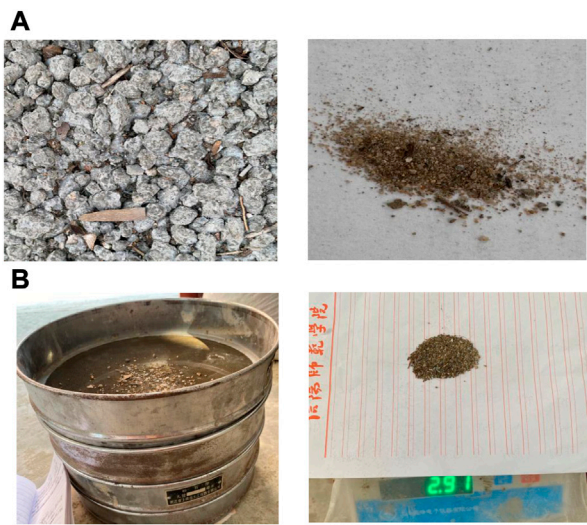


FIGURE 2 Collection and screening of clogging materials: (A) collection of clogging materials; (B) screened clogging materials.

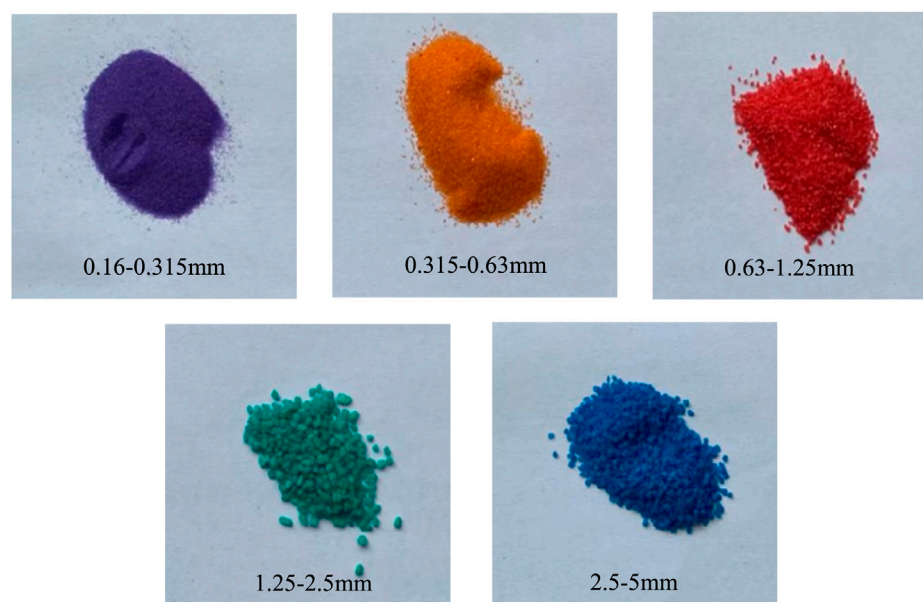


FIGURE 3
Colored sand with different particle sizes.

TABLE 3 Colored sand with different particle sizes.

Particle size (mm)	Proportion (%)	Sand color
0.16–0.315	40.5	Purple
0.315–0.63	25.5	Orange
0.63–1.25	14.2	Red
1.25–2.5	7.4	Blue
2.5–5	12.4	Green

2.3 Pervious concrete production and optimization

2.3.1 Pervious concrete production

The mixing method of this experiment is the cement paste wrapping method. First, the cement is poured into the mixer, and 1/2 the total quantity of water is added and stirred for 1 min to moisten the cement. At this point, coarse aggregate and cement paste may be well combined. Then, the aggregate is added and stirred for the 1 min. The aggregate is fully mixed with cement. Finally, the remaining water is poured and stirred for 2 min to get the PC mixture. In this experiment, there are nine specimens in each group, and the mold size of the specimens is 100 mm × 100 mm × 100 mm.

2.3.2 Pervious concrete optimization

The design point and mixed coarse aggregate analysis were carried out in this study using Design-Expert software, as shown in Table 4. The compressive strength and permeability of PC were predicted and optimized using regression equations and the response surface model. The basic mechanical properties and permeability of PC are optimally balanced by optimizing. After

optimization, the proportions of the three groups of mixed aggregates are 5–10 mm:15–20 mm = 7:3, 5–10 mm,10–15:15–20 mm = 3:1. Laboratory experiments verify the reliability of the optimization result. The error relative to the result was controlled by 5%, indicating that the prediction of the measured data of the confirmatory test of PC can be realized through the optimization results of the response surface design and has high accuracy. The optimum thickness of wrapped slurry is selected in the experiment, and the design porosity is 20%. Finally, three groups of PC with high compressive strength and good permeability are obtained and used as representative samples for the clogging test. The optimization results are shown in Table 5.

2.4 Laboratory clogging experiment

Based on the optimization in Section 2.3.2, three groups of PC specimens with high compressive strength and good permeability were chosen for the anti-clogging test. The simulation test was carried out using the pervious clogging device, as shown in Figure 4. The steps of the laboratory clogging experiment are as follows.

- (1) The specimen was sealed with adhesive tape, placed into the self-made pervious clogging device, and the container was lowered into the device. The mixture of clogging particles was collected as shown in Figure 4A.
- (2) Around 10 g clogging particles were obtained and spread evenly on the surface of the specimen. The spray intensity of the sprinkler simulating rainfall was kept unchanged and sprayed for 10 min, as shown in Figure 4B.
- (3) After the clogging test, the test water was filtered by a 0.16-mm sieve, and then, the collected colored sand was put into a

TABLE 4 Simplex centroid design point of aggregate gradation.

Notation	Different aggregate gradations (%)			Compressive strength (MPa)	Permeability coefficient (mm/s)
	Size A	Size B	Size C		
BC	0.000	0.500	0.500	14.64	6.69
ABC ₁	0.167	0.167	0.667	13.98	5.83
C	0.000	0.000	1.000	8.43	7.04
AB	0.500	0.500	0.000	15.14	5.27
B	0.000	1.000	0.000	14.78	6.37
B	0.000	1.000	0.000	14.86	6.03
ABC ₂	0.167	0.667	0.167	16.21	5.80
ABC ₃	0.667	0.167	0.167	17.71	4.07
AC	0.500	0.000	0.500	17.86	3.95
AB	0.500	0.500	0.000	15.34	5.13
A	1.000	0.000	0.000	16.98	3.4
A	1.000	0.000	0.000	16.85	3.21
C	0.000	0.000	1.000	10.71	6.58
ABC ₄	0.333	0.333	0.333	17.43	4.03

TABLE 5 Optimal performance result of permeable concrete.

Serial number	Aggregate gradation	Design porosity (%)	Compressive strength (MPa)	Permeability coefficient (mm/s)
P _{A1}	A:B = 7:3	20	29.14	1.48
P _{A2}	A		27.92	1.69
P _{A3}	B:C = 3:1		23.07	2.67

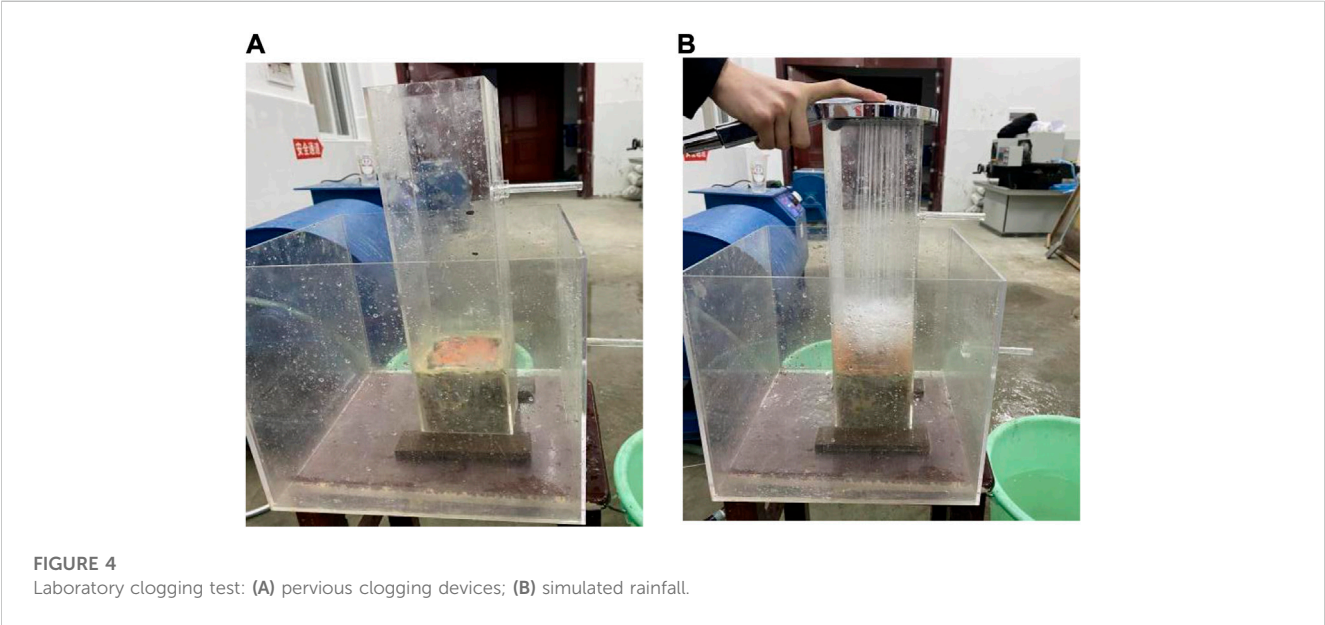
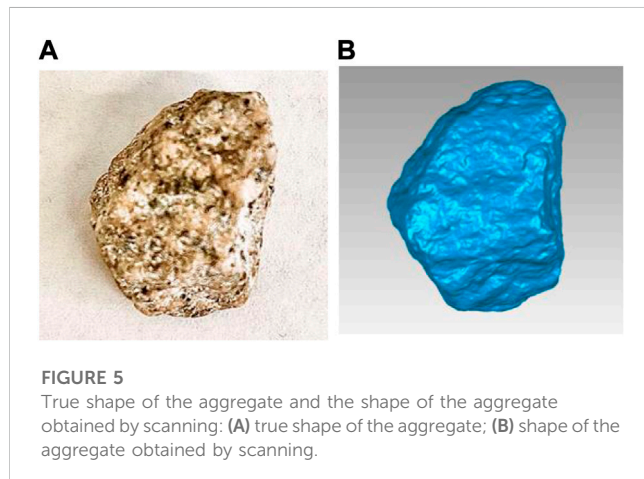


TABLE 6 Mass of each particle size range of the clogging material in the specimen.

Particle size (mm)	0.16–0.315	0.315–0.63	0.63–1.25	1.25–2.5	2.5–5
Clogging ratio of P_{A1} (%)	42.36	39.19	13.47	0	0
Clogging ratio of P_{A2} (%)	53.69	49.19	46.47	0	0
Clogging ratio of P_{A3} (%)	22.31	21.69	24.16	15.34	0



stainless steel tray and placed in the oven. After drying, its mass is a, and it is screened.

- (4) The specimen was removed from the device and dried. The colored sand on the surface of the specimen was gently swept. After drying, its mass is b, and it is screened.

The mass of the colored sand left inside the specimen is 10-a-b. The mass ratio of each particle size range of the internal clogging of the three groups of specimens is shown in Table 6.

3 Test and the simulation design

PFC can be considered a simplified implementation of the DEM. As the skeleton of pervious concrete, the size and shape of aggregate have an important influence on the performance of pervious concrete. The effective performance of the size and shape of the aggregate itself in the numerical simulation determines the effect of the numerical simulation of PC. The CFD module is included in the PFC3D program.

3.1 Discrete element model of pervious concrete

3.1.1 Aggregate scanning

In this study, the particle flow modeling method is adopted. In this experiment, a 3D laser scanner was used to scan the aggregate to obtain the STL file of aggregate outline information, and the corresponding aggregate model was reconstructed by PFC3D5.0 software, as shown in Figure 5.

3.1.2 Establishment of the aggregate cluster template

In this study, the STL file, which characterizes the outline information of the aggregate, is imported into PFC3D5.0 software to reconstruct the real shape of the aggregate. The specific steps are as follows.

- (1) Using the geometry import command built in to create geometry in PFC3D5.0, the STL file of aggregate is imported into software, as shown in Figure 6A.
- (2) The imported geometry is the surface outline of the aggregate, while the real aggregate is solid. Therefore, in order to simulate aggregate, it is necessary to fill the geometry with spherical particles, which are discrete elements in PFC3D5.0 software and can be realized by the command of a clump template created in PFC3D5.0. The geometry created in step (1) is imported into PFC5.0 through the keyword geometry, and the particles are automatically filled into the geometry to create an aggregate cluster template, as shown in Figure 6B.
- (3) The average aggregate volume was measured by the net basket method after weighing 100 g of each of the three kinds of aggregates. According to the mass ratio of mixed particle size aggregates, the volume fraction of each particle size in three 100 mm × 100 mm × 100 mm samples was calculated, as shown in Table 7. In the discrete element program, each particle's aggregate size and volume are input, and the samples with different aggregate size ratios are generated according to the aggregate cluster template.

3.1.3 Modeling of pervious concrete specimen

The STL file of the outer profile of the aggregate was introduced into PFC3D5.0 to establish the cluster template to characterize the aggregate. Based on the different particle sizes and porosity of the specimen in the test, the compaction process of permeable concrete was simulated, and the cube specimen of 100 mm × 100 mm × 100 mm was obtained. The specific steps are as follows.

- (1) A compression mold is generated. Because of the irregular shape of the aggregate unit, the number of coarse aggregates with a fixed volume in the fixed-volume mold must be less than the ratio of the two volumes; so the volume of the virtual mold is enlarged. After repeated experiments, the mold volume is three times the sample volume, and a cuboid box of 100 mm × 100 mm × 300 mm is generated by using the wall generate command, as shown in Figure 7A.
- (2) Coarse aggregate is added. Using the clump distribute command, according to the volume fraction of the particle size in different samples in Table 7, a certain number of aggregate models are generated in the box, as shown in Figure 7B.

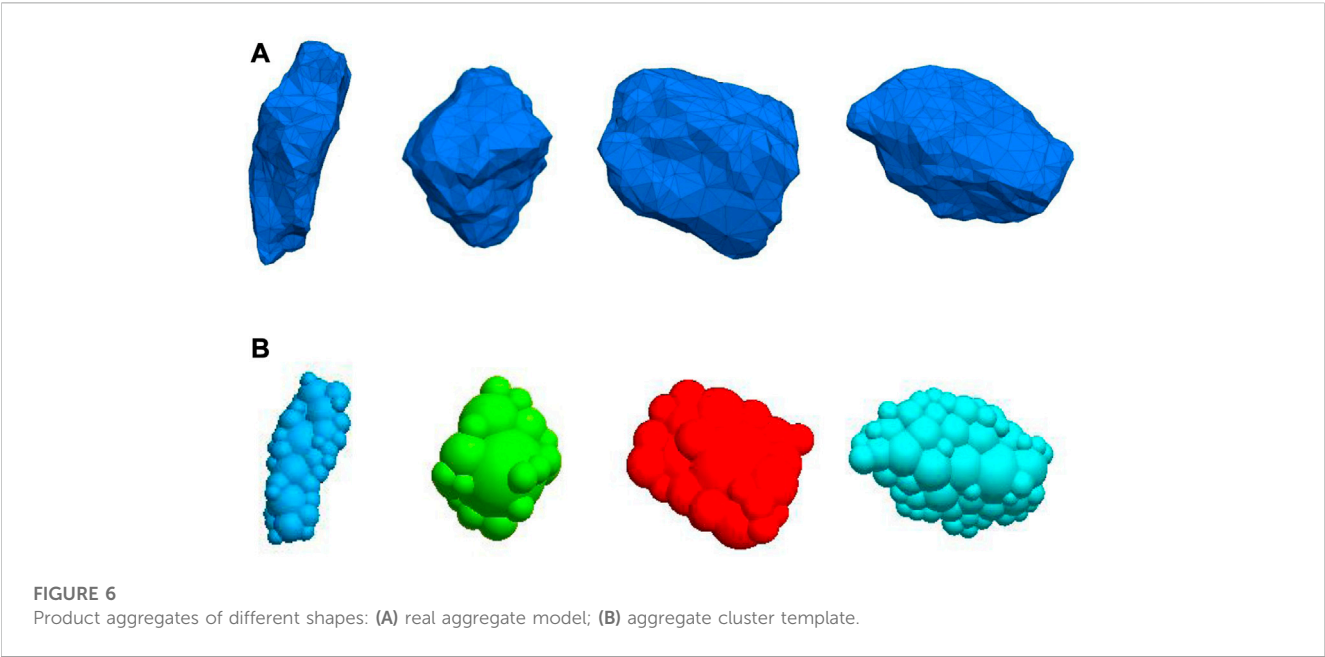


TABLE 7 Volume fraction of each particle size in the sample.

Particle size (mm)	5–10 mm	10–15 mm	15–20 mm
Volume fraction of P _{A1} (%)	70	0	30
Volume fraction of P _{A2} (%)	100	0	0
Volume fraction of P _{A3} (%)	0	75	25

and the cube test block model of 100 mm × 100 mm × 100 mm is obtained, as shown in Figure 7C.

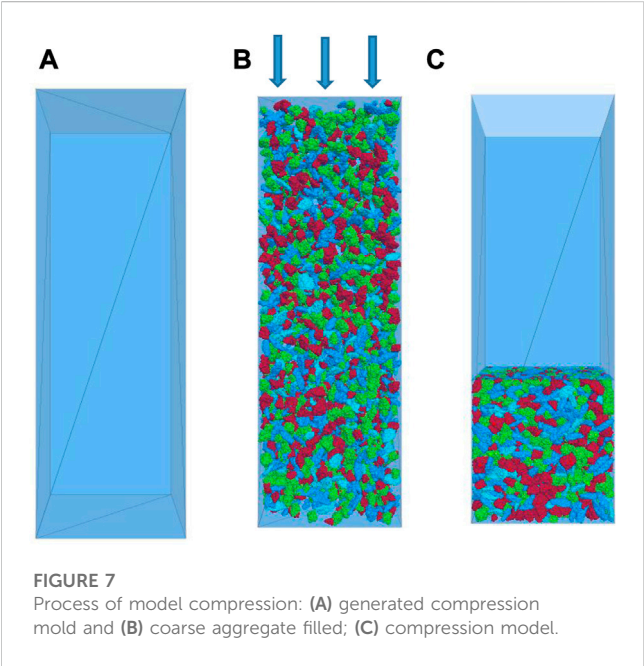
The contact model used in this study mainly involves the linear stiffness model, and the linear stiffness contact parameters of the aggregate model are shown in Table 8.

3.2 Modeling of the sediment

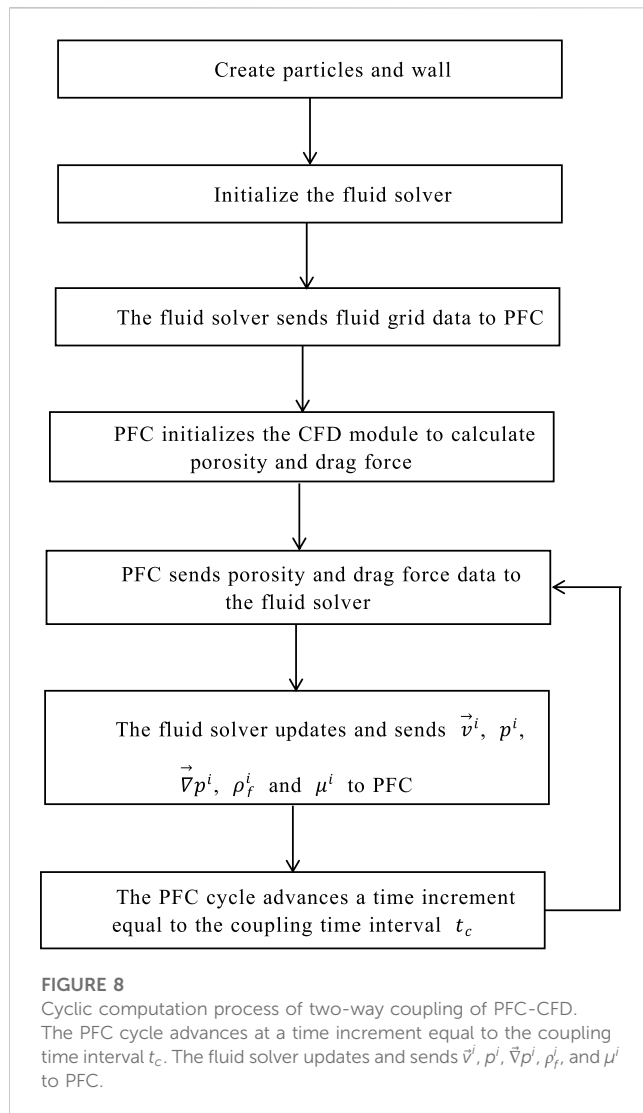
In PFC3D, the clogging material is represented by balls of different sizes. The contact between the clogging particles and the clump that makes up the pavement structure is set as a linear stiffness model. The contact parameters are analogous to coarse aggregates. The diameter of clogging particles is 0.16–5 mm. According to the proportion of the particle size of each clogging material in Section 2.2, it is assumed that 2 g clogging material is poured into the virtual specimen. According to the gradation of the clogging material, the median of the two adjacent sieve sizes is taken as the result of the average particle size [32]. The number of clogging materials and contact parameters for each particle size range are shown in Table 9.

3.3 Mathematical equations in the PFC-CFD model

In fact, under the action of rainwater and gravity, clogging particles flow into the interior of PC through the pores of pervious concrete, resulting in the clogging of pervious concrete. However, it is impossible to know the clogging inside the pores. In this study, the clogging simulation test uses the CFD module in PFC3D to visualize the clogging process, and the interaction between particles and fluid is considered.



- (3) The specimen is compressed. After the aggregate model is generated in the cuboid box, the direction, speed, and time are applied to the upper wall through the servo mechanism. When the mold height reaches 100 mm, the loading is stopped,



PFC3D gives the equation of motion of particles:

$$\frac{\partial \vec{u}}{\partial t} = \frac{\vec{f}_{mech} + \vec{f}_{flud}}{m} + \vec{g}, \quad (1)$$

$$\frac{\partial \vec{\omega}}{\partial t} = \frac{\vec{M}}{I}, \quad (2)$$

where \vec{u} is the velocity of the particle, m is the mass of the particle, \vec{f}_{flud} is the total force exerted by the fluid on the particle, \vec{f}_{mech} is the sum of the external forces acting on the particle (including the external force and contact force), \vec{g} is the acceleration of gravity, $\vec{\omega}$ is the angular velocity of rotation of the particle, I is the moment of inertia, and \vec{M} is the moment of inertia.

In order to calculate the fluid-particle interaction force, the particle cluster (clump) in PFC is regarded as a single spherical particle (calculating the equivalent radius at the same volume). The fluid-particle interaction force acts on the centroid of the particle cluster (clump) without considering the bending moment. The force exerted by the fluid on the particle (fluid-particle interaction) \vec{f}_{flud} consists of two parts: the drag force and the fluid pressure gradient force.

Drag force is defined as follows:

$$\vec{f}_{drag} = \vec{f}_0 \varepsilon^{-x}, \quad (3)$$

where \vec{f}_0 is the drag force on a single particle, ε is the porosity of the fluid unit in which the particle is located, and ε^{-x} is the empirical coefficient considering local porosity.

$$\vec{f}_0 = \left(\frac{1}{2} C_d \rho_f \pi r^2 |\vec{u} - \vec{v}| (\vec{u} - \vec{v}) \right), \quad (4)$$

where C_d is the drag force coefficient, ρ_f is the fluid density, r is the particle radius, \vec{v} is the fluid velocity, and \vec{u} is the particle velocity.

$$C_d = \left(0.63 + \frac{4.8}{\sqrt{Re_p}} \right), \quad (5)$$

TABLE 8 Linear stiffness contact parameters of the aggregate model.

Aggregate type	Density (kg/m ³)	Normal stiffness coefficient (N/m)	Tangential stiffness coefficient (N/m)	Friction coefficient	Poisson's ratio
Coarse aggregate	2,700	1e ⁹	1e ⁹	0.5	0.18

TABLE 9 Number of clogging materials and contact parameters in each particle size range.

Size range (mm)	Average diameter (mm)	Particle volume (m ³)	Number of particles	Density (kg/m ³)	Normal stiffness coefficient (N/m)	Tangential stiffness coefficient (N/m)	Friction coefficient	Poisson's ratio
0.16–0.315	0.24	1.38e ⁻¹¹	21,740	2,700	1e ⁹	1e ⁹	0.5	0.18
0.315–0.63	0.47	1.04e ⁻¹⁰	1817					
0.63–1.25	0.94	8.3e ⁻¹⁰	127					
1.25–2.5	1.88	6.64e ⁻⁹	9					
2.5–5	3.75	5.27e ⁻⁷	2					

where R_{ep} is the Reynolds number of the particles.

$$\chi = 3.7 - 0.65 \exp\left(-\frac{(1.5 - \lg R_{ep})^2}{2}\right), \quad (6)$$

$$R_{ep} = \frac{2\rho_f r |\vec{u} - \vec{v}|}{\mu_f}, \quad (7)$$

where μ_f is the dynamic viscosity coefficient of the fluid. The physical force applied to the fluid unit is as follows:

$$\vec{f}_b = \frac{\sum_j \vec{f}_{drag}^t}{V}, \quad (8)$$

where V is the volume of the fluid unit, and the summation object on the molecule is the particles overlapping with the fluid unit.

$$\vec{f}_{fluid} = \vec{f}_{drag} + \frac{4}{3}\pi r^3(\nabla p - \rho_f \vec{g}). \quad (9)$$

The physical strength per unit volume of each fluid unit is determined by drag and drag in the PFC3D:

$$\vec{f}_b^t = \frac{\sum_j \vec{f}_{drag}^t}{V_i}, \quad (10)$$

where V_i is the volume of the fluid unit, \vec{v}^i is the fluid velocity, p^i is the fluid pressure, $\vec{\nabla} p^i$ is the fluid pressure gradient, ρ_f^i is the fluid density, and μ^i is the hydrodynamic viscosity coefficient. Fluid software determines these parameters.

The flow with a low Reynolds number in porous media can usually be described by Darcy's law.

$$\vec{v} = \frac{K}{\mu \varepsilon} \vec{\nabla} p^i, \quad (11)$$

where \vec{v} is the flow velocity of the fluid, K is the permeability matrix, μ is the fluid viscosity, ε is the porosity matrix, and p is the fluid pressure. The cyclic calculation process of two-way coupling of PFC-CFD is shown in Figure 8.

3.4 The setup of the PFC-CFD simulation

The CFD module in PFC can be used to calculate porous media flow under three-dimensional conditions. Generate the boundary of the model wall; the size is 100 mm × 100 mm × 300 mm. A total of 2 g full-grade clogging particles are released on the top of the sample. It is found that the average void velocity of pervious pavements with 20% porosity is 0.015 m/s. At the speed of 0.015 m/s, water flows vertically into the wall from the entrance of the x-y plane located at zonal 0.22 m and flows out from the exit of the x-y plane at zonal 0 m. Except for the entrance and exit, the other wall boundaries are impervious. In the process of two-way coupling, the PC pavement structure composed of clumps always remains at rest, and the clogging particles enter the interior of the PC pavement with the flow of water, as shown in Figure 9.

The speed of the clump that makes up the pervious pavement is set to 0. The displacement of the clogging particles only changes when there is a collision between the clogged particles and the clump of the pavement. In this study, the time step of the fluid calculation is 2.0×10^{-4} s. In the actual calculation process, the time step of PFC3D is generally smaller than that

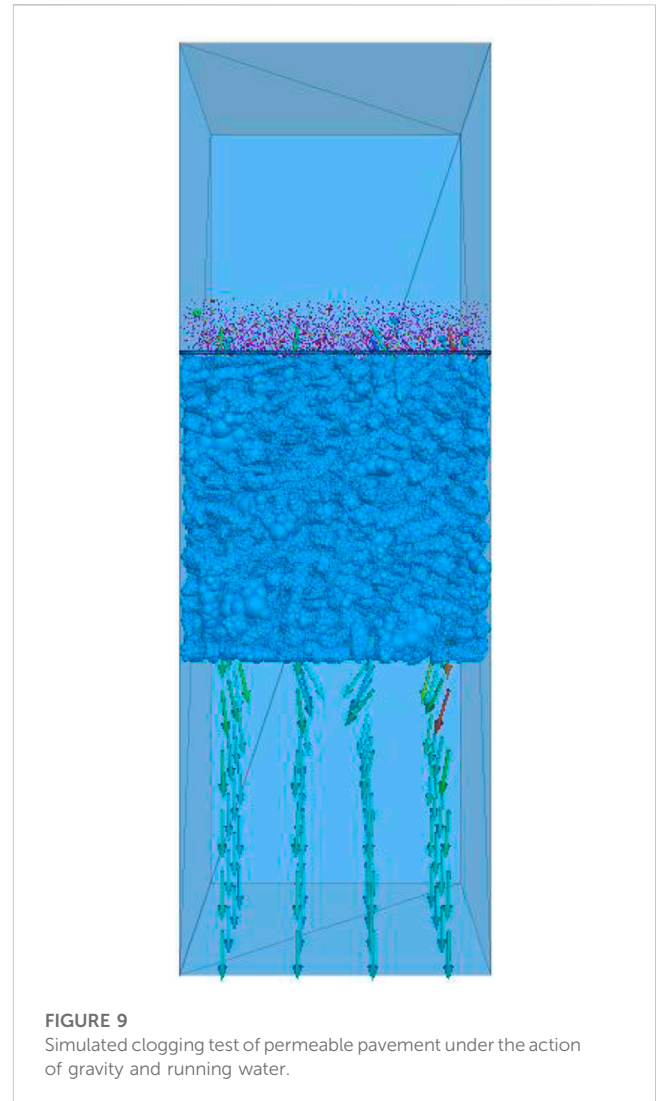


FIGURE 9
Simulated clogging test of permeable pavement under the action of gravity and running water.

of the fluid [32], and the time step of particle calculation is 2.0×10^{-6} s. The model is preserved every 100,000 time steps until the residual clogging particles in the pavement structure no longer move. The whole process of the two-way coupling calculation was carried out for 6 s.

Based on the optimization of Section 2.3.2, three groups of PC specimens with high compressive strength and good permeability were obtained for the anti-clogging test. In this study, the thickness of the designed pavement was 100 mm, and the pavement structure is divided into five layers along the vertical direction, namely, I layer (0–20 mm), II layer (20–40 mm), III layer (40–60 mm), IV layer (60–80 mm), and V layer (80–100 mm). The simulation test of clogging of three groups of specimens under the action of gravity and running water is shown in Figure 10.

4 Experimental results and analysis

4.1 Verification of the clogging simulation and test

Based on the same experimental conditions, laboratory and numerical simulation clogging experiments were carried out on

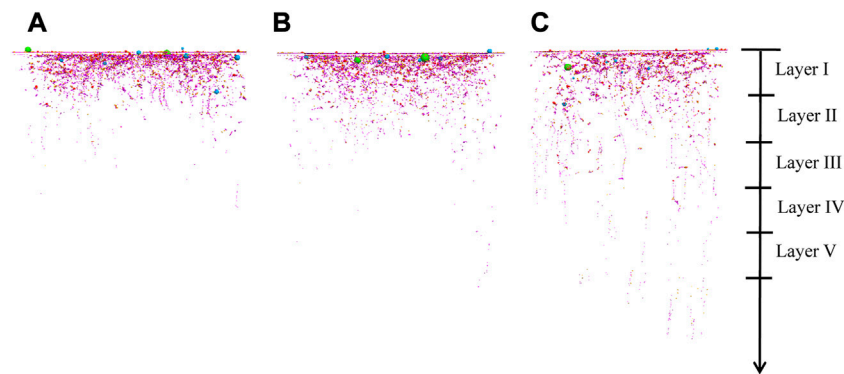


FIGURE 10

Clogging simulation test under the action of gravity and running water. (A) P_{A1} ; (B) P_{A2} ; (C) P_{A3} .

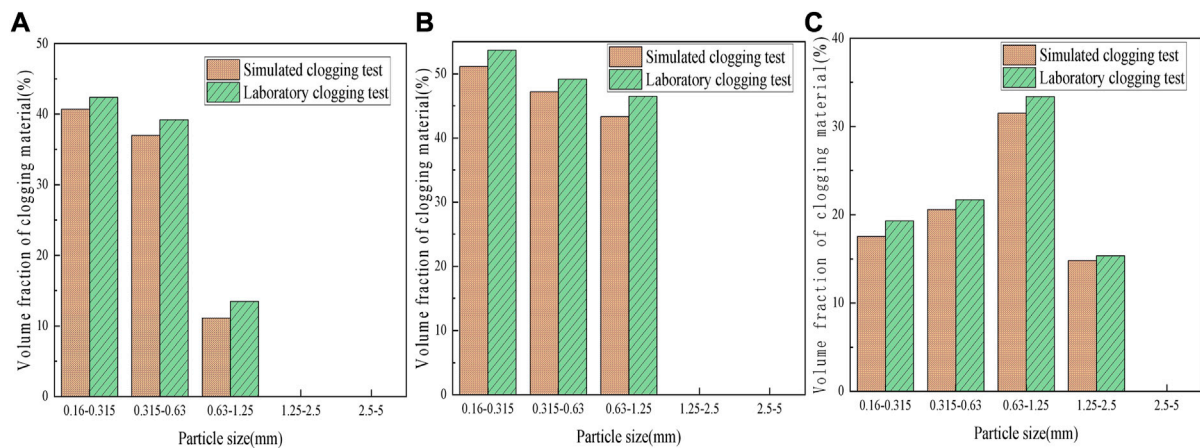


FIGURE 11

Comparison of clogging experiment results between laboratory and numerical simulation. (A) P_{A1} ; (B) P_{A2} ; (C) P_{A3} .

three groups of PC specimens. The comparison of the results is shown in Figure 11. Due to the different masses of clogging material between the laboratory clogging test and numerical simulation clogging test, there will be some errors in the results, but the error between the two results is less than 5%. It is proved that the PFC-CFD module in PFC3D can accurately simulate the clogging of PC specimens.

4.2 Clogging state in the pervious pavement

As shown in Figure 12, there are three states of deposition of clogging materials on the surface of pervious concrete. Figure 12A shows the clogging of the large particle size clogging material. As shown in Figure 13A, the diameter of the clogging material is larger than the size of the pores. The pores of the PC pavement are directly clogged by the clogging material, resulting in a sudden clogging of the pavement. Figure 12B shows the clogging material's clogging with mixed particle size. The clogging substances of mixed particle size are gathered together; the diameter of the clogging material is smaller than the pore size but very close to the pore diameter. At the

same time, the clogging material with a small particle size is also deposited around it, which is equivalent to forming a large particle size clogging material. Figure 12C shows the clogging of small particle size clogging material. As shown in Figure 13B, the diameter of the clogging material is smaller than the pore size of the road. A lot of small particle size clogging material is gathered together; small particle size clogging material easily forms an arch when passing through the pore structure [33], leading to clogging.

4.3 Influence of coarse aggregate gradation

The zigzag degree and diameter of pores of PC pavement with different aggregate gradations may be different, and the clogging in the pervious pavement will be different. In this study, clogging simulation experiments were carried out on three groups of PC pavement with different aggregate gradations, and the clogging material is full-grade sand. The variation curve of the volume fraction of clogging particles during the development of road structure clogging over time is shown in Figure 14. The volume

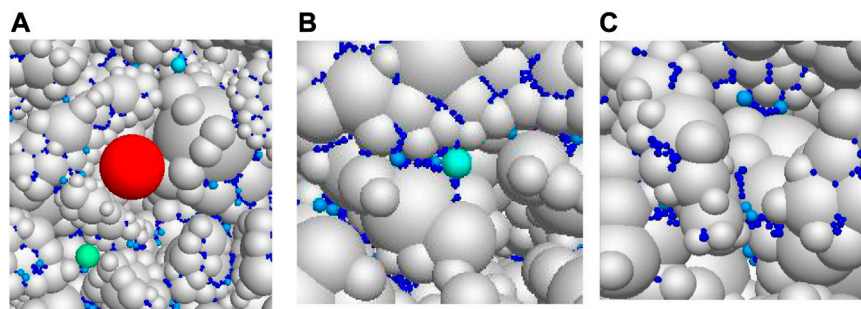


FIGURE 12

Clogging state of clogging materials with different particle sizes in permeable pavement structure: (A) large particle size clogging; (B) mixed particle size clogging; (C) small particle size clogging.

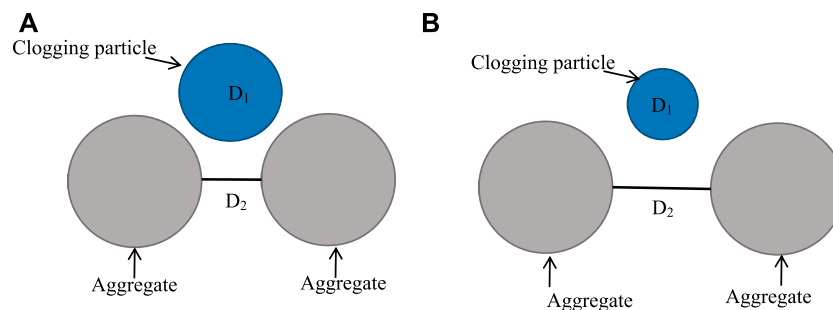


FIGURE 13

Relationship between the diameter of clogging particles and the distance between two aggregates: (A) $D_1 > D_2$; (B) $D_1 < D_2$.

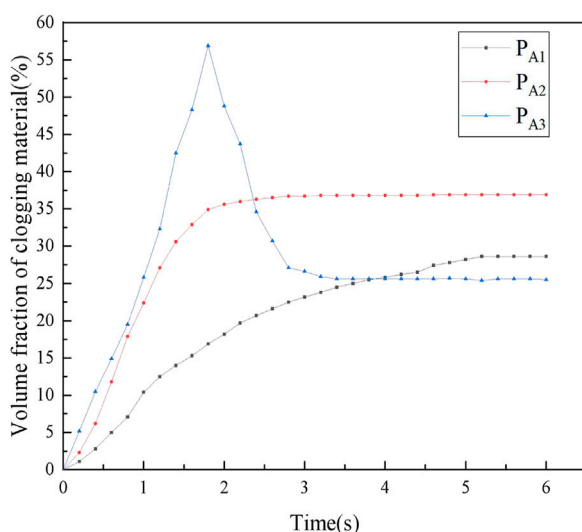


FIGURE 14

Clogging development of different aggregate gradation.

fraction of clogging particles in P_{A1} and P_{A2} tends to increase and stabilize because there are coarse aggregates with small particle sizes in both P_{A1} and P_{A2} . The relatively large contact area of small-size

aggregate can form relatively small pores, and the clogging material moves slowly down under the action of water flow; so, it is not easy to move out of the pervious pavement structure under the action of water flow. Therefore, the number of clogged particles on the pavement surface will only increase to a certain number but will not decrease. The volume fraction of the clogging substance in P_{A1} is 8.3% less than that in P_{A2} . P_{A1} is a kind of PC with discontinuous gradation, and the particle size ratio of coarse aggregate is 5–10 mm: 15–20 mm = 7:3 in which small coarse aggregate accounts for the majority. In the PC with mixed particle size aggregate, the contact area between large-size coarse aggregates is small, and it is easy to form large pores. Small-size coarse aggregate is smaller than the pore between the large-size aggregate. The small-size coarse aggregate fills the pores so that the pore size becomes smaller, and it is difficult for clogging material to enter the pores. P_{A2} is a PC pavement with a single aggregate, and the particle size of coarse aggregate is 5–10 mm. The pores formed are more uniform, and the clogging material enters the pores more easily. Therefore, the volume fraction of the clogging substance in P_{A2} reaches the maximum first. The volume fraction of clogging particles in P_{A3} increased rapidly first and then reached a maximum of 56.9% at 1.8 s. It decreased sharply by 31% at 1.2 s and then gradually stabilized. Large-size aggregate concrete with the continuous gradation of P_{A3} and coarse aggregate particle size ratio is 10–15 mm:15–20 mm = 3:1. Large aggregate size forms a small zigzag degree of pore, and the particle size of

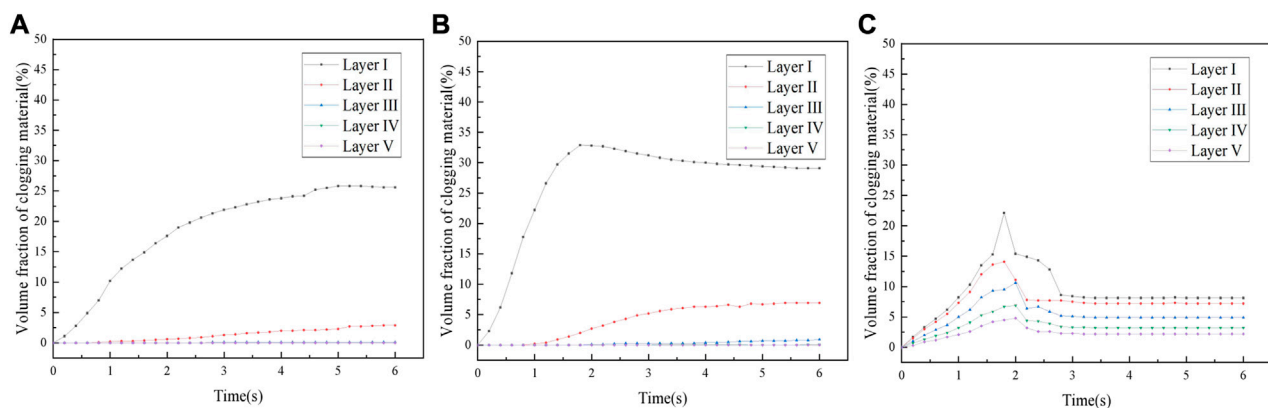


FIGURE 15

Distribution of clogging substances at different pervious pavement depths. (A) P_{A1} ; (B) P_{A2} ; (C) P_{A3} .

secondary aggregate is larger than that between superior aggregates; so, it is impossible to fill the pores and form large pores. Some of the clogging particles migrate out of P_{A3} under the action of water flow.

The aggregate gradation in P_{A1} is a discontinuous gradation; the small-size aggregate fills the pores produced by the large-size aggregate, the large pores are separated by the small-size aggregates to form a smaller pore structure, and the zigzag degree of the pores increases. P_{A2} is a coarse aggregate with a small particle size and single gradation, so it can form a uniform pore structure with smaller pores but smaller zigzag degree. P_{A3} is composed of coarse aggregate with large particle sizes and continuous gradation. The diameter of pores formed in permeable pavement structures is larger, and the zigzag degree is small. Therefore, the greater the zigzag degree in the pervious pavement structure, the slower the clogging development, the smaller the pores, and the more clogging materials can block the outside. When aggregate gradation in the pervious pavement is different, the time when the volume fraction of clogging material reaches the maximum is also different. The time when the volume fraction of clogging material in three kinds of pervious pavement reaches the maximum is $P_{A1} > P_{A2} > P_{A3}$, which is related to the zigzag degree and diameter of pores in the pervious pavement. After the clogging material in the pervious pavement tends to stabilize, the volume fraction of the clogging material is 28.8%, 36.9%, and 25.5%, respectively. The results show that the smaller the particle size of coarse aggregate in the pervious pavement is, the easier it is to be clogged.

Figures 15A,B,C show the distribution of clogging substances at different pavement depths of P_{A1} , P_{A2} , and P_{A3} , respectively. By comparing the distribution of clogging particles in three kinds of pervious pavement, there are clogging particles in each layer of P_{A3} and clogging particles in the first three layers of P_{A2} , but only in the first and second layers of P_{A1} . The volume fraction of clogging particles in the first layer of P_{A2} is larger than that in the first layer of P_{A3} because the aggregate size of P_{A2} is smaller than that of P_{A3} . P_{A2} can block the entry of clogging particles with large particle sizes, and clogging particles with small particle sizes accumulate in the pavement. Due to the large pore size in P_{A3} , most of the clogging particles can migrate smoothly to the next layer under the action of water flow, and some of the clogging particles pass directly through each layer of the pavement structure. P_{A1} is a kind of PC with discontinuous gradation, forming the smallest pore diameter and improving the barrier effect. After the occurrence of

clogging, the volume proportion of clogging material of P_{A1} , P_{A2} , and P_{A3} is 28.6%, 36.9%, and 25.5%, respectively, and the anti-clogging performance of P_{A1} and P_{A3} is better.

4.4 Influence of clogging material gradation

The three states of clogging material in pervious pavements introduced in Section 4.2 show that the grade of clogging has a certain influence on the clogging development of PC pavement. Different clogging material gradations have different effects on the clogging of pervious pavement. Figures 16A,B,C show the clogging distribution of different gradations of clogging substances in P_{A1} , P_{A2} , and P_{A3} , respectively. The particle size range of fine sand is 0.16–0.63 mm, that of coarse sand is 0.63 mm–5 mm, and that of full-grade is 0.16–5 mm. The results show that the volume fraction of clogging material in P_{A1} and P_{A2} has the same trend. P_{A1} and P_{A2} are more likely to be clogged by fine sand. Because the pores of these two kinds of pavement are small, they cannot migrate out of the pavement structure under the action of water flow. Fine sand accumulates in the pervious pavement over time, causing serious clogging. When the fine sand is the clogging material, the volume fraction of the clogged material in P_{A1} and P_{A2} is larger than that in full-grade sand. Because full-grade sand contains sand with larger particle sizes, the larger sized sand particles are clogged in the pores of the pavement surface layer. They cannot enter the pervious pavement, so part of the smaller-sized sand cannot enter the pore. Therefore, when the full-grade sand is used as the clogging material, the volume fraction of the clogging material decreases by 7.4% and 13.4%, respectively, and the clogging effect of fine sand on P_{A2} is greater than that of P_{A1} .

When the coarse sand is the clogging material, the volume fraction of the clogging material in P_{A1} and P_{A2} is the lowest of the three clogging conditions, which are 11.97% and 17.3%, respectively. Most of the particles in coarse sand are larger than the pores of P_{A1} and P_{A2} , so it is clogged in the surface layer of the pervious pavement and rarely enters the interior and distributes in the first pavement layer. The change of the volume fraction of clogging substance in P_{A3} is opposite to that of P_{A1} and P_{A2} . When the clogging material is coarse sand, the volume fraction of clogging material in P_{A3} is a maximum of 28.45%. The pores formed

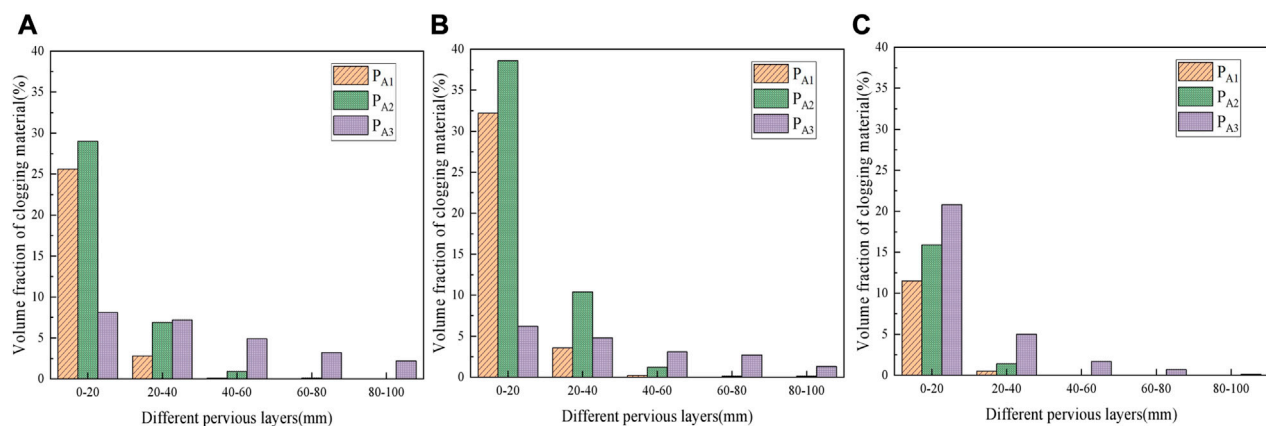


FIGURE 16

Distribution of clogging substances with different gradation in each layer: (A) full-grade sand; (B) find sand; (C) coarse sand.

by P_{A3} are relatively large, and some large clogging materials can enter its interior to cause clogging. However, when the clogging material is full-grade sand and fine sand, the sand with a smaller particle size is more likely to migrate out of the pervious pavement structure and is less likely to cause clogging. When the full-grade sand is the clogging material, the small particle size and the large particle size aggregates enter the P_{A3} together, and the small particle size aggregates migrate out of the pervious pavement structure. As a result, when full-grade sand is the clogging material, the volume fraction of the clogging material increases by 7.41%.

As shown in Figure 16A, the clogging substances of the three pervious pavements are full-grade sand. The clogging substances in P_{A1} are distributed in the first and second layers and can reach a depth of 40 mm. The clogging substances in P_{A2} are distributed within 60 mm, and the volume fraction of the clogging material in each layer is larger than that in P_{A1} . The clogging substances in P_{A3} can migrate out of the pervious pavement structure. The distribution of clogging substances in Figure 16B is roughly the same as that of full-grade sand. Figure 16C shows that coarse sand is distributed within 80 mm of P_{A3} . Among the three pervious pavements, coarse sand cannot migrate out of the pervious pavement structure under the action of water flow but is clogged inside it. Among the gradations of the three clogging substances, only coarse sand cannot migrate out of the P_{A3} structural layer under the action of water flow, which significantly impacts the anti-clogging performance of P_{A3} .

5 Conclusion

The clogging simulation experiments of different pervious pavements are carried out using the two-way coupling method of PFC-CFD. Three clogging states of pervious pavements are obtained, and the effects of coarse aggregate gradation and clogging material gradation on the anti-clogging ability of pervious pavements are analyzed. The conclusions are as follows:

- (1) The three states of the deposition of clogging material on the surface of PC are the clogging by large particle size clogging

material, the clogging by mixed particle size clogging material, and the clogging by small particle size clogging material. It shows that the gradation of clogging material has a certain influence on the clogging development of PC pavement.

- (2) When the aggregate gradation in the pervious pavement is different, the time when the volume fraction of clogged material reaches the maximum is also different. The time when the clogging material in the three kinds of pervious pavement reaches the maximum is $P_{A1} > P_{A2} > P_{A3}$, which is related to the zigzag degree and diameter of pores. After the clogging material in the pervious pavement tends to stabilize, the volume fraction of the clogging material is 28.8%, 36.9%, and 25.5%, respectively, indicating that the smaller the particle size of the coarse aggregate in the pervious pavement is, the more likely it is to be clogged.
- (3) Different clogging material gradations have different effects on the clogging of pervious pavement. Therefore, selecting the mix ratio of pervious pavement based on the particle size range of clogging materials in a certain area is necessary for preparing pervious pavement with anti-clogging performance.
- (4) The results of this experiment show that P_{A1} has the highest compressive strength and has a strong barrier effect on full-grade sand and coarse sand. The compressive strength of P_{A2} is slightly lower than that of P_{A1} , but the anti-clogging ability is the worst. The lowest compressive strength of P_{A3} is 23.07 MPa, and the clogging material is full-grade sand and fine sand, showing good anti-clogging performance. According to the aforementioned research results, researchers can select different mix ratios of anti-clogging PC according to different areas of use. The law obtained from the experiment can provide a reference for the further study of the design of double-layer pervious pavement structures.

Data availability statement

The original contributions presented in the study are included in the article/Supplementary Materials, further inquiries can be directed to the corresponding author.

Author contributions

QX: supervision, writing—review and editing, conceptualization, and resources; YX: writing—original draft, data curation, and formal analysis; GZ: investigation, validation, and visualization; XL: resources, investigation, and validation; JZ: resources and investigation. All authors contributed to the article and approved the submitted version.

Funding

This research was sponsored by the Training Scheme for Young Backbone Teachers in Colleges and Universities in Henan Province, no. 2019-163; the Excellent Teaching Case Project of Professional Degree Postgraduates in Henan Province (2022-115); the Scientific Research Foundation of Graduate School of Xinyang Normal University (2021KYJJ73); Special Projects of Key R & D and

Promotion in Xinyang City (20220055); and Key Scientific and Technological Projects in Henan Province (232102320196).

Conflict of interest

The authors declare that the research was conducted in the absence of any commercial or financial relationships that could be construed as a potential conflict of interest.

Publisher's note

All claims expressed in this article are solely those of the authors and do not necessarily represent those of their affiliated organizations, or those of the publisher, the editors, and the reviewers. Any product that may be evaluated in this article, or claim that may be made by its manufacturer, is not guaranteed or endorsed by the publisher.

References

- Kia A, Wong HS, Cheeseman CR. Clogging in permeable concrete: A review. *J Environ Manage* (2017) 193:221–33. doi:10.1016/j.jenvman.2017.02.018
- Chen LM, Chen JW, Lecher T, Chen TH, Davidson P. Assessment of clogging of permeable pavements by measuring change in permeability. *Sci Total Environ* (2020) 749:141352. doi:10.1016/j.scitotenv.2020.141352
- Afonso ML, Fael CS, Dinis-Almeida M. Influence of clogging on the hydrologic performance of a double layer porous asphalt. *Int J Pavement Eng* (2020) 21(6):736–45. doi:10.1080/10298436.2018.1508843
- Hatanaka S, Kamalova Z, Harada M. Construction of a nonlinear permeability model of pervious concrete and drainage simulation of heavy rain in a residential area. *Results Mater* (2019) 3(9):100033. doi:10.1016/j.rinma.2019.100033
- Debnath B, Sarkar PP. Clogging in pervious concrete pavement made with non-conventional aggregates: Performance evaluation and rehabilitation technique. *Arabian J Sci Eng* (2021) 46(11):10381–96. doi:10.1007/s13369-021-05380-6
- Hung VV, Seo SY, Kim HW, Lee GC. Permeability and strength of pervious concrete according to aggregate size and blocking material. *Sustain* (2021) 13(1):426–13. doi:10.3390/su13010426
- Brunetti G, Šimunek J, Piro P. A comprehensive numerical analysis of the hydraulic behavior of a permeable pavement. *J Hydrol* (2016) 540:1146–61. doi:10.1016/j.jhydrol.2016.07.030
- Zhang J, She R, Dai Z, Ming R, Ma G, Cui X, et al. Experimental simulation study on pore clogging mechanism of porous pavement. *Constr Build Mater* (2018) 187:803–18. doi:10.1016/j.conbuildmat.2018.07.199
- Sandoval GFB, Galobardes I, Campos A, Toralles BM, 29. January (2020). p. 101203. doi:10.1016/j.job.2020.101203 Assessing the phenomenon of clogging of pervious concrete (Pc): Experimental test and model proposition *J Build Eng*
- Coughlin JP, Campbell CD, Mays DC. Infiltration and clogging by sand and clay in a pervious concrete pavement system. *J Hydrol Eng* (2012) 17(1):68–73. doi:10.1061/(asce)he.1943-5584.0000424
- Lee JW, Yang E, Jang J, Yun TS. Effect of clogging and cleaning on the permeability of pervious block pavements. *Int J Pavement Eng* (2022) 23(9):3147–56. doi:10.1080/10298436.2021.1884861
- Kayhanian M, Anderson D, Harvey JT, Jones D, Muhunthan B. Permeability measurement and scan imaging to assess clogging of pervious concrete pavements in parking lots. *J Environ Manage* (2012) 95(1):114–23. doi:10.1016/j.jenvman.2011.09.021
- Nan X, Wang Z, Hou J, Tong Y, Li B. Clogging mechanism of pervious concrete: From experiments to CFD-DEM simulations. *Constr Build Mater* (2021) 270:121422. doi:10.1016/j.conbuildmat.2020.121422
- Yang Q, Beecham S, Liu J, Pezzaniti D (2019). The influence of rainfall intensity and duration on sediment pathways and subsequent clogging in permeable pavements. *J Environ Manage* 246, 730–6. doi:10.1016/j.jenvman.2019.05.151
- Bugrin M, Marchioni M, Becciu G, Giustozzi F, Toraldo E, Andrés-Valeri VC. Clogging potential evaluation of porous mixture surfaces used in permeable pavement systems. *Eur J Environ Civ Eng* (2020) 24(5):620–30. doi:10.1080/19648189.2017.1411834
- Cui X, Zhang J, Huang D, Tang W, Wang L, Hou F. Experimental simulation of rapid clogging process of pervious concrete pavement caused by storm water runoff. *Int J Pavement Eng* (2019) 20(1):24–32. doi:10.1080/10298436.2016.1246889
- Zhang J, Cui X, Li L, Huang D. Sediment transport and pore clogging of a porous pavement under surface runoff. *Road Mater Pavement Des* (2017) 18:240–8. doi:10.1080/14680629.2017.1329878
- Sandoval GFB, Galobardes I, De Moura AC, Toralles BM. Hydraulic behavior variation of pervious concrete due to clogging. *Case Stud Constr Mater* (2020) 13:e00354. doi:10.1016/j.cscm.2020.e00354
- Huang J, Zhang Y, Sun Y, Ren J, Zhao Z, Zhang J. Evaluation of pore size distribution and permeability reduction behavior in pervious concrete. *Constr Build Mater* (2021) 290:123228. doi:10.1016/j.conbuildmat.2021.123228
- Singh A, Sampath PV, Biligiri KP. A review of sustainable pervious concrete systems: Emphasis on clogging, material characterization, and environmental aspects. *Constr Build Mater* (2020) 261:120491. doi:10.1016/j.conbuildmat.2020.120491
- Hu N, Zhang J, Xia S, Han R, Dai Z, She R, et al. A field performance evaluation of the periodic maintenance for pervious concrete pavement. *J Clean Prod* (2020) 263:121463. doi:10.1016/j.jclepro.2020.121463
- Sandoval GFB, de Moura AC, Jussiani EI, Andreollo AC, Toralles BM. Proposal of maintenance methodology for pervious concrete (PC) after the phenomenon of clogging. *Constr Build Mater* (2020) 248:118672. doi:10.1016/j.conbuildmat.2020.118672
- Kia A, Wong HS, Cheeseman CR. High-strength clogging resistant permeable pavement. *Int J Pavement Eng* (2021) 22(3):271–82. doi:10.1080/10298436.2019.1600693
- Barišić I, Grubeša IN, Dokšanović T, Zvonarić M. Influence of clogging and unbound base layer properties on pervious concrete drainage characteristics. *Materials (Basel)* (2020) 13:2455–11. doi:10.3390/MA13112455
- Elango KS, Revathi V. Infiltration and clogging characteristics of pervious concrete. *Asian J Civ Eng* (2019) 20(8):1119–27. doi:10.1007/s42107-019-00170-w
- García A, Aboufoul M, Asamoah F, Jing D. Study the influence of the air void topology on porous asphalt clogging. *Constr Build Mater* (2019) 227:116791. doi:10.1016/j.conbuildmat.2019.116791
- Zhou H, Li H, Abdelhady A, Liang X, Wang H, Yang B. Experimental investigation on the effect of pore characteristics on clogging risk of pervious concrete based on CT scanning. *Constr Build Mater* (2019) 212:130–9. doi:10.1016/j.conbuildmat.2019.03.310
- Chen L, Wang Z, Peng X, Yang J, Wu P, Lian H. Modeling pressurized fracture propagation with the isogeometric BEM. *Geomech Geophys Geo-energy Geo-resources* (2021) 7(3):51. doi:10.1007/s40948-021-00248-3
- Parvan A, Jafari S, Rahnama M, Norouzi apourvari S, Raoof A. Insight into particle retention and clogging in porous media; a pore scale study using lattice Boltzmann method. *Adv Water Resour* (2020) 138:103530. doi:10.1016/j.advwatres.2020.103530
- Ma G, Zhang J, Dai Z, She R, Xia S, Hu N (2019). Reply to the Comment on 'Numerical study on pore clogging mechanism in pervious pavements. *J Hydrol* 578, 124050. doi:10.1016/j.jhydrol.2019.124050

31. Xu J, Kong C, Xu T. Effects of deposition states and distribution regularity of clogging substances on pore clogging behaviors of double-layer drainage asphalt pavement. *Constr Build Mater* (2021) 314:125701. doi:10.1016/j.conbuildmat.2021.125701
32. Hu J, Ma T, Ma K, 595. January (2021). p. 126028. doi:10.1016/j.jhydrol.2021.126028 DEM-CFD simulation on clogging and degradation of air voids in double-layer porous asphalt pavement under rainfall *J Hydrol*
33. Remond S. DEM simulation of small particles clogging in the packing of large beads. *Phys A Stat Mech Its Appl* (2010) 389(21):4485–96. doi:10.1016/j.physa.2010.06.033
34. Nan X, Zhang M, Liu Y, Wang J, Wang L, Jing L. Flow field analysis of micro particles passing through pervious concrete. *IOP Conf Ser Mater Sci Eng* (2019) 493(1): 012006. doi:10.1088/1757-899X/493/1/012006
35. Zhang J, Xia S, Hu N, Hao W, Han R, Meng B, et al. Optimization of anti-clogging pervious pavement structure based on numerical evaluation. *Constr Build Mater* (2021) 275:122186. doi:10.1016/j.conbuildmat.2020.122186
36. Zhang J, Ma G, Dai Z, Ming R, Cui X, She R. Numerical study on pore clogging mechanism in pervious pavements. *J Hydrol* (2018) 565(5):589–98. doi:10.1016/j.jhydrol.2018.08.072
37. Zhao W, Chen L, Chen H, Marburg S. Topology optimization of exterior acoustic-structure interaction systems using the coupled FEM-BEM method. *Int J Numer Methods Eng* (2019) 119(5):404–31. doi:10.1002/nme.6055
38. Chen L, Zheng C, Chen H. FEM/wideband FMBEM coupling for structural-acoustic design sensitivity analysis. *Comput Methods Appl Mech Eng* (2014) 276:1–19. doi:10.1016/j.cma.2014.03.016
39. Chen L, Marburg S, Chen H, Zhang H, Gao H. An adjoint operator approach for sensitivity analysis of radiated sound power in fully coupled structural-acoustic systems. *J Comput Acoust* (2017) 25(1):1750003–24. doi:10.1142/S0218396X17500035
40. Chen L, Zhao W, Liu C, Chen H. 2D structural acoustic analysis using the FEM/FMBEM with different coupled element types. *Arch Acoust* (2017) 42(1):37–48. doi:10.1515/aoa-2017-0005



OPEN ACCESS

EDITED BY

Leilei Chen,
Huanghuai University, China

REVIEWED BY

Qingwei Bu,
Anhui University of Science and
Technology, China

Zhijun Liu,
Heilongjiang University of Science and
Technology, China

*CORRESPONDENCE

Zhenghe Liu,
✉ liuzhenghe@tyut.edu.cn

SPECIALTY SECTION

This article was submitted to Statistical
and Computational Physics,
a section of the journal
Frontiers in Physics

RECEIVED 06 February 2023

ACCEPTED 08 March 2023

PUBLISHED 24 March 2023

CITATION

Liu B, Liu Z and Yang L (2023),
Accelerating fracture simulation with
phase field methods based on Drucker-
Prager criterion.
Front. Phys. 11:1159566.
doi: 10.3389/fphy.2023.1159566

COPYRIGHT

© 2023 Liu, Liu and Yang. This is an open-
access article distributed under the terms
of the [Creative Commons Attribution
License \(CC BY\)](https://creativecommons.org/licenses/by/4.0/). The use, distribution or
reproduction in other forums is
permitted, provided the original author(s)
and the copyright owner(s) are credited
and that the original publication in this
journal is cited, in accordance with
accepted academic practice. No use,
distribution or reproduction is permitted
which does not comply with these terms.

Accelerating fracture simulation with phase field methods based on Drucker-Prager criterion

Bin Liu¹, Zhenghe Liu^{1*} and Lusheng Yang²

¹Key Laboratory of In-situ Property Improving Mining of Ministry of Education, Taiyuan University of Technology, Taiyuan, China, ²Shanxi Institute of Energy, Yuci, China

The paper presents a framework for accelerating the phase field modeling of compressive failure of rocks. In this study, the Drucker-Prager failure surface is taken into account in the phase field model to characterize the tension-compression asymmetry of fractures in rocks. The degradation function that decouples the phase-field and physical length scales is employed, in order to reduce the mesh density in large structures. To evaluate the proposed approach, four numerical examples are given. The results of the numerical experiments demonstrate the accuracy and efficiency of the proposed approach in tracking crack propagation paths in rock materials under Drucker-Prager criterion.

KEYWORDS

phase field method, fracture, Drucker-Prager, degradation function, large scale

1 Introduction

The phase-field fracture model gains great popularity in computational fracture mechanics in recent years due to its capability of capturing complex fracture patterns including crack initiation, propagation, bifurcation and coalescence. Because the conventional form of phase field is based on the assumption of tension and compression symmetry, it is not applicable to rock materials [1], whose tensile and compressive strengths show significant differences [2]. To reproduce the fracture behaviors exhibiting asymmetric tension-compression characteristics, Zhou et al. [3] and Wang et al. [4] developed new driving force formulations, whereby Mohr-Coulomb criterion can be introduced to phase field fracture modeling. Navidtehrani et al. [5–7] proposed a general framework for decomposing the strain energy density under multi-axial loading, which enables us to simulate compressive failure in rocks under Drucker-Prager criterion.

The phase-field fracture model has limitations for simulating large-scale rock models [1]. In the traditional formulation, the phase field length scale is linked with the physical process zone length scale for a given material strength [8–10]. In the analysis of the structures whose sizes are orders of magnitude larger than their physical length scales, the mesh density can be prohibitively high, leading to an unaffordable computational cost in practice. To address this issue, Wu et al. proposed a new type of degradation function which is insensitive to the length scale [11–20]. After that, Lo et al. [18, 20] presented a degradation function that decouples the phase field length scale from the physical length scale, which reduces the mesh density and thus enables one to simulate crack propagation in large-scale rock masses with phase field methods [21–28].

In this paper, we combine the work of Navidtehrani et al. [5–7] and Lo et al. [18, 20] to accelerate the fracture phase field modeling of Drucker-Prager failure by using the degradation functions decoupling the phase field and physical length scales. The remainder of the paper is organized as follows. Section 2 introduces the phase field fracture model for Drucker-Prager failure. Section 3 explains the degradation function that separates phase field length scales from physical length scales. The numerical experiments were conducted in Section 4, followed by the

conclusions in Section 5. To demonstrate the accuracy of this method in capturing the crack patterns of rock materials.

2 Phase field fracture model

According to [29], the total potential energy of an elastic body is composed of the elastic energy of the elastic body and the crack surface energy

$$\Pi(\mathbf{u}, \Gamma) = \int_{\Omega} \psi_e(\boldsymbol{\varepsilon}(\mathbf{u})) d\Omega + \int_{\Gamma} G_c d\Gamma \quad (1)$$

where: ψ_e is the elastic energy density of the elastomer, $\boldsymbol{\varepsilon}(\mathbf{u})$ is the strain tensor, \mathbf{u} is the displacement, the range of \mathbf{u} is $\in \mathbb{R}^d$ ($\{1,2,3\}$), and G_c is the fracture energy release rate of the material. We can obtain from the variational method that at time $t \in [0, t]$, crack $\Gamma(x, t)$ has any behavior of $x \in \mathbb{R}^d$ at any position. Once the crack is formed, it cannot be recovered, so an irreversible condition needs to be imposed. For energy, minimizing the total potential energy will only increase but not decrease. This condition is $\Gamma \cap \Gamma(x, s) \subset \Gamma(x, t)$, ($s < t$).

Here we use the fracture variational criterion inherited and developed from the traditional Griffith theory, which is still based on the elastic strain energy and energy release rate. Griffith believes that there are many small cracks or defects in actual materials. Under the action of external forces, stress concentration will occur near these cracks and defects. When the stress reaches a certain level, the cracks will start to expand and cause fracture. However, Griffith theory [29] has the defect that it cannot solve the problems of crack generation, propagation angle and instability bifurcation, so the fracture of materials is further studied by using the fracture variational criterion.

2.1 Estimation of fracture surface energy using phase field variables

B. Bourdin et al. [30] realized the fracture variational criterion numerically for the first time by introducing phase field variables. In this paper, we define a scalar variable that changes in the interval of $[0, 1]$ to be a phase field variable, and use ϕ to represent the topology of the crack, when $\phi = 1$ to represent the crack, and when $\phi = 0$ to represent the material is intact, and then use ϕ to represent the crack surface density in unit volume γ [31]:

$$\gamma(\phi, \nabla \phi) = \frac{\phi^2}{2l_0} + \frac{l_0}{2} |\nabla \phi|^2 \quad (2)$$

$l_0 \in \mathbb{R}^+$ is an important model parameter to control the range of crack diffusion fracture transition zone ($0 < \phi < 1$), as shown in Figure 1. l_0 characterizes the crack diffusion range. In short, when l_0 is small, the crack is thinner, while the larger l_0 is, the fatter the crack is. In this way, the crack surface Γ acts as a time-varying scalar field, or phase field, in space.

From formula (2), we can express the total crack surface energy in the elastic body with the following equation

$$\int_{\Gamma} G_c d\Gamma \approx \int_{\Omega} G_c \left[\frac{(\phi - 1)^2}{2l_0} + \frac{l_0}{2} |\nabla \phi|^2 \right] d\Omega \quad (3)$$

2.2 Elastic strain energy decomposition

According to the above fracture variational criteria, the crack surface energy and elastic strain energy are tied closely. If the elastic strain energy is not decomposed, the pseudo bifurcation of the crack will occur. To solve this problem, this paper decomposes the elastic strain energy in tension and compression based on the method proposed by C. Miehe et al. [32], so that the tensile part of the elastic strain energy drives the evolution of the phase field. To this end, the strain tensor is first spectral decomposed [33]:

$$\boldsymbol{\varepsilon}_{\pm} = \sum_{i=1}^d \langle \boldsymbol{\varepsilon}^i \rangle_{\pm} \mathbf{n}^i \otimes \mathbf{n}^i \quad (4)$$

In the formula, $\boldsymbol{\varepsilon}_{+}$ and $\boldsymbol{\varepsilon}_{-}$ are tensile strain tensors and compression strain tensors respectively. $\boldsymbol{\varepsilon}^i$ and \mathbf{n}^i are the main strain values and their corresponding directions. d is an independent parameter, namely the spatial dimension. When $d = 2$, this is a two-dimensional problem. When $d = 3$, this is a three-dimensional problem. Macaulay brackets in the formula are defined as: $\langle \bullet \rangle_{+} = (\bullet + |\bullet|)/2$, $\langle \bullet \rangle_{-} = (\bullet - |\bullet|)/2$.

The strain after spectral decomposition can decompose the elastic strain energy density:

$$\psi_e^{\pm}(\boldsymbol{\varepsilon}) = \frac{\lambda}{2} \langle \text{tr}(\boldsymbol{\varepsilon}) \rangle_{\pm}^2 + \mu \text{tr}(\boldsymbol{\varepsilon}_{\pm}^2) \quad (5)$$

Here λ and μ is the Lamé constant, $\text{tr}(\bullet)$ represents the trace of the matrix. In the process of material failure, the stiffness will also decrease. At this time, the material stiffness weakening is related to the phase field variable. If we assume that only the tensile strain energy density in the elastic body receives the weakening of the phase field variable, the elastic strain energy at this time is

$$\psi_e(\boldsymbol{\varepsilon}) = [(1 - \phi)^2 + \kappa] \psi_e^{+}(\boldsymbol{\varepsilon}) + \psi_e^{-}(\boldsymbol{\varepsilon}) \quad (6)$$

Where: κ is a parameter model parameter, $0 \leq \kappa < 1$. Avoid generating numerical singularity when $\phi = 1$.

2.3 Characterization of Drucker-Prager fracture surface

According to Navidtehrani [5–7] Drucker-Prager fracture criterion applicable to brittle or quasi-brittle materials, such as rock or concrete, is shown as follows

$$\sqrt{J_2}(\boldsymbol{\sigma}) = A + BI_1(\boldsymbol{\sigma}) \quad (7)$$

I_1 and J_2 are the first tensor and the second partial derivative of the invariant, respectively.

A is the equation about uniaxial tension (σ_t). B is the equation about uniaxial compression (σ_c). The specific form is as follows

$$A = \frac{2}{\sqrt{3}} \left(\frac{\sigma_c \sigma_t}{\sigma_c + \sigma_t} \right); B = \frac{1}{\sqrt{3}} \left(\frac{\sigma_t - \sigma_c}{\sigma_c + \sigma_t} \right) \quad (8)$$

For quasi-brittle materials, the mechanical properties within the Drucker – Prager failure range can still be regarded as linear elastic. Only when the stress reaches the failure surface, the linear elastic behavior will be transformed into non-linear action. At the same time,

the failure of the material will lead to the weakening of the tensile strength and compressive strength. We can get the relationship between the material strength and the phase field damage by using the degradation function $g(\phi)$ in the numerical calculation:

$$\begin{aligned} A(\phi) &= \frac{2}{\sqrt{3}} \left(\frac{g(\phi)\sigma_c g(\phi)\sigma_t}{g(\phi)\sigma_c + g(\phi)\sigma_t} \right) = g(\phi) \frac{2}{\sqrt{3}} \left(\frac{\sigma_c \sigma_t}{\sigma_c + \sigma_t} \right) = g(\phi) A(\phi = 0) \\ B(\phi) &= \frac{1}{\sqrt{3}} \left(\frac{g(\phi)\sigma_t - g(\phi)\sigma_c}{g(\phi)\sigma_c + g(\phi)\sigma_t} \right) = \frac{1}{\sqrt{3}} \left(\frac{\sigma_t - \sigma_c}{\sigma_c + \sigma_t} \right) = B(\phi = 0) \end{aligned} \quad (9)$$

The phase field parameter ($\phi = 0$) represents the integrity of the material. ($\phi = 1$) represents the complete destruction of the material. At this time, the Drucker – Prager parameters are as follows

$$A(\phi = 1) = 0; B(\phi = 1) = B(\phi = 0) \quad (10)$$

Governing equations of phase field fracture model.

Under the condition of considering kinetic energy T at the same time, according to the crack surface energy expressed in Eq. 3 and the elastic strain energy density expressed in Eq. 6, the following formula can be obtained:

$$T(\dot{\mathbf{u}}) = \int_{\Omega} \frac{1}{2} \rho \dot{\mathbf{u}} \cdot \dot{\mathbf{u}} dV \quad (11)$$

In the formula: ρ is the material density. Thus, the expression of Lagrange function can be written:

$$\begin{aligned} L &= T - \Pi \\ &= \int_{\Omega} \frac{1}{2} \rho \dot{\mathbf{u}} \cdot \dot{\mathbf{u}} dV - \int_{\Omega} \left\{ \left[(1 - \phi)^2 + \kappa \right] \psi_e^+(\boldsymbol{\varepsilon}) + \psi_e^-(\boldsymbol{\varepsilon}) \right\} dV \\ &\quad - \int_{\Omega} G_c \left[\frac{\phi^2}{2l_0} + \frac{l_0}{2} |\nabla \phi|^2 \right] dV \end{aligned} \quad (12)$$

According to Hamilton's principle and ignoring the physical force, the Lagrangian function L takes the variation of $\{\dot{\mathbf{u}}, \phi\}$, and the control equation of the phase field fracture model can be obtained:

$$\text{Div} [\boldsymbol{\sigma}] = \rho \ddot{\mathbf{u}} \left(\frac{G_c}{l_0} + 2\psi_e^+ \right) \phi - G_c l_0 \Delta \phi = 2\psi_e^+ \quad (13)$$

In the formula: $\boldsymbol{\sigma}$ is Cauchy stress tensor. We can obtain the stress from the partial derivative of the elastic strain energy corresponding to the strain

$$\begin{aligned} \boldsymbol{\sigma} &= \left[(1 - \phi)^2 + \kappa \right] \partial_{\boldsymbol{\varepsilon}} \psi_e^+(\boldsymbol{\varepsilon}) + \partial_{\boldsymbol{\varepsilon}} \psi_e^-(\boldsymbol{\varepsilon}) = \\ &= \left[(1 - \phi)^2 + \kappa \right] (\lambda \langle \text{tr}(\boldsymbol{\varepsilon}) \rangle_+ \mathbf{I} + 2\mu \boldsymbol{\varepsilon}_+) + \lambda \langle \text{tr}(\boldsymbol{\varepsilon}) \rangle_- \mathbf{I} + 2\mu \boldsymbol{\varepsilon}_- \end{aligned} \quad (14)$$

Where: \mathbf{I} is the second order unit tensor. The control Eq. 13 is a set of partial differential equations composed of the dynamic balance equation and the phase field evolution equation. In order to make the control equation equal to the aforementioned variational method, the irreversible condition should be added, that is, when the elastomer is under pressure or unloading, the crack healing should be prevented. The simplest and most effective way to deal with the irreversibility of variables is to introduce historical state variables:

$$\mathcal{H}(\mathbf{x}, t) = \max_{s \in [0, t]} \psi_e^+[\boldsymbol{\varepsilon}(\mathbf{x}, s)] \quad (15)$$

The state variable H represents the maximum tensile elastic strain energy. The maximum value of the \mathcal{H} variable from loading to the

current time is also related to the relative position and time, that is, $\mathcal{H}(\mathbf{x}, t)$. The irreversibility condition can be satisfied by replacing the value of ψ_e^+ in Eq. 13 with $\mathcal{H}(\mathbf{x}, t)$ in the control equation. It is also because of the previous irreversible and only increase monotonically. Because of the irreversibility of the state variable \mathcal{H} , ϕ also has the same irreversibility and will only increase monotonically. At this time, the control equation should be rewritten as:

$$\text{Div} [\boldsymbol{\sigma}] + \mathbf{b} = \rho \ddot{\mathbf{u}} \left(\frac{G_c}{l_0} + 2\mathcal{H} \right) \phi - G_c l_0 \Delta \phi = 2\mathcal{H} \quad (16)$$

Where: \mathbf{b} is the body force. The phase field fracture model can describe any behavior of the fracture only by a set of partial differential equations. The separated fracture is equivalent to the fracture field coupled with the displacement field, and no additional tracking of the geometric shape of the tracking crack is required. Therefore, any propagation path of the fracture can be calculated.

2.4 Principle of virtual work. Balance of forces

Now, we will use the principle of virtual work to derive the equilibrium equations of the coupled deformation fracture system. Cauchy stress is introduced $\boldsymbol{\sigma}$, It is related to the strain $\boldsymbol{\varepsilon}$ Work conjugation. In addition, the traction force \mathbf{T} is defined as partial $\partial \Omega$ on the solid boundary. We introduce scalar stress into the fracture model ω . This stress ω And phase field ϕ and phase field micro-stress vector $\boldsymbol{\xi}$, which conjugate with the phase field gradient $\nabla \phi$. It is assumed that the phase field ϕ is only driven by the solution of the displacement problem. Therefore, there is no external traction and ϕ relevant. In the absence of external force, the principle of virtual work is as follows:

$$\int_{\Omega} \{ \boldsymbol{\sigma} : \delta \boldsymbol{\varepsilon} + \omega \delta \phi + \boldsymbol{\xi} \cdot \delta \nabla \phi \} dV = \int_{\partial \Omega} (\mathbf{T} \cdot \delta \mathbf{u}) dS \quad (17)$$

Among δ Represents a virtual quantity. This equation must be applicable to any field Ω and any kinematically permissible change of virtual quantity. Therefore, by applying the Gauss divergence theorem, the local force balance is given by the following formula:

$$\begin{aligned} \nabla \cdot \boldsymbol{\sigma} &= 0 \\ \nabla \cdot \boldsymbol{\xi} - \omega &= 0 \end{aligned} \quad \text{in } \partial \Omega \quad (18)$$

boundary conditions:

$$\begin{aligned} \boldsymbol{\sigma} \cdot \mathbf{n} &= \mathbf{T} \\ \boldsymbol{\xi} \cdot \mathbf{n} &= 0 \end{aligned} \quad \text{on } \partial \Omega \quad (19)$$

2.5 Constitutive theory

Based on the phase field crack modeling and theoretical framework, we first discuss the relationship between the change of phase field variables around the crack and the length scale by modifying the degradation function. It is feasible to modify the degradation function under our phase-field model to affect the peak stress of the phase-field model. The following is our equilibrium equation, free energy and related constitutive equation. The balance equation is as follows:

$$\sigma_{ji,j} + b_i = 0 \text{ in } V \text{ and } t_i = \sigma_{ji}n_j \text{ on } S \quad (20)$$

V is the volume of the object, S is its boundary surface, n_i is the unit component (perpendicular to the surface), b_i is the physical strength per unit volume, t_i is the traction vector, σ_{ji} is the component of Cauchy stress tensor. Assuming small deformation and deformation gradient, make infinitesimal strain tensor ε_{ij} can be determined by the deformation gradient of the displacement vector u_i is expressed as,

$$\varepsilon_{ij} = \frac{1}{2}(u_{i,j} + u_{j,i}) \quad (21)$$

Phase field parameters usually introduced by phase field method ϕ . It is used to describe the degradation of materials, and is generally set ϕ . When the boundary changes from 1 to 0, 1 indicates that the material is intact without cracks $\phi = 0$ indicates that the material has been completely destroyed. According to Gurtin's [34] research, the micro-forces cited at the same time are: a group of micro-forces on the outer surface λ and body micro-force γ , the micro force on the inner surface is π and ξ_i . The following is the point direction balance equation of these micro forces:

$$\xi_{i,i} + \gamma + \pi = 0 \text{ in } V \text{ and } \xi_i n_i = \lambda \text{ on } S \quad (22)$$

It can be seen from the second law of thermodynamics in isothermal form that for the system, the sum of the work done by mechanical traction and body force and the work done by external surface and body force is greater than or equal to Helmholtz free energy ψ Total change of. The integral form of the second law is

$$\int_V \dot{\psi} dV \leq \int_V (b_i \dot{u}_i + \gamma \dot{\phi}) dV + \int_S (t_i \dot{u}_i + \lambda \dot{\phi}) dS \quad (23)$$

Assume that for any volume ψ depends on ε_{ij} , ϕ , and $\dot{\phi}$. Under the condition of applying divergence theory, we can determine that Eq. 23 is bound to hold.

$$\frac{\partial \psi}{\partial \varepsilon_{ij}} \dot{\varepsilon}_{ij} + \frac{\partial \psi}{\partial \phi} \dot{\phi} + \frac{\partial \psi}{\partial \dot{\phi}} \dot{\dot{\phi}} + \frac{\partial \psi}{\partial \dot{\phi}} \dot{\dot{\phi}} \leq \sigma_{ji} \dot{\varepsilon}_{ij} - \pi \dot{\phi} + \xi_i \dot{\phi}_{,i} \quad (24)$$

According to the standard Coleman and Noll procedure [35], if,

$$\sigma_{ji} = \frac{\partial \psi}{\partial \varepsilon_{ij}}, \xi_i = \frac{\partial \psi}{\partial \phi_{,i}}, \text{ and } \frac{\partial \psi}{\partial \dot{\phi}} = 0 \quad (25)$$

The remaining items lead to unequal reduced dissipation,

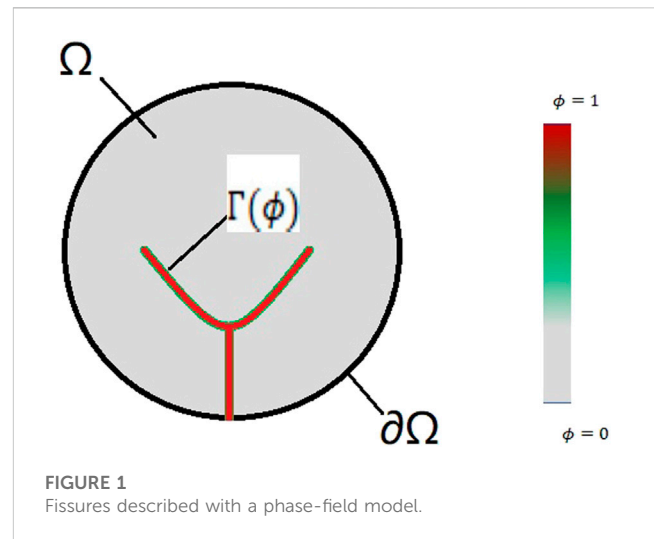
$$\left(\pi + \frac{\partial \psi}{\partial \dot{\phi}} \right) \dot{\phi} \leq 0. \quad (26)$$

The attenuation of this dissipative inequality always satisfies the following conditions

$$\pi = -\frac{\partial \psi}{\partial \dot{\phi}} - \beta(\phi, \dot{\phi}, \varepsilon_{ij}) \dot{\phi} \quad (27)$$

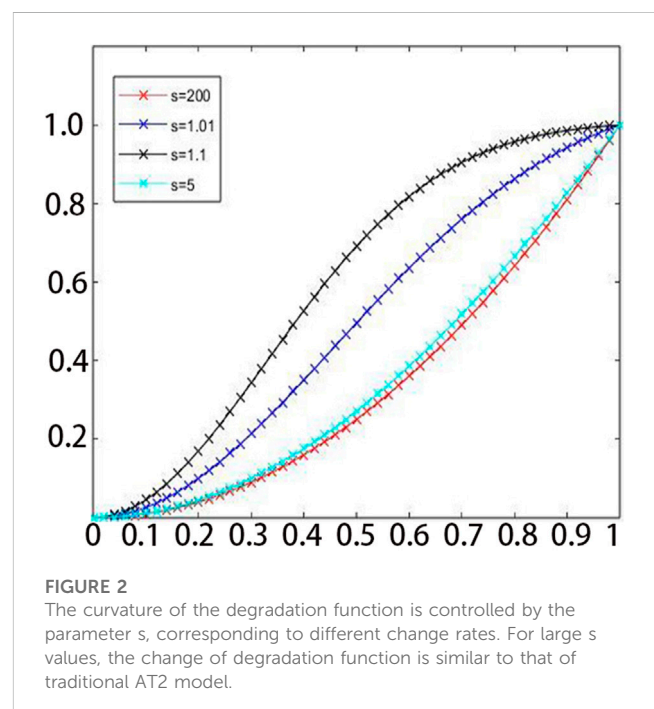
In the fracture phase field method of brittle materials similar to rock, the value of the β is zero.

The following formula introduces a form of Helmholtz free energy to apply the frame to brittle fracture



$$\psi = [g(\phi)\psi_e^+ + \psi_e^-] + G_c \left[\frac{3}{8\ell_0} (1 - \phi) + \frac{3}{8}\ell_0 \phi_{,i} \phi_{,i} \right] \quad (28)$$

Among ψ_e^+ represents the effect of tensile stress on elasticity, ψ_e^- represents the effect of compression on elastic strain energy. The study of strain energy decomposition by Borden et al is very profound. For the numerical simulation of brittle fracture, we usually introduce the physical quantity representing the tensile or compressive strength of the material within the elastic limit, namely the elastic modulus E , into the linear elastic isotropic material, as well as the elastic constant Poisson's ratio ν reflecting the transverse deformation of the material. For our phase-field simulation, we also need to introduce physical quantities such as the effective fracture surface energy G_c per unit area, and the length scale parameter ℓ_0 . For phase-field fracture simulation, we have mentioned that the variation range of phase-field



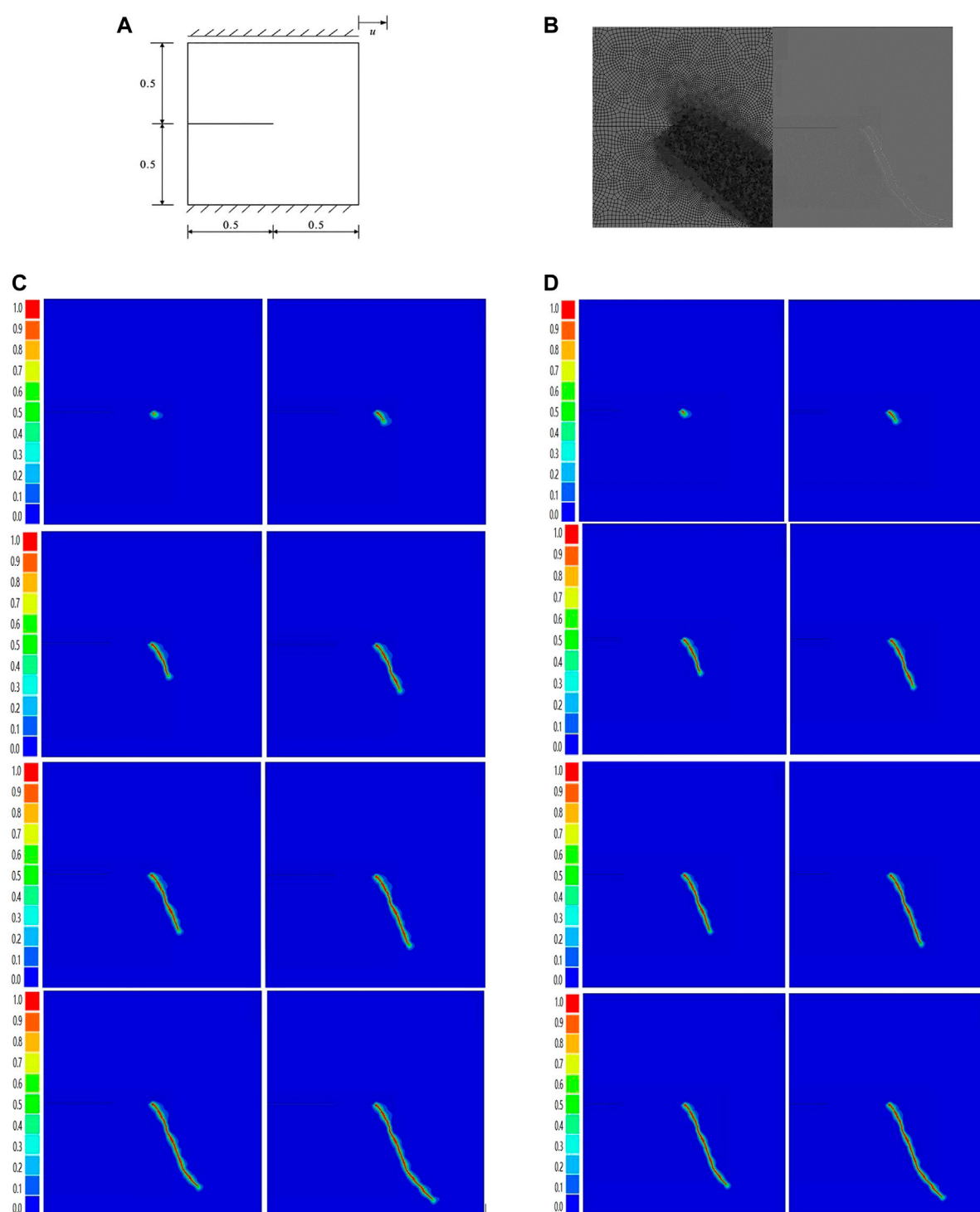


FIGURE 3

(A) Square plate under tension/m. (B) Meshing diagram (Tight zone dimensions = 0.2, other = 1) (C) Crack propagation path ($S = 5$). (D) Crack propagation path ($S = 200$). (E) Crack propagation path (traditional degradation).

parameters is between 0 and 1, and the length scale affects the influence range of phase-field parameters.

Rooted in the variational principle of linear elastic fracture energy proposed by Francfort and Marigo [30], and referring to the elliptic regularization method of Mumford-Shah functional in computer image

segmentation, it is called AT2 model [36–42], and its manifestation in the phase-field fracture model is $(1 - \phi)^2$. With the failure of the material, the physical properties of the material itself will also change. At this time, we need to use the degradation function, namely g , to determine the weakening of the physical properties of the material.

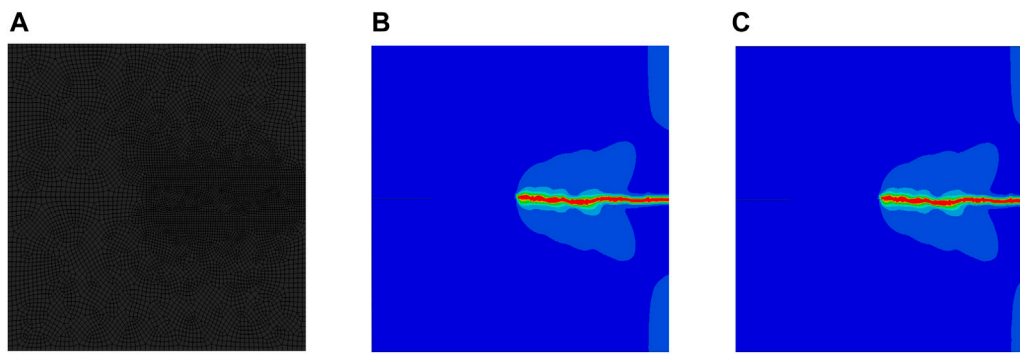


FIGURE 4

(A) Meshing diagram = 0.4. (B) Crack propagation path ($S = 1.107$). (C) Crack propagation path ($S = 1.01$).

Obviously, our degradation function is related to the phase field parameters. Just as the phase field parameters ϕ only change from 0 to 1, so is our degradation function g . When the material is completely destroyed, the degradation function $g(\phi) = 0$, we can easily realize the weakening of the elastic property by multiplying it by the elastic energy. The following is the function of the degradation function and the elastic energy equation:

$$g(\phi) = (1 - \phi)^2 \quad (29)$$

According to our degradation function, it is easy to obtain the peak stress:

$$\sigma_c = \sqrt{\frac{3G_c E}{8\ell_0}} \quad (30)$$

The final governing equation is as follows:

$$\left(\phi^2 \frac{\partial \psi_e^+}{\partial \varepsilon_{ij}} + \frac{\partial \psi_e^-}{\partial \varepsilon_{ij}} \right) + b_i = \beta \dot{\phi} \text{ in } V \left(\phi^2 \frac{\partial \psi_e^+}{\partial \varepsilon_{ij}} + \frac{\partial \psi_e^-}{\partial \varepsilon_{ij}} \right) n_j = t_i \text{ on } S \quad (31)$$

And

$$\frac{3}{8} G_c \ell_0 \phi_{,ii} + \frac{3G_c}{8\ell_0} - 2\phi \psi_e^+ + \gamma = 0 \text{ in } V, \frac{3}{8} G_c \ell_0 \phi_{,i} n_i = \lambda \text{ on } S \quad (32)$$

3 The degradation function

For the sake of completeness, we introduce the degradation function proposed by Lo et al [18, 20]. In this section, Eq. 30 shows that the peak stress is not only related to the properties of the material itself, such as material strength σ_c . Breaking energy G_c is related to Young's modulus E , and also to the phase field length scale ℓ_0 . Because of our need for numerical simulation of large-scale rock phase field fracture, the phase field length scale is usually a very small physical quantity. This has brought a great burden to our actual calculation. We can easily associate whether we can decouple the peak stress and the phase field length scale if we adopt a new degradation function to ensure more efficient calculation results. Therefore, we adopt the following degradation function:

$$g(\phi) = s \left[1 - \left(\frac{s-1}{s} \right)^{\phi^2} \right] \quad (33)$$

As shown in Figure 2, the function curve under different s values. The characteristic of this degradation function is that a parameter s is introduced to control the specific peak stress through different values of s . We can easily calculate the peak stress of different s values by the following formula.

$$\sigma_c^* = \frac{\sqrt{\frac{3G_c E}{8\ell_0}}}{\sqrt{(s-1) \ln \left(\frac{s}{s-1} \right)}} \quad (34)$$

we separate the phase field length scale ℓ_0 and the physical length scale ℓ_p . In the traditional phase field simulation, $\ell_0 = \ell_p$, and we choose different s values, the corresponding phase field length scale ℓ_0 and the physical length scale ℓ_p ratio are also different, and the corresponding physical length scale ℓ_p formula is

$$\ell_p = (s-1) \ln \left(\frac{s}{s-1} \right) \ell_0 \quad (35)$$

At this time, the ratio of peak stress is also different. We use the new peak stress symbol σ_c^* to distinguish,

$$\sigma_c^* = \sqrt{\frac{3G_c E}{8\ell_p}} \quad (36)$$

For the value of s , we can find that when $s \approx 1.0148$, ℓ_0 increase by 16 times with the peak stress unchanged. This has increased by an order of magnitude, and if we want to increase ℓ_0 100 times while maintaining the same peak stress, when $s \approx 1.00155$. With different values of s , we can easily simulate a larger scale model, which has many advantages for the phase field modeling of our large-scale rock mass model.

4 Numerical examples

4.1 Tension square plate with unilateral crack

Consider the tension square plate containing initial cracks as shown in Figure 3A with a side length of 50 mm, which is divided into

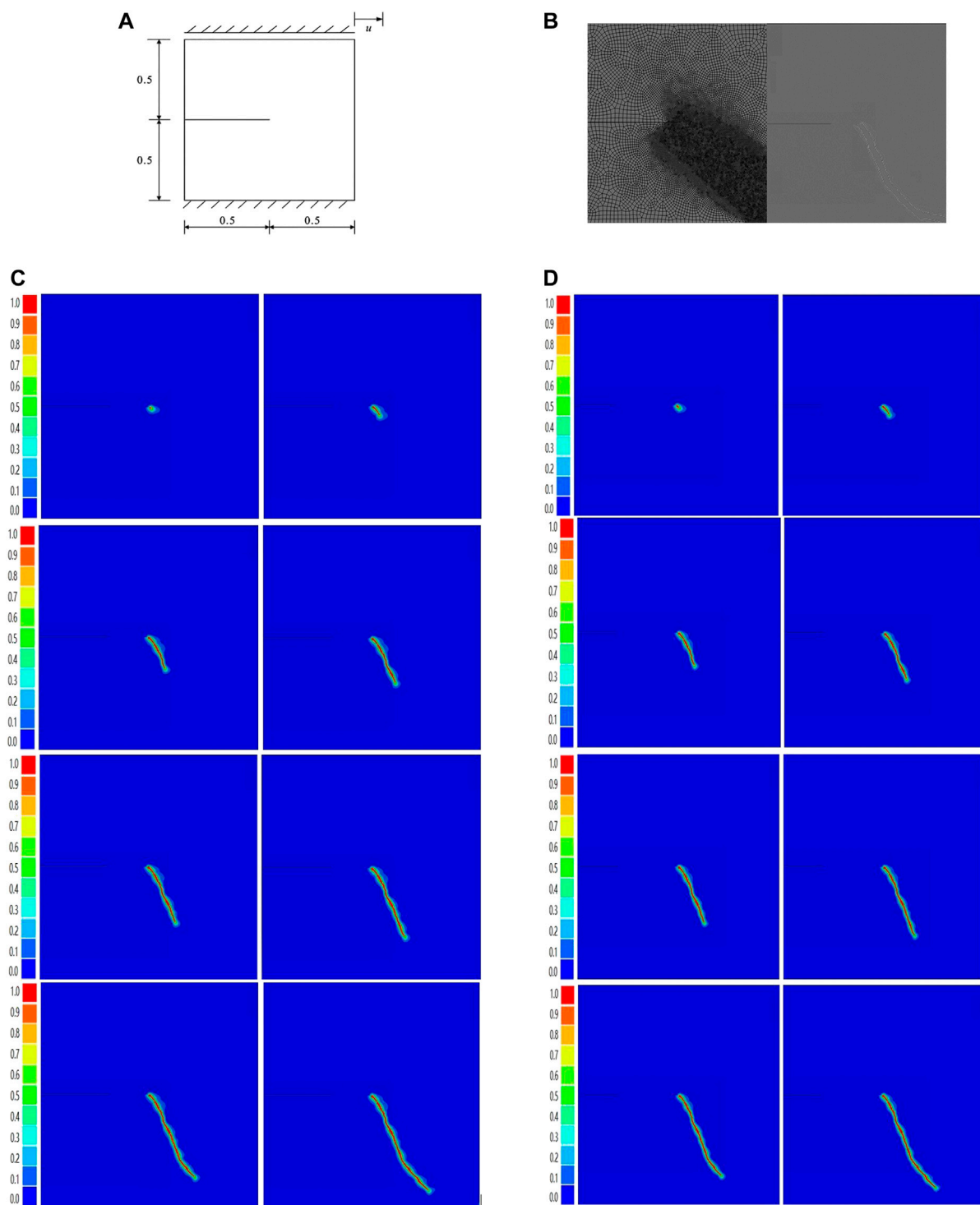


FIGURE 5

(A) Sheared square plates. (B) Meshing diagram (Tight zone dimensions = 0.2, other = 1) (C) Crack propagation path ($S = 200$). (D) Crack propagation path (traditional degradation).

46118 quadrilateral elements as shown in Figure 3B, and locally densified at the predicted crack growth path, where the grid size is about 0.1 mm. Let the problem be a plane strain problem, with an elastic modulus of 250 kN/mm², a Poisson's ratio of 0.2, and a fracture toughness of $G_c = 2.5 \times 10^{-3}$ kN/mm². Using displacement loading method, $t = 1$ s, $\Delta U = 0.15$ mm until complete failure. During the calculation, $l_0 = 0.2$ mm is

taken. First, the geometric discontinuity method is used to preset the initial crack, that is, the upper and lower elements are geometrically separated at the crack. The calculated crack growth process is shown in Figure 3.

Based on the numerical simulation results presented in Figures 3, 4, it can be observed that the model employing our proposed phase-field fracture method generates a crack propagation path that is more

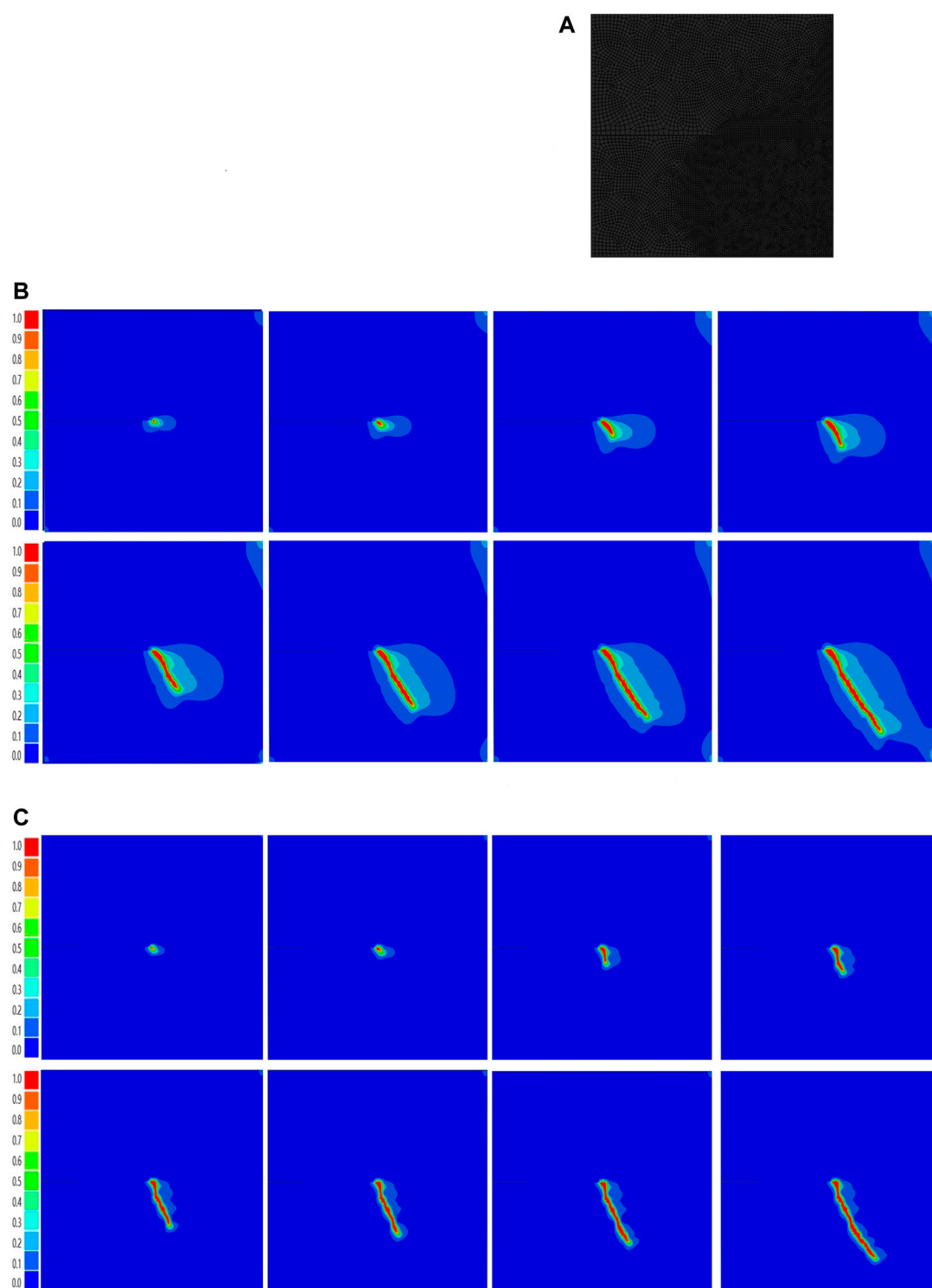


FIGURE 6

(A) Meshing diagram (Tight zone dimensions = 0.4). (B) Crack propagation path ($S = 1.107$). (C) Crack propagation path ($S = 1.01$).

complex and closely resembles a rock fracture section during the simulation of the tensile square plate. Conversely, the crack growth path generated by the traditional degradation function appears more linear. These findings indicate that our proposed phase-field fracture model possesses distinctive characteristics in accurately capturing crack

propagation under complex stress-displacement boundary conditions, which enables it to fit large-scale rock models while maintaining crack tracking precision. Consequently, further numerical simulations will be conducted to comprehensively investigate, analyze and compare the performance of our proposed model.

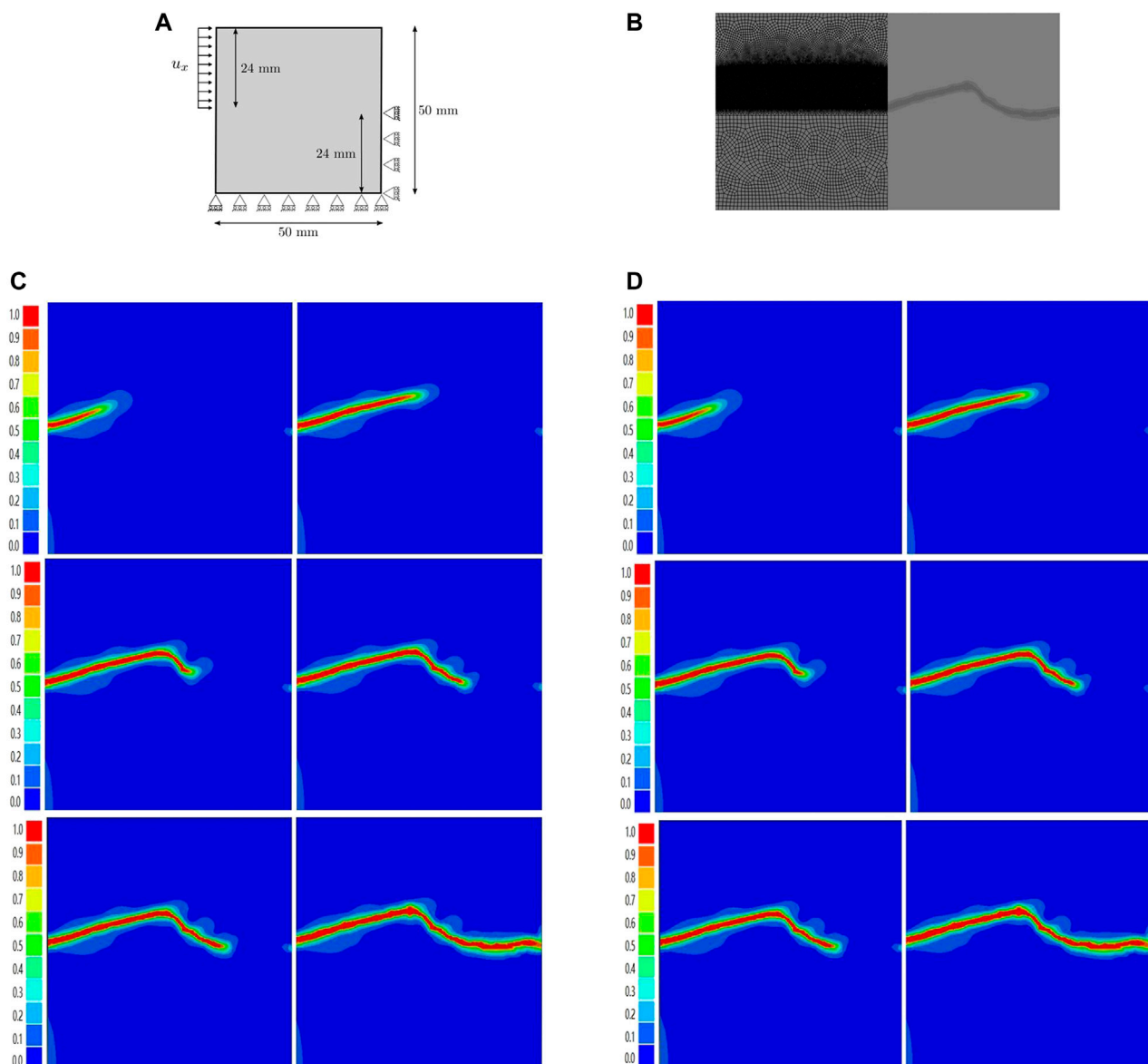


FIGURE 7

(A) Direct shear test (DST). (B) Meshing diagram (Tight zone dimensions = 0.1, other = 1) and the calculated crack growth process. (C) Crack propagation path ($S = 200$). (D) Crack propagation path (traditional degradation).

4.2 Shear square plate with unilateral crack

The same material parameters as in Example 4.1 are used to study the crack growth process of square plates under shear. The calculation model is shown in Figure 5A, and the vertical displacement on all boundaries is constrained to zero. The displacement loading method is adopted, and the displacement increment of each loading step is $\Delta U = 2.5\text{ mm}$, the non-uniform grid is adopted, and the grid is densified at the position where the crack growth is expected. The minimum grid size is about 0.2 mm. The grid model is shown in Figure 5B.

In the experiment involving a shear square plate with a unilateral crack, numerical simulations were conducted by varying the S value ($S = 200$), and the results obtained are shown in Figures 5D, E. Comparison of these results with those obtained by the traditional degradation function,

such as Figure 5C, reveals that the tracked crack propagation path remains the same. This observation is consistent with our theoretical calculations of the relationship between S value and peak stress.

For the following research, we plan to investigate the effect of varying the S value on the physical and phase field scales. Specifically, we will choose values of $S = 1.01$ and 1.1 to expand the physical scale and the multiple of the phase field scale. The choice of $S = 1.01$ will result in a phase field scale that is 16 times the physical scale, while $S = 1.107$ will yield a phase field scale that is 4 times the physical scale. The model cell mesh size will be set to 0.4 mm. Through this verification process, we aim to demonstrate that our phase-field model has lower demands for mesh accuracy than the traditional phase-field model.

Based on the results presented in Figure 6, it can be observed that a gradual decrease of parameter S leads to an increase in the proportion of

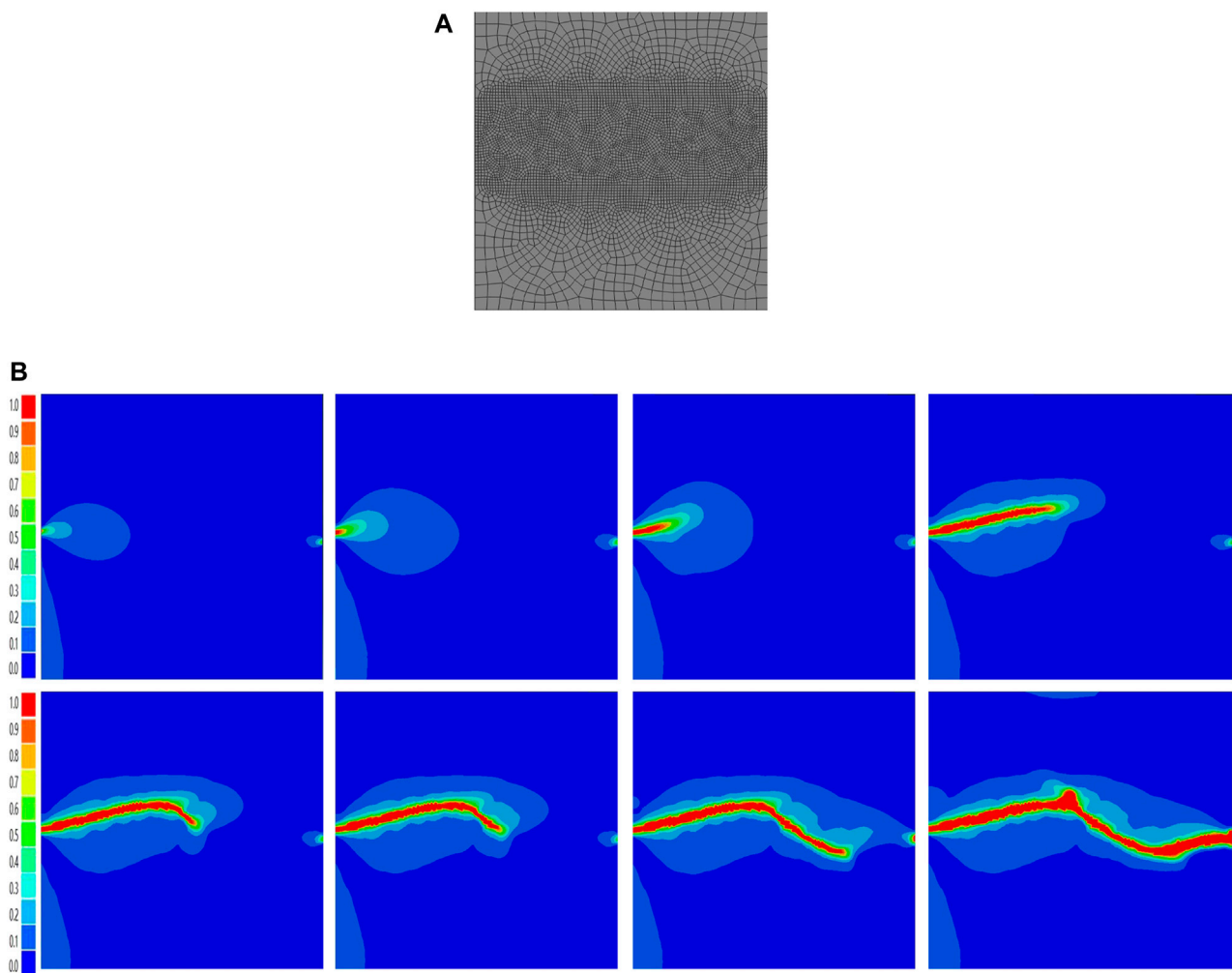


FIGURE 8
(A) Meshing diagram (Tight zone dimensions = 0.5, other = 2). (B) Crack propagation path ($S = 1.107$).

phase field length to physical length. This results in the phase field length being several times or even ten times greater than the physical length. As the proportional relationship between the mesh density and phase field length is a key factor affecting fracture tracking accuracy in the phase-field method, it is possible to reduce the mesh density without compromising the accuracy of crack tracking, as long as the proportion of mesh density and phase field length is maintained. This outcome is highly valuable for large-scale rock numerical simulations, as it results in significant computational resource savings and enhances the efficacy of the phase-field method for such applications.

4.3 Direct shear test of cracked plates

Next, direct shear tests are simulated to evaluate the degradation function changes in the test configuration. The geometry and boundary conditions of the model are shown in Figure 7A. Apply a lateral displacement on the top edge, which is equal to 0.15 mm. The boundary conditions are vertical constraints at the top and fixed constraints at the bottom. Modulus of elasticity $E = 25$ GPa and Poisson's ratio $\nu = 0.2$,

fracture parameters are given by $G_c = 0.15$ kJ/m² and $l = 0.2$ mm. In order to save computing resources, the predicted crack propagation area is encrypted, and the cell size of the encrypted part is at least half of the phase field scale, so as to save computer resources without affecting the computing accuracy.

The crack initiation and propagation mode observed in the simulation is in line with the rock shear fracture experiment, where the crack initiates from the edge and progresses towards the center. The simulation results presented in the figure above compare the crack growth path obtained using the specific degradation function with $S = 200$ and the traditional degradation function. The result display that the crack propagation paths traced by the traditional degradation function are similar when $S = 200$.

As the value of S approaches 1, the phase field characteristic length and the physical characteristic length become decoupled, resulting in a change in the quantitative relationship between the phase field length and physical scale. This leads to a significant increase in the phase field scale, which can become several times or even dozens of times larger than the physical scale. For instance, when $S = 1.107$, the phase field scale is observed to be four times larger than the physical scale. To accurately track the crack propagation path using the phase field

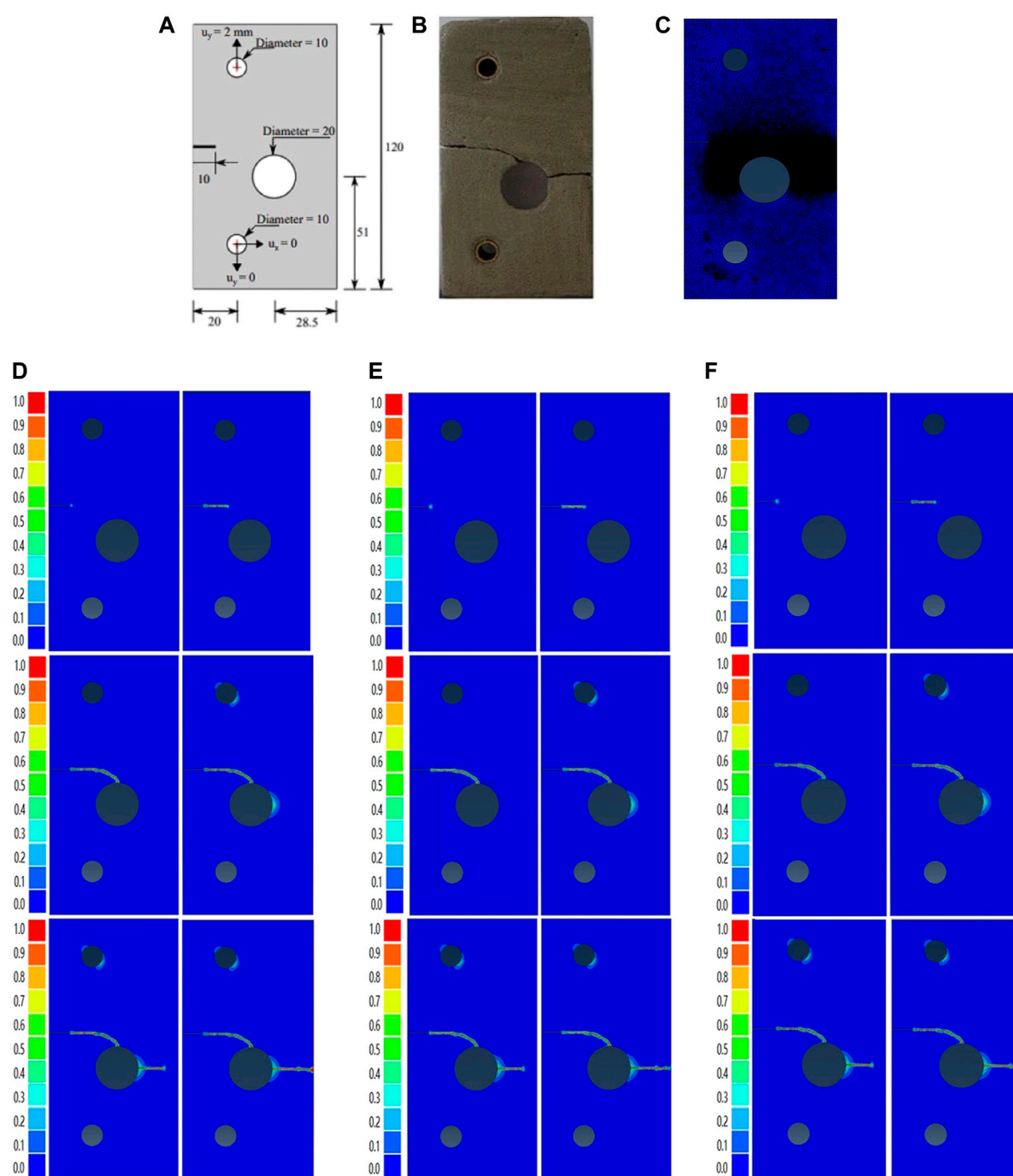


FIGURE 9

(A) Boundary conditions and geometric parameters (B) actual experimental results (C) Meshing diagram (Tight zone dimensions=0.1, other=1) (D) Crack propagation path (S=5) (E) Crack propagation path (S=200) (F) Crack propagation path (traditional degradation).

method, a smaller mesh size than the phase field scale is required. Therefore, with the increase in phase field scale, excessively dense grids can be discarded. By maintaining the proportion between the phase field scale and mesh size, a mesh size of 0.4 mm can be set to achieve equally accurate crack propagation path tracking.

As shown in Figure 8, when using a smaller S value, increase the cell size of the model and use a 0.04 mm mesh size. At this time, very accurate crack tracking curve of rock direct shear test can still be

obtained. It is verified that this phase field model can more effectively simulate large-scale rock fracture.

4.4 Notched plate with eccentric holes

In this case, we model the rock plate with holes, as shown in the figure. This is an eccentric plate with three holes with a length of 120 mm

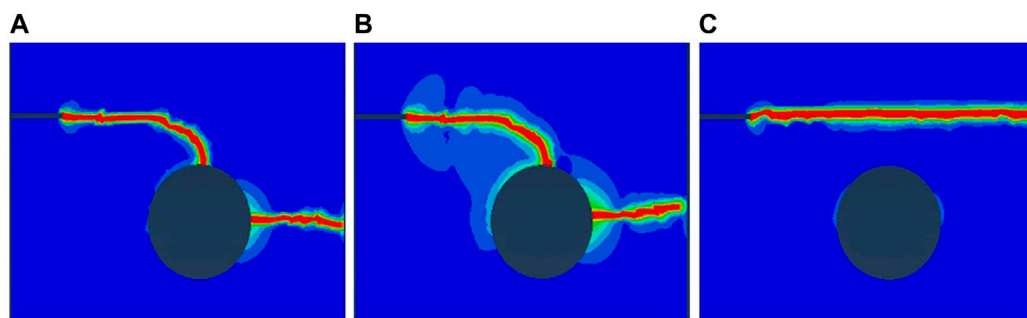


FIGURE 10

(A) Crack propagation path $S = 1.107$ (element size 0.4). (B) Crack propagation path $S = 1.107$ (element size 0.4). (C) Crack propagation path $S = 1.107$ (element size 1.0).

and a width of 70 mm. The size and distribution of the holes are indicated in the Figure 9 below. The boundary condition is that the bottom is fixed vertically and horizontally, and 0.15 mm vertical displacement is applied to the top. The material property parameter in this simulation is Young's modulus $E = 25$ GPa, Poisson's ratio $\nu = 0.20$, Phase field scale $\ell_0 = 0.25$ mm and energy release rate $G_c = 0.15$ kJ/m². At the same time, we compare the different degradation functions affected by multiple S and the cracks tracked by the traditional degradation functions, and use the same division ratio for the element, that is, the mesh size is equal to 0.1 mm. See the figure below for the specific numerical simulation results.

In notched rock slabs with eccentric holes, obtaining accurate crack information is crucial, as multiple factors affect the crack propagation process. In this simulation, we employed the traditional phase field model of Drucker-Prager fracture criterion and the traditional degradation function for numerical simulation, and the simulation results are depicted in Figures 9, 10. Comparing Figures 10 B, C, if we exaggerate the phase field length while maintaining the original set mesh density, our crack path will shift. At this time, we can alleviate this problem by keeping the proportion of the enlarged grid density and the phase field length the same, that is, the grid density is less than half of the phase field scale. Even so, the mesh density after densification is still much smaller than the initially given mesh density, which is more conducive to obtaining the correct crack path and more efficient numerical simulation. However, we can overcome this issue by densifying the mesh. Through multiple sets of experimental simulations, we determined that a phase field scale with a grid density less than half can accurately track the crack propagation path.

5 Conclusion

This study effectively accelerates the fracture phase field modeling for compressive failure of rocks materials. By splitting the strain energy using the approach introduced by [18, 20], the asymmetric tension-compression behaviors in rock fracture processes can be characterized. To decouple the phase-field length with the physical length scale, the degradation function proposed by [18, 20] were adopted and thus the mesh density is reduced for the structures much larger than the physical process

zone. In the future, we will extend the present approach to the applications of hydraulic fracturing in quasi-brittle materials [43]. In addition, the combination of isogeometric analysis will be considered to solve high-order problems [44].

Data availability statement

The original contributions presented in the study are included in the article/supplementary material, further inquiries can be directed to the corresponding author.

Author contributions

BL: optical experiment, ZL and LY: guidance and revision.

Funding

The authors are grateful for the support of National Natural Science Foundation of China (Nos. 52174213, 51574174).

Conflict of interest

The authors declare that the research was conducted in the absence of any commercial or financial relationships that could be construed as a potential conflict of interest.

Publisher's note

All claims expressed in this article are solely those of the authors and do not necessarily represent those of their affiliated organizations, or those of the publisher, the editors and the reviewers. Any product that may be evaluated in this article, or claim that may be made by its manufacturer, is not guaranteed or endorsed by the publisher.

References

- Jaeger JC, Cook NJ. *Fundamental of rock mechanics* (1979). doi:10.1016/j.mineng.2009.02.015
- León Baldelli AA, Maurini C. Numerical bifurcation and stability analysis of variational gradient-damage models for phase-field fracture. *J Mech Phys Sol* (2021) 152: 104424. doi:10.1016/j.jmps.2021.104424
- Zhuang XY, Zhou SW, Sheng M, Li GS. On the hydraulic fracturing in naturally-layered porous media using the phase field method. *ENGINEERING GEOLOGY* (2020) 266:105306. doi:10.1016/j.enggeo.2019.105306
- Zhang Q, Wang D, Zeng F, Guo Z, Wei N. Pressure transient behaviors of vertical fractured wells with asymmetric fracture patterns. *JOURNAL ENERGY RESOURCES TECHNOLOGY-TRANSACTIONS ASME* (2020) 142(4). doi:10.1115/1.4045226
- Navidtehrani Y, Betegon C, Martinez-Paneda E. A unified abaqus implementation of the phase field fracture method using only a user material subroutine. *MATERIALS* (2021) 14(8):1913. doi:10.3390/ma14081913
- Navidtehrani Y, Betegon C, Martinez-Paneda E. A general framework for decomposing the phase field fracture driving force, particularised to a Drucker-Prager failure surface. *THEORETICAL APPLIED FRACTURE MECHANICS* (2022) 121. doi:10.1016/j.tafmec.2022.103555
- Navidtehrani Y, Betegon C, Zimmerman RW, Martinez-Paneda E. Griffith-based analysis of crack initiation location in a Brazilian test. *INTERNATIONAL JOURNAL ROCK MECHANICS MINING SCIENCES* (2022) 159:105227. doi:10.1016/j.ijrmms.2022.105227
- Cundall PA. A computer model for simulating progressive large-scale movements in blocky rock systems. In: *Proceedings of the Symposium of the International Society for Rock Mechanics, Society for Rock Mechanics (ISRM); 1971; France, Paris (1971)*. p. 11–8.
- Li H, Huang Y, Yang Z, Yu K, Li QM. 3D meso-scale fracture modelling of concrete with random aggregates using a phase-field regularized cohesive zone model. *Int J Sol Structures* (2022) 256:111960. doi:10.1016/j.ijsolstr.2022.111960
- Carlsson J, Isaksson P. A statistical geometry approach to length scales in phase field modelling of fracture and strength of porous microstructures. *Int J Sol Structures* (2020) 200–201:83–93. doi:10.1016/j.ijsolstr.2020.05.003
- Borden MJ, Hughes TJR, Landis CM, Anvari A, Lee IJ. Corrigendum to “A phase-field formulation for fracture in ductile materials: Finite deformation balance law derivation, plastic degradation, and stress triaxiality effects. *Comp Methods Appl Mech Eng* (2017) 324:712–3. doi:10.1016/j.cma.2017.06.023
- Jiang D, Kyriakides S, Landis CM. Propagation of phase transformation fronts in pseudoelastic NiTi tubes under uniaxial tension. *Extreme Mech Lett* (2017) 15:113–21. doi:10.1016/j.eml.2017.06.006
- Jiang D, Kyriakides S, Landis CM, Kazinakis K. Modeling of propagation of phase transformation fronts in NiTi under uniaxial tension. *Eur J Mech - A/Solids* (2017) 64: 131–42. doi:10.1016/j.euromechsol.2017.02.004
- Landis CM, Beyerlein IJ, McMeeking RM. Micromechanical simulation of the failure of fiber reinforced composites. *J Mech Phys Sol* (2000) 48(3):621–48. doi:10.1016/S0022-5096(99)00051-4
- Landis CM, Huang R, Hutchinson JW. Formation of surface wrinkles and creases in constrained dielectric elastomers subject to electromechanical loading. *J Mech Phys Sol* (2022) 167:105023. doi:10.1016/j.jmps.2022.105023
- Li W, Landis CM. Nucleation and growth of domains near crack tips in single crystal ferroelectrics. *Eng Fracture Mech* (2011) 78(7):1505–13. doi:10.1016/j.engfracmech.2011.01.002
- Li W, McMeeking RM, Landis CM. On the crack face boundary conditions in electromechanical fracture and an experimental protocol for determining energy release rates. *Eur J Mech - A/Solids* (2008) 27(3):285–301. doi:10.1016/j.euromechsol.2007.08.007
- Lo Y-S, Borden MJ, Ravi-Chandar K, Landis CM. A phase-field model for fatigue crack growth. *J Mech Phys Sol* (2019) 132:103684. doi:10.1016/j.jmps.2019.103684
- Woldman AY, Landis CM. Thermo-electro-mechanical phase-field modeling of paraelectric to ferroelectric transitions. *Int J Sol Structures* (2019) 178–179:19–35. doi:10.1016/j.ijsolstr.2019.06.012
- Lo Y-S, Hughes TJR, Landis CM. Phase-field fracture modeling for large structures. *J Mech Phys Sol* (2023) 171:105118. doi:10.1016/j.jmps.2022.105118
- Ai W, Wu B, Martínez-Pañeda E. A coupled phase field formulation for modelling fatigue cracking in lithium-ion battery electrode particles. *J Power Sourc* (2022) 544: 231805. doi:10.1016/j.jpowsour.2022.231805
- Cui C, Ma R, Martínez-Pañeda E. A generalised, multi-phase-field theory for dissolution-driven stress corrosion cracking and hydrogen embrittlement. *J Mech Phys Sol* (2022) 166:104951. doi:10.1016/j.jmps.2022.104951
- Isfandbod M, Martínez-Pañeda E. A mechanism-based multi-trap phase field model for hydrogen assisted fracture. *Int J Plasticity* (2021) 144:103044. doi:10.1016/j.jiplas.2021.103044
- Kristensen PK, Niordson CF, Martínez-Pañeda E. A phase field model for elastic-gradient-plastic solids undergoing hydrogen embrittlement. *J Mech Phys Sol* (2020) 143: 104093. doi:10.1016/j.jmps.2020.104093
- Martínez-Pañeda E, Fuentes-Alonso S, Betegón C. Gradient-enhanced statistical analysis of cleavage fracture. *Eur J Mech - A/Solids* (2019) 77:103785. doi:10.1016/j.euromechsol.2019.05.002
- Navidtehrani Y, Betegón C, Martínez-Pañeda E. A simple and robust Abaqus implementation of the phase field fracture method. *Appl Eng Sci* (2021) 6:100050. doi:10.1016/j.applsc.2021.100050
- Navidtehrani Y, Betegón C, Martínez-Pañeda E. A general framework for decomposing the phase field fracture driving force, particularised to a Drucker-Prager failure surface. *Theor Appl Fracture Mech* (2022) 121:103555. doi:10.1016/j.tafmec.2022.103555
- Tan W, Martínez-Pañeda E. Phase field fracture predictions of microscopic bridging behaviour of composite materials. *Compos Structures* (2022) 286:115242. doi:10.1016/j.compstruct.2022.115242
- Espadas-Escalante JJ, Van Dijk NP, Isaksson Pjcs T. A phase-field model for strength and fracture analyses of fiber-reinforced composites. *Compos Sci Technol* (2019) 174(APR.12):58–67. doi:10.1016/j.compscitech.2018.10.031
- Bourdin B, Francfort GA, Marigo JJ. Numerical experiments in revisited brittle fracture. *J Mech Phys Sol* (2000) 48(4):797–826. doi:10.1016/S0022-5096(99)00028-9
- Miehe C, Welschinger F, Hofacker M. Thermodynamically consistent phase-field models of fracture: Variational principles and multi-field FE implementations. *Int J Numer Methods Eng* (2010) 83(10):1273–311. doi:10.1002/nme.2861
- Miehe C, Hofacker M, Welschinger F. A phase field model for rate-independent crack propagation: Robust algorithmic implementation based on operator splits. *Comp Methods Appl Mech Eng* (2010) 199(45):2765–78. doi:10.1016/j.cma.2010.04.011
- Bernard PE, Moës N, Chevaugeon N. Damage growth modeling using the Thick Level Set (TLS) approach: Efficient discretization for quasi-static loadings. *Comp Methods Appl Mech Eng* (2012) 233–236:11–27. doi:10.1016/j.cma.2012.02.020
- Gurtin ME. Generalized Ginzburg-Landau and Cahn-Hilliard equations based on a microforce balance. *Physica D: Nonlinear Phenomena* (1996) 92(3):178–92. doi:10.1016/0167-2789(95)00173-5
- Coleman BD, Noll W. The thermodynamics of elastic materials with heat conduction and viscosity. In: W Noll, editor. *The foundations of mechanics and thermodynamics: Selected papers*. Berlin, Heidelberg: Springer Berlin Heidelberg (1974). p. 145–56.
- Feng D-C, Wu J-Y. Phase-field regularized cohesive zone model (CZM) and size effect of concrete. *ENGINEERING FRACTURE MECHANICS* (2018) 197:66–79. doi:10.1016/j.engfracmech.2018.04.038
- Vinh Phu N, Wu J-Y. Modeling dynamic fracture of solids with a phase-field regularized cohesive zone model. *COMPUTER METHODS APPLIED MECHANICS ENGINEERING* (2018) 340:1000–22. doi:10.1016/j.cma.2018.06.015
- Wu J-Y. A unified phase-field theory for the mechanics of damage and quasi-brittle failure. *JOURNAL MECHANICS PHYSICS SOLIDS* (2017) 103:72–99. doi:10.1016/j.jmps.2017.03.015
- Wu J-Y. A geometrically regularized gradient-damage model with energetic equivalence. *COMPUTER METHODS APPLIED MECHANICS ENGINEERING* (2018) 328:612–37. doi:10.1016/j.cma.2017.09.027
- Wu J-Y. Robust numerical implementation of non-standard phase-field damage models for failure in solids. *COMPUTER METHODS APPLIED MECHANICS ENGINEERING* (2018) 340:767–97. doi:10.1016/j.cma.2018.06.007
- Wu J-Y, Vinh Phu N. A length scale insensitive phase-field damage model for brittle fracture. *JOURNAL MECHANICS PHYSICS SOLIDS* (2018) 119:20–42. doi:10.1016/j.jmps.2018.06.006
- Wu J-Y, Vinh Phu N, Nguyen CT, Sutula D, Sinaia S, Bordas SPA. Phase-field modeling of fracture. In: SPA Bordas DS Balint, editors, 53 (2020). p. 1–183. *ADVANCES APPLIED MECHANICS*
- Yang J, Lian H, Nguyen VP. Study of mixed mode I/II cohesive zone models of different rank coals. *Eng Fracture Mech* (2021) 246:107611. doi:10.1016/j.engfracmech.2021.107611
- Chen L, Wang Z, Peng X, Yang J, Wu P, Lian H. Modeling pressurized fracture propagation with the isogeometric BEM. *Geomechanics Geophys Geo-Energy Geo-Resources* (2021) 7(3):51. doi:10.1007/s40948-021-00248-3



OPEN ACCESS

EDITED BY

Leilei Chen,
Huanghuai University, China

REVIEWED BY

Haifeng Gao,
Taiyuan University of Technology, China
Zhao Binghao,
Beijing Institute of Technology, China

*CORRESPONDENCE

Qingyuan Hu,
✉ qingyuanhu@jiangnan.edu.cn

SPECIALTY SECTION

This article was submitted to Statistical and Computational Physics, a section of the journal Frontiers in Physics

RECEIVED 26 February 2023

ACCEPTED 21 March 2023

PUBLISHED 31 March 2023

CITATION

Hu Q, Meng X and You Y (2023),
Isogeometric multi-patch topology
optimization based on pix2pix.
Front. Phys. 11:1174262.
doi: 10.3389/fphy.2023.1174262

COPYRIGHT

© 2023 Hu, Meng and You. This is an open-access article distributed under the terms of the [Creative Commons Attribution License \(CC BY\)](#). The use, distribution or reproduction in other forums is permitted, provided the original author(s) and the copyright owner(s) are credited and that the original publication in this journal is cited, in accordance with accepted academic practice. No use, distribution or reproduction is permitted which does not comply with these terms.

Isogeometric multi-patch topology optimization based on pix2pix

Qingyuan Hu^{1*}, Xin Meng¹ and Yangxiu You²

¹School of Science, Jiangnan University, Wuxi, China, ²School of Artificial Intelligence and Computer Science, Jiangnan University, Wuxi, China

We present a novel approach that combines the power of pix2pix, an image-to-image translation framework, with the advanced capabilities of isogeometric multi-patch analysis for topology optimization. The proposed method adds the Nitsche's methods into the advantages of Isogeometric analysis (IGA), thus gaining the ability to handle complex geometries by generating locally smooth and well-converged results. Additionally, the usage of generative adversarial network based pix2pix allows for a more efficient representation of the design space, reducing the computational cost of the optimization process. This approach has shown promising results in various numerical examples. This technique aims to improve the efficiency of conceptual design in complex engineering applications.

KEYWORDS

isogeometric, topology optimization, Nitsche, GaN, pix2pix

1 Introduction

Nowadays, topology optimization is becoming a powerful computational technique for designing structures with optimal properties by iteratively redistributing material within a given design space. It has many practical applications in the design of structures for aerospace, automotive, civil engineering and many other projects [1]. However, accurately representing complex geometries can be challenging, especially when utilizing traditional finite element methods (FEM) that require a high number of elements. Isogeometric analysis (IGA), which uses the same basis functions for both the geometry field and displacement field, has emerged as a promising alternative to traditional FEM [2]. Isogeometric based topology optimization offers several advantages over traditional topology optimization methods. Firstly, the usage of Non-Uniform Rational B-Splines (NURBS) basis functions offers improved accuracy, as NURBS provide a smooth and flexible representation of geometry that can accurately capture complex features. Additionally, isogeometric topology optimization reduces meshing efforts and achieves faster convergence rates than traditional topology optimization methods, thanks to the higher accuracy of the NURBS-based representation. Finally, isogeometric topology optimization can be seamlessly integrated with CAD systems, making it a potential tool for designers and engineers to create more accurate and efficient designs for a wide range of engineering applications [3]. However, one significant issue with isogeometric topology optimization is its computational cost. The NURBS basis functions bring a high number of control points, leading to an increased number of degrees of freedom and computational complexity, especially for large-scale problems. Additionally, the optimization iteration itself is time consuming, especially when convergence issues occur, the computational costs could be badly increased.

To address these challenges, the deep learning technique is introduced into the IGA and topology optimization. Liao et al. [4]. Proposed a deep-learning-based inverse design approach for auxetic materials, using a surrogate model based on deep neural networks. The deep learning framework called IGA-Reuse-Net was presented by Wang [5], which combined IGA and UNet3+ architecture, and achieved a good trade-off between accuracy and efficiency in solving Poisson equations on different topologies. Gasick and Qian [6] introduced a physics-based machine learning approach that combines isogeometric representation with deep learning to solve parameterized PDEs over changing domains. As for topology optimization, Sosnovik and Oseledets [7] proposed a deep learning-based approach to accelerate topology optimization by treating it as an image segmentation problem, which demonstrates significant acceleration. In the study of Sasaki and Igarashi [8], a novel approach of topology optimization was proposed, which combined the power of deep learning with traditional optimization techniques to accelerate the design process and achieved optimal solutions for complex electromagnetic systems. Nie et al. [9] proposed a new method for topology optimization using generative adversarial networks, leveraging physical fields over the initial design domain to generate high-quality optimized structures. In the recent contribution of Yan et al. [10], a new method for real-time topology optimization driven by deep learning is introduced, by utilizing initial stress learning to achieve efficient and accurate optimization, marking a significant step forward in the development of intelligent design systems.

The pix2pix framework is a type of conditional generative adversarial network (cGAN) that maps an input image to an output image with high resolution, in our case, an optimized topology of a structure [11]. It has been specifically designed for image-to-image translation, such as converting a black-white image to a color image or converting a low-resolution image to a high-resolution image. The generator network produces a high-resolution image of the optimized structure, while the discriminator network evaluates the generated image and provides feedback to the generator network to iteratively improve its performance. Pix2pix has been successfully used in a variety of applications, including the translation of sketches to photorealistic images, the generation of realistic images of 3D objects from 2D images, and the restoration of degraded or low-resolution images [12]. By considering the mechanical structures in the form of images as input, the pix2pix proves its effectiveness in topology optimization applications. Hertlein et al. [13] presented an approach for topology optimization, which enables designers to explore design flexibility in the early stages of the additive manufacturing process. Ye et al. [14] accelerated the topology optimization process by utilizing a pix2pix network to generate high-quality optimized designs. Li et al. [15] developed a cross-resolution Pix2pix neural network, enabling efficient and accurate optimization of geometrically nonlinear systems.

In engineering common practice, complex design spaces are usually represented by a set of NURBS patches, and each patch has its own parameterization, such as different degrees of continuity or geometric shape. Isogeometric multi-patch methods have been proposed to address the challenges of complex geometries. Ruess et al. [16] utilized weak coupling to enable accurate analysis of complex multi-patch geometries with non-matching and trimmed

boundaries. Brivadis et al. [17] used the mortar method for the coupling between different subdomains, paving the way for advanced numerical simulation in a variety of fields. In the study of Kargaran et al. [18], a new approach to isogeometric analysis using overlapping multi-patch structures is proposed, which enables efficient and accurate simulation of complex geometries.

The Nitsche's method is usually adopted in FEM for weakly imposing boundary conditions and handling non-matching meshes between different subdomains. The method involves adding energy terms to the weak form of the partial differential equation being solved, which helps to enforce the boundary conditions and reduce the effect of the non-matching meshes. The Nitsche's method has been shown to be robust, accurate, and flexible, and has become a popular method in the FEM community. Chouly and Hild [19] solved unilateral contact problems using a Nitsche-based approach, enabling accurate and efficient numerical analysis of complex systems. Nguyen et al. [20] presented a new approach to patch coupling using the Nitsche's method, allowing for efficient and accurate analysis of complex two and three-dimensional systems. Guo and Ruess [21] tried to couple isogeometric thin shells and blended shell structures using the Nitsche's method, facilitating efficient and accurate simulation of complex structures. Du et al. [22] presented a new approach to isogeometric analysis of Reissner-Mindlin plates with non-conforming multi-patches by the Nitsche's method. Back to our study in 2018 [23], we proposed a skew-symmetric Nitsche's formulation for isogeometric analysis, which allows for the incorporation of Dirichlet and symmetry conditions, patch coupling, and frictionless contact in IGA simulations.

In this research, the pix2pix framework is adopted for fast topology optimization in the context of multi-patch IGA. Our goal is to expedite the conceptual design process and enhance efficiency. The analysis process begins with multiple NURBS patches, each with its own local isogeometric basis functions. These patches are then merged by the Nitsche's method under a continuity condition to ensure a smooth and seamless design across patch interfaces. Subsequently, a well-trained pix2pix network is used to generate an image of the desired design from an initial image of element-wise strain energy distribution. Finally, the generated image is projected back onto the multi-patch domain together with some post-processing treatment. This approach offers multiple benefits. Firstly, the isogeometric basis functions and multi-patch technique provide a more accurate representation of the geometry, resulting in clear designs. Secondly, the adoption of the pix2pix significantly reduces the computational efforts of the calculation process while maintaining relatively high-quality outcomes. Lastly, combining these techniques leads to an efficient and accurate topology optimization process, enabling faster and more cost-effective design iterations. This method has yielded promising results in various problems.

2 Isogeometric multi-patch analysis

2.1 Basic theory of IGA

FEM is widely utilized in structural mechanics, but it requires careful consideration of mesh quality in order to keep good analysis accuracy. IGA, on the other hand, overcomes this drawback using

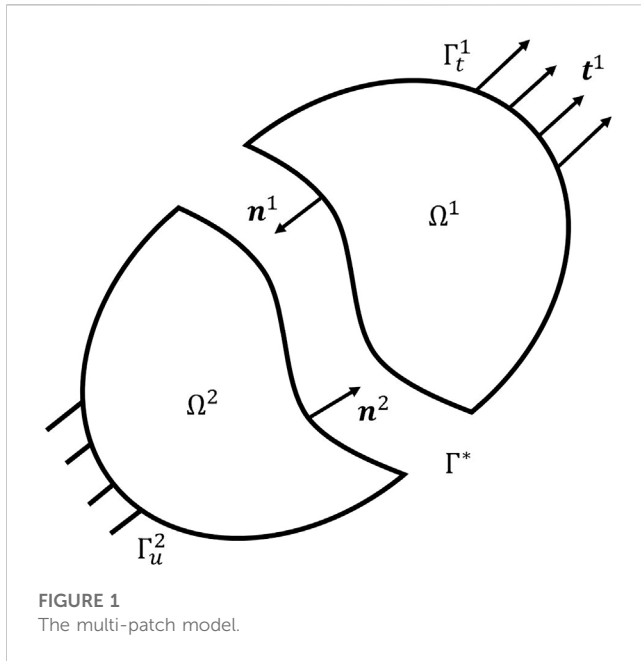


FIGURE 1
The multi-patch model.

the inherent meshes naturally from the CAD model. Moreover, by utilizing NURBS as shape functions, IGA gains the ability to construct high-order continuous approximations. This paper focuses specifically on two-dimensional structures. For three-dimensional problems, the extension can be naturally achieved by incorporating an additional dimension.

The IGA process starts with a parametric representation for its geometric model, which is constructed by the NURBS interpolation as

$$\mathbf{S}(\xi, \eta) = \sum_{i=1}^n R_i(\xi, \eta) \mathbf{P}_i(x, y), \quad (1)$$

where R_i are NURBS basis functions, (ξ, η) represent the coordinates frame in the parameter space, and n denotes the number of base functions. $\mathbf{P}_i(x, y)$ are called control points. In IGA, the mesh division is done naturally in the parametric domain, which eliminates the need for special mesh division procedures utilized in classical FEM, resulting in faster analysis cycles.

IGA can be considered as a special isoparametric version of FEM, meaning that the interpolation basis functions used in geometry discretization, i.e., NURBS, are consistent with the shape functions used in displacement discretization. Then the following formula expresses the physical field

$$\mathbf{u}(\xi, \eta) = \sum_{i=1}^n R_i(\xi, \eta) \mathbf{u}_i(x, y), \quad (2)$$

where $\mathbf{u}_i(x, y)$ are the displacement values at the control points.

Isogeometric analysis offers superior accuracy in representing the geometric features of a given model. Unlike traditional FEM, it provides a wider range of mesh refinement strategies, including the commonly used h-refinement and p-refinement, as well as the unique k-refinement strategy. This innovative approach allows for higher accuracy and faster refinement speeds. From an optimization perspective, isogeometric analysis offers an

integrated approach to design and simulation. In this way, the geometry of the structure being designed gains the potential to be directly modified based on the results of the simulation, resulting in greater efficiency in structural design optimization.

2.2 Multi-patch analysis based on the Nitsche's method

In practice, most complex geometric models are represented by multiple patches of distinct material properties. Furthermore, patches with different meshes reveal the potential of parallel computation, although not considered in this study. Consider an interface problem, as indicated in Figure 1, the domain Ω is decomposed into two sub-domains Ω^m , where the superscript $m = 1, 2$ is used to mark the divided domain and corresponding variables. The governing equations are listed as follows

$$\begin{aligned} -\nabla \cdot \boldsymbol{\sigma}^m &= \mathbf{b}^m & \text{on } \Omega^m, \\ \mathbf{u}^m &= \bar{\mathbf{u}}^m & \text{on } \Gamma_u^m, \\ \boldsymbol{\sigma}^m \cdot \mathbf{n}^m &= \bar{\mathbf{t}}^m & \text{on } \Gamma_t^m, \\ \mathbf{u}^1 &= \mathbf{u}^2 & \text{on } \Gamma^*, \\ \boldsymbol{\sigma}^1 \cdot \mathbf{n}^1 &= -\boldsymbol{\sigma}^2 \cdot \mathbf{n}^2 & \text{on } \Gamma^*, \end{aligned} \quad (3)$$

Where the $\boldsymbol{\sigma}^m$ are stress fields, \mathbf{b} stands for the body force, \mathbf{u}^m denote the displacement fields, the \mathbf{n}^1 and \mathbf{n}^2 are unit normal vectors along Γ^* , the interface of Ω^m .

In order to glue the two patches, according to the Nitsche's method [23], we define the trial function on the domain Ω as \mathbf{V} , then the weak form of the problem reads:

Find $\mathbf{u} \in \mathbf{V}$:

$$a(\mathbf{u}, \mathbf{v}) = L(\mathbf{v}), \quad \forall \mathbf{v} \in \mathbf{V}. \quad (4)$$

By defining the displacement jump and stress average operators as

$$[\![\mathbf{u}]\!] := \mathbf{u}^1 - \mathbf{u}^2 \quad (5)$$

and

$$\langle \boldsymbol{\sigma}(\mathbf{u}) \rangle := \frac{1}{2} (\boldsymbol{\sigma}^1(\mathbf{u}) \mathbf{n}^1 - \boldsymbol{\sigma}^2(\mathbf{u}) \mathbf{n}^2), \quad (6)$$

we obtain the Nitsche's formulation as

Find $\mathbf{u} \in \mathbf{V}$:

$$\begin{aligned} a(\mathbf{u}, \mathbf{v}) - \int \langle \boldsymbol{\sigma}(\mathbf{u}) \rangle \cdot [\![\mathbf{v}]\!] \, ds - \theta \int [\![\mathbf{u}]\!] \cdot \langle \boldsymbol{\sigma}(\mathbf{v}) \rangle \, ds + \int \gamma [\![\mathbf{u}]\!] [\![\mathbf{v}]\!] \, ds \\ = L(\mathbf{v}), \quad \forall \mathbf{v} \in \mathbf{V}, \end{aligned} \quad (7)$$

where the θ is the Nitsche parameter, and the γ is called the stabilization parameter.

For the Nitsche parameter θ , taking different values results in different Nitsche formulations. In this paper, we set $\theta = 1$ in order to use the standard Nitsche's method which can keep the stiffness matrix symmetric. For the stabilization parameter γ , we adopt the experienced formula in [24]. For more details about the derivation and theory of the Nitsche's method, please refer to [23].

From the matrix point of view, original discrete IGA formula in matrix form is given by

$$\mathbf{KU} = \mathbf{F}, \quad (8)$$

where \mathbf{K} is the global stiffness matrix, \mathbf{U} is the vector of nodal displacement degrees of freedom, and \mathbf{F} is the nodal force vector. Since we are considering two NURBS patches, the above formula can be decomposed as follows

$$\begin{bmatrix} \mathbf{K}^1 & \\ & \mathbf{K}^2 \end{bmatrix} = \begin{bmatrix} \mathbf{U}^1 & \\ & \mathbf{U}^2 \end{bmatrix} \begin{bmatrix} \mathbf{F}^1 \\ \mathbf{F}^2 \end{bmatrix}, \quad (9)$$

where the superscripts are used to show the patch indexes as before. After marking the interface elements by subscripts s and m along the two patches respectively, we can rewrite discretized Eq. 10 as follows

$$\begin{bmatrix} \tilde{\mathbf{K}}^1 & & & \\ & \mathbf{K}_s^1 & & \\ & & \mathbf{K}_m^2 & \\ & & & \tilde{\mathbf{K}}^2 \end{bmatrix} = \begin{bmatrix} \tilde{\mathbf{U}}^1 & & & \\ & \mathbf{U}_s^1 & & \\ & & \mathbf{U}_m^2 & \\ & & & \tilde{\mathbf{U}}^2 \end{bmatrix} \begin{bmatrix} \tilde{\mathbf{F}}^1 \\ \mathbf{F}_s^1 \\ \mathbf{F}_m^2 \\ \tilde{\mathbf{F}}^2 \end{bmatrix}, \quad (10)$$

here the tilde indicates the remaining elements which are not involved into the interface coupling, for illustration $\tilde{\mathbf{K}}^1 = \mathbf{K}^1 - \mathbf{K}_s^1$.

3 Topology optimization based on pix2pix

3.1 Pix2pix driven topology optimization

Structural topology optimization is a more advanced optimization technique than size and shape optimization, which operates at the conceptual design stage of a structure, and its output serves as the foundation for future designs. This study focuses on the topology optimization of elastic structures, aiming to identify the optimal structural type generated within the design domain under given conditions. This paper uses the minimum structural compliance as the objective function to optimize the topology, i.e., the density distribution. The optimization formula is written by

$$\begin{aligned} \min: \Phi(\rho, \mathbf{U}) &= \mathbf{F}(\rho, \mathbf{U})^T \mathbf{U} = \mathbf{U}^T \mathbf{KU} = \sum_{e=1}^N \mathbf{u}_e^T \mathbf{k}_e \mathbf{u}_e, \\ \text{s.t.}: \sum_{e=1}^N \rho_e v_e - V^* &\leq 0, \\ 0 < \rho_{\min} \leq \rho_e &\leq 1, \quad e = 1, \dots, N, \\ \mathbf{K}(\rho) \mathbf{U} &= \mathbf{F}, \end{aligned} \quad (11)$$

where subscript e represents the corresponding physical quantity of element e , and N is the total number of finite elements. The ρ is a vector of density variables, which represents the relative density of materials of each element in the structure. ρ_e is the density of element e , and ρ_{\min} is the minimum relative density of a single element. v_e stands for the volume of element e . \mathbf{k}_e is the element stiffness matrix. V^* denotes the upper limit of the allowable material volume.

Pix2pix algorithm, proposed by Phillip Isola of the AI Laboratory in Berkeley, is a typical image migration algorithm based on GAN [11]. The pix2pix algorithm consists of two components: a generator network and a discriminator network. The generator network takes an input image and attempts to generate a corresponding output image, while the discriminator network evaluates the output image to determine whether it is a

qualified image or not, according to the training data. During the training process, the generator network is trained to generate output images that the discriminator network is unable to distinguish from qualified images, while the discriminator network is trained to accurately differentiate between qualified and unqualified images. Figure 2 shows the network structure of pix2pix, which includes 8 convolution layers and 7 deconvolution layers. In order to better retain the information of the input image, a jump connection structure is added between the convolution layers and the deconvolution layers.

In this paper, we are using pix2pix to accelerate the topology optimization process. This approach is divided into the following three steps:

- i. We calculate the strain energy for each element by

$$c_e = \mathbf{u}_e^T \mathbf{k}_e \mathbf{u}_e \quad (12)$$

from the first iteration of topology optimization through (multi-patch) IGA, since the strain energy is a part of the structural compliance, and it reveals the sensitivities of the objective function to a certain extent. The strain energy matrix is normalized and then scaled as an input image for pix2pix.

- ii. The pix2pix model is trained together with the well-calculated topology optimization results served as reference for the discriminator. In the model, the strain energy data is used as the training image, and the topology optimization results obtained by the sequential integer programming and canonical relaxation algorithm proposed by Liang and Cheng [25], are used as the reference results, since it provides clear black-white results.
- iii. Based on the well-trained pix2pix model obtained in step ii, for the topology optimization problem that needs to be predicted, we carry out isogeometric analysis, and input the strain energy heat map into the trained pix2pix model. According to the input, the model will quickly output the probable distribution of the element densities of the structure. Finally, we convert this distribution into topology optimization results.

3.2 Data training and testing

As illustrated in Figure 3, the pix2pix network is trained by a single-patch cantilever beam example. In order to provide training and testing samples for the pix2pix model, and to get as many data as possible, we fix the left side of the cantilever beam and apply a variable concentrated force at the midpoint of the right side of the beam, with a force magnitude of $F = 1$. Furthermore, different loads, load types, boundary conditions and constraints are also considered to perform topology optimization. Together with the strain energy in the first isogeometric analysis, the final topology optimization results are labeled, then be used to train the pix2pix model.

In this study, we trained the input data using a batch size of 1 and a maximum epoch of 200, and the final prediction result comprises images measuring $256 \times 256 \times 1$. To verify the effectiveness of the training process, we take a glance during the early stage of the training process, as shown in Figure 4. Here we randomly choose 3 cases, each case is lined by a column. The top row is the element-

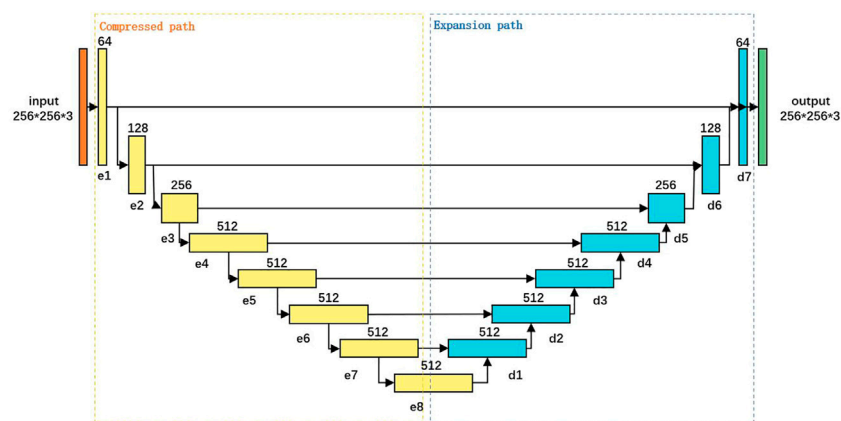


FIGURE 2
Pix2pix network structure.

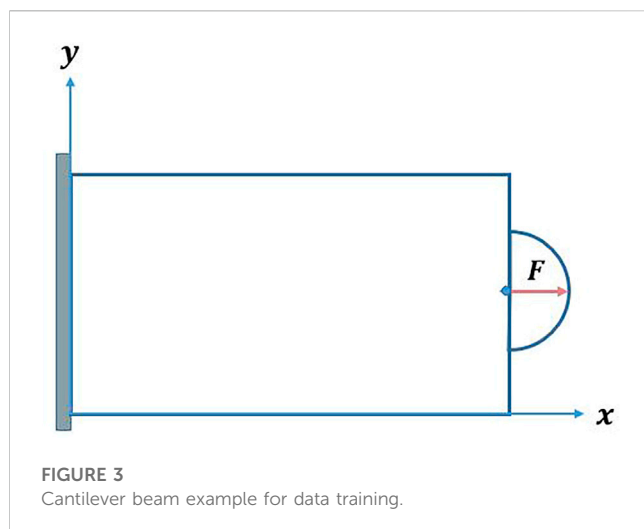


FIGURE 3
Cantilever beam example for data training.

wise strain energy heat map, the middle row describes the predicted results by pix2pix, and the bottom row shows the reference results obtained by traditional IGA topology optimization. Note that this is just the early stage of the training process, as training goes on, the predicted results are quite distinguishable.

3.3 Special treatment for multi-patch cases and post-processing

For multi-patch topology optimization in IGA, the Nitsche's method is firstly adopted to couple patches. Since the mesh resolutions of different patches are usually different, the magnitudes of the sensitivity values corresponding to meshes of different densities are also different. If these sensitivities are directly substituted into the topology optimization algorithm, it could lead to inappropriate optimization results, especially along the coupling interfaces. To overcome this problem, a simple method to filter the interface sensitivities is used [26].

The deep learning toolbox is commonly used as a black box, it just learns from big data and predicts a result according to a

given input, thus it is difficult to impose direct constraints, such as volume constraints in our topology optimization applications. In our practice, the pix2pix accepts a heat map of the element-wise strain energy matrix, then feeds back an element-wise density distribution matrix. To address this matter, we firstly sort the densities by their numbers, then keep and drop out the elements according to the desired volume constraint.

4 Numerical examples

4.1 Cantilever beam

In this study, we present the results of testing our proposed method on a cantilever beam model, the left side of the beam is fixed, and the bottom right is subjected to a downward concentrated force. The model is fixed at the left end and subject to a concentrated force at the lower right corner. The mesh is shown in Figure 5. The topology optimization result obtained by the pix2pix method is shown in Figure 6. By comparing the result obtained through normal calculation (Figure 7) and our proposed method, we observed that the material topology of both results is similar, with the pix2pix result exhibiting some jagged boundaries and finer details.

However, the pix2pix result accurately reflects the material distribution. Our method demonstrates significant potential for accelerating the optimization process, while simultaneously maintaining high accuracy and generalizability.

4.2 One-quarter ring

As our next example, the proposed method is used to test the one-quarter ring model. The bottom of the ring is fixed to the ground, and its upper left corner is applied by a concentrated force. This model serves to evaluate the efficacy of isogeometric analysis for models with curved edges. The mesh partitioning is presented in Figure 8, and the topology optimization result

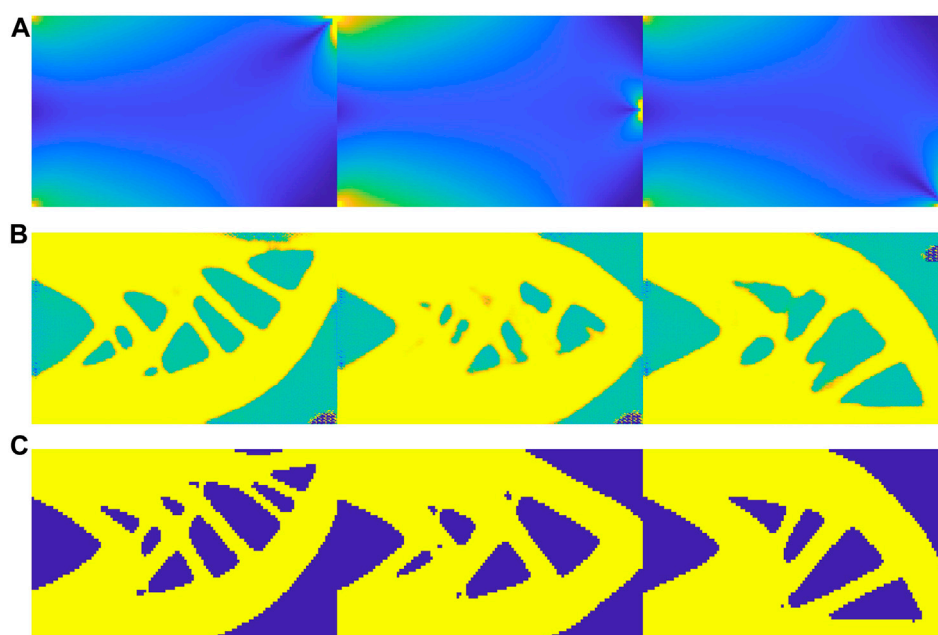


FIGURE 4

A glance during the early stage of the train process. (A) element-wise strain energy heat map. (B) predicted results by pix2pix. (C) reference results.

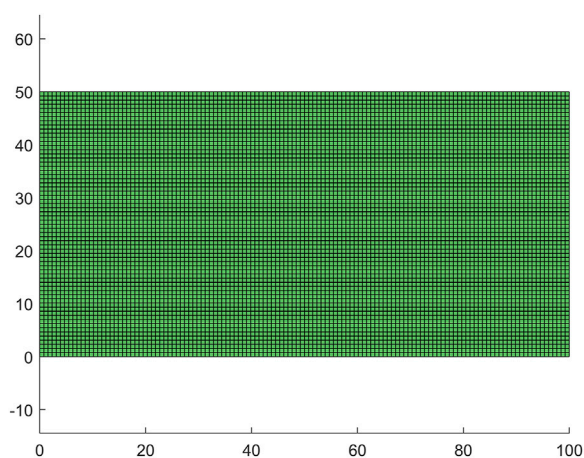


FIGURE 5

Cantilever beam mesh.

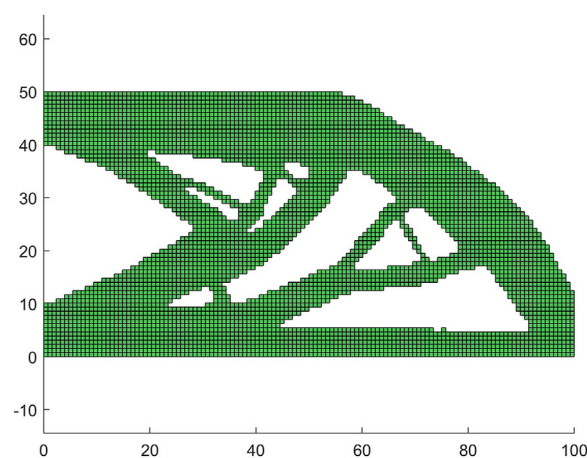


FIGURE 6

Cantilever beam topology optimization result by pix2pix.

obtained through the application of pix2pix can be found in Figure 9.

Despite the inherent limitations of the method, such as the occurrence of unsmoothness at certain boundaries and occasional holes at individual locations, the pix2pix results are still commendable, especially when compared to the reference result obtained through conventional calculations in Figure 10. However, it is worth noting that the use of the element-wise strain energy as the sole predictor in pix2pix does make it challenging to obtain entirely smooth boundaries even with post-processing.

4.3 Double-beam structure

To further assess the performance of our proposed method in multi-path scenarios, we conducted experiments on a divided cantilever beam model, as depicted in Figure 11. The upper patch of the beam is subjected to a sparser mesh division, while the lower patch is subjected to a denser mesh division. The result obtained from pix2pix prediction are presented in Figure 12.

Notably, the two patches exhibit a seamless connection, indicating that the pix2pix prediction is able to maintain the smoothness of the



FIGURE 7
Cantilever beam topology optimization result for reference.

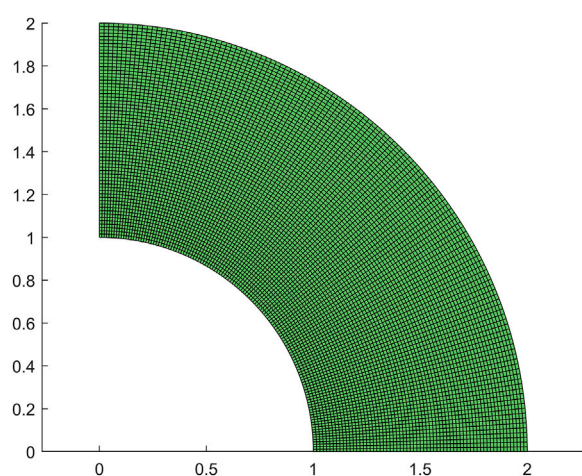


FIGURE 8
One-quarter ring mesh.

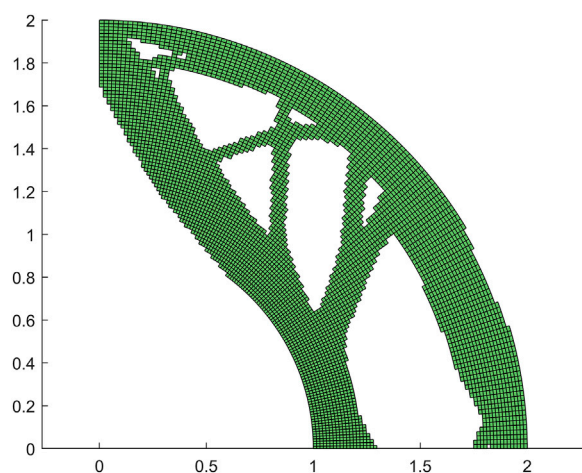


FIGURE 9
One-quarter ring topology optimization result by pix2pix.



FIGURE 10
One-quarter ring topology optimization result for reference.

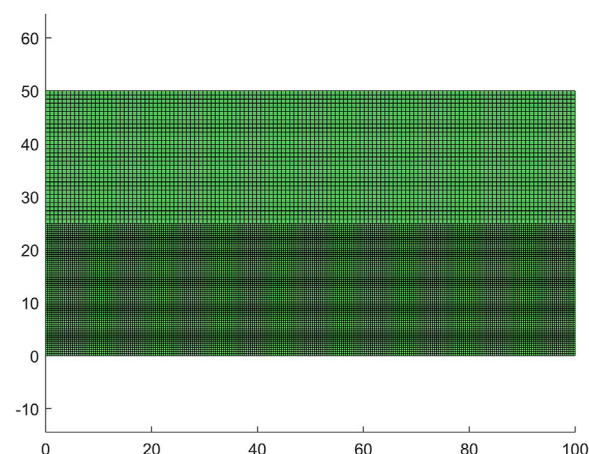
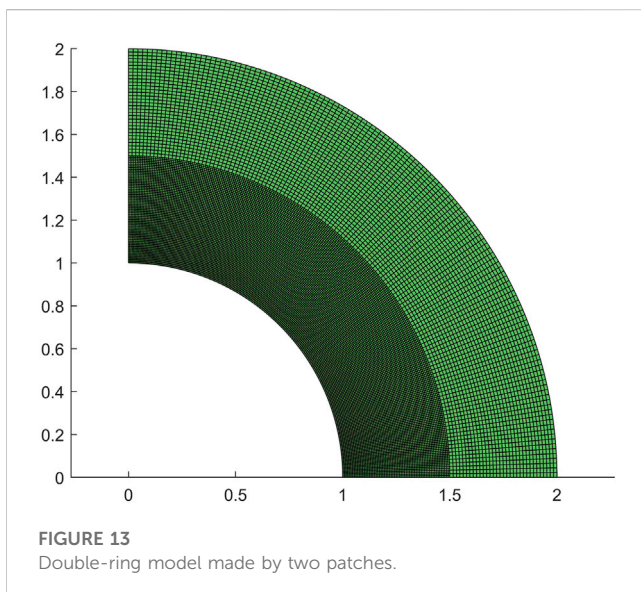
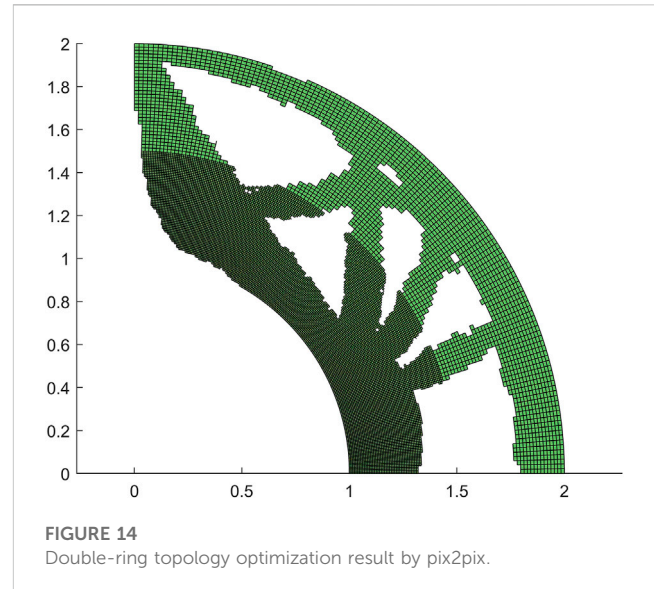
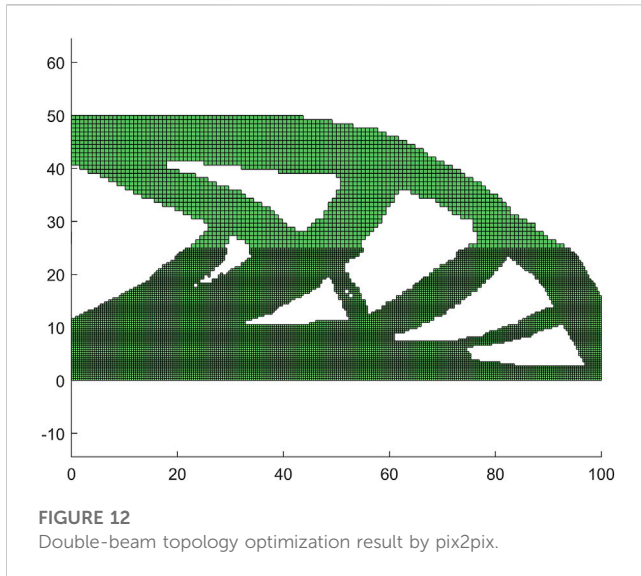


FIGURE 11
Double-beam model made by two patches.

overall structure despite the differing mesh divisions in the separate patches. These results highlight the potential of our method to provide accurate predictions for complex, multi-patch models. The approach we propose not only resolves the topology optimization problem for the training model but also accomplishes a range of topology optimization problems within a shorter computational time compared to conventional optimization procedures.

4.4 Double-ring structure

The double one-quarter ring problem, as depicted in the accompanying Figure 13, has been partitioned into two distinct



segments, with corresponding mesh divisions, in order to address its computational complexity. However, despite its utility, the performance of the pix2pix model in predicting the outcome of this problem is suboptimal, as evidenced by the accompanying predicted outcome of Figure 14. The model's limited efficacy is characterized by a heavily jagged boundary and localized discontinuities arising from a lack of edge connectivity, which compromises the accuracy of its predictive capacity.

Despite these shortcomings, the material distribution resultant from this exercise provides a clear conceptual framework for further analyses and serves as a dependable guide for subsequent investigations. By generating a clear and coherent spatial representation of the material distribution, it enables researchers to identify relevant features of the problem and evaluate its overall complexity. Thus, while the pix2pix model may not be fully optimized for this task, the insights gleaned from this exercise demonstrate its potential for application in a range of related problems, and serve as a stepping stone for further research in this area.

5 Conclusion

In this article, we provide a comprehensive evaluation of the isogeometric multi-patch topology optimization based on the pix2pix method and discuss its potential applications in the design of complex structures.

The Nitsche's method is adopted for multi-patch coupling, enabling isogeometric analysis (IGA) to analyze complex geometries. Within the IGA framework, element density is treated as the design variable, resulting in topology optimization geometries with smooth, curved boundaries that are used as training data for the generative adversarial network (GAN). Finally, the pix2pix algorithm is used to quickly evaluate a complex model by inputting a heat map of element-wise energy. However, due to the limitations of GANs, controlling the volume constraint directly is not straightforward. Therefore, a post-processing step is applied by sorting and filtering the element densities. Our results demonstrate the efficiency and the effectiveness of the proposed approach.

Overall, the combination of IGA, Nitsche-based multi-patch technique, and pix2pix image-to-image translation provides a powerful tool for engineers and designers to efficiently and effectively optimize complex engineering designs, and we believe that it represents an exciting area of research for topology optimization with a wide range of potential applications.

Data availability statement

The raw data supporting the conclusion of this article will be made available by the authors, upon reasonable request.

Author contributions

QH, XM, and YY contributed to the conception and design of the study. QH proposed the original idea and the code framework. XM developed further the algorithm, performed the computation, and wrote the draft. YY helped with the training and computation, the result

analysis, as well as the draft of the manuscript. All authors contributed to the manuscript revision, read, and approved the submitted version.

Funding

QH is supported by the National Natural Science Foundation of China (No. 12102146), the Natural Science Foundation of Jiangsu Province (No. BK20200611), and the Fundamental Research Funds for the Central Universities (No. JUSRP12038).

Acknowledgments

The authors wish to express their appreciation to the reviewers for their helpful suggestions which greatly improved the presentation of this paper.

References

1. Bendsoe MP, Sigmund O. *Topology optimization: Theory, methods, and applications*. Berlin: Springer Science and Business Media (2003). doi:10.1007/978-3-662-05086-6
2. Hughes TJ, Cottrell JA, Bazilevs Y. Isogeometric analysis: CAD, finite elements, NURBS, exact geometry and mesh refinement. *Comp Methods Appl Mech Eng* (2005) 194(39-41):4135–95. doi:10.1016/j.cma.2004.10.008
3. Cottrell JA, Hughes TJ, Bazilevs Y. *Isogeometric analysis: Toward integration of CAD and FEA*. Chichester: John Wiley and Sons (2009). doi:10.1002/9780470749081
4. Liao Z, Wang Y, Gao L, Wang ZP. Deep-learning-based isogeometric inverse design for tetra-chiral auxetics. *Compos Structures* (2022) 280:114808. doi:10.1016/j.compstruct.2021.114808
5. Wang D, Xu J, Gao F, Wang CC, Gu R, Lin F, et al. IGA-reuse-NET: A deep-learning-based isogeometric analysis-reuse approach with topology-consistent parameterization. *Comp Aided Geometric Des* (2022) 95:102087. doi:10.1016/j.cagd.2022.102087
6. Gasick J, Qian X. Isogeometric neural networks: A new deep learning approach for solving parameterized partial differential equations. *Comp Methods Appl Mech Eng* (2023) 405:115839. doi:10.1016/j.cma.2022.115839
7. Sosnovik I, Oseledets I. Neural networks for topology optimization. *Russ J Numer Anal Math Model* (2019) 34(4):215–23. doi:10.1515/rnam-2019-0018
8. Sasaki H, Igarashi H. Topology optimization accelerated by deep learning. *IEEE Trans Magnetics* (2019) 55(6):1–5. doi:10.1109/TMAG.2019.2901906
9. Nie Z, Lin T, Jiang H, Kara LB. Topologygan: Topology optimization using generative adversarial networks based on physical fields over the initial domain. *J Mech Des* (2021) 143(3). doi:10.1115/detc2020-22675
10. Yan J, Zhang Q, Xu Q, Fan Z, Li H, Sun W, et al. Deep learning driven real time topology optimisation based on initial stress learning. *Adv Eng Inform* (2022) 51:101472. doi:10.1016/j.aei.2021.101472
11. Isola P, Zhu JY, Zhou T, Efros AA. Image-to-image translation with conditional adversarial networks. In: Proceedings of the IEEE conference on computer vision and pattern recognition (2017). doi:10.1109/CVPR.2017.632
12. Pan W, Torres-Verdin C, Pyrcz MJ. Stochastic pix2pix: A new machine learning method for geophysical and well conditioning of rule-based channel reservoir models. *Nat Resour Res* (2021) 30:1319–45. doi:10.1007/s11053-020-09778-1
13. Hertlein N, Buskohl PR, Gillman A, Vemaganti K, Anand S. Generative adversarial network for early-stage design flexibility in topology optimization for additive manufacturing. *J Manufacturing Syst* (2021) 59:675–85. doi:10.1016/j.jmsy.2021.04.007
14. Ye HL, Li JC, Yuan BS, Wei N, Sui YK. Acceleration design for continuum topology optimization by using Pix2pix neural network. *Int J Appl Mech* (2021) 13(04):2150042. doi:10.1142/S1758825121500423
15. Li J, Ye H, Yuan B, Wei N. Cross-resolution topology optimization for geometrical non-linearity by using deep learning. *Struct Multidisciplinary Optimization* (2022) 65(4):133. doi:10.1007/s00158-022-03231-y
16. Ruess M, Schillinger D, Oezcan AI, Rank E. Weak coupling for isogeometric analysis of non-matching and trimmed multi-patch geometries. *Comp Methods Appl Mech Eng* (2014) 269:46–71. doi:10.1016/j.cma.2013.10.009
17. Brivadis E, Buffa A, Wohlmuth B, Wunderlich L. Isogeometric mortar methods. *Comp Methods Appl Mech Eng* (2015) 284:292–319. doi:10.1016/j.cma.2014.09.012
18. Kargaran S, Jüttler B, Kleiss SK, Mantzaflaris A, Takacs T. Overlapping multi-patch structures in isogeometric analysis. *Comp Methods Appl Mech Eng* (2019) 356:325–53. doi:10.1016/j.cma.2019.07.010
19. Chouly F, Hild P. A nitsche-based method for unilateral contact problems: Numerical analysis. *SIAM J Numer Anal* (2013) 51(2):1295–307. doi:10.1137/12088344X
20. Nguyen VP, Kerfriden P, Brino M, Bordas SP, Bonisoli E. Nitsche's method for two and three dimensional NURBS patch coupling. *Comput Mech* (2014) 53:1163–82. doi:10.1007/s00466-013-0955-3
21. Guo Y, Ruess M. Nitsche's method for a coupling of isogeometric thin shells and blended shell structures. *Comp Methods Appl Mech Eng* (2015) 284:881–905. doi:10.1016/j.cma.2014.11.014
22. Du X, Zhao G, Wang W. Nitsche method for isogeometric analysis of Reissner–Mindlin plate with non-conforming multi-patches. *Comp Aided Geometric Des* (2015) 35:121–36. doi:10.1016/j.cagd.2015.03.005
23. Hu Q, Chouly F, Hu P, Cheng G, Bordas SP. Skew-symmetric Nitsche's formulation in isogeometric analysis: Dirichlet and symmetry conditions, patch coupling and frictionless contact. *Comp Methods Appl Mech Eng* (2018) 341:188–220. doi:10.1016/j.cma.2018.05.024
24. Hu Q, Baroli D, Rao S. Isogeometric analysis of multi-patch solid-shells in large deformation. *Acta Mechanica Sinica* (2021) 37:844–60. doi:10.1007/s10409-020-01046-y
25. Liang Y, Cheng G. Topology optimization via sequential integer programming and canonical relaxation algorithm. *Comp Methods Appl Mech Eng* (2019) 348:64–96. doi:10.1016/j.cma.2018.10.050
26. Hu Q, Liang Y, Liu M, Hu M, Mao Y. Multi-patch black-white topology optimization in isogeometric analysis. *CMES-Computer Model Eng Sci* (2023) 134(1):459–81. doi:10.32604/cmesci.2022.020327

Conflict of interest

The authors declare that the research was conducted in the absence of any commercial or financial relationships that could be construed as a potential conflict of interest.

Publisher's note

All claims expressed in this article are solely those of the authors and do not necessarily represent those of their affiliated organizations, or those of the publisher, the editors and the reviewers. Any product that may be evaluated in this article, or claim that may be made by its manufacturer, is not guaranteed or endorsed by the publisher.



OPEN ACCESS

EDITED BY

Pei Li,
Xi'an Jiaotong University, China

REVIEWED BY

Yunfei Gao,
Hohai University, China
Chuang Lu,
University of Science and Technology of
China, China

*CORRESPONDENCE

Yujing Ma,
✉ jingleyeah198@163.com

SPECIALTY SECTION

This article was submitted to Statistical
and Computational Physics,
a section of the journal
Frontiers in Physics

RECEIVED 02 March 2023

ACCEPTED 31 March 2023

PUBLISHED 18 April 2023

CITATION

Yuan X, Ma Y, Huang Y, Huo R and Wang Z
(2023), The method of moments for
electromagnetic scattering analysis
accelerated by the polynomial chaos
expansion in infinite domains.
Front. Phys. 11:1178466.
doi: 10.3389/fphy.2023.1178466

COPYRIGHT

© 2023 Yuan, Ma, Huang, Huo and Wang.
This is an open-access article distributed
under the terms of the [Creative
Commons Attribution License \(CC BY\)](#).
The use, distribution or reproduction in
other forums is permitted, provided the
original author(s) and the copyright
owner(s) are credited and that the original
publication in this journal is cited, in
accordance with accepted academic
practice. No use, distribution or
reproduction is permitted which does not
comply with these terms.

The method of moments for electromagnetic scattering analysis accelerated by the polynomial chaos expansion in infinite domains

Xiaohui Yuan¹, Yujing Ma^{1*}, Yajun Huang², Ruijin Huo¹ and
Zhongwang Wang^{3,4}

¹College of Architecture and Civil Engineering, Xinyang Normal University, Xinyang, China, ²College of Intelligent Construction, Wuchang University of Technology, Wuhan, China, ³Henan International Joint Laboratory of Structural Mechanics and Computational Simulation, Huanghuai University, Zhumadian, China, ⁴School of Architecture and Civil Engineering, Huanghuai University, Zhumadian, China

An efficient method of moments (MoM) based on polynomial chaos expansion (PCE) is applied to quickly calculate the electromagnetic scattering problems. The triangle basic functions are used to discretize the surface integral equations. The polynomial chaos expansion is utilized to accelerate the MoM by constructing a surrogate model for univariate and bivariate analysis. The mathematical expressions of the surrogate model for the radar cross-section (RCS) are established by considering uncertain parameters such as bistatic angle, incident frequency, and dielectric constant. By using the example of a scattering cylinder with analytical solution, it is verified that the MoM accelerated by PCE presents a considerable advantage in computational expense and speed.

KEYWORDS

method of moments, polynomial chaos expansion, radar cross-section, surrogate model, electromagnetic scattering

1 Introduction

In recent decades, the research of electromagnetic scattering is playing a crucial role in the stealth system of military structures [1, 2], exploration of underground resources and stratum structures, target recognition, antenna radiation, electromagnetic compatibility, etc. Higher target detection ability and lower detection risk are currently considered important indicators for its design [3], manufacture, and inspection. Research on electromagnetic scattering analysis [4], especially theoretical calculation, practical testing, and uncertainty analysis of radar cross-section (RCS), is the focus of the current research [5, 6]. The RCS is a scalar quantity representing the scattering ability of the target to the incident electromagnetic wave, which can be regarded as the virtual area of the measured object. It plays a vital role in the whole life cycle of equipment design, production, testing, inspection, and use. The theoretical calculation has a lower research cost than the experimental test method.

In the field of electromagnetic scattering analysis, the differential equation methods mainly include the finite element method [7] and finite difference time domain method [8]. These methods require meshing within the domain, which leads to mesh truncation error and mesh dispersion error, which are large. Moreover, it is difficult to accurately fit the

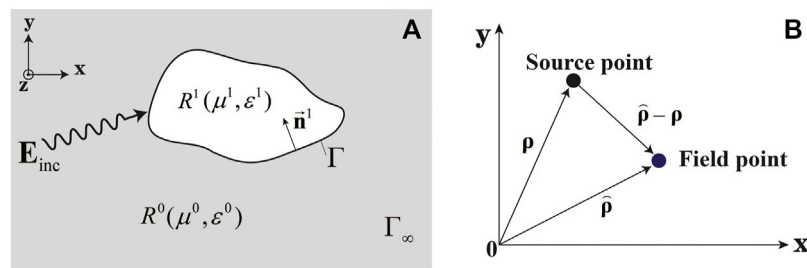


FIGURE 1

Diagram of the electromagnetic scattering. (A) Two regions R : R^0 is an unbounded domain in which the free space parameters are assigned (μ^0, ϵ^0) ; Γ denotes the boundary of R^1 . On each of its interfaces, the normal vector \vec{n}^1 points into R^1 . (B) Near-field diagram.

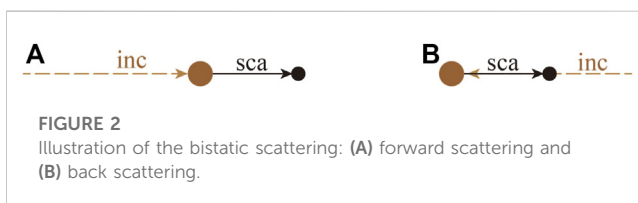


FIGURE 2

Illustration of the bistatic scattering: (A) forward scattering and (B) back scattering.

complex target surface. In addition, high-frequency methods such as graphical electromagnetic computing (GRECO) [9, 10], method of geometrical optics (GO), geometrical theory of diffraction (GTD), physical optics (PO), physical theory of diffraction (PTD), uniform theory of diffraction (UTD) [11], and the bouncing ray method (SBR) [12] are widely used to analyze the electromagnetic scattering characteristics of various complex targets due to their advantages of fast calculation speed and low memory requirement. However, the disadvantage of high-frequency methods is the lower accuracy of the calculation results [13]. The method of moments (MoM) [14–19], using integral equations, has the advantages of automatically satisfying the boundary conditions, relatively few unknowns, and high calculation accuracy. Therefore, it is widely adopted in piezoelectric materials [20], dynamics [21], and acoustics [22–24]. However, the traditional MoM needs to solve huge matrix systems [25–28], which requires a large amount of calculation and memory [29]. Considering the limitations of the aforementioned methods in rapidly solving the RCS of arbitrary targets, the polynomial chaos expansion method with model universality is adopted. According to statistical correlation, a high-precision surrogate model is established with a small number of samples, which can be used to replace the accurate analysis model with high consumption of computing resources to approximate the output results, which can significantly improve the research efficiency.

The polynomial chaos expansion with strong mathematical support was originally proposed by Wiener to construct turbulence computational models [30]. It offers a robust framework for uncertainty quantification of complex engineering problems with its mathematical elegance and global convergence behavior. The method uses basis orthogonal polynomials to expand the uncertain variable and transfers the random characteristics of the variable to polynomial coefficients through the properties of orthogonal polynomials [31]. The polynomial chaos expansion

method has the advantages of constructing surrogate models with high accuracy, computing system responses efficiently, and handling systems with cross-terms effectively. It has been widely used in different engineering fields, such as heat conduction [32], structural mechanics [33, 34], fluid mechanics [35], environmental and acoustic fields [36, 37], electrical properties of nanomaterials [38], flexoelectric materials [39], and stochastic difference equations [40].

In summary, a series of research results and relatively formed mature method have been developed in the field of electromagnetic scattering analysis. However, the accuracy and efficiency of these numerical methods are difficult to be balanced in the problems with the complex model due to the large computational matrix. In this paper, the PCE is applied to accelerate the electromagnetic scattering calculation by constructing surrogate models using a small number of samples. These samples are accurately obtained by the MoM. The main novelties of this paper are as follows:

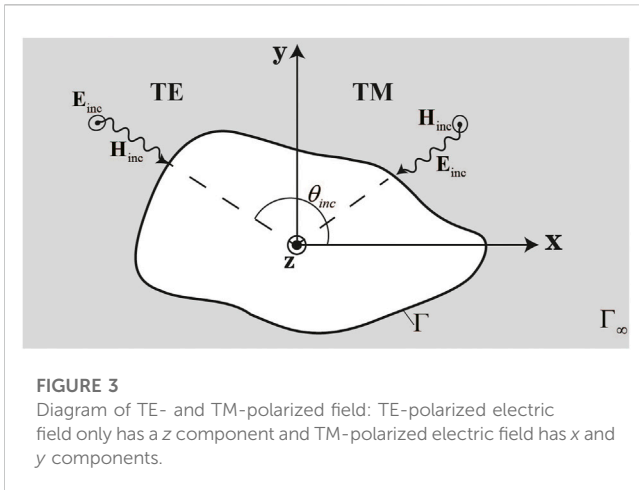
1. The surrogate model of the RCS is established using PCE based on the MoM, which achieves high precision and high-efficiency calculation.
2. Univariate and multivariate analysis of the RCS are carried out considering several different parameters.

The rest of the paper is organized as follows. Section 2 provides the computational expression of the RCS. The MoM is introduced in Section 3 to solve the unknown scattering field. Section 4 includes the PCE method and the specific orthogonal polynomials. The accuracy and efficiency of the proposed method are verified by numerical examples in Section 5, followed by the conclusion in Section 6.

2 Objective function description

In this paper, a perfect electric conductor (PEC) or dielectric conductor (DIE) in the infinite domain is considered for electromagnetic scattering analysis as shown in Figure 1.

The RCS is an important quantity in electromagnetism to quantify how detectable an object is to a radar signal in a given direction. It is a scalar quantity representing the scattering ability of an object, which can be understood as the equivalent scattering area



of the target under the incident wave, and it is measured in square meters. It can be expressed as

$$\text{RCS}(\text{m}^2) = 2\pi\rho \frac{|\mathbf{E}_{\text{sca}}|^2}{|\mathbf{E}_{\text{inc}}|^2}, \quad (1)$$

where $\rho = |\boldsymbol{\rho} - \hat{\boldsymbol{\rho}}|$ is the distance between the source point and the field point shown in Figure 1B. \mathbf{E}_{sca} is the unknown intensity of the scattering electric field and \mathbf{E}_{inc} is the known intensity of incident electric waves. It is often expressed as Eq. 2, as given here.

$$\text{RCS} = \text{RCS}(\text{dBsm}) = 10 \times \lg \text{RCS}(\text{m}^2). \quad (2)$$

The bistatic RCS depends on the location of the source and field points. The angle between the incident and the scattered wave is called the bistatic angle θ_{sca} . In Figure 2, the bigger brown ball denotes the source point and the smaller black point represents the field point. It can be seen that forward scattering is denoted by $\theta_{\text{sca}} = \pi$ and $\theta_{\text{sca}} = 0$ denotes backscattering.

3 MOM for the electromagnetic scattering problems

In this section, we first investigate scattering problems in the context of two-dimensional structures. The MoM is used to calculate the electromagnetic field required for the RCS.

3.1 Surface integral equations

We consider a PEC cylinder with the section contour Γ of arbitrary shape impinged by a TM- or TE-polarized plane wave as illustrated in Figure 3.

We first assume a PEC domain R^1 with connected boundary Γ residing within an unbounded domain R^0 with permittivity and permeability given by the scalar quantities ϵ^0 and μ^0 , respectively. We further assume a polarized time-harmonic electromagnetic plane wave \mathbf{E}_{inc} of angular frequency ω , which is imposed on the PEC body with a wavenumber $k = \omega\sqrt{\epsilon\mu}$. The entire setup is depicted in Figure 1. The surface integral equations on R^i could be expressed as

$$\left[i\omega\mu^i (\mathcal{P}\mathbf{J}')(\hat{\boldsymbol{\rho}}) + (\mathcal{H}\mathbf{M}')(\hat{\boldsymbol{\rho}}) \right]_{\text{tan}} + \frac{1}{2}\hat{\mathbf{n}} \times \mathbf{M}'(\hat{\boldsymbol{\rho}}) = \left[\mathbf{E}'_{\text{inc}}(\hat{\boldsymbol{\rho}}) \right]_{\text{tan}}. \quad (3)$$

$$\left[i\omega\epsilon^i (\mathcal{P}\mathbf{M}')(\hat{\boldsymbol{\rho}}) - (\mathcal{H}\mathbf{J}')(\hat{\boldsymbol{\rho}}) \right]_{\text{tan}} - \frac{1}{2}\hat{\mathbf{n}} \times \mathbf{J}'(\hat{\boldsymbol{\rho}}) = \left[\mathbf{H}'_{\text{inc}}(\hat{\boldsymbol{\rho}}) \right]_{\text{tan}}. \quad (4)$$

where \mathbf{J}' and \mathbf{M}' denote the electric and magnetic current in R^i , respectively, and $\mathbf{E}'_{\text{inc}}(\boldsymbol{\rho})$ and $\mathbf{H}'_{\text{inc}}(\boldsymbol{\rho})$ are the fields, respectively, generated by the incident wave and zero everywhere, except in R^0 . The operators \mathcal{P} and \mathcal{H} are

$$\begin{aligned} (\mathcal{P}\mathbf{J}')(\hat{\boldsymbol{\rho}}) &= \left[1 + \frac{1}{k^2} \nabla \nabla \cdot \right] \int G(\hat{\boldsymbol{\rho}}, \boldsymbol{\rho}) \mathbf{J}'(\boldsymbol{\rho}) d\Gamma'(\boldsymbol{\rho}) \\ (\mathcal{H}\mathbf{M}')(\hat{\boldsymbol{\rho}}) &= \nabla \times \int G(\hat{\boldsymbol{\rho}}, \boldsymbol{\rho}) \mathbf{M}'(\boldsymbol{\rho}) d\Gamma'(\boldsymbol{\rho}), \end{aligned} \quad (5)$$

where $G(\hat{\boldsymbol{\rho}}, \boldsymbol{\rho})$ denotes Green's function. For 2-D problems, it is expressed as

$$G(\hat{\boldsymbol{\rho}}, \boldsymbol{\rho}) = -\frac{i}{4} H_0^{(2)}(k\rho), \quad \text{with } \rho = |\hat{\boldsymbol{\rho}} - \boldsymbol{\rho}|. \quad (6)$$

Equations 3, 4 are called the electric field integral equation (EFIE) and the magnetic field integral equation (MFIE), respectively, yielding a result free of spurious solutions for DIEs. However, on closed conductors, the EFIE and MFIE cannot produce a unique solution for all frequencies, which is called the interior resonance problem. The most popular method for handling the problem is a linear combination of the EFIE and MFIE, which yields the combined field integral equation (CFIE) given by Eq. 7.

$$\alpha \text{EFIE} + (1 - \alpha) \eta' \text{MFIE}, \quad (7)$$

where $\eta' = \sqrt{\mu^i/\epsilon^i}$ and $0 \leq \alpha \leq 1$, with $\alpha = 0.5$, are commonly used.

3.2 Discretization of MoM

The MoM is used to convert Eqs 3, 4 into a matrix system using Galerkin-type testing in each region. Expanding the electric and magnetic currents in R^i using a sum of weighted basis functions yields

$$\mathbf{J}'(\boldsymbol{\rho}) = \sum_{n=1}^N \alpha_n^{J(i)} \mathbf{f}_n(\boldsymbol{\rho}), \quad \mathbf{M}'(\boldsymbol{\rho}) = \sum_{n=1}^N \alpha_n^{M(i)} \mathbf{g}_n(\boldsymbol{\rho}), \quad (8)$$

where N is the number of electric and magnetic basis functions in R^i , and the basic functions \mathbf{f}_n and \mathbf{g}_n are triangle functions. We next test the EFIE and nMFIE with the electric testing functions \mathbf{f}_m , and the MFIE with the magnetic testing functions \mathbf{g}_m . This yields the matrix system in R^i as follows:

$$\begin{bmatrix} A^{J(i)} & A^{M(i)} \end{bmatrix} \begin{bmatrix} \alpha^{J(i)} & \alpha^{M(i)} \end{bmatrix}^T = \mathbf{S}^{(i)}, \quad (9)$$

where

$$A^{J(i)} = \begin{bmatrix} A_{\text{EFIE}}^{J(i)} & A_{\text{EFIE}}^{M(i)} \end{bmatrix}^T. \quad (10)$$

$$A^{M(i)} = \begin{bmatrix} A_{\text{MFIE}}^{J(i)} & A_{\text{MFIE}}^{M(i)} \end{bmatrix}^T. \quad (11)$$

$$S_{\text{EFIE}}^{(i)}(m) = \int \mathbf{f}_m(\hat{\boldsymbol{\rho}}) \cdot \mathbf{E}'_{\text{inc}}(\hat{\boldsymbol{\rho}}) d\Gamma'(\hat{\boldsymbol{\rho}}). \quad (12)$$

$$S_{\text{MFIE}}^{(i)}(m) = \int \mathbf{g}_m(\hat{\boldsymbol{\rho}}) \cdot \mathbf{H}'_{\text{inc}}(\hat{\boldsymbol{\rho}}) d\Gamma'(\hat{\boldsymbol{\rho}}). \quad (13)$$

and

$$A_{EFIE}^{I(i)}(m, n) = i\omega\mu' \left[1 + \frac{1}{k^2} \nabla \nabla \cdot \right] \int \mathbf{f}_m(\hat{\rho}) \times \int G(\hat{\rho}, \rho) \mathbf{f}_n(\rho) d\Gamma'(\rho) d\Gamma'(\hat{\rho}). \quad (14)$$

$$A_{EFIE}^{M(i)}(m, n) = \int \mathbf{f}_m(\hat{\rho}) \int \nabla G(\hat{\rho}, \rho) \times \mathbf{g}_n(\rho) d\Gamma'(\rho) d\Gamma'(\hat{\rho}) + \frac{1}{2} \int \mathbf{f}_m(\hat{\rho}) \cdot \left[\vec{\mathbf{n}}(\hat{\rho}) \times \mathbf{g}_n(\hat{\rho}) \right] d\Gamma'(\hat{\rho}). \quad (15)$$

$$A_{MFIE}^{I(i)}(m, n) = - \int \mathbf{g}_m(\hat{\rho}) \int \nabla G(\hat{\rho}, \rho) \times \mathbf{f}_n(\rho) d\Gamma'(\rho) d\Gamma'(\hat{\rho}) - \frac{1}{2} \int \mathbf{g}_m(\hat{\rho}) \cdot \left[\vec{\mathbf{n}}(\hat{\rho}) \times \mathbf{f}_n(\hat{\rho}) \right] d\Gamma'(\hat{\rho}). \quad (16)$$

$$A_{MFIE}^{M(i)}(m, n) = i\omega\varepsilon' \left[1 + \frac{1}{k^2} \nabla \nabla \cdot \right] \int \mathbf{g}_m(\hat{\rho}) \times \int G(\hat{\rho}, \rho) \mathbf{g}_n(\rho) d\Gamma'(\rho) d\Gamma'(\hat{\rho}). \quad (17)$$

It should be noted that all blocks of the matrix in Eq. 9 are square with rank of N . If we now combine the previously mentioned matrix for the two regions, a block-diagonal system is obtained as

$$\begin{pmatrix} A^{(0)} & \mathbf{0} \\ \mathbf{0} & A^{(1)} \end{pmatrix} \begin{pmatrix} \alpha^{(0)} \\ \alpha^{(1)} \end{pmatrix} = \begin{pmatrix} S^{(0)} \\ S^{(1)} \end{pmatrix}. \quad (18)$$

The coefficient α can be found by solving the previously mentioned system. Then, the expressions of electric and magnetic current can be obtained by substituting the obtained α in Eq. 8.

3.3 Scattering field

In the previous section, the expressions of electric and magnetic current are obtained, and we will further obtain numerical solutions for scattered fields in this section by using the 2-D near-field radiation equation as Eqs 19, 20.

$$\begin{aligned} H_{sca}^x(\rho) &= i \frac{k}{4} \int \left([\sigma_y J^z] \frac{H_1^{(2)}(k\rho)}{\rho} \right) d\Gamma'(\hat{\rho}) \\ H_{sca}^y(\rho) &= i \frac{k}{4} \int \left([-\sigma_x J^z] \frac{H_1^{(2)}(k\rho)}{\rho} \right) d\Gamma'(\hat{\rho}) \\ H_{sca}^z(\rho) &= i \frac{k}{4} \int \left([\sigma_x J^y - \sigma_y J^x] \frac{H_1^{(2)}(k\rho)}{\rho} \right) d\Gamma'(\hat{\rho}). \end{aligned} \quad (19)$$

$$\begin{aligned} E_{sca}^x(\rho) &= \frac{k^2}{8\omega\varepsilon} \int \left(([\sigma_y^2 - \sigma_x^2] J^x - 2\sigma_x \sigma_y J^y) \frac{H_2^{(2)}(k\rho)}{\rho^2} - J^x H_0^{(2)}(k\rho) \right) d\Gamma'(\hat{\rho}) \\ E_{sca}^y(\rho) &= \frac{k^2}{8\omega\varepsilon} \int \left(([\sigma_x^2 - \sigma_y^2] J^y - 2\sigma_x \sigma_y J^x) \frac{H_2^{(2)}(k\rho)}{\rho^2} - J^y H_0^{(2)}(k\rho) \right) d\Gamma'(\hat{\rho}) \\ E_{sca}^z(\rho) &= -\frac{k^2}{4\omega\varepsilon} \int (J^z H_0^{(2)}(k\rho)) d\Gamma'(\hat{\rho}), \end{aligned} \quad (20)$$

where

$$\sigma_x = x - \hat{x}, \quad \sigma_y = y - \hat{y}. \quad (21)$$

The $E_{sca}^x(\rho)$, $E_{sca}^y(\rho)$, and $E_{sca}^z(\rho)$ aforementioned represent the 2-D scattering electric field in x , y , and z directions, respectively. Substituting the obtained scattered field into Eq. 1, the objective function-RCS is solved successfully.

TABLE 1 Orthogonal polynomials with respect to the different distributions.

Orthogonal polynomial	Distribution	Range
Hermite	Normal	$(-\infty, +\infty)$
Jacobi	Beta	$[-1, 1]$
Legendre	Uniform	$[-1, 1]$
Laguerre	Gamma	$(0, +\infty)$
	Weibull	$(0, +\infty)$
Charlier	Poisson	$\{0, 1, 2, \dots\}$
Krawtchouk	Binomial	$\{0, 1, 2, \dots, n\}$
Meixner–Chaos	Negative binomial	$\{0, 1, 2, \dots\}$
Hahn–Chaos	Hypergeometric	$\{0, 1, 2, \dots, n\}$

4 Polynomial chaos expansion

PCE is a method to describe the uncertainty of random variables by constructing random spaces with polynomial bases. The original non-linear problem is transformed into a weighted summation of polynomials, which is actually a process of coefficient fitting. Orthogonal polynomials are often used as the orthogonal basis of the space to express the mapping between independent variables and dependent variables.

In general, different distributions of random variables lead to different orthogonal polynomials. Table 1 lists the classical families of distributions and the corresponding univariate orthogonal polynomials.

In this section, the Legendre orthogonal polynomial is adopted to construct the surrogate model of the scattered field. The uniform input variable of the system is $\mathbf{x} = (x_1, x_2, \dots, x_N)$, and RCS is the corresponding response. There is an expression constructed by polynomial chaos as

$$\text{RCS} = f(\mathbf{x}) = \sum_{i=0}^{\infty} \alpha_i \Phi_i(\mathbf{x}), \quad \mathbf{x} = (x_1, x_2, \dots, x_N). \quad (22)$$

where $\Phi_i(\mathbf{x})$ is the multi-dimensional Legendre orthogonal polynomial with vector $\mathbf{x} = (x_1, x_2, \dots, x_N)$, and each variable x_i belongs to the interval $[-1, 1]$; α_i is the coefficient of the polynomial chaos expansion and RCS is square integral. The previously mentioned expansion can be truncated to K th order as Eq. 23.

$$\widehat{\text{RCS}} = \alpha_0 \Phi_0(\mathbf{x}) + \alpha_1 \Phi_1(\mathbf{x}) + \dots + \alpha_{K-1} \Phi_{K-1}(\mathbf{x}) = \Phi \alpha, \quad (23)$$

where

$$\Phi = \begin{pmatrix} \Phi_0(x_1) & \Phi_1(x_1) & \dots & \Phi_{K-1}(x_1) \\ \Phi_0(x_2) & \Phi_1(x_2) & \dots & \Phi_{K-1}(x_2) \\ \vdots & \vdots & \ddots & \vdots \\ \Phi_0(x_N) & \Phi_1(x_N) & \dots & \Phi_{K-1}(x_N) \end{pmatrix}_{N \times K} \quad (24)$$

and

$$\alpha = (\alpha_0 \quad \alpha_1 \quad \dots \quad \alpha_{K-1})'_{K \times 1}, \quad (25)$$

where K is the number of orthogonal polynomials, which can be calculated as $K = C_{m+k}^k$ and m is the dimension of \mathbf{x} . There are two

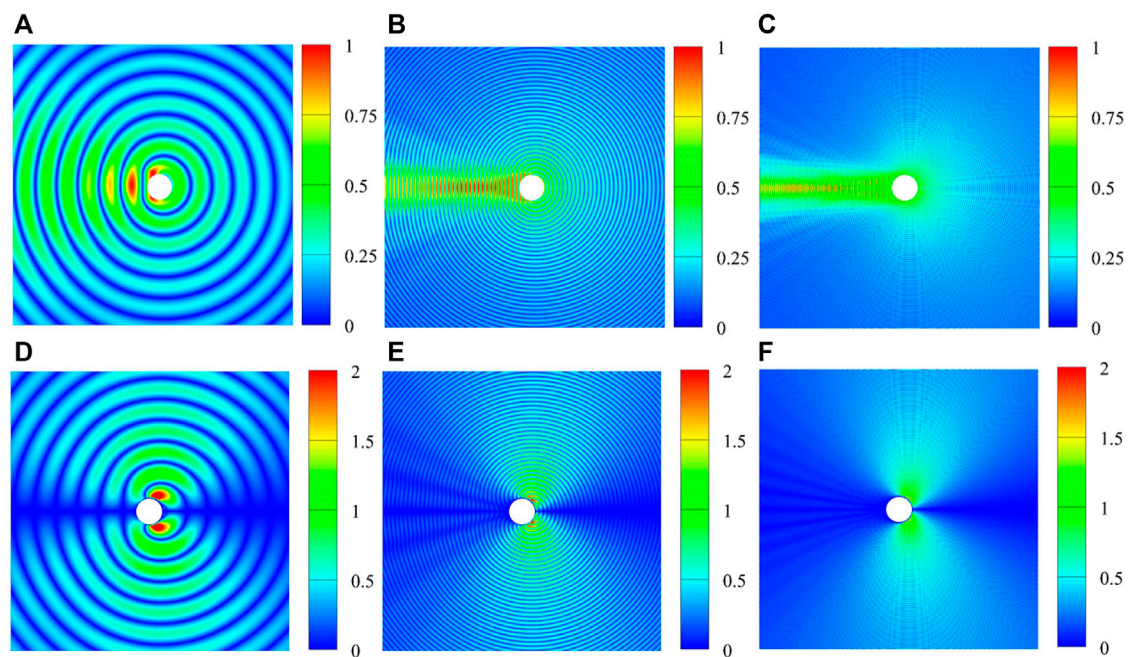


FIGURE 4 Scattering electric and magnetic field distribution under TE polarization with $\theta_{sca}=0$. (A) Electric field, $f=100\text{MHz}$; (B) electric field, $f=500\text{MHz}$; (C) electric field, $f=1000\text{MHz}$; (D) magnetic field, $f=100\text{MHz}$; (E) magnetic field, $f=500\text{MHz}$; (F) magnetic field, $f=1000\text{MHz}$.

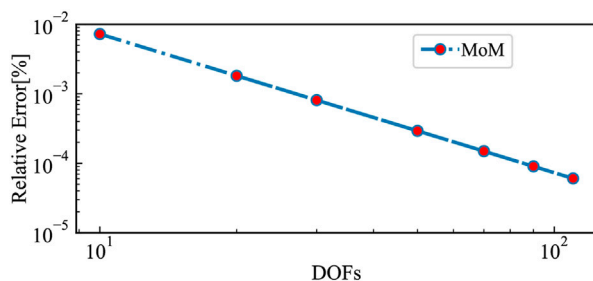


FIGURE 5 Convergence results of the average error in terms of the MOM calculation DoFs.

key steps of the PCE method according to Eq. 23: constructing the multi-dimensional Legendre orthogonal polynomial $S \Phi_i(\mathbf{x})$ and solving the coefficient α_i of the expansion.

The common recurrence relation of the Legendre polynomial system $\{L_k(x)\}_{k=0}^{\infty}$ in the interval $[-1, 1]$ is expressed as

$$L_0(x) = 1, \quad L_1(x) = x, \\ L_{k+1}(x) = \frac{2k+1}{k+1}xL_k(x) - \frac{k}{k+1}L_{k-1}(x) \quad k \geq 1. \quad (26)$$

For the 1-D surrogate model, $L_i = \Phi_i$. The truncated polynomial chaos expansion shown in Eq. 23 is actually a predicted value rather than a true solution, and the error between them is

TABLE 2 One dimensional Legendre polynomials of the first eight orders (k goes from 0 to 8).

k	Legendre polynomials $L_k(x)$
0	1
1	x
2	$(3x^2 - 1)/2$
3	$(5x^3 - 3x)/2$
4	$(35x^4 - 30x^2 + 3)/8$
5	$(63x^5 - 70x^3 + 15x)/8$
6	$(231x^6 - 315x^4 + 105x^2 - 5)/16$
7	$(429x^7 - 693x^5 + 325x^3 - 35x)/16$
8	$(6435x^8 - 1201x^6 + 7080x^4 - 1260x^2 - 35)/128$

$$\boldsymbol{\varepsilon} = \text{RCS} - \widehat{\text{RCS}} = f(\mathbf{x}) - \sum_{i=1}^{K-1} \alpha_i \Phi_i(\mathbf{x}), \quad \mathbf{x} = (x_1, x_2, \dots, x_N). \quad (27)$$

The residual $\boldsymbol{\varepsilon}$ is assumed to be a zero-mean variable and $\boldsymbol{\alpha}$ is the unknown coefficient vector. The smaller absolute value of the residual indicates the more accurate estimation of the surrogate model. The coefficient $\boldsymbol{\alpha}$ should minimize the expectation of the sum of squares of the residual $\boldsymbol{\varepsilon}$.

$$\hat{\boldsymbol{\alpha}} = \arg \min E(\boldsymbol{\varepsilon}^2). \quad (28)$$

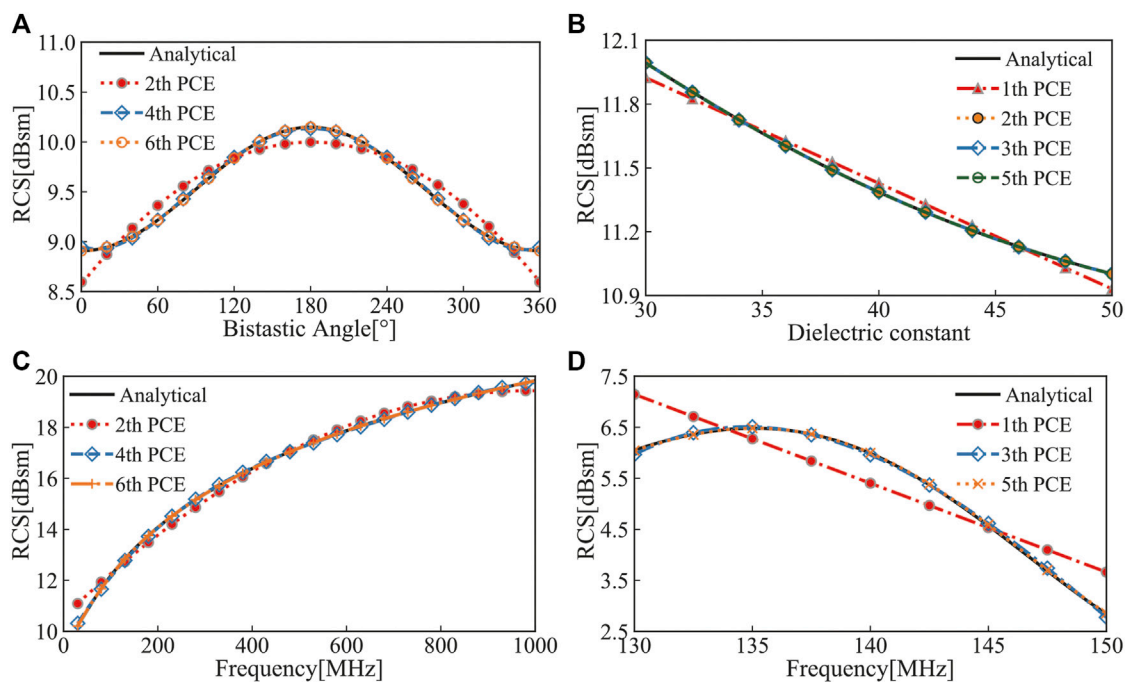


FIGURE 6

RCS value at the field point $(1 \times 10^5, 0)$ in terms of four uniform random variables: (A) $f=10\text{MHz}$, $\epsilon^1=\infty$; (B) $f=10\text{MHz}$, $\theta_{SCA}=0$; (C) $\theta_{SCA}=\pi$, $\epsilon^1=\infty$; and (D) $\epsilon^1=2.56$, $\theta_{SCA}=0$.

Thus, the polynomial chaos expansion coefficient α can be determined by the following equation.

$$\hat{\alpha} = (\Phi^T \Phi)^{-1} \Phi^T \text{RCS}. \quad (29)$$

The response from the surrogate model can be obtained with the solved coefficient α and Eq. 23. The measure used to describe the accuracy of the final model named CV (RSMD) is expressed in Eq. 30.

$$\text{CV (RSMD)} = \sqrt{\frac{\sum_{i=1}^N (y_i - \hat{y}_i)^2}{N}} / \frac{\sum_{i=1}^N y_i}{N}, \quad (30)$$

where y_i is the output of the MoM, which is the input of PCE, and \hat{y}_i is the output of the obtained surrogate model using PCE. A lower value of CV means a better effect of the surrogate model. If the CV value is lower than 5%, it is considered that the expansion converges under the current order and has great fitting accuracy.

5 Numerical examples

In this section, the output of the MoM with the cylinder model in the infinite domain is used to construct the PCE surrogate model. The univariate and bivariate analyses are adopted to verify the high accuracy and efficiency of the surrogate model. The uniform incident frequency, bistatic angle, and dielectric constant are considered the input variables. The coordinate system is established with the source point (object) as the origin, and its distance to the field point is taken as 1×10^5 .

The Fortran 90 language is used for MoM programming, and the non-embedded PCE programming in MATLAB is utilized to obtain

the polynomial expression, and all the programs are implemented on a desktop computer with Intel (R) Core (TM) i7-8700 CPU and 16 GB RAM.

5.1 Univariate analysis

The electric and magnetic field distribution scattered by the infinite PEC cylinder with a radius of 1 is depicted in Figure 4. The results under several incident frequencies ($f = 100, 500, 1000\text{MHz}$) are first considered. Figures 4A–C represent the electric field in the z-direction around the cylinder with the same level, and the magnetic field in the x-direction is shown in Figures 4D–F. It can be seen that the distribution strongly depends on the frequency and becomes more complex with increase in the incident frequency. The distribution is symmetric with respect to the x-axis, which verifies the proposed method.

No analytical solution is proposed for most of the electromagnetic problems, especially with complex problems. It is necessary to find a rapid calculation method with high accuracy. The MoM is one of the effective numerical approaches with small errors, shown in Figure 5. The convergence result of the relative error in terms of the MoM calculation degrees of freedom (DoFs) is given in Figure 5 to verify the accuracy of the MoM. The considered DoFs range from 10 to 110. The relative error for the MoM decreases with DoF increase, and the logarithmic values present a significant linear correlation. The data computed with the MoM are considered the true value when the analytical solution does not exist. However, the CPU time consumption is huge because of the calculation of the

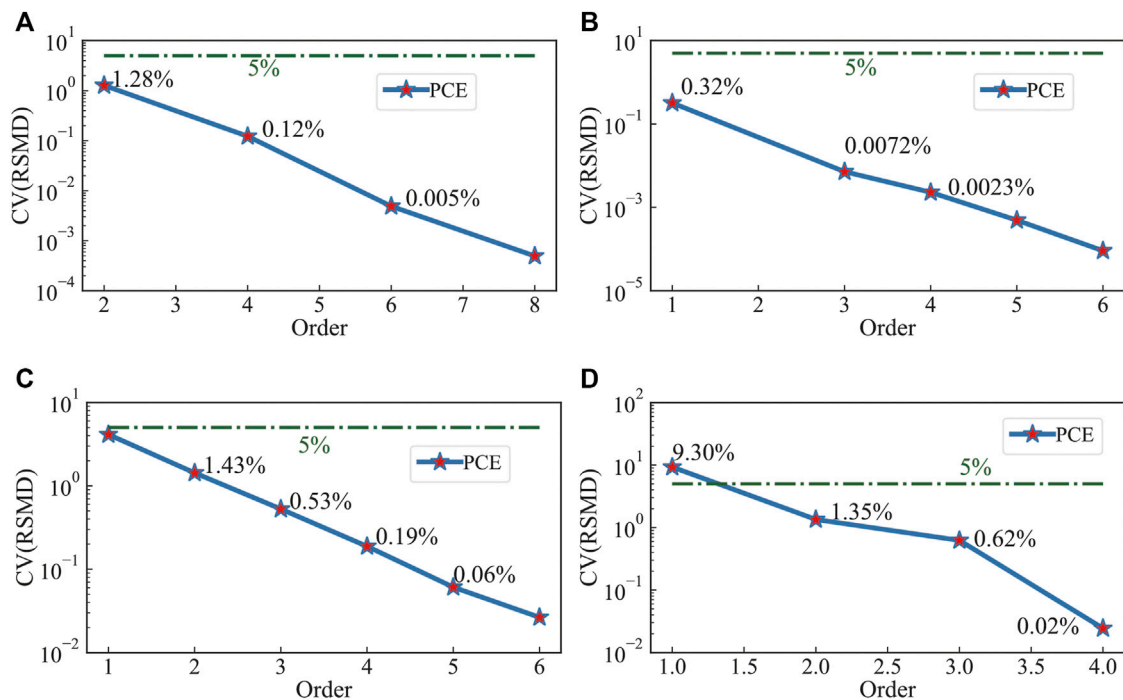


FIGURE 7

CV (RSMD) with respect to different variables. (A) PEC model, $\theta_{sca} \in [0, 2\pi]$, $f = 10$ MHz; (B) DIE model, $\epsilon^1 \in [30, 50]$, $f = 10$ MHz, $\theta_{sca} = 0$; (C) PEC model, $f \in [1, 1000]$ MHz, $\theta_{sca} = \pi$; (D) DIE model, $f \in [130, 150]$ MHz, $\epsilon^1 = 2.56$, $\theta_{sca} = 0$.

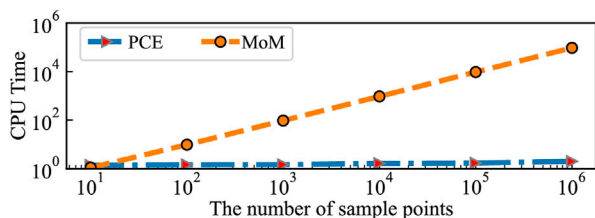


FIGURE 8

CPU time used to calculate the RCS value.

large matrix system. On the contrary, the PCE method only needs the input data irrespective of the complexity of the problem is, which makes it more efficient.

We should select a set of suitable orthogonal polynomials according to Section 4. Table 2 lists the first eight orders of Legendre polynomials of 1-D random variables for univariate analysis.

Figure 6 presents the comparison RCS results of analytical and MoM-PCE for an infinite cylinder with three random variables. We first compute the bistatic RCS for $0 \leq \theta_{sca} \leq 2\pi$ and $\theta_{inc} = 0$ at 10 MHz. The $\epsilon^1 = \infty$ denotes that the cylinder is a perfect conductor. It can be seen in Figure 6A that the RCS is symmetric with respect to θ_{sca} . The 2nd PCE performs badly, and the accuracy increases from the 4th order. The expression of the 4th PCE shown in Figure 6A is

$$\begin{aligned} \text{RCS}_A^{[4]} \approx & 1.51 \times 10^{-9} x^4 - 1.09 \times 10^{-6} x^3 + 2.09 \times 10^{-4} x^2 \\ & - 4.59 \times 10^{-3} x + 8.95, \end{aligned} \quad (31)$$

where x denotes the bistatic angle θ_{sca} and $\text{RCS}_A^{[4]}$ represents the 4th PCE results with respect to x in Figure 6A.

It can be seen in Figure 6B that the back-scattering RCS value decreases as the dielectric constant increases. The 1st order of the PCE model shows some errors and the 2nd PCE performs fairly well, which can be expressed as Eq. 32.

$$\text{RCS}_B^{[2]} \approx 1.12 \times 10^{-3} x^2 - 0.14x + 15.17. \quad (32)$$

Figure 6C shows the back-scattering RCS in terms of frequency. The 2nd PCE shows errors again, but they are not quite as apparent as they were in case (A). The 4th order model fits well, at least within the range of frequencies considered. The 6th PCE is free of errors as expected and expressed as Eq. 33. The higher frequencies correspond to higher results, which is approximately 19.8 dBsm at 1000 MHz.

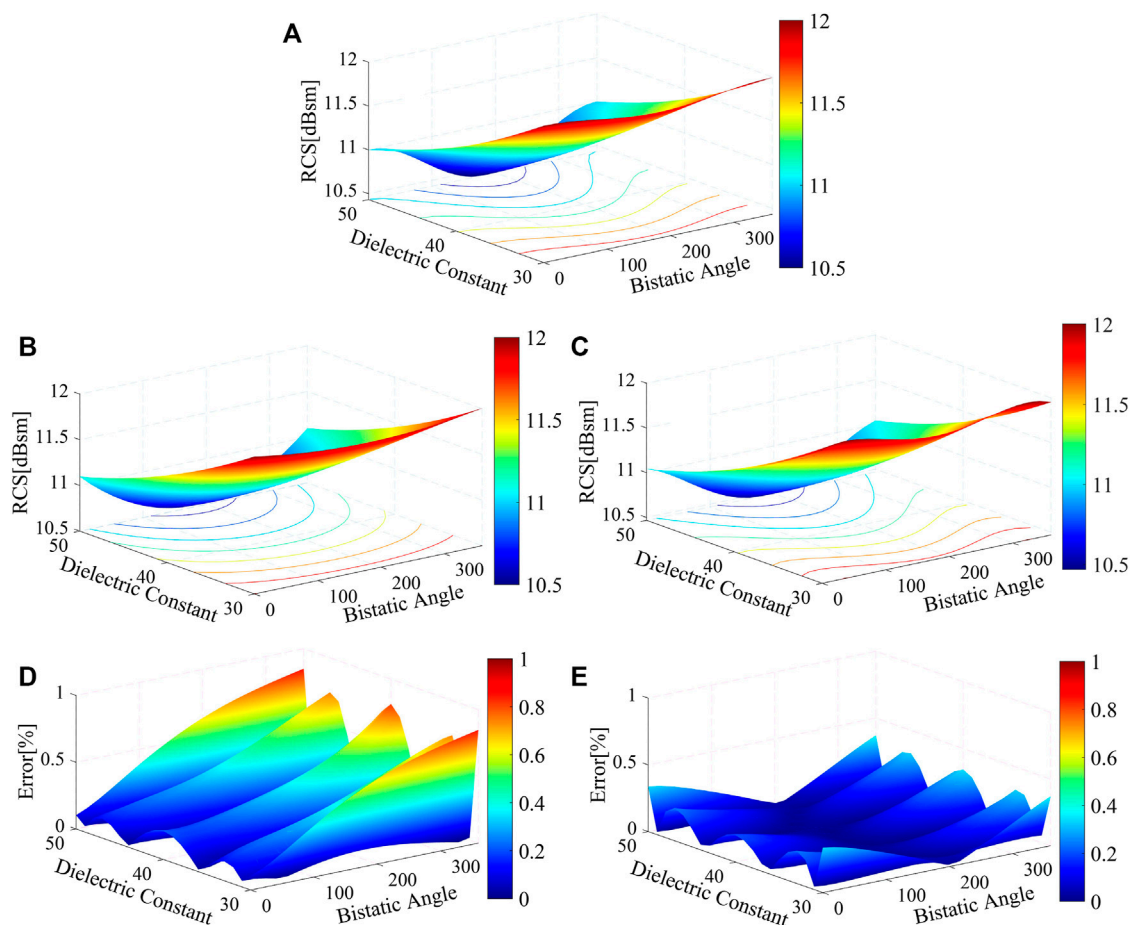
$$\begin{aligned} \text{RCS}_C^{[6]} \approx & -3.46 \times 10^{-17} x^6 + 1.34 \times 10^{-13} x^5 - 2.16 \times 10^{-10} x^4 \\ & + 1.88 \times 10^{-7} x^3 - 9.98 \times 10^{-5} x^2 + 3.88 \times 10^{-2} x + 9.13. \end{aligned} \quad (33)$$

Contrary to Figure 6C, the RCS does not follow a straight direction in terms of frequency, which is shown in Figure 6D. With the increase of frequency, the RCS value increases first and then decreases in the interval [130, 150] MHz. The 1st PCE shows more errors with CV = 9.3% illustrated in Figure 7D. It can be seen that the 4th PCE performs fairly well, which can be expressed as Eq. 34.

$$\text{RCS}_D^{[4]} \approx 4.04 \times 10^{-5} x^4 - 2 \times 10^{-4} x^3 + 4.562x^2 - 414.5x + 14070. \quad (34)$$

TABLE 3 Four Legendre polynomials Φ_j with two variables (k goes from 0 to 4).

$k = 0$	$k = 1$	$k = 2$	$k = 3$	$k = 4$
$\Phi_0 = 1$	$\Phi_1 = x_1$	$\Phi_3 = (3x_1^2 - 1)/2$	$\Phi_6 = (5x_1^3 - 3x_1)/2$	$\Phi_{10} = (9x_1^2x_2^2 - 3x_1^2 - 3x_2^2 + 1)/4$
	$\Phi_2 = x_2$	$\Phi_4 = (3x_2^2 - 1)/2$	$\Phi_7 = (5x_2^3 - 3x_2)/2$	$\Phi_{11} = (35x_2^4 - 30x_2^2 + 3)/8$
		$\Phi_5 = x_1x_2$	$\Phi_8 = x_1(3x_2^2 - 1)/2$	$\Phi_{12} = (35x_1^4 - 30x_1^2 + 3)/8$
			$\Phi_9 = x_2(3x_1^2 - 1)/2$	$\Phi_{13} = x_1(5x_2^3 - 3x_2)/2$
				$\Phi_{14} = x_2(5x_1^3 - 3x_1)/2$

**FIGURE 9**

Surface results of the bivariate analysis with dielectric constant and bistatic angle: (A) analytical solution, (B) 3rd PCE result, (C) 4th PCE result, (D) relative error of the 3rd PCE model, and (E) relative error of the 4th PCE model.

Figure 7 shows the CV values corresponding to Figure 6. The green line represents $CV = 5\%$, which is much higher than most of the constructed models. Only one result in Figure 7D created by the 1st PCE introduced higher CV, but the accuracy improved rapidly with the increase in the order. While ensuring accuracy, the PCE combined with the MoM could also increase the speed, which can be seen in Figure 8.

The aforementioned comparison is between the analytical and the PCE method solution with 1-D independent variables. The PCE method can also fit well and even the independent variable is 2-D data.

5.2 Bivariate analysis

In this section, the MOM-PCE method is used to construct a surrogate model of the dielectric cylinder for electromagnetic scattering analysis. The frequency is 11 MHz, ϵ^0 and μ^0 values of the outer region are 1, and the radius of the cylinder model is 1. We assume the dielectric constant ϵ^1 as $x_1 \in [30, 50]$ and bistatic angle θ_{scat} as $x_2 \in [0, 360]$. The random sample points put into the PCE module are obtained from the MoM results. Table 3 lists the 2-D Legendre expressions.

The final expressions of the surrogate model with the 3rd and 4th order can be written as

$$\begin{aligned} \text{RCS}^{[3]} \approx & -8.1 \times 10^{-7} x_1^3 - 7.6 \times 10^{-14} x_2^3 - 7.5 \times 10^{-7} x_1 x_2^2 \\ & - 7.1 \times 10^{-12} x_2 x_1^2 - 2.7 \times 10^{-4} x_1 x_2 + 1.1 \times 10^{-3} x_1^2 \\ & - 1.9 \times 10^{-5} x_2^2 + 6.8 \times 10^{-3} x_1 - 0.13 x_2 + 14.85. \end{aligned} \quad (35)$$

$$\begin{aligned} \text{RCS}^{[4]} \approx & -8.9 \times 10^{-7} x_1^4 - 3.8 \times 10^{-10} x_2^4 + 7.8 \times 10^{-15} x_1 x_2^3 \\ & - 1.6 \times 10^{-13} x_2 x_1^3 + 1.1 \times 10^{-8} x_1^2 x_2^2 + 1.4 \times 10^{-4} x_1^3 \\ & + 2.7 \times 10^{-7} x_2^3 - 1.17 \times 10^{-7} x_1 x_2^2 - 3.9 \times 10^{-6} x_2 x_1^2 \\ & - 6.4 \times 10^{-5} x_2^2 - 7.2 \times 10^{-3} x_1^2 + 4.3 \times 10^{-5} x_1 x_2 \\ & + 5.5 \times 10^{-3} x_2 + 7.8 \times 10^{-2} x_1 + 12.97. \end{aligned} \quad (36)$$

The bivariate results with surrogate models of the 3rd and 4th order are shown in Figure 9A–C, which show the surface and contour solution with the same chromatic level of [10.5,12]. The red region represents a higher value of the corresponding model, and the blue region represents a lower value. It can be seen that the 4th PCE fits better as its trend and color distribution are more similar to those of the analytical solution. The relative errors are shown in Figures 9D, E using the same chromatic level of [0, 1%]. It can be clearly seen that the 4th PCE results have much higher accuracy. In addition, the CV (RMSD) of the 3rd PCE is 0.32%, and that of the 4th PCE is 0.12%, which are both much lower than 5%. In addition, it shows good agreement near the specular angles but fair to poor elsewhere, as shown in Figure 9E. It is also clear from the red region in Figure 9D that the margin of error in the interval is higher, which may be due to the Runge phenomenon.

6 Conclusion

In this paper, the method of moments is accelerated by polynomial chaos expansion to construct a surrogate model for electromagnetic scattering analysis. The triangle basic functions are used to discretize the surface integral equations (EFIE, MFIE, and CFIE) with MoM, and the input variables are sampled uniformly combined with Legendre orthogonal polynomials to construct the surrogate model of electromagnetic RCS. Bistatic angle, incident frequency, and dielectric constant are considered the source of systematic uncertainty. First, three different parameters are considered for univariate analysis to construct the corresponding surrogate model. The RCS and CV results of the MoM–PCE method are compared with the analytical solutions to verify the correctness of the algorithm proposed in this work, which performs fairly well. Then, the CPU time consumption of the MoM–PCE method is compared with that of MoM. It is found

that the PCE method has a significant advantage in the calculation speed, especially when the number of sample points is huge. Finally, the bivariate analysis is carried out with the bistatic angle and dielectric constant with a dielectric conductor. The result shows that the PCE method is still efficient, and high order of PCE often leads to high accuracy. In general, it is verified that the MoM based on PCE presents great accuracy and efficiency.

Future work is required to extend the proposed algorithm into 3D electromagnetic sensitivity analysis and optimization analysis for practical engineering problems.

Data availability statement

The original contributions presented in the study are included in the article/Supplementary Material, further inquiries can be directed to the corresponding author.

Author contributions

Conceptualization, XY; data curation, YM; formal analysis, YH and RH; investigation, YH and ZW; methodology, XY and ZW; project administration, XY, software, YM and ZW; supervision, XY and YH; validation, YH and RH; visualization, YM and RH; writing—original draft, XY, YM, and ZW. All authors have read and agreed to the published version of the manuscript.

Conflict of interest

The authors declare that the research was conducted in the absence of any commercial or financial relationships that could be construed as a potential conflict of interest.

Publisher's note

All claims expressed in this article are solely those of the authors and do not necessarily represent those of their affiliated organizations, or those of the publisher, the editors, and the reviewers. Any product that may be evaluated in this article, or claim that may be made by its manufacturer, is not guaranteed or endorsed by the publisher.

References

- Chen H, Li G, Lu LJ, Liang DF, Weng X, Xie H, et al. Design of tapered periodic meta-surfaces for suppressing edge electromagnetic scattering. *Mater Sci Forum* (2020) 998:203–8. doi:10.4028/www.scientific.net/msf.998.203
- Li M, Yue X, Ding F, Ning B, Wang J, Zhang N, et al. Focused lunar imaging experiment using the back projection algorithm based on sanya incoherent scatter radar. *Remote Sensing* (2022) 14:2048. doi:10.3390/rs14092048
- He Y, Yang Q, Gao X. Comprehensive optimization design of aerodynamic and electromagnetic scattering characteristics of serpentine nozzle. *Chin J Aeronautics* (2021) 34:118–28. doi:10.1016/j.cja.2020.10.010
- Bahret WF, Sletten CJ. A look into the future of radar scattering research and development. *Proc IEEE* (2005) 53:786–95. doi:10.1109/proc.1965.4056
- Ma J, Jin K, Zheng X. Radar cross-section of a target and attenuation of electromagnetic waves in sandstorms. *J Quantitative Spectrosc Radiative Transfer* (2023) 294:108388. doi:10.1016/j.jqsrt.2022.108388
- Wang X, Yang F, Liu C, Liu Y, Gong H, Zhang H. Fast wide-band rcs analysis of the coated target based on pbr using efie-pmchwt and the Chebyshev approximation technique. *Electronics* (2023) 12:923. doi:10.3390/electronics12040923

7. Gedney S. The finite element method in electromagnetics [book review]. *Antennas Propagation Mag IEEE* (1994) 36:75–6. doi:10.1109/MAP.1994.1068064
8. Hadi MF, Esmaeili SA. Cuda fortran acceleration for the finite-difference time-domain method. *Comput Phys Commun* (2013) 184:1395–400. doi:10.1016/j.cpc.2013.01.006
9. Rius JM, FerrandoGreco M, Jofre L. Greco: Graphical electromagnetic computing for RCS prediction in real time. *IEEE Antennas Propagation Mag* (1993) 35:7–17. doi:10.1109/74.207645
10. Andersh D, Moore J, Kosanovich S, Kapp D, Bhalla R, Kipp R, et al. Xpatch 4: The next generation in high frequency electromagnetic modeling and simulation software. In: Record of the IEEE 2000 International Radar Conference [Cat. No. 00CH37037]; 12–12 May 2000; Alexandria, VA, USA (2000). p. 844–9. doi:10.1109/RADAR.2000.851945
11. Tabakcioglu M. Extensive comparison results of coverage map of optimum base station location of digital terrain with utd based model. *Prog Electromagnetics Res M* (2020) 97:69–76. doi:10.2528/PIERM20080405
12. Ling H, Chou RC, Lee SW. Shooting and bouncing rays: Calculating the rcs of an arbitrarily shaped cavity. *IEEE Trans Antennas Propagation* (1989) 37:194–205. doi:10.1109/8.18706
13. Brem R, Eibert T. A magnetic field integral equation based iterative solver for scattered field prediction. *Prog Electromagnetics Res M* (2014) 40:27–35. doi:10.2528/pierm14072506
14. Chen L, Lian H, Xu Y, Li S, Liu Z, Atroshchenko E, et al. Generalized isogeometric boundary element method for uncertainty analysis of time-harmonic wave propagation in infinite domains. *Appl Math Model* (2023) 114:360–78. doi:10.1016/j.apm.2022.09.030
15. Harrington RF. *Field computation by moment methods*. Hoboken: Wiley (1968).
16. Chen L, Lian H, Natarajan S, Zhao W, Chen X, Bordas S. Multi-frequency acoustic topology optimization of sound-absorption materials with isogeometric boundary element methods accelerated by frequency-decoupling and model order reduction techniques. *Comput Methods Appl Mech Eng* (2022) 395:114997. doi:10.1016/j.cma.2022.114997
17. Chen L, Lian H, Liu Z, Gong Y, Zheng C, Bordas S. Bi-material topology optimization for fully coupled structural-acoustic systems with isogeometric FEM-BEM. *Eng Anal Boundary Elem* (2022) 135:182–95. doi:10.1016/j.enganabound.2021.11.005
18. Miller EK, Medgyesi-Mitschang LN, Newman EH. *Computational electromagnetics: Frequency-domain method of moments*. Piscataway: IEEE Press (1992).
19. Wang J. Generalised moment methods in electromagnetics. *Microwaves Antennas Propagation Iee Proc H* (1990) 137:127–32. doi:10.1049/ip-h-2.1990.0024
20. Chen L, Li H, Guo Y, Chen P, Atroshchenko E, Lian H. Uncertainty quantification of mechanical property of piezoelectric materials based on isogeometric stochastic FEM with generalized nth-order perturbation. *Eng Comput* (2023) 1–21. doi:10.1007/s00366-023-01788-w
21. Chen L, Wang Z, Peng X, Yang J, Wu P, Lian H. Modeling pressurized fracture propagation with the isogeometric BEM. *Geomechanics Geophysics Geo-Energy Geo-Resources* (2021) 7:51. doi:10.1007/s40948-021-00248-3
22. Chen L, Zhang Y, Lian H, Atroshchenko E, Ding C, Bordas SP. Seamless integration of computer-aided geometric modeling and acoustic simulation: Isogeometric boundary element methods based on catmull-clark subdivision surfaces. *Adv Eng Softw* (2020) 149:102879. doi:10.1016/j.advengsoft.2020.102879
23. Chen L, Lu C, Lian H, Liu Z, Zhao W, Li S, et al. Acoustic topology optimization of sound absorbing materials directly from subdivision surfaces with isogeometric boundary element methods. *Comput Methods Appl Mech Eng* (2020) 362:112806. doi:10.1016/j.cma.2019.112806
24. Chen L, Lu C, Zhao W, Chen H, Zheng CJ. Subdivision surfaces—Boundary element accelerated by fast multipole for the structural acoustic problem. *J Theor Comput Acoust* (2020) 28:2050011–1. doi:10.1142/S2591728520500115
25. Xu Y, Li H, Chen L, Zhao J, Zhang X. Monte Carlo based isogeometric stochastic finite element method for uncertainty quantization in vibration analysis of piezoelectric materials. *Mathematics* (2022) 10:1840. doi:10.3390/math10111840
26. Chen L, Cheng R, Li S, Lian H, Zheng C, Bordas SP. A sample-efficient deep learning method for multivariate uncertainty qualification of acoustic-vibration interaction problems. *Comput Methods Appl Mech Eng* (2022) 393:114784. doi:10.1016/j.cma.2022.114784
27. Chen L, Liu C, Zhao W, Liu L. An isogeometric approach of two dimensional acoustic design sensitivity analysis and topology optimization analysis for absorbing material distribution. *Comput Methods Appl Mech Eng* (2018) 336:507–32. doi:10.1016/j.cma.2018.03.025
28. Chen L, Marburg S, Zhao W, Liu C, Chen H. Implementation of isogeometric fast multipole boundary element methods for 2d half-space acoustic scattering problems with absorbing boundary condition. *J Theor Comput Acoust* (2018) 27:1850024. doi:10.1142/S259172851850024X
29. Chen L, Lian H, Liu Z, Chen H, Atroshchenko E, Bordas S. Structural shape optimization of three dimensional acoustic problems with isogeometric boundary element methods. *Comput Methods Appl Mech Eng* (2019) 355:926–51. doi:10.1016/j.cma.2019.06.012
30. Wiener N. The homogeneous chaos. *Am J Maths* (1938) 60:897. doi:10.2307/2371268
31. Kim T, Han WS, Piao J, Kang PK, Shin J. Predicting remediation efficiency of Inapls using surrogate polynomial chaos expansion model and global sensitivity analysis. *Adv Water Resour* (2022) 163:104179. doi:10.1016/j.advwatres.2022.104179
32. Xiu D, Karniadakis GE. A new stochastic approach to transient heat conduction modeling with uncertainty. *Int J Heat Mass Transfer* (2003) 46:4681–93. doi:10.1016/s0017-9310(03)00299-0
33. Nath K, Dutta A, Hazra B. Iterative polynomial dimensional decomposition approach towards solution of structural mechanics problems with material randomness. *Probabilistic Eng Mech* (2021) 66:103159. doi:10.1016/j.proengmech.2021.103159
34. Ghanem R. Ingredients for a general purpose stochastic finite elements implementation. *Comput Methods Appl Mech Eng* (1999) 168:19–34. doi:10.1016/s0045-7825(98)00106-6
35. Nabil EM, Seaid M. Data-driven polynomial chaos expansions for characterization of complex fluid rheology: Case study of phosphate slurry. *Reliability Eng Syst Saf* (2021) 216:107923. doi:10.1016/j.res.2021.107923
36. Trinh VH, Li D, He M, Li X. Modeling sound absorption of graded foam absorbers via polynomial surrogate technique. *J Theor Comput Acoust* (2022) 30:2150027. doi:10.1142/S2591728521500274
37. Mocayd NE, Mohamed MS, Seaid M. Non-intrusive polynomial chaos methods for uncertainty quantification in wave problems at high frequencies. *J Comput Sci* (2021) 53:101344. doi:10.1016/j.jocs.2021.101344
38. Stievano IS, Manfredi P, Canavero FG. Carbon nanotube interconnects: Process variation via polynomial chaos. *IEEE Trans Electromagn Compatibility* (2012) 54:140–8. doi:10.1109/temc.2011.2171490
39. Li H, Zhao J, Guo X, Cheng Y, Xu Y, Yuan X. Sensitivity analysis of flexoelectric materials surrogate model based on the isogeometric finite element method. *Front Phys* (2022) 10. 1111159. doi:10.3389/fphy.2022.1111159
40. Xiu D, Karniadakis GE. The wiener–askey polynomial chaos for stochastic differential equations. *SIAM J Scientific Comput* (2002) 24:619–44. doi:10.1137/s1064827501387826

Appendix A. Analytical solution

In this section, we consider the PEC and DIE infinite cylinder impinged by electromagnetic plane waves with different polarization directions. The analytical solution of the scattering electric field is described in detail. The scattered electric field under TE-polarized incident waves can be expressed as

$$E_{sca}^z(\rho, \theta_{sca}) = \sum_{n=0}^{\infty} i^n c_n A_n H_n^{(2)}(k_0 \rho) \cos(n\theta_{sca}), \quad (37)$$

where $|E_{sca}^z| = 1$ for convenience, θ_{sca} is the bistatic scattering angle, and $c_n = 1$ for $n = 0$ and $c_n = 2$, otherwise. For the conducting cylinder, the coefficient A_n^{PEC} is

$$A_n^{PEC} = -\frac{J_n(k_0 r)}{H_n^{(2)}(k_0 r)}. \quad (38)$$

For a dielectric cylinder, the series coefficients A_n^{DIE} are

$$A_n^{DIE} = -\frac{(k_1/\mu^1)J_n(k_0 r)J'_n(k_1 r) - (k_0/\mu^0)J'_n(k_0 r)J'_n(k_1 r)}{(k_1/\mu^1)H_n^{(2)}(k_0 r)J'_n(k_1 r) - (k_0/\mu^0)H_n^{(2)}(k_0 r)J'_n(k_1 r)}, \quad (39)$$

where r is the radius of the cylinder. The scattered far electric field is

$$E_{sca}^z(\rho, \theta_{sca}) = \sqrt{\frac{2}{\pi}} \frac{e^{-i(k_0 \rho - \pi/4)}}{\sqrt{k_0 \rho}} \sum_{n=0}^{\infty} (-1)^n c_n A_n \cos n\theta_{sca}. \quad (40)$$

The aforementioned expression is the analytical solution of the scattered electric field under TE polarization, and the expressions of the scattered magnetic field under TM polarization are as follows.

$$H_{sca}^z(\rho, \theta_{sca}) = \frac{1}{\eta_0} \sum_{n=0}^{\infty} i^n c_n B_n H_n^{(2)}(k_0 \rho) \cos(n\theta_{sca}), \quad (41)$$

where H_{sca}^z means the scattered magnetic field with a z-directed incident magnetic field. $|E_{inc}| = 1$ for convenience. For the conducting cylinder, the coefficients B_n^{PEC} are

$$B_n^{PEC} = -\frac{J'_n(k_0 r)}{H_n^{(2)}(k_0 r)}. \quad (42)$$

For the dielectric cylinder, the coefficients B_n^{DIE} for TM polarization are

$$B_n^{DIE} = -\frac{(k_1/\epsilon^1)J_n(k_0 r)J'_n(k_1 r) - (k_0/\epsilon^0)J'_n(k_0 r)J'_n(k_1 r)}{(k_1/\epsilon^1)H_n^{(2)}(k_0 r)J'_n(k_1 r) - (k_0/\epsilon^0)H_n^{(2)}(k_0 r)J'_n(k_1 r)}. \quad (43)$$

The scattered far magnetic field is

$$H_{sca}^z(\rho, \theta_{sca}) = \frac{1}{\eta_0} \sqrt{\frac{2}{\pi}} \frac{e^{-i(k_0 \rho - \pi/4)}}{\sqrt{k_0 \rho}} \sum_{n=0}^{\infty} (-1)^n c_n B_n \cos n\theta_{sca}. \quad (44)$$

Frontiers in Physics

Investigates complex questions in physics to understand the nature of the physical world

Addresses the biggest questions in physics, from macro to micro, and from theoretical to experimental and applied physics.

Discover the latest Research Topics

[See more →](#)

Frontiers

Avenue du Tribunal-Fédéral 34
1005 Lausanne, Switzerland
frontiersin.org

Contact us

+41 (0)21 510 17 00
frontiersin.org/about/contact

